Synthesis and Characterisation of Nanomaterials Produced Using Laboratory and Pilot Scale Continuous Hydrothermal Flow Reactors

Robert I. J. Gruar

A thesis submitted to University College London for the degree of Doctor of Philosophy

Supervised by Professor J. A. Darr

2012

Department of Chemistry,
University College London,
20 Gordon Street,
London, WC1H OAJ

Abstract

Due to their small particle size, nanoparticles (< 100 nm in diameter) have an increased surface area to volume ratio compared to larger particles, meaning that surface attributes become increasingly important over bulk properties. Chemically, this means more atoms in the material have unsatisfied coordination environments compared to atoms in the bulk of the particle. In many cases, this leads to materials with significantly different bulk properties compared to much larger particles; some of these unique properties are desirable in high technology applications such as sun screens, catalysts, etc.

This thesis explores the use of Continuous Hydrothermal Flow Synthesis (CHFS) reactors as a niche technology to controllably produce nanoparticles at different process scales. In CHFS, a metal ion feed is mixed with superheated water (the latter is typically above the critical temperature and pressure of water, *i.e.* 374 °C, 22.1 MPa), and nanoparticles are precipitated. This thesis presents data relevant to an evaluation of a laboratory scale CHFS process (able to produce *ca.* 100 g a day of nanoparticles). This included the development of a new type of mixer for this type of process suitable for the continuous precipitation of nanoparticles. The knowledge gained from *in situ* measurements and particle property measurements was then applied to the successful scale up of the technology to produce up to *ca.* 2 kg per hour of nanoparticles. It was demonstrated that the versatility of a flow process and the rapid crystallising environment in a CHFS system could be effectively exploited for the production of target nanoparticles when appropriate synthesis conditions were used. This thesis has also demonstrated the versatility of CHFS in that as formed particles could be surface functionalised in flow by use of an additional feed in process. The outcomes of this thesis have been demonstrated using a variety of material compositions; Hydroxyapatite, ZnO, iron oxides, yttrium oxyhydroxide, yttrium oxide and the binary oxide series Ce-Zn. Where each material composition was used to probe different aspect of the continuous hydrothermal process reported in this work.

In summary, the CHFS process has been evaluated and developed to allow for synthesis of a wide range of nanoparticle compositions with different particle properties. Process modifications have been evaluated and shown to be suitable for the synthesis of target materials.

I certify that the research in this thesis is the product of my own work and that any words and figures from the work of other people are fully acknowledged according to standard referencing.

Robert Gruar

Acknowledgements

During the completion of work for this thesis many people have helped to foster ideas and generated ideas on which I have acted. The following paragraphs are dedicated to people who have given significant amounts of time in guiding me towards completion of this thesis.

First of all, I will thank my supervisor, Professor Jawwad Darr for his support and guidance throughout. He has been exceptionally welcoming to some of my process ideas a few of which are included in the body of this thesis.

I would like to thank Dr Christopher Tighe a person whom I have spent a great deal of time with over the last 3 years, mostly with spanners at hand in the construction of the pilot scale CHFS process. I would also like to acknowledge the members and ex-members of the clean materials technology group (CMTG) all of whom have contributed to a nice working environment.

For technical help at UCL I would like to thank, Dr Steve Firth, Professor Quentin Pankhurst, Dr, Paul Southern, Dr Josie Goodall, Dr Christopher Tighe, Dr Sam Alexander amongst others.

I would like to thank the EPSRC for funding as the completion of this work would not be possible without their support.

On the personal side, I would like to thank my parents and family for their support, my girlfriend Laurie for putting up with me, and all my housemates and friends for doing the same.

Table of Contents

List of Figures

Chapter 3

Chapter 4

Chapter 5

Chapter 6

Chapter 8

List of Tables

Chapter 6

Chapter 7

Chapter 8

List of Symbols

List of Symbols:

Nomenclature:

A_o	Outside surface area of inner pipe (m^2)
Fr	Froude number (dimensionless)
G	Mass flowrate (kg s^{-1})
h	Specific enthalpy (kJ kg^{-1})
Q	Volumetric flowrate (ml min^{-1})
ΔQ	Rate of heat transfer (W)
Re	Reynolds number (dimensionless)
Gr	Grashof number (dimensionless)
C_{tn}	Thring Newby Parameter (dimensionless)
T	Temperature (°C)
T'	Temperature calculated by heat balance (°C)
ΔT_{lm}	Log-mean temperature difference (K)
U_o	Overall heat transfer coefficient based on A_o (W m^{-2} K^{-1})
z	Distance from outlet of superheated water (mm)
z/d_i	Normalised position of thermocouple (for comparison of mixers)

Greek symbols:

μ	Viscosity (Pa s)
θ	Temperature difference (K)
ρ	Density (kg m^{-3})

Subscripts:

sw	Superheated water
in	Inlet to mixer
mix	Mixture of superheated water and ‘precursors’

out	Outlet of mixer
p	Precursor
q	Quench

Magnetic properties:

M_s	Saturation magnetisation (emu g^{-1})
μ	Ferromagnetic diameter (nm)
χ	Paramagnetic susceptibility (dimesionless)
σ	Ferromagnetic diameter distribution (nm)

Spectroscopy:

Δ	Wavenumber separation (cm^{-1})
λ	Wavelength (nm)

List of Abbreviations

Abbreviation	**Meaning**
BET	Brunauer-Emmitt-Teller (theory)
BPR	Back Pressure Regulator
CFD	Computational Fluid Dynamics
CHFS	Continuous Hydrothermal Flow Synthesis
CA	Citric Acid
Cit	Citrate anion
CJM	Confined Jet Mixer
COS7	Cos 7 cell line
DLS	Dynamic light scattering
DNA	Deoxyribonucleic Acid
DSC	Differential Scanning Calorimetry
EDX/EDS	Energy Dispersive Spectroscopy
HPLC	High Pressure Liquid Chromatography
Fe:CA	Ratio of iron to citric acid
FTIR	Fourier Transform Infra Red Spectroscopy
HA	Hydroxyapatite
HREM	High Resolution Electron Microscopy
HRTEM	High Resolution Transmission Electron Microscopy
JCPDS	Joint Committee on Powder Diffraction Standards
ICDS	International Crystallography Association Structural Database
IAPWS	International Association for the Properties of Water and Steam
LSW	Lifshitz, Slyozov, Wagner (theory)
NOx	Nitrogen oxides
NH_2-PEG	NH_2 mono end functionalised PEG
NPs	Nanoparticles
pH	Power of Hydrogen
PL	Potoluminescence
PpRV	Proportional Pressure Relief Valve
PSD	Particle Size Distribution

QMUL	Queen Mary, University of London
QD	Quantum Dot
UCL	University College London
RT1	Residence Time 1
RT2	Residence Time 2
SA	Surface Area
SCF	Supercritical Fluid
SCW	Supercritical Water
SD	Standard Deviation
SEM	Scanning Electron Microscope/Microscopy
SS	Stainless Steel
STA	Simultaneous Thermal Analysis
SQUID	Vibrating Sample Magnetometry
TEM	Transmission Electron Microscopy/Microscope
T_{mix}	Theoretical Mixture Temperature
T_{mix1}	Theoretical Mixture Temperature 1
T_{mix2}	Theroretical Mixture Temperature 2
TGA	Thermogravimetric Analysis
TRPL	Time Resolved Photoluminesence
UV-VIS	Ultra Violet-Visible Spectroscopy
XPS	X-ray Photoelectron Spectroscopy
XRD	X-Ray Diffraction

Chapter 1

Literature Review of Methods for Nanoparticle Synthesis and Processing

1.1 Introduction to Nanoparticles:

Materials with a least one dimension less than 100 nm (100 x 10^{-9} m) are collectively known as nanomaterials. The term “nanomaterial” can be used to describe materials with almost any elemental composition of almost any architecture; ribbons, wires, rods etc. It is only recently that an understanding of the science and properties of nanomaterials has developed, alongside many analytical methods to study the properties and physical characteristics of these materials. In 1963, Richard Feynman, gave his famous lecture at the Institute of technology in California where he stated "there is plenty of room at the bottom”. (Feynman & Vernon, 1963) Since then, nanotechnology and investigations into the properties of nanosized materials has seen rapid progression culminating in the increasing use of nanosized materials in high technology applications ranging from; high-density data storage in computers, UV attenuators, probes for biochemical processes, drug delivery and catalysts. (Lester *et al.*, 2006) The scope of application and the demand for nanoscale metals and metal oxides has greatly expanded in the last 10 years, and significant research effort is focused on developing processes for the large scale synthesis of nanomaterials.

One aspect of nanotechnology is focused on inorganic and ceramic materials, as both building blocks and useful standalone materials. These are reviewed in greater detail, as this is the field of nanomaterials referred to throughout this thesis. The very small size of inorganic nanomaterials means that they have a very high surface area, and most of the atoms are at the surface, leading to unique surface effects in many nanomaterials. This means surface properties dominate over those of the bulk, and the properties exhibited by nanomaterials can be very different from that of the bulk material. A good example is that of inert materials such as gold which become catalytically active as their dimensions approach the nanoscale. (Kamat, 2002) A significant portion of the research into nanotechnology has focused on the production of inorganic materials on a nanometric scale, either as potential building blocks for nanoscale devices or for their useful or interesting properties as nanomaterials. A vast number of material compositions have been produced and evaluated as nanoparticles. (Byrappa & Adschiri, 2007) The numerous application areas of nanoparticles are summarised in figure 1.1, demonstrating how widespread investigation into the application of nanomaterials has become. (Tsuzuki, 2009)

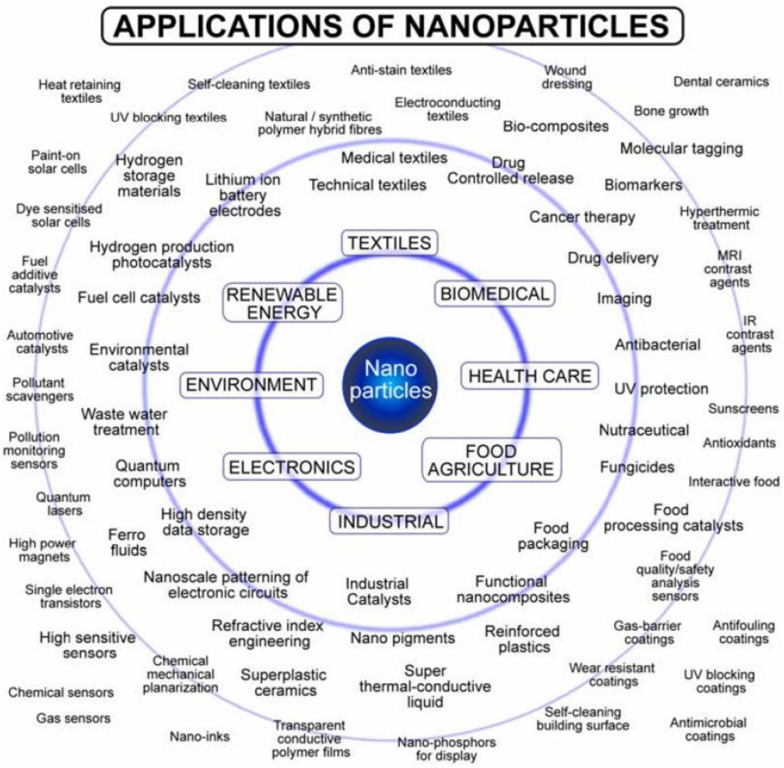

Figure 1.1: Web diagram of nanoparticle application areas. (Tsuzuki, 2009)

1.2 Properties and Applications of Inorganic Nanomaterials:

Quantum confinement and the dominance of surface properties mean that nanomaterials can have unique optical, mechanical, electrical and magnetic properties. (Alivisatos, 1996) Many of the unique physical properties of nanomaterials can be exploited in a variety of applications. For example, materials that are not magnetic in the bulk form can become magnetic as their dimensions approach the nanoscale (*e.g.* NiO). (Kodama, 1999) Equally materials such as titania and zinc oxide, which scatter visible light when micrometre sized can become transparent when nanosized. (Wang *et al.*, 2003) Nanoparticles can also exhibit effects not seen at all in larger particles, such as quantum confinement effects, which only arise through the reduction in the bulk of the material and limits the number of possible energy states within the materials structure. The reduction in possible energy states means that the particle behaves somewhat like an atom. This is important in materials known as quantum dots (QDs) and quantum wires (Qw) which have become technologically important. A slightly more detailed examination of quantum effects in semiconductor quantum dots is presented here to serve as a description of some of the physical characteristics resulting in unique properties of nanomaterials. QDs are semiconductor nanocrystals composed of atoms from groups II–VI or III–V of the periodic table and their composition can be varied to tune a material to a given application. QDs are generally defined as particles having physical dimensions smaller than the exciton Bohr radius of the material, which is composition dependent (typically 1–5 nm). (Parak *et al.*, 2003) Due to this small size of only a few nanometres, which is of the same order of magnitude as the de -Broglie wavelength of electrons and holes at room temperature, the states of the free charge carriers in QDs are quantized and the movement of these carriers is entirely determined by quantum mechanics. Conceptually, this quantum confinement effect can be described as the fate of a photon as it is absorbed by a semiconductor. Where, static electrons from the valence band become mobile and are excited into the conduction band within the semiconductor matrix. As the electron becomes mobile it leaves behind a hole. After a certain period of time (usually in nano seconds), the electrons and holes recombine. As such, the small size of these QDs leads to a quantum confinement effect where an energy loss, at recombination of the electron and hole, results in the emission of a down converted photon. This energy loss, endows the nanocrystals with unique optical and electronic properties as summarised by figure 1.2.

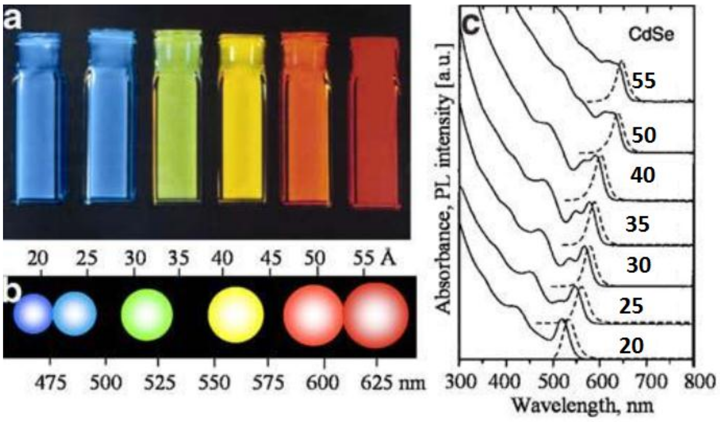

Figure 1.2: Optical properties of CdSe-ZnS quantum dots of different particles sizes **a)** Size-dependent photoluminescence emission wavelengths **b)** schematic presentation of size, colour, and photoluminescence emission wavelengths of CdSe–ZnS quantum dots of different sizes **c)** Absorption (solid lines) and emission spectra (broken lines) of CdSe QDs with various size. (Parak *et al.*, 2003)

1.3 Strategies for Inorganic Nanoparticle Manufacture:

The unique properties of nanoparticles have led to significant interest in exploiting many of their properties. As such, many methods have been developed to produce target materials. There are two general methods for production of nanoparticles called "top down" and "bottom up", respectively. "Top down" refers to methods which involve taking a bulk material, and making it smaller, by grinding or milling. "Bottom up" refers to methods in which nanoparticle form as a result of a chemical reaction which form nanoparticles from a molecular or atomic level precursors. The bottom up and are typically divided into two major classifications, as reactions conducted in the gas and liquid phases, respectively. These methods are shown schematically in figure 1.3.

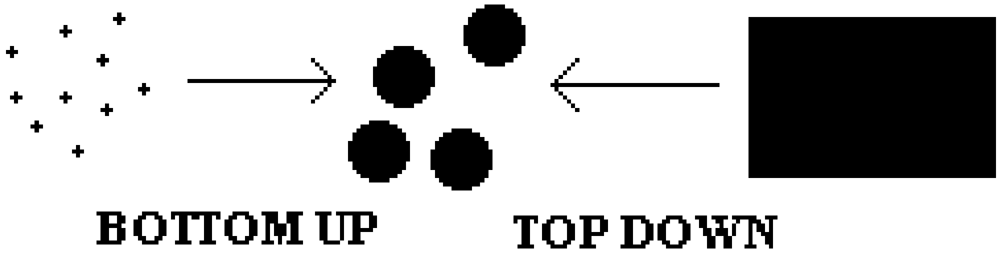

Figure 1.3: Schematic comparing "bottom up" and "top down" schemes for nanoparticle production.

1.3.1 Top down Strategies:

Top down methods have been used to produce nanomaterials of many compositions (magnetic, catalytic and structural). (Yoshimura *et al.*, 2000) Where, examples of top down strategies include ball milling (many embodiments), lithography (adding functional elements to a substrate) and etching (adding functional structures). (Malow & Koch, 1998) Although, lithography and etching are becoming exceptionally versatile techniques for the addition of nano and micron sized structures to substrates, they are seldom used for the production of nanoparticles as such only a detailed review of ball milling is presented here.

Top down methods such as ball milling are often seen as a poor methods for the production of nanomaterials due to problems with contamination from the milling media. Ball milling as a process, tends to produce partially amorphous particles with a low surface area and a high particle size polydispersity, these characteristics have limited application industrially as many of the unique properties of nanomaterials identified to date rely on homogeneity of the nanoparticles and are often determined by material size. The method is also energy inefficient for the production of nanoparticles as milling times in excess of days are sometimes required to produce a sufficient yield of "nanoparticles". (Zhang, 2004) Ideally nanoparticles formation methods should be reproducible, with batch-batch homogeneity being a key issue. Top-down methods are not favoured for the synthesis of many nano-materials as the structural defects and polydispersity of the products limits application where certain size dependent or structural properties are to be exploited. (Souza *et al.*, 2001) Although technologically simple, ball-milling and related top-down strategies provide limited control of particle properties when compared to other bottom up methodologies. (Souza, Aranda, & Schmal, 2001, Zhang, 2004) As such, the bottom up methods are reviewed in greater detail in the following sections.

1.3.2 Bottom-up Synthesis of Nanoparticles

The aim of this section is to provide a brief and succinct description of methods used for the manufacture of nanoparticles. However, first it is important to review the mechanism of nanoparticle formation and the theories associated with nanoparticle nucleation and growth.

1.3.2.1 Mechanisms of Nanoparticle Formation (bottom up):

The synthesis and formation of any nanoparticle from solution or reactive gasses involves four main stages which are divided and defined as follows; nucleation, growth, coarsening and termination (shown schematically in figure 1.4). Where, nucleation is the initial formation of solid from liquid or gas. Growth is the addition of atoms from the solution or carrier to the nuclei. Larger particles begin to grow using material from smaller particles rather than the solution which is commonly referred to as coarsening or ripening. Termination is the end of the reaction where no more growth occurs and can be influenced by many chemical events. Many methods for the production of bottom up synthesis of nanomaterials (solution or gas phase) allow for the control of one or many of these steps through different mechanisms. (Sun & Zeng, 2002)

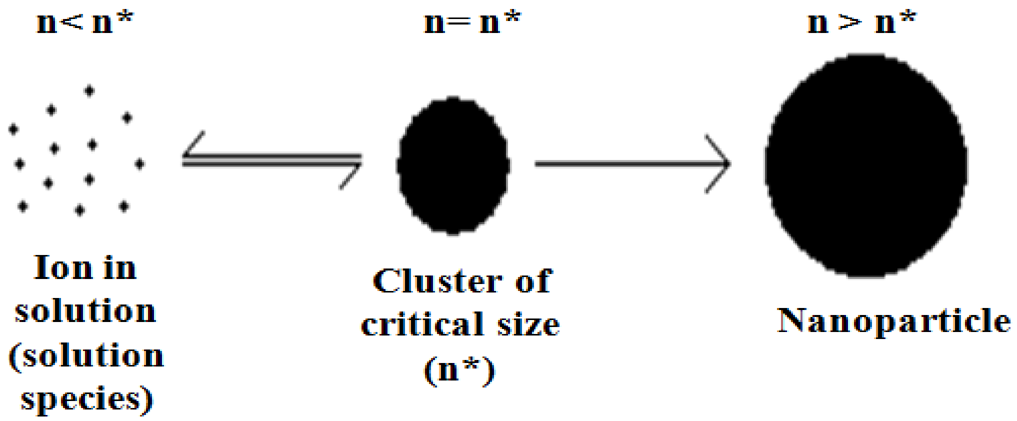

Figure 1.4: Schematic showing the nucleation of a nanoparticle from solution including formation of a cluster of critical size (n*) which is in equilibrium with ions in solution but can grow irreversibly into a stable particle under appropriate chemical conditions.

Particle nucleation begins with the formation of a cluster of molecules of a critical size (n*) this cluster is formed through a chemical reaction and in some cases this reaction is reversible (figure 1.4), the driving force for the formation of a cluster is dependent on the method chosen for the synthesis of nanoparticles. Initiation of cluster formation for example can be heating a solution containing precursors (initiating decomposition reactions) or a change in the chemical environment (*i.e.* the addition of reducing agents) a good example of the latter is the Brust-Schiffrin method, where sodium borohydride is used to reduce a solution of $HAuCl_4$ in a single phase reaction leading to rapid cluster formation and minimal growth through reduction of the Au salt forming insoluble Au^0 and the nucleation of Au clusters from solution. (Brust *et al.*, 1994) The driving force for nucleation in this context arises from a difference in chemical potential of a molecule in a cluster (μ_c) compared to the chemical potential of the species in solution (μ_g). Thermodynamically, this is the driving force ($\Delta\mu$) for the nucleation of a nanoparticle (equation 1.1) as defined by Kashchiev & van Rosmalen. (Kashchiev, 1982, Kashchiev & van Rosmalen, 2003)

$$\Delta\mu = \mu_g - \mu_c \quad \textbf{(Equation 1.1)}$$

The driving force for cluster formation can also be written as equation 1.2, k is the Boltzmann constant, T is the absolute temperature and S is the supersaturation (equivalent to $\Delta\mu$ in equation 1.1). Supersaturation in this context is a non-equilibrium state, and provides a driving force for nucleation (*i.e.* cluster formation) and can be induced by many methods which are detailed later in this review. Often, if the cluster is of the critical nucleus (n*) or above the cluster is stable and will grow, and conversely if the extent of supersaturation is not sufficient to produce stable cluster dissolution is likely to occur, this occurs if the chemical force driving the potential is removed (figure 1.4). (Kashchiev & van Rosmalen, 2003) Supersaturation of a system is defined in equation 1.3, where there are ‘i’ types of ions in solution (i = 1, 2, 3…j) with n_i ions in a cluster. The actual and equilibrium activities are “a” and “a_e” respectively. Equation 1.2 and 1.3 show that if the product of the actual concentration is greater than the product equilibrium concentration then S is greater than 1. Therefore, lnS is greater than zero and the driving force ($\Delta\mu$) is greater than zero and the nucleation of particles is favoured. This suggests that nucleation will occur in a supersaturated solution and can be potentially controlled either by chemical reaction or by the change in state of the salvation of ions. Change in free energy in the nucleation of an ion depends on the energy gained in creating a cluster ($-n\Delta\mu$) and the excess energy of the cluster ($\varphi(n)$) as described by equation 1.4. The work (W) in forming a critical cluster is defined in Equation 1.5, and $\varphi(n^*)$ is the excess energy of the critical cluster. (Ho *et al.*, 2007)

$$\Delta\mu = kT\ln S \qquad (\textbf{Equation 1.2})$$

$$S = {a_1}^{n_1}{a_2}^{n_2}\ldots{a_j}^{n_j} \Big/ {a_{1e}}^{n_1}{a_{2e}}^{n_2}\ldots{a_{je}}^{n_j} \qquad (\textbf{Equation 1.3})$$

$$W(n) = -n\,\Delta\mu + \varphi(n) \qquad (\textbf{Equation 1.4})$$

$$W(n^*) = -n^*\,\Delta\mu + \varphi(n^*) \qquad (\textbf{Equation 1.5})$$

Although conceptually simple, the term $\varphi(n)$ is hard to define experimentally and it is often regarded as method dependent, alongside synthesis condition dependent. Consequently, to the experimentalist the quantification of particle nucleation and critical cluster formation is only evaluated experimentally in terms of the effect of different synthesis condition on particle size inferring a difference in the nucleation and growth phases of the particles.

The definition of the term φ(n) is further complicated by the fact it depends on the type of nucleation (heterogeneous or homogeneous), the morphology and structure of the cluster, the interface between the cluster and the ions involved. Thus, in theoretical work these terms are often estimated. For example, the interface energy is often approximated to that of a 1d material (*i.e.* single atomic plane) although this only holds true for sufficiently large clusters to be relevant for a typical nanoparticle synthesis. (Wang & Yang, 2005)To overcome the problem of the interface energy, nucleation theory was developed and is described in equation 1.6; (Kashchiev & van Rosmalen, 2003)

$$\frac{dW^*}{d\Delta\mu} = -n^* \qquad \textbf{(Equation 1.6)}$$

Where, dW* is the work involved in the formation of a cluster, -n* is the work required to form a cluster and dΔμ is the change in the driving force required to form a cluster. In general, this relationship holds true for most nucleation models and is referred to in the experimental observations of many publications relating to the synthesis of size controlled nanomaterials in the liquid and gas phase. (Lester *et al.*, 2006) Nucleation theory (equation 1.6) can be related to the extent of supersaturation in a given system by substitution into equation 1.2 leading to equation 1.7.

$$\frac{dW^*}{d\ln S} = -n^* kT \qquad \textbf{(Equation 1.7)}$$

In many cases, nucleation is evaluated as the ideal case where a spherical cluster which shows isotrophic surface tension and interface energy with a radius (r) in solution which is nucleating (*i.e.* supersaturated). In this case the critical cluster size n* corresponds to a critical cluster r*, the free ions in solution γ_{SL} and the change in Gibbs free energy (ΔG_v) as described by equation 1.8. This equation is governed by two dominant terms, the first term on the right of equation 1.8 is the energy gained to create the volume of solid in the solution and is equivalent to the term (-nΔμ) defined in equation 1.5, the second term is the excess energy due to the creation of an interface and equivalent to φ(n) defined in Equation 1.5. (Porter & Easterling, 1992**)**

$$\Delta G(r) = -\frac{4}{3}\pi r^3 \Delta G_V + 4\pi r^2 \gamma_{SL} \qquad \textbf{(Equation 1.8)}$$

The critical cluster size can be calculated for a given synthesis condition by differentiation of Equation 1.8. This equation is strictly only valid for spherical nucleation but it shows the balance between volume and interface creation effects. Figure 1.5 shows graphically the formation of a critical cluster under this approximation of homogenous and spherical nucleation. (Kashchiev & van Rosmalen, 2003) However, in the case of isotropic heterogeneous nucleation there is a shape factor, which will reduce the optimum energy needed because the volume is no longer a full sphere so the contribution from interface effects is greater (it does not account for crystal facet polarity), but this will not affect the determination of n*.

Critical issues in the synthesis of nanoparticles include control of size, composition, interfaces and size distributions, later in this chapter these issues are reviewed in relation to individual synthetic methodologies. However, in any method intended for the production of nanoparticles it is important to have control over nucleation and growth and forms a justification why certain methods are preferred for the synthesis of nanomaterials. (Yoshimura, Suchanek, & Byrappa, 2000) In a chemical reaction, the extent of nanoparticle growth is often constrained by the exhaustion of reactants, or when the system reaches a state of equilibrium (*i.e.* the free energy gained in forming the particle from the solution is insufficient and often occurs as the concentration of a reactant is reduced). For the formation of particles, the equivalent physical parameter is supersaturation, *i.e.* the nucleation and growth processes will stop when the level of supersaturation reaches zero this is particularly relevant to nanoparticle synthesis methods which use vanishingly short reaction times to constrain the growth of nanoparticles. The extent of supersaturation is not necessarily determined by the concentration of a reactant, so precipitation can be affected by changing reaction conditions such as temperature, pressure or solvent composition. (Byrappa & Adschiri, 2007) Also, since “bottom-up” formation of particles often involves an *in situ* chemical reaction to produce the feedstock for the precipitation, it is possible that the production of particles can be halted by stopping the chemical reaction (*i.e* in a high temperature process this is conveniently achieved by quenching the reaction through a reduction in temperature). (Sun & Zeng, 2002)

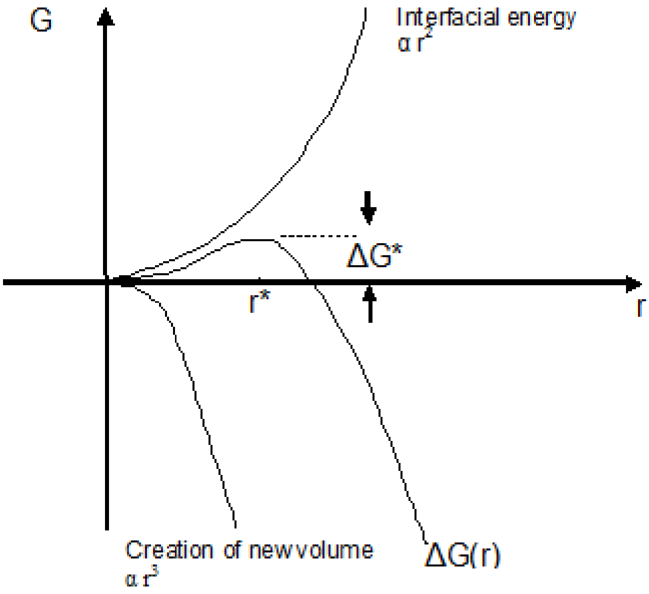

Figure 1.5: The balance of interfacial energy and energy for creation of a volume of solid in nucleation theory leading to a critical nucleus size r* or n* and the change in free energy derived from this process. (Porter and Easterling, 1992)

The control of nanoparticle size and size distribution is further complicated by processes in which particles grow by a mechanism of coarsening in which discrete nanoparticles crystallize together an event commonly referred to as Ostwolds ripening. The predominant theory describing Ostwald ripening is known as LSW theory, after Lifshitz and Slyozov and Wagner. (Lifshitz, 1956, Lifshitz & Slyozov, 1961, Wagner, 1961) The mathematics of this theory are complex, model based and beyond the scope of this review, but a number of the findings of the theory can be conveniently simplified. For example, the average particle diameter is proportional to the cube root of time, and the number of particles is inversely proportional to time. (Lifshitz & Slyozov, 1961) This simplification allows the mechanism of growth to be determined in a particular synthesis and allows a system to be defined as nucleation or growth/coarsening dominated. (Cushing *et al.*, 2004)

Similarly, loss of control of particle morphology and size can also be further complicated by agglomeration where particles can continue to agglomerate even when there is no supersaturation. (Lifshitz, 1956) Agglomeration of nanoparticles is primarily due to the high surface energy (attributed to partially coordinated surface atoms) of nanoparticles driving their tendency to form agglomerates. (Dzyaloshinskii *et al.*, 1961) Upon contact the primary particles of an agglomerate form bonds which can be of different nature and depend heavily on the method of particle preparation. In this embodiment, under severe processing conditions particle agglomeration can lead to the formation of solid state necks. Alternatively, Chemical bonds between the particle surfaces may also form and magnetic dipole forces can potentially contribute to the inter-particle forces leading to agglomeration. The strength of these inter-particle bonds determines to a large part their physical properties and applicability of many materials in a given application. To combat agglomeration and coarsening, nanoparticle production methods often use capping agents which bind to the surface of nascent nanoparticles increasing the energy barrier and preventing agglomeration. (Pankhurst *et al.*, 2009) Capping agents may also serve to direct the growth of nanoparticles along surface facets or as a method to control the growth of a particle by excluding the surface. These molecules can be coordinating surfactants, polymers or other organic molecules. In general they work by binding to the outside of the particle and preventing further particle growth by steric hindrance or serve as a charged species in solution providing an electrostatic mechanism to the prevention of agglomeration and are reviewed later. (Thanh & Green, 2010)

1.3.3 Gas Phase Synthesis of Nanomaterials:

Gas phase syntheses, usually involve nucleation of particles from gasses containing precursors in a vapourised or atomic form, particle formation is often initiated by combustion. The gas phase methods allow synthesis of nanomaterials at high production capacities (some are operated commercially). (Tsuzuki, 2009) The advantages of nanomaterials synthesis using gas phase reactions can be summarised as follows; particle formation is generally rapid, the products are largely of high compositional purity, product collection and consolidation is simple and there is no contaminated effluent. One drawback of gas phase synthesis is that nanoparticles are not contained as they are produced which increases the extent of engineering measured required to isolate workers from nanoparticles, in light of the largely unknown health effects of many nanomaterials (reviewed later). (Teow *et al.,* 2011) This review is limited to the operation of gas phase methods for the production of metal oxide nanoparticles and only a brief summary of the methods used for metal oxide particles are presented. Chemical Vapour Deposition (CVD), Flame reactions, spray pyrolysis and plasma syntheses are all examples of gas phase processes used for the production of nanomaterials and each of the aforementioned methods have their own caveats which are briefly described below:

- CVD deposits nanomaterials onto a substrate either as a nanostructured film or as nanoparticles imbedded in a substrate grown from the gas phase, reactant streams “precursor” and “O_2” are segregated until over the substrate. (Mills *et al.*, 2002) This technique has been to produce a variety of nanoparticles including; TiO_2, Al_2O_3, Cu_2O, ZnO, Carbon nanotubes and a variety of transition metal oxides. (Kafizas & Parkin, 2010) This technique is limited by the availability of suitable volatile precursor materials (organometallic complexes) and choice is further limited as materials with low melting points or high boiling points and nanomaterials are exclusively produced on a substrate. (Palgrave & Parkin, 2006)
- Flame based methodologies result in particle formation from the combustion and oxidation of an organometallic precursor. Flame based processes are typically continuous and a degree of control over particle properties such as shape and morphology is afforded by control of flame temperature, residence time, additives and precursor concentration. (Pratsinis & Vemury, 1996) Although, sintering of nanoparticles produced in high temperature synthesis causes significant issues with particle consistency and morphology. (Rosner, 2005, Vemury *et al.*, 1994)
- In Spray pyrolysis soluble precursors are first atomized (often into a mist) and delivered to a reaction furnace using a carrier gas. (Eroglu *et al.*, 1996) Particles form as the solvent evaporates leading to the formation of a precipitate within the droplet. Thereafter, the particles are calcined at high temperature to complete the reaction and form crystalline nanoparticles, porous networks or dense ceramic materials. (Messing *et al.*, 1993)
- In plasma based syntheses a reactant is vaporized in a plasma (using solid or solution based precursors). Unlike the other gas phase processes nanoparticle formation nanoparticles are not formed in plasma based syntheses until the precursors quenched at the end of the plasma. Only after quenching the precursor materials nucleate and grow in the gas phase. (Vissokov *et al.*, 1988) The particle formation processes can be controlled to some degree by the plasma temperature and reaction quench rate. However, intimate control over reaction variables is not practicable as particle formation occurs in the transition from plasma to near ambient temperature. (Pratsinis & Vemury, 1996)

The gas phase methods offer relatively simple processes for the production of nanoparticles and nanomaterials. In many ways the liquid phase synthesis methods for the synthesis of nanoparticles are favored and are now reviewed.

1.3.4 Liquid Phase Methods:

Liquid phase routes for the synthesis of nanoparticles include precipitation, chemical reaction, sol-gel methods, emulsion synthesis and hydrothermal routes. (Masala & Seshadri, 2004) There are many different liquid phase techniques which can produce nanoparticles, usually involving synthesis of insoluble products from soluble reactants. This section describes some of the liquid phase methods for the production of metal oxide nanoparticles.

1.3.4.1 Precipitation of Nanoparticles from Aqueous Solutions:

One of the most common methods for the preparation of nanoparticles are the aqueous precipitation routes. Aqueous precipitation has many embodiments and can be conveniently divided as follow **1)** Direct precipitation of the desired material from the aqueous phase (with or without a capping agent being present) **2)** precipitation of metal ions in a desired composition ratio (often as hydroxides) which are used as precursor nanomaterials for further processing *via* calcination. (Cushing, Kolesnichenko, & O'Connor, 2004)

Direct precipitation is a method favored for the synthesis of homometallic oxides (such as ZnO, TiO_2, Fe_2O_3 and Fe_3O_4). For example, Fe_3O_4 can be produced directly from the precipitation of Fe^{2+} and Fe^{3+} from soluble salts (Iron chlorides) by the addition of NH_4OH or NaOH at a temperature of *ca.* 70 °C under an inert atmosphere. (Kuo & Tsai, 1989) Direct precipitation is difficult to control and suffers from large batch to batch variation in relation to particle size and composition. (Darr & Poliakoff, 1999) The direct co-precipitation method is typically limited in relation to mixtures of metal ions as different ions show different solubilities and often precipitate separately leading to composition in-homogeneity resulting in further commination strategies being employed to produce a desired material (hetrometallic systems). (Gu *et al.*, 2000) Typical co-precipitation reactions are often time consuming 2h – 6 days and require stringent control over reaction conditions to produce a desired material. (Jang *et al.*, 1998) The long reaction times have lead to the development of “assisted” coprecipitation reactions. In “assisted” reactions a further chemical or physical process is used to drive the precipitation reaction. For example, the application of ultrasound to a coprecipitation mixture results in the formation of hot-spots through ultrasonic cavitation leading to localised heating which increases the rate of the coprecipitation reaction. (Hoffmann *et al.*, 1996) Similarly, microwave assisted co-precipitaion is also a method commonly employed for the synthesis of nanoparticles although the mechanism of heating is different from the former, similar results have been demonstrated. (Yoshimura, Suchanek, & Byrappa, 2000)

1.3.4.2 Sol-Gel Processing:

The sol-gel method is based on the hydrolysis and condensation of an organic-metal precursor sol. This process involves the dissolution of a metal precursor in a solvent, a gelation phase in which a matrix material is added, an ageing phase in which gelation and cross linking occurs to from the sol-gel matrix, a drying step to remove the solvent and a heating step to dehydrate the metal complex to form a oxide (simultaneously pyrolysing the matrix material). Many nanomaterials have been produced using sol-gel methodologies and is far too complex a field of literature to review here, as sol gel methods have been extensively modified for the production of desired nanomaterials. Further information on sol-gel processing is available in several notable review articles published by Yoshimura and Cushings amongst others. (Casas *et al.*, 2002, Corrias *et al.*, 2003, Cushing, Kolesnichenko, & O'Connor, 2004, Si *et al.*, 2004, Yoshimura, Suchanek, & Byrappa, 2000) However, certain sol-gel methods such as the pechini method are almost exclusively applied to the synthesis of nanomaterials and as such a slightly more detailed review of this process is presented here.

The Pechini method is a widely adopted alteration of the core sol-gel method outlined above. The Pechini method does not rely on a hydrolysis equilibrium to form the gel matrix. In a typical synthesis, a complex mixture of precursor materials (metal-citrate complexes), citric acid (or another complexing agent) and a polyalcohol such as ethylene glycol are used for the formation of a gel phase from solution as shown in figure 1.6. (Lessing, 1989) In this process the polyalcohol serves as a linker to from a gel from the metal-citrate complex through poly-esterification. The reaction to form metal oxides is completed by calcination which also serves to remove the organic templating phase. Many materials have been produced by the Pechini method and are reviewed in detail by

Yoshimura. (Yoshimura, Suchanek, & Byrappa, 2000) The Pechini method confers several advantages for the synthesis of nanomaterials including; the use of simple metal complexes, the reaction is not as sensitive to pH as co-precipitation or conventional sol-gel methods and higher order phases (hetrometallic oxides) can be produced. However, little control over particle properties such as size distribution and morphology can be achieved and is essentially a batch process for nanomaterial production. The requirement for calcination results in the unavoidable formation of particle agglomerates. (Cushing, Kolesnichenko, & O'Connor, 2004)

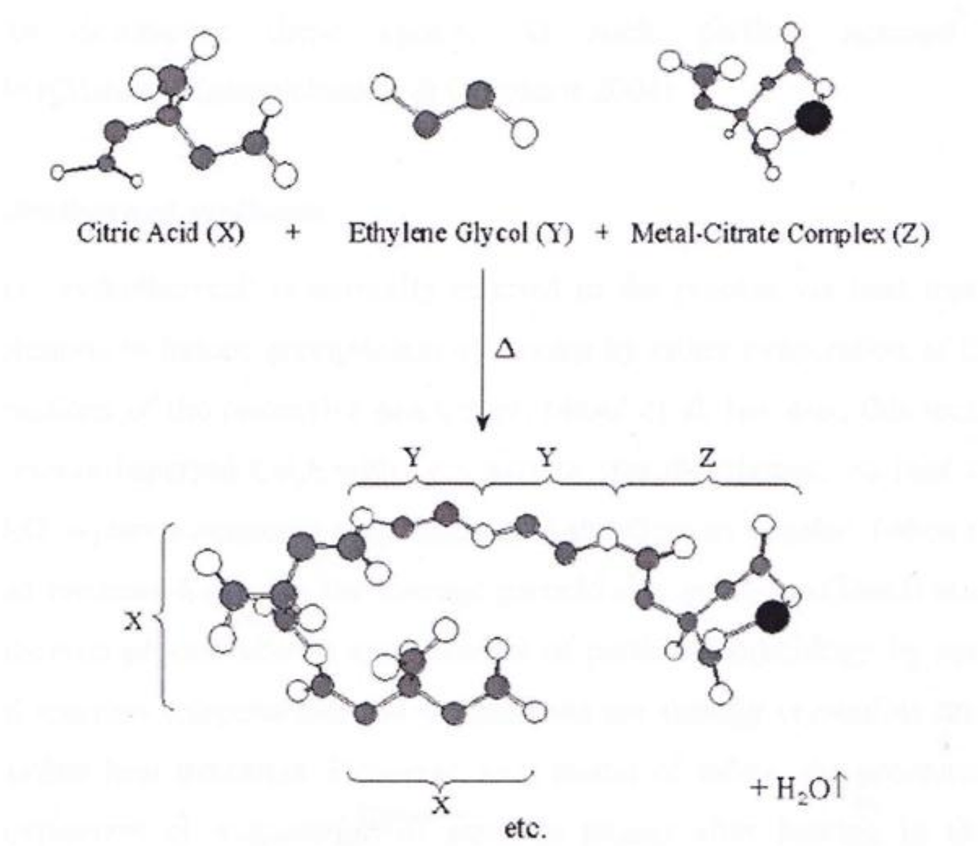

Figure 1.6: Schematic representation of the poly-esterification of a metal-cation, citric acid and polyol forming the basis of the Pechini method. (Lessing, 1989)

As the near ambient solution phase methods often form precursor materials which require calcination to either form or crystallise a desired reaction product, agglomeration and particle growth are unavoidable which in some cases can introduce material properties which are not desirable in many applications. Solution phase processes which allow for the introduction of capping agents after the formation of nanoparticles often mitigate many of the effects of particle coarsening and growth observed in near ambient temperature processes and these are reviewed next.

1.3.5 Methods for the Production of Surface Functionalised Nanoparticles:

As the application of many nanoparticles is dependent upon the particle being dispersed in an appropriate medium, capping agents are commonly employed to prevent agglomeration of nanoparticles and to some extent allow control of particle growth and formation from solution. (Lu *et al.*, 2007) Capping agents which confer stability to a dispersion of nanoparticles in an appropriate solvent, can be used to either electrostatically stabilise nanoparticles (charge based mechanism) or confer a steric mechanism (physical separation) to stability. (Thanh & Green, 2010) For example, the deprotination of a free carboxylic acid group conjugated to the surface of a nanoparticle resulting in a negative surface charge this charge results in hydration (aqueous dispersion) of the particle surface leading to the formation of an energy barrier to particle agglomeration. Conversely, the steric mechanism exploits the bulk of the capping agent (high molecular weight aliphatic compounds) to provide physical separation of the surface of nanoparticles preventing interparticle interaction / agglomeration. (Lu, Salabas, & Schueth, 2007) Metal oxide and nanoparticles of other compositions often have high surface energy where agglomeration occurs to minimise free surface energy, as such both steric and electrostatic mechanisms are effective to prevent agglomeration of nanoparticles. (Ho, Huang, & Carter, 2007) However, as the stabilisation mechanism is highly solvent dependent, methods which produce surface functionalised dispersion of metal oxide nanoparticles in various media are required. (Pankhurst, Thanh, Jones, & Dobson, 2009)

The ligand molecules bound to the nanoparticle surface not only control the growth of the particles during synthesis, but also prevent aggregation of the nanoparticles. The repulsive force between particles can in principle be due to electrostatic repulsion, steric exclusion, a hydration layer on the surface (*i.e.* in the case of a hydrophilic shell such as SiO_2) or combinations of the aforementioned mechanisms. (Parak, Gerion, Pellegrino, Zanchet, Micheel, Williams, Boudreau, Le Gros, Larabell, & Alivisatos, 2003) Many capping agents have been employed to stabilise nanoparticles and a summary of the chemical groups commonly used to coordinate ligands to a nanoparticle surface are presented in figure 1.7. (Lu, Salabas, & Schueth, 2007, Masala & Seshadri, 2004) Depending on the particle system, *i.e.* the core material, and the solvent in which the particles are to be dispersed, the choice of an appropriate capping agents showing a suitable chemical moiety should confer stability to a particle dispersion. (Hirai *et al.*, 1992) Typically, the capping agents have to be bound to the particle surface by some attractive interaction, either chemisorption, electrostatic attraction or hydrophobic interaction, most commonly provided by a head group of the ligand molecule (figure 1.7). Various chemical functional groups possess affinity to inorganic surfaces, the most famous example being a thiol to gold, many functional groups are reported to bind to inorganic surfaces. (Brust, Walker, Bethell, Schiffrin, & Whyman, 1994) In many cases, this principle is already exploited during synthesis and a number of methodologies have been developed to allow for the direct synthesis of surface functionalised nanoparticles. (Lu, Salabas, & Schueth, 2007)

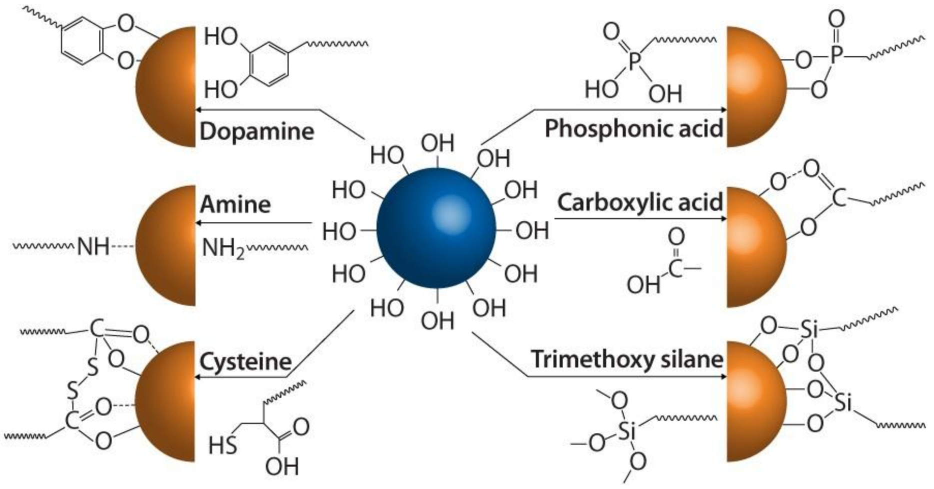

Figure 1.7: Common capping agents used for the surface functionalisation of metal oxide nanoparticles. (Lu, Salabas, & Schueth, 2007)

1.3.5.1 Thermal Decomposition:

The thermal decomposition methods are principally inspired by the synthesis of high-quality semiconductor nanocrystals (QDs) and has been applied to the synthesis of many nanoparticles, allowing control over particle size and morphology. (Hyeon *et al.*, 2001, Masala & Seshadri, 2004) Many, monodisperse nanomaterials with can essentially be synthesized through the thermal decomposition of organometallic compounds (*e.g.* metal acetylacetonates amoungst others, [M(acac)n], M = Fe, Mn, Co, Ni, Cr; n = 2 or 3, acac = acetylacetonate) in high-boiling organic solvents containing capping agents (fatty acids, oleic acid, and hexadecylamine as an ancillary reagent). (Hyeon, Lee, Park, Chung, & Bin Na, 2001, Sun *et al.*, 2000, Sun *et al.*, 2004, Sun & Zeng, 2002) The purpose of the capping agent can be either as a method of controlling particle growth or as an agent to template the preferential growth of a material along a preferential crystal facet. (Thanh & Green, 2010) As with many “assisted” synthesis methodologies thermal decomposition reactions involving the application of heat in conjunction with ultrasound allow further chemistries to become accessible to this methodology. In principle, the ratios of the starting reagents including organometallic compounds, surfactant, and solvent are the decisive parameters for the control of the size and morphology of many of the nanoparticles synthesised using this methodology. (Masala & Seshadri, 2004) Intrinsic parameters such as reaction time, reaction time (aging) or heating rate (pseudo-decomposition rate) can also influence particle properties. (Hyeon, Lee, Park, Chung, & Bin Na, 2001) The production of either oxide or metallic nanoparticles can be controlled by the valence of the metal ion in the organometallic precursor(s). (Sun, Murray, Weller, Folks, & Moser, 2000) If the metal in the precursor is zerovalent, such as in carbonyls, thermal decomposition initially leads to formation of the metal, but two-step procedures can be used to produce oxide nanoparticles *e.g.* iron pentacarbonyl can be decomposed in a mixture of octyl ether and oleic acid at 100 °C, subsequent addition of trimethylamine oxide $(CH_3)_3NO$ as a mild oxidant at elevated temperature *ca.* 180 , results in formation of monodisperse Fe_2O_3 nanoparticles. Whereas, decomposition of precursors with cationic metals leads directly to the oxides, Fe_3O_4, is formed as the reaction product if $[Fe(acac)_3]$ is decomposed in the presence of 1,2- hexadecanediol, oleylamine, and oleic acid in phenol ether. (Burda *et al.*, 2005) The thermal decomposition methods confer several advantages for the synthesis of nanomaterials including; the product is obtained from the reaction directly, the reactions are relatively rapid and the experimental apparatus is relatively simple. However, many of the organometallic precursors used are toxic and reactions require very careful control of reaction conditions to yield a desired material and the process is inherently a batch processing method.

1.3.5.2 Microemulsion Methods:

A microemulsion is a thermodynamically stable isotropic dispersion of two immiscible liquids, where the micro-domain of either or both liquids is stabilised by an interfacial film of surfactant molecules and a number of material composition have been produced using this methodology. (Fletcher *et al.*, 1987) Water-in-oil microemulsions, are the most commonly used media for the synthesis of nanoparticles, the aqueous phase is dispersed as micro-droplets (typically 1– 50 nm in diameter) surrounded by a monolayer of surfactant molecules in the continuous hydrocarbon phase and vice versa, defining micelle and reverse micelle routes, respectively (shown schematically in figure 1.8). (Zarur & Ying, 2000) The size of the reverse micelle is determined by the molar ratio of water to surfactant and provides a method to constrain particle growth as the precursors are confined within a single phase (the surfactant can also serve as a capping agent in this context or a separate capping agent can be added). (Bandow *et al.*, 1987) Primarily, the size of each micelle is determined by the behaviour of the surfactant at a given concentration as long as the surfactant is at a concentration greater than the CMC (Critical Micelle Concentration). (Fletcher, Howe, & Robinson, 1987) In this sense, a microemulsion can be used as a vehicle for the formation of nanoparticles. The microemulsion methods are typically limited in the materials that can be produced by the low temperatures of reaction. (Zarur & Ying, 2000) Where, not all material types can be precipitated directly or are precipitated as amorphous materials. In this embodiment post processing results in the agglomeration of nanoparticles limiting further application. Where, metal oxides, metal carbonates, metal sulphides and other non-metal nanoparticles can be synthesised inside reverse micelles by hydrolysis and precipitation procedures outlined above. (Bandow, Kimura, Konno, & Kitahara, 1987) For example, the formation of maghemite nanoparticles was demonstrated by Santra *et al*. In the reported reaction $FeCl_3.6H_2O$ was initially hydrolysed in a aqueous phase and subsequently formulated into a reverse micelle through the addition of dibenzylether using oleic acid as a surfactant or silanes. (Santra *et al.*, 2001) Iron hydroxide formation was initiated and promoted by propylene oxide (proton scavenger) which was dissolved in the oil phase. The final material phase was produced by refluxing of the obtained hydroxide in tetralin solvent at above 200 °C for 2 h. (Santra *et al.*, 2001)

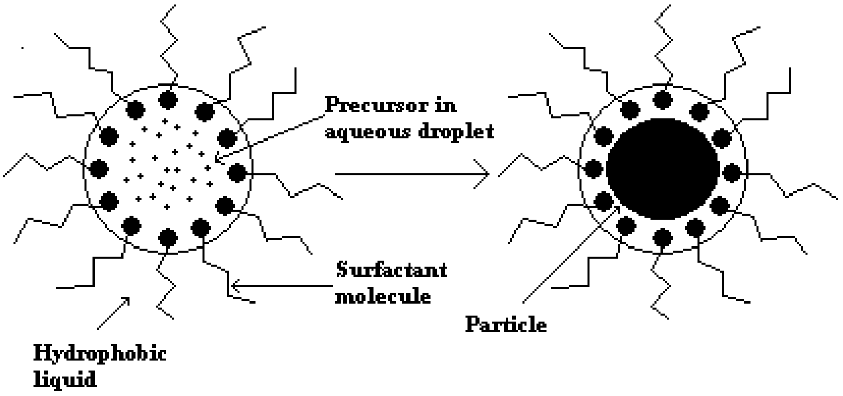

Figure 1.8: Diagram showing an idealised reverse micelle emulsion synthesis reaction. (Fletcher, Howe, & Robinson, 1987)

1.3.5.3 Polyol Synthesis Methods:

The Polyol processes encompass a large variety of solution compositions. In a typical polyol processes, secondary alcohols are used as high boiling point solvents. Examples of polyols used for the synthesis of nanoparticles include; 1,2-propanediol, 1,2-docecanediol, 1,2-hexanedecanediol, 1,2-octanediol *etc*. (Sun *et al.*, 2004) In all cases the polyol chosen for the reaction serves two purposes; **1)** to act as the solvent and **2)** to act as a mild reducing agent. (Mizuno *et al.*, 2005) Particles are formed by conventional nucleation processes as the decomposition of precursor materials (typically acetylacetonates although other metal sources can also be used), occuring at the relatively high reaction temperatures (*ca.* 300 °C). (Mizuno *et al,.* 2005) Nanoparticles of many different materials can be readily produced through the judicious control of reaction conditions (*i.e.* reducing, oxidising or inert). The decomposition approach of metal source is readily extended to the preparation of metal oxides and hetrometallic oxides, they are obtained by the thermal decomposition of metal complex. For example, the synthesis of magnetite nanoparticles was reported by Robinson et al. (Robinson *et al.*, 2009) In this report iron(III) acetylacetonate, 1,2-hexadecanediol, oleic acid, oleyl amine were dissolved in dioctyl ether and heated to reflux for 30 minutes to allow the formation of magnetite nanoparticles where magnetite was surface functionalised by oleic acid. In a similar reaction, Hyeon *et al.* presented the synthesis of various MFe_2O_4 nanoparticles which were produced, by altering the metal salt stoichiometry in the starting solution (Where , M = Zn, Cu, Ni, Co, Mn, Cr, V, Ti, Mg, or Ba). (Hyeon *et al.*, 2001) The polyol methods also allow for the relatively simple synthesis of surface functionalised nanoparticles, although intimate control over the reaction conditions is required to control variation.(Sun & Xia, 2002) As with the thermal decomposition methods the particles produced are highly dependent upon many intrinsic reaction conditions which are often difficult to independently control. Inherently, polyol methods are batch processes which also suffer batch to batch variation limiting the wide spread application of the technique.

1.3.5.4 Modification of surface chemistry:

Alongside all the direct surface functionalisation methods reviewed above there are several strategies for transferring stable dispersions of nanoparticles produced in any media to a desired suspending medium. As it is often more convenient to produce a nanomaterial in a given solution phase with intended application in another. (Lu, Salabas, & Schueth, 2007, Masala & Seshadri, 2004) Phase transfer takes nanoparticles dispersed in a given solvent A to a different, non-miscible solvent B, either from non-polar organic solvents to the aqueous phase or vice versa, and is commonly achieved by alteration of the chemical species present at the surface of a nanoparticle (either coupling a new chemical moiety to the particle surface through ligand exchange, amidation coupling (EDC), Click chemistry or another chemical strategy. (Hirai, Aizawa, & Shiozaki, 1992, Thanh & Green, 2010) In the ligand exchange strategy, the molecules stabilising the particles in one phase are replaced by other capping agents that allow the transfer to the second phase and provide dispersion stability. (Zhang *et al.*, 2007) Ligand exchange occurs successfully if the incoming ligand has a higher affinity towards the surface of the nanoparticles and displaces the former ligand. Le-chatelliers principle can also be exploited in this context to drive displacement of a high affinity ligand by a lower affinity ligand by using the lower affinity ligand in large excess. (Thanh & Green, 2010) An alternative approach to phase transfer is ligand modification through either covalently coupling a ligand to a free chemical moiety present on the capping agent used to initially stabilise the particle (e.g. EDC (amidation coupling), Click Chemistry, *etc.*). Using coupling based strategies allows the ligand molecule to be modified relatively simply with many examples of modified surface groups being presented in the literature. (Lu, Salabas, & Schueth, 2007) For example, Hydrophilic nanoparticles electrostatically stabilised by a mercaptocarboxylic acid can be modified by a hydrophobic molecule that is chemically bound to its carboxylic terminal groups (*e.g.* dicyclohexylamine to mercaptoacetic acid), or the addition of amphiphilic/ bulky hydrophilic coating layer can also be used to confer a steric mechanism to particle stability which is desirable in many biological applications of nanoparticles. (McMahon & Emory, 2007) Coupling strategies are not limited to simple organic molecules and many proteins or enzymes are readily conjugated to the surface of nanoparticles using appropriate coupling methodologies. Nanoparticles of different core materials can also be modified with a silica shell, which can be considered as an inorganic polymer and can be readily condensed onto the surface of electrostaically stabilised nanoparticles. The method of silination can also take the form of a first ligand exchange procedure in which a layer of silanes is bound to the nanoparticle surface displacing the capping agent used during synthesis. Then, using this first layer, a polymeric, cross-linked inorganic silica shell is deposited on the particles which can be further derivatised to allow further application. (Wooding *et al.*, 1991) This section severs to demonstrate the diversity of chemistries explored to produce nanoparticles suitable for an intended application and how common syntheses are built upon to expand the application of nanoparticles obtained from a single synthesis strategy.

As reviewed both liquid phase and gas phase syntheses have disadvantages for the production of nanoparticles. Typically, the application of any synthetic methodology requires thorough assessment prior to it being efficiently used for the synthesis of a desired material. However, both subcritical and supercritical fluids, which can be described as being intermediate between a gas and a liquid phase synthesis methods, are also attractive for the synthesis of nanomaterials and collectively these are known as hydrothermal processes. Hydrothermal methods either overcome or mitigate (to some degree) many of the disadvantages of conventional methods for the manufacture of nanoparticles. (Byrappa & Adschiri, 2007) Before, detailed review of processes which utilise hydrothermal fluids for the synthesis of nanoparticles it is important to highlight the unique properties of supercritical/hydrothermal fluids as a reaction medium for the synthesis of nanoparticles as this forms the body of the work presented in this thesis.

1.4: Properties of Sub and Supercritical Water:

Supercritical fluids (SCFs) are fluid phases that exists above a critical point defined by a critical temperature (T_c), and critical pressure (P_c). Many fluids have a supercritical point above which the properties of the fluid vary significantly from those observed at ambient temperatures and pressures. Figure 1.9 depicts the general physical state of a fluid transitioning through its critical point. A number of SFCs have been used for the synthesis of nanomaterials (ethanol, methanol, CO_2 and mixtures *i.e.* ethanol / water or methanol/water). (Byrappa *et al.*, 2008, Byrappa & Adschiri, 2007) SCFs have found application materials processing ranging from; chemical synthesis, polymerisation, film generation, nanoparticle generation, nanoencapsulation, mesoporous material generation to the impregnation or deposition of nanoparticles in porous materials. (Fukushima & Wakayama, 1999) Thorough reviews on the application of SCFs focusing on different classes of materials other than metal oxides (such as polymeric materials, pharmaceutics, and porous materials) are available in the literature and are beyond the scope of this review. (Byrappa, Ohara, & Adschiri, 2008, Yoshimura, Suchanek, & Byrappa, 2000)

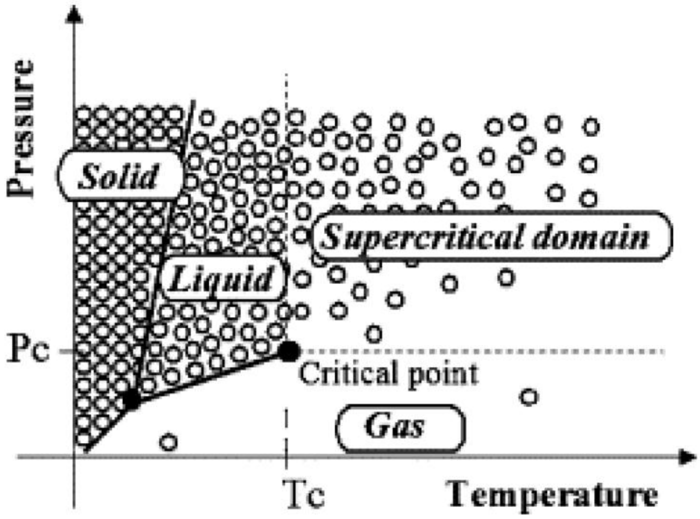

Figure 1.9: Pictographic representation of the phases of water at elevated temperatures and pressures.

Interest in SCFs as a medium for chemical reactions stems from primarily an ecological point of view, as reactions conducted in water are considered to be “green” reactions. Byrappa and Adschiri, identified SCF processes being environmentally benign when compared to many processing methods outlines previously (Section 1.3). (Byrappa & Adschiri, 2007) Above the critical point of pure water [274 °C, 22.1 MPa] the phase boundary between gas and liquid disappears (figure 1.9) and the resultant single phase displays properties which can be described as continuous phase showing intermediate properties of liquid water and a gas (steam). (Hoffmann & Conradi, 1997) The thermochemical and transport properties of water vary significantly around the critical point and many of these form the foundation of particle synthesis in SCFs.

Many of the unique properties of water approaching its critical point are associated with density changes. The density of water begins to change from a relatively low temperature, *e.g.* at 200 °C showing a density of 712 kg m^{-3} at the saturation curve, to the critical point (T_c=374 °C, P_c=22.1 MPa) where the density drops to 322 kg m^{-3}. (Weingartner & Franck, 2005) The fluctuation of density as a function of temperature for a series of isobaric pressures is presented in figure 1.10. The dielectric constant of water is another important parameter at elevated temperatures and pressures which dictates the solubility of solutes by describing the polarity of water. At ambient conditions in the liquid phase, water is a polar solvent, capable of dissolving ionic solids and mixing with other polar liquids. (Weingartner & Franck, 2005) The reduction in dielectric constant as water is heated towards its critical point is thought to be the dominant driving force controlling particle nucleation in hydrothermal systems. (Adschiri *et al.*, 2001) At ambient conditions water has a dielectric constant of around 80. Under the minimum pressure required to keep it as a liquid (*i.e.* on the saturation curve), the dielectric constant falls to a similar value as that of methanol at a temperature of 210°C with a dielectric constant of 33. At the critical point of water (374 °C, 22.1 MPa), its dielectric constant is around 5 similar to polar organic solvents such as ethyl acetate and THF and drives the precipitation of ionic solids. At 500 °C, water has a similar dielectric constant to non-polar solvents (*e.g.* hexane, with a dielectric constant of 1). This relationship between pressure, temperature and dielectric constant is shown graphically in figure 1.10b.(Fukushima & Wakayama, 1999) Figure 1.10b also represents two values for the dielectric constant below T_c and P_c and shows the liquid and gas phase transitions, respectively. Around the critical point the dielectric constant varies largely through only small changes in temperature. With, the largest changes occurring just above the critical temperature and pressure as shown in figure 1.10b. Hence, hydrothermal methods using both near and supercritical water are useful for the synthesis of nanoparticles as the properties of water lead to precipitation of ionic solids from solution and the high temperatures are generally sufficient to crystalise the precipitate.

Another interesting effect shown by water as it approaches its critical point is a large change in the ion product (*K),* the ratio of the concentrations of the dissociation products of water H^+ and OH^- as shown in equation 1.10.

$$K = [H^+][OH^-]$$ **(Equation 1.10)**

Water at ambient temperature and pressure has an ion product of *ca*. 10^{-14} mol^2 dm^{-6}. The corresponding pH of an aqueous solution is determined using equation 1.11. The pH of water at this condition is 7 due to the ion product as the concentration of [H^+] are equal *ca.* 10^{-7} mol^2 dm^{-6}.(Wagner & Pruss, 2002a) Similarly, the relationship between K and pressure and temperature are well characterised allowing the pH of SCFS to be determined.(Wagner & Pruss, 2002a) However, the presence of other dissociated species such as KOH, metal salts and organic species the determination of the ion product and thus accurate description of pH is complicated by interactions of the dissociated products with these and effective methods for determining reaction pH do not exist. (Hakuta *et al.*, 1999a) This is discussed in greater detail later where the importance of “pH” is highlighted in several materials syntheses (as discussed later).

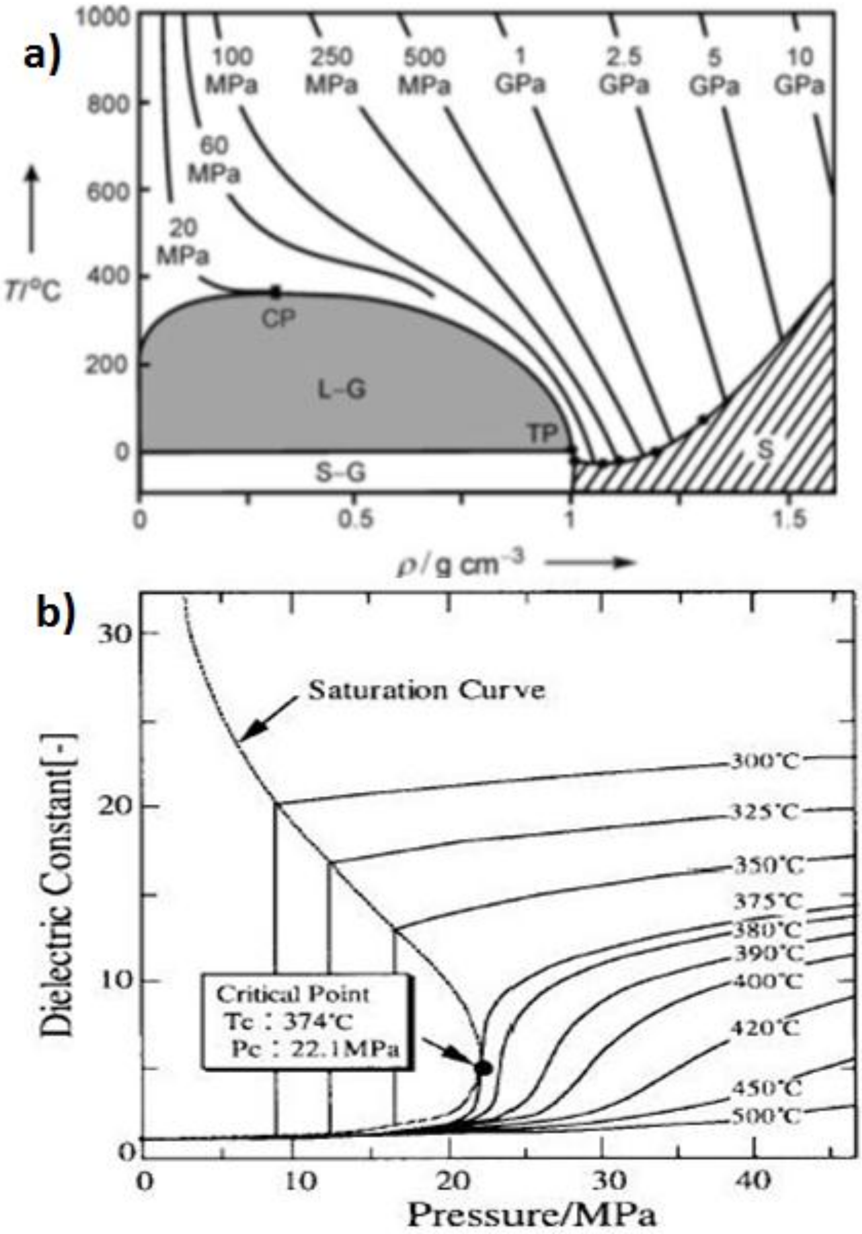

Figure 1.10: a) Plot of density (ρ) vs. temperature (T) for pure water at a variety of pressures (taken from Weingartner & Franck 2005) showing the phase boundaries of pure water **b)** Plot of dielectric constant *vs.* pressure for a given temperature. (Weingartner & Franck, 2005)

$$\mathrm{pH} = -\log_{10}[\mathrm{H}^+] \qquad \textbf{(Equation 1.11)}$$

The ion product of water is important in many materials synthesis applications, the ion product is known to vary non-linearly with temperature and pressure until at *ca.* 300 °C it reaches a maximum of 10^{-11} mol^2 dm^{-6}, which equates to an increase in concentration of around 30 times for both H^+ and OH^- ions from ambient temperature and pressure. (Wagner & Pruss, 2002a) Thus, near-critical water shows traits of both an acid and an alkali. However, above 300 °C the ion product varies greatly with temperature and pressure, with the effect the ion product can vary from 10^{-11} to 10^{-22} mol^2 dm^{-6} with water in a supercritical state, this variation is presented graphically in figure 1.11 (variation of log K with temperature for different isobaric pressure). (Fukushima & Wakayama, 1999) Demonstrating that large variation in the ion product are realised over narrow pressure and temperature range. Where, it is postulated that the structure around solutes determined by K controls the solubility and thus the precipitation of hydrated ions at near critical temperatures. (Hakuta, Adschiri, Hirakoso, & Arai, 1999a)

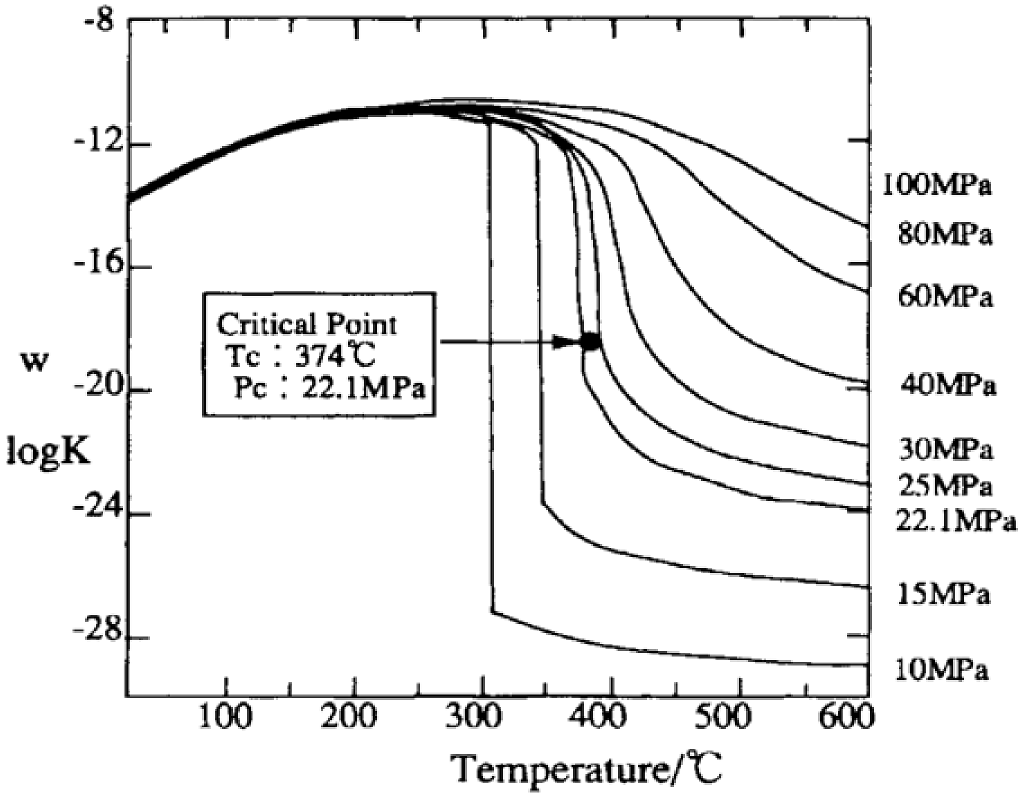

Figure 1.11: Variation in the ion product of pure water (logK) vs. temperature of water at a variety of pressures. (Fukushima & Wakayama, 1999)

Alongside the physiochemical characteristics of SCFS presented above the structure of water at elevated temperatures in the presence of solutes has been studied to shed light on some of the mechanisms responsible for the behavior of ionic solids in SCFs. Water at low temperatures has long been known to form short lived clusters held together with dative hydrogen bonds, and water molecules aggregate around ions where the charged particle forms a centre for coordination forming a hydration shell. Quantitative experimental studies of H-bonding in supercritical water by techniques such as neutron diffraction, Raman spectroscopy and NMR suggest that *ca.* 30% of the H-bonds are retained in supercritical water as compared to ambient water and hydration of ionic solids is reduced through the transition to a more gas like state. (Hoffmann & Conradi, 1997, Ikushima *et al.*, 1998a, Yamaguchi, 1998) These experimental studies indicate that the structure of water is composed of short-lived H-bonded clusters, with a medium-to-long range structure (*i.e.* extending beyond one hydration shell) being effectively disordered or gas-like in state. This structure is largely dependent on the density and is inherently a function of temperature and pressure. As such, the behavior of cationic and anionic species in both sub and supercritical environments has also been studied. (Ikushima *et al.*, 1998b) Regarding the changes to hydrated anions when in sub or supercritical water, the first coordination shells remain intact, while the hydration shells which extend further into the bulk solution *i.e.* second and further shells become largely disrupted initiating precipitation or hydrothermal reaction of the anion. (Balbuena *et al.*, 1996) Whereas, cations in ambient water are mainly around surrounded by water molecules and the presence of anions within the hydration shell is highly unlikely. However, approaching the critical point, cations become surrounded by anions (OH^- derived from the dissociation of water). For example, the Ni^{2+} ions in $NiBr_2$ solutions have *ca.* 6 water molecules and no anions at ambient conditions (in octahedral coordination) constituting the hydration shell, whereas, at near critical temperatures Ni^{2+} has 2 water molecules and two anions forming the hydration shell (with tetrahedral coordination) initiating precipitation on hydrolysis of $Ni(OH)_2$. (Hoffmann & Conradi, 1997) Similar results have been presented for Zn^{2+} ions, at ambient temperature Zn^{2+} is coordinated by 4 water molecules whereas at near critical conditions hydration is reduced and Zn^{2+} coordinates only 2. (Hoffmann & Conradi, 1997, Simonet *et al.*, 2002a, Simonet *et al.*, 2002b). The aformentioned, change seems to offer a straight forward explanation as to why hydrolysis reactions occurring between the metal and the oxygen on the water are favoured and as such precipitation of cationic metals in SCF occurs.

The key to the production of nanoparticles using both sub and supercritical processes is the maximisation of supersaturation, in this context achieved through temperature and pressure resulting in a decrease in the dielectric constant and the change in the structure of hydration leading to hydrolysis of cationic species in solution. (Byrappa & Adschiri, 2007) The increase in supersaturation leads to an increases the nucleation rate and many authors suggest that effective control of supersaturation could lead to controlled nucleation and control over particle properties in both hydrothermal and supercritical water based processes. (Cushing, Kolesnichenko, & O'Connor, 2004, Kashchiev & van Rosmalen, 2003) The low dielectric constant (controlling the solubility of solutes) and highly hydrolysing (high ion product) environment afforded by super-critical water means that many of the inorganic materials produced by hydrothermal methodologies from solutes result in the formation of nanoparticles as the reaction product. (Yoshimura, Suchanek, & Byrappa, 2000) A detailed review of the use of sub and supercritical fluids for the synthesis of nanoparticles in both batch and continuous systems are reviewed in the following section.

1.5 Hydrothermal Synthesis of Inorganic Nanoparticles:

The properties described in section 1.4, show that near-critical and supercritical water could be useful for a wide range of materials synthesis reactions. Hydrothermal methods can be conveniently divided into modes of operation *i.e.* batch wise and continuous syntheses. In this section a review of batch processes is presented first as many of the reactions undertaken in batch hydrothermal processes are readily recreated in continuous systems.

A number of researchers have investigated the formation of metal oxides from metal salts such as nitrates under hydrothermal conditions. (Darr & Poliakoff, 1999) Typically, the formation of a metal oxide from aqueous metal salts follows a two-step reaction mechanism, with hydrolysis (as a result of a chemical reaction (addition of KOH) or as a reaction occurring as a function of temperature), described by equation 1.12. Hydrolysis is rapidly followed by dehydration which is dictated by reaction temperature and described by equation 1.13. (Adschiri *et al.*, 2000, Darr & Poliakoff, 1999)

Hydrolysis: $M(NO_3)_{x\ (aq)} + xH_2O \rightarrow M(OH)_{x\ (s)} + xHNO_3$ **(Equation 1.12)**
Dehydration: $M(OH)_{x\ (s)} \rightarrow MO_{(x/2)\ (s)} + (x/2)H_2O$ **(Equation 1.13)**

Unlike reactions conducted in ambient or near ambient water, it is much easier to produce metal oxides and related nanomaterials under hydrothermal conditions, and a generic mechanism of reaction from aqueous metal salts results in the formation of metal hydroxides, oxy-hydroxides and oxides. (Yoshimura, Suchanek, & Byrappa, 2000) Typically, for a given synthesis condition the formation of either an oxide or hydroxide is governed by thermodynamics, in certain cases the comparatively low reaction temperatures cannot yield oxide phases directly. (Hakuta, Adschiri, Hirakoso, & Arai, 1999a) Simple metal oxides are straightforward to make by batch hydrothermal synthesis according to the mechanism described by equations 1.12 and 1.13. Nitrates of metals which have been reported to decompose to oxides in batch reactions include many of the transition metals, Fe (III), Co (II), Ni (II), Ti (IV), and Ce (IV) forming the corresponding oxides in many cases. (Byrappa & Adschiri, 2007) The synthesis of complex mixtures of metal oxides is also possible *via* batch hydrothermal methods. (Si *et al.,* 2004) Most species which can be produced separately as oxides by hydrothermal synthesis can also be synthesised as mixed oxides. Interest in doping host lattices stems from the structural changes enforced by the inclusion of a guest metal in a host lattice which has been shown to alter the physical properties of metal oxides for a wide range of applications especially in semiconductor nanomaterials. (Sorescu *et al.*, 2005) Lattice defects, such as oxygen vacancies, induced by doping have a major impact in the performance of these materials and often allow access to novel material properties. (Si *et al.*, 2004) As such, numerous examples of doped transition metal oxides are reported in the literature. In certain circumstances complete solid solutions can be produced using this methodology as reported by Zhang *et al.* where, $(ZrO_2)_{(1-x)}(Y_2O_3)_x$ solid solutions were prepared from $Zr(NO_3)_3$ and $Y(NO_3)_3$ with the addition of KOH at 180 °C for 12 hours. (Si *et al.*, 2004) However, under hydrothermal conditions not all metals can be precipitated directly as oxides, for example Wang *et al*., found that Gd, Na, Nd, Cs, Ba, La, Sm, Sr, Y, Eu, Cd or Ag could not be precipitated as oxides, although there could be a number of reasons for this, including that the oxides are soluble under the conditions used and many were obtained as hydroxides (stemming from the complexity in defining pH within the reaction as defined in section 1.4). (Wang *et al.*, 2002) Usually, these materials require additional heat treatment to turn them into their respective oxides. For example, Li *et al.* reported the dehydration of $Y(OH)_3$ produced by the hydrothermal treatment of $Y(NO_3)_3$ at 180 °C for 10 hours, by calcining at 700 °C for 2 hours to produce phase pure Y_2O_3. Similarly, Wang and Li synthesised 13 different rare earth hydroxides in a hydrothermal batch reactor at 180 °C without any evidence of oxidic phases in the samples even with reaction times of *ca.* 48 h. (Wang & Li, 2003) However, Meng *et al*. showed that they can be incorporated into host oxide lattices and produced sodium titanate by reacting NaOH with TiO_2 in a hydrothermal batch reactor at 180 °C for 12 days. (Meng *et al.*, 2004) Typically, batch hydrothermal processes produce nanoparticles at the limit of the definition. (Byrappa, Ohara, & Adschiri, 2008) The long reaction times required for the crystallization of materials result in significant particle growth and agglomeration. (Reverchon & Adami, 2006) Hence, there is significant interest in modifying the reaction durations allowing the synthesis of nanosized materials.

The synthesis of surface functionalised metal oxide nanoparticles has been reported in batch hydrothermal processes and in selected materials has been shown to effectively surface functionalise the materials. The hydrothermal approaches simply take advantage of the increased solubility and reactivity of metal salts and complexes at elevated temperatures and pressures without bringing the solvent to its critical point. (Adschiri *et al.*, 2011) Several studies conducted in batch hydrothermal processes discuss the synthesis of surface functionalised inorganic nanoparticles, such as TiO_2, ZnO, and $CoAl_2O_4$, under supercritical conditions primarily for application in MOFs (Metal organic frameworks) where carboxylic acids are used as the capping agent. (Adschiri & Byrappa, 2009, Arita *et al.*, 2010a, Arita *et al.*, 2010b, Sahraneshin *et al.*, 2012, Taguchi *et al.*, 2012, Togashi *et al.*, 2011) The capping agents used in these reports were long chain (C4-12) di-carboxylic acids, oleyl-amine and phosphonated acids (*e.g.* ethyl 11-diethoxyphosphorylundecanoate). The low dielectric constant of water at near-critical conditions realises high miscibility of the organic capping agents at synthesis temperature and has been put forward as the explanation of the capping results (figure 1.10a). (Adschiri & Byrappa, 2009) The authors reported transparent solutions were obtained for well-crystallized and nanoparticles when they are dispersed and a compilation of examples are presented in figure 1.12.

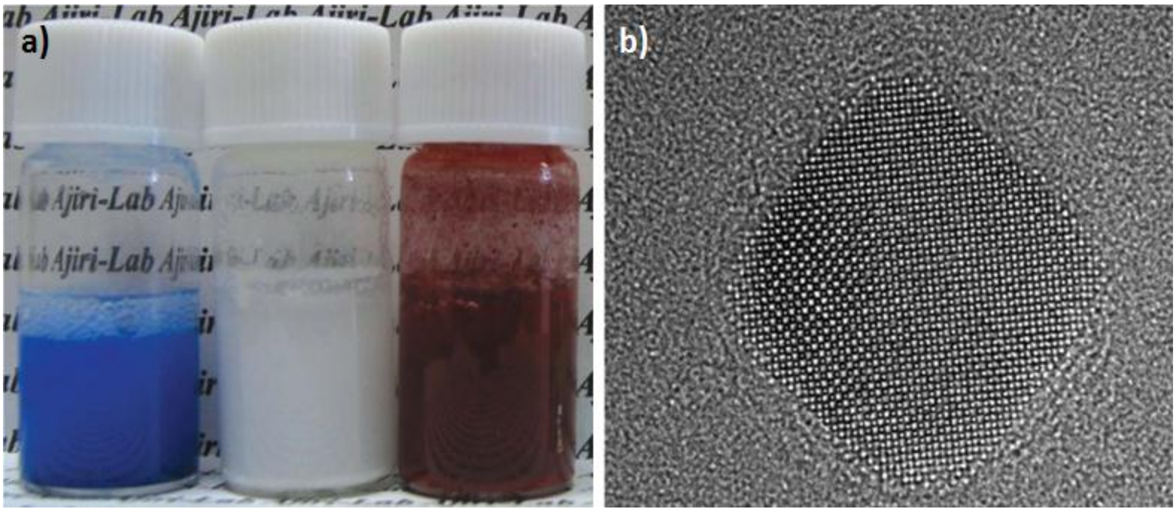

Figure 1.12: a) Images of nanoparticle dispersions in water: $CoAl_2O_4$ (blue), ZnO (white), Fe_2O_3 (brown) [image has been taken from (Sahraneshin *et al.,* 2012)]. **b)** HRTEM image of CeO_2 nanoparticles obtained by supercritical hydrothermal synthesis at 300°C and 30 MPa when dodecanoic acid is used as a capping agent(Image taken from (Taguchi *et al.*, 2011a).

Taguchi *et al.* and Arita *et al.,* whom studied the synthesis of surface-modified CeO_2 nanocrystals in the presence of dicarboxylic acids with various chain lengths in supercritical water, showed the crystal growth could be affected by the presence of the organic compound (figure 1.12 b). (Arita, Yoo, & Adschiri, 2010b, Taguchi *et al.*, 2011b) In particular, they investigated the relationship between the alkyl chain length of dicarboxylic acids and the morphologies of the CeO_2 nanocrystals produced using a batch supercritical water process where the morphology of the particles could be controlled by the choice of di-carboxylic acid, discussion by the authors suggested capping resulted in stabilisation of different crystal facets leading to morphology and crystallite size (capping agent preventing particle growth) differences.

The surface-modified nanoparticles produced by the detailed methods can be easily recovered when long chain carboxylic acids are used by extraction from the water suspension phase with an organic solvent which leads to ease in separation and purification processes or by another precipitation strategy if hydrophilic capping agents are chosen. (Arita, Yoo, & Adschiri, 2010b, Taguchi *et al.*, 2011b) However, the choice of capping agent is dominated by the chemical reactions of capping agent end groups, thermal decomposition or oxidation leading to a physical imitation in the choice of capping agent. For example, alkyl phosphates are easily hydrolyzed in supercritical water so that they cannot be effectively used. (Arita *et al.*, 2010a) Hydrothermal strategies for the synthesis of nanoparticles show several notable benefits as; the processes typically use water soluble metal precursors and water is used as the only solvent, the nanoparticles are produced in the aqueous phase and crystalline nanoparticles are the reaction product.

This section has shown the diverse chemistry that is available for particle formation and processing in both hydrothermal and supercritical fluids. The next section explains a continuous variant and its application to the synthesis of nanoparticles.

1.6: Continuous Hydrothermal Synthesis and Related Methods

Japanese researchers working in the Arai group at Tohoku University were the first to develop the continuous hydrothermal flow synthesis (CHFS) systems in the early 1990s. (Adschiri *et al.*, 1992a) Since then, a number of research groups have adopted and modified CHFS systems to expanded the range of materials that can be synthesised. (Cote *et al.*, 2003, Darab & Matson, 1998, Hao & Teja, 2003, Lin *et al.*, 2010, Matson *et al.*, 1992, Weng *et al.*, 2008) CHFS and related methods, have been shown to be capable of exploiting the diverse chemistry practicable in hydrothermal solutions, showing a notable benefit, in that they require significantly shorter synthesis times and are continuous processes almost exclusively producing nanoparticles as the reaction products. (Adschiri, Lee, Goto, & Takami, 2011) Many additions and iterative refinement of the CHFS processes have allow for the production of materials with increasing complexity in both morphology and composition. (Adschiri, Hakuta, Sue, & Arai, 2001) This section reviews the available literature on both the physical processes resulting in the formation of nanoparticles and the engineering solutions currently employed to control particle formation.

1.6.1 Description of the CHFS Process:

In 1992, Arai's group in Japan published the synthesis of a number of metal oxides in a continuous manner by mixing a flow of metal salt solution with a preheated supercritical water feed. (Adschiri, Kanazawa, & Arai, 1992a) Since then, a number of other groups have built hydrothermal flow reactors along similar lines, and due to the bespoke nature of many CHFS processes the design of each system varies by publication. Many of the reported CHFS systems are based on the same concept as that of the work of Adschiri. (Adschiri, Kanazawa, & Arai, 1992a) Figure 1.13 shows a simple scheme for a hydrothermal flow reactor initially used in the work of Arai's group. In this process DI water (resistivity >18 Mega Ohms) is pumped into the system at *ca.* 20 – 30 MPa, this feed is heated to the required temperature by the preheater (up to 500 ºC) and is pumped to the reaction point, it meets a metal salt solution at ambient temperature and process pressure. The mixed stream, a slurry containing nanoparticles (formed through the hydrolysis and dehydration of the metal salt) is then cooled down to ambient temperature (*ca.* 20-50 °C), larger particles are filtered out and the slurry then flows through the back pressure regulator so the nanoparticles can be collected at ambient pressure. This reactor design has mainly been used for homometallic oxides and the oxide precipitates from solution without additional reagents *i.e.* base, but can also be used for heterometallic oxides where the metals are soluble in the same precursor solution. (Adschiri *et al.*, 1992b, Cabanas *et al.*, 2000) This process description provides sufficient detail relevant to all reported CHFS processes and forms the basis of their operation in many laboratories.

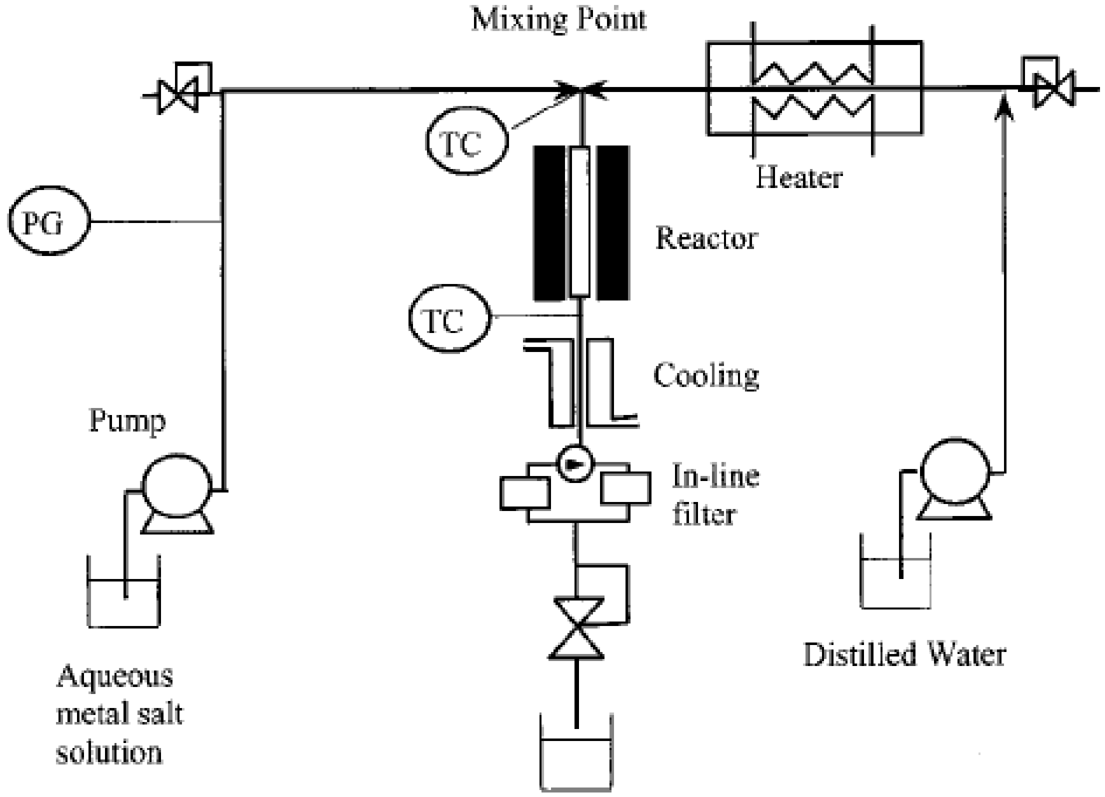

Figure 1.13: A CHFS system with one feed for metal ions and one for superheated water (taken from (Adschiri, Kanazawa, & Arai, 1992a).

In a number of publications, additional feeds have been added to the basic design presented by Arai's research. Many reports have been presented where combinations of precursor feed are used to allow for the introduction of mixtures of metal salts or for the addition of individual metal salt solutions for inline mixing (prior to contact with supercritical water). Several notable examples of the requirement for multiple feeds have been presented in the literature and are reviewed here to highlight some of the limitations which are overcome through system modification. The addition of two or more feedlines allows the mixing of two reagents in the reactor which, if placed in the same precursor solution, would react and would not be suitable medium to be pumped (primarily a limitation of equipment). (Weng *et al.*, 2008) The main reason this has been done is that the precipitation of metal oxide powders often requires basic conditions, so a separate feed for a base (usually a hydroxide) is used to aid the hydrolysis and dehydration of metal salts, common to many hydrothermal reactions. (Reverchon & Adami, 2006) For example, the work of Sue *et al.* used a setup consistent with the core process presented by Arai's research group (figure 1.13), the process was modified to allow the use of two precursor feeds, and correspondingly there are two mixing zones one at ambient temperature and one at high temperature where the supercritical feed is mixed with the combined precursor feed. (Sue *et al.*, 2004c) This particular setup was used to produce ZnO from $ZnSO_4$ and KOH aqueous feeds and investigated the effect of mixing the feeds in a different order showing that control of particle size could be affected by the combinations of feeds yielding some control over the particle formation reaction. Other researchers have used similar equipment configurations to investigate the effect of reagent addition sequences on the phase of materials produced. For example, Cote *et al.* investigated the effect of mixing the two solutions before feeding them into the superheated water (cold mixing), compared to heating the hydroxide solution before feeding in the metal cations (hot mixing). They found that hot mixing gave a higher percentage of Fe_2O_3 as an impurity when the target material was $CoFe_2O_3$. (Cote *et al.*, 2003) From the available literature it is suggested that hot mixing resulted in the preferential precipitation of Fe resulting in phase separation as cobalt species are known to exhibit greater solubility in hydrothermal media.(Cote *et al.*, 2003) They also noted that in the hot mixing experiments, the proportion of Fe_2O_3 increased with the supercritical water feed temperature. Hence, in more complex flow reactor designs, the order of mixing can profoundly affect the products of the reaction in terms of product composition. Many designs are optimised for a given synthesis and the number of reports presented to date makes it infeasible to review all configurations. Along a similar line, the CMTG research group based at UCL have developed a semi-automated CHFS system which allows for the sequential synthesis of upto 66 sample, each with a unique composition in a single day through a simple process modification of the core process presented in figure 1.13. (Weng *et al.*, 2009) This process is drawn schematically in figure 1.14. The process called RAMSI (Rapid Automated Materials Synthesis Instrument) has been specifically designed to rapidly produce hetrometallic oxides and hydroxides as nanosized precursor materials for solid state chemistry, as the homogenous co-precipitated produced through the CHFS process reduce comminutation steps through effectively reducing the ion diffusion distances in solid-state reactions. (Weng *et al.*, 2007) The use of this system is limited to small amounts of samples *ca.* 0.1 - 0.2 g which is sufficient for preliminary investigation of materials properties. The high throughput capacity of this instrument is related to the mixing of precursor solutions prior to being fed into a reactor analogus to the one shown in figure 1.13. (Weng *et al.*,2009)

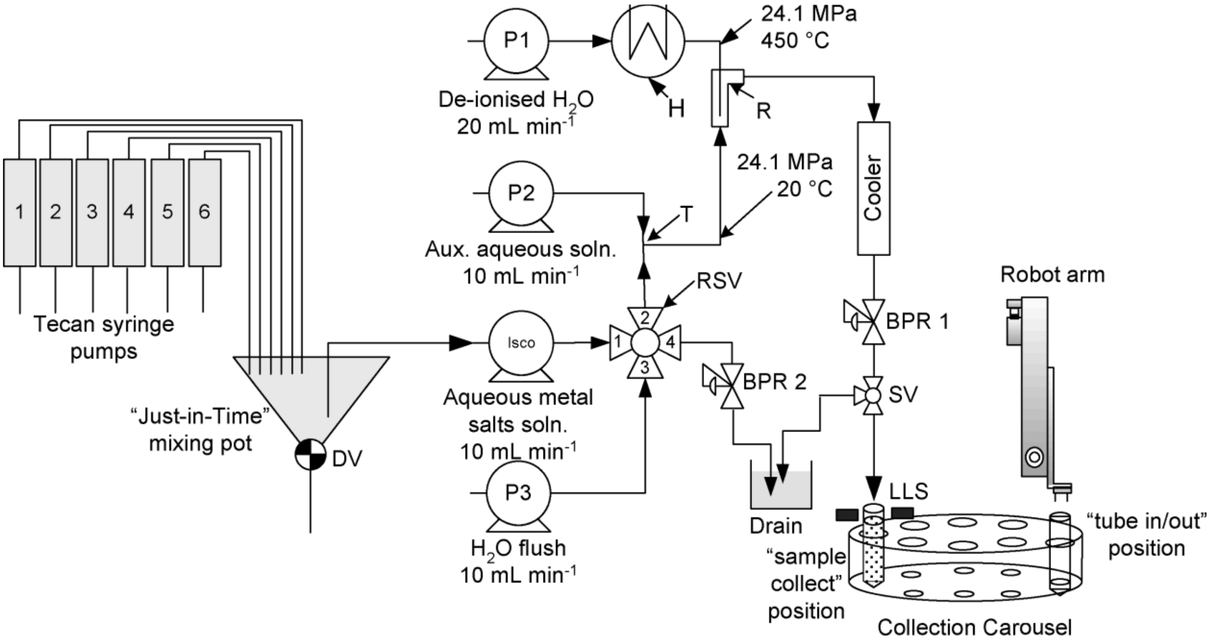

Figure 1.14: Schematic representation of the synthesis and collection part of RAMSI that was used to prepare 66 compositionally unique samples. Key: P) Gilson pump, Isco) Isco syringe pump, H) heater, R) counter-current mixer, T) T-piece, RSV) Rheodyne switch valve, BPR) back-pressure regulator, DV) drain valve, SV) two way switch valve, LLS) liquid level sensor. Each high pressure line also contains non return valves, pressure relieving safety devices, electronic pressure transducer, and manual pressure gauges which are not shown here for clarity.

1.6.2 Materials Produced by CHFS:

There are numerous reviews discussing the synthesis of materials in batch hydrothermal processes. (Darr & Poliakoff, 1999, Reverchon & Adami, 2006, Yoshimura, Suchanek, & Byrappa, 2000) Many of the materials produced in batch hydrothermal reactions are accessible as nanomaterials when a continuous hydrothermal process is used. (Byrappa, Ohara, & Adschiri, 2008) In this section comparisons will be drawn between the two bodies of literature to highlight common compositions produced using both methods.

The first reactions reported using continuous hydrothermal synthesis produced simple metal oxides and hydroxides. Such as, AlO(OH), Fe_2O_3, Fe_3O_4, Co_3O_4, NiO, ZrO_2 and TiO_2. (Adschiri, Kanazawa, & Arai, 1992a, Adschiri, Kanazawa, & Arai, 1992b) The study of homometallic systems has proved useful in describing the effect of processing conditions on the properties of the nanomaterials *i.e.* material phase, particle size and size distribution. Adschiri *et.al* have extensively studied the formation of, Al_2O_3 and AlO(OH) using the CHFS process presented in figure 1.13 in several publications (Adschiri, Kanazawa, & Arai, 1992b, Adschiri, Hakuta, & Arai, 2000, Adschiri *et al.,* 2001, Hakuta *et al.,* 1999a) The original publication of Arai produced particles of AlO(OH) in the size range 0.1 – 1.5 µm, with considerable variation is particle size as a function of temperature and pressure, correspondingly particle morphology also differed as a function of processing variables such as temperature and concentration of $Al(NO_3)_3$. (Adschiri, Kanazawa, & Arai, 1992b) Later, the same research group detailed the synthesis of AlO(OH) in total 38 reactions were presented, with particle sizes ranging from *ca*. 60 – 70 nm to *ca*. 450 nm, with much smaller size distribution with higher reaction point temperatures and lower-precursor concentrations producing AlO(OH) with smaller crystallite sizes and narrower particle size distributions. (Hakuta *et al.*,1999a) In many papers related to CHFS, particle properties are often discussed in relation to the solubility and supersaturation levels of precursor metal salts before, during and after the reaction point (defined as where the precursors and preheated water mix) and it was reported by Hakuta *et al.* that smaller and narrower particle size distributions were obtained in the latter report by improved control over the mixing of supercritical water and the precursor solutions *i.e.* leading to more homogenous nanoparticle nucleation and growth. (Hakuta *et al.,* 1999a)

ZnO a material which is difficult to produce as a nanoparticle in batch hydrothermal processes has been the subject of a number of publications related to CHFS and many of these publications serve to highlight how the CHFS processes operated by different groups yield remarkably different results. (Sue *et al.*, 2004a, Sue *et al.,* 2004c)Viswanathan and Gupta were the first to successfully produce nanosized ZnO from $Zn(Ac)_2$ in with the addition of KOH as a mineraliser using a reaction point temperature of *ca.* 380 °C with nanoparticles ranging from 39-320 nm being produced and the difference in each synthesis was attributed to differences in mixing events (mixing or the precursor solution and supercritical water) occurring within the reactor altering the nucleation and growth of nanoparticles. (Viswanathan & Gupta, 2003) Arai's group have also published work relating to the synthesis of ZnO nanoparticles using $Zn(NO_3)_2$ and KOH as precursor materials, in the reported reactions the precursors were premixed in a tee-piece mixer before encountering the supercritical water feed (*ca.* 400 °C). The particles produced ranged from 20 – 60 nm with narrower particle size distributions to those presented by Viswanathan & Gupta. (Sue *et al.*, 2004c) In a later publication Arai's group also managed to produce ZnO without base using $Zn(NO_3)_2$ as the precursor material using a furnace to increase the reaction point temperature (*ca.* 500 °C) of the process after the precursors and preheated water were mixed, showing higher temperatures are required to dehydrate the zinc precursors in the absence of a mineraliser. (Ohara *et al.*, 2004) In this publication ZnO nanoparticles with a rod like morphology were produced in the µm size range. Later, the same laboratory added KOH to act as a minerliser in the reaction (Sue et al. 2004c), but instead of pre-mixing the $Zn(NO_3)_2$ and KOH, they were only mixed after one of them had encountered the supercritical water feed. It was found that if the KOH was heated first *i.e* addition of $Zn(NO_3)_2$ to a preheated KOH solution, then small spherical particles were produced *ca.* 90 nm, whereas if the $Zn(NO_3)_2$ was heated first, then rods were produced, presumably the observed difference was due to the former reaction being nucleation dominated and the latter showing evidence of particle growth (images of the products of these reactions are shown in figure 1.15). (Sue *et al.*, 2004b) Comparative work between ZnO nanoparticles produced in both hydrothermal batch and flow reactors has also been presented by Sue *et al.* and showed that a CHFS reactor gave significantly smaller particles than the batch reactor presumably due to the higher supersaturation and shorter reaction times afforded by using a continuous process. (Sue *et al.*, 2004c)

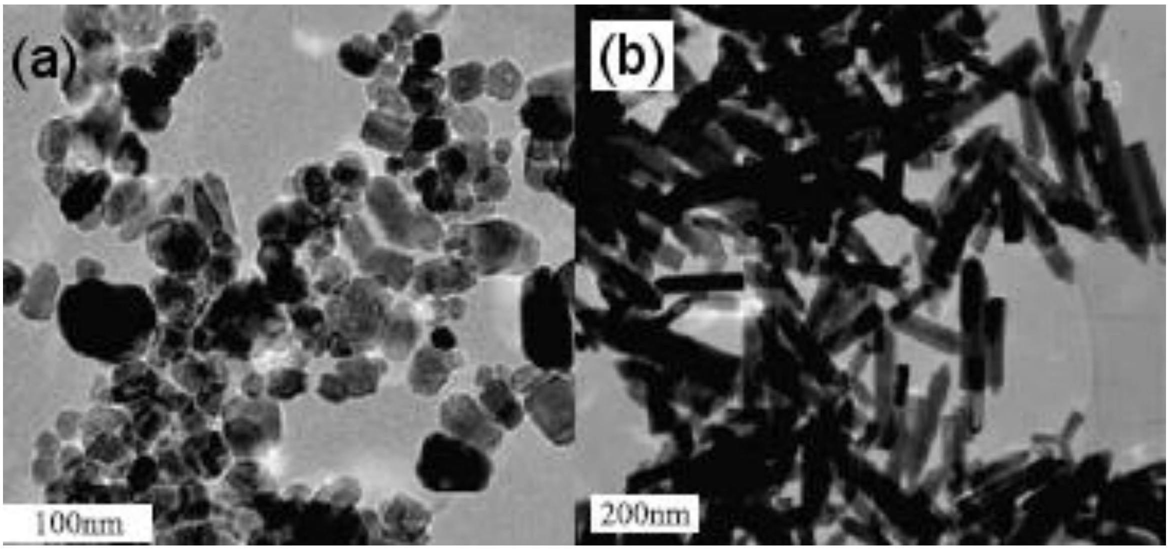

Figure 1.15: TEM image of ZnO nanoparticles particles produced in a CHFS reactor a) with KOH heated first and b) with $Zn(NO_3)_2$ heated first as reported by Sue *et al.* (Sue *et al.*, 2004c)

Further, the study of other homometallic systems has highlighted a number of issues related to synthesis parameters for the formation of a desired material phase. Nanoparticles of the following have all been produced using CHFS or CHFS like methodologies; Fe_2O_3, (Adschiri, Kanazawa, & Arai, 1992a, Cabanas & Poliakoff, 2001, Cote *et al.*, 2003, Darab & Matson, 1998, Hao & Teja, 2003) Fe_3O_4, (Adschiri, Kanazawa, & Arai, 1992a) Co_3O_4, (Adschiri, Kanazawa, & Arai, 1992a, Cote *et al.*, 2003, Hao & Teja, 2003) NiO, (Adschiri, Kanazawa, & Arai, 1992a, Reverchon & Adami, 2006) ZrO_2, (Adschiri, Hakuta, & Arai, 2000, Cabanas *et al.*, 2000, Darab & Matson, 1998, Lester *et al.*, 2006) and CuO (Lester *et al.*, 2006). These investigations have highlighted the diversity in reactions that can be performed in hydrothermal systems, and have identified some interesting phase behaviour. As an example, the synthesis of Fe_2O_3 and Fe_3O_4 indicates that different oxidation states can be obtained in CHFS systems as a function of temperature and the presence of reducing species formed through the thermal decomposition of the precursor anion. (Adschiri, Kanazawa, & Arai, 1992a) Similarly, the choice of precursor has also been shown to influence the material phase produced in the formation of iron oxides. If $Fe(SO_4)_3$ is used, Fe_2O_3 was obtained as the product, whereas when a Fe^{2+} salt is used, Fe_3O_4 (magnetite) can be produced. (Adschiri, Kanazawa, & Arai, 1992a, Cote *et al.*, 2003)

The rapid and uniform precipitation of metal ions in continuous hydrothermal processes also leads to some interesting observations in the structure and solubility of guest ions in host lattices. The Cerium Zirconium Oxides are a good example of solid solutions produced directly by Continuous hydrothermal methods from soluble Ce and Zr salts (ammonium cerium nitrate and zirconium nitrate). (Cabanas *et al.*, 2000) Interesting phase behaviour is observed in the $Ce_{(1-x)}Zr_xO_2$ in conventional hydrothermally precipitated ions after heat treatment, where $x > 0.8$ monoclinic crystal structures are typically the reaction products. (Si *et al.*, 2004) However, analogous materials produced in CHFS for $x > 0.90$ in $Ce_{(1-x)}Zr_xO_2$ tetragonal Ceria zirconia is observed. (Cabanas *et al.*, 2000, Si *et al.*, 2004) Other mixed metal (heterometallic) oxides can be also be synthesised in the CHFS system and have shown that careful control over the chemical conditions is required to control the phase of materials produced. An example, Yttrium Aluminium Garnet or YAG ($Y_3Al_5O_{12}$) needs to be made be made under specific conditions. The Y: Al precursor ratio needs to be that required in the product (3:5) and 1.0M KOH is added, lower KOH concentrations result in the formation of boehmite (AlO(OH)) as an impurity phase, and excess base results in YOOH impurities. In addition supercritical conditions are needed as particles formed in the sub critical region have AlOOH impurities. Where the interplay between temperature and the presence of other reagents are required to control the material phase. (Hakuta *et al.,* 1999a) Demonstrating the requirement for careful control over reaction conditions to produce co-precipitated phases.

More recently CHFS has been used as a method for the production of nanosized heterometaillic oxides and hydroxides as precursor materials for solid state reactions and other solid solutions, exploiting the homogenous distribution (afforded by rapid and uniform coprecipitation upon mixing with supercritical water) of the component metal ions in the coprecipitate. The ability of CHFS to produce intimate mixtures of metal ions as nanosized coprecipitate has been shown to greatly reduce the materials processing times when compared to conventional solid state reactions. (Weng, *et al.*, 2008) For example, the Lanthanum nickelates are oxygen ion and electron conductors with the general formula $La_{n+1}Ni_nO_{3n+1}$ and are often used as a cathode material in solid oxide fuel cells. (Weng *et al.*, 2008) The structure of these compounds consists of stacked layers along the c-axis of n finite $LaNiO_3$ perovskite layers separated by LaO rock salt-like layers. (Lacorre 1992) As n increases, the phases become more difficult to access without prolonged and multiple comminuation steps leading to long materials processing times. (Weng *et al.*,2007) Lanthanum and Nickel hydroxides formed in the CHFS process as either a single phase or a phase separated mixture containing La and Ni species, was shown to form the relevant lanthanum nickelate (depending on the La:Ni ratio) in a single heat treatment step at an appropriate temperature. (Weng *et al.*, 2008) It is thought that the short elemental diffusion distances are a valid explanation of reduced processing time and mitigation of comminuation strategies. (Parker *et al.*, 2011) The CHFS system can therefore be used to access hard to make phases in more efficient ways. Another example of nanoparticles precursor materials was presented by Lin *et al*. The authors showed that CHFS could rapidly produce phosphor nanoparticles precursors doped with europium $(Eu_{1-x})Y(OH)_3$ (where, x = 0-0.20) allowing the rapid optimisation of fluorescence intensity with heat treatment temperature and Eu^{3+} mol %.(Lin *et al.*, 2010) Figure 1.16 a shows a photograph of the nanosized precursors produced and the samples heat treated at different temperatures for 6h under 254 nm excitation. Figure 1.16 b shows a contour plot of fluorescence intensity extracted from figure 1.16a (arbitrary units on *z* axis). The plot suggests a gradual change of properties exists and that the most intense phosphor at lower temperatures is the 3 mol % Eu^{3+} sample heat treated at 500 °C, while the brightest sample was the same sample composition heat treated at 1200 °C. Results were obtained far more rapidly than equivalent experiments using conventional nanoparticle processing methodologies. (Lin *et al.,* 2010)

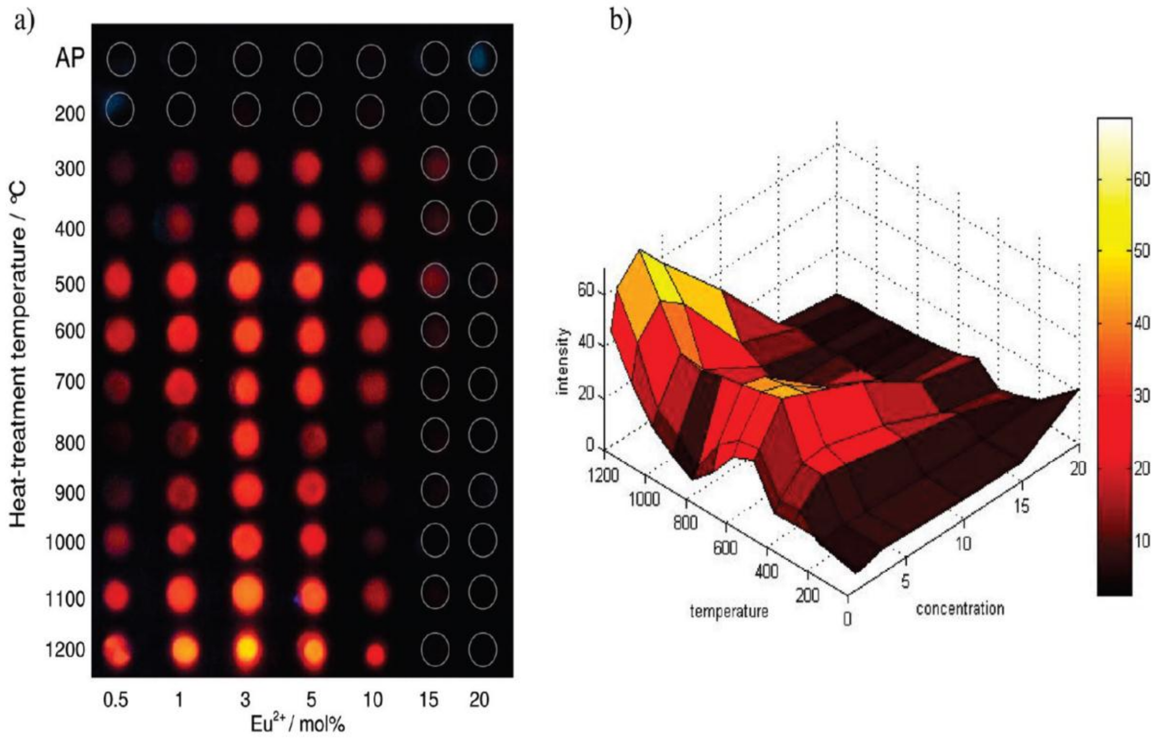

Figure 1.16: a) Photograph of a $(Eu_{1-x})Y(OH)_3$ nanoparticle precursor library under UV light illumination (254 nm) showing the changes in intensity with heat-treatment temperature and Eu^{3+} mol % (AP = as prepared sample with no further heat-treatment). **b)** A contour plot showing the extracted image intensities (arbitrary units on *z* axis) from the photograph versus heat-treatment temperature (°C) and Eu^{3+} dopant concentration in yttria (mol %). Image adapted from (Lin *et al.*, 2010).

In CHFS, heterometallic phases with alkali or alkali earth metals can also be produced where a large excess of the alkali metal is required for precipitation in the reactor due to the high solubility of group 1 and 2 metals in both sub and supercritical water. (Meng, Wang, Liu, & Zhang, 2004) There are several examples of materials which demonstrate the excesses of group 1 and 2 required to produce a material incorporating the alkali metal. $LiCoO_2$ and $LiMnO_4$ are examples of such materials and can be made in CHFS type synthesis with a large excess of LiOH (>20 x [Co] or [Mn]) and reaction temperatures of > 330 °C. (Adschiri, Hakuta, Sue, & Arai, 2001, Adschiri, Lee, Goto, & Takami, 2011) It was found for $LiCoO_2$ formation low concentration of lithium resulted in a Cobalt phases such as ($Co(OH)_3$ and $CoO(OH)$ and Co_3O_4. (Adschiri, Hakuta, Sue, & Arai, 2001) Similarly, Hakuta *et al.* produced Potassium titanate, $K_2Ti_6O_{13}$, from $Ti(OH)_4$ with a 20 x excess of KOH. (Hakuta, Hayashi, & Arai 2004) More recently, the CMTG group based at UCL produced sodium titanate ($Na_2Ti_3O_7$) made with excess NaOH and TiBALD precursor. (Zhang *et al.*, 2010) this reaction compared to other methods and equivalent excesses of NaOH were required as noted in previous reports.

As demonstrated above the synthesis of metal oxide nanoparticles under hydrothermal conditions is relatively simple to achieve. However, the synthesis of metallic nanoparticles using this processing methodology is less well described principally due to the oxidizing conditions present in many continuous hydrothermal reactions. (Darr & Poliakoff, 1999) Many examples of metal particles produced using batch reactors have been published, comparatively few publications detail synthesis using continuous methods. In a review article referenced earlier, preliminary, but as yet unpublished, results were reported that it was possible to precipitate metal nanoparticles directly from scH_2O using metal-organic salts (*e.g.* acetates) to date this data has not been published. (Darr & Poliakoff, 1999) The report inferred that if the reaction conditions were suitably reducing metallic nanoparticles could be produced. The work of Dr Goodall in the CMTG group using many of the processes and methodologies developed in this thesis has recently shown that the synthesis of metal sulphides (of many compositions) is possible in CHFS if suitably reducing and oxygen free solutions (degassed solutions) are used in the reaction.

Although the chemistries accessible in continuous hydrothermal systems are comparatively well defined. (Byrappa, Ohara, & Adschiri, 2008) The subject of particle size and the control thereof is complex due to the discontinuity in both process design and suitable definitions of reaction conditions presented in each publication. (Lester *et al.*, 2006) This subject was briefly discussed alongside the review of ZnO formation in CHFS where reproduction of results between laboratories is rare. However, one particularly important paper presented by Sue *et. al.* studied a range of homometallic oxides produced using a single reactor design and more importantly a single reaction point geometry (used for mixing the supercritical water and precursor feeds) and measured the particle size produced while varying conditions such as pressure, metal ion concentration, anion concentration, base concentration and starting materials. In this report the authors found the particle size (of all oxides) decreased reliably with increasing supersaturation as defined through empirical relationships, regardless of the material being produced. (Sue *et al.*, 2006) They concluded that for a particle size of less than 10 nm, a supersaturation of greater than 10^4 (equation 1.7) was necessary, as shown in figure 1.16. The size ranges presented for different materials in this publication showed consistency with those produced before the publication and after the publication. Demonstrating the role of controlling supersaturation within a reaction, and how the solubility of the metal ion in the reaction influences its final size as a crystalline nanoparticle either through increasing the presence of mineralisers or through the changes in the physical properties of water as it transitions to a supercritical temperature. (Adschiri, Hakuta, Sue, & Arai, 2001)

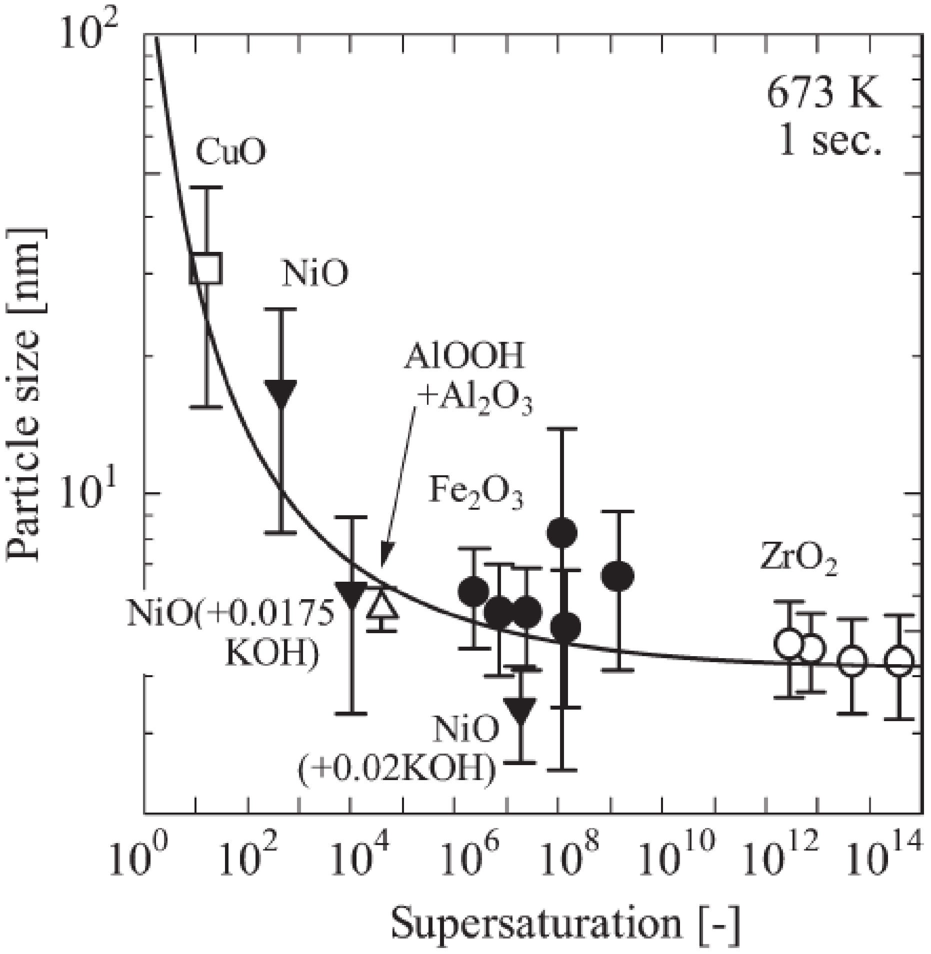

Figure 1.16: Graph of particle size plotted against supersaturation for various materials produced at 400 ºC in a CHFS reactor (taken from (Sue *et al.,* 2006)

In CHFS the physical process of mixing supercritical water with the precursor feed is thought to be the largest single contributory factor for the synthesis of nanoparticles. As such, the following section details the literature concerning the mixing of the supercritical water feed and precursor and the different methods employed to achieve rapid mixing and thus uniform nanoparticle formation in CHFS systems. The following section also details the myriad of complications of mixing flows of significantly different physiochemical properties.

1.6.3 Continuous Hydrothermal Synthesis Mixing Point Designs:

As particle properties such as size, size distribution and composition are critical to the performance of many nanomaterials, there is a strong push towards achieving greater control over particle properties such as size, shape and polydispersity. (Burda *et al.*, 2005) In the context of CHFS, it is widely accepted that the physical process of mixing a preheated water feed and a precursor feed is the largest factor in determining the particle size distribution of materials produced. (Lester *et al.*,2006, Lester *et al.*, 2010, Takami *et al.*, 2012) Resultantly, many methods for ensuring homogenous mixing between the preheated water and precursor feeds have been presented, and are collectively known as reaction points. Reaction point geometries found to be suitable for the formation of nanoparticles in CHFS include designs based upon; Cross type reactors with movable inlets, (Mae *et al.*, 2007), swirl type mixers, (Kawasaki *et al.*, 2010a, Wakashima *et al.*, 2007), classical tee mixers, (Aimable *et al.*, 2009, Takami *et al.*, Saito, 2012, Toft *et al.*, 2009), confined impinging jet reactors (used predominantly for sc CO_2 processes relevant to pharmaceutical particle formation) and nozzle-type mixers, (Lester *et al.*, 2006, Lester *et al.*, 2010, Middelkoop *et al.*, 2009) many suffer from experimental limitations arising through “poor mixing” of the component streams within the reaction point geometry leading to material deposition (through hydrothermal reaction of the precursors) and reactor blockage which severely limits the continuous operation of these reactors. Many of the heat and mass transfer processes that lead to complications in the operation of CHFS systems are poorly described and collectively it is difficult to elude these processes from the scant experimental details presented in many publications.(Lester *et al.*, 2010) For information, many of the geometries used for the synthesis of nanoparticles are presented schematically in figure 1.17, alongside a representation of empirical data taken from each publication detailing complications in the operation of each geometry *i.e.* particle nucleation and deposition regions are highlighted.

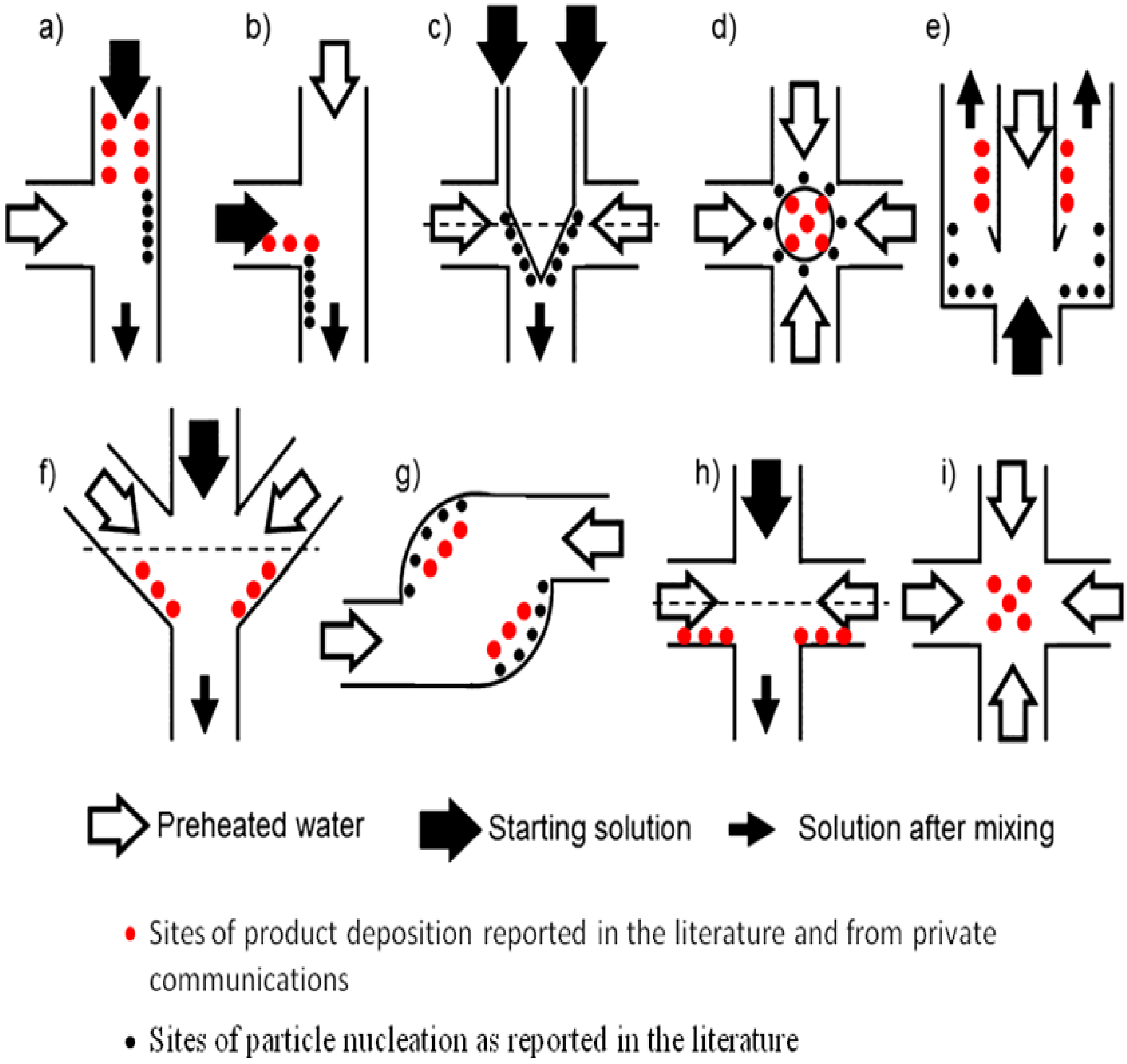

Figure 1.17: Schematic representations of reaction point geometries developed for the continuous hydrothermal synthesis of nanoparticles **a)** horizontal cross-section of a conventional "tee" reaction point and **b)** "tee" reaction point with the inlets of different feeds entering the geometry (Adschiri, Hakuta, & Arai, 2000) **c)** A vertical cross section and d) a horizontal cross section (dassghed line in c) of a mixer with a movable needle (Mae, 2007) **e)** Vertical cross section of the nozzle mixer (Lester, Blood, Denyer, Giddings, Azzopardi, & Poliakoff, 2006) **f)** and **g)** A vertical cross section of a swirling micro mixer and the corresponding horizontal cross section (Kawasaki, Sue, Ookawara, Wakashima, & Suzuki, 2010a) **h)** and **i)** Vertical cross section of a central collision type mixing point and the horizontal cross section (Sue *et al.*, 2010).

A large number of reaction point geometries reported as suitable for the synthesis of nanoparticles in CHFS have experimental limitations associated with them to overcome key operational issues, and many reaction point geometries are not comparatively evaluated making it difficult to select an optimal geometry for a given synthesis. For example, Kawasaki *et al.* overcame the problem of material deposition and reactor blockage in a tee type mixing geometry through using high flow rates for the preheated water stream (*e.g.* 100 mL min^{-1}) and lower concentrations for the metal salts (e.g. 0.01 M). (Kawasaki *et al.*, 2010b) However, the flexibility of the system was reduced in terms of possible flow rates and precursor concentrations limiting the efficiency of synthesis (product per unit volume waste). Resultantly, authors working with these continuous hydrothermal systems have defined empirical criteria for the “ideal” heating / mixing of precursor feeds in an engineered mixer which result in the formation of nanoparticles. (Lester *et al.*, 2006, Lester *et al.*, 2010) The criteria state that an optimal geometry for the synthesis of nanoparticles would show the following empirical characteristics; near instantaneous and uniform mixing of reactant streams with a supercritical water feed (essential for the formation of many nanosized and uniform particle nuclei), short reaction residence times are required to limit particle growth (if the synthesis is not nucleation dominated), minimal heating of precursor feeds prior to rapid mixing with a preheated supercritical water feed ensuring rapid uniform nuclei formation and minimal product deposition within the reaction point, and a high flow velocity from the reaction point to prevent the accumulation of reagents and products at the reaction point through highly turbulent flow. These empirical characteristics have been adopted by many researches trying to find suitable reaction points for the synthesis of nanoparticles. (Kawasaki *et al.*, 2010a, Toft *et al.*, 2009, Wakashima *et al.*, 2007)

Many researchers have attempted to understand the mixing between the precursor and preheater water feeds in CHFS and the effects of different mixing processes on the formation of nanoparticles. These endeavours, have led to the development of several experimental methods to visualise the properties of a hydrothermal system working at the temperatures and pressures used for the synthesis of nanoparticles. Many of the identified complications with mixing in CHFS stem from large differences in thermodynamic and transport properties of water between the preheated water feed and the ambient temperature precursor feed. For information, the normalised thermodynamic and transport properties for water at 24.1 MPa at variable temperature are presented in figure 1.18 and demonstrates the differences in properties between the ambient temperature feed (precursor) and the preheated water feed. Mixing between these feeds in light of the properties summarised in figure 1.18 suggest that in CHFS processes mixing analogous to mixing a gas like state (low density) with water (high density). However, strictly speaking at temperatures and pressures used for the synthesis of nanoparticles is a liquid - liquid mixing process. It has been reported that in CHFS poor mixing between the feeds results in different degrees of supersaturation, leading to broad particle size distributions and larger average particle sizes due to particle growth after nucleation. (Lester *et al.,* 2010) Mixing in CHFS is almost a unique problem due to both the temperature and density difference between the two feeds and defies direct comparison to much of the available mixing literature. (Ma *et al.*, 2011) However, authors working with these systems have suggested turbulent flows of preheated water and a turbulent flow of the mixture when (preheated water and precursors) yields the most appropriate flow types for the formation of nanoparticles. (Takami *et al.,* 2012) Typically, dimensionless numbers are used to evaluate the type of flow occurring within a system, and are especially useful in determining the flow in pipes. Flow in pipes, including mixing of flows, is determined by a complex mixture of factors and in the case of supercritical fluids evaluation of the dominant factors on mixing and the behavior is complicated further by the significant changes in the thermodynamic and transport properties of water as its temperature reaches the critical point (Figure 1.18). This section now moves forward to describe the current state of the art in the evaluation reaction point geometries for the synthesis of nanoparticles.

The flow regimes occurring within a pipe can be expressed as a single dimensionless number called the Reynolds number. For a flow in a pipe, the Reynolds number is calculated equation 1.14.

$$\mathrm{Re} = \mathrm{D}v\rho / \mu \quad \textbf{(Equation 1.14)}$$

Where, *Re* is the Reynolds number (dimensionless), *D* is the “characteristic length” (in the case of a CHFS reaction point is the diameter of the pipe), *v* is the velocity, *ρ* is the density, and μ is the viscosity. The value of *Re* determines which type of flow is present for any given system and values of *Re* < 2000 are considered laminar flow regimes, values > 4000 are considered turbulent flows and transitional flow straddle the values between these regions. When operating at near critical conditions (< 373 °C, 24.1 MPa), many of the reactions reported in the literature operate in a turbulent flow regime with relatively high *Re* > 3500, after the precursors and the preheated water are completely mixed, these reports often yield the smallest nanoparticle size. (Blood *et al.*, 2004) However, the exact definition of the mixing processes between precursor and preheated water with regard to time scales is rather ambiguous. This is primarily due to the difficulty in taking observation based measurements at the high working temperatures and pressures of CHFS systems. As such, there is uncertainty in defining the 'true' reaction conditions inside many of the reactions and reaction points identified as suitable for the production of nanoparticles, and more importantly the dominant forces influencing mixing behaviour and the formation of nanoparticles (*i.e.* buoyancy, momentum, viscosity, turbulence and sheer). (Blood *et al.*, 2004)

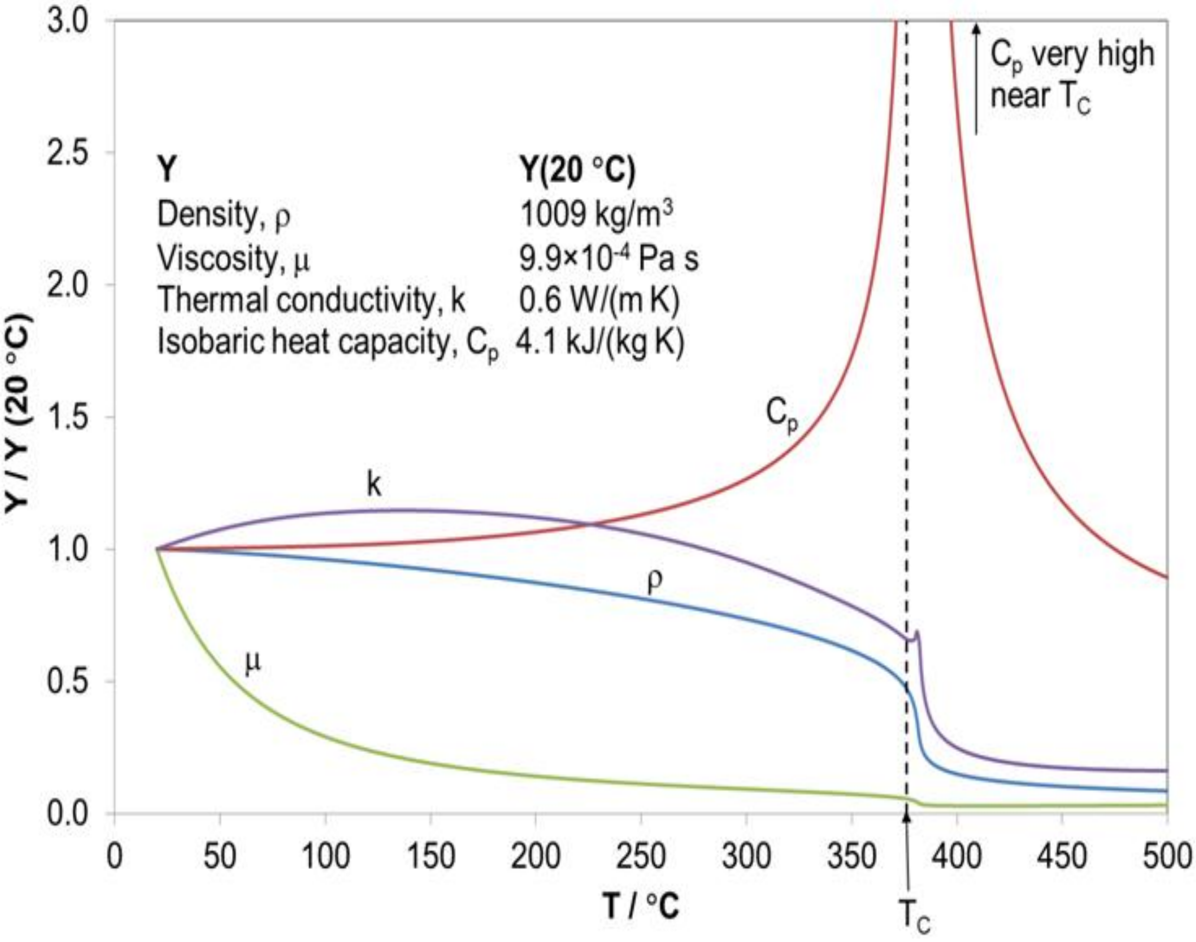

Figure 1.18: Normalised thermodynamic and transport properties of water as a function of temperature at the typical operating pressure of CHFS systems (24.1 MPa) calculated using the IAPWS formulations. (Wagner & Pruss, 2002b)

Several attempts have been made to study the flow within reaction points used for the synthesis of nanoparticles with a specific emphasis on the interface between the preheated water and precursor feeds. Blood *et al*. modeled a reactor at typical operating temperatures and pressure using a ambient pressure analogue. (Blood *et al.,* 2004) In this report, methanol and sucrose solution were chosen as they have “similar” Re numbers to the fluids (supercritical water and metal salt solution respectively) and the observations made in this publication are presented in figure 1.19a and 1.19b which also show the effects of orientation on the mixing between the precursor and preheated water feeds. In figure 1.19 it can be clearly seen that the effect of buoyancy on the mixing process is quite significant, this observation is not surprising as the density of water changes dsignificantly around the critical point. In figure 1.19b it can be seen that the orientation of flows within the Tee reaction point can significantly ifluence the effects of buoyancy on mixing and the direction of flows. In figure 1.19a the orientation of flows meant that the buoyancy forces drive the recirculation of the mixture into the precursor annuli, at a process level this would lead to rapid reactor blockage through hydrothermal reaction of the precursors. (Lester *et al.,* 2006) However, using transparent plastic mock ups at ambient temperature and pressure must be approached with caution because the changes in transport and thermochemical properties of water, which are significant near the critical temperature are largely ignored (figure 1.18). The results of Aizawa *et al*. superseeded the work of blood *et al.* and used sapphire reactor components to visualise the mixing process at typical CHFS system temperatures and pressures. (Aizawa *et al.,* 2007) These obsservations are presented in figure 1.19c to e and again show the large contribution of buoyancy in determining the flow pattern within the ractor. These direct observation also show some intersting feateures in that the data clearly shows phase separation (between the preheated water feed and the precursor) in the mixer. This observation suggests that “mixing” does not strictly occur in this reaction point and the heating of the precursors is influenced to a greater degree by heat transfer occuring between the feeds, and the distribution of a passive scalar (dye) was shown to be influence by both the flow rate of each of the feeds and the orientation of the flows within the reaction point.

In both the publication of Aizawa *et al*. and Blood *et al*. the Grashof number was used to compare the contribution of buoyancy on the mixing processes occuring with a reactors under different flow orientation, preheated water temperatures and flow rates in light of the data generated by direct observation. The derivation of which was taken as being the theroetical mixture temperature although from observation this was unlikely to be reached until significantly after the introduction of preheated water (figure 1.19). (Aizawa *et al., 2007,* Blood *et al.*, 2004) The Grashof number is defined in equation 1.15;

$$\mathrm{Gr} = \frac{g\alpha\Delta T L^3}{v^2}$$ **(Equation 1.15)**

Where, *Gr* is the Grashof number, *g* is the acceleration due to gravity (9.81 ms^{-2}), *α* is the thermal expansion coefficient, *ΔT* is the temperature difference between the two fluids mixing, *L* is the characteristic length (In the case of CHFS systems the diameter of the pipe), and *v* is the kinematic viscosity (absolute viscosity/density). In general, when the *Gr* >> 1 in any given flowing system, then buoyancy forces are dominant over inertial (viscous) forces. The higher the temperature difference the more buoyancy forces will dominate. In all publications related to materials synthesis using such systems buoyancy in the preheated water feed is dominant and as such certain for orientations allow for more efficient operation than others as shown in figure 1.19. Although due to the nature of the mixers used other forces may supersede the effect of buoyancy and will be discussed later.

Further to the work of Aizawa *et al.*, neutron absorption measurements have also been applied to experimentally evaluate the mixing between component streams in a “Tee” piece reaction point geometry. Takami *et al.* mapped the density of water as a function of distance using the neutron adsorption coefficient and produced spatial maps representing the density fluctuation (indicative of temperature) in a Tee piece reactor and studied the effects of flow and temperature as shown in figure 1.20 Figure 1.20 clearly shows the difference in density distribution across the reactor for different experimental conditions. The results suggest that the backflow of preheated water is dependent upon the balance between the volumentric flow rates of preheated water / precursor feeds (influencing the Gr number within the system) and the orientation of the flows, respectively. These measurements although informative provide time averaged data (over 3 hours) which is not representative or any turbulence or transient flow events and provides comparatively limited information when compared to the direct observation measurements presented in figure 1.19.

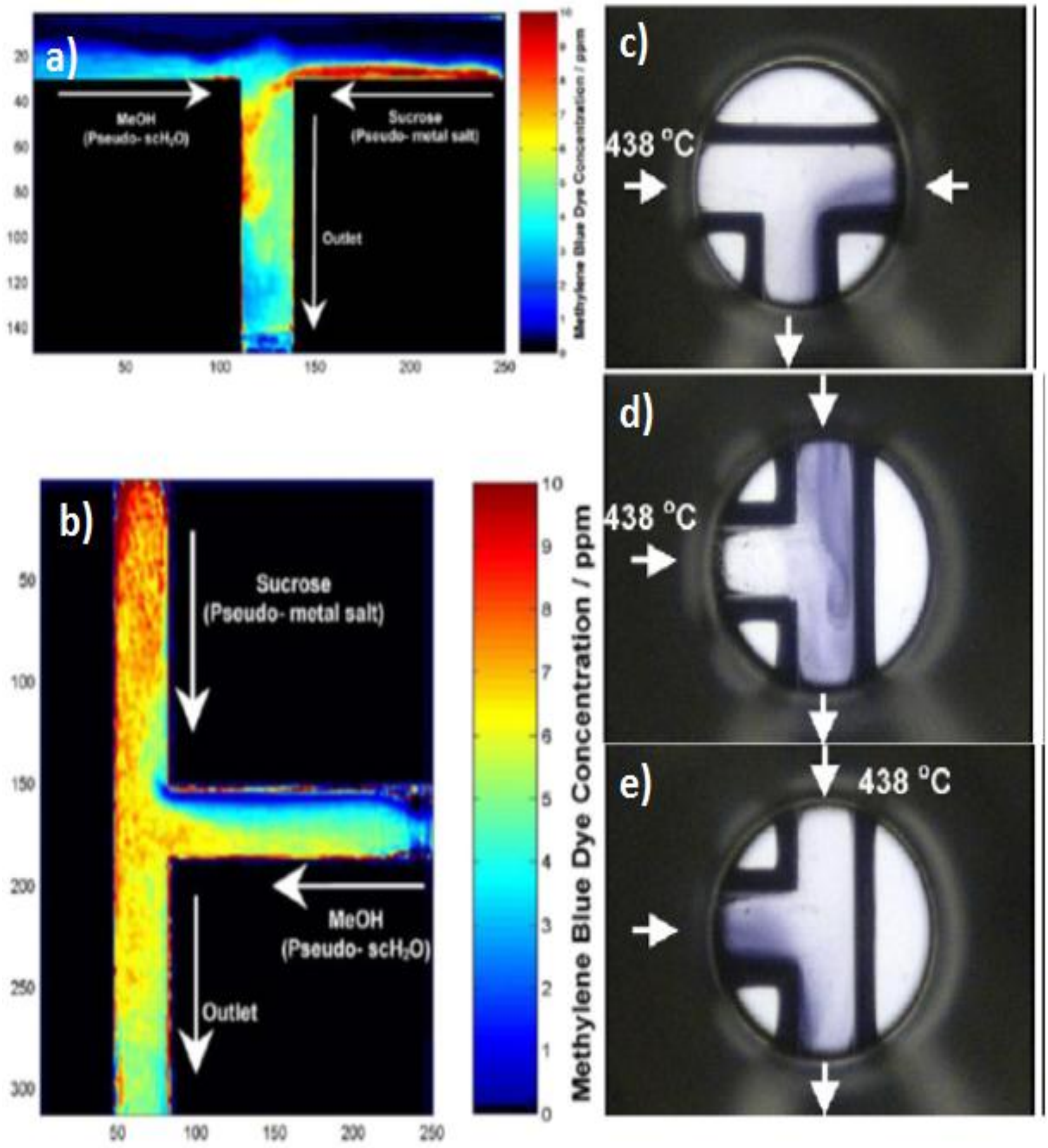

Figure 1.19: a) Images showing the concentration profile of a tracer within a tee mixing design with the simulated metal salt solution feed and the simulated preheated water feed showing inefficient mixing between the component streams and **b)** the most efficient tee-piece inlet configuration showing almost complete mixing, **c)** Inefficient tee-piece mixing observed using a tracer in a tee piece used under typical nanoparticle synthesis conditions using sapphire windows to observe a tracer, **d)** mixing observed as in c with a different

inlet configuration **e)** mixing observed as in a with the most complete mixing. (Images a and b were taken from Blood et al. 2004 and images c-e were taken from Aizawa et al. 2007)

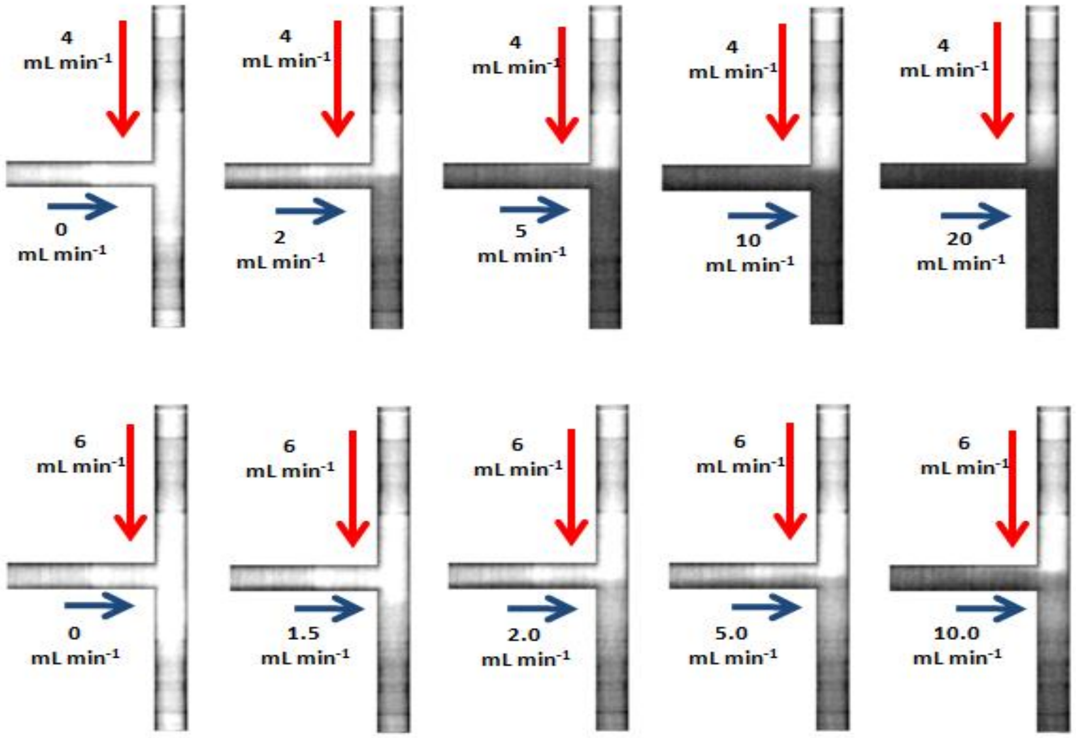

Figure 1.20: Absorbance of water inside reactor (indicative of density) during experiments with neutron absorption at different ratios of volumetric flow rates in a conventional "tee" piece. Colour gradient is indicative of density (light = low density and dark = high density).

Alongside many of the experimental evaluations of reaction points presented in the literature, there are many examples of modelling approaches which allow finer interpretation of the flow regimes at the interfaces responsible for mixing in reactors. From a fundamental point of view modelling has limitations, although its largest benefit is more rapid evaluation / screening and optimisation of a process. Reducing, significantly the experimental cost of optimising a process or material. Modelling strategies, have been employed to study reaction point geometries of the following types; Tee, cross, swirling micro mixers and inlet type mixers (counter current flows). (Kawasaki *et al.,* 2010b, Masuda *et al.*, 2009) Much of the literature focuses on finding an optimal geometry for the synthesis of nanoparticles. Kawasaki *et al.* have used Computational Fluid Dynamics (CFD) to visualise the processes of momentum, heat and mass transfer occurring inside a

Tee piece mixing geometry. (Kawasaki *et al.*, 2010b) Such simulations are not trivial, because the transport properties of water change considerably around the critical temperature (figure 1.19) often complicating interpretation of the data, in their work, the flow and the reaction of an organometallic precursor used for the synthesis of NiO in supercritical water was analysed in a tee type reaction point and the results were coupled to size distribution data that showed that particles with lower polydispersity and primary crystallite size were synthesised when the velocity of the reacting mixture was high through the reaction point, and that the polydisperity of particles was very much affected by the flow pattern in the mixer (*i.e.* when the flow of the mixture was more “turbulent” (implying good mixing) the particles were smaller *ca.* 10 nm and “transient” flow resulted in particles which were *ca.* 30 nm (determined through calculation of the Reynolds number of the mixture). The orientation of inlet directions for the precursors and preheated water was also shown to influence the particle size and polydispersity of the material attributed to the buoyancy of the mixture and these results correlated well with the conclusions of direct observation experiments. (Aizawa *et al.*, 2007) The authors also suggested an optimal flow regime for the synthesis of nanoparticles (achieving a small crystallite size), in which the preheated water inlet had a significantly higher volumetric flowrate than the precursor solution (ratio >10:1).(Kawasaki *et al.*, 2010b)

Wakashima *et al*. have also applied CFD modeling to improving the crystallite size distribution and defined three key design criteria for a new mixer from their modeling work; **1)** newly formed particles should be prevented from coming into contact with the walls of the mixer, as this causes deposition and blockages a common issue presented throughout this review (from the review presented thus far other explanations for reactor blockage and deposition are also valid), **2)** the mixing of the two feeds should be as near instantaneous as possible in order to minimise inhomogenous particle nucleation and **3)** there should be a “smooth and quick” discharge of the flow from the mixing zone. The latter two points are consisted with the desired mixing criteria highlighted earlier. The design which Wakashima *et al.* defined as fulfilling these criteria was named a swirling mixer as shown in figure 1.21 (the inlet positions for the precursors and preheated water can be identified through the temperature key). The swirling mixer rapidly achieves a uniform green colour equating to a temperature of around 400 ºC as calculated from enthalpy balance, whereas the tee-piece mixer contains sections of the flow which are still at the same temperature as the inlet hot water feed demonstrating segregated flows, and sections where the temperature is still subcritical for a long distance after the initial mixing point (as inferred from previous reports the conduction of heat may be significant). This design was comparatively tested using AlOOH (bohemite) as a particle system and compared the obtained characterization data to previous results using a tee-piece mixer. (Hakuta *et al.*, 1999b, Wakashima *et al.*, 2007) It was found that the new mixer gave both a smaller overall particle size (60 nm compared to 126 nm for an equivalent reaction in a tee-piece mixer) and a significantly narrower particle size distribution. The main disadvantage with this type of mixer is that it cannot readily be made with off the shelf parts and requires substantial reengineering to be used at different flow rates to maintain the turbulent environment within the reaction zone.

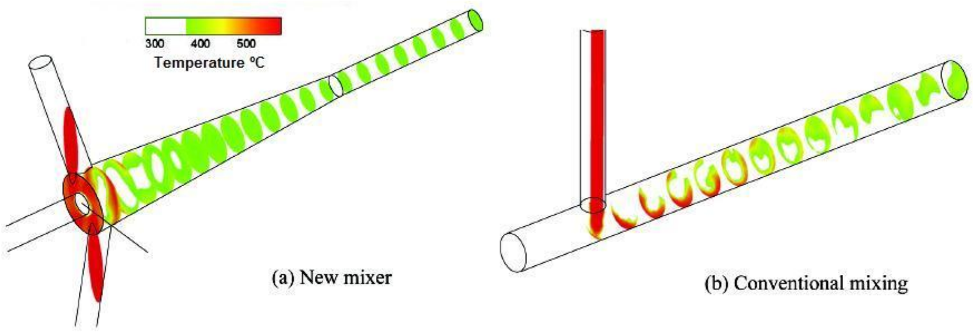

Figure 1.21: Modeled cross-sectional temperature contours of (a) the new “swirling” mixer design compared to b) a conventional tee-piece mixer. White spaces in the cross-sections equate to temperatures below 374 ºC. (Wakashima *et al.*, 2007)

One result of the work detailed above was the development of a well known engineering reactor design, which introduced the preheated water and precursors in a co-axial counter-current arrangement as shown in figure 1.22. In this mixing design, one tube passes inside another tube, and the mixing takes place where the inner tube ends, with the mixed fluid passing back up the outside of the inner tube. (Lester *et al.*, 2006) The purpose of having the superheated water flow vertically downwards is to exploit the buoyancy of near critical water which means that back flow is almost impossible as the hot water will naturally flow upwards around the outside of the pipe. This mixing system was modeled in the same way as the “tee” piece mixers described earlier in the work of Blood *et al.* as shown in figure 1.22 and served to demonstrate the mixing processes occurring in this reactor at ambient temperature. Coupled to this design and evaluation, nanoparticle characterisation data for several metals and metal oxides were produced using a counter-current reactor and a tee piece reaction point. In particular, CeO_2 was synthesised in a number of different runs under identical conditions, and the surface area measured, to assess the reproducibility of the results (another key factor in defining a suitable reaction point for the synthesis of nanoparticles. It was found that the surface area of the powders produced was 90 ± 5 m^{2}g^{-1}, which is a marked improvement on the tee-piece mixers, which varied between 52 and 104 m^{2}g^{-1}.(Lester et al. 2006). These results suggested a significant influence of the type of mixing influencing the properties of nanoparticles produced in different reactors(Lester *et al.*, 2006, Lester *et al.*, 2010).

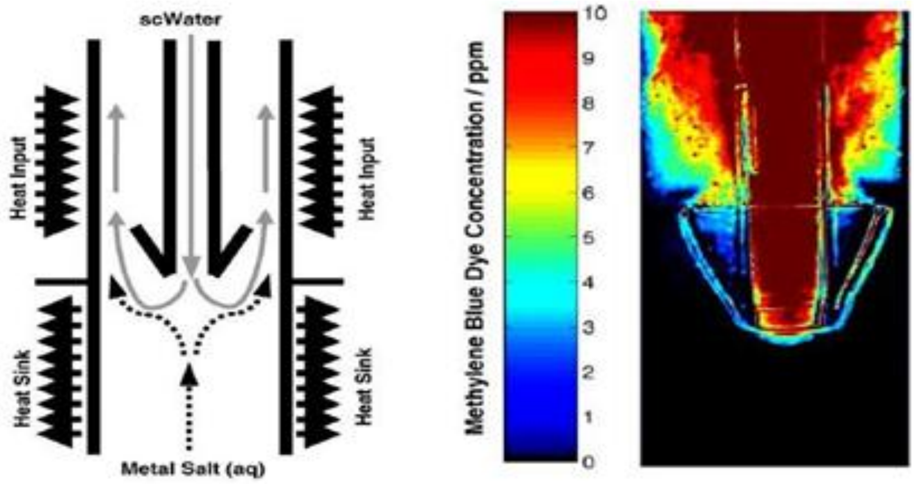

Figure 1.22: Design of counter-current "nozzle" mixer (left) and image of the result of modeling the reactor (right) as per the method of Blood *et al.*. (Lester, Blood, Denyer, Giddings, Azzopardi, & Poliakoff, 2006)

As the counter current reactor identified by Lester et al. showed some notable benefits in the synthesis of nanoparticles further work has been conducted to define the regions of particle nucleation and growth. (Middelkoop *et al.*,2009) This has been achieved by using high energy synchrotron radiation, and arguably this has been more informative than any of the modelling experiments which proceeded this analysis. (Middelkoop *et al.*, 2009) In the experiment, the steady state formation of CeO_2 nanoparticles was followed at a reaction point temperature of 335 °C, and a system pressure of 24 MPa. The results identified the location of particle growth and the distribution of particle growth across the mixer as shown in figure 1.23. The crystallite size distribution across the reactor was determined by calculating the crystallite size form narrowing of the CeO_2 (113) reflection. In figure 1.23 it can be seen that the highest concentration of ceria (nascent nanoparticles) is observed just above the terminus of the inner-tube (highlighted in grey) and in the annulus bound by the outer tube. In this experiment it was also evident that build up of material on the reactor wall occurs during long syntheses. The imaging represents a significant achievement in that information of this kind can be gleaned defining the regions within a reaction point where the nucleation and growth of nanoparticles occurs. Where, nucleation appears to occur at the interface between the preheated water and precursor, respectively. Showing that particle growth is complete within the window of observation when compared to data obtained from the product at the exit of the reactor.

From this review, publications highlighting results amalgamated from both modelling and experimental approaches are the most valuable, as they provide the greatest insight into particle formation. However, the difference in methods used to study mixing processes all have significant limitations. Although not explicitly stated above even designs of reactors are not exactly replicated by laboratories as such direct comparisons and true definition of the events leading to either undesirable mixing events (reactor blockage through material deposition) and the formation of true nanoparticles are very difficult to elude. For this reason much of the data presented in this thesis is focused towards further understanding of the particle formation reactions in different reaction points for the continuous hydrothermal synthesis of nanoparticles.

1.7 Advantages of CHFS as a Potential Manufacturing Process:

CHFS is a continuous flow process in which reactants undergo a rapid change to a condition of high supersaturation which typically leads to the formation of nanoparticles. As highlighted in the literature presented previously CHFS can be adapted to many synthetic challenges often forming products which are not readily accessible through more conventional methodologies (*e.g.* nanopartricles of kinetic or metastable products). The high supersaturation afforded by continuous hydrothermal methods generally leads to a large number of nucleation events and results in smaller particles than equivalent reactions performed on much longer time-scales (*i.e.* batch reactions). CHFS reactions are rapid with residence times in the order of a few seconds which means many reactions are complete and the desired material can often be made directly. Similarly, the literature suggests that because of the continuous nature of flow methods batch to batch variations can be reduced although not necessarily eliminated. (Lester *et al.*, 2006)

There are certain safety issues associated with operating a process of this nature. However, the hazards are difficult to assess and compare in any meaningful manner. Depending on many variables which vary as a function of pressure, temperature and volume CHFS and related methods are noted as being no more dangerous than comparable synthetic routes (*i.e.* batch hydrothermal processes). As long as appropriate precautions and maintenance procedures are put into place there should be no safety issues, the reaction volumes used in CHFS systems are much smaller than comparable batch reactions the process is a lot less hazardous as the operator has significant control over the reaction.

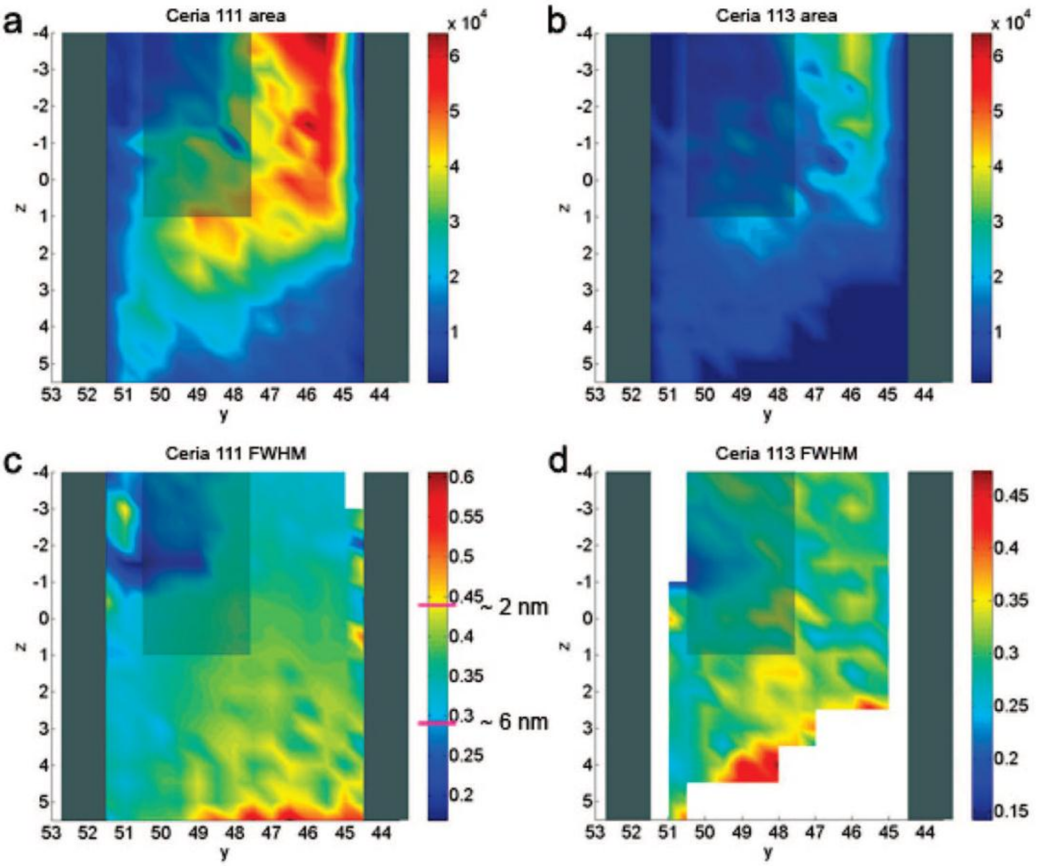

Figure 1.23: Images a and b show the distribution of the strongest ceria reflections, 111 and 113 appearing at 2θ) 5.14 and 9.75°, respectively, defining the regions where crystalline particles are present in the flow. Images c and d show the distribution of crystallite sizes within the window of observation determined from the peak widths of the ceria 111 and 113 reflections; in both cases, the smallest peak widths, which equates to largest average crystallite size, are found to be in the same region of highest intensity in of particles in images a and b. (Middelkoop *et al.*, 2009)

1.8 Disadvantages of CHFS as a Manufacturing Process:

The CHFS process and related flow methods typically produce materials at high temperature and pressure where particle formation is controlled by the solubility of ions (at a given synthesis condition). Where, as shown by Sue *et al.* the solubility of a metal ion precursor is an intrinsic property of the material this appears to limit the particle size range a typical CHFS process can produce if there are no other external process factors. Similarly, there are limits in the precursors available when the process is operated using water as conventional pumping equipment is not suitable to feed slurries or emulsions into a reactor. There are also limits as to what type of materials can be made; generally the process is limited to hydroxides, oxy-hydroxides and oxides of metals, although some phosphates (*e.g.* hydroxyapatite) can also be made. Additionally, other chemical processes which occur inside CHFS reactors are also poorly described and are known as experimental limitations although not exclusively stated as such within the academic literature. For example, halide ions cause significant corrosion in steel reactors and further limit the precursors that can be used. Nevertheless continuous and aqueous processing routes are attractive for the synthesis of nanomaterials as highlighted in Section 1.7.

1.9 Methods for the Large Scale Synthesis of Nanoparticles:

As the application areas of inorganic nanoparticles are expanding there is a greater demand for large quantities of nanoparticles (*ca.* > 100g) to allow for thorough commercial evaluation of nanomaterials identified in laboratory scale processes. (Tsuzuki, 2009) Inorganic nanoparticles have reached annual production volumes of several metric megatons. Most of the worldwide production of nanomaterials on an industrial scale can be assigned to carbon black, silica (SiO_2) and titania. (Kreuter, 1990, Liu *et al.*, 2009) These compounds are used in a wide range of application areas including the automotive (fuel additives) and food industry (packaging) or pharmaceutics (whitening/thickening agents). (Journet *et al.*, 1997) The large production volume of the highlighted nanopowders is counter balanced by the high production capacity of a very limited range of elemental compositions at an industrial scale. (Tsuzuki, 2009) One of the major reasons for the lack of composition variance (with the exception of the aforementioned materials) often arises due to a complication with the scale up of a previously identified process for their manufacture. (Dirksen & Ring, 1991, Kreuter, 1990)

This section aims to review the methods employed by academic groups or companies for the large scale production of nanoparticles. Although, many academic reports claim the large scale synthesis or facile scale up of a process the actual process in many cases operates at a production capacity of >1 g per batch or in flow processes 1-10g/h (low in comparison to the production capacities of carbon nanotubes for example). (Journet *et al.*, 1997). Currently there are over 100 commercial companies that produce large quantities (> 0.1 tonne/annum) of inorganic nanoparticles and achieve this through either direct volumetric or mass scale up, or scale out of the processes. (Jongen *et al.*, 2003, Tsuzuki, 2009) Figure 1.24 shows the distribution of methods used for the production of nanoparticles from *ca.* 100 companies as reported by Tsuzuki. (Tsuzuki, 2009) The output volumes are not reviewed as no reliable data has been sourced. However, liquid phase syntheses are dominated by the production of colloidal gold, silver and quantum dots. (Li *et al.*, 2003, Marchisio *et al.*, 2006, Pennemann *et al.*, 2004) Vapour phase methods are dominated by carbon-black (including nanotubes) and TiO_2 manufacture (specifically, Degussa P25). (Liu *et al.*, 2009, Tsuzuki, 2009)

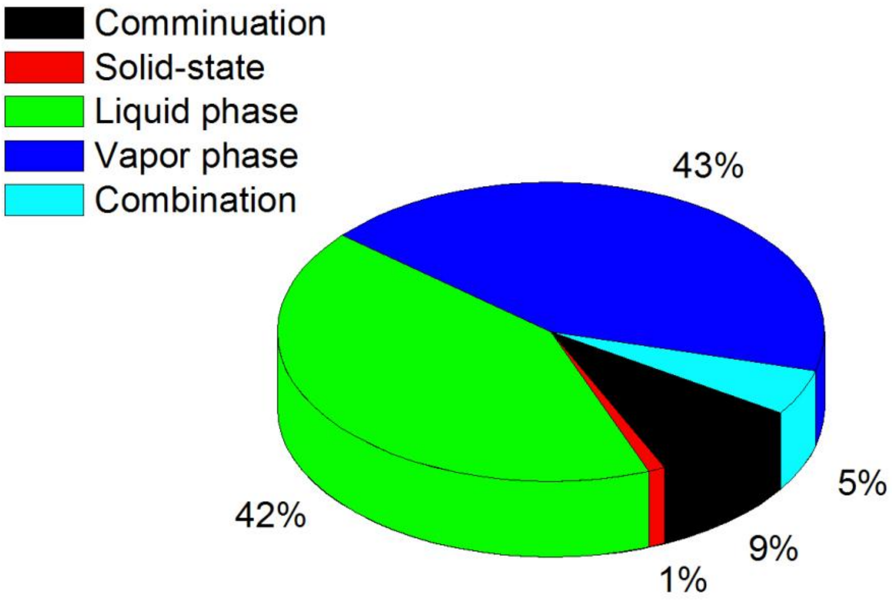

Figure 1.24: Distribution of nanoparticles production methods adopted for the industrial synthesis of nanoparticles. (Tsuzuki, 2009)

In almost all chemical processes, the difficulty in scaling up the production lies in achieving stable and uniform reaction environment, whether this takes the form of nanoparticles synthesis in large chemical baths (liquid phase) or combustion of precursors in a flame, most endeavours of scale up strive to ensure uniform quality of the resulting nanoparticles across production scales. (Kreuter, 1990, Marchisio, Rivautella, & Barresi, 2006) Although there are many general complications with increase in production rate; particle agglomeration during particle growth, elongated particle growth phases, loss of control over particle nucleation, compositional differences in materials (*e.g* material phase and homogeneity detailed reports of these phenomena are rarely published in any form). (Dirksen & Ring, 1991) The production of nanoparticles on a commercial scale often produces materials which are different to those produced by small scale processes requiring almost complete process optimisation. (Tsuzuki, 2009) The following section describes the issues associated with high output nanomaterials processing as divided in figure 1.24. A more detailed description of many of these process has been presented earlier within this review.

As the mechanical methods offer certain advantages for scale up including; relatively simple operation, ease of process enlargement and the ability to form slurries in liquid matrices they constitute *ca.* 10 % of commercial nanomaterial output. (Tsuzuki, 2009) In recent years, significant improvement have been made in adapting milling instruments and grinding media allowing for increases in process scale, which has led to significant progress in the use of this technique for the production of a wide range of nanoparticles. (Basset *et al.*, 1993, Konya *et al.*, 2002, Zhang, 2004) However, the top-down approach still suffers issues with process reproducibility and a production of a homogenous product (size and composition) stemming from low milling equivalency even when long processing times are used (several days) and several adverse effects in SiO_2 nanoparticles produced by milling have been identified when compared to other solution based methods. (Lam *et al.*, 2000) As initially noted in section 1.3.1, milling almost universally results in polydisperse particle size distributions, un-milled precursors in the final products and inhomogeneous materials. (Basset, Matteazzi, & Miani, 1993) In addition, longer milling times will result in more milling impurities (trace contamination) and structural defects in the materials processed which often add to the number of processing steps. (Lam, Zhang, Tang, Lee, Bello, & Lee, 2000) Although milling is a well known process for the production of nanoparticles compared to other solution and gas phase methods the materials produced show significant limitations if a certain size dependent material property is desirable.

The gas / vapour phase methods are more advantageous for the production of nanoparticles in an industrial context than milled materials. As materials produced in the gas phase are often produced directly with high crystallinity, low levels of contaminants and as particles with low polydispersity and as such find wider application (*i.e.* TiO_2 nanoparticles produced in the gas phase are used was whitening agents in paint for example). (Gupta & Tripathi, 2011) However, the method suffers from the inevitable trade-off between particle size/quality and throughput, as the throughput changes in many cases the flame and nucleation environments within a reactor also change. (Geohegan *et al.*, 1998, Kruis *et al.*, 1998) It is reported that particle growth is evident at high process yields, due to high temperature operations and lack of a solid medium that hinders agglomeration. (Pratsinis & Vemury, 1996) Normally the resulting nanoparticles in commercial scale production have characteristics of high crystallinity, a wide size distribution and evidence of agglomeration or particle sintering. (Kruis, Fissan, & Peled, 1998) The materials are exclusively produced as dry powders and this limits the versatility of the synthesis for some applications of nanoparticles. Similarly, as the nanomaterials are produced in the gas phase the processes require heavy capital investment in engineering measures to isolate workers from nanoparticle production. (Pratsinis & Vemury, 1996)

Of the three main methodologies for the commercial synthesis of nanoparticles, the liquid phase methods are the most attractive in terms of scale up due to the diverse chemistry accessible in the liquid phase. (Xia *et al.*, 2003) However, the difficulty in scaling up production is associated with achieving stable and uniform reaction environment in the synthesis medium. (Park *et al.*, 2004) Where, stringent control is difficult to achieve due to concentration gradients, thermal gradients and inhomogeneity in mixing reagents in large volumes. (Dirksen & Ring, 1991) Increasing the production rate in this context requires high particle concentration which causes particle agglomeration, particle growth and in some cases loss of control of particle polydispersity. (Park *et al.*,2004) As a result, nanoparticles in commercial scale production have characteristics of spherical shapes, a narrow size distribution of primary particles but high degrees of agglomeration if they are produced without effective surface functionalisation. As much of the commercial production of nanoparticles form the solution phase is related to the synthesis of colloidal dispersions of nanoparticles. A notable example of a moderate scale solution based process is the thermal decomposition technique developed by Hyeon’s group in Korea, to data it is the largest reported batch synthesis of surface functionalised nanoparticles. (Hyeon *et al.*, 2001, Park *et al.*, 2004) A scheme showing the process is presented in figure 1.25. These functionalised nanoparticles were prepared as batches of upto 40g by decomposition of iron-oleate salt precursors in octadecane solution heated to 320°C for the decomposition of the complex to metal oxide using oleic aide as a capping agent for a reaction time of 6 h. In this report the crystallite size could be controlled by using various solvents with different boiling points. The corresponding metal nanoparticles can be prepared by the self reduction at higher reaction temperature. This route is presented as it is widely reported as a general process for the industrial production of metals, metal oxides and multi-metallic oxides without further size-selection steps.

As some methods have now been applied to the synthesis of large quantities of nanoparticles it is important to review the health and environmental aspects of production of nanoparticles. A review of this nature serves to identify processing methodologies which would be favoured for long term manufacture and processing. From this section it was identified that the scale up of liquid phase synthesises would be the most attractive in terms of the chemistries accessible and the diverse range of chemical compositions that are accessible and the materials *(sic)* produced by these strategies would probably find the widest application.

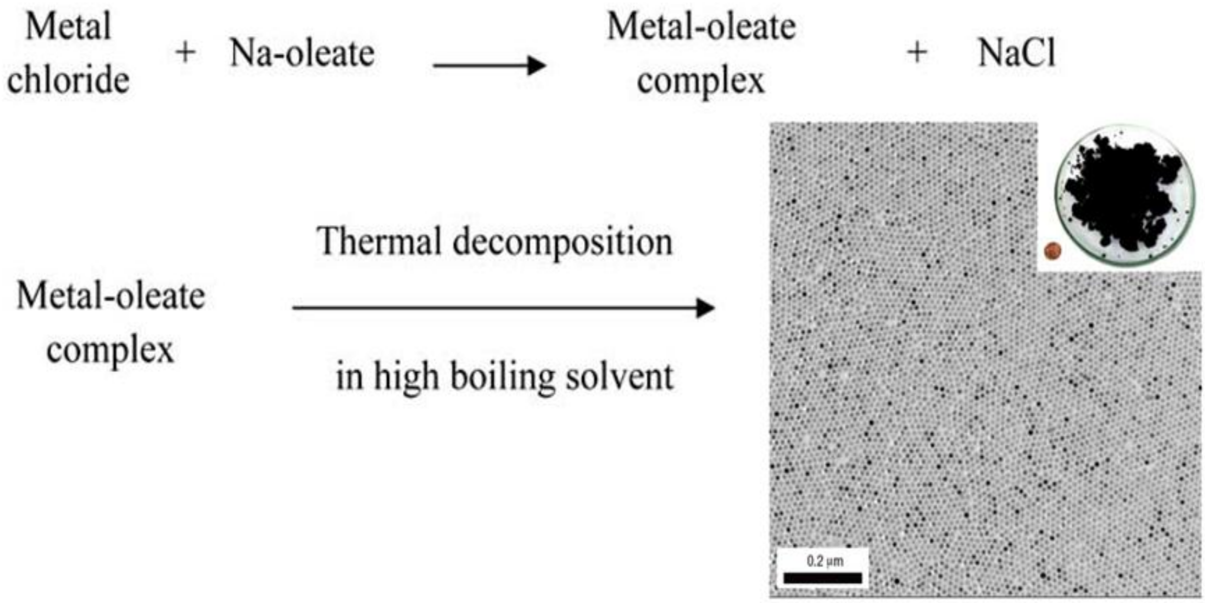

Figure 1.25: The overall preparation scheme of monodisperse nanoparticles by decomposition of metal oleate precursors. 12 nm magnetite monodisperse nanoparticles.

Inset is a photograph showing a Petri dish containing 40 g of the monodisperse magnetite nanoparticles. (Park *et al.*, 2004)

1.10 Safety and Cytotoxicity of Nanomaterials:

There are many unique hazards associated with nanoparticles, in addition to the normal chemical hazards associated with the corresponding bulk materials and are manifested by many mechanisms of cytotoxicity. A summary of the known mechanisms of nanoparticle interaction with biological tissues are presented in figure 1.26, which shows the diversity in the mechanisms of nanoparticles toxicity. (Nel *et al.*, 2006) In several notable examples the toxicity of certain nanomaterials have been evaluated in great detail. (Oberdorster *et al.*, 2005a) For example, it is well known that cadmium selenide quantum dots can lead to cadmium poisoning in the body and free radicals (ROS) generated on the surface of semiconductor nanoparticles can cause DNA damage. (Xia *et al.*, 2006) However, broader and more generalised descriptions of the toxicity of nanomaterials are well accepted due to the vast compositional space present in the field. (Warheit *et al.*, 2009) Where, all nanomaterials are thought to be a pulmonary hazard. (Sayes & Warheit, 2009) The work of Lin *et al.* showed that nanoparticles of ZnO cause dose and time dependent cytotoxicity in human lung tissue when particles of 70 and 420 nm were evaluated. (Lin *et al.*, 2006) Oxiditative stress is thought to be a large contributory factor in the cytotoxicity of nanoparticles (carbon black, carbon nanotubes, silica and ZnO). (Oberdorster *et al.*, 2005b) The properties of fiberous nanomaterials (*i.e.* carbon nanotubes) have also been found to have carcinogenic effects analogous to asbestos fibres. (Poland *et al.*, 2008) As nanoparticles can gain access to cells and blood through inhalation and ingestion and for nanoparticles such as quantum dots possibly through skin penetration, it is generally considered best practice to ensure exposure is minimised in the route chosen for their manufacture in an attempt to minimise the risk of nanoparticle toxicity. (Oberdorster, Oberdorster, & Oberdorster, 2005a, Oberdorster *et al.*, 2005b) The composition, shape surface structure charge aggregation and solubility all effect the cytotoxicity so it is difficult to generalise in the hazards of nanoparticles and often nanoparticles of many materials are simply treated as hazardous with no knowledge of specific toxicity *i.e.* tetratogenic effects, mutagenic effects, *etc*. (Nel, Xia, Madler, & Li, 2006) Hence, it is reasoned that the safest and most effective strategies for the production of nanoparticles are those which produce nanomaterials in the liquid phase to minimise the potential for exposure.

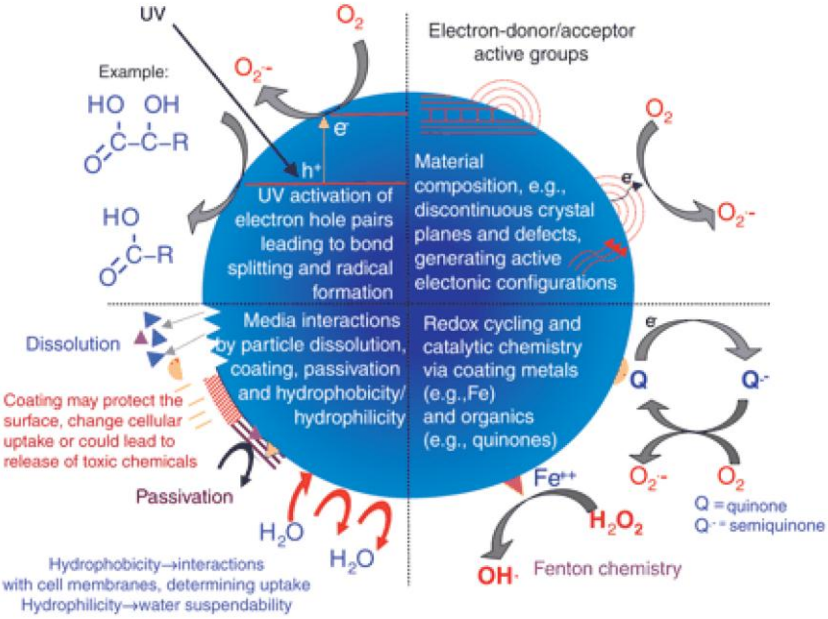

Figure 1.26: Summary of the mechanisms by which nanomaterials interact with biological tissue. The quadrants of the figure illustrate the importance of material composition, electronic structure, bonded surface species (e.g., metal-containing), surface coatings (active or passive), and solubility, including the contribution of surface species and coatings and interactions with other environmental factors. The figure also highlights how different materials mediate toxicity. (Nel, Xia, Madler, & Li, 2006)

1.11 Environmental Impact of Nanomaterials:

The environmental impacts of the release of nanomaterials and wastes which contain nanomaterials is a subject that has not been evaluated as thoroughly as the potential human health aspects to exposure to nanomaterials. (Biswas & Wu, 2005) As many unique hazards are associated with nanoparticles in addition to the normal chemical hazards associated with the corresponding bulk materials in complex ecosystems are far more difficult to evaluate or predict the acute or chronic effects of nanoparticle release. (Klaine *et al.*, 2008, Lam *et al.*, 2006, Navarro *et al.*, 2008) However, an increase in funding by research bodies has spurred development of this area. There have been several notable studies which have shown that nanoparticle containination even at low level affect microflora and the release of nanoparticle wastes or effluent containing nanoparticles should be avoided. (Navarro *et al.*, 2008) However, the fate and persistence of nanomaterials within food-chains and aquatic systems is of ongoing debate and the subject of many reviews. (Biswas & Wu, 2005) Recently, a study published by Jarvie *et al.* found that nanoparticles of common cosmetic additives (silica nanoparticles) could effectively be removed from waste water through the introduction of a flocculent before introducing them into sewage meant that the nanoparticles interacted with components of the sewage to form a solid sludge. This sludge can was separated from the waste water and disposed of by common sedimentation clarification procedures preventing entirely the release of nanoparticles. (Jarvie *et al.*, 1997) By contrast, uncoated nanoparticles stayed dispersed in the wastewater and were likely to continue through the effluent stream. This study showed the complications of adapting waste treatment protocols to deal with effluents contaminated by wastes. (Jarvie *et al.,*1997)

Within the United Kingdom the disposal of nanoparticulate waste and wastes contaminated with nanoparticles (RPE, Gloves, Spillage kits, etc) is governed by best practices rather than being legislated. Guidance provided by the Environment Agency provides a framework for assessing whether a waste material is hazardous and a process by which it can be disposed of (HWR01). Where, typically all waste contaminated by nanomaterials is to be disposed of as chemical waste (ICS 13.100; 71.100.99). However, there are currently no legal requirements to dispose of nanomaterials or effluents contaminated by nanomaterials in any particular manner (as long as the constituent metals are not classified as hazardous) and the volume of effluent does not exceed 1000 Tonnes/annum. (Oberdorster *et al.*, 2007)

In light of the available environmental impacts of nanoparticle release and the subject of this thesis. Several protocols were adapted to mitigate the environmental impacts of the work. Throughout this thesis, effective sedimentation and effluent clarification protocols have been devised to limit the disposal of aqueous waste contaminated with nanoparticles. No metals listed as toxic to aquatic organisms are used throughout this thesis. This section has been included for the interest of the reader due to the nature of the work presented. The work presented herein has as close to practicable been conducted in accordance with these guidelines.

1.12 Summary of Literature:

The literature review presented has highlighted the benefits of nanoparticles in certain applications, the methods used for manufacture and the progress to date in the development of continuous processes for their manufacture. Current techniques for producing many nanomaterials are sufficiently well characterised and optimised to allow control over particle properties. However, many methods are not applied to the synthesis of large volumes of nanomaterials limiting meaningful application of the nanoparticles produced by many methodologies. Similarly, the evaluation of many material compositions as nanomaterials is constrained by difficulty in producing the material with dimensions approaching the nanoscale. Many techniques are being developed to produce “improved” nanosized materials, but these suffer from their own problems; they may be time consuming, multi-step, produce free nanoparticles which are potentially hazardous, or suffer batch variation, use expensive chemicals or are poorly scalable (volumetrically or otherwise) limiting the amount of material available for characterisation or through evaluation in any given application.

From the preceding literature review it was concluded that Continuous Hydrothermal Flow Synthesis (CHFS) is an efficient methodology for the synthesis of a large variety of metal oxide nanoparticles. Typically, nanomaterials are produced directly through the use of both sub and supercritical water to rapidly and continuously precipitate homogenous nanomaterials (in both size and composition if > 1 component metal ions are present). Moreover, the nature of the process being; **1)** a flow system (*i.e* method of continuous synthesis) and **2)** process where particles form by rapid reaction on time-scales of < 2 s may be able to produce nanomaterials of equivalent size and composition at higher scales of synthesis. However, despite being relatively high temperature (*ca.* 380 ºC), the process is still conducted in aqueous solution, and therefore will not produce free nanoparticles, will not require environmentally damaging solvents or otherwise expensive reagents. When compared to many of the large scale processes currently employed for the production of nanoparticles CHFS confers certain key benefits in terms of both the breadth of chemistries accessible by the methodology and the fact that nanoparticle synthesis is contained. A review of the concerns relating to nanoparticle manufacture suggests that aqueous processing methodologies will be favored in the long term as both efficient effluent treatment and containment protocols can be applied to mitigate many concenrns.

1.13 Hypotheses:

In the proceeding literature review it was highlighted that CHFS is a versatile technique for the synthesis of nanoparticles of many compositions. As CHFS is a continuous process it also confers certain advantages for control over the reaction and unlike batch processes can be used continually to produce a desired quantity of material. It was postulated that the rapid nucleating and crystallising environment within a hydrothermal flow reactor maybe a scalable methodology for the synthesis of a broader range of nanomaterials than are produced by liquid or gas phase methods. Furthermore, the large number of variable system parameters and the high degree of control afforded by flow processes may provide control over particle properties. In addition, there is a large amount of flexibility in the design and operation of CHFS systems such that, for example, improvements to such systems could also be made to allow for the production of materials of specific interest. The overall hypothesis of this thesis can be broken down into the following objectives, presented alongside a statement of how each theme contributes to the main subject of the thesis:

- Investigations into the design and application of reaction points suitable for the continuous hydrothermal synthesis of nanoparticles. These investigations will define the process conditions which can be used to produce nanoparticles. These investigations are performed with a specific emphasis on the effects of different processing conditions by linking other observation based measurements to process outcomes. Investigations of this type will allow the formulation of a better description of particle formation dynamics in continuous hydrothermal systems. This will provide a more coherent description of particle synthesis dynamics than can be mined from the literature. These definitions will then be used to investigate if the process is amenable to volumetric enlargement, forming the basis of scale up reactions.
- The addition of other feeds to continuous hydrothermal processes has also been under explored in the literature. As such, investigations into the modification of a CHFS process to allow for the introduction of reagents after the formation of nanoparticles is also presented. The purpose of these investigations is to evaluate if continuous processes are amenable to further refinement, allowing the synthesis of surface functionalised materials. As the surface functionalisation of nanoparticles is desirable in many applications, the characterisation of surface functionalized materials produced using CHFS and their utility in biomedical and other applications is presented.
- As hydrothermal processes are often limited by thermodynamics, often by the reaction temperatures usable in hydrothermal systems are not being sufficintly high

to produce oxides of many metals. An investigation of materials produced by CHFS as nanosized precursor materials for conversion to nanosized oxides, through a moderate heat treatment strategy is also presented. The post processing is evaluated in terms of its effect on material properties with a specific emphasis on size and agglomeration and the formulation of stable nanoparticle dispersions.

- The final aspect of this thesis is an investigation into the development an application of a pilot scale CHFS. Particular attention has been paid to the scale up of nanomaterials using two strategies; Volumetric scale up and increasing the product per-unit volume (concentration) and the effect of scale up strategy is highlighted with respect to the properties of nanoparticles. These investigations serve to define the limits of scale up using CHFS and to assess if many of the process attributes developed within the thesis are suitable for the large scale synthesis of nanoparticles.

In summary, this thesis will describe the evaluation of the CHFS process and evaluate if the process is amenable to scale up. This thesis will also investigate whether further process adaptations can allow for the synthesis of materials of interest. This thesis draws correlations between the properties of nanomaterials produced at different scales and provides explanations for the observations based on various process aspects.

CHAPTER 2

Materials and Methods

2.1 Introduction:

This chapter concerns the experimental methods and processes used in this thesis. This includes details of the continuous hydrothermal flow synthesis (CHFS) systems, different synthesis methodologies (certain calculations and reaction conditions), characterisation techniques (sample preparation and measurement details) and any modifications to methods and procedures used. In certain cases, for clarity the methods are also described briefly within the chapters they feature as this thesis is largely concerned with the development of aspects of the CHFS process to produce desired materials. As such, the results obtained in later chapters are often derived from modified methods or alterations to methods identified in preceding chapters. However several pieces of equipment were used extensively alongside simple analysis. Thus, the purpose of this chapter is to describe these.

2.2 CHFS Process Equipment:

2.2.1 Description of the CHFS Process:

The first CHFS process used as the core design throughout this thesis was built by Professor J.A. Darr and Dr P. Boldrin at Queen Mary University London. (Boldrin *et al.*, 2007) The modification and evaluation of this system to produce a variety of materials is described as the subject of this thesis (a schematic diagram of this process has been presented in Chapter 1 section 1.3). CHFS systems based on a number of pump configurations were used throughout this thesis and the purpose of this section is to describe the core design of the apparatus used for the production of nanomaterials and identify the key components of each reactor.

2.2.2 CHFS System 1:

Stemming from the initial design constructed by Boldrin *et al.* the CHFS process used by the CMTG group has been incrementally modified and improved. (Boldrin *et al.*, 2007) This section will describe the core system design used to synthesise materials and investigate the properties of the CHFS process. A flow diagram of CHFS system 1 is shown in figure 2.1, it shows a three-pump configuration, each of which being used as an independent feed line to allow for the introduction of reagents to the CHFS process. All pumps were fitted with 25 ml piston pump heads, (Gilson, SC-type) unless otherwise stated. Pump 1 was exclusively used to provide a feed of > 10 Mega Ohm DI water to the heaters, allowing the feed to be preheated prior to entering the main body of the process. Pump 2 was exclusively used to supply an aqueous metal ion solution (precursor) feed, and Pump 3 was used as a supplementary feed (auxiliary) feed which could also be used to supply reagents (base, metal salts, *etc.*). Feeds were contained in appropriate beakers and the HPLC pumps required priming prior to system start-up (all feeds could be independently controlled). Each “feed line” was constructed from 1/8” 316 stainless steel seamless tubing, hereafter referred to as 316 SS (Swagelok, UK) and swagelok fractional fittings (316 SS, Swagelok). The Gilson pumps were connected to the system using a 1/16″ SSI fittings and 1/16″ outer diameter (OD) tubing to minimise total system volume. The 1/16″ tube was converted into 1/8″ at a reducing union and passed through a check valve (1/8″ fittings), as a safety feature to prevent backflow, and into a 1/8″ cross piece. Of the other three arms of each cross piece; one was connected to a Swagelok proportional pressure release valve (1/4″ fittings), which were connected to the system in parallel, the relief valves were set to a relief pressure of *ca.* 28.2 MPa. A 40 MPa pressure gauge (RS components, London) was also installed allowing continuous monitoring of the system pressure during a reaction, connected in series to each of the feed lines (figure 2.1). The final arm for the precursor and auxiliary feed lines was connected to a tee-piece to the premix the precursor feeds at this point, this design feature was included in all CHFS systems as it allowed in-line premixing of precipitation agents (e.g. KOH, NaOH etc.) with a metal ion feed. HPLC pumps are not suitable to pump slurries, hence the requirement for this addendum. The final arm of the scH_2O feed was connected to the heater at this point (the design of the heater is described in section 2.2.3). All reagents were brought together to mix in a specified reaction point geometry. A list of the reaction point geometries and their construction is presented in a later sections.

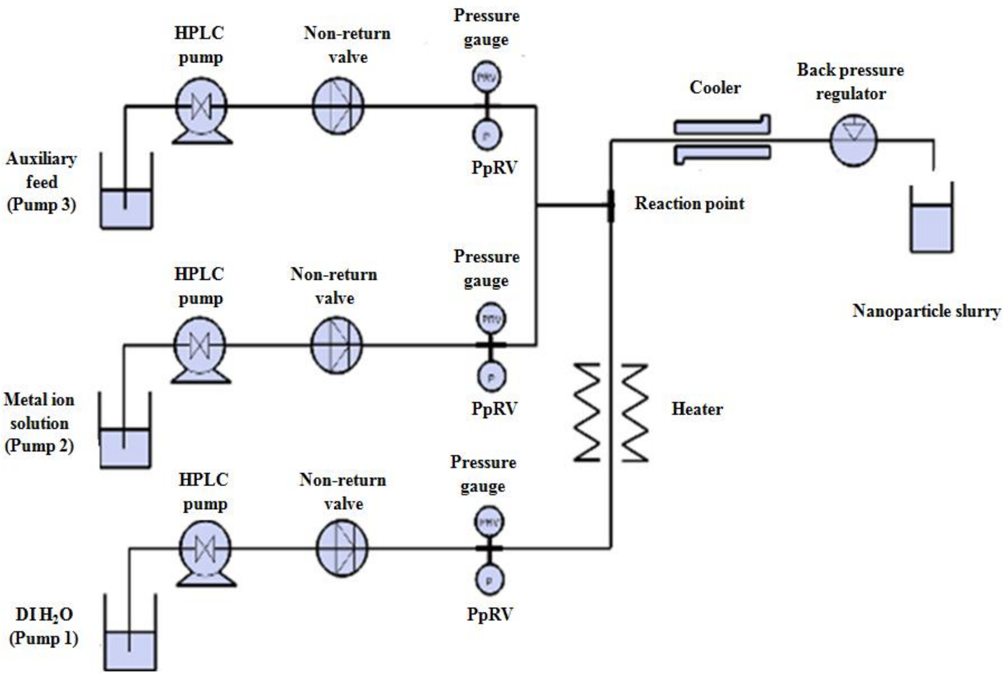

Figure 2.1: Schematic diagram of the laboratory scale CHFS process. PpRV = proportional pressure relief valve.

The products issuing from the reaction point were fed into a heater exchanger to cool the reaction mixture to near room temperature before exiting the system. The mixing point was connected to the cooler *via* a suitable reducing union constructed of 316SS and was dependent upon the reaction point geometry chosen for synthesis. Figure 2.2 shows a labeled schematic of the coolers construction in all experiments the cooler was operated in a counter-flow configuration. The cooler was made entirely from Swagelok™ parts. As shown in figure 2.2 the reaction product flowed through an inner tube. The inner tube was constructed of 1/4” 316SS Swagelok™, which passes through the middle of a 3/4” 316SS Swagelok™ tube. Cooling water flows in between the inner and outer tubes at a nominal flow rate of 6 L min^{-1}. At the ends of the outer tubing are two brass 3/4” tee pieces, with a 1/4” – 3/4” bored through reducer at each end to allow the 1/4” inner pipe to pass through whilst forming a seal to maintain the cooling water pressure (*ca.* 4 - 7 bar). To the other outlet of the tee pieces are attached 3/4” – 3/8” reducers which were used to connect the cooling unit to an external recirculating chiller. The total cooler length used for the synthesis of all nanomaterials on the laboratory scale processes were 55 cm. Under all given synthesis conditions this length was shown to maintain the outlet water temperature below 30 °C. (Ma *et al.*, 2011) The coolant (5 % ethylene glycol in water) was maintained at a constant temperature of 10 °C by a Thermoflex 5000 chiller (4.4 kW

Thermoscientific). The cooled suspension of nanoparticles passed through a manually operated back pressure regulator (BPR, Tescom) which was used to maintain the system pressure at 24.1 MPa. After each reaction or set of reactions the mixing point was removed for cleaning and maintenance.

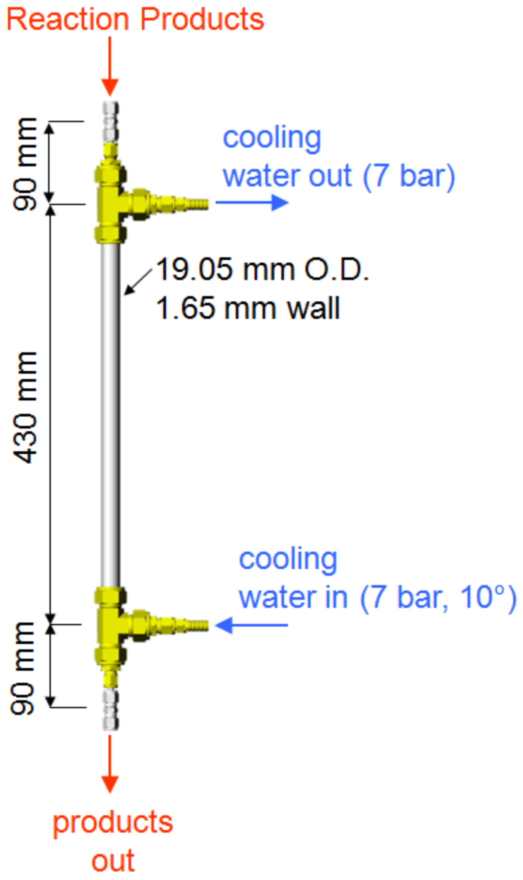

Figure 2.2: Schematic diagram of the pipe-in-pipe cooler used in for laboratory scale CHFS systems.

2.2.3 Heater Design:

A custom-built electrically powered pre-heater was used to heat the feed issuing from pump 1 as defined in figure 2.3 in all laboratory scale CHFS systems. The design is shown in figure 2.3 a (as a photograph of the complete heating unit) and schematically in figure 2.3 b-c. The heater was controlled by a digital heater controller (Watlow) with an alarm trip which was controlled by the alarm thermocouple (defined in figure 2.3 c). The alarm was set to just above the maximum working temperature of the heater (*ca.* 460 °C). The heater core was made of duralumin for good thermal conductivity. A cartridge heater (1 kW Firerod ™, Watlow) was inserted into the centre of the core and the output of two 'J' type thermocouples (Watlow) were used to both monitor and control the temperature. One was inserted in to the top of the heater to control the temperature and one was inserted into the base of the core as a safety feature and connected to the alarm. The heating coil thorough which the feed issuing from pump 1 passed was approximately 6 m of ¼" (OD) tubing was coiled tightly around the core (ensuring intimate contact) as shown in Figure 2.3. To add capacity to the heater two 750 W band heaters (10.1 cm deep, by 6.35 cm diameter, Watlow) were fixed around the coil. The whole assembly was then insulated to mimimise heat loss by using a microtherm flexible insulating quilt (RS components, London) and ceramic blanket insulation (Kitsons thermal supplies, Dawlish). The components of the heater were secured between two circular stainless steel end plates were held together with brass studding (figure 2.3 a).

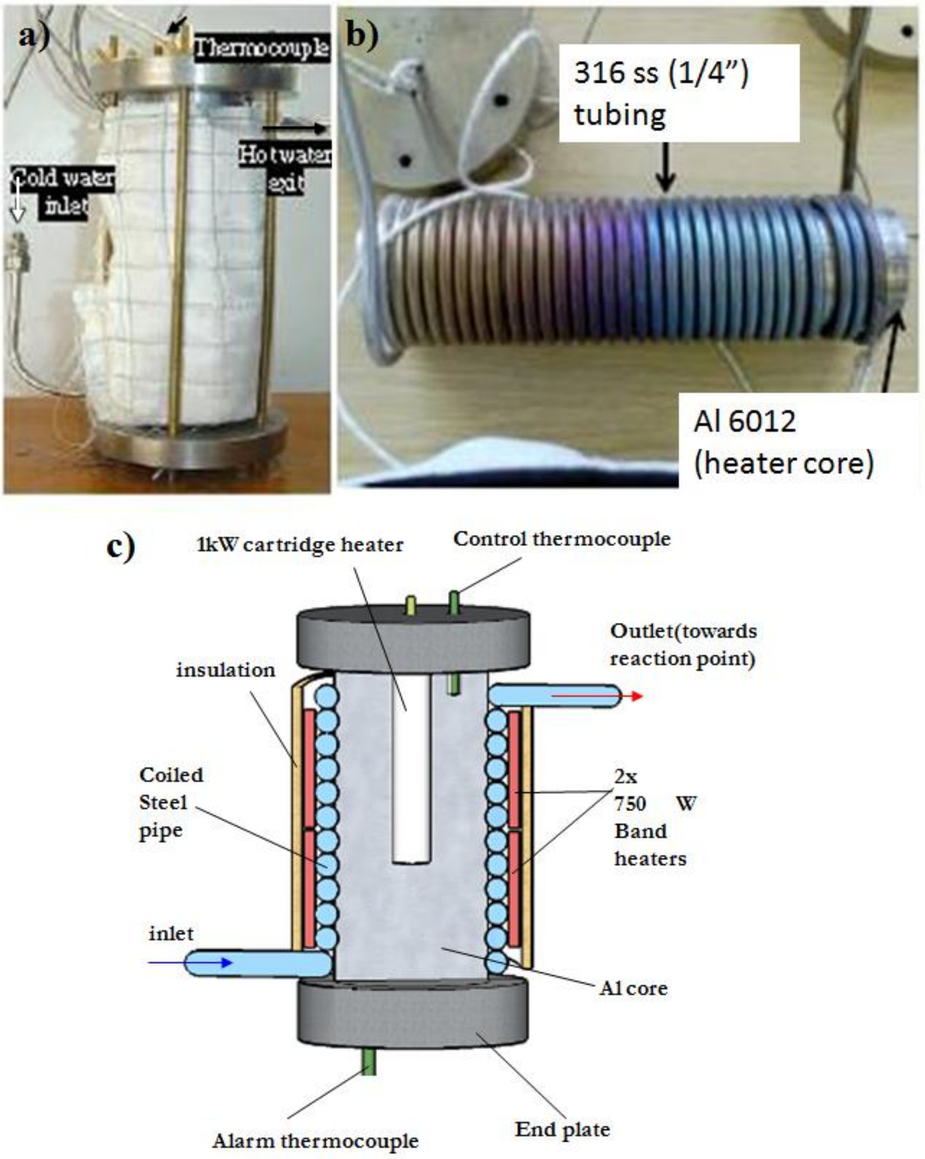

Figure 2.3: The custom made heater used on the laboratory scale CHFS process **a**) a photograph of the complete heater assembly **b**) diagram of the heater construction showing the Al core and wound 316 SS tubing **c**) A schematic diagram of the completed heater graphically representing the position of all components (Adapted from Kellici 2006).

2.2.4 Reaction Point Geometries:

All reaction points used in this work are used in conjunction with CHFS system design 1 (section 2.2.2). Where, the system was designed to allow different reaction points to be substituted by simply modifying the position of feed lines issuing from any of the pumps. Within this thesis reaction point geometries of two main types were evaluated; a counter-current geometry where the precursors and hot water were mixed in opposing flows and a co-current type where the precursors and pre-heated water were introduced co-axially. The co-axial type geometries are hereafter referred to as “Confined Jet mixers” (CJM) stemming from the mechanism of mixing defined in chapter 4 (the terms co-current reactor and CJM are used interchangeably and depend on the subject of the discussion).

2.2.4.1 Counter Current Reaction Point Geometries:

The counter-current reaction point used in this thesis was developed from a counter-current reactor based on a concept by Lester *et al*. and is shown pictorially in figure 2.4a and schematically in figure 2.4.b. (Lester *et al.*, 2006) The counter-current reactor was constructed of a 1/8” 316SS swagelok pipe swaged into a 3/8” 316SS Swagelok cross-piece through the use of a bored through reducing union. The superheated water (from the feed issuing from pump 1 and passing through the heater) flows downwards into the mixing point through the inner 1/8″ tube, and the metal salt solution flows upwards through the 3/8″ tube as the combined output of pumps 2 and 3 (within the reaction point the precursor meeting the pre-heated water was either a soluble metal salt or a precipitate formed by mixing a metal salt with a precipitation agent such as KOH). The exit of the reaction point where the products of the reaction pass is connected to the cooling apparatus through 3/8” 316SS tubing with an approximate length of 220 mm. The total reactor volume defined from the terminus of the pre-heated water inlet and the start of the cooler was 26.4 cm^3.

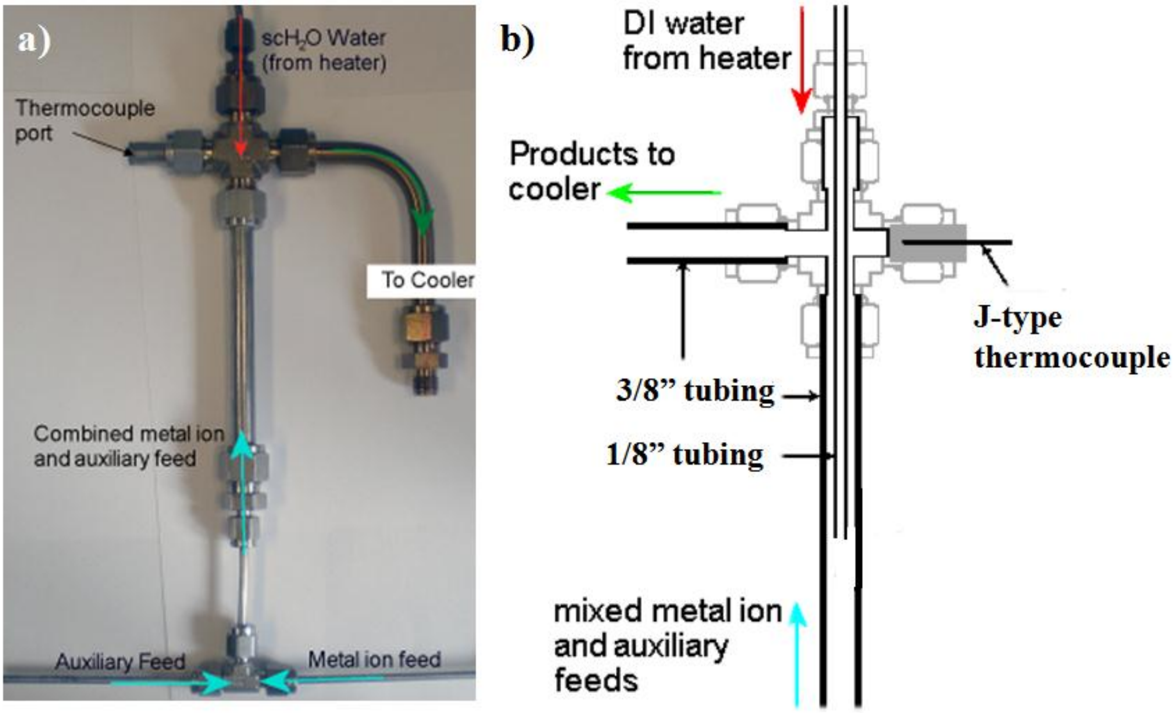

Figure 2.4: a) A photograph of the counter-current reactor showing the orientation of feeds **b)** A technical drawing of the counter-current reactor showing the terminus of the preheated water inlet (as a mirror image of figure 2.4a).

2.2.4.2 Confined Jet Mixer:

The CJM reaction point geometries used in this work were developed through the course of Chapter 4. This section aims to provide a brief description of the geometry and combinations of components used in their construction. Figure 2.5 shows a schematic representation of the reaction point type used in this work, defining the components used in construction. The CJM reaction points were constructed of fractional 316SS swagelok components. The size of the components varied according to the physical size reaction point chosen for evaluation. In general, the feed issuing from the heater was reduced from ¼" tubing to either 1/16" or 1/8" in. tubing thus forming the inlet to the reactor. The inlet to the reactor was passed into a cross piece ¼" or 3/8" by the use of an appropriate bored through union. The precursor solutions were fed into the reactor through the cross piece symmetrically using the inlets perpendicular to the pre-heated water feed inlet (as shown in figure 2.5). The inlet tubing issuing from the pumps was 1/8" Swagelok and was connected to the arms of the cross piece using an appropriate union. The cross-piece was connected to the cooling apparatus by an appropriate length (*ca.* 220 mm) of either ¼" or

3/8” Swagelok tubing. The tubing connecting the cross piece to the cooling apparatus contained the flow issuing from all pumps after mixing in the annulus shortly beyond the terminus of the inlet of pump 1. In this configuration the metal salt solution (combined flow issuing from pumps 2 and 3) flows upwards through the cross piece in the annulus formed around the inlet of the feed issuing from pump 1.

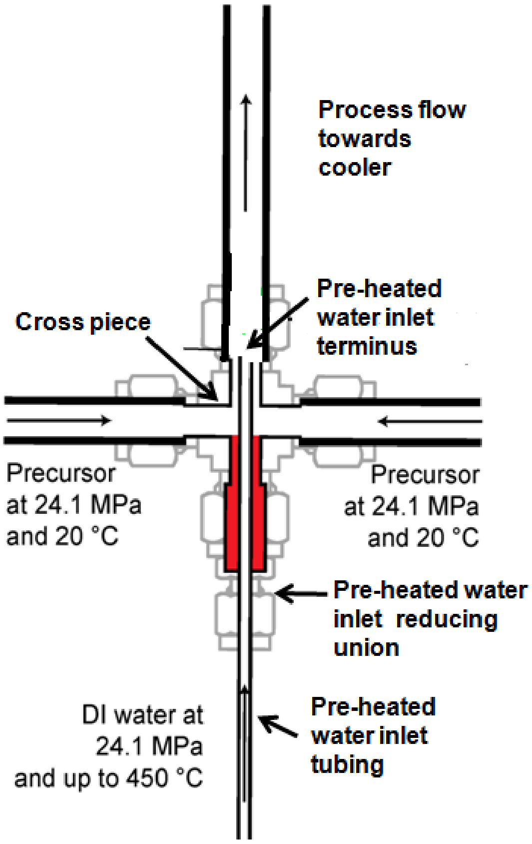

Figure 2.5: Schematic diagram of the CJM type reaction point geometries used in this work.

2.2.5 CHFS System 2:

The second CHFS system built during the course of this work is identified as CHFS system 2 and a schematic of the modified process is presented in Figure 2.6. It was designed and built by R. Gruar and Professor. J. A. Darr. The design is similar to that of CHFS system 1 in relation to all components upstream of the reaction point and down-stream of the cooler. However, instead of using a 1/4” 316SS Swagelok cross-piece and tubing in the CJM reaction point, a ¼” 316SS Swagelok tee-piece and tubing was added upstream of where the precursors and preheated water mix allowing the introduction of another reagent feed to the system shortly after the formation of nanoparticles. The added feed line (feed line 4) was analogous to the construction of other feed lines. The added feed line consisted to two Gilson pumps (25 mL pump heads) which were connected in series and subsequently connected to the CHFS system through the use of 1/16″ tube tubing. The flow from feed line 4 passed through a check valve (1/8″ fittings), as a safety feature to prevent backflow, and into a 1/8″ cross piece consistent with the assembly used in CHFS system 1. This feed also had a independent Swagelok proportional pressure release valve (PpRV, 1/4″ fittings) set to a relief pressure of 28.8 MPa and a 40 MPa pressure gauge (RS components) which allowed continuous monitoring of the system pressure during a reaction as detailed in the process diagram (figure 2.6). The cooler design used in this system was identical to that outline previously for CHFS system 1 and was shown to be suitable to maintain the slurry exit temperature below *ca.* 40 °C under all experimental conditions reported. (Ma *et al.*, 2011)

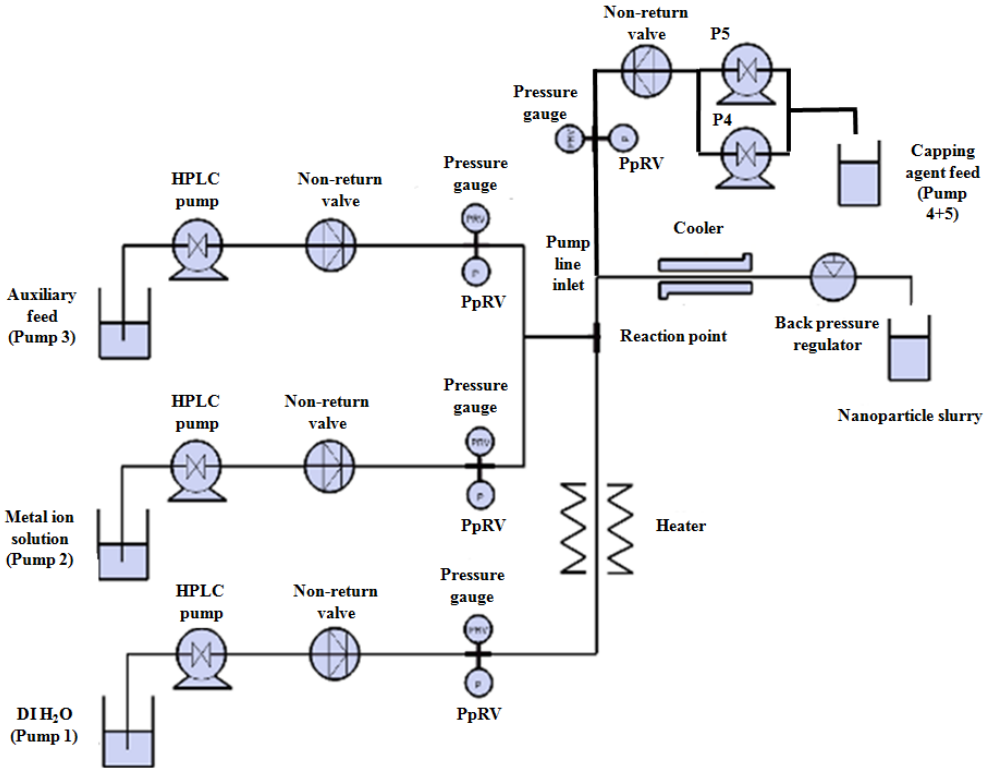

Figure 2.6: Schematic of the 5 pump CHFS system (CHFS system 2).

The modified reaction point geometry used for the introduction of the feed issuing from pumps 4 + 5 was based on a counter current reaction point. A schematic of the reaction point is presented in figure 2.7. The modification of the geometry used on the laboratory scale process consisted of a 1/16” 316SS swagelok tube swaged into a 1/4” 316SS

Swagelok Tee-piece using a 1/16” bored through reducer allowing the tube to extend into the stream of nascent nanoparticles coming from a ¼” CJM type reaction point. The superheated water flow issues upward into the mixing point through the inner 1/6″ tube, and the metal salt solution flows upwards through the 1/4″ tube. The exit of the reaction point where the products of the reaction pass was connected to the cooling apparatus through a variable length of 1/4” 316SS tubing (explained further in Chapter 6). The total reactor volume defined from the terminus of the preheated water inlet to the inlet of feed line 4 was varied from 4.5 cm to 35 allowing variation of the residence time. Similarly, variation of the length of tubing between the inlet of feed 4 and the cooler could be used to vary the residence time after the addition of feed 4. Dimensions used to referrer to this geometry state the reactor volume in each reference.

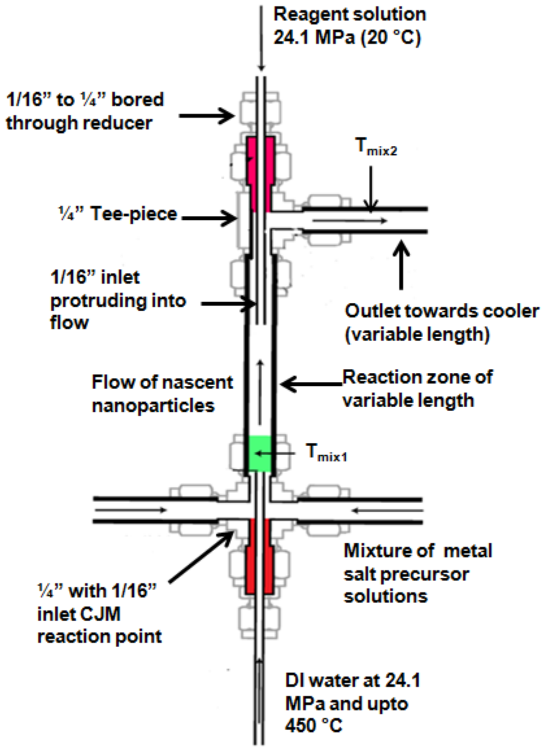

Figure 2.7: The modified reaction point geometry used for the introduction of feed 4 into the CHFS system. The green zone represents the region in which nanoparticles form and the red zones represent region of low flow velocity (stagnation zones). $T_{mix\ 1}$ defines the reaction point temperature (for the formation of nanoparticles and T_{mix2} defines the temperature after mixing the products of the reaction with feed 4.

2.2.6 Measurement of Temperature within Reaction Points:

Temperature profiles were measured inside different reaction points by inserting four fine thermocouples (type J, stainless steel sheath, 0.5 mm OD, 1.0 m length) into the apparatus, between the cooler and the BPR as indicated in Figure 2.8 a, each of which terminated at a different position within the reaction point, the positions of each thermocouple are defined in chapter 3 and 4 and were chosen on the basis of preliminary observations. These measurments were used to provide an indication of the mixing processes occuring within reaction points. A spectite MF series thermocouple port (Spectite , UK) was used to insert the termocouples into CHFS system 1 and a VITON (spectite, UK) seal was used to allow measurements at pressure. A diagram of the fitting is presented in figure 2.8 b. Sufficient measurements were taken in runs of 4 to allow for evaluation of the heat and mass transfer processes occuring in a reaction point, in the case of the pilot scale CHFS process (described later) 8 simultaneous measurements of temperature could be taken. The cross-sectional area of the four thermocouples combined was 0.8 mm^2 wich is *ca.* ~ 2% of the cross sectional area of any reaction points used in this work. The tips of the thermocouples were not fixed to a surface and were angled such that they would protrude into the flow during an experiment. This permitted the temperature to be measured in the bulk flow, this meant that slight radial movement of the tip may occur under the flow conditions, thus, the positions of the thermocouples are quoted to *ca.* ± 2 mm since the stiffness in the thermocouples inhibited their movement to some degree. The response time of the thermocouples (the time taken to reach 63.2% of the temperature steady-state when plunged into a batch of boiling water) was quoted by the manufacturers as ~ 25 ms. The temperature at each location was recorded every 500 ms and recorded using a labview data logger. Typically, 30 s time averages temperature measurments were taken once the system reached a steady state or what was deemed a steady state and these are the values reported within this thesis. The same general method was used to place thermocouples in CHFS system 2.

The IAPWS Formulation 1995 for the Thermodynamic Properties of Ordinary Water Substance for General and Scientific Use using the associated FLUIDCAL^{TM} software was used to calculate the physical and transport properties of water at elevated temperatures and pressures. (Wagner & Pruss, 2002) The calculations used to determine the physical properties of water are included in each chapter in which they appear.

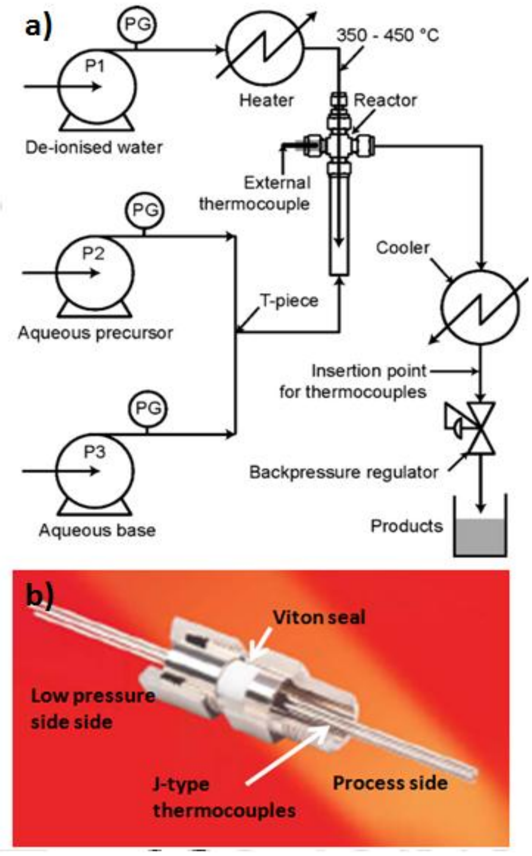

Figure 2.8: a) Schematic representation of the position for thermocouple insertion into CHFS system 1, **b)** Annotated diagram of the Spectite fitting used for the insertion of thermocouples into pressurised CHFS systems.

2.3: Pilot Scale CHFS Process Equipment

The pilot scale CHFS system described in this section was designed and in collaboration with Dr Christopher Tighe. I was heavily involved in the construction and commissioning of the CHFS pilot plant which included the synthesis and characterisation of all materials produced by the process. The purpose of this section is to describe the pilot scale process equipment and the configurations in which the equipment was used.

2.3.1 Description of the Core Pilot Scale Process Equipment:

The pilot scale CHFS process is an analogue of the laboratory scale process presented in the previous section. Figure 2.9 shows a simplified flow diagram of the pilot scale process highlighting process control elements used in both commissioning and the synthesis of nanoparticles. A summary of the large components used in the construction of this process are detailed in Table 2.1 alongside the supplier which also serves as a key for Figure 2.9.

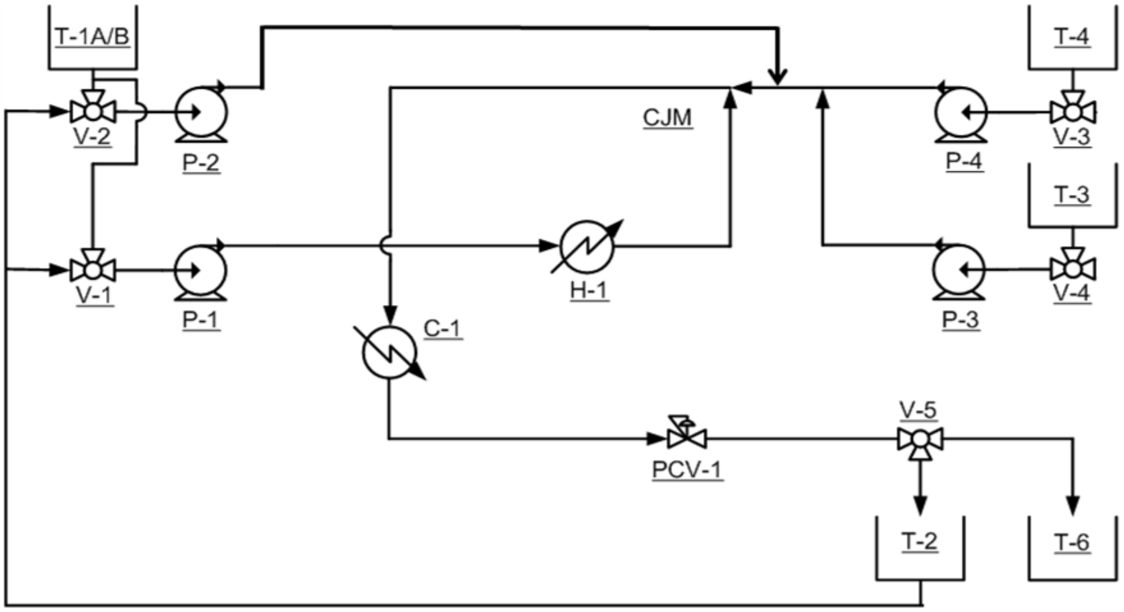

Figure 2.9: Schematic diagram of the basic pilot scale process in the dual pump configuration (analogous to the design of CHFS system 1)

Figure 2.9 shows a schematic of the pilot scale process set-up in the dual pump configuration. This pump configuration allows experiments to be performed in an analogous manner to those performed using CHFS system 1 described in section 2.2. The chemical dosing pumps (Milton Roy / Primeroyal K) were connected to the pilot scale process equipment using Swagelok/Gasket fittings. The feeds from the precursor/storage tanks (T1-4) were connected to the pumps using ¼” seamless tubing. The pumps were connected to the pulsation dampeners (Liquid Dynamics / Pipehugger HP) precharged to a pressure of 192 bar (N_2 Gas, BOK UK) using gasket fittings. The pulsation dampener was connected to ¼” Swagelok tubing using another gasket fitting as shown in figure 2.10a. The 1/4″ tubing passed through a non-return valve constructed of 1/4″ fittings (Swagelok, UK), as a safety feature to prevent backflow. Downstream of the non-return valve a pressure transducer was fitted to each of the feed lines to allow independent pressure monitoring of each feed. A Category IV proportional pressure relief valve (Parker / HPRV) was connected in series to each feed line. The set pressure of the relief valves differed for the H1 feed line has a relief valve set at 300 Bar each other feed had the relief pressure set at 280 Bar. This arrangement is pictured in figure 2.10 b which also indicates the flow direction.

Table 2.1: Key to pilot scale process schematic including the manufacturer and model of major components used

Tag	Description	Manufacturer/Model
T-1A&B	De-ionised water tanks	Millipore / 60 litre PE
T-2	Recycle water tank	Cole Parmer / 07240-95
T-3 & T-4	Precursor tanks	Vogue / 40 cm stainless
T-6	Product tank	Vogue / 40 cm stainless
P-1	Main scH_2O pump	Milton Roy / Primeroyal K
P-2	Backup scH_2O pump / running spare	Milton Roy / Primeroyal K
P-3	Precursor pump	Milton Roy / Primeroyal K
P-4	Precursor pump	Milton Roy / Primeroyal K
PD-1 to 4	Pulsation dampeners for P-1 to 4	Liquid Dynamics / Pipehugger HP
SV-1 to 4	Category IV relief valves for P-1 to 4	Parker / HPRV set @ 4000 psi
SV-5	Category IV relief valve	Parker / HPRV set @ 4350 psi
NRV-1A to 4A	1st non-return valve for P-1 to P-4	Swagelok / CH series
NRV-1B to 4B	2nd non-return valve for P-1 to P-4	Swagelok / 50 series
H-1A to D	Electrical heaters	Watlow / bespoke CastX 2000
CJM	Confined Jet Mixer	Swagelok / assembled by UCL
C-1	Cooler	Swagelok / assembled by UCL
C-2	Recirculating chiller	MTA / TAEevo50
PCV-1	Backpressure regulator	Swagelok / KHB 6000 psi C_v 0.06

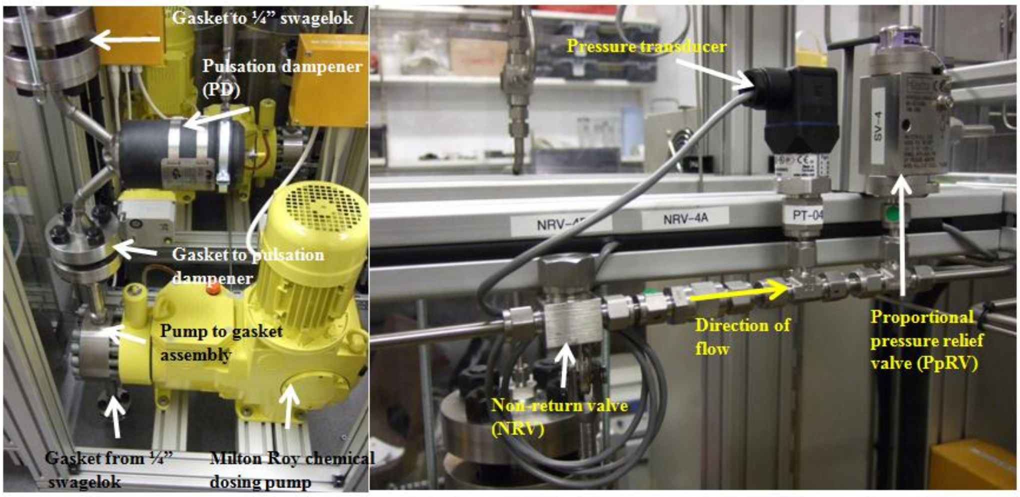

Figure 2.10: **a)** Photograph showing the pump position relative to the pulsation dampeners (including gasket joints), **b)** Photograph showing a feed line safety component assembly and pressure monitoring position (the image indicates the direction of flow).

The preheated water feed in the pilot scale process is produced by pumping deionised water, stored in tanks T-1A&B, though an electrical heater H-1 operating at a pressure of 240 Bar (24.1 MPa). The design of the heaters used on the pilot scale process was similar to the heater design used on the laboratory scale. However, on the pilot scale process consisted of four custom made heating units professionally fabricated (Watlow, UK). The bank of heating units provides a total heating capacity of 24 kW. Each heating unit could provide *ca.* 6 kW of heating capacity. Each heating unit was connected in parallel and the outlet temperature from the combined flow of the heating unit was used to control heater output. This design allowed up to 400 mL min^{-1} of deionised water to be heated to a maximum temperature of 450 °C. The heating units were constructed from six meters of ½” Inconel seamless tubing (Swagelok, UK) tightly wound around a Bronze core into which 4 x 1.5 kW heating rods (Firerod ™, Watlow) and K-type thermocouples were cast. The heating units were cast in Bronze to ensure good thermal conductivity between the water flowing within the Inconell tubing and the heating block. The thermocouples inserted into each heating unit were used to ensure equal flow between each of the units in parallel and to monitor the heating block temperature. An annotated photograph of the complete process is presented in figure 2.11.

In the dual pump configuration T-3 is used to store the dilute salt of a metal (*e.g.* zinc nitrate) and T-4 contains a dilute acid, base or oxidant (*e.g.* ammonia, citric acid or hydrogen peroxide). The contents of T-3 and T-4 are pumped by P-3 and P-4 (fitted with pulsation dampeners), respectively, to a tee-piece followed by a static mixer (Swagelok). The combined feed had an analogue pressure gauge (40 MPa) connected (RS components) to allow for the operator to see the system pressure (insulated from high temperature by a 3 m length of 1/8” seamless tubing). Using certain precursors, precipitation of a solid may occur at this point, and the purpose of static mixer was used to ensure homogenisation of the reagents entering the reaction point. The scH_2O issuing from H-1 is rapidly mixed with the pre-mixed precursors in the “Confined Jet Mixer” (CJM) of the same basic core design as that presented in figure 2.3 the dimensions of which are provided later. The products from the reaction point (R-1) are cooled to room temperature in C-1, where C-1 consists of a bank of two coolers (*ca.* 1.5 m in length) where the flow issuing from R-1 is fed through two units in series. The product produced in R-1 flowed through a pipe in each cooling unit, cooled externally by an outer jacket through which cooling water (supplied by a recirculating chiller) flowed at 100 L min^{-1} with an inlet temperature of 15 °C. Under all quoted synthesis conditions the cooling water exited the heat exchanger at ~20-40 °C dependent on the mass flow rate of the system. The design of each cooling unit was identical to that which has been previously described in detail on the lab scale apparatus except the total length of each unit was 1.5 m and the outer diameter of the cooling water jacket was 25.4 mm. The cooled product flowed through a backpressure regulator (PCV-1) after which it was collected in a suitable product tank (PVC or stainless steel). The back-pressure regulator was obtained from Swagelok UK and a custom made electronic actuator unit was fitted to remotely control pressure through a GUI (described later in this section).

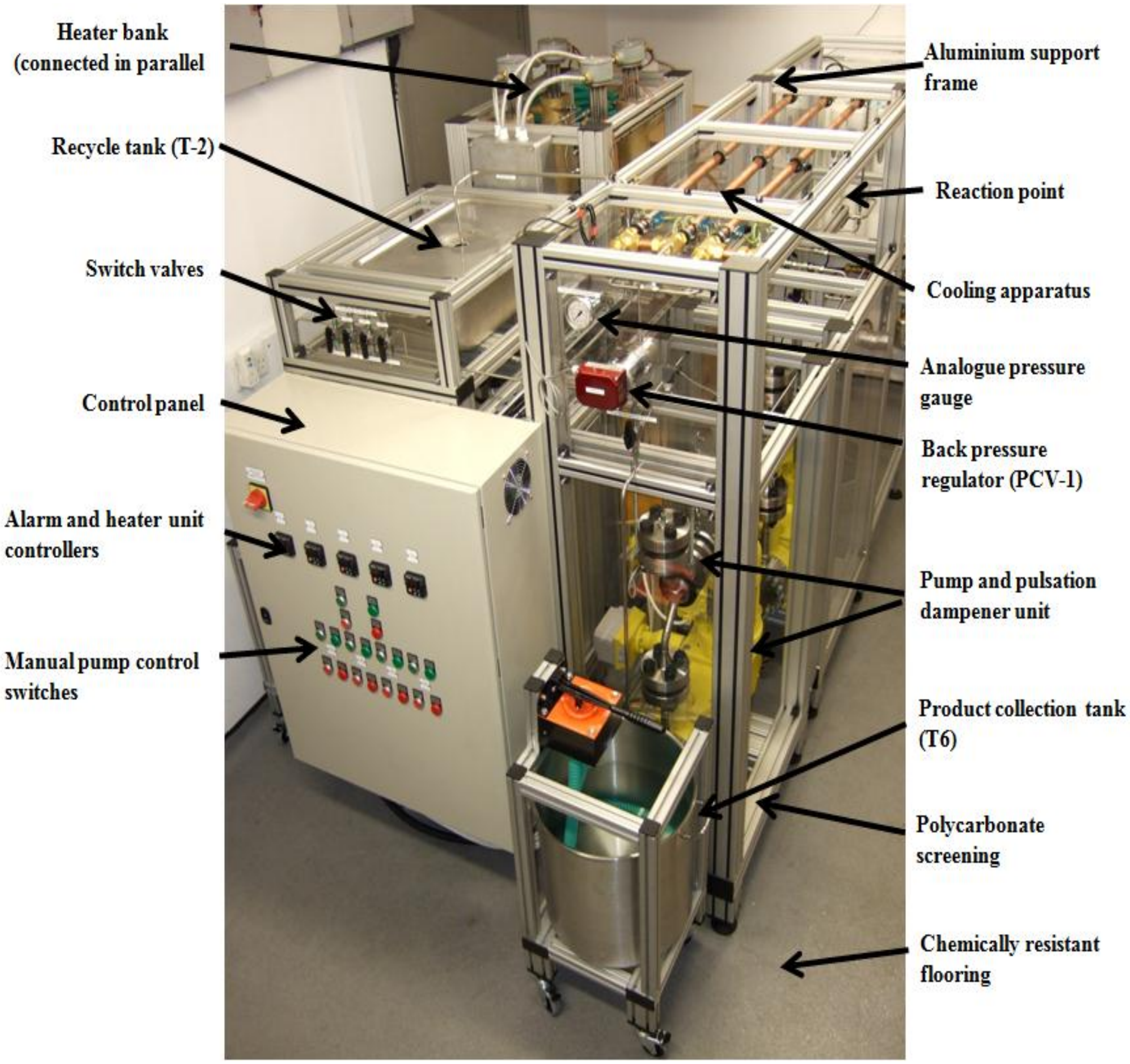

Figure 2.11: Annotated photograph showing the pilot scale CHFS process used in this work

In the dual pump configuration the system was always brought upto operational temperature and pressure using an internal recycling loop constructed from 3/8” tubing connected from T2 to pumps 1 and 2 via V-1 and V-2. Where, the output of pump 2 was used to replace the flow issuing from pumps P-3 and P-4. To change the process to synthesis mode the start-up pumps were isolated using switch valve (V-2) precursors could be pumped into the system through the use of pumps P-3 and P-4. All feed lines and pumps were primed against atmospheric pressure before start-up. V-5 was used to switch the process from total internal recycle (feeding T-1) to product collection T-6. Figure 2.12 shows the valve assembly used to isolate and direct feeds within the process. Internal recycle was not used during cooling the system due to possible contamination of fixed process components by residual products in the process tubing. This system was implemented to increase the overall water efficiency of the process as under the highest flow regime (*ca.* 800 mL) min to save *ca.* 55 L of DI water which would have previously been lost during start up.

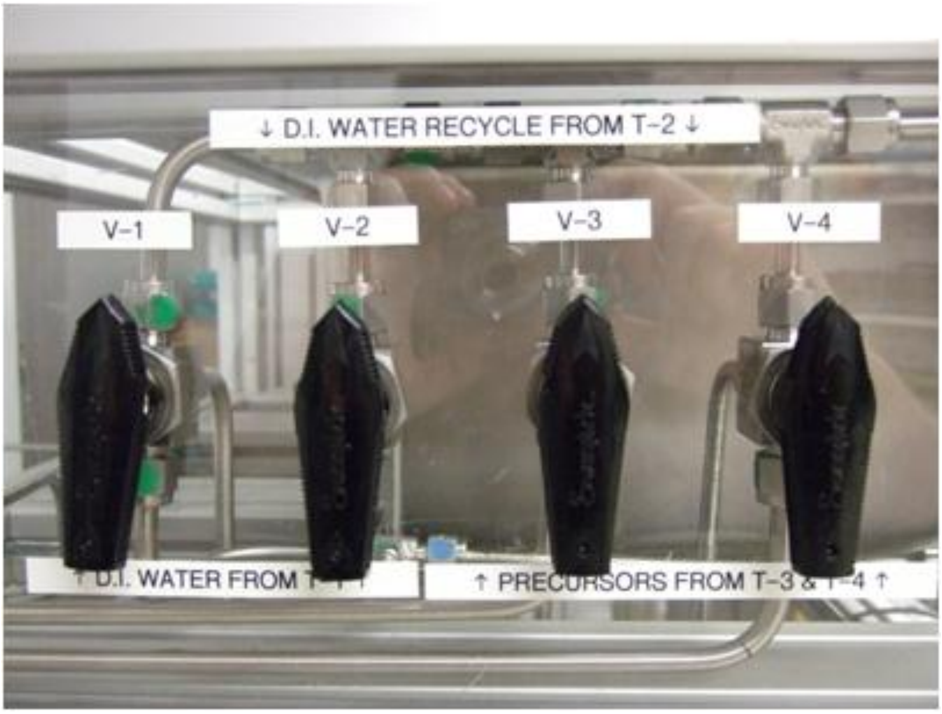

Figure 2.12: Photograph of the switch valve assembly used to isolate and direct feeds within the pilot scale CHFS process.

The automated pilot scale CHFS process was entirely controlled by a LAB View GUI developed by Dr C Tighe. The control software automatically controlled heater out-put and the solenoid controlling the Swagelock BPR dependent on the required temperature and pressure defined by the user. The flow-rates of each of the pumps could also be independently controlled though this interface. The process was designed to include a deployable programme which could run independently of the GUI in case of power failure via the Compact Rio control unit which was built into a custom made control panel constructed by Claremont Eves (London, UK). The complete process is annotated in figure 2.10.

2.3.2 Description of Process Modifications for Materials Synthesis:

The pilot scale process was also modified to allow for the addition of a capping agent into the process shortly after the formation of nanoparticles in a system analogous to CHFS system 2. This reactor configuration is presented schematically in figure 2.5. In this configuration the feed from pump 4 was directed into the reaction point shortly after the formation of nanoparticles. Briefly, the CJM type reaction point used in this work consisted of a ¾” cross piece into which a ¼” inlet was used to supply a preheated water feed into the reactor. The inlet of the feed from pump 4 consisted of ¼” tubing fed into the centre of the flow issuing from the reaction point consistent with the design presented in figure 2.7. In this configuration all ancillary process equipment remained situated as described in section 2.2.3 and as shown in figure 2.10. In this configuration the process was brought upto operational temperature and pressure using the feeds form pump 1, 2 and 4 (feed directed from T-1 for the pre-heated water feed and precursor feeds respectively. To change the process to synthesis mode the start-up pump (P-2) was isolated using switch valve 2 (v-2) and precursors could be pumped into the system into the using pumps P-3 and P-4 by switching the origin of P-4 to T-4.

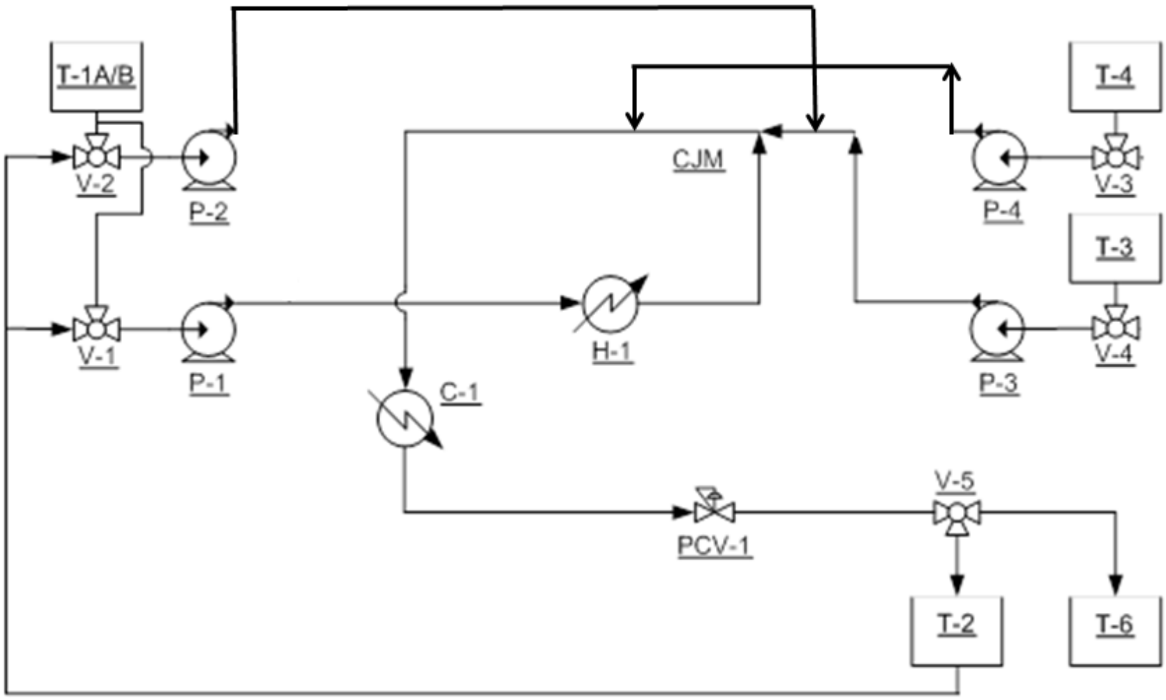

Figure 2.13: process schematic for the pilot scale-process used for the production of surface functionalised nanoparticles.

The pilot scale process was also modified to allow for the combinatorial synthesis of nanoparticles using a three pump configuration in which each pump and feed line contained a different reagent. Similarly, this three pump set-up could also be used for the online dilution of reagents allowing solution concentrations to be varied during a single experiment. This process configuration is presented schematically in figure 2.14. In this embodiment the feeds issuing from pumps P-3 and P-4 (typically containing metal salts) were mixed in a Tee piece prior to being diluted inline with the addition of the feed issuing from pump P-2 (typically and auxillary feed such as KOH). The solution compositions entering the reaction point as well mixed solutions after passing through a static mixing device could be controlled by the output of each pump. In this configuration the process was brought to operational temperature and pressure using the feeds form pump 1 and 2 (All feeds were directed from T-1 for the pre-heated water feed and precursor feeds respectively). To change the process to synthesis mode the start-up pump (P-2) was isolated using switch valve 2 (v-2) and precursors could be pumped into the system into the using pumps P-3 and P-4 by switching the origin of P-4 to T-4. The feed tank for P-2 was switched using V-2 to come from an ancillary tank containing a reagent.

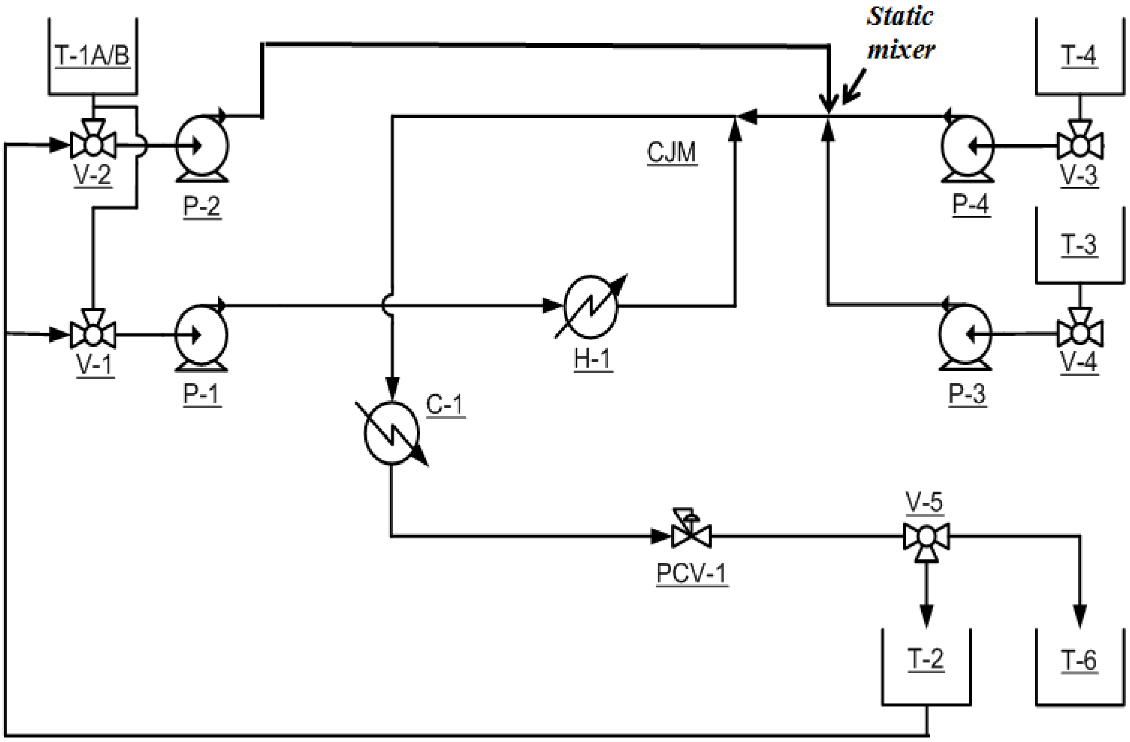

Figure 2.14: process schematic for the pilot scale-process used for the combinatorial production of nanoparticles or for scale-up via concentration studies.

2.4 Sample Preparation and Clean-up:

The purpose of this section is to detail the product recovery methods used in this thesis owing to the relatively large volumes of nanoparticle laden slurry which had to be processed.

2.4.1 Salt/non-solvent Precipitation:

Salt precipitation was used in the recovery of surface functionalised nanoparticles produced in chapters 6, 7 and 8. The optimisation of the salt/solvent precipitation and product cleaning processes are not presented (available on request). Briefly, in the optimisation of precipitation processes, methanol, ethanol and NaCl were used as precipitation agents. In the case of experiments involving solvent precipitation the evolution of precipitates was followed using DLS as a function of time where it was found that the volume of non-solvent required to effectively precipitate particles was too large to be economically used on the scales required in this thesis. Hence, NaCl based flocculation was used in the recovery of all surface functionalised nanomaterials. Where, a total salt concentration in the range of 0.5-1.0 M in the nanoparticle laden slurry was sufficient to induce complete sedimentation (under gravity) on time scales of < 24 h. After the addition of salt the particle suspension was allowed to precipitate under gravity. The precipitate was concentrated by centrifugation at 4500 rpm for 5 minutes prior to being re-suspended for dialysis. This procedure was applied for volumes of nano-particle laden slurry in excess of 80 L although many are not reported.

2.4.2 Dialysis:

Dialysis tubing with different molecular weight cut-off was used in different applications (MW. range 12,400-200,000, (obtained from SLS)). In a typical preparation the sample dispersion was sealed into dialysis tubing with an appropriate molecular weight cut-off. The sealed tubing was secured and fastened at both ends and a magnetic stirrer attached. The membrane was placed into an appropriate beaker (ca. 100 x nominal volume of the dialate) 15 Mega Ohm distilled water was used as the buffer and stirred to ensure rapid equilibrium between the dialate and buffer. The buffer solution (typically >15 Mega Ohm DI water) was exchanged at regular time intervals and the conductivity of the dialate and buffer were measured until no change in conductivity was measured (*ca.* 3-5 cycles). Upon completion of the dialysis, the membrane was removed and either freeze dried for further characterisation or retained as particle dispersion. Materials produced on the pilot scale process were initially dialysed against tap water before a final dialysis against > 15 Mega Ohm DI water due to the large processing volumes.

2.4.3 Centrifugation and Cleaning:

A Sigma 4K15 Centrifuge with a rotor housing four buckets, each with a capacity of seven 50 ml Falcon tubes each (28 tubes in total), was used to centrifuge the suspensions after collection from CHFS systems. Each of the slurries (*ca.* 1-10 wt% in water) either precipitatd autogenously or with the addition of a flocculant were placed in falcon tubes. Samples were centrifuged for *ca.* 5-10 min (material dependent) at a speed of 4500 rpm (6800 g). The supernatant was removed and replaced with DI water (>10 Mega Ohm) and centrifuged. This step was repeated *ca.* 3-10 times to ensure the removal of all residual ions. The solids were redispersed using a VWR analogue vortex mixer (model VM-3000) on its maximum setting for 1 minute between reach round of centrifugation. Samples were washed until either the pH of the slurry approached 7 or the conductivity of the sample was stable for 3 rounds of centrifugation. In the case of materials produced on the pilot scale process the same centrifugation procedure was applied. However, the falcon tubes were replaced by 0.75 L centrifuge buckets and the samples were placed in bucket liners giving a nominal volume of *ca.* 0.70 L. Samples were retained as consolidated slurries which were *ca.* 10-40 wt% particles. The consolidated slurry was either freeze-dried or retained for further analysis or dialysed depending on the material.

2.4.4 Freeze Drying:

After centrifugation or cleaning to remove residual ions as defined in sections 2.4.1-2.4.3 samples were freeze-dried prior to characterisation unless otherwise stated. The samples in this thesis were frozen by placing them in a Virtis Genesis 35 XL freeze drier and allowing the samples to freeze to a preset temperature *ca.* -40-60 °C. for at least 1 hour prior to freeze drying. All drying was carried out against a condenser compartment set at *ca.* -60 °C. Freeze drying was carried out for 22.5 hours under a *ca.* 1.3×10^{-7} MPa vacuum. However, in the case of materials produced on the pilot scale process the drying duration was extended to 48-72 hours depending on the amount of material. Alternatively, some samples required freezing in liquid nitrogen prior to freeze drying and this was added as a step prior to the freeze drier cycle (Citric acid coated magnetite produced on the pilot scale CHFS process).

2.5 Materials Characterisation and Equipment:

2.5.1 X-ray Diffraction:

The purity and phase composition of the samples were determined by powder X-ray diffraction (XRD). X-ray diffraction patterns were collected using a Bruker D4 Diffractometer (CuKα_1, λ=1.540598 Å). This diffractometer was used as it allowed the diffraction patterns of materials which normally fluoresce under CuKα_1, λ=1.540598 to be characterised due to controllable diffraction slits and a secondary monochromator. The aperture size of the slit was set usually set to 0.5 mm in each data collection unless otherwise stated. The diffractometer was equipped with an automated sample holder allowing large numbers of samples to be processed rapidly. In all diffraction data presented within this thesis step scans were collected and the scan parameters were altered as required for each material investigated. The scan parameters used for all the samples in this thesis are summarised in table 2.2. Samples were prepared for analysis by grinding and mounting in either plastic or amorphous silica holders.

Table 2.2: Scan parameters [2θ range, step size and count time per step] and diffractometers used for all samples.

Sample series [corresponding section]	**Scan parameters**		
	2 θ range (°)	**Step (°)**	**time (s)**
Hydroxyapatite samples [Chapter 3 + 4]	10-80	0.04	2
ZnO [Chapter 3 + 4]	10-80	0.02	2
Iron oxide nanoparticles [Chapter 5]	10-70	0.05	2
Magnetic iron oxides[Chapter 6]	10-80	0.06	1
(Eu_x Y_{1-x})OOH [Chapter 7]	20-70	0.04	2
Magnetic iron oxides [Chapter 8]	10-70	0.05	2
Citric acid coated Magnetic iron oxides [Chapter 8]	10-70	0.05	2

Ce-Zn Oxides [Chapter 8]	10-70	0.04	3
ZnO [Chapter 8]	10-80	0.02	2

Phases were identified using the Joint Committee on Powder Diffraction Standards (JCPDS) database, the ICDD database, in the XRD or evaluation program Diffracplus EVATM Version 5.0 (Bruker-AXS, Germany). Refinement of selected diffraction patterns using the Le-bail method was done using GSAS/EXPGUI. In each case a standard material (Y_2O_3) was used to estimate instrumental broadening and peak shift to refine the diffractometers zero. The volume weighted mean crystallite size was estimated using the Scherrer equation:

$$t = \frac{0.9\lambda}{B\cos\theta}$$ **(Equation 2.1)**

Where, t = crystallite size in nm, λ= wavelength of X-rays, B = full-width at half maximum in radians, θ = angle corresponding to the peak. Alternatively, estimates of particle size were made using equation 2.2, where the contribution of sample induced broadening was defined by the term X determined for the overall profile fit from GSAS. This method was used for samples which had complete diffraction profile fits (as indicated within this thesis).

$$\rho = \frac{18000\kappa\lambda}{\pi X}$$ **(Equation 2.2)**

Where ρ is the crystallite size (Å), x is the Lorentsian broadening ($° \times 10^{-2}$), the constant (κ) in this equation was dependent upon the symmetry of the material and values appropriate to each crystal system were chosen.

2.5.2 FTIR:

FTIR spectra were recorded on a Perkin Elmer Spectrum 1 fitted with an ATR accessory. This equipment is located in the department of chemistry, UCL. Prior to use on the ATR accessory samples were ground into a fine powder and a sufficient quantity was used to ensure complete coverage of the sample window. Spectra were obtained in the wave number range 4000 - 600 cm^{-1} with 64 scans and a spectral resolution of 4 cm^{-1}. Backgrounds were collected using the sample accessory mirror alone and all spectra were automatically corrected adjusted and accordingly. Table 2.3 provides a summary of the scan parameters used in this thesis alongside the data location within the text.

Table 2.3: summary of scan parameters used in ATR-FTIR and the data location within the thesis:

Sample series [Corresponding section]	**Number of scans**	**Spectral resolution (cm^{-1})**
Citric acid coated magnetite [Chapter 6]	64	4
Citric acid coated ($Y_{1-x}Eu_xOOH$) [Chapter 7]	64	4
Pegylated ($Y_{1-x}Eu_xOOH$) [Chapter 7]	162	4
Citric acid magnetite pilot plant [Chapter 8]	64	4

2.5.3 Raman Spectroscopy:

Raman spectra were collected in a Renishaw InVia Raman Spectrometer equipped with a 785 nm diode laser. The output laser power was 80 mW (*i.e.* 100%). The experimental parameters used were dependent on the material under study and a summary of the measurement conditions is presented alongside the data generated using each measurement condition is presented in table 2.4. The Raman system was calibrated against the mode of silicon at 520 cm^{-1} and the spectral resolution was 1 cm^{-1}. Materials were all evaluated as freeze dried powders mounted and pressed flat on glass microscope slides.

Table 2.4: Summary of Raman scan parameters and the data location within the thesis

Sample series	**Scans**	**Scan time (s)**	**Laser power (% of 80 mW)**	**Resolution (cm^{-1})**
Hydroxyapatite [Chapter 3]	10	10	100	1
ZnO [Chapter 3]	10	10	50	1
Pilot scale ZnO [Chapter 8]	5	10	50	1
Ce-Zn Oxides [Chapter 8]	5	10	5-50	1

2.5.4 BET surface area measurements:

Brunauer, Emmet, Teller (BET) surface area measurements (using N_2 gas adsorption method), were performed on a Micromeritics Gemini Micromeritics ASAP 2420 analyser. Freeze dried powders were degassed at 120-180 °C for at least 12 hours prior to analysis. After the degas procedure the samples were weighed (to calculate dry weight) and then analysed for nitrogen absorption. Liquid nitrogen was supplied by BOC, UK. Data for absorption isotherms and derivation of surface area was recorded. Typically the adsorption type maybe referred to demonstrate that typically solid materials were produced. Hence, limited data from these measurements is presented (most measurements were type II isotherms unless otherwise stated). This protocol was applied to all materials studied in this thesis. The BJH adsorption/desorption method mentioned in Chapter 7 was also measured using the ASAP 2410 analyser and both the adsorption and desorption isotherms were recorded to provide an estimate of pore size. The crystallite could be estimated using the equivalent sphere approximation as described by equation 2.3:

$$Ds = \frac{6000}{S_{bet}\rho} \quad \textbf{(Equation 2.3)}$$

Where, D_S (nm) is the equivalent sphere diameter, S_{BET} ($m^2\ g^{-1}$) is the BET surface area and ρ ($g\ cm^{-3}$) is the density of the material (either assumed to be that of the bulk material or calculated from the diffraction data [theoretical material density]). In certain cases this approximation is presented for materials which do not show a spherical morphology and this is presented only to provide the reader with an interpretable number derived from surface area.

2.5.5 Dynamic light scattering (DLS):

The particle size distribution of nanoparticles in suspension either obtained directly from the CHFS process or as formulated using the strategies presented in within respective chapter sections were determined using a Malvern Zetasizer Nano (ZEN3600). The sizes were measured using dynamic light scattering (also called quasi elastic light scattering [QELS] and Photon Correlation Spectroscopy [PCS]) using a measurement angle of 173°. The instrument was calibrated using a size standard (Nanosphere™ 3200A 199±6 nm) before each days use. The measurement of dispersions was optimised for each material analysed using this method and depended heavily on sample adsorption. Samples were prepared for measurement by an appropriate dispersion protocol which typically involved a round of sonication (*ca.* 5 minutes) followed by filtration (1.2 μm pore size) to remove dust and other large particle detritus. All measurements were performed in disposable plastic cuvettes with a nominal path length of *ca.* 1 cm. Each measurement was taken using a backscatter geometry and the intensity of light scattered by the sample was recorded at a measurement angle of 173 ° decreasing the sensitivity of the measurement to slight variation in colloidal number concentration.(Holthoff *et al.*, 1996) All measurements of hydrodyanamic diameter are reported as an average of 25 measurements of 10s duration. Typically, hydrodynamic diameter is reported as the distribution calculated from the raw scattering data as a distribution based on total scattered light (633 nm). However, in certain cases number weighted distributions are reported by correcting the intensity weighted distribution to a number weighted distribution by acknowledging the contribution of Mei scattering to the interpretation of the sample data. The following paragraph provides a justification for the number weighted conversion used to support some of the discussion presented.

Scattering from a colloidal sample can be described in terms of two theories; Rayleigh scattering and Mie scattering. If the particles are small compared to the wavelength of the laser used (typically less than $d = \lambda/10$ *ca.* 63nm for a He-Ne laser (633 nm) as used in the Malvern instrument), Rayleigh scattering applies. In the Rayleigh approximation, intensity $I \alpha d^6$ and also that $I \alpha 1/\lambda^4$, where I = intensity of light scattered, d = particle diameter and λ = laser wavelength. (Lin *et al.*, 1990) The d^6 relationship shows that scattering is non-linear and larger particles scatter significantly more light that smaller particles *i.e.* a 50 nm particle will scatter 10^6 times as much light as a 5 nm particle. Hence, the sensitivity of the measurement to the presence of a small population of larger nanoparticles or agglomerated nanoparticles. (Lin, Lindsay, Weitz, Ball, Klein, & Meakin, 1990) This d^6 factor also means it is difficult with DLS to accurately measure samples showing polydispersity because the contribution to the total light scattered by the small particles will be negligible. To allow estimation of the distribution of particles scattering in a sample a Cumulants analysis is performed on the raw light scattering data (Malvern's DTS software V5.1) This analysis yields a plot of the relative intensity of light scattered by particles in various size classes and is therefore known as an intensity size distribution (based upon the diffusion rate of a hard sphere in a medium of known viscosity). (McNeil-Watson & Kaszuba, 2010) However, if the plot shows a substantial tail, or more than one peak, then Mie theory can make use of the input parameter of sample refractive index to convert the intensity distribution to a volume weighted size distribution or a number weighted distribution by modeling the complex scattering of a population of particles based on scattering angle per the size classes identified from cumulant analysis. This will then give a more realistic view of the importance of the tail or second peak present by accounting for the differences in scattering at different angle by particles of different sizes. Hence, distributions based on both interpretations of the scattering data are provided. (McNeil-Watson & Kaszuba, 2010)

2.5.5.1 Colloidal Stability Measurements:

The colloidal stability of nanoparticle dispersions was assessed in a variety of buffer solutions. This was achieved by measuring the evolution of hydrodynamic diameter as a function of time (sample dependent) for a known solution condition. (Holthoff *et al.*, 1996) Colloidal stability measurements were performed using DLS and all measurements were taken on a Malvern Zetasizer Nano (ZEN3600). Each measurement condition was optimised using trail runs prior to data collection. Typically, a suitable measurement position and attenuator setting was used over the entire intended measurement range. In a typical experiment a known concentration of particles *ca.* 0.05 mg mL $^{-1}$ was dispersed in the appropriate buffer in a disposable cuvette (PMMA) with a nominal path length of *ca.* 1 cm and all measurements were performed in a backscatter configuration. Typically, the duration of each measurement was 10 s. The results were recorded as the samples average hydrodynamic size (un-weighted) and the measured sample polydispersity. Interpretation of the evolution of hydrodynamic diameter is provided alongside the relevant discussion presented in the body of the thesis.

2.5.6 Zeta-Potential Measurement:

The zeta potential measurements were performed using a Malvern Zetasizer Nano (ZEN3600) using disposable electrophoretic mobility cells (DTS1060). A zeta-potential standard (Malvern DTS1050, -50 ±5 mV) was run to calibrate the instrument prior to each days use. All samples prepared for zeta-potential measurement were further cleaned by dialysis against >10 Mega Ohm DI Water. Samples of particle dispersions were dispersed ultrasonically in 0.005M NaCl aqueous solution to ensure sufficient conductivity to a concentration of *ca.* 0.001 g L^{-1} nanoparticles (ensuring sample transparency). The zeta-potential (ξ) was typically measured as a titration in series from pH 3 to 10 by using 0.01M NaOH and HCl as titrants and the pH of each dispersion was measured by a calibrated pH Probe (Malvern, DTS1230). All solutions containing nanoparticles for zeta-potentail measurements were subjected to three measurements taken sequentially with a pause of 30 s between each measurement and the results were averaged (mean). Each measurement was a composite of 10-20 runs each lasting *ca.* 10 s. The calculations of zeta-potential were performed by the software where the measured electrophoretic mobility was converted to zeta-potential by application of the Smoluchowski approximation (f(Ka) =1.5) to Henry's equation shown in equation 2.4, as this was the most valid interpretation of the electrophoretic mobility data under the measurement conditions chosen.(McNeil-Watson & Kaszuba, 2010) The relationship between electrophoretic mobilitiy and zeta-potential is described by equation 2.4:

$$u_e = \frac{2\,\varepsilon\, z\; f(k_a)}{3\omega} \quad \textbf{(Equation 2.4)}$$

Where, U_e is the electrophoretic mobility of the sample, z is the zeta-potential, ε the dielectric constant of the suspending medium (assumed to be that of water at 25 °C), ω is the viscosity of the suspending medium and F(ka) is the Smoluchowski approximation (1.5). All quoted measurements are reported as zeta-potential values.

2.5.7 Microscopy and Related Methods:

2.5.7.1 Transmission Electron Microscopy (TEM):

Nanoparticles synthesised using the CHFS system at both a laboratory and pilot scale were studied using various TEM instruments. The electron microscopes used in this thesis are identified in the list below and data coming from each instrument is identified within the body of the thesis.

1. JEOL 100cx operated at an acceleration voltage of 100 KeV (tungsten filament), this instrument is located in the department of chemistry UCL. Images generated using this microscope were film based and scanned in as negatives prior to image calibration.

2. JEOL 1200 operated at an acceleration voltage of 120 KeV (tungsten filament), this instrument is located at the Royal institution of Great Britain. Images generated using this microscope were collected on a Gatan CCD camera. Similarly, SEAD diffraction patterns were obtained using a 5 µm aperture and the pattern was captured using a GATAN CCD camera. The camera length was calibrated for the diffraction setting using Al foil.
3. JEOL 4000x is a high resolution TEM instrument based at the department of Materials university of Oxford. The instrument was operated using an acceleration voltage of 400 KeV with a LaB_6 crystal as the electron source for the generation of high resolution images. SAED patterns were taken using this microscope on film and were calibrated using a Si wafer as a standard. Access to this instrument was funded under the EPSRC access scheme (grant reference EP/F01919X/1).
4. JEOL 2010 high resolution transmission electron microscope based at the department of Materials university of Oxford. The instrument was operated using an acceleration voltage of 200-300 KeV using a LaB_6 electron gun. SEAD patterns were taken using this microscope as digital images captured using a Gatan CCD camera and the images were calibrated using a Si wafer as a standard. Access to this instrument was funded under the EPSRC access scheme grant reference EP/F01919X/1.

Sample preparation for TEM differed between the microscopes used and the objective of the work undertaken. As an example, samples which were stable aqueous dispersions were either dropped onto TEM grids (Agar scientific, 400 mesh) as dispersions and allowed to dry prior to analysis (TEM preparation method 1). However, samples prepared from stable aqueous dispersions for HRTEM were first freeze dried and re-dispersed ultrasonically in methanol prior to mounting on grids (TEM preparation method 2). This was essential as polymerization of adventitious carbonaceous material on the film resulted in “fogging “of the image making image capture difficult. Powders produced from freeze dried materials were mounted using the same procedure as for the preparation of samples for HRTEM. In microscopes 2, 3 and 4, SAED (Selected area electron diffraction patterns) were take simultaneously to images to confirm the phase of the material under observation. In the case of microscope 4 it was possible to select a small enough aperture to allow for diffraction from individual nanoparticles and generate structural data.

2.5.7.2 Scanning Electron Microscopy and Energy dispersive X-ray Spectroscopy:

In this work, SEM was carried out on samples using a JEOL-5410LV SEM apparatus, with the accelerating voltage of 20 kV. Prior to analysis, the samples were mounted onto a 0.5 cm circular aluminium stubs using a double-sided adhesive carbon tape and then coated with a thin layer of carbon using an Edwards (ED100) sputter coater to render them electrically conductivity. The SEM was not used for imaging particles due to the low resolution (*ca.* 30 nm), however it was used as a platform to perform EDX. Energy Dispersive X-ray (EDX) spectroscopy coupled with scanning electron microscopy (SEM) was conducted on a JEOL-5410LV SEM apparatus, equipped with an Oxford Instruments Inca 400 EDX unit operating at 20 kV and a 15 mm working distance (backscatter). Averages of 10 area scans (1 × 1 μm areas) were used to calculate average elemental compositions. Dependent on the objective of the work the atomic percentages of elements were calculated using the microscopes internal calibration references and typically only metallic elements of interest were quantified in the analysis.

2.5.8 Fluorescence Microscopy:

In this work fluorescence microscopy was used to evaluate various phosphor materials. Fluorescence was captured using an Olympus BX51 microscope (BX51WI) using standard continuous excitation from a mercury arc lamp (HBO-1001). The microscope was equipped with a dichroic narrow pass filter centred at 470 nm and interchangeable emission filters (wide pass 640 nm or wide pass 540 nm). Observations were made with an Olympus UVFL 60 x PL, N.A. 1.30 silicon oil immersion lens which resulted in a total magnification of 350 x to the CCD camera used to capture fluorescence. The dichroic mirror was suitable for visualisation at all chosen wavelengths. Digital images of phosphor particle or cellular autofluroescence were taken with a EM-CCD camera (Ixon, Andor) and the exposure was optimized for each experiment. COS7 cells were used in visualization experiments and this culture was maintained and mounted by Dr James Muir.

2.5.9 Photo Luminescence Spectroscopy:

A Perkin Elmer LS55 spectrometer was used for fluorescence measurements on as synthesised powder samples. Scans were conducted at appropriate wavelength spreads for emission spectra. Excitation spectra were recorded at the wavelength of peak emission for each sample. The scan speed was set at 100 nm min^{-1} for all samples. The sample preparation protocol varied due to the nature of the material under investigation and are described the different measurement methods are presented below. The spectrometer settings were fixed with both excitation and emission slits set at 10, 10 which served as *ca.* 20 % signal attenuation and allowed all measurements to be performed within the optimal sensitivity window of the detector.

2.5.9.1 Powders:

Quantative photoluminescence measurements were performed on powdered samples. The samples were prepared by pressing the sample flat in well plates of 6 mm nominal diameter and 2 mm depth. Ensuring equivalency in the relative sample height relative to the excitation and emission fibers (nominal width, 2 mm) of the spectrometer (LS55 detailed above). In each measurement *ca.* 1 g of powder was used and comparative work was performed on samples in series. Each measurement was performed at a scan rate of 100 nm min^{-1} for both excitation and emission spectra. Exitation spectra for emission at a given wavelength and vice versa were recorded for each sample.

2.5.9.2 Dispersions:

Quantitative photoluminescence measurements were performed on colloidal dispersions of nanoparticles in DI water (10 MΏ resistivity). The samples were prepared by dispersing the nanopowder to a known particle concentration (the relative proportion of nanomaterial excluding capping agent was previously quantified using TGA). Measurements were performed on samples with a nominal volume of *ca.* 2 mL in quartz cuvettes (6030-UV, obtained from SLS) each measurement was performed at a scan rate of 100 nm min^{-1} and comparative work was performed on samples in series.

2.5.10 Time Resolved Photoluminescence Spectroscopy (TRPL):

Samples were prepared for TRPL measurements by mounting powder between two glass slides (microscope coverslips, SLS). PL measurements were performed using a 473 nm excitation source (DPSS laser) passed through a Bentham M300 single grating monochromator, emission spectra were recorded using a Hamamatsu photomulitiplier. Time resolved measurements were taken using a 473 nm excitation source monochromated using a Bentham M300 single grating emission, transitions were recorded using a digital oscilloscope. The most intense emission wavelength of each sample was identified and time resolved measurements were performed at that wavelength unless otherwise stated. Exponential decay curves were fitted to the data obtained from time resolved emission measurements to obtain a time constant for the radiative decay of the sample. All PL measurements were taken at room temperature.

2.5.11 UV-Vis:

UV-Visible absorbance (200 - 800 nm) spectra were recorded using an Ocean Optics spectrophotometer (USB 4000) with a deuterium halogen light source (DH-2000-BAL) and 6 μm fibre optic cables, white Spectralon^{TM} was used as a reference material for any spectrometer calibration. Samples were all measured as powders which were pressed flat onto glass microscope slides.

The band gap of materials evaluated using data obtained from UV-Vis were calculated using the Kubelka-Munk method. The Kubelka-Munk (K-M) function, and Tauc plots are derived from equations 2.5 and 2.6 as shown below:

$$F(R) = \frac{(1-R)^2}{2R}$$ **(Equation 2.5)**

$$\mathrm{R} = 1/10^{\mathrm{A}}$$ **(Equation 2.6)**

Where, A is the measured value of absorbance and R is the calculated value of reflectance. The K-M function, (F(R)) used is shown in equation 2.5 was calculated from the reflectance R and is determined from the absorption data using equation 2.6. The factors used for the determination of indirect ($F(R).E^{\frac{1}{2}}$) and direct ($F(R).E^{2}$) band gaps, were used to draw Tauc plots and the value of the factor was plotted against photon energy (eV). The K-M function defined above for direct and indirect energy transitions was plotted against the photon energy (eV) and E_g and the band gap was extrapolated by a linear fit of the point on the low energy side of F(R) curve at which the linear increase starts. However, all presented band-gap measurements are derived from the direct bandgap calculation unless otherwise stated. Similarly, CIE L*a*b* colour data was also calculated from the reflectance spectra using the Ocean Optics Spectrasuite software and a D65 light source. Data generated from this derivation is only presented in Chapter 8.

2.5.12 X-ray Photoelectron Spectroscopy:

X-ray photoelectron spectroscopy (XPS) experiments were performed on selected samples using a Kratos Axis Ultra-DLD photoelectron spectrometer using monochromatic Al-Kα radiation (1486.6 eV, 150 W). Survey scans were performed at a pass energy (PE) of 160 eV, whilst detailed scans were performed at PE 40 eV. All data were analyzed using CasaXPS^{TM} software (Version 2.3.14). Spectra were acquired using the Kratos immersion lens charge neutralisation system, and all spectra were calibrated to the C (1s) signal, which was assigned a value of 284.7 eV, and attributable to either adventitious carbon or a capping agent such as citric acid. Curve fits were performed using a Shirley background and a Gaussian peak shape with 30 % Lorentzian character. The XPS was located at Cardiff University and all the samples (in this thesis) were run by Dr David Morgan.

2.5.13 Magnetic Property Measurements:

2.5.13.1 SQUID-VSM:

A Quantum Design MPMS7 SQUID Magnetometer allowing DC magnetisation measurements at temperatures of 2-400 K in magnetic fields of 0-7 T was used in the evaluation of all samples presented in this thesis and all measuremnts were performed on samples loaded into plastic capsules. Both M(H) curves and ZFC/FC measurements were performed on materials prepared in this fashion. The measurements of M(H) curves was typically performed at 300 K unless otherwise stated and measurements were performed upto a maximum applied field strength of 5-7 T. The number of data point recorded in each M(H) measurement were determined experimentally to provide sufficient resolution for analysis. ZFC/FC measurements were performed on selected samples and measurements were performed at constant applied field of 100 Oe. Each sample was measured consecutively from low temperature (5-10 K) to high temperature (300 K), ZFC measurements were performed in the absence of an applied field and FC measurements were performed at constant field.

The ferromagnetic volume fractions (σ_{FM}) and a paramagnetic-like susceptibility (χ), the latter accounting for the non-saturating behaviour observed in samples, were calculated by fitting the experimental magnetization curve assuming a volume weighted log-normal ferromagnetic diameter distribution as described by equation 2.7. This method of ferromagnetic fitting was initially described by Chen *et al.* (Chen *et al.*, 2009)

$$P(v;\ \sigma,\mu) = \frac{1}{x\,\sigma\sqrt{2\pi}}\, e^{\frac{-(\ln x-\sigma)^2}{2\sigma^2}} \quad \textbf{(Equation 2.7)}$$

Where, x is the ferromagnetic size, σ is the average ferromagnetic diameter determined from the Langevin equation and μ is the ferromagnetic polydispersity and v is the ferromagnetic volume diameter. The equation which described the over-all fitting procedure is shown below.

$$M(H) = \int_0^\infty p(v;\ \mu,\sigma)v^{-1}\,[M_s v L_x + v_s \chi\, H]\; d_v \quad \textbf{(Equation 2.8)}$$

Where, p is the probability density function (equation 2.7), M_s is the saturation magnetization, χ is a term which describes the paramagnetic component, L_x is the langevain function (defined in equation 2.9), h is the applied field and d_v is the volume weighted diameter. This fitting was performed using a programme written by Dr P. Southern which allowed iterative fitting based upon least squares. Fits were judged on their quality by reduced χ^2. The fitting is done by iteratively changing the values of σ, M, d (the diameter of the median volume) and χ (the paramagnetic component). Langevin function weighted by the log normal distribution of ferromagnetic size is described by equations 2.9 and 2.10, respectively.

$$L(x) = \left(cothx - \frac{1}{x}\right) \quad \textbf{(Equation 2.9)}$$

Where, x is defined by (Equation 2.10)

$$x = \frac{M_o H}{K_b\ T} \quad \textbf{(Equation 2.10)}$$

Where, M_o is the magnetisation of the sample, M_s is the saturation magnetisation assumed to be the bulk value of magnetite (92 emu g^{-1}), T is the absolute temperature, χ is a term which describes the paramagnetic component on approach to saturation and H is the applied field strength. Values determined from the fitting procedure reported are the ferromagnetic diameter (μ), ferromagnetic diameter polydispersity (σ) and χ which describes the paramagnetic component of the magnetization curve.

2.5.13.2 Calorimetric Measurements for the Determination of Hyperthermia Performance:

The efficacy of magnetite nanoparticles from magnetic hyperthermia was evaluated by placing a ferrofluid sample into an alternating magnetic field. Figure 2.15 shows a photograph of the measurement set-up using the MACH (Magnetic Alternating Current Heating) system developed by Kallamundil *et. al.* (Kallumadil *et al.*, 2009) The AC magnetic field amplitude and frequency was controlled by patented circuitry and measurements were performed at a field frequency of 1.05 MHz and a field amplitude of 12 kA m^{-1} and powered a supply of 150 Volts at *ca.* 0.8 Amps. The AC field was actuated with a 2 cm water-cooled 6 turn solenoid and the sample was placed in the centre of the coil in an eppendorf tube. The heat-rise per unit volume magnetic fluid was measured using fluoro-optic thermocouples obtained from Luxtron and measurements were recorded every 0.1 s. Both the temperature of the magnetic fluid and the 6 turn solenoid was recorded to ensure that heating of the sample was not due to the inductive heating of the solenoid. The temperature of the solenoid was controlled by using a re-circulating chiller unit set at 20 °C. Samples were prepared for measurement by dispersing surface functionalised magnetic nanoparticles in distilled water to a particle concentration of 50 mg mL^{-1} by a moderate sonication protocol using a 4.5 kW ultrasonic bath on it’s maximum power setting (*ca.* 2 mins).

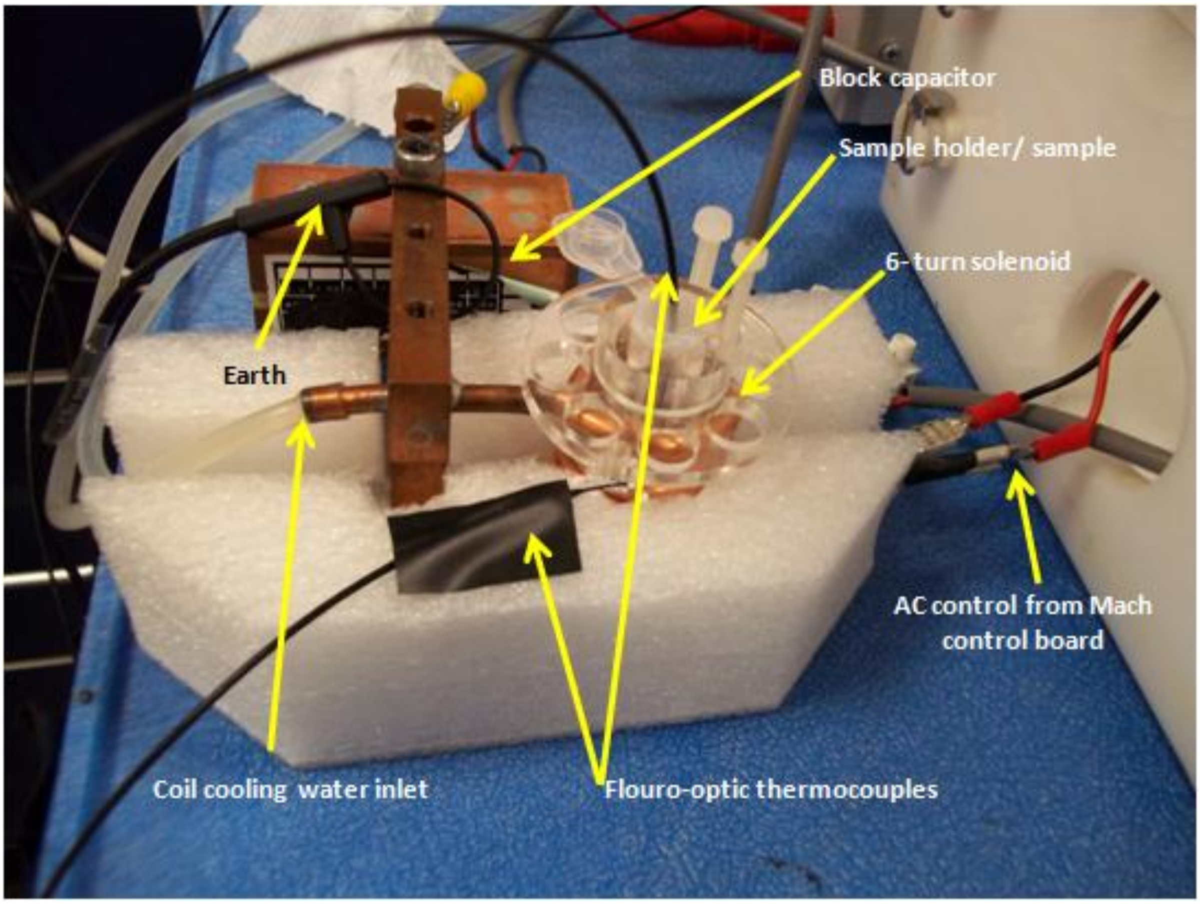

Figure 2.15: An annotated photograph of the calorimetric measurement used in the magnetic AC hyperthermia (MACH) system to induce heating from a sample.

The heating efficiency of ferrofluids determined by calorimetric measurements is typically compared using a value termed the SAR (specific absorption rate) of the material under evaluation, alternatively the same measure is also called the specific loss power (SLP) and is defined as the energy dissipated per unit mass of magnetic material (Typically W g^{-1}). Within the literature, either the mass of the magnetic phase (*e.g.* Magnetite (Fe_3O_4)/maghemite (Fe_2O_3)) present within the sample is used or the mass of the magnetic element the definition used seems to be dependent on the laboratory in which the work originated. The SAR value is calculated using equation 2.11:

$$SAR = \frac{\Delta t}{\Delta T}\frac{c}{m_{fe}}$$ **(Equation 2.11)**

Where, C is the heat capacity of the fluid per unit mass of fluid, m_{fe} is the iron mass in the fluid per unit mass of fluid (defined as either the mass of the magnetic element or mass of the magnetic phase) m_{fe} is defined as the mass of the magnetic element present in the sample when the material phase is assumed to be stoichiometric magnetite. Δt/ΔT is the initial heat rise rate determined from calorimetric measurements by fitting with a phenomelogical box lucas equation:

$$T(t) = A(1 - e^{-bt})$$ **(Equation 2.12)**

Where, T is the measured temperature, t is time, A is the saturation temperature and B is a parameter related to the curvature of the heating curve. The product (A x B at T = 0) is also known as the initial heat rise rate and is equivalent to the ratio Δt/ΔT defined in equation 2.11. Pankhurst *et al.* suggested that although the SAR value is widely used in the literature to characterise the heating efficiency of ferrofluids, it has a significant limitations in that it is an extrinsic parameter and will vary for the same magnetic fluid when measured in AC magnetic field systems with different frequencies and strengths.(Kallumadil, Tada, Nakagawa, Abe, Southern, & Pankhurst, 2009) The influence of the extrinsic parameters on the SAR value calculated for a ferrofluid can be deduced from the formula for volumetric power dissipation described by equation 2.13:

$$p = \mu_o \pi \chi^{"}(f) f H^2$$ **(Equation 2.13)**

where μ_o is the permeability of free space, $\chi^{"}$ is the out-of-phase (imaginary) component of susceptibility, and H is the applied field strength. Where, $\chi^{"}$ is intrinsically a function of f. The SAR parameter is proportional to P divided by the density of the magnetic material, hence the value of SAR varies with both H, and f thus making comparative work difficult without large numbers of measurements over various field strengths and frequencies. Pankhurst *et al,* subsequently derived a new formulation of the SAR value termed ILP which allows for the effects of field strength and frequency to be accounted for in a comparative measure.(Kallumadil, Tada, Nakagawa, Abe, Southern, & Pankhurst, 2009) This approximation relies on the work of Rosenwieg who showed to a good approximation, $\chi^{"}$ is largely frequency independent in the measurement ranges used for the evaluation of ferrofluids (*ca.* 10^5–10^6 Hz) when the sample shows a polydispersity index > 0.1 (this approximation was experimentally validated).(Rosensweig, 2002) In such cases, the SAR parameter can be regarded as a function of f and the square of magnetic field strength only as described by equation 2.14:

$$ILP = \frac{p}{\rho H^2 f} = \frac{SAR}{H^2 f}$$ **(Equation 2.14)**

The ILP is a step towards an intrinsic, system-independent parameter, derived to allow a direct comparison between materials which have been developed and evaluated in independent laboratories and under different measurement conditions. Hence, the ILP formulation has been used to compare samples presented in presented in this thesis.

2.5.14 Thermal Gravimetric Analysis:

Thermal analyses were carried out in order to study thermal behaviour of phases, their decomposition temperatures and weight loss. Simultaneous differential scanning calorimetric (DSC) and thermogravimetric analyses (TGA) were carried out using a Netesch STA 1500 using a heating rate of between 5-10 ºC min^{-1} from 30 to 800-1500 °C in air. The measurement conditions are identified within the text. Samples were analysed under a constant flow of air unless otherwise stated. Samples were analysed as freeze dried powders and typically 20 mg of a sample was used in each analysis. All samples were prepared and analyzed in alumina crucibles. In the case of the materials presented in chapter 7 section 7.3 a dynamic step was inserted into the heating rate which allowed the sample to be held at 400°C so the decomposition of an organic could be accurately quantified near a phase change.

2.6: Contributions of others

The contributions of other academics presented in this thesis is clearly identified within the text of each chapter.

Chapter 3

An Evaluation of Counter-Current Reaction Points for the Continuous Hydrothermal Synthesis of Nanoparticles

3.0 Aim:

The purpose of this chapter is to develop an experimental understanding of the mixing and particle synthesis dynamics in hydrothermal flow reactors. This chapter presents both *in-situ* temperature measurements and the characterisation of materials produced under different synthesis conditions to identify if temperature differences at the point of particle nucleation lead to changes in the physical properties of the products. This is because the bespoke nature of many continuous hydrothermal systems makes it very difficult to compare materials synthesised in different laboratories as many system parameters used for the synthesis of nanoparticles differ and are rarely standardised (*i.e.* temperature, flowrates (including flow types), type of reaction point, heating systems and cooling systems).

3.1: Introduction

As particle properties such as size, size distribution and composition are critical to the performance of many nanoceramics, there is a strong push towards achieving greater control over particle properties such as size, shape and polydispersity. (Darr and Poliakoff 1999) The resultant growth in the demand for "high quality" nanomaterials has prompted investigation into synthetic routes which are scalable and highly reproducible. To this end, many synthetic methods have been optimised to produce certain materials as reviewed in greater detail within Chapter 1. (Adschiri *et al.*, 2011, Byrappa and Adschiri 2007)

CHFS is a method based upon the rapid hydrothermal reaction of water soluble metal salts and a preheated water feed and can be used for the synthesis of many nanomaterials. (Adschiri *et al.*, 2011, Lester *et al.*, 2006) Nanoparticles are produced in CHFS when a feed of preheated water is mixed with a solution containing precursors under flow, or, alternatively a precursor flow is continually heated to produce nanoparticles. (Adschiri *et al.*, 2000, Lester *et al.*, 2006) Formation of nanoparticles occurs through the rapid hydrolysis and dehydration reactions of the metal salts upon contact with the preheated water to form the corresponding metal oxide. (Darr & Poliakoff 1999) Precipitation of the metal ion as either a hydroxide or oxide occurs when the precursor feed and preheated water feed mix due to the insolubility of the oxide in both near and supercritical water. (Lester *et al.,* 2006; Lester *et al.,* 2010) However, the contribution of hydrolysis and dehydration reactions to precipitation is not clear in the literature. (Sue *et al.,* 2004a; Sue *et al.,* 2004b; Sue *et al.,* 2006) It is widely reported that the reaction point geometry and the degree of mixing between the component streams influences the size distribution of materials produced through discrete differences in the particle nucleation and growth reactions. Although, little conclusive work has been presented for a single geometry operated over a range of process conditions as reviewed in Chapter 1. (Kawasaki *et al.,* 2010b; Lester *et al.,* 2006; Lester *et al.,* 2010)

Different reaction point designs are reported in the literature allowing the precipitation of nanoparticles when the preheated water feed and precursors mix. These designs are based on geometries with movable inlets, (Mae *et al.,* 2007) swirl type mixers, (Kawasaki *et al.,* 2010a) classical tee mixers, (Ohara *et al.,* 2004; Takami *et al.,* 2012) and nozzle type mixers, (Blood *et al.,* 2004; Lester *et al.,* 2006). Many of these designs suffer from experimental limitations arising through "poor mixing" of the component streams within geometry leading to material deposition and reactor blockage.(Lester *et al.,* 2006; Lester *et al.,* 2010) In the context of CHFS, it is widely accepted (not often stated) that the extent / efficiency of mixing between the preheated water feed and the precursor feed is the dominant step in the formation of nanoparticles. Subsequently, much effort has focused on achieving rapid and intimate mixing between to two component streams and a number of engineering solutions have been adopted which allow for the synthesis of nanoparticles. (Blood *et al.,* 2004; Lester *et al., 2*006) Consequently, authors working with these systems have defined empirical criteria for the "ideal" mixing within a mixer that result in the formation of nanoparticles, these can be summarised as follows: near instantaneous and uniform mixing of reactant streams with a supercritical water feed (essential for the formation of uniform particle nuclei), short reaction residence times are required to limit particle growth, minimal pre-heating of precursors prior to mixing with a supercritical water feed ensuring rapid uniform nuclei formation and minimal product deposition within the reactor, high flow velocity from the reaction point to prevent the accumulation of reagents and products at the reaction point. (Lester *et al.,* 2006; Toft *et al.,* 2009)

Very little work has been reported of *in-situ* investigations of mixing, therefore the effects of different processing conditions on the formation of nanoparticles and can be attributed to the difficulty of taking measurements at the conditions typically required for the synthesis of nanoparticles. (Middelkoop *et al.,* 2009; Takami *et al.,* 2012) As such, novel experimental methods have been used to visualise certain properties of a hydrothermal system at working temperatures and pressures. For example, the formation of CeO_2 nanoparticles within a counter-current mixer has been mapped using *in-situ* X-rays from a synchrotron. This analysis showed CeO_2 formed around the point at which the precursor was contacted with supercritical water and provided evidence of the initial nucleation and subsequent growth of the nanoparticles as they travelled through the mixer. (Middelkoop *et al.,* 2009) However, much of the investigation of mixers used for the synthesis of nanoparticles takes the form of comparative work *i.e.* the synthesis of nanoparticles in different mixers. (Mae *et al.,* 2009) For example, Toft *et al.* detailed a comparison between titania (TiO_2) nanoparticles synthesised using counter current and tee type reaction point geometries using supercritical isopropanol/water mixtures which showed that smaller particles were produced using a tee type geometry and suggested that the tee piece was a better reaction point geometry for this specific system. (Toft *et al.,* 2009) Similarly, Wakashima *et al.* published results on an experimental comparison between a “tee” and swirling micromixer which showed smaller NiO particles with narrower particle size distributions were produced in the latter, these observations were attributed to more uniform particle nucleation. (Kawasaki, Sue, Ookawara, Wakashima, & Suzuki 2010a) As such, attempts to evaluate different mixers are few and far from supplying a complete insight into the changes in temperature and chemical environment experienced by reagents in these systems, or the experimental observation of any adverse mixing/product deposition issues predominantly due to the difficulties of observation type measurements at typical synthesis conditions. (Middelkoop *et al.,* 2009)

The objective of this Chapter is to gain a deeper understanding of the temperature profile and physical properties of the mixture of the precursor and preheated water occurring inside a counter current reaction point, with measurements relevant to the synthesis of nanoparticles, and supplement the data with materials characterisation. Initially an operational envelope for the synthesis of two materials ZnO (hydrothermal dehydration) and hydroxyapatite (hydrothermal crystallisation) was established using the counter-current geometry and the physical characteristics of the particles produced were evaluated by XRD, Raman spectroscopy, UV-vis (ZnO samples) and TEM. Allowing, a coherent analysis of both the effects of temperature distributions within a mixer and the consequent effects of these observations on the formation of nanoparticles.

3.2 Materials and Methods:

3.2.1 Description of Mixer:

Figure 3.1 presents a schematic representation of the counter-current mixer used in this Chapter, showing all relevant dimensions used in the analysis. The details of its construction are presented in Chapter 2. This configuration was first used by Lester *et.al.* and has been applied to the synthesis of many nanoparticles and was deemed appropriate for further investigation.(Lester *et al.,* 2006) Figure 3.2 is a schematic of the process equipment used, into which the reaction point was located.

3.2.2 *In-situ* Temperature Measurements:

Temperature profiles were measured inside the counter-current mixer by inserting four long thermocouples into the reaction point at different positions as shown in Figure 3.3. The difficulties encountered in measuring the temperatures *in-situ* with fine thermocouples at such a high temperature and pressure were overcome by inserting the four thermocouples into the apparatus between the cooler and the BPR as indicated in figure 3.2, using a high pressure feed-through fitting (Spectite MF, viton elastomer seal, also supplied by TC Direct).

The temperature at eight different locations in the mixer was measured in two separate runs and the data amalgamated. The flows from pumps P1, P2 and P3 (figure 3.2) were all de-ionised water for these experiments, as it was found that during the synthesis of nanoparticles the thermocouples fouled (reducing reliability). The positions of the thermocouples are quoted relative to the outlet of the inner tube in shown in figure 3.3, and the terminus of the inner tube is defined as z = 0 with positive z in the direction towards the outlet. This strategy permitted the temperature to be measure in the bulk flow, the positions of the thermocouples are quoted to *ca.* ± 2 mm in the z direction and could be situated at any point along the axis in the x direction as summarised in figure 3.3 (limiting the interpretation of the measurements). The temperature measurements reported herein were of a non-insulated mixing point as insulation of the mixing point is not normally used during synthesis as it has to be removed after each use (for maintenance and the identification of leaks). Furthermore, measurements obtained from an insulated mixing point consistently showed temperatures which were only *ca.* 6-12 °C higher than those obtained without insulation suggesting only negligible heat loss through radiation (data not shown).

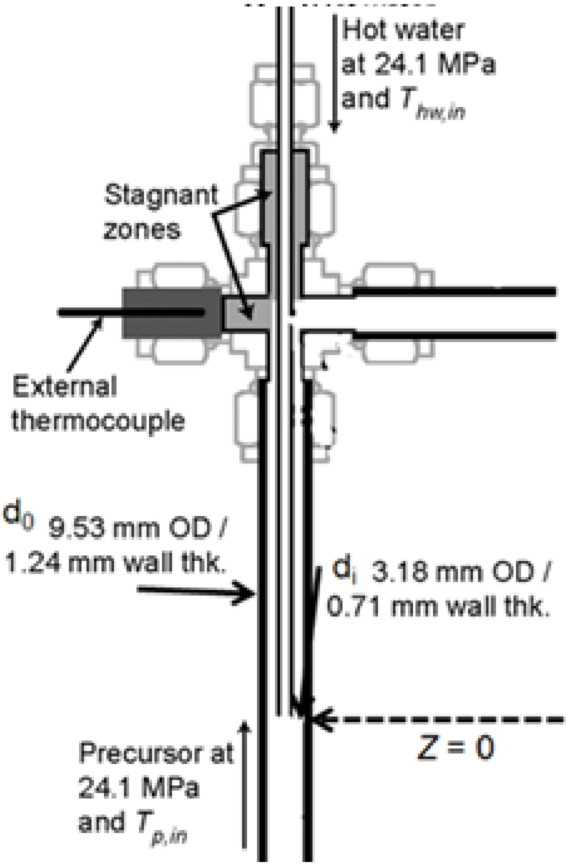

Figure 3.1: Schematic representations of the counter current mixer

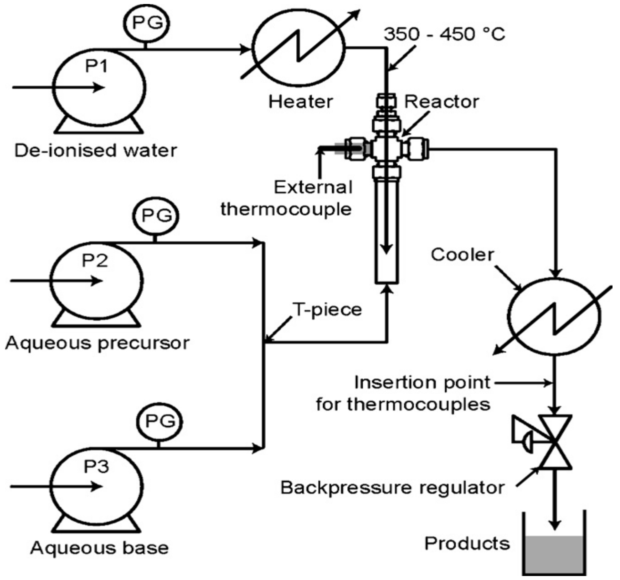

Figure 3.2: Schematic diagram of the CHFS process that was used for the synthesis of ZnO and Hydroxyapatite nanoparticles.

3.2.3 Operational Envelopes for the Synthesis of Hydroxyapatite and ZnO:

3.2.3.1 Reagents:

Diammonium hydrogen phosphate ($(NH_4)_2HPO_4$, 98.3 %), calcium nitrate tetrahydrate ($Ca(NO_3)_2.4H_2O$, 99.0 %), Zinc nitrate hexahydrate ($Zn(NO_3)_2\cdot6H_2O$, 99 %)) and potassium hydroxide (KOH (96 %)) were obtained from Sigma-Aldrich (Dorset, UK). Ammonium hydroxide solution (NH_4OH, 30% w/w) was obtained from VWR International (Lutterworth, UK). Tables 3.1 and 3.2, provide details of the experimental conditions used for the synthesis of hydroxyapatite and ZnO samples, respectively. In total, 23 reactions were run to define an operational space for the synthesis of hydroxyapatite and 15 reactions defined an operational space for the synthesis of ZnO nanoparticles. Descriptions of the procedure used for the synthesis of each system are presented in sections 3.2.1.2 and 3.2.1.3, for ZnO and hydroxyapatite samples, respectively.

3.2.3.2 Synthesis of ZnO:

Zinc oxide nanopowders were synthesised as detailed in table 3.1. The schematic diagram of the CHFS reactor used in this work is presented in figure 3.1. Pump 2 was used to feed Zn salts to meet a feed of KOH issuing from pump 3. Flow regimes are referred to as the volumetric ratio of the feeds issuing from P1 (supercritical water feed [Q_{sw}]) and the combined flow from P2 and P3 (hereafter referred to as precursor [Q_p]). Sample volumes of *ca.* 500 mL nanoparticle laden slurry were collected from the exit of the CHFS system and recovered using the method detailed in Chapter 2. Samples were labelled according to synthesis condition and are identified alongside the condition used for synthesis in table 3.1. Reaction yields were calculated from the recovered dry particle mass from a fixed volume of raw slurry.

Table 3.1: Summary of the synthesis and characterisation data for ZnO nanoparticles.

ID	Q_{sw}	Precursors		Qp		T_{mix1} (°C)	RT (s)	Crystallite size (nm)			Yield (%)	E_g (eV)
	P1	[Zn] (M)	[KOH] (M)	P2	P3			Cs	TEM	SD		
ZnO1	20	0.1	0.00	10	10	199	4.19	-	-	-	-	-
ZnO2	20	0.1	0.00	10	10	305	3.48	-	-	-	-	-
ZnO3	20	0.1	0.00	10	10	335	3.16	-	-	-	-	-
ZnO4	20	0.1	0.10	10	10	199	4.19	-	-	-	-	-
ZnO5	20	0.1	0.10	10	10	305	3.48	-	-	-	-	-
ZnO6	20	0.1	0.10	10	10	335	3.16	44.2	65.7	13.3	58	3.26
ZnO7	20	0.1	0.25	10	10	335	3.16	31.7	49.5	11.2	90	3.26
ZnO8	20	0.1	1.50	10	10	335	3.16	31.9	54.4	16.7	85	3.26
ZnO9	20	0.1	2.00	10	10	335	3.16	30.5	61.4	12.2	94	3.27
ZnO10	20	0.05	0.10	10	10	335	3.16	30.6	68.8	14.2	83	3.27
ZnO11	20	0.1	0.10	10	10	335	3.16	31.4	64.6	11.9	89	3.26
ZnO12	20	0.2	0.10	10	10	335	3.16	30.6	60.1	9.70	90	3.27
ZnO13	15	0.1	0.10	7.5	7.5	335	4.22	33.2	67.1	13.5	90	3.27
ZnO14	10	0.1	0.10	5	5	335	6.33	31.4	62.1	15.8	89	3.26
ZnO15	20	0.1	0.10	10	10	335	6.33	33.2	59.3	14.8	91	3.27
ZnOAP1	20	0.1	0.05	10	10	22	4.80	-	-	-	86	-
ZnOAP1	20	0.1	0.10	10	10	22	4.80	-	-	-	85	-
ZnOAP1	20	0.1	0.20	10	10	22	4.80	-	-	-	83	-

Key: T_{mix1} = reaction point temperatures (°C) determined by enthalpy balance (Equation 3.1), RT = Residence time (assuming complete mixing at the terminus of the preheated water inlet). Eg = Bandgap (eV) determined from the Kubelka-Munk function detailed in Chapter 2. Cs = the crystallite size determined from the application of the Scherrer equation, Q_{sw} = flow rate of preheated water (mL min^{-1}) and Q_p = combined flow rate of precursor (P2 + P3).

3.2.3.3 Synthesis of Hydroxyapatite:

Hydroxyapatite nanoparticles were synthesised using the conditions presented in table 3.2. Initially reactions were based on the work of Chaudhry *et al*. (Chaudhry *et al.,* 2006) The CHFS system used to evaluate the synthesis of hydroxyapatite was the same as that used for the synthesis of ZnO (section 3.2.1.2). Calcium nitrate and diammonium hydrogen phosphate solutions were pumped by pumps 2 and 3, respectively. Hereafter, these are referred to as precursor (Q_p) and P1 was used to supply supercritical water feed (Q_{sw}). The pH of the solution is quoted as that of the mixture and was iteratively adjusted by the addition of NH_4OH solution (28 % v/v). Samples were labelled incrementally and are listed grouped per variable in table 3.2. After collection at the end of the back pressure regulator (BPR), the particles were washed, centrifuged, and then freeze dried according to the method details given in Chapter 2. Materials were characterised using TEM, Raman, XRD and XPS.

3.3 Results and Discussion:

3.3.1 *In-Situ* Measurements of Temperature

Figure 3.3 b shows a sample of four simultaneous measurements at locations within the counter-current mixer corresponding to z = 0, - 10, - 20 and - 22 mm, as described pictorially in figure 3.3a and provides an indication of the noise associated with the measurements in different flow regimes. At t = 0 (Figure 3.3b), the flowrates of superheated water, Q_{sw}, and 'precursors', Q_p, were both 20 mL min^{-1}, at t = 150 s Q_{sw} was increased to 25 mL min^{-1} and Q_p was reduced to 10 mL min^{-1}. As can be seen the transition from a balanced to unbalanced flow regime saw a substantial increase in the "noise" associated with the measurements. The fluctuations are most likely the result of inhomogeneity in the fluids due to the time taken for the positive displacement HPLC pumps to refill (125 ms). Serving to represent the noise observed in the measurements for each theoretical mixture temperature, as determined from enthalpy balance (equation 3.1):

$$\overline{H}_{out,calc}(T_{out,calc},24.1\,\mathrm{MPa}) = \frac{G_{sw}\overline{H}_{sw,in}(T_{sw,in},24.1\,\mathrm{MPa}) + G_p\overline{H}_{p,in}(20\,^{\circ}\mathrm{C},24.1\,\mathrm{MPa})}{G_{sw}+G_p}$$

(Equation 3.1)

Where, Gs_w and G_p are the mass flow rates of the preheated water and precursor feeds. The specific enthalpies $\overline{H}_{sw,in}$ and $\overline{H}_{p,in}$ and the temperature $T_{out,,calc}$ at which the specific enthalpy is $\overline{H}_{m,out}$ at 24.1 MPa were determined for from the IAPWS Formulation 1995 as described in Chapter 2. All interpretation presented from here is subject to the limitations associated with the noise observed in each measurement condition.

Table 3.2: Summary of the synthesis conditions used for the production of Hydroxyapatite nanoparticles using CHFS system 1.

ID	**Q_{sw}**	**Q_p**		**[Ca] (M)**	**[P] (M)**	**pH**	**$T_{mix\ 1}$ (°C)**	**RT (s)**	**Crystallite size (nm)**			**Aspect ratio (SD)**	**Yield (%)**
		Ca (P2)	**P (P3)**						**C_s**	**TEM**	**SD**		
HA1	20	10	10	0.1	0.05	10	199	4.19	-	261	92.3	3.89 (1.23)	86
HA2	20	10	10	0.1	0.05	10	305	3.48	-	208	73.3	4.16 (1.35)	87
HA3	20	10	10	0.1	0.05	10	335	3.16	-	235	74.4	4.61 (1.54)	98
HA4	25	5	5	0.1	0.05	10	383	2.16	-	252	83.9	4.02 (1.48)	90
HA5	20	10	10	0.1	0.05	11	335	3.16	-	261	77.6	4.34 (2.02)	97
HA6	20	10	10	0.1	0.05	10	335	3.16	-	223	79.6	5.13 (2.31)	86
HA7	20	10	10	0.1	0.05	9	335	3.16	-	221	74.7	4,56 (1.75)	88
HA8	20	10	10	0.1	0.05	8	335	3.16	-	203	62.1	4.46 (1.78)	83
HA9	20	10	10	0.1	0.05	6	335	3.16	-	271	95.1	4.23 (1.39)	80
HA10	15	7.5	7.5	0.1	0.05	10	335	4.22	-	246	78.5	4.67 (1.89)	89
HA11	10	5	5	0.1	0.05	10	335	6.33	-	230	78.5	4.56 (1.32)	83
HA12	20	10	10	0.1	0.05	10	335	6.33	-	219	73.8	3.92 (1.69)	89
HA13	20	10	10	0.1	0.058	10	335	3.16	-	234	86.3	4.04 (1.57)	87
HA14	20	10	10	0.1	0.055	10	335	3.16	-	269	92.7	4.56 (2.10)	81
HA15	20	10	10	0.1	0.052	10	335	3.16	-	247	73.4	4.34 (1.89)	86
HA16	20	10	10	0.1	0.05	10	335	3.16	-	282	87.3	4.29 (145)	84
HA17	20	10	10	0.1	0.045	10	335	3.16	-	261	84.3	4.11 (1.54)	87
HA18	20	10	10	0.2	0.1	10	335	3.16	-	254	78.2	4.14(1.34)	82
HA19	20	10	10	0.05	0.025	10	335	3.16	-	249	92.7	4.26 (1.58)	89
HA20	20	10	10	0.025	0.0125	10	335	3.16	-	278	80.2	4.28 (1.49)	74
Ap9	20	10	10	0.1	0.05	9	22	8.80	-	89	22	3.72(1.10)	32
Ap10	20	10	10	0.1	0.05	10	22	8.80	-	78	15	3.14 (1.34)	35
Ap11	20	10	10	0.1	0.05	11	22	8.80	-	84	21	3.69(1.56)	42

Key: T_{mix1} = reaction point temperatures (°C) determined by enthalpy balance (Equation 3.1), RT = Residence time (assuming complete mixing at the terminus of the preheated water inlet). Cs = the crystallite size determined from the application of the Scherrer equation, Q_{sw} = flow rate of preheated water (mL min^{-1}) and Q_p = combined flow rate of precursor (P2 + P3), Aspect ratio = the length / width of particles viewed using TEM, P = diammonium hydrogen phosphate solution and Ca = calcium nitrate tetrahydrate solution.

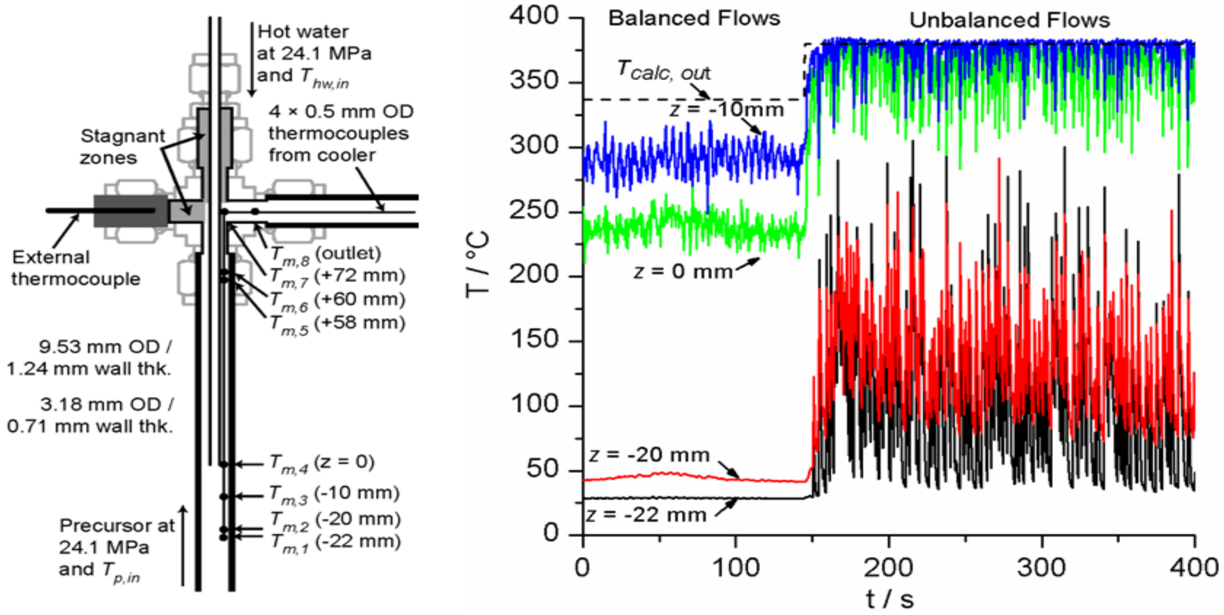

Figure 3.3: a) locations of thermocouples placed within the mixer **b)** graphical representation of the noise associated with the measurements for a transition from a balanced to un-balanced flow regime ($T_{p,in}$ = 20 °C for all experiments). $T_{calc,out}$ is the outlet temperature calculated from Equation 3.1.

The temperature profiles measured as a function of z within the mixer point are shown in figure 3.4 for heater temperatures (T_{sw}) of 400 and 450 °C. The dashed lines in Figures 3.4 show the theoretical temperature (T_{mix}) at the outlet of the entire mixer for each flow condition, assuming complete mixing and any heat losses from the outer pipe to the surroundings are negligible as determined by equation 3.1. It is apparent from the temperature profiles shown in figures 3.4 a and b that the mixture ($Q_p + Q_{sw}$) flowing through the annulus between the inlet tube and the outer pipe is not isothermal and the temperature at z = 0 of the combined flow $Q_p + Q_{sw}$ is much lower than that at the outlet from the mixer (*z* = 72 mm). This observation suggests dynamic variation of the temperature and flow properties occur as a function of Q_p, Q_{sw} and T_{sw}. These observations also suggest that differences in the properties of nanoparticles should be observed, principally as the largest variation in temperature and thus particle formation would occur around the point of particle nucleation. (Adschiri *et al.*, 1992a; Adschiri *et al.*, 1992b; Takami *et al.*, 2012) As in CHFS, mixing results in rapid changes in temperature which are regarded as the dominant force for particle nucleation and growth. (Lester *et al.*, 2006)

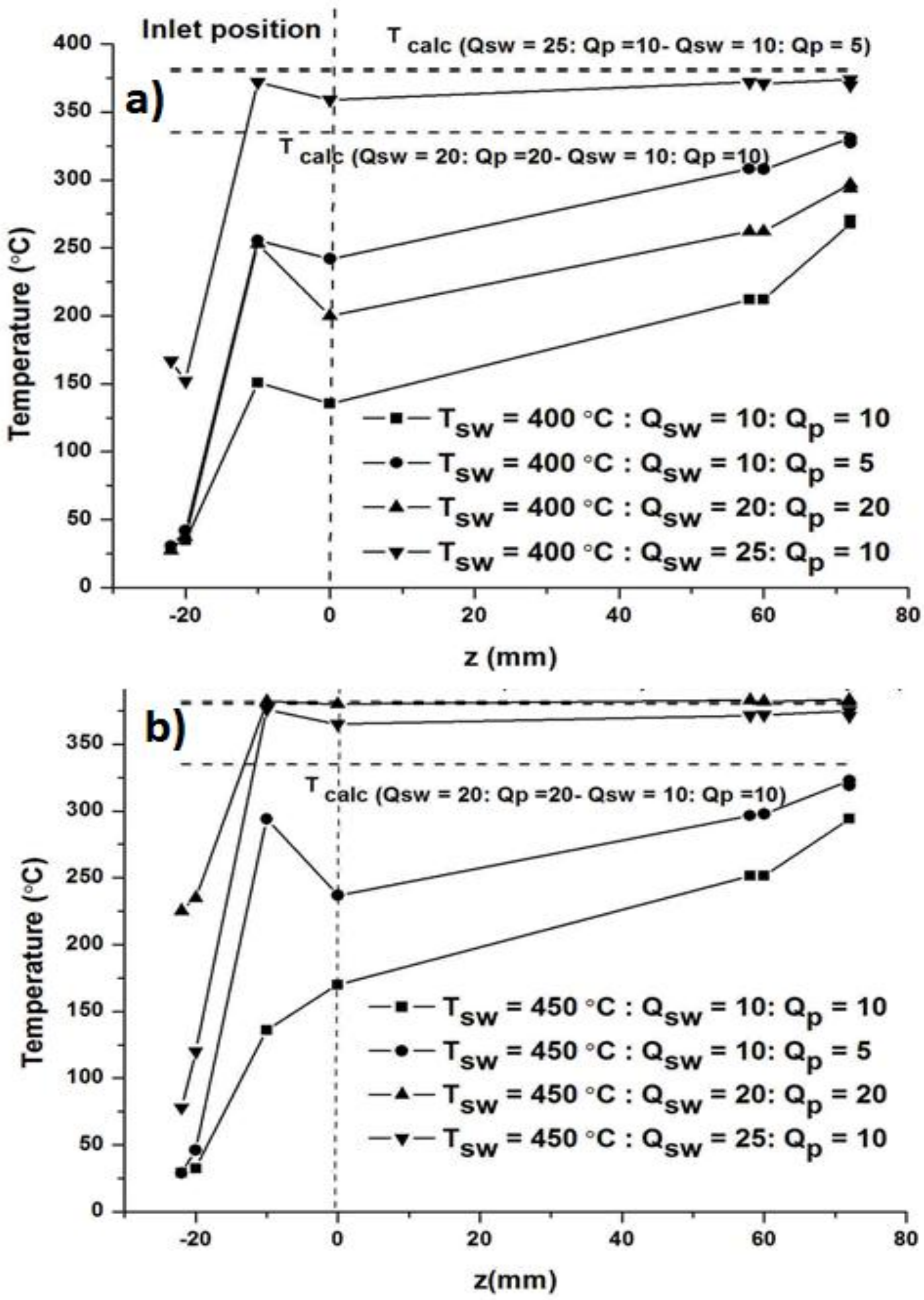

Figure 3.4: Temperature profiles measured within the counter-current reaction point geometry using preheated water temperatures of **a)** 450 and **b)** 400 °C, respectively. Dashed lines represent the theoretical mixture temperature determined by Equation 3.1 and each measurement condition is defined within the figure.

From the measurements presented in figures 3.4 a and b, it is interesting to consider the processes of mass and heat transfer underpinning mixing in the counter-current reaction point, to better define events occurring at z = 0 (*i.e.* around the point of particle nucleation) and explain some of the observation made in figure 3.4. As the superheated water exits the inner tube it is acted upon by three dominant forces; **i)** drag due to the difference in velocity between the downward moving superheated water and the upward moving mixture, **ii)** buoyancy due to differences in density and **iii)** the net pressure gradient. As shown in the temperature measurement the apparent penetration of Q_{sw} into Q_p depends on both T_{sw} and Q_{sw}, and Q_p as there is a significant difference in density between Q_{sw} and the cooler mixture flowing around it $Q_{sw} + Q_p$ which is highly dependent upon the magnitude of heat transfer occurring between the flows. To estimate the temperature and thus the properties of Q_{sw} exiting the inner tube the apparent contribution of heat transfer was determined. Where, the mixer is treated as a counter-current heat exchanger. Assuming all heat lost from the superheated water (ΔQs_w) equals that gained by the cooler mixture (ΔQ_m) as determined by enthalpy balance (the cooler mixture is defined as $Q_{sw} + Q_p$) (equation 3.2):

$$\Delta Q_m = \Delta Q_{sw} = G_p[h_p(T_{z=0}, 24.1\,\mathrm{MPa}) - h_p(T_{z=72}, 24.1\,\mathrm{MPa})]$$. **(Equation 3.2)**

The specific enthalpy and thus the temperature of the superheated water exiting the inner tube at z = 0 may subsequently be determined from (Equation 3.3):

$$H_{sw}(T_{sw,z=0}, 24.1\,\mathrm{MPa}) = H_{sw}(T_{sw,in}, 24.1\,\mathrm{MPa}) - \frac{\Delta Q_{sw}}{G_{sw}}$$ **(Equation 3.3.)**

Values of $T'_{sw,z=0}$ determined from equations 3.2 and 3.3 are given in table 3.3. Values of $T'_{sw,z=0}$ for unbalanced flows at $T_{sw,in}$ = 400 and 450 °C have been excluded, as the temperature rise from z = 0 to 72 mm was only a few degrees, but the magnitude of ΔQ_m from equation 3.2 was large owing to the increase in the specific heat capacity of water near to its critical temperature as described further in Chapter 1. The measurements presented for low Q_{sw} and Q_p are also omitted, as it is apparent significant heat loss is occurring within the system.

Table 3.3: Temperature profiles (30-second time averaged) in counter current mixer as a function of Q_p and Q_{sw} ($T_{p,in}$ = 20 °C for all experiments). $T_{calc,out}$ is the outlet temperature calculated from Equation 3.1. $T_{sw\ (z\ =\ 0)}$ is the temperature of the superheated water leaving the inner pipe calculated from Equation 3.2 and 3.3. $\mathrm{Re}_{sw(z\ =\ 0)}$ and $(\mathrm{Fr}_{sw(z\ =\ 0)})^2$ are the dimensionless Reynolds and Froude numbers of Q_{sw} at z = 0.

No.	Ts_w	Q_{sw}	Q_p	$T_{z=0}$	$T_{z=72}$	$T^{'}_{m,out}$	$T^{'}_{sw,z=0}$	$\mathrm{Re}_{sw,z=0}$	$(\mathrm{Fr}_{sw,z=0})^2$
	(°C)	mL min^{-1}		(°C)	(°C)	(°C)	(°C)	x 10^3	
1	400	10	10	135	268	307	323	1.5	1.6
2	400	20	20	200	297	307	362	3.6	6.2
3	400	10	5	280	310	367	-	6.3	?
4	400	25	10	359	374	377	-	9.8	21.8
5	450	10	10	170	294	337	373	2.1	1.3
6	450	20	20	237	323	337	381	5.9	6.5
7	450	10	5	250	350	382	-	7.4	?
8	450	25	10	380	383	382	-	10.5	44.9

From the measurements presented in figure 3.4 and calculation of the temperature of Q_{sw} exiting the inner tube at z = 0 it is possible to assess the behaviour of the flow of Q_{sw} which from much of the available literature should influence the precipitation of nanoparticles. (Kawasaki *et al.,* 2010b; Lester *et al.,* 2006; Sue *et al.,* 2006) The relative magnitude of the momentum of the flow of Q_{sw} water at $z = 0$ compared to the viscous drag force can be represented by the Reynolds number, $\mathrm{Re}_{sw,z=0}$, of the flow as described by equation 3.4:

$$\mathrm{Re}_{sw,z=0} = \frac{\rho_{sw} u_{sw} d_i}{\mu_{sw}} = \frac{4G_{sw}}{\pi d_i \mu_{sw}} \quad \textbf{(Equation 3.4)}$$

Where, ρs_w, u_{sw} and μ_{sw} are the density, velocity and dynamic viscosity, of the superheated water exiting the inner tube at z = 0 determined from the IAPWS formulations and d_i is the internal diameter of the inlet (1.76 mm). The values of $\mathrm{Re}_{sw,z=0}$ are summarized in table 3.3. Similarly, the relative magnitude of the momentum of the jet acting downwards compared to the buoyancy force acting upwards (due to differences in fluid density) can be represented by the square of the Froude number, $(\mathrm{Fr}_{sw,z=0})^2$ as defined in equation 3.5:

$$(\mathrm{Fr}_{sw,z=0})^2 = \frac{\rho_{sw} u_{sw}^{\ 2}}{g d_i (\rho_m - \rho_{sw})} = \frac{16 G_{sw}^{\ 2}}{\pi^2 d_i^{\ 5} \rho_{sw} (\rho_m - \rho_{sw}) g} \quad \textbf{(Equation 3.5)}$$

Where, ρ_m is the density of the mixture determined from the temperature measured at $z = 0$ in each run (table 3.3). When the value of $(\mathrm{Fr}_{w,z=0})^2$ is > 1, the momentum of the flow dominates, resulting in greater penetration of into the oncoming flow of Q_p, whilst a magnitude of $(\mathrm{Fr}_{w,z=0})^2 << 1$ suggests buoyancy forces dominate, and a rapid reversal in the direction of the flow is expected under this condition.

The magnitudes $\mathrm{Re}_{sw,z=0}$ in table 3.3 suggest that the superheated water exiting the inlet at Z = 0 is either laminar ($\mathrm{Re}_{sw} < 2300$) or turbulent ($\mathrm{Re}_{sw} > 5000$) depending on the flowrates and temperatures used. In particular, the superheated water flow appears to be turbulent ($\mathrm{Re}_{sw,z=0} \approx 1 \times 10^4$) in the experiments using unbalanced flows and $T_{sw} \geq 400$ °C. Expressed in terms of the mass flowrate of superheated water, G_{sw}, it is clear from Equation 3.4 that Re_{sw} depends heavily on dynamic viscosity, μ_{hw}, (*i.e.* the temperature at z = 0) at constant d_i, and G_{sw}. This shows the process is dynamic around the magnitude of heat transfer occurring between Q_{sw} and $Q_{sw} + Q_p$. More interesting are the variations in the magnitude of $(\mathrm{Fr}_{sw,z=0})^2$ given in table 3.3 shows that at the lowest, but balanced, flowrates, the momentum of the jet and the buoyancy force opposing it are of a similar magnitude, *i.e.* $(\mathrm{Fr}_{sw,z=0})^2 \approx 1$ and the flow of Q_{sw} at Z = 0 would behave more as a plume. Whereas, at the higher balanced flowrates, momentum begins to dominate over the buoyancy force, *i.e.* $(\mathrm{Fr}_{sw,z=0})^2 > 1$ and the flow would behave more like a jet. Under this approximation it would be assumed that a higher degree of mixing and thus a more rapid change in the temperature of Q_p would be expected when the flow issuing from the inlet behaves more like a jet. (Strykowski and Niccum 1991) Similarly, the penetration of the jet of superheated water deep into the precursor when the flowrates are unbalanced and at $T_{sw} \geq 400$ °C, evident in the temperature measurements shown in figure 3.4 a and b, appears to result from two factors: **i)** a transition from a situation in which the momentum of the jet of superheated water is approximately in balance with the drag and buoyancy forces opposing it ($\mathrm{Re}_{sw,z=0} \approx 2000$ and $(\mathrm{Fr}_{sw,z=0})^2 \approx 1$) to one in which momentum dominates

($Re_{sw,z=0} \approx 10000$ and $(Fr_{sw,z=0})^2 >> 1$) and **ii)** the effect of thermal dilation due to entrainment of the mixture of 'precursors' and superheated water into the jet of superheated water issuing from the inner pipe is less significant when the mixture is above the critical temperature of water (low density) than when it is below the critical temperature (much higher density). Suggesting that in a counter-current geometry the mixture flowing upwards past the jet (containing nanoparticles under reaction conditions) may under some flow regimes be pulled back into the jet, resulting in re-circulation and a broadening of the residence time distribution of the mixer, which may serve to dynamically influence the synthesis conditions used for the production of nanoparticles. Similarly under these conditions recirculation of the flow in the region z = -10 to -20 would be expected as the combined flow of $Q_p + Q_{sw}$ would be entrained into the rear of the issuing jet. (Sreenivasan *et al.,* 1989a; Sreenivasan *et al.,* 1989b)

In light of these observations *i.e.* the noted differences in both temperature profile and possible differences in mixing events at z = 0, this chapter now moves forward to assess the effects of mixing near the terminus of the preheated water inlet on the formation of nanoparticles produced under different flow and chemical conditions. Materials synthesis performed in an unbalanced flow regime as the synthesis of both ZnO and HA resulted in rapid reactor blockage at *ca.* z = -20 mm and it was deemed unsafe to produce materials under these conditions. However, reference is made to the synthesis of HA under this flow condition although the reactor rapidly blocked.

3.3.2 Synthesis of Nanoparticles:

3.3.2.1 Synthesis of ZnO Nanoparticles:

The purpose of this section is to define an operational envelope for the synthesis of ZnO nanoparticles using CHFS, in light of the temperature analysis presented in section 3.3.1, the samples presented in this section are identified in table 3.1.

All syntheses reported in this section yielded products which were identified as Wurtzite structure ZnO. XRD patterns of the products reported in this section are shown in figure 3.5a and all show good agreement with JCPDS pattern 76-0704. To confirm the structure of ZnO, Raman spectra obtained for the samples are shown in figure 3.5b, and confirmed the phase assignment made through XRD. The two modes centred at 435 and 404 cm^{-1} are attributable to the $E_{2(high)}$ and $E_{1(TO)}$ phonons of ZnO with the hexagonal space group *Pmm6/3* and a mode centred at 327 cm^{-1} is attributable to the (E_{2H} - E_{2L}) second order phonon. (Calleja and Cardona 1977) UV-Vis was used to further assess the similarity of the reaction products (data not shown). All the samples showed a good absorption over the entire range of UV and little or no visible absorbance consistent with that expected for ZnO. The calculated band-gap values are shown in table 3.1 for the samples reported in this section. The bandgap values were all slightly red shifted when compared to reported bulk ZnO band gap of 3.37 eV, yet internally consistent providing a further measure of the structural and compositions similarity in the products. (Hale *et al.,* 2005)

To confirm the reported mechanism of ZnO formation in hydrothermal solution described by equations 3.6 - 3.8, several control reactions were performed to ensure that the formation of ZnO nanoparticles was not internally limited by any chemical factor. In CHFS, no product was recovered from the process regardless of reaction point temperature (reactions ZnO1 - 3) in the absence of KOH and a clear solution was formed, thought to be a Zn peroxide species (ZnO_2^{2-}). (Demianets *et al.,* 2002; Kolb *et al.,* 1967; Sue *et al.,* 2004a; Sue *et al.,* 2006) However, the addition of KOH to the reaction yielded crystalline ZnO at reaction temperatures > 305 °C (reactions ZnO4 - 6). To ensure that the coprecipitation reaction of ZnO with KOH prior to hydrothermal reaction did not limit the particle size formed through the process the co-precipitate formed upon mixing KOH and Zn feeds within the CHFS process were characterised, samples ZnOAP1 - 3 (table 3.1). These materials were amorphous as determined by XRD and were likely to be $Zn(OH)_2$, formed through equation 3.6 (data not shown). TEM images taken of the coprecipitate formed at a KOH concentration of 0.1 M, showed no resolvable crystallites (data not shown). Reactions ZnO4 - 6 (table 3.1) demonstrated that although a coprecipitate was formed by mixing KOH and ZnO at ambient temperature the formation of ZnO was shown to transition through a soluble intermediate (ZnO_2^{2-}) described by equation 3.7. (Demianets *et al.,* 2002) These observations are consistent with the reported reactions leading to the formation of ZnO in hydrothermal systems. Where, equations 3.6 and 3.7 define the hydrolysis (formation of insoluble zinc species) and dehydration reactions responsible for ZnO_2^{2-} formation under hydrothermal conditions, which occur upon mixing the precursor solution with supercritical water, and the concentration of KOH contribute to the formation of the product (possibly by aiding nucleation of ZnO from solution) described by equation 3.8. (Demianets *et al.,* 2002) The crystallisation of ZnO only at occurring at reaction point temperatures > 305 °C suggest that the increased supersaturation afforded by both KOH and the low dielectric constant of water at > 305 °C (*ca.* 23, deterimed from IAPWS formulations), suggests a synergistic effect between both lower solubility of Zn (through increasing temperature) and chemically induced supersaturation, which are both required for the formation of ZnO *via* CHFS.

$$Zn(OH)_2 + 2OH^- \rightarrow Zn(OH)_4^{2-}.$$ **(Equation 3.6)**

$$Zn(OH)_4^{2-} \rightarrow 2H^+ + ZnO_2^{2-}.$$ **(Equation 3.7)**

$$Zn(NO_3)_2 \bullet 6\,H_2O + 4OH^- \rightarrow Zn(OH)_2^{4-} + O^{2-} \rightarrow Zn(OH)_2 + 2OH- \rightarrow ZnO_2^{2-} + 2H \rightarrow ZnO\ (crystal) + 2e^-$$ **(Equation 3.8)**

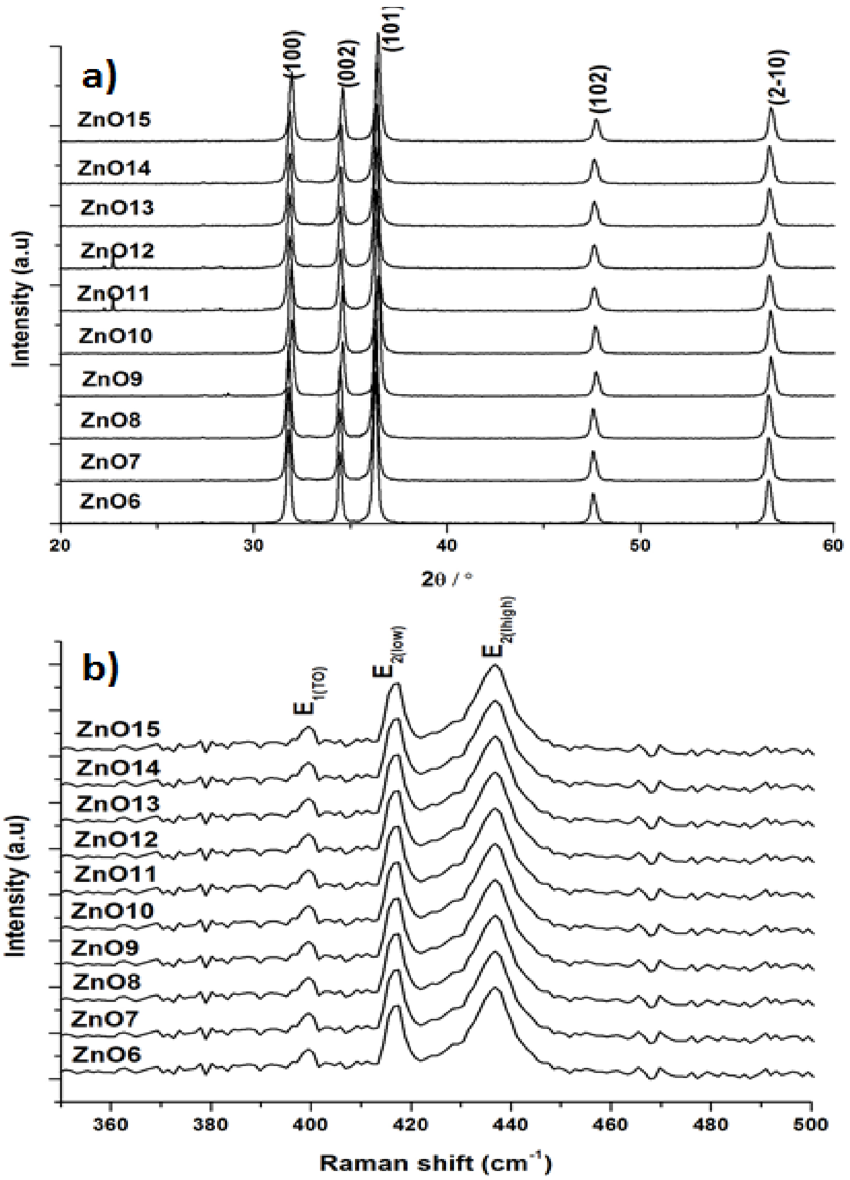

Figure 3.5: a) XRD patterns of ZnO nanoparticles produced using CHFS under the conditions stated in table 3.2, **b)** Raman spectra of ZnO.

To ensure that particle formation of ZnO was not significantly influenced by KOH concentration a series of samples were produced in which the concentration of KOH was varied, represented by reactions ZnO7 - 11. Characterisation of the particles produced under these conditions using TEM showed that the concentration of KOH marginally affected the crystallite size and only a slight trend in crystallite size and sample polydispersity were observed on variation of Zn : KOH concentration, with crystallite sizes of 49.5, 54.4, 65.7 and

61.5 nm obtained for samples when the KOH concentrations of 0.25, 0.1, 1.0 and 2.0 M, were used (table 3.1). A similar observation has been made previously, where in a continuous hydrothermal tubular reactor ZnO particle size was shown to decrease on increasing KOH concentration, and was attributed to greater supersaturation and the dominance of particle nucleation in the synthesis. The data presented here shows the opposite trend (suggesting the interpretation put forward previously was biased by some intrinsic system parameter *i.e.* the temperature profile as the reported nanomaterials were larger than those presented here). (Ohara *et al.,* 2004; Sue *et al.,* 2006) The observations presented herein suggest that increasing KOH in counter current reactor, influenced to a greater degree the growth phase of ZnO, in that growth appears retarded in the presence of low concentrations of KOH as inferred by the lower reaction yield (*ca.* 58.6 %). Suggesting that in the formation of ZnO via CHFS is codependent upon both a chemical driving force for precipitation or addition of Zn species to particle nucleates and the reaction temperature an observation well reported in the literature. (Demianets *et al.*, 2002)

Reactions ZnO12 - 14 present the synthesis of ZnO under variable flow rates, in these reactions samples with striking similarity in both the primary crystallite size and sample polydispersity (sd) (*ca.* 60.1 (9.7), 67.1 (13.5) and 62.1 (15.7) nm for materials produced using $Q_p + Q_{sw} = 40$, 30 and 20 mL min^{-1}, respectively) were obtained (figure 3.6). The similarity in both crystallite size and size distribution is surprising in light of the differences in temperature profile measured between the highest and lowest flow rates, as a comparatively large temperature deviation was observed as a function of both T_{sw} and $Q_p : Q_{sw}$ around the point of particle nucleation (figure 3.4). These observations suggests that the particle nucleation is less sensitive to slight differences in mixing before a critical temperature is reached (*ca.* >305 °C). In effect making the formation of Zn species independent of the events occurring at the terminus of the preheated water inlet. Inference from these observations suggest that particle nucleation and growth are similar over the processing range due to high degrees of supersaturation and upon onset of particle nucleation and a rapid particle growth phase occurs, limited by exhaustion of Zn species in solution. (Demianets *et al.,* 2002; Liu and Zeng 2003) Although, from the temperature measurements presented in section 3.1 it is evident that the time scale of this transition to a supersaturated state would differ considerably between flow rates. To confirm that growth was constrained by exhaustion of the Zn species in solution and the particles do not grow *via* coarsening, a sample was produced increasing the residence time of the reaction by lengthening the reaction zone (reaction ZnO15). This sample showed that particles with similar physical characteristics to those produced in other reactions were obtained at a similar reaction yield (summarised in table 3.1). Confirming that particle growth was constrained by a reduction in the driving for particle growth caused by near exhaustion of the Zn species in solution and the particles did not grow *via* a coarsening mechanism.

3.3.2.2 Summary:

In summary, the synthesis of ZnO nanoparticles was used to assess the effect of different CHFS processing conditions on the formation of nanoparticles. This analysis also assessed the effect of differences in the mixing between the preheated water feed and the precursor feed as identified in the previous section. The mechanism of ZnO formation was found to be consistent with the growth processes of ZnO produced in both batch and other hydrothermal processes. In this CHFS process it was observed that particles showing similar characteristics are formed over a wide range of experimental variables. The results suggest that the initial mixing between the component streams in a counter-current reaction point are not critical to the synthesis of ZnO under the experimental conditions evaluated, and are in fact governed by the terminal temperature. However, it is speculated that this may not be the case in the continuous hydrothermal synthesis of all metal oxides using CHFS. This chapter now moves forward to evaluate the synthesis of a non-oxide based nanomaterial (hydroxyapatite) to assess if observed differences in mixing result in different particle characteristics in materials which are formed through a different mechanism.

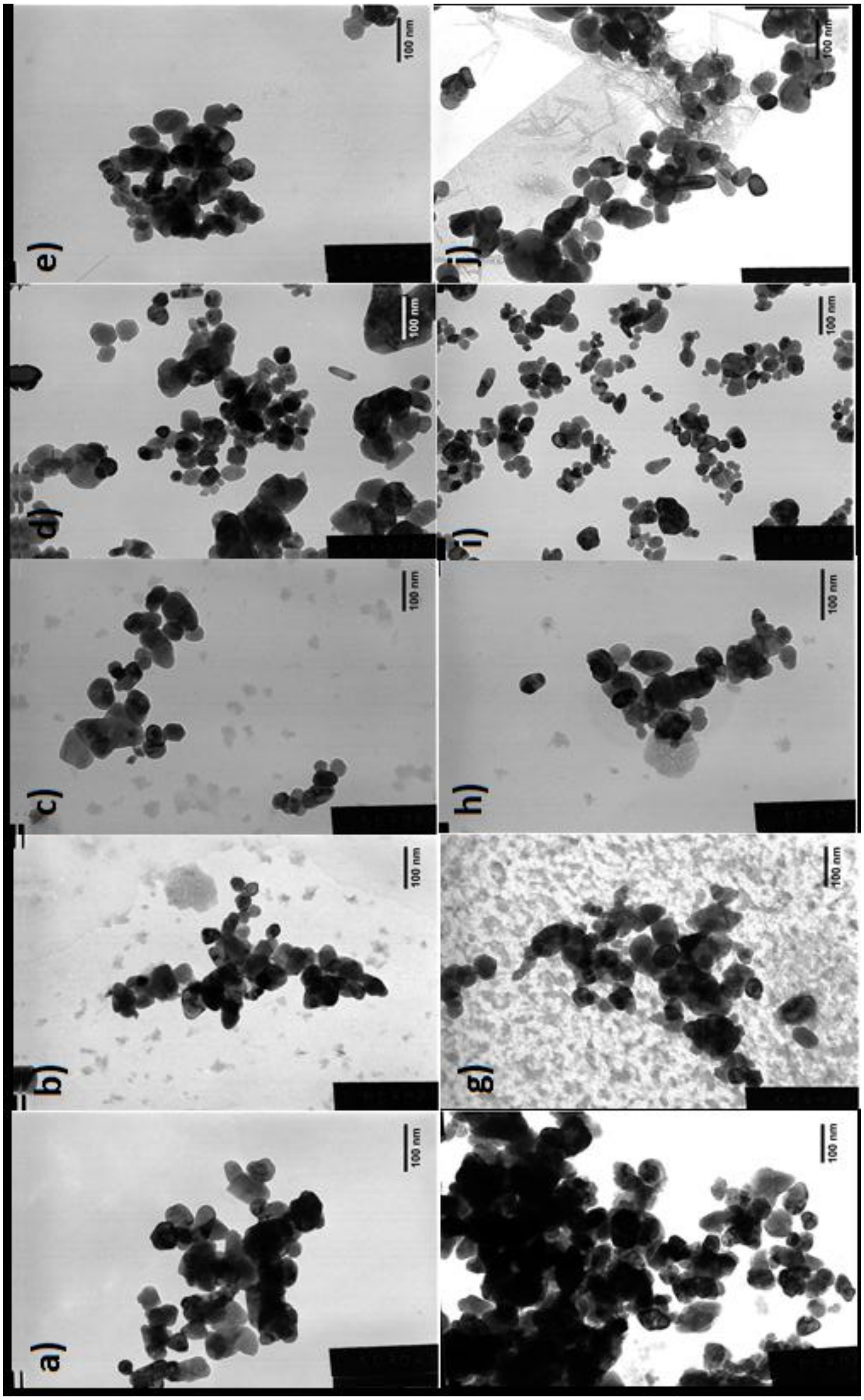

Figure 3.6: TEM images of ZnO nanoparticles produced in reactions; **a)** ZnO6, **b)** ZnO7, **c)** ZnO8, **d)** ZnO9, **e)** ZnO10, **f)** ZnO11, **g)** ZnO12, **h)** ZnO13 and **i)** ZnO14 as summarised in table 3.2.

3.3.3 Synthesis of Hydroxyapatite

The aim of this section is to study the effect of different CHFS processing and synthesis conditions on the particle characteristics of hydroxyapatite. In total, 23 reactions were performed to establish an operational envelope for the synthesis of hydroxyaptite using CHFS. These reactions were used to assess the effect of different synthesis conditions on the particle phase, size and size distribution. Table 3.2 summarises the reaction conditions and characterisation data obtained for samples reported in this section.

The formation of hydroxyapatite ($Ca_{10}(PO_4)_6(OH)_2$) in CHFS is described by equation 3.9. The mechanism of particle formation in this context is thought to arise from the rapid crystallisation and growth of a coprecipitate formed by the mixture of $Ca(NO_3)_2$ and $(NH_4)_2HPO_4$ under hydrothermal conditions, as initially reported by Chaudhry *et al.* (Chaudhry *et al.,* 2006) At ambient conditions the mixture of $Ca(NO_3)_2$ and $(NH_4)_2HPO_4$ at pH > 8 forms a precipitate composed of either, brushite [$CaHPO_4.2H_2O$] described by equation 3.10 or its dehydrated form, monetite [$CaHPO_4$] described by equation 3.11. (Liu *et al.*, 2001; Yoshimura *et al.*, 1994) Characterisation of control experiments for the precipitation of Ca and P sources within the reactor yielded amorphous monotite/brushite mixtures as identified by Raman (data not shown). (Koutsopoulos 2002) Further characterisation via TEM (figure 3.7) of the products showed some structure to the precipitates forming needle like precipitates with a size of *ca.* 89 (22), 78 (15), and, 84 (21) (SD) for materials produced from ambient precipitation at pH 9, 10 and 11, respectively (50 precipitates measured) which is consistent with many ambient temperature precipitation reactions for the formation of hydroxyapatite. (Kay *et al.,* 1964) This observation is presented here as it forms the basis of much of the analysis presented for this hydrothermal crystallisation reaction. The low reaction yields under ambient precipitation suggests incomplete precipitation of the component ions and a degree of growth would be observed in hydrothermal solution (table 3.2).(Koutsopoulos 2002)

$$10Ca(NO_3)_2 + 6(NH_4)_2HPO_4 + 2H_2O = Ca_{10}(PO_4)_6(OH)_2 + 12\ NH_4NO_3 + 8\ HNO_3$$

(Equation 3.9)

$$Ca(NO_3)_2 + (NH_4)_2HPO_4 + 2H_2O = CaHPO_4 \cdot 2H_2O + 2\ (NH_4)\ NO_3$$ **(Equation 3.10)**

$Ca(NO_3)_2 + (NH_4)_2HPO_4 = CaHPO_4 + 2\,(NH_4)NO_3$ **(Equation 3.11)**

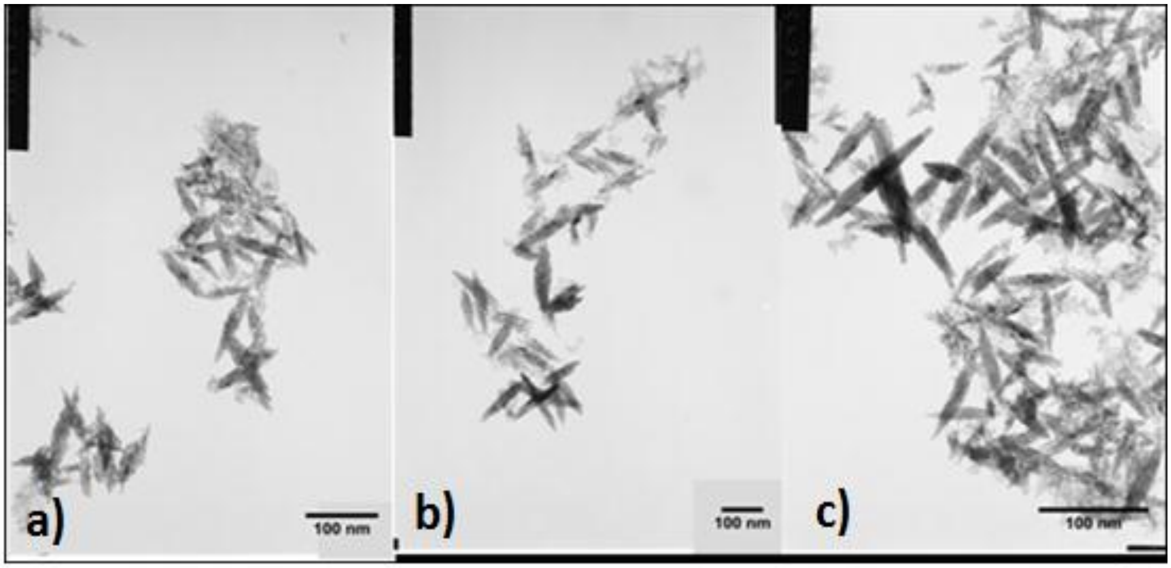

Figure 3.7: TEM images of the products of co-precipitation obtained from the CHFS system; **a)** HAAP1, **b)** HAAP2 and **c)** HAAP3.

To assess the effect of reaction point temperature on the crystallisation of hydroxyapatite using CHFS the reaction point temperature was controlled by varying $T_{sw,}$ (350 – 450 °C) as described in table 3.2 (samples HA1 - 4). Diffraction patterns of samples (HA1 - 4) synthesised at reaction point temperatures of 199, 305, 335 and 383 °C are shown in figure 3.8, showing an increase in material crystalinity with reaction point temperature. Low reaction temperatures (HA1 - 2) produced an apatite like phase similar to those produced at higher temperatures (HA3 - 4). However, no evidence of a crystalline brushite or monotite phase was observed (all diffraction patterns are compared to JCPDS pattern 09-0432) suggesting complete re-crystallisation of the monotite precipitate initially formed on mixing the Ca and P sources at ambient temperature.(Yoshimura *et al.,* 1994)

TEM images (figure 3.9) of the products obtained from reactions HA1 - 4 showed a rod like particle morphology. The particle size distributions obtained for the materials were 261.6 (92.35), 208.6 (73.34), 235.21 (74.44) and 252 (83.9) nm for the materials synthesised at reaction point temperatures of 199, 305, 335 and 383 °C, respectively. Hydroxyapatite is known to preferentially grow along the 0001 (c-axis) directions forming rod like or needle like structures. (Kay, Young, & Posner 1964) The preferential growth of the particles in this direction stems from the charge associated with different crystal facets. (Liu, Troczynski, & Tseng 2001) The observed morphology is consistent with the anisotropy observed between families of reflections in XRD (figure 3.8). Where the observed particle size is significantly larger than that observed for the products of the coprecipitation reaction (figure 3.7) showing a degree of growth related to hydrothermal reaction. To further evaluate the effect of reaction point temperature on particle growth the aspect ratio distribution was assessed to see if slight differences in the morphology of the reaction products could be resolved, the aspect ratio distributions are summarised in table 3.2 (*ca.* 150 particles measured) and was largely invariant of reaction point temperature. These observations also suggest the complete precipitation of Ca and P sources within the reaction as evidenced by the high reaction yields (table 3.2) with the temperature effecting particle crystalinity rather than absolute particle size.

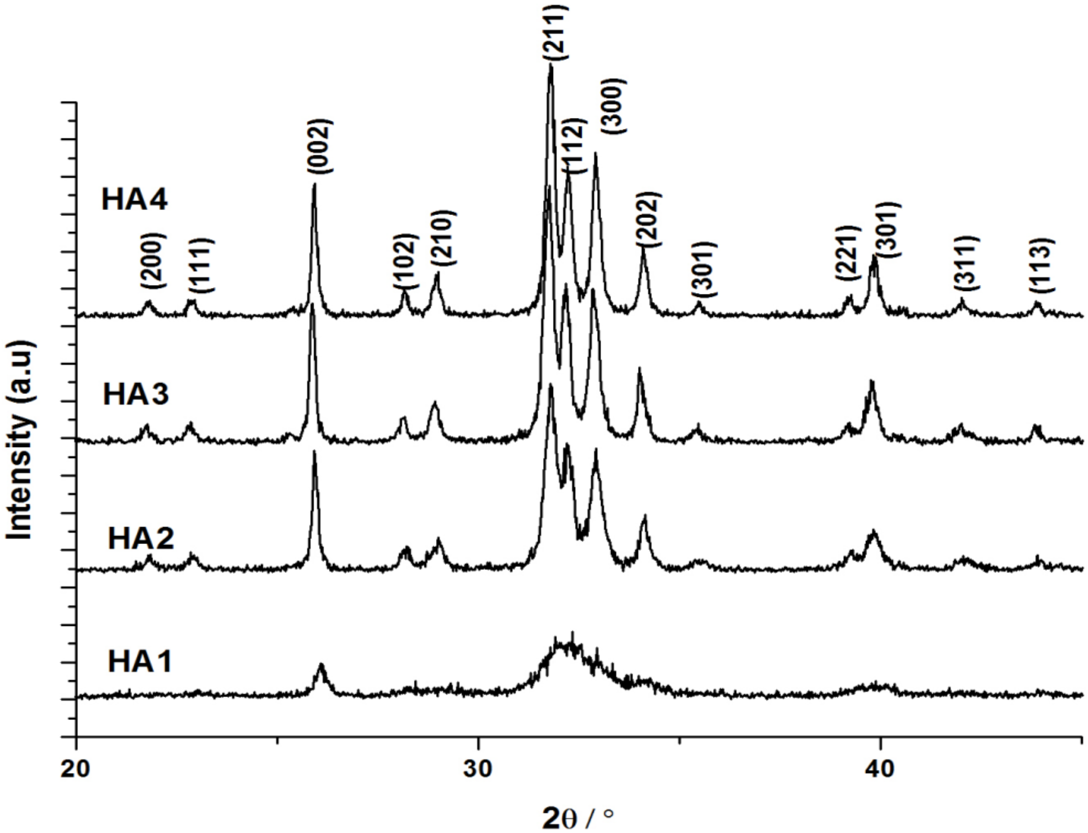

Figure 3.8: XRD patterns of HA samples HA1 - 4 produced at reaction point temperatures of 199, 305, 335 and 383 °C, respectively.

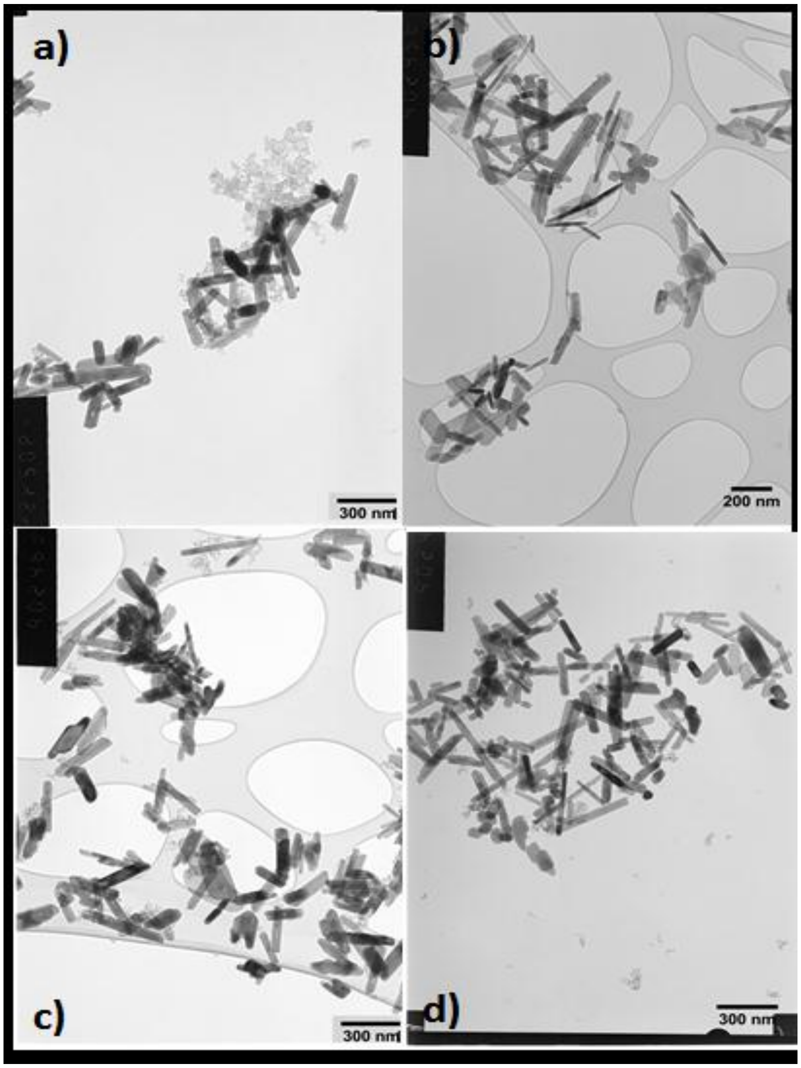

Figure 3.9: TEM images of hydroxyapatite synthesised at a reaction point temperature of **a)** 199 °C (HA1), **b)** 305 °C (HA2), **c)** 335 °C, (HA3) and **d)** 383 °C (HA4).

To further investigate the effect of reaction point temperature on the structure of the product Raman spectra were collected as shown in figure 3.10.a. The Raman spectra of the materials produced at reaction point temperatures of 199, 305, 335 and 383 °C showed all the expected modes for hydroxyapatite. Peaks centred at 965 cm^{-1} correspond to the symmetric stretching mode (ν_1) of the P-O bond in phosphate. Peaks at 610, 593 and 583 cm^{-1} observed as 1 broad peak corresponds to the bending mode (ν_4) of the O-P-O in phosphate. (Penel *et al.,* 1998; Tsuda and Arends 1994) Similarly, the bending mode (ν_2) of the O-P-O in phosphate resulted in peaks at 450 and 433 cm^{-1}. Lattice based modes were observed in the spectra of hydroxyapatite synthesised at reaction point temperatures of 305, 335 and 383 °C but were absent in the material synthesised at 199 °C (typically observed in the 200 - 300 cm^{-1} region) confirming observations using XRD and are indicative of sample crystalinity increasing as a function of temperature. The mode positions observed were slightly shifted when compared to the mode positions observed for samples precipitated at ambient temperature (samples AP1 - 3) and are consistent with those reported in the literature. (Tsuda & Arends 1994)

As shown in Section 3.3.1 slight variance in the temperature profile of the reaction point was observed as a function of Q_p / Qs_w for a given T_{sw}. To assess the effect of this observed temperature profile the synthesis of hydroxyapatite a fixed reaction point temperature of *ca.* 335 °C was used and Q_p and $Q_{hw,in}$ were varied (Reactions HA3, 10 - 11). XRD patterns of the products of these reactions are presented in figure 3.11 and confirmed that highly crystalline hydroxyapatite phase was obtained as the reaction product, Raman spectra confirmed the phase assignment made using XRD (figure 3.10 c). Direct observation of the particles (figure 3.12) of the reaction products showed that similar crystallite sizes were obtained; 235 (74.4), 246 (78.5)and 230 (78.5) nm for samples HA3, 10-and 11 respectively. Similarly, the aspect ratio distributions also highlighted the similarity in crystallite morphology, with aspect ratios of 4.61, 4.67 and 4.56 being obtained for reactions HA3, HA10 and HA11, respectively. These observations are surprising in light of the temperature differences at the terminus of the pre heated water inlet defined in Figure 3.4 where in the lowest flow regime ($Q_p + Q_{sw} = 20$ [HA11]) a reaction point temperature at the terminus of the preheated water inlet was *ca.* 100 °C lower than that measured in the high flow regime ($Q_p + Q_{sw} = 40$). Conceptually this would suggest that smaller materials would be produced in the high flow regime as a transition to temperature where precipitation of Ca and P sources would occur more rapidly. However, from these results it appears that almost complete and instantaneous precipitation of the product occurs as evidenced by the high reaction yields (table 3.2). This suggests that particle formation processes are once again governed by a transition within the reaction point to a condition of rapid precipitation and crystallisation. Increasing the residence time was shown to have little effect on any of the physical properties of the materials produce in terms of both greater crystalinity and an increase in particle size due to coalescence (table 3.2). Overall these observations are consistent with that made in the synthesis of ZnO where a rapid and swift transition to a condition of rapid particle growth occurs within the reactor although through *in-situ* measurements identified quite large differences in temperature profile within the reactor however, the measured difference shows very little effect on the hydrothermal crystallisation of HA in CHFS.

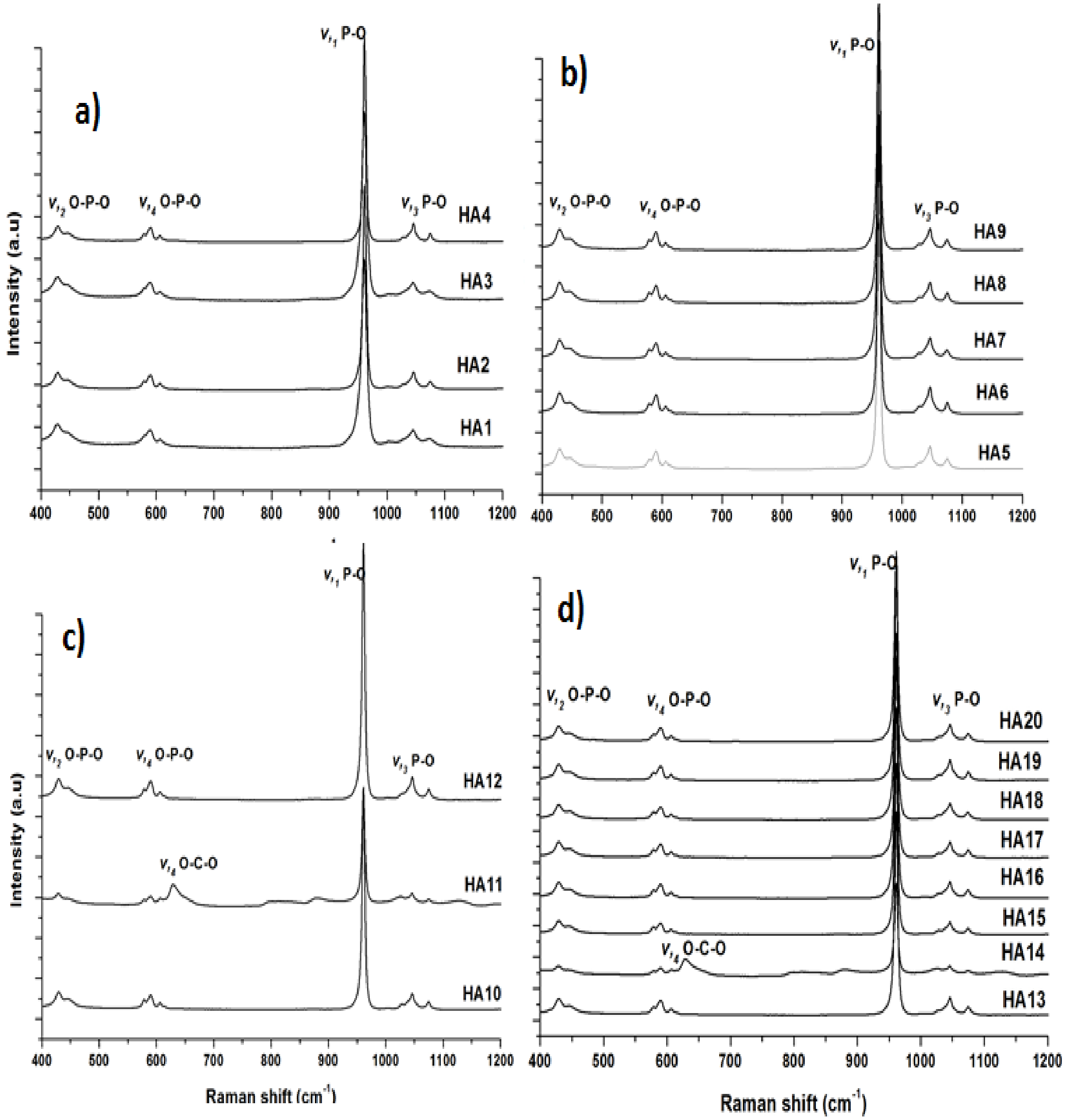

Figure 3.10: Raman spectra of hydroxyapatite synthesised using CHFS; **a)** HA1 – 4, **b)** HA5 – 9, **c)** HA10 – 12 and **d)** HA13 - 20

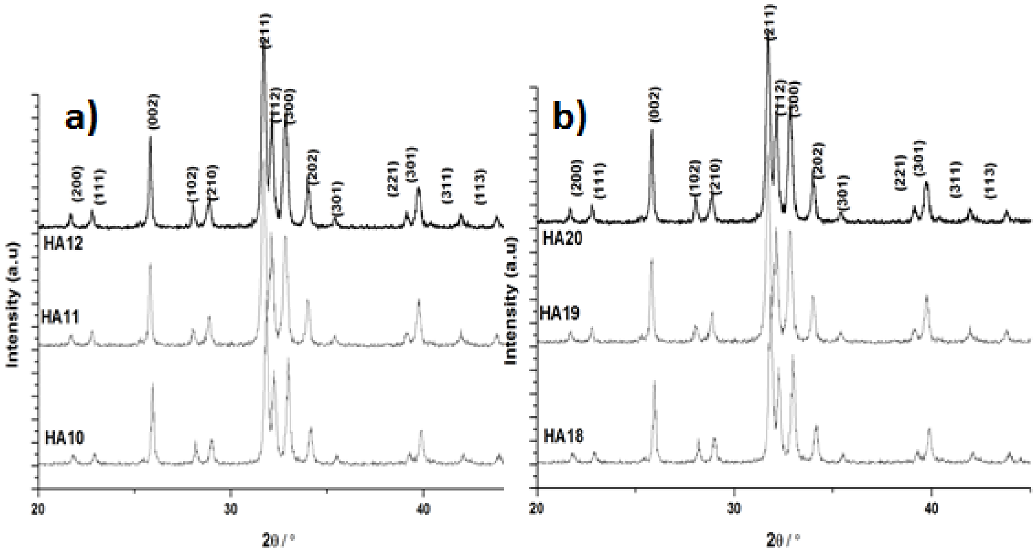

Figure 3.11: XRD patterns of Hydroxyapatite nanoparticles produced under different synthesis conditions; **a)** variation of flow rate (HA 10-12), **b)** variation of precursor concentration (HA18-20).

To ensure that the particle size was not dominated by the comparatively low concentration of precursors used several experiments were conducted to assess the effect of increasing precursor concentration on the reaction. Diffraction patterns of the products are shown in figure 3.11b and show significant similarity to the materials produced previously, the structure of the reaction products was also confirmed using Raman (figure 3.10b). Similar to previous observations the crystallite size was shown to be largely independent of precursor concentration. The crystallite sizes determined for reactions HA 18, 19 and 20 were 254 (78.2), 249 (92.7), and 278(80.2) nm, the similarity in particle size and size distribution was also mirrored in the similarity of particle aspect ratios 4.14, 4.26 and 4.28 nm for samples HA 18, 19 and 20, respectively. Although this is counter intuitive (as growth is expected to be proportional to [Ca and P] it could be explained by dynamic equilibrium within the system in that the number concentration of precipitates would likely increase with increasing concentration. This observation suggests that the similarly sized crystallites are produced as a result of an increase in the number of particle nucleates ↔ precursor concentration. The degree of particle growth in this context is constrained by the compete precipitation of Ca and P sources adding to a variable nucleate number concentration.

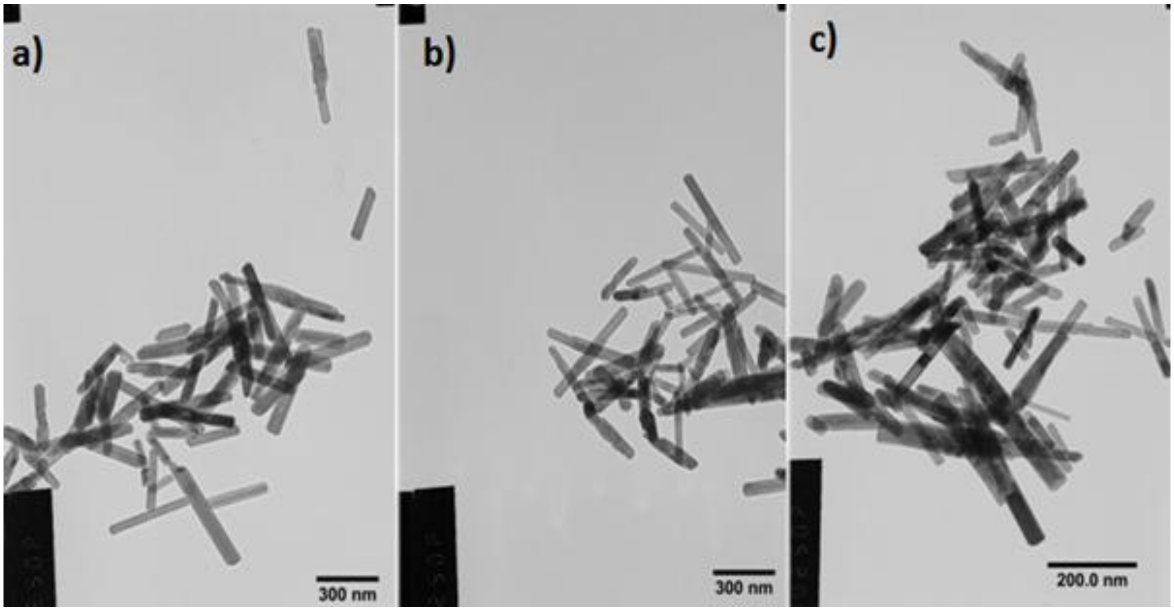

Figure 3.12: TEM images of hydroxyapatite nanoparticles synthesised at different flow rates; **a)** HA3 ($Q_{sw} + Q_p = 40$), **b)** HA10 ($Q_{sw} + Q_p = 30$) and **c)** HA11($Q_{sw} + Q_p = 20$).

As the temperature profile within the reaction point was shown to have little effect on the hydrothermal crystallisation reaction a broader investigation into the hydrothermal crystallisation of hydroxyapatite was performed in which the Ca:P ratio, and the pH of the reaction were investigated. The Ca:P ratio was varied (1.8-2.2) to assess the effect of elemental composition on the hydrothermal crystallisation (samples HA 13 to 17). Similarly, the effect of changing the pH of the reaction mixture was also investigated (HA 5 to 9) to assess the effect of precipitation prior to hydrothermal crystallisation (***n.b.*** no precipitation at ambient temperature was observed when the pH of the mixture ≤ 8). XRD patterns of the products from reactions HA13 - 17 and HA5 - 9 are presented in figure 3.13. All diffraction patterns were in good agreement with JCPDS 09-0432. Consistent with observations made on previous samples. Raman spectra of the series shown in figure 3.10 b and 3.10 d showed all expected raman modes, suggesting significant structural similarities between samples. TEM images of selected samples from each series HA13-17 and HA 5-9 are shown in figure 3.14 and show a particle morphology consistent with that observed in all other materials presented in this section. The crystallite size determined from the measurement of *ca.* 300 particles was also consistent between series and consistent with the mean size from all other samples. Similarly, the aspect ratio of the particles was also similar as summarised in table 3.2 with both size determinations being internally consistent, suggesting a high dependence of particle formation on the hydrothermal precipitation reaction.

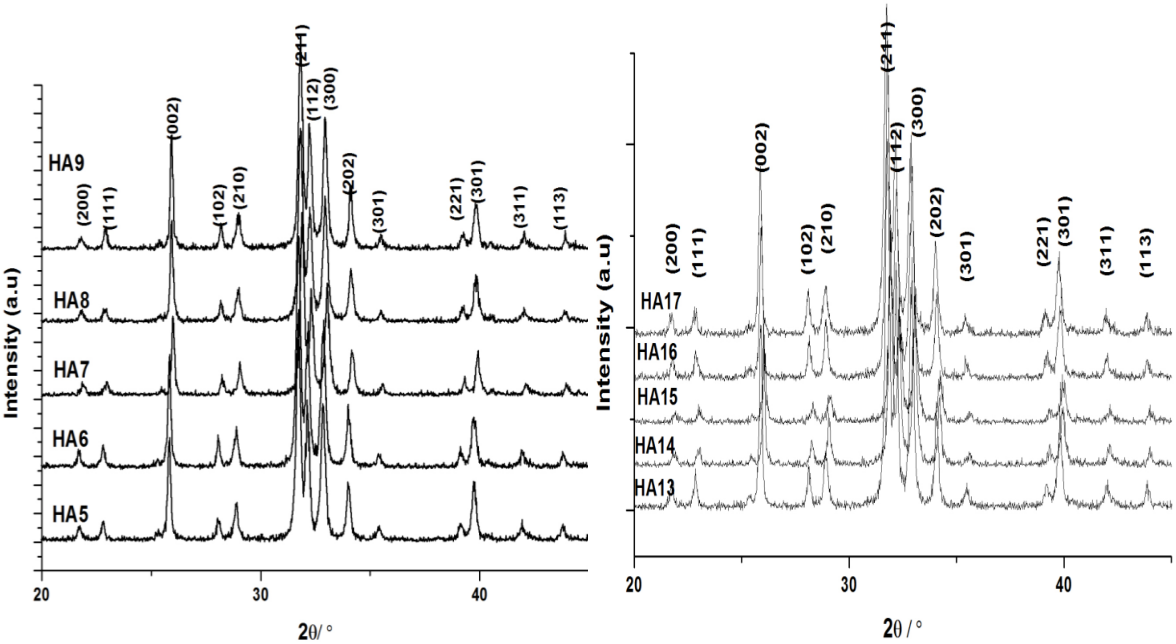

Figure 3.13: Powder XRD patterns of hydroxyapatite samples **a)** HA5-9 and **b)** HA13-17.

To confirm the stoichiometry of the reaction products produced in sample series HA13 - 17 and HA5 - 9 the elemental compositions of selected samples was measured using a calibrated EDX. Table 3.4 provided a summary of the elemental compositions measured for the materials synthesised using Ca:P ratios in the range 1.8 - 2.2, samples synthesised. Ca:P ratios of > 2.0 produced a material which showed an elemental composition close to that of stochiometric hydroxyapatite (Ca:P = 1.67) being slightly calcium deficient. XRD showed no difference in primary material phase even when different Ca:P ratios or concentrations were used in the synthesis. It is well known that the apatite structure can accommodate significant cation and anion vacancies under conservation of the apatite structure, this appears mirrored by the results presented in table 3.4. (Kay, Young, & Posner 1964) The similarity in crystallite size, suggests that the crystallisation reaction of HA in CHFS occurs at a rate independent of anion to cation ratio, with the crystallite growth occurring accommodating Ca deficiencies within the lattice. (Liu, Troczynski, & Tseng 2001) Similarly, elemental compositions measured for the samples produced at pH 6 - 11 (through the addition of NH_4OH solution) showed a variation of Ca stoichiometry as a function of pH (with Ca:P ratio increasing as the pH of the reaction increases) consistent with the observations made in samples HA13 - 17. The calcium content of the sample decreasing with reaction temperature is unsurprising as Ca is highly soluble in aqueous media and is known to be difficult to precipitate in hydrothermal solution. (Suchanek *et al.,* 2002; Yoshimura *et al.,* 1994) It is well known in the hydroxyapatite synthesis literature, that careful control of reaction pH is required to produce stoichiometric hydroxyapatite. (Liu, Troczynski, & Tseng 2001) Again the variation in product stoichiometry and the similarity of hydroxyapatite size suggests the crystallisation reaction is not heavily influenced by Ca:P stoichiometry (within the limits evaluated) with material and crystallite growth occurring rapidly, and independent of most process conditions. Whereas, many other processing methodologies such as co-precipitation and sol-gel methods observe variation in crystallite size an morphology as a function of Ca:P ratio suggesting that the crystallisation reaction in CHFS is heavily driven by temperature and the short reaction times (*ca.* 1.4 seconds) yielding complete precipitation of the component ions as a crystalline nanomaterial accommodating cation deficiencies in the lattice. (Yoshimura *et al.,* 1994)

Table 3.4: Summary of compositions obtained from EDX for hydroxyapatite samples synthesised under different conditions using CHFS. The quantification of each element was obtained through the relative intensities of the K lines.

Sample ID	**Atomic (%)**			**Ca:P ratio**
	Ca	**P**	**O**	
HA5	15.43	10.41	74.16	1.48
HA6	16.43	10.73	72.84	1.53
HA7	15.49	9.68	74.83	1.60
HA8	15.87	9.74	74.39	1.63
HA9	16.45	10.03	73.52	1.64
HA15	10.98	8.45	80.57	1.30
HA16	11.78	8.12	80.10	1.45
HA17	16.63	10.27	73.10	1.62
HA18	16.78	10.11	73.11	1.66

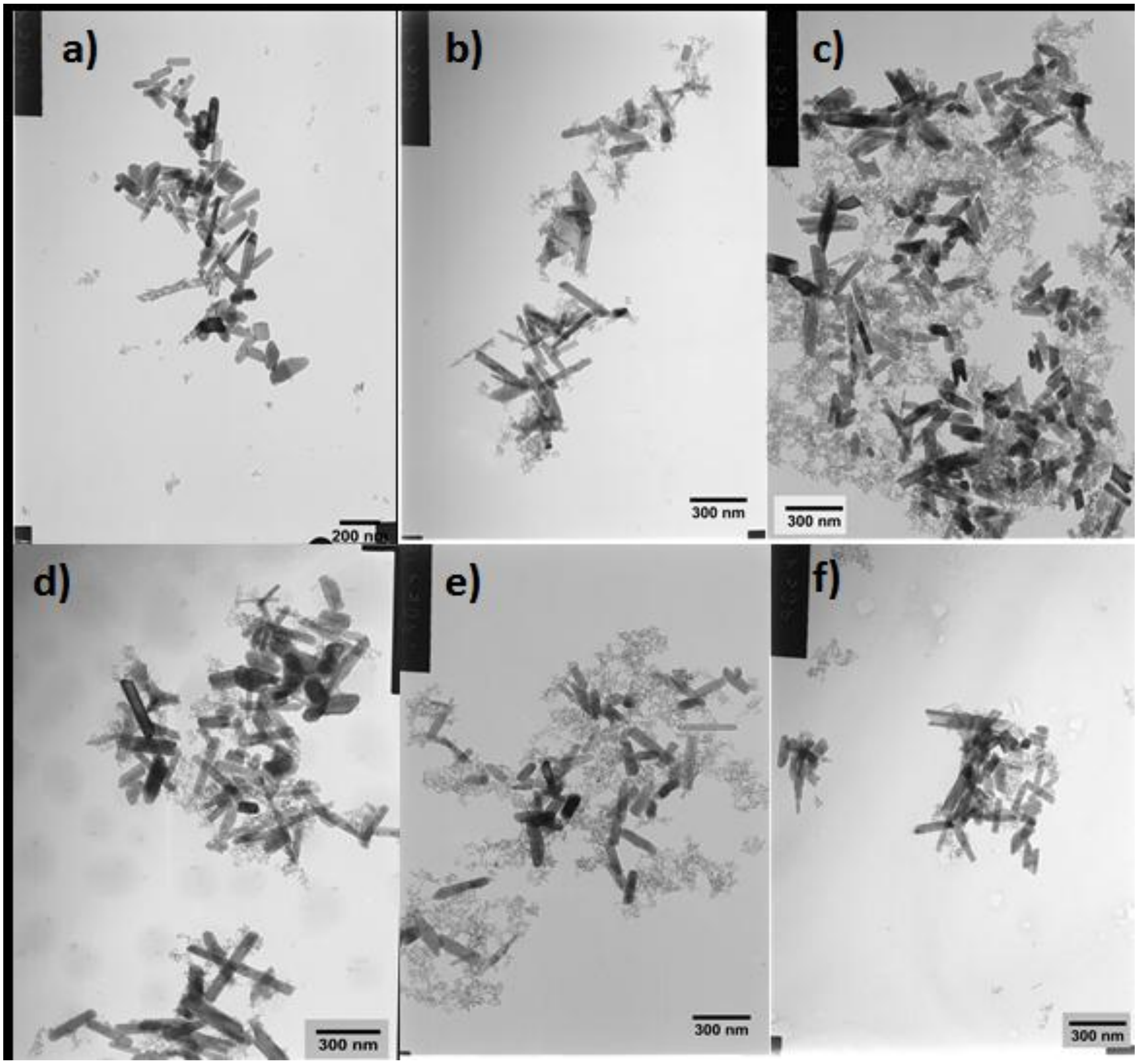

Figure 3.14: TEM images synthesised at different pH **a)** HA6, **b)** HA7, **c)** HA8 and TEM images of hydroxyapatite nanoparticles synthesised at different Ca:P ratios **d)** HA13, **e)** HA14 and **f)** HA15 **(*n.b.*** the amorphous content of this sample is likely to be from the presence of residual ions in the solution**).**

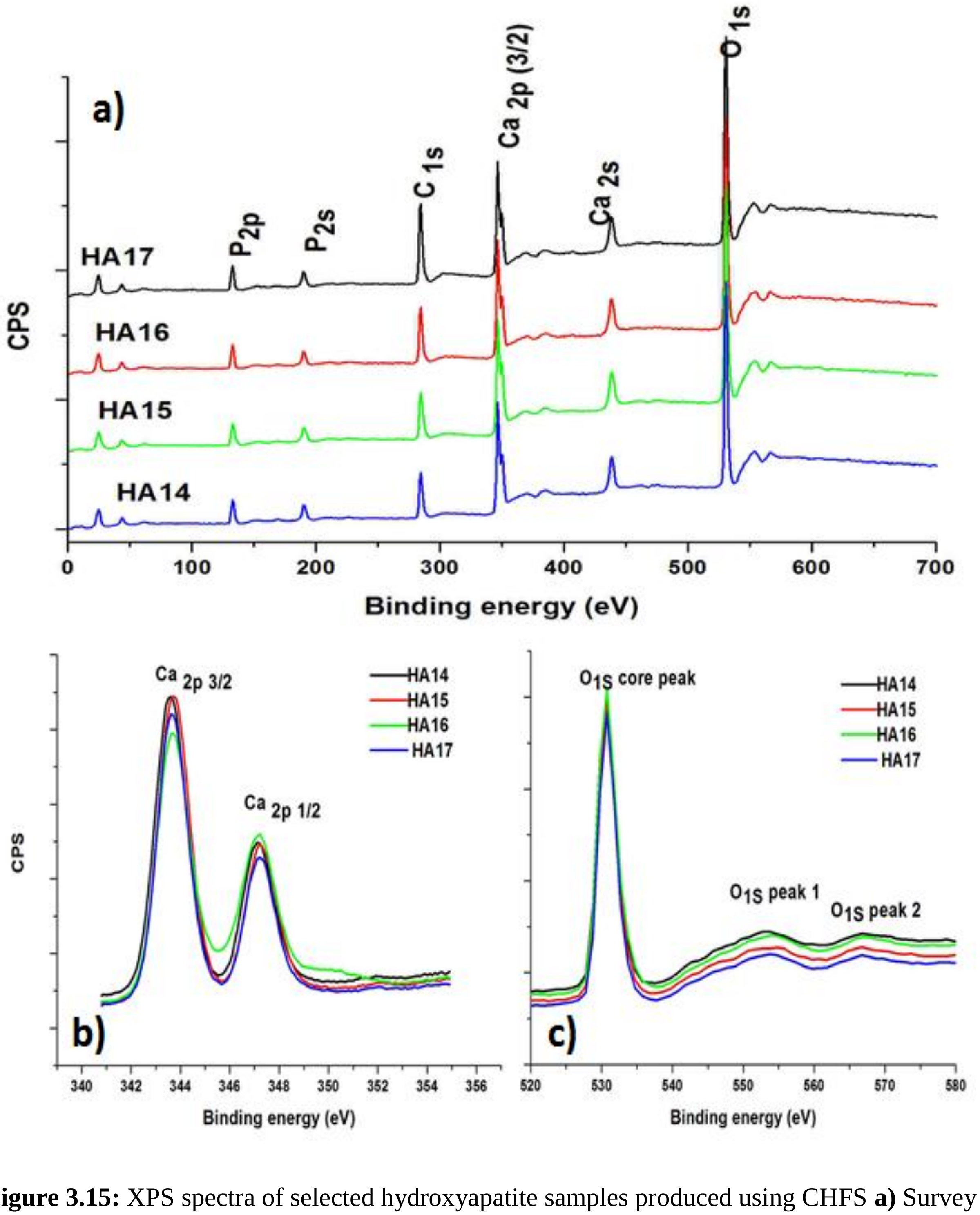

Figure 3.15: XPS spectra of selected hydroxyapatite samples produced using CHFS **a)** Survey scan, **b)** High resolution data of the Ca 2P region and **c)** high resolution data of the O1s region.

To provide further clarification on the crystallisation the differences between the bulk stoichiometry of HA (measured by EDX) and the surface of the particles was measured using XPS as shown in figure 3.15. The composition of the surface of samples HA15 - 18 was determined from survey spectra and the composition analysis is summarised in table 3.5. The mole fractions of the powders were obtained from intensities of the P 2p and Ca 2p3/2 core levels. High resolution spectra of the O 1s regions and Ca 2p regions are shown in figures 3.15b and 3.15c, respectively. Analysis of the Ca 2p region showed significant similarity between samples HA15 - 18 consistent with many reports of the characterisation of Ca deficient apatites, as the Ca 2p loss peak is not sensitive to slight differences in Ca:P coordination. (Casaletto *et al.,* 2002; Lu *et al.,* 2000; Zeng and Lacefield 2000) The O 1s spectrum (shown in figure 3.15c) consists of three components at binding energies of 531.5, 532.3 eV, which can be assigned to hydroxide and phosphate groups (OH^-, PO_4^{3-}), and adsorbed water (H_2O) all features which could be expected from the synthesis. However, analysis of the O 1s energy loss peak can provided useful information about the differences in the surface structure of hydroxyapatite as described previously by Zeng *et al.* (Zeng & Lacefield 2000) The characteristic energy loss peaks observed at *ca.* 554 eV (peak I) and *ca.* 568 eV (peak II) with higher BE than the main O 1s peak are shown in Figure 3.15c. These peaks exhibit unique area ratios of (O 1s peakII) / O(1s) or (O 1s peak II) / (O 1s total), O 1s total = O 1s + peak I + Peak II. The difference in this ratio arises from differences in the energy loss peak related to the phosphate oxygen content, and for this sample series the ratios determined are summarised in table 3.5. (Lu *et al.,* 2000; Ong *et al.,* 1994) Typically, loss ratios of < 3.5 are indicative of monotite (Ca : P = 1) like calcium phosphates, and ratios > 3.5 are indicative of HA (Ca : P = 1.67) and is attributed to variance in the PO_3/ PO_4 anion composition of the samples (although in these samples this could not be independently measured). (Lu *et al.,* 2000) These observations suggest a difference in stoichiometry between the bulk of the particle and the surface which could either be attributed to a segregated surface phase from precipitation of monetite from solution or from the presence of a cation deficient hydroxyapatite at the surface of the particle. The discontinuity between the elemental ratios determined from EDX and the surface composition and phase identified using XPS, these observations suggest further complexities in the crystallisation of Hydroxyapatite in CHFS and further work is required to understand the differences in the bulk and surface structures.

However, it is interesting to consider the phase behaviour of calcium deficient hydroxyapatite at elevated temperatures, as thermal treatment of calcium deficient hydroxyapatite leads to phase separation forming a stoichiometric hydroxyapatite and monotite or tricalcium phosphate it could be that hydrothermal crystallisation of these Ca deficient phases leads to nanoscale phase separation at the particle surface.

Table 3.5: Relative proportions of Ca, P and O measured using XPS for samples synthesised at a reaction point temperature of 335 °C using Ca:P of 1.8, 1.9, 2.0 and 2.2 (samples HA15, HA16, HA17 and HA18 respectively).

ID	(at %)			Binding energy (eV)				O1s $_{(II)}$/ O1s ratio	Ca:P ratio	Surface phase
	Ca	P	O	P $_{2p}$	Ca $_{2p}$ $_{1/2}$	Ca $_{2p}$ $_{3/2}$	O 1s			
HA15	19.73	18.03	62.2	133.5	350.7	347.2	531.0	0.067	1.09	monetite
HA16	24.46	17.24	58.3	133.5	350.7	347.1	530.9	0.062	1.41	monetite
HA17	24.77	18.02	57.2	133.5	350.7	347.2	531.1	0.071	1.37	monetite
HA18	24.11	19.52	56.3	133.5	350.6	347.1	530.8	0.075	1.23	monetite

Compositions were determined by using the Ca 2p, P 2p and O 1s peaks from the survey spectra (figure 3.15).

3.3.3.1 Summary:

In summary, from the data presented in this section it is clearly shown that crystalline hydroxyapatite is produced above reaction point temperatures of *ca.* 305 °C. The effect of different synthesis conditions, Q_p and Q_{sw} were shown to have little effect on the particle size. The particle size appeared to be dominated by the formation of monotite nucleates which upon contact with supercritical water recrystallised to form hydroxyapatite with addition of material from solution with almost complete crystallisation of the reaction products. Where, the low apparent solubility of both Ca and P sources in the reaction yielded particles of similar size under most processing conditions. In light of the *in-situ* analysis performed using temperature measurements the results suggest that the reactions governing particle formation and crystallisation are largely independent of the rate of temperature change experienced by reagents and are more influenced by the final temperature consistent with the observations presented for ZnO. Using control reactions it was possible to identify the nucleates (*ca.* 30-60 % of mass balance) onto which atoms are added upon mixing with supercritical water and crystallisation of hydroxyapatite from monotite occurs. Suggesting the crystallisation reactions occurring for the production of hydroxyapatite using CHFS are largely independent of all processing conditions when the material is produced using CHFS. Elemental analysis of the reaction products also suggested that cation deficiency within the lattice can be accommodated and the particles form in the presence of these atomic vacancies yielding overall similarly sized materials showing that crystallisation in this reaction is not overall sensitive to atomic ratios in the hydrothermal solution. Further analysis of some of the reaction products suggests the surface phase is not strictly hydroxyapatite and from the available literature the analysis of the XPS spectra suggests the surface phase of the products is monotite. However it is still unclear whether this observation stems from simply cation deficiency within the structure or from the presence of a separate phase at the surface and requires further work.

3.4 Conclusions:

The work in this chapter has demonstrated some of the complexities in controlling the size of nanoparticles produced using CHFS. *In-situ* temperature measurements were useful in defining the key differences in the temperature profile within a counter-current reactor over a spread of conditions and allowed a much finer analysis of the events occurring around the point of mixing precursors with supercritical water. This region is commonly defined as the point of particle nucleation as such much time and effort has been spent on ensuring rapid changes in the temperature of hydrothermal solutions at this point *i.e.* driving the formation of nanoparticles. Many of the results presented here contravene the ideal reaction conditions for reagents to experience in CHFS resulting in the formation of nanoparticles as resolvable differences in the distribution of temperature within the reaction point were measured. *In-situ* temperature measurements showed that the CHFS process and the mixing process in the reactor are dynamic and are highly system dependent, showing that even simple variation in the flow rate yields significant differences in the temperature at the point of particle formation and the distribution of temperature within the reaction point. Although the empirical criteria (stated in the introduction to this chapter) used by many to guide the development and evaluation of reaction points for nanoparticles in CHFS the criteria appear over simplified. Ultimately, the results presented in this chapter have provided the only conclusive evidence of the dominance of precipitation process occurring in the reactor and have elucidated that the short-time scale of the reactions probably dominate all other process often cited within the within the literature as crucial for the formation of nanoparticles. These results span a much broader and better defined set of reaction conditions experienced by reagents in CHFS and have served to demonstrate that many of the microscale mixing processes are probably not important for the formation of nanoparticles, as such the kinetics of particle formation probably play a greater role. Although this chapter has not definitively addressed the time scales of mixing the span of reaction parameters suggest significantly different temperature profiles are required before significant difference in the nucleation and growth of nanoparticles are resolved.

In this chapter the crystallisation of two materials ZnO and hydroxyapatite was studied, these model systems served to assess the effect of different CHFS processing conditions on the formation of nanoparticles in light of the temperature profile within the reactor identified by *in-situ* temperature measurements. The mechanism of ZnO was also suggested to be consistent with the growth processes of ZnO produced in both batch and other hydrothermal processes. It was observed that particles showing similar characteristics are formed over a large number of experimental variables. The results also suggest that the initial mixing between the component streams in a counter-current reaction point are not critical to the synthesis of ZnO under the experimental conditions evaluated and are in fact governed by the terminal temperature. Similarly, the hydrothermal crystallisation of hydroxyapatite was also studied and clearly showed a connection between ion precipitation and the formation of a crystalline material. In all cases it was shown that materials with a similar crystallite size were produced over the process variables evaluated which was attributed to complete precipitation of the component ions and overall material phase and crystalinity were governed by reaction temperature. The effect of slight differences in the temperature at the point of contact with supercritical water were once again shown to have little effect on the particle size. The particle size appeared to be dominated by the formation of monotite nucleates which upon contact with supercritical water recrystallised to form hydroxyapatite with addition of material from solution with almost complete crystallisation of the reaction products as observed by the high reaction yields. In light of the *in-situ* analysis performed using temperature measurements the results suggest that the reactions governing particle formation and crystallisation are largely independent of the rate of temperature change experienced by reagents and are more influenced by the final temperature consistent with the observations presented for ZnO. Using control reactions it was possible to identify the nucleates (*ca.* 30-60 % of mass balance) onto which atoms are added upon mixing with supercritical water and crystallisation of hydroxyapatite from monotite occurs further suggesting the complete precipitation of the component ions in solution was the driving force for the similarity in particle size between experiments. This was further emphasised by changes in monetite coprecipitate size as a function of the pH which was also shown to have little effect on the precipitation reaction. However, this analysis yield some interesting observations in that crystallite size was also largely independent of the stoichiometry of the reaction product and suggests the lattice can be accommodate significant vacancies on conservation of the structure showing that the reaction is not overall sensitive to atomic ratios in the hydrothermal solution. However, further investigation into the hydrothermal crystallisation mechanism is required as analysis of the XPS spectra suggests the surface phase of the products is monotite or another calcium deficient phosphate phase. However it is still unclear whether this observation stems from simply cation deficiency within the structure or from the presence of a separate phase at the surface and requires further work.

3.5 Future work:

The largest single contribution to this work would come from CFD (Computational Fluid Dynamics) modelling of the reaction point operated at a variety of temperature and flow regimes. Although, the presented *in-situ* temperature measurement strategy highlighted some useful information the data was significantly limited (pertaining to a further understanding of the mixing processes) and the exact placement of thermocouples within the system could not be determined allowing only an empirical comparison. The use of CFD would also allow the visualisation of complex flow patterns, fluid velocity contours to be mapped and the addition of tracers would the state of complete mixing to be modelled on the experimental results obtained. Ultimately, these endeavours would not significantly influence the physical characteristics of materials produced by this process, they could possibly aide in further understanding of the process as a whole and could be useful in rapidly assessing the effects of other process such as material deposition within the reactor. In section 3.3.1 it was mentioned that an unbalanced flow regime yielded jetting of the supercritical water feed in materials synthesis this resulted in plugging of the reactor limiting the operational range and more significantly the reaction point temperature. Further work is required to fully understand the formation of nanoparticles in CHFS systems as some of the results presented herein are ambiguous and it would be beneficial to extend the analysis of the effects of particle size to materials which have lower crystallisation temperatures which would allow the influence of temperature to be further understood (this is briefly addressed later in the thesis).

Chapter 4

An Experimental Evaluation of Confined Jet Mixers for the Continuous Hydrothermal Synthesis of Nanoparticles

4.0 Aim:

The aim of this chapter is to describe the application of alternative mixers (reaction points) for the continuous hydrothermal synthesis of nanoparticles. Following on from Chapter 3, where it was found that particle formation in CHFS not sensitive to local variation in temperature profile. Hence, it was reasoned that other mixer designs may be more versatile in terms of the flow regimes they are able to utilise without adverse effects on reactor operation. These investigations were undertaken to mitigate the adverse jetting behaviour observed in the previous chapter. In this chapter, the systematic assessment of co-axial type mixers is evaluated and the practical limitations of materials synthesis in such mixers are defined.

4.1 Introduction:

Many different reaction point designs are reported in the literature that are suitable for the continuous hydrothermal synthesis of nanoparticles. (Lester *et al.*, 2006; Lester *et al.*, 2010) These geometries take many forms, with many orientations of flows to overcome some of the difficulties associated with mixing supercritical and ambient temperature water as reviewed earlier in Chapter 1. (Lester *et al.*, 2010) Geometries based on movable inlets, (Mae *et al.*, 2007) swirl type mixers, (Kawasaki *et al.*, 2010) classical tee mixers (Adschiri *et al.*, 1992a; Takami *et al.*, 2012; Toft *et al.*, 2009) and nozzle-type mixers (Blood *et al.*, 2004; Lester *et al.*, 2006; Middelkoop *et al.*, 2009), are all well represented in the literature. Many of the aforementioned methods of mixing for CHFS type processes give “poor mixing” of the component streams within the reaction point leading to material deposition and reactor blockage (these complications are often poorly described), and often arise through hydrothermal reaction of precursors prior to entering the mixer as discussed further in Chapter 1. (Blood *et al.*, 2004; Lester *et al.*, 2006; Takami *et al.*, 2012) As shown in Chapter 3, mixing supercritical water and ambient temperature water is complex and many of the heat and mass transfer processes governing the formation of nanoparticles are poorly described due to the high operating temperatures and pressures required for the synthesis of nanoparticles in CHFS. The large differences in the physical and transport properties of the flows that are mixing and the need to prevent “preheating” of the incoming precursor feed are at the heart of the problem which prevents the efficient use of mixers in CHFS.

Although, accurate data of the mixing processes occurring within CHFS systems are difficult to acquire, a set of empirical criteria have been defined to satisfy nanoparticle synthesis in CHFS and define the “ideal” mixing of precursor feeds in a CHFS system which result in the formation of nanoparticles. (Takami *et al.*, 2012) Although, in Chapter 3 it was shown that a large distribution of temperature within a counter current reactor showed little apparent effect on the nucleation and growth of nanoparticles, the criteria are widely applied in the development of novel reaction points for the synthesis of nanoparticles using CHFS. The criteria include the following characteristics; near instantaneous and uniform mixing of reactant streams with a supercritical water feed, short reaction residence times to limit particle growth (through coarsening or growth from solution), minimal heating of precursor feeds prior to rapid mixing with a preheated supercritical water feed ensuring rapid and uniform nuclei formation, high flow velocity from the reaction point to prevent the accumulation of reagents and products at the reaction point. (Lester *et al.*, 2006) As initially discussed in chapter 3, defining limits with many of the ideal conditions for the formation of nanoparticles is difficult as such these empirical criteria have been used to guide the development of a novel reaction point suitable for the synthesis of nanoparticles presented in this Chapter. Nevertheless, it is widely reported that the reaction point geometry and the degree of mixing between the component streams influences the size distribution of materials produced although independently in a counter-current reactor large temperature variations in and around the point of particle nucleation did not yield measurable effects on particle size or distribution. (Adschiri *et al.*, 1992b; Lester *et al.*, 2006; Takami *et al.*, 2012; Toft *et al.*, 2009)

In this Chapter an experimental evaluation of co-axial mixers is presented for the continuous hydrothermal synthesis of nanoparticles. Coaxial mixers often find application in combining a laminar flow with a turbulent flow, and at ambient conditions mixing is governed by the mass flow rate ratio of laminar and turbulent feeds, respectively. (Zhdanov and Chorny 2011; Chorny and Zhdanov 2012; Pitts 1991a) As initially discussed in Chapter 3, this could be beneficial for the synthesis of nanomaterials in CHFS as mixing a ambient temperature feed of precursors ($\rho \approx 1010$ kg m^{-3}) and a high temperature low density feed of supercritical water ($\rho \approx 166$ kg m^{-3}) is complicated by the large differences in the physical properties of the component streams. (Takami *et al.,* 2012) Mixing a feed of supercritical water and a denser precursor flow in a co-axial flow orientation would confer a similar variation in the mass flow rate ratio normally used to control mixing, especially if the low density feed flowed through a narrow inlet. In co-axial jet mixers the inner flow always supplies the most turbulent feed and the mixing of the turbulent inner flow with its laminar co-flow occurs through entrainment into the rear of the emerging turbulent jet. (Pitts 1991b; Sreenivasan *et al.,* 1989) Although, in many co-axial mixing applications a degree of recirculation within the turbulent jet flow is expected especially at high Re numbers, in CHFS this recirculation could be tolerated if no adverse effects on particle properties were measured as this was initially evidenced in Chapter 3. (Takami *et al.,* 2012) As suggested in Chapter 3, zones of recirculation are inferred from an *in-situ* temperature profile analysis of a mixer that has been used in the synthesis of nanoparticles.

This Chapter describes an experimental evaluation of a co-axial type reaction point and the steps taken to select an optimal geometry for the synthesis of nanomaterials (yielding a novel application of this mixing configuration). Hereafter, co-axial jet mixers are referred to as CJM or confined jet mixers. Data obtained from operational envelope studies of the formation of ZnO and hydroxyapatite is presented in Chapter 3 has been used to explain experimental observation made here. The synthesis of both hydroxyapatite and ZnO nanoparticles have been used to study the effects of nanoparticle synthesis in CJM. All materials reported in this section were characterised by XRD, Raman spectroscopy and TEM.

4.2 Materials and Methods:

4.2.1 Reagents:

Diammonium hydrogen phosphate $(NH_4)_2HPO_4$ (98.3 wt %), calcium nitrate tetrahydrate $Ca(NO_3)_2{\cdot}4H_2O$ (99.0 wt %), Zinc nitrate hexahydrate ($Zn(NO_3)_2{\cdot}6H_2O$, 98 %) and potassium hydroxide (KOH; 96%) were obtained from Sigma Aldrich (Dorset, UK). Ammonium hydroxide solution (NH_4OH, 30 % w/w) was obtained from VWR International (Lutterworth, UK).

4.2.2 Materials Synthesis:

Sample of both hydroxyapatite and ZnO produced using CJM type reaction point geometries are presented and have both been used as model systems to validate the use of CJM for the synthesis of nanoparticles. Samples of ZnO were produced under equivalent conditions to those used in the preparation of samples ZnO8 and ZnO12 (Chapter 3), where Q_p (combined precursor (P2 + P3) flow rate) and Q_{sw} (supercritical water flowrate) were equal. All reactions were conducted using a 0.1 M metal salt concentration and an equal concentration of KOH. Similarly, the conditions chosen for the synthesis of hydroxyapatite were equivalent to those used to produce samples HA4 and HA6 (chapter 3) and Q_p (combined precursor (P2 + P3) flow rate) and Q_{sw} were equal and all syntheses were conducted using 0.1M metal salt concentrations. All materials synthesis was performed using CHFS system 1 into which a CJM was inserted (shown schematically in figure 4.1). The materials are identified by the flow regime chosen for the synthesis and further identified by the ratio of the diameters (d_o-d_i) of the preheated water inlet (d_i) and the diameter of the confining tube (d_o) of the CJM used in the synthesis, if the material was produced in a reaction point with a different physical dimension *e.g.* A hydroxyapatite sample produced in a CJM with a 0.99 mm diameter inlet and a 4.97 mm confining tube using a flow rate of $Q_p + Q_{sw} = 40$ is identified as 40HA3.98.

4.2.3 CJM Reaction Point Geometries:

A schematic diagram of the CJM used in this work is presented in figure 4.1. The schematic shows the typical arrangement of the reaction points defined as CJM type which were substituted into CHFS system 1. The details of the components used for the construction of all CJM are presented in greater detail within Chapter 2. In this Chapter several attributes of CJM were evaluated, the first being the position of the supercritical water inlet (d_i) relative to the other process feeds, and the second was the physical dimensions of the mixer. In this Chapter data, is presented from two inlet positions defined as confined and unconfined, in the unconfined position the inlet of preheated water was below the level of the precursor annuli, in the confined position the inlet was positioned above the precursor inlet annuli and confined by the diameter of the outer tube d_o as shown in figure 4.1. Data from these analyses is presented in Section 4.3.1 for a reaction point constructed from ¼” components and a 1/16” inlet (d_o = 4.97 and d_i = 0.99). CJM constructed to be of different dimensions are presented in section 4.3.2. The reaction point geometries used in this work are identified by the ratio of the diameters (d_o - d_i) of the preheated water inlet (d_i) and the diameter of the confining tube (d_o) as summarised in table 4.1.

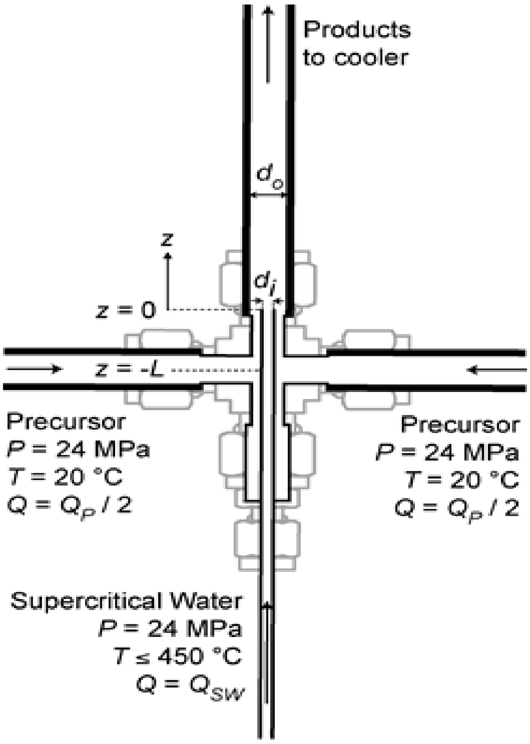

Figure 4.1: Schematic representation of CJM reaction point geometries defining the key dimensions used within the text (drawn to a relative scale). Key: d_i = the diameter of the preheated water inlet, d_o = the diameter of the confining tube, z = position within reactor, Q = flowrate, Q_{sw} = flow rate of preheated water, Q_p = flow rate of precursors.

Table 4.1: Summary of inner pipe diameters and components used for the construction of CJM presented in this chapter.

Geometry identifier (d_o-d_i)	Inlet (“)	Confining tube (“)	d_i (mm)	d_o (mm)
3.98	1/16	1/4	0.99	4.97
6.63	1/16	3/8	0.99	7.62
3.57	1/8	1/4	1.4	4.97
6.22	1/8	3/8	1.4	7.62

4.2.4 *In-situ* Temperature Measurements:

Temperature profiles were measured inside different CJM mixers by inserting four long thermocouples into the reaction point at positions relative to the terminus of the preheated water inlet (defined as z = 0 in figure 4.1) and described in greater detail within Chapter 2. CJM reaction point geometries were evaluated in the same manner as that presented in Chapter 3 for the evaluation of the counter-current mixer. However, many more measurements were taken and the thermocouple positions used in each analysis are either presented graphically within the text or described relative to z = 0. As initially described in Chapter 2 and applied in Chapter 3, the IAPWS Formulation 1995 for the Thermodynamic Properties of Ordinary Water Substance for General and Scientific Use, were used alongwith the associated FLUIDCAL^{TM} software to determine the physical and transport properties of water at elevated temperatures and pressures. (Wagner and Pruss 2002)

4.3 Results and Discussion:

In this section, the experimental evaluation of Confined Jet Mixers (CJM) for the continuous hydrothermal synthesis of nanoparticles is discussed. Initially, the effects of inlet position within the geometry are identified, and an analysis of flow events leading to undesirable conditions for the synthesis of nanoparticles are presented. This chapter then moves forward to assess the effect of several reaction point geometries, which differed in physical dimensions. Analysis is presented from both *in-situ* temperature measurements and from materials characterisation.

4.3.1 Effects of Inlet Position:

Initially, the effects of inlet height on the practical aspects of reactor operation were evaluated. The inlet positions used are depicted graphically in figure 4.3, where the low inlet position level with the annuli of the precursor inlets (hereafter know as unconfined) and the high inlet position, which was sited just above the upper part of the precursor inlet annuli (hereafter referred to as confined).

The effect of inlet position during materials synthesis was evaluated using both the synthesis of HA and ZnO nanoparticles to define the experimental limits of the CJM geometry with the inlet positioned in both the confined and unconfined position. The reactions chosen for the evaluation of the system were the same as reactions ZnO12 and

HA6 (presented in Chapter 3), the products of the reaction were characterised by XRD and TEM. Diffraction patterns showed the expected material phase for the reaction products obtained from both the confined and unconfined inlet positions (data not shown). However, it was observed that significant material deposition occurred in syntheses conducted using the unconfined inlet position (*ca.* 10-15 minutes of operation) as shown in figure 4.2a (synthesis of ZnO), whereas figure 4.2b shows the same experiment conducted with the inlet confined within the annulus. The mean crystallite sizes of these samples determined by TEM were 68.9 ±14.2 nm (±SD) and 65.7± 31. 3(±SD) for ZnO synthesized with confined and unconfined inlet positions (figure 4.2 c), with more polydisperse particle size distributions being produced in the unconfined geometry. Similarly, in the case of hydroxyapatite crystallite sizes of 269.1 ± 92.7 (±SD) and 308.2 ± 80.3 (±SD) were obtained from materials produced in the confined and unconfined inlet positions, respectively (figure 4.2d). These observations suggest a degree of particle growth occurred when the inlet was in the unconfined environment. However, the measured difference in particle size is not as severe as would be anticipated by a review of the available literature. However, the data presented in Chapter 3 supports this observation. (Takami *et al.*, 2012) In both cases the increase in particle size and crystallite polydispersity has been attributed to particle growth. This could be attributed to either recirculation occurring within the reaction point (broadening the residence time distribution around the point of particle nucleation) or through differences in the nucleation and growth processes of nanoparticles arising from inhomogenous particle nucleation. (Adschiri *et al.*, 1992) Similarly, the observed deposition is likely caused by particle nucleate formation and growth in an Ostwald ripening type process possibly induced by recirculation of the flows of Q_{sw} and Q_p within the geometry. (Adschiri, Kanazawa, & Arai 1992)

To explain further the differences observed in material deposition and particle-size, *in-situ* temperature measurements were performed to assess if any heat or mass transfer processes could be attributed to these observations. Figures 4.3 a and b show the temperature measured at different points within the geometry using both the confined and unconfined inlet positions as a function of T_{sw}, Q_{sw} and Q_p and the theoretical mixture temperature (T_{mix}) defined by enthalpy balance for each temperature and flow condition is summarised in table 4.2. From figure 4.3, it can clearly be seen that T_{sw}, Q_p, Q_{sw} and the ratio of $Q_p : Q_{sw}$ affect the mixing environment and the distribution of temperature across the geometry in both the confined and unconfined positions. The increase in measured temperature from thermocouples at z = -5 and -10 (figure 4.3 a) suggests flow of the pre-heated water into the precursor annuli with the increase in temperature linked to both T_{sw}, Q_p, Q_{sw} and the ratio of $Q_p : Q_{sw}$ increasing as would be expected for increasing T_{sw} and G_{sw}, owing to the thermal dilation of Q_{sw} issuing from the inlet. In the case of the confined inlet (figure 4.3b) a degree of heat transfer was observed between the inlet and Q_p in annulus between the inlet and confining tube (d_o - d_i). Identifying compromises in both inlet position choices in

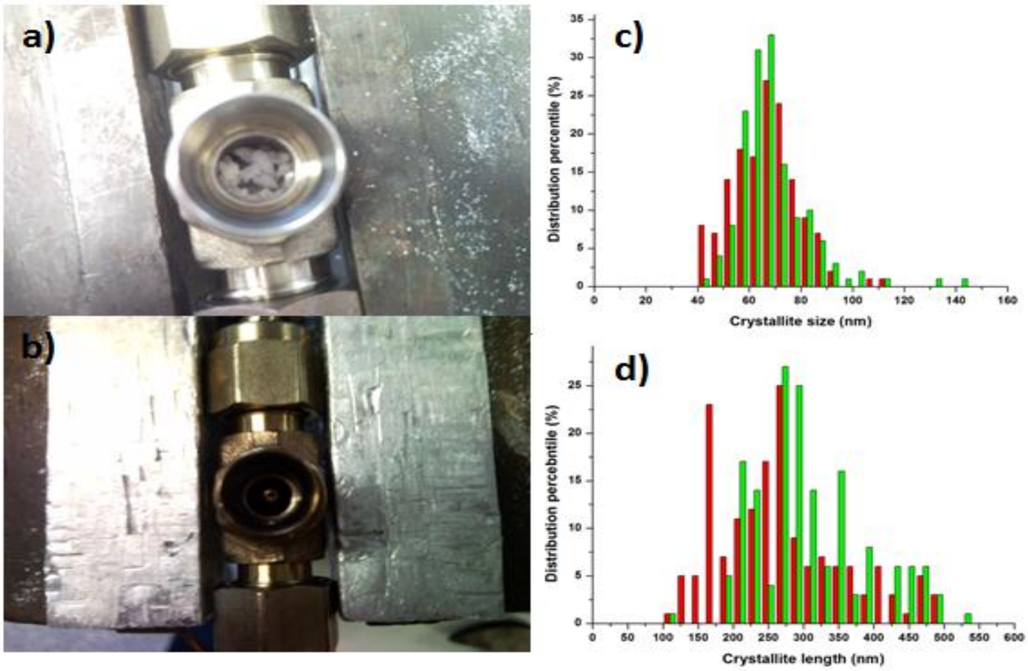

Figure 4.2: Photographs showing the differences in deposition between inlet position and material deposition **a)** synthesis of ZnO when the inlet was unconfined, **b)** synthesis of ZnO when the inlet was confined, **c)** histogram representations of ZnO nanoparticles with a confined (red) and unconfined inlet (green), **d)** histogram representations of HA with a confined (red) and unconfined inlet (green).

satisfying the ideal reaction criteria outlined previously. At first glance, the flow pattern expected to issue from the supercritical water inlet in figures 4.3 a) and b) can be simplified to a, vertical, axisymmetric, buoyant, and turbulent jet which entrains a co-flow (*i.e.* the precursors). Estimates of the events leading to the observed distribution of temperature can be made if the dominant forces influencing jet behaviour can be identified *i.e.* velocity, temperature difference and density differences. For clarity, a representation of the events occurring within the reactor is presented in figure 4.4 which also serves to define the position of thermocouples referenced.

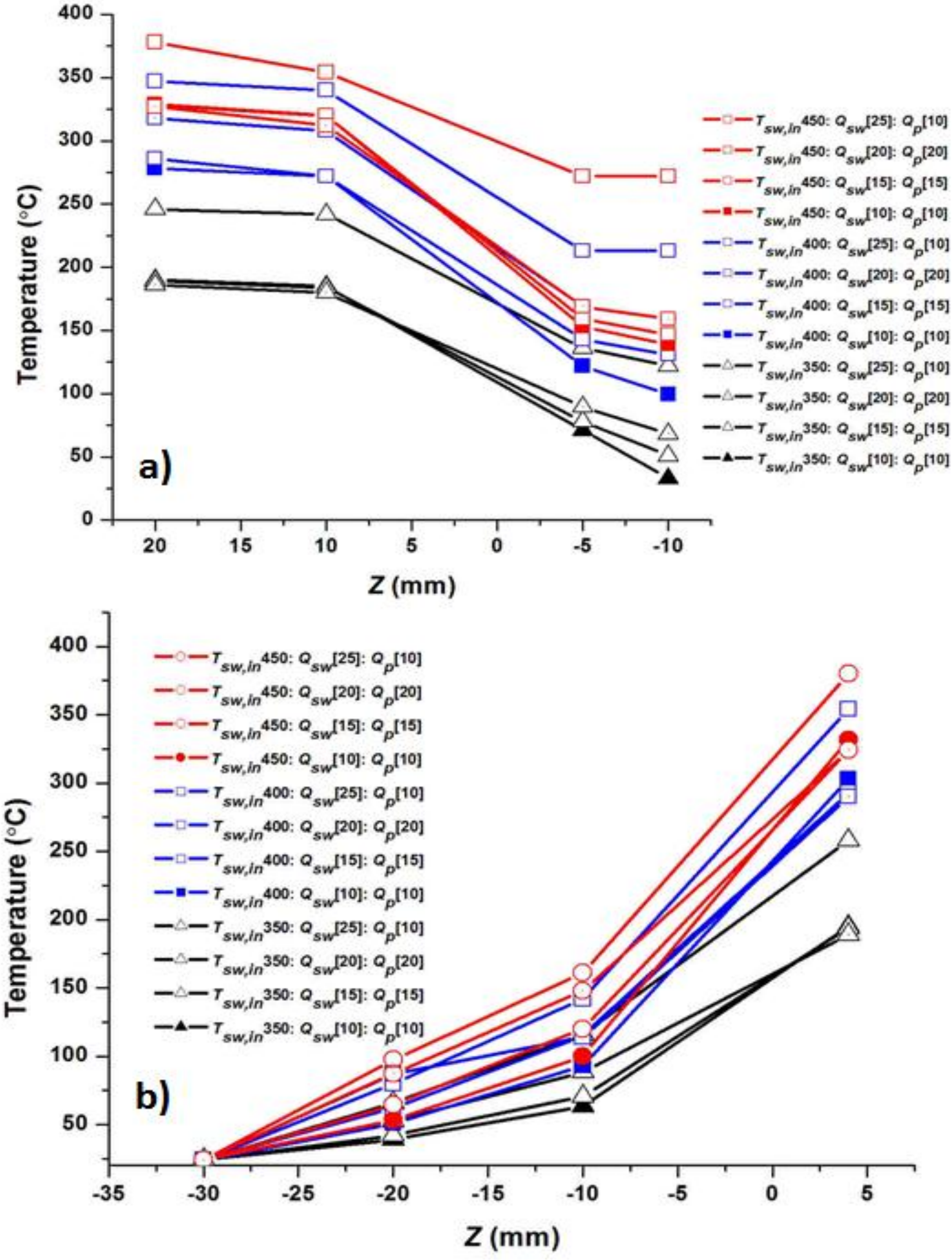

Figure 4.3: The 30 second time averaged temperatures recorded for a ¼” geometry with the inlet (1/16”) position set at different heights **a)** inlet level with the annuli of precursor inlets (unconfined), **b)** inlet confined within the outlet annulus (confined).

Table 4.2: Summary of T_{mix} temperatures (°C) for different process conditions determined from overall enthalpy balance for each temperature of Q_{sw} and flow regime (Q_{sw}: Q_p).

Flow regime Q_{sw}:Q_p	**Heater set temperature (°C)**		
	350	***400***	***450***
10:10	199	320	338
15:15	199	320	338
20:20	199	320	338
25:10	256	352	383

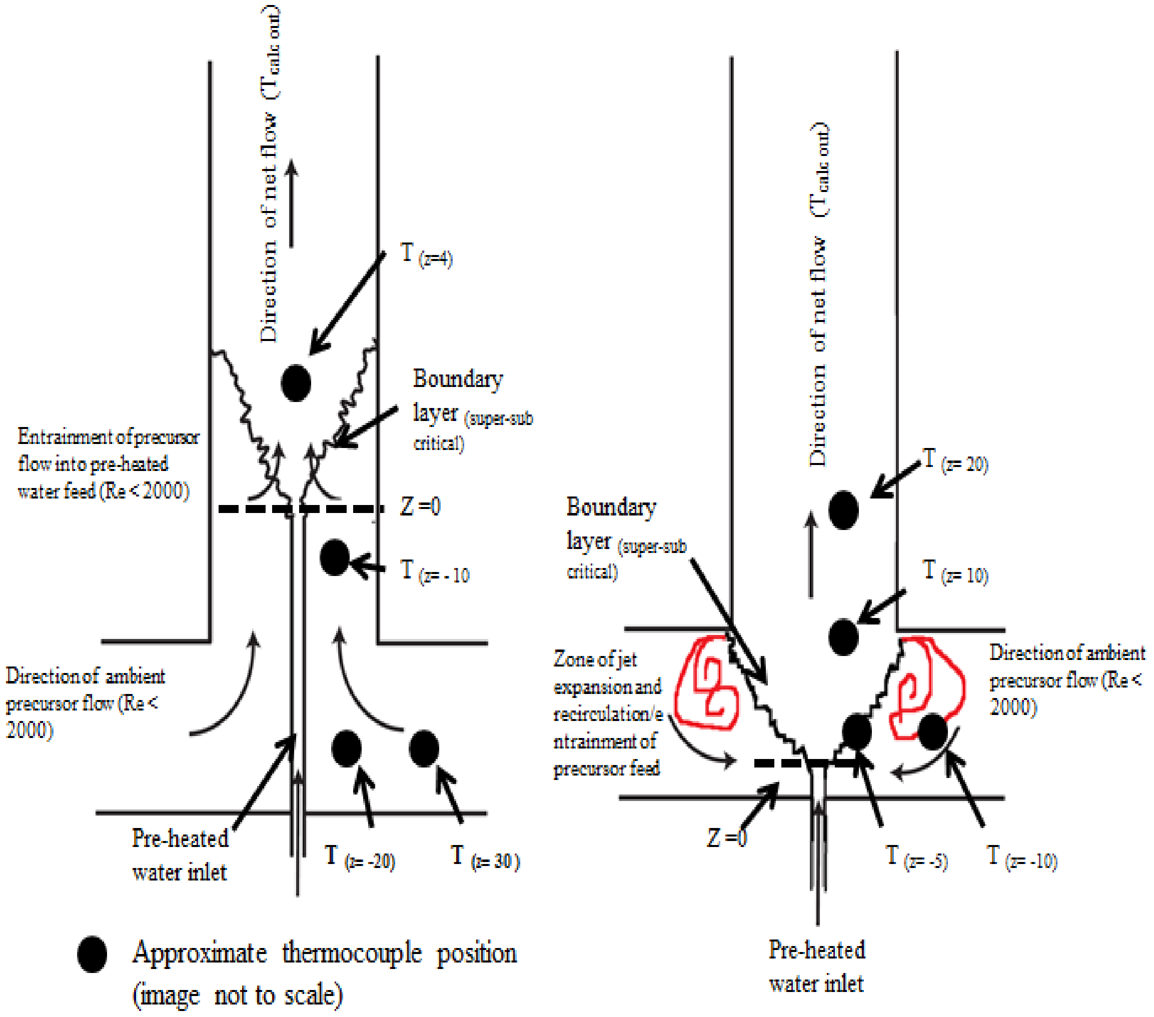

Figure 4.4: Drawing representing the possible mechanism of observations from temperature measurements (approximately to scale) of the confined inlet position (left) and unconfined (right) indicating the relative placement of thermocouples (T).

Accurately, determining the effects of supercritical jet exit temperatures are difficult in this system as the temperature and density of Q_{sw} are subject to change over both Q_{sw}: Q_p especially in light of the heat transfer (ΔQ) occurring in the confined inlet geometry (figure 4.3 b). However, in the unconfined inlet geometry the loss of heat from Q_{sw} can be assumed to be minimal, as the inlet does not penetrate into the cooler precursor flow (as indicated by T_{mix} being reached in the annulus of the outlet). As such, the temperature at the point of issue is assumed to be that of T_{sw} from the heater. Where, under this assumption the relative magnitude of the momentum of the flow of $Q_{sw\ z=0}$ (where z = 0 is defined as the terminus of the preheated water inlet) compared to the viscous drag force can be represented by the Reynolds number, $\mathrm{Re}_{sw\ z=0}$, of the flow (Equation 4.1); (Coulson *et al.*, 1999)

$$\mathrm{Re}_{\mathrm{sw\,z=o}} = \frac{\rho_{\mathrm{sw\,z=o}} u_{\mathrm{sw\,z=o}} di}{\mu_{\mathrm{sw\,z=o}}} = \frac{4G_{\mathrm{sw\,z=o}}}{\pi di \mu_{\mathrm{sw\,z=o}}}$$ **(Equation 4.1)**

Where, $\rho_{sw\ z=o}$, $u_{sw\ z=o}$ and $\mu_{sw\ z=o}$ are the density, velocity and dynamic viscosity of Q_{sw} , respectively, and d_i is the internal diameter of the inlet (0.99 mm in this case). Similarly, the relative magnitude of the momentum of the jet acting upwards compared to the buoyancy forces can be represented by the square of the Froude number, $(\mathrm{Fr}_{sw\ z=0})^2$ (equal to the reciprocal of the Richardson number, Ri (*i.e.* the ratio of sheer to buoyancy in the flow) as described by equation 4.2; (Coulson *et al.*, 1999)

$$(\mathrm{Fr}_{\mathrm{sw\,z=o}})^2 = \mathrm{Ri}^{-1} = \frac{\rho_{\mathrm{sw\,z=o}} u_{\mathrm{sw\,z=o}}^{\ 2}}{g d_i (\rho_p - \rho_{hw})} = \frac{16 G_{\mathrm{sw\,z=o}}^{\ 2}}{\pi^2 d_i^{\ 5} \rho_{sw} (\rho_p - \rho_{sw}) g},$$ **(Equation 4.2)**

Where, μ_{sw} is the density of $Q_{sw,\ z=0}$. As summarised in table 4.3 the magnitude of $\mathrm{Re}_{sw,\ z=0}$ ranged from 3.0 to 18.8 x 10^3 increasing as expected for G_{sw} and T_{sw}, defining the flow in the mixer as turbulent at the point of issue under all evaluated flow and temperature regimes. Similarly, the magnitude of $(\mathrm{Fr}_{sw\ z\ =0})^2$ for the mixer increased as expected with T_{sw} and Q_{sw}. This suggests that over the range of T_{sw} and Q_{sw}, the rapid movement of flow towards the outlet of the mixer is driven by momentum $(\mathrm{Fr}_{sw,\ z=0})^2 >> 1$. The influence of buoyancy on the behaviour of the jet issuing from the inlet can be largely ignored in this context as in all evaluated flow and temperature regimes the magnitude of $(\mathrm{Fr}_{sw,\ z=0})^2 >> 1$, suggesting a large dominance of momentum over buoyancy. A review of axisymmetric buoyant jets by Rodi *et al.* suggested that the contribution of buoyancy to jet behaviour can be ignored if the $Fr^2 > 5$, as shown in table 4.3 this was calculated to be the case for all measurements. (Ljuboja and Rodi 1980; Rodi and Srivatsa 1980)

Table 4.3: Summary of supercritical water jet behaviour calculated for the CJM with an unconfined inlet.

Q_{hw}	Q_p	*Tmix*	$T'_{sw,z=0}$	$Re_{hw,z=0}$	$(Fr_{hw,z=0})^2$
mL min^{-1}		°C	°C	x 10^3	
10	10	199	350	3.0	21
20	20	199	350	5.9	89
25	10	256	350	7.5	133
10	10	320	400	7.6	40
20	20	320	400	15.3	159
25	10	352	400	19.1	248
10	10	338	450	7.5	55
20	20	338	450	15.0	219
25	10	383	450	18.8	313

The study of vertical, axisymmetric, buoyant jets is of particular relevance in understanding the measured temperature distribution within the CJM in the unconfined inlet position. Coaxial turbulent jets are well known to entrain a co-flow (*i.e.* the precursor flow in this case) which leads to the thermal and spatial dilation of the jet. (Ricou and Spalding 1961) It is well known that jets entrain fluid in their wake, often resulting in re-circulation and a broadening of the residence time distribution of the mixer with more turbulent jets environments leading to greater degree of recirculation as summarised in table 4.3. This was shown to increase with both $Re_{sw,\ z\ =\ 0}$ and $Fr^2_{\ sw,\ z\ =\ 0}$. (Pitts 1991;Ricou & Spalding 1961) From this analysis, dilation and relatively poorly controlled recirculation of the jet is expected due to the flow issuing into a unconfined environment. Similarly, in the unconfined position the temperature of the medium into which the jet is issuing would also affect the behaviour of the jet, although this is beyond the resolution of the measurements. However, if the jet is unable to entrain a sufficient co-flow, greater recirculation would be expected as is observed when $Q_{sw} > Q_p$ (figure 4.3 a). Suggesting, that the observed increase in nanoparticle polydispersity using a CJM with an unconfined inlet arises partly due to the thermal gradient across the mixer (leading to inhomogenous particle nucleation) and the formation of zones of recirculation leading to steady material buildup (through Otswolds ripening) and material growth through recirculation *i.e.* a local increase in reagent concentration in zones of recirculation. Nevertheless, the measured effect on particle size was smaller than expected for the degree of deposition observed within the reactor. Although recirculation caused issues the residence time distribution in the mixer was still sufficiently short to prevent nanoparticles growing to much greater than the nm scale.

As shown in figure 4.2, the confined inlet showed properties more desirable for the formation of nanoparticles in CHFS in terms of minimal material deposition within the reactor and a comparatively narrower PSD for the materials produced. However, accurately determining the effect of supercritical water inlet temperature on the behavior of the jet issuing from the confined inlet is more complicated than the simplified analysis of the unconfined inlet. This is due to heat transfer occurring between the feeds (Q_{sw} and Q_p) and the possible influence of the confining wall. Figure 4.5 provides a sketch of the processes of heat and mass transfer expected in the confined inlet mixer. The measurements presented in figure 4.3 have shown that complete mixing of the feed issuing from the inlet and the precursor flow reach T_{mix} within 4 mm of the terminus of the inlet. A magnitude of heat transfer (ΔQ) was also observed to increase with both increasing $Q_p + Q_{sw}$ and T_{sw}. This suggests that events occurring shortly after issue at the terminus of the inlet are responsible for the fully mixed stream at $z = 4$ mm. The observation of complete mixing and beyond $z = 4$ mm is consistent with the findings of previous studies. (Chorny and Zhdanov 2012; Zhdanov and Chorny 2011) Where, highly turbulent jets have been shown to rapidly entrain a co-flow leading to a uniform concentration of a passive scalar at and beyond five inner pipe diameters for ambient flows and between 1.8 - 2.4 inner pipe diameters in near critical flows (issuing into a cold co-flow). (Augustine and Tester 2009;

Chorny and Zhdanov 2012; Zhdanov and Chorny 2011) In the case of the confined inlet, it was possible to estimate the magnitude of the heat transfer occurring between the inlet and the precursor feed by the measurements taken at z = -20 and z = -10 over a heat transfer area (A_o) of 7.85 x 10^{-8} m^{-2} (calculated using a simple co-axial heat exchanger model). (Coulson *et al.*, 1999) Correspondingly, the estimates of heat transfer coefficients ranged from 1.75 to 2.35 kW m^{-2} k^{-1} increasing as expected with an increase in $T_{sw,in}$ and G_{sw}. The values obtained from this estimation agreed well with those measured for the counter-current reactor (0.9 - 2.0 kW m^{-2} k^{-1}) derived from the measurements presented in Chapter 3 (not reported in detail). However, the complications with accurately placing a thermocouple at z = 0 influenced this analysis, as an apparent temperature step between just below the terminus of the preheated water inlet and the mixture was observed. This step will now be shown to be due to rapid and complete entrainment of the precursor flow.

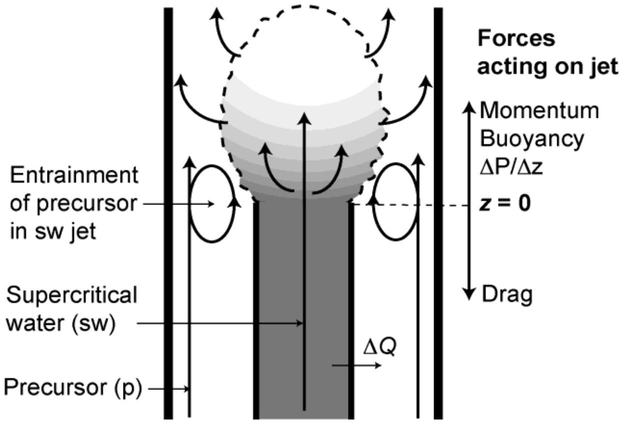

Figure 4.5: Representation of the processes of heat and mass transfer occurring within the confined jet reactor.

As the streams of Q_{sw} and Q_p meet at the terminus of the inlet the temperature of the mixture ($Q_p + Q_{sw}$) may reach $T_{mix,}$ simply by conduction of heat between the supercritical water and aqueous precursor feed, even if no mixing occurred between the two streams. This has in fact been observed in direct observation measurements performed in CHFS systems as reviewed in Chapter 1. Consequently, the magnitude of the distance required to closely approach T_{mix} through the conduction of heat between the inlet (diameter d_i) of and an annulus (width $d_o - d_i$) has been estimated to ensure the rapid transition to T_{mix} is not governed by conduction. This situation represents a simple pipe-in-pipe co-current heat exchanger. In stratified flows of steam and water, it has been reported that U_o (heat transfer coefficient) can vary between 3 and 30 kW m^{-2} K^{-1} giving a length to approach within 95% of T_{mix} ranging from 200- 33 mm ($Q_p + Q_{sw}$ = 20 (T_{sw} = 350) and $Q_p + Q_{sw}$ (Q_{sw} > Qp) = 35 (T_{sw} = 450), respectively, *i.e.* much greater than the measured 4 mm suggesting events occurring near the terminus governed the rapid mixing. (Chorny & Zhdanov 2012; Viollet 1987) The work of Thring and Newby assessed the flow of co-axial turbulent jets of different densities, similar to the densities and velocities presented here and described a parameter which can predict whether a jet issuing into a co-flow can entrain all the available co-flow as described by equation 4.3: (Thring and Newby, 1980)

$$C_{tn} = \frac{G_p + G_{sw}}{G_{sw}} \left(\frac{\rho_{sw}}{\rho_p}\right)^{0.5} \frac{d_i}{d_o} \quad \textbf{(Equation 4.3)}$$

Where, C_{tn} is the Thring-Newby parameter, G_p is the mass flow-rate of the precursor, G_{sw} is the mass flowrate of the preheated water , ρ_{sw} is the density of the preheated water at the outlet, ρ_p is the density of the precursor flow, d_i is the inlet diameter and d_o is the diameter of the confining tube. According to Thring and Newby's analysis, there is insufficient co-flowing fluid if $C_{tn} < 0.9$ and it is likely that a recirculation zone is formed downstream of the inlet. However, in this case slight recirculation could be tolerated if no adverse effects on particle size were measured. If it is assumed that no heat transfer occurs between Q_p and Q_{sw} as is the case in the unconfined mixer the values of C_{tn} ranged from 0.128 – 0.08, suggesting that the jet issuing from the inlet will entrain all the precursor flow and could possibly entrain a significantly greater co-flow than its own mass flow rate. Similarly, a relationship was put forward in which the distance required for the Jet to entrain all available co-flow as defined by equation 4.4; (Thring and Newby, 1980)

$$X_0 = 2.5\ d_0\, C_{tn} \quad \textbf{(Equation 4.4)}$$

Where, X_0 is an estimate of the distance required by the jet to entrain the fluid, d_o is the diameter of the confining tube and C_{tn} is the Thring-Newbury parameter. In the unconfined mixer distances in the order of a few mm (range 0.99 – 2.54 mm) were calculated assuming the confining tube could be represented by d_o. However, in the case of the confined inlet, the density and velocity of the jet issuing from the inlet is subject to large variation near the critical temperature and the effect of ΔQ could not be readily resolved. For this reason, calculation of the effect of supercritical water exit temperature were estimated assuming different magnitudes of heat transfer occurring between Q_p and Q_{sw} (arbitrarily defined) resulting in a distribution of temperatures and densities between

Q_{sw} and Q_p. An analysis is presented on the basis of differences in density between Q_p and Q_{sw} determined from enthalpy balance and an indication of the total heat transfer yielding different mixing lengths is presented. The specific enthalpy and thus the temperature and density at 24.1 MPa of the superheated water exiting the inner tube at $z = 0$ (within these bounds) was determined using equation 4.5:

$$h_{sw,z=0}(T'_{sw,z=0}, 24.1\,\mathrm{MPa}) = h_{sw}(T_{sw}, 24.1\,\mathrm{MPa}) - \Delta Q_p / G_p \quad \textbf{(Equation 4.5)}$$

Where ΔQ_p is the heat transferred from Q_{sw} to Q_p. Similarly, the temperature of Q_p may be determined by adding the heat transferred to known enthalpy of ambient temperature water. The calculation of all relevant physical properties is presented in table 4.4 assuming different magnitudes of heat transfer through defining the temperature of $Q_{p\ z=0}$. From this analysis is can be seen that even at relatively large magnitudes of ΔQ substantial entrainment between the precursors and preheated water is expected, owing principally to the large density change in water around the critical point as discussed further in Chapter 1. These calculations suggest that the behaviour of Q_{sw} issuing from the inlet is responsible for the mixture rapidly achieving T_{mix}. Similarly, the estimated distances for entrainment fall within the measured mixing lengths determined experimentally. This analysis showed that even if *ca.* 90% of the mixture temperature was reached by Q_p the flow regime at issue would yield a Re and Fr^2 similar in magnitude to those assumed for the adiabatic case *i.e.* the flow would be turbulent and the flow would show a $(Fr_{sw\ z=0})^2 >>1$ and be dominated by momentum, and that rapid entrainment was caused by the momentum of the jet. (Pitts 1991) Although a significant simplification this analysis suggests that in all reported cases this mixer geometry operates in a regime where, **1)** rapid entrainment of the precursor solutions into the issuing jet is occurring and **2)** that the jet could potentially entrain a greater flow of precursors relative to its own mass flow rate. To further support the discussion presented here a brief description of CFD modeling data for the CJM is presented in section 4.3.2. From a particle formation point of view it was shown in chapter 3 that ZnO formation occurs through the formation of a soluble intermediate which in the CJM operated in the confined position would form through preheating of the precursor in the annulus bound by d_o-d_i and dehydration would only occur above a temperature of 305 °C suggesting that deposition in this reaction would be unlikely. However, similar observations were also made in the synthesis of hydroxyapatite which suggests this reaction point is suitable for the efficient and clean (lack of material deposition) of many nanoparticle compositions. However, this analysis also suggested that recirculation would occur under all reaction conditions downstream of the inlet. However, recirculation downstream of the particle formation could be tolerated if no adverse effects in particle properties or evidence of particle growth were measured. This chapter now moves forward to evaluate this aspect of the application of CJM for the synthesis of nanoparticles.

Table 4.4: Summary of the variation in entrainment length and C_{tn} as a function of density difference at z = 0. All calculations are derived from a defined temperature difference at z = 0.

Q_{sw}	Q_p	T_{sw}	T_{mix}	$T_{pz=0}$ (°C)	$T_{sw, z=0}$ (°C)	$(Fr_{sw, z=0})^2$	$Re_{sw, z=0}$ x 10^4	C_{tn}	X_o (mm)
25	10	450	383	100	419	288	1.9	0.15	1.78
20	20	450	338	100	392	142	1.5	0.18	2.08
10	10	450	338	100	392	35	0.74	0.25	2.78
25	10	450	383	200	399	241	1.9	0.30	3.43
20	20	450	338	200	381	88	1	0.34	3.58
10	10	450	338	200	381	22	0.5	0.38	3.98
25	10	450	383	300	387	178	1.8	0.32	3.92
20	20	450	338	300	351	85	0.6	0.36	4.04
10	10	450	338	300	351	21	0.3	0.45	4.32

4.3.2 Preliminary modelling data:

The modelling data presented for the CJM was completed by Dr Caiyun Ma and Professor Xue Wang (University of Leeds). CFD models of the mixing in the CJM were generated using the FLUENT software package and constructed as described in our previous work. (Ma *et al.,* 2011) Figure 4.6, shows the velocity, temperature and density vector distribution in the region near the terminus of the preheated water inlet modelled independently of the *in situ* temperature analysis presented here. This preliminary modelling work supports the above discussion of a large temperature (Figure 4.6 c) and density difference (figure 4.6 c) still occurring at the terminus of the inlet. This preliminary modelling data has served to demonstrate, both entrainment and recirculation (figure 4.6 a) lead to the step change in temperature measured at z = 0 which made accurate (and reproducible measurements in the near z = 0 range impossible). Similarly, the modelling also supports the analysis presented above, which suggested that entrainment and vanishingly small mixing lengths would be observed in the region near the terminus even if high heat transfer was anticipated. In the model depicted below the temperature of Q_p at z = 0 is in the region of 140 - 180 °C and still shows rapid entrainment and mixing. For comparison the heat transfer co-efficient determined from the model was 2.13 kW m^{-2} k^{-1} and mid-range for the estimation presented earlier. Suggesting a valid interpretation of the experimental data presented earlier.

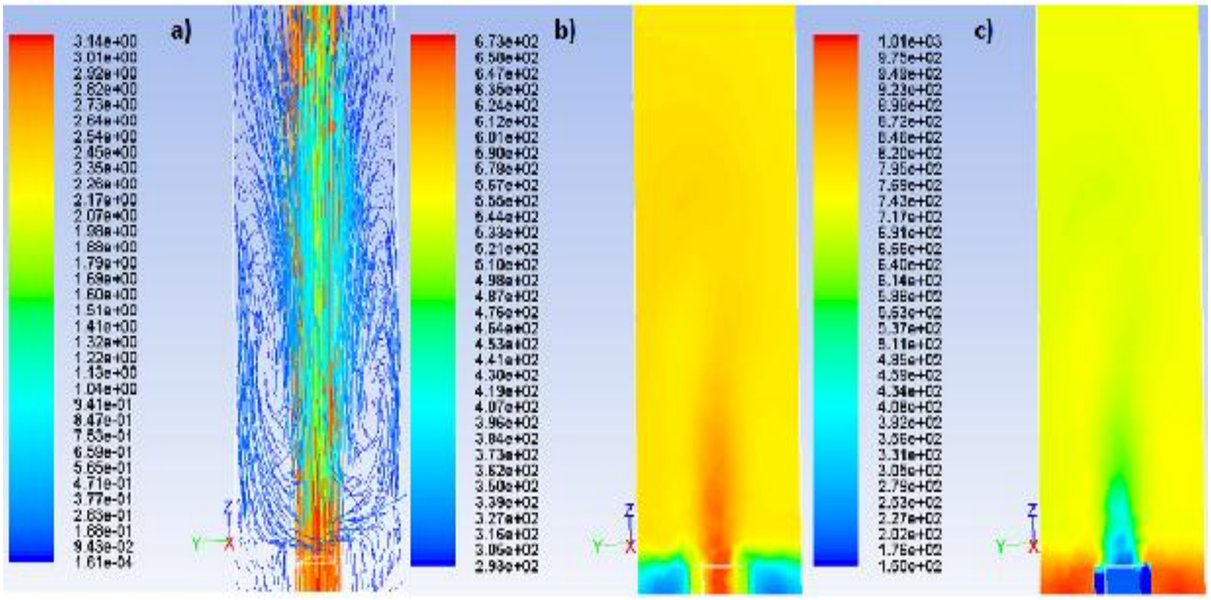

Figure 4.6: **a)** Velocity vectors (m s^{-1}) **b)** temperature vectors (scale in K) and **c)** density distributions (kg m^{-3}) in the supercritical water exit regions of a confined jet mixer (d_i = 0.99, d_o = 4.97 mm). This modelling work is of the T_{sw} = 450 $Q_{sw} + Q_p$ = 40 process condition.

4.3.3 Effects of CJM mixers on the continuous hydrothermal synthesis of nanoparticles:

To evaluate the effects of both materials synthesis in the CJM and to assess if the preheating of Q_p prior to the terminus of the preheated water inlet influenced particle size, ZnO was chosen as a model system to evaluate the effect of processing variables. Samples were produced a flow rates ranging from $Q_p + Q_{sw}$ = 20 to $Q_p + Q_{sw}$ = 40 at three precursor concentrations as summarised in table 4.5 alongside the characterisation data obtained for each sample. The reactions governing the formation of ZnO in hydrothermal systems have been described previously in Chapter 3 and by others. (Demianets *et al.*, 2002; Li *et al.*, 1999)

Table 4.5: Summary of the synthesis conditions used for the production of ZnO on the laboratory scale CHFS process (mixer 1/16” inlet within ¼” components).

ID	[Zn] (M)	Q_{sw}	$Q_{p(zn)}$	Q_{p} (KOH)	C_s (nm)	TEM (nm)	TEM SD (nm)	AR	Eg (eV)	Yield (%)
0.05M40	0.05	20	10	10	32.0	68.8	14.2	1.01	3.27	92
0.1M40	0.1	20	10	10	37.7	64.6	11.9	1.06	3.26	88
0.2M40	0.2	20	10	10	33.6	60.1	9.7	1.2	3.26	91
0.05M30	0.05	15	7.5	7.5	37.8	67.1	13.5	1.04	3.26	90
0.1M30	0.1	15	7.5	7.5	34.1	62.1	15.8	1.08	3.26	83
0.2M30	0.2	15	7.5	7.5	33.2	59.3	14.8	1.1	3.26	96
0.05M20	0.05	10	5	5	34.0	63.9	10.3	1.16	3.27	94
0.1M20	0.1	10	5	5	33.6	69.2	11.7	1.18	3.27	92
0.2M20	0.2	10	5	5	35.5	64.6	9.3	1.08	3.27	95

Key: C_s is the crystallite size determined by application of the Scherrer equation, AR is the aspect ratio measured by TEM, E_g is the direct bandgap calculated using the KM method. The concentration of KOH was equal to the Zn concentration used in each synthesis. TEM is the average particle size determined by TEM and TEM (SD) is the standard deviation determined from a particle size distribution taken from *ca.* 300 particles.

The diffraction patterns of the materials summarised in table 4.5 could be indexed to the Wurtzite structure of ZnO (ICDD 26170) and showed significant similarity to those of ZnO produced in Chapter 3. Significant similarity in particle size of ZnO produced in the CJM was inferred from calculation of the diffraction peak FWHM of the (101) reflection giving estimates of particle size consistent across the sample series as summarised in table 4.5. The similarity in the reaction products was also reaffirmed by their UV-VIS spectra which all showed striking similarity, the band gaps of each of the samples are summarized in table 4.5 and showed no significant differences in any of the samples inferring no size dependent absorption effects. (Hale *et al.*, 2005) TEM images representative of samples 0.05M20 – 0.2M40 (table 4.5) are shown in figure 4.7 and were used to confirm the similarity in particle size and size distribution inferred from powder XRD. A summary of the particle size distributions taken from the measurement of *ca.* 300 particles of each sample are summarised in table 4.5, showing that crystallite size and size distribution is largely invariant over the experimental conditions presented. The observations infer that the particle nucleation and growth steps of ZnO are largely unaffected by slight variation in the mixing processes occurring within the CJM and that heat transfer occurring between Q_{sw} and Q_p within the reactor has little effect on the formation of nanoparticles in this reactor. From the data presented in Chapter 3, the formation of ZnO nanoparticles was shown to proceed *via* a soluble Zn peroxide species the dehydration and crystallization of which was shown to occur at temperatures above 305 °C. From the measurements presented in figure 4.3 and the temperature calculations presented in table 4.4, it is unlikely that the reagents in the CJM only reach a temperature >305 °C when almost completely mixed with Q_{sw}. As such, it is unsurprising that little effect in the variation both Q_{sw} and Q_p is seen in the properties of ZnO produced using this reactor.

The anisotrophic growth of ZnO is observed in many syntheses, and is expected if there are distinct particle nucleation and growth phases present. (Demianets *et al.*, 2002) To confirm that no slight anisotropic particle growth occurred in the samples produced using the CJM, the aspect ratio distributions of each of the samples were measured (*ca.* 150 particles), yielding values close to 1 (range 1.0 - 1.2) for all samples as summarised in table 4.5. As ZnO rods, bars and whiskers have been synthesised in other continuous hydrothermal systems, these observations imply that a particle growth phase can be observed in CHFS systems, arising through differences *(sic)* in the nucleation of particles. (Ohara *et al.,* 2004; Sue *et al.,* 2004a; Sue *et al.,* 2004b; Sue *et al.,* 2004a) As these observations were not made in this sample series (0.05M20 – 0.2M40), the data suggests that the nucleation and growth of nanoparticles was not sufficiently different to observe a change in the characteristics of the reaction products. Although, from the calculations presented in table 4.4 slight differences in the behavior of Q_{sw} exiting the preheated water inlet could be expected, but do not appear to be significant enough to observe differences in the nucleation and growth of the nanoparticles even when the precursor concentration was varied (an attempt to exaggerate any particle growth phases). These observations are consistent with the observations made in Chapter 3. It is inferred that the differences in mixing behavior in the CJM as a function of flow rate and the degree of heat transfer occurring with the CJM were not large enough to observe differences in the growth of nanoparticles. This chapter now moves forward to assess the effects of the physical geometry of CJM mixers and the effects of variation in flow rate.

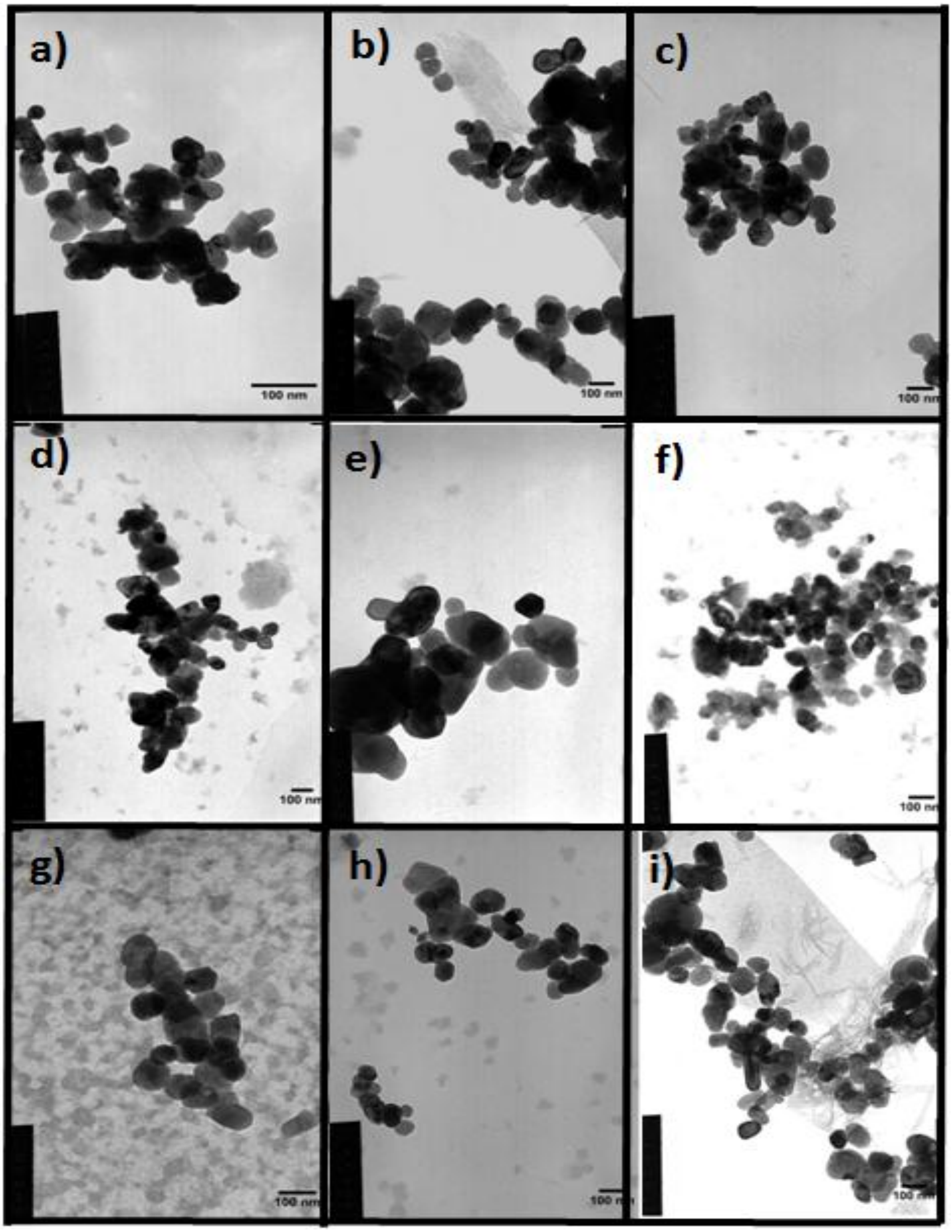

Figure 4.7: TEM images representative of ZnO nanoparticles produced on the laboratory scale CHFS process through a variation of flow rate and precursor concentration, **a)** 0.05M40, **b)** 0.1M40, **c)** 0.2M40, **d)** 0.05M30, **e)** 0.1M30, **f)** 0.02M30, **g)** 0.05M20, **h)** 0.1M20 and **i)** 0.2M20.

4.3.4: Evaluation of CJM on Particle Synthesis

In this section the effect of the physical dimensions of the reaction points are assessed for a fixed T_{sw} (450 °C) and at two flow regimes $Q_p + Q_{hw} = 40$ and $Q_p + Q_{hw} = 20$. Tabulated characterisation data for the materials presented in this section is provided in Table 4.6 alongside the synthesis conditions. This section presents data from four distinct geometries of CJM (identified in Table 4.1). These experiments were performed to assess if the slight variation inferred from *in-situ* temperature measurements and calculation of the flow regimes influenced the properties of nanoparticles obtained from the process. The application of CJM to the synthesis of nanoparticles was evaluated using both hydroxyapatite and ZnO as model systems to supplement the data reported in table 4.5.

Table 4.6: Summary of the synthesis and characterisation details of the nanoparticles produced for the evaluation of CJM of different dimensions as summarised in table 4.1

ZnO									
[CJM] (d_o-d_i)	Q_{sw}	$Q_{p(zn)}$	Q_p (KOH)	Cs (nm)	TEM (nm)	TEM SD (nm)	AR	Eg (eV)	Yield (%)
3.98	20	10	10	29.6	65.7	13.3	1.06	3.27	90.3
3.98	10	5	5	31.1	68.8	14.2	1.10	3.26	87.6
6.63	20	10	10	30.5	64.6	11.9	1.03	3.26	90.2
6.63	10	5	5	34.2	60.1	9.7	1.08	3.26	87.8
3.57	20	10	10	33.5	67.1	13.5	1.13	3.26	93.4
3.57	10	5	5	33.6	54.4	16.7	1.13	3.26	92.4
6.22	20	10	10	29.6	68.6	13.1	1.02	3.27	90.9
6.22	10	5	5	34.2	65.9	14.2	1.15	3.26	79.2
Hydroxyapatite									
3.98	20	10	10	-	187.3	24.9	3.23	-	88.9
3.98	10	5	5	-	183.8	21.2	4.01	-	94.6
6.63	20	10	10	-	212.4	42.3	3.56	-	92.2
6.63	10	5	5	-	218.3	45.0	3.42	-	93.1
3.57	20	10	10	-	198.6	32.6	3.56	-	89.6
3.57	10	5	5	-	241.5	46.4	3.78	-	90.8
6.22	20	10	10	-	226.5	36.7	3.47	-	93.2
6.22	10	5	5	-	234.0	41.02	3.58	-	87.3

Key: All metal salt precursor concentrations were fixed to 0.1M, AR = aspect ratio, Cs crystallite size determined from the application of the Scherrer equation.

Measurements of temperature taken from the four distinct CJM mixers are presented in figure 4.8. The characteristic mixing length (defined as the distance taken for the mixture preheated water and precursors) to reach the theoretical maximum temperature T_{mix} was used as a measure of the performance of each CJM. Where, in figure 4.8 complete mixing (the mixture achieving T_{mix} as summarised in table 4.1) is shown to occur within 5 internal pipe diameters (d_i) in each geometry over a large range of T_{sw} and $Q_p : Qs_w$ ratios ($Q_p + Q_{sw} = 20$, $Q_p + Q_{sw} = 40$ and $Q_p (10) + Q_{sw} (25) = 35$) and suggests significant similarity in the mixers with the notable exception of the mixer 6.22 (figure. 4.8d) in which T_{mix} is achieved at *ca.* 10 internal pipe diameters. The similarity in temperature measurements for different mixers is unsurprising in light of the analysis presented for the confined inlet reaction point presented in Section 4.3.1. If it is assumed that the magnitude of heat transfer ΔQ is similar in each geometry the variation in (d_i / d_o) over each geometry is comparatively small (0.9 - 1.2 mm) and as such it is expected by equations 4.1 and 4.2 that slight dilation of the inlet would yield comparatively small effects on the jet of preheated water issuing from the inlet as neither the Re of the flow or $(Fr)^2$ would not change significantly in magnitude. Although, a degree of variation in the $(Fr_{sw\ z=0})^2$ of Q_{sw} issuing from inlets of different internal diameters would suggest slight variations in the length of entrainment, in many cases these variations are anticipated to be much smaller than the resolution of the temperature measurements (equation 4.4). However, these measurements have served to identify the dynamics in mixing in CJM of different size ratios. In this evaluation, “equivalent mixing behaviour” is observed in reactors with d_o-d_i ratios of 3.98, 3.57 and 6.63. In these geometries either a higher magnitude of $Re_{sw\ z=0}$ and correspondingly greater $(Fr_{sw\ z=0})^2$ or a narrower annulus bound by d_o-d_i was used when compared to the 6.22 reactor (figure 4.8 d). This suggests a dynamic interplay between jet behaviour at the terminus of the inlet and the influence of the confining wall. As in the 6.22 reaction point geometry, on increasing d_i it is anticipated that in an adiabatic case (*i.e.* no heat transfer) that the $(Fr)^2$ of the jet issuing from the inlet would decrease and the contribution of momentum in the flow would reduce when compared to that of mixer 6.63 (not sufficiently to induce buoyancy driven flow). Similarly, an increase in d_i would also have the effect of lowering the Re of the flow (equation 4.2) leading in certain cases to a more transient flow (*i.e.* Re > 2000 but < 4000) which would have the effect of altering jet behaviour at the terminus of the inlet and possibly altering entrainment effects. Hence, it is reasoned that the increase in mixing length observed in the 6.22 reactor is due to the flow of Q_{sw}

behaving in a more plume like manner (rather than jet like) and not interact with the confining wall until further from the terminus of the Q_{sw} inlet due to less rapid entrainment. This effect is likely complex and cannot be adequately addressed using this strategy. However, inference made from the modelling data presented in figure 4.6 suggests the confining wall influences the flow pattern as shown in the velocity vector diagram (figure 4.6a) and confining the jet issuing from the inlet yields a large local temperature rise. Whereas, in a reactor with a broader d_o this region is extended until the flow of Q_{sw} interacts with the confining wall.

To confirm that these geometries give similar outcomes under the conditions used for the synthesis of nanoparticles. Samples of both HA and ZnO were produced at two flow rate ratios ($Q_{sw} + Q_p = 20$ and $Q_{sw} + Q_p = 40$) spanning a range of flow rates commonly used for the synthesis of nanoparticles (as summarised in table 4.6). Powder Diffraction patterns of the samples produced using the four distinct CJM's showed significant similarity and could either be indexed as the hexagonal wurtzite structure of ZnO (ICDD: 26170) or as hydroxyapatite (JCPDS pattern 09-0432). In both materials no evidence of contaminating phases in the reaction products was observed consistent with the work of Chapter 3. However, consistent with the data presented in Chapter 3, slight anisotropy was observed for hydroxyapatite samples in reflections related to the c-axis (001, etc) suggesting materials with a similar morphology were obtained to those detailed in Chapter 3 (data not shown). In ZnO samples, similarity in particle size was inferred from calculation of the diffraction peak FWHM from the (101) reflection giving estimates of particle size consistent across the sample series (table 4.6) and further suggested by the similarity in the absorbance of the samples determined by UV-Vis, the band-gaps for each of the samples (determined using the KM method) are presented in table 4.6.

To confirm again the similarity in particle properties inferred from XRD and the similarity in temperature profiles within each of the reactors. TEM was used to assess the crystallite morphology and crystallite size distributions of both the ZnO and hydroxyapatite samples, the crystallite size determined from the measurement of *ca.* 300 particles is summarised in table 4.6. TEM images representative of the ZnO samples are shown in Figure 4.9 which all show striking similarity in both size distribution and morphology.

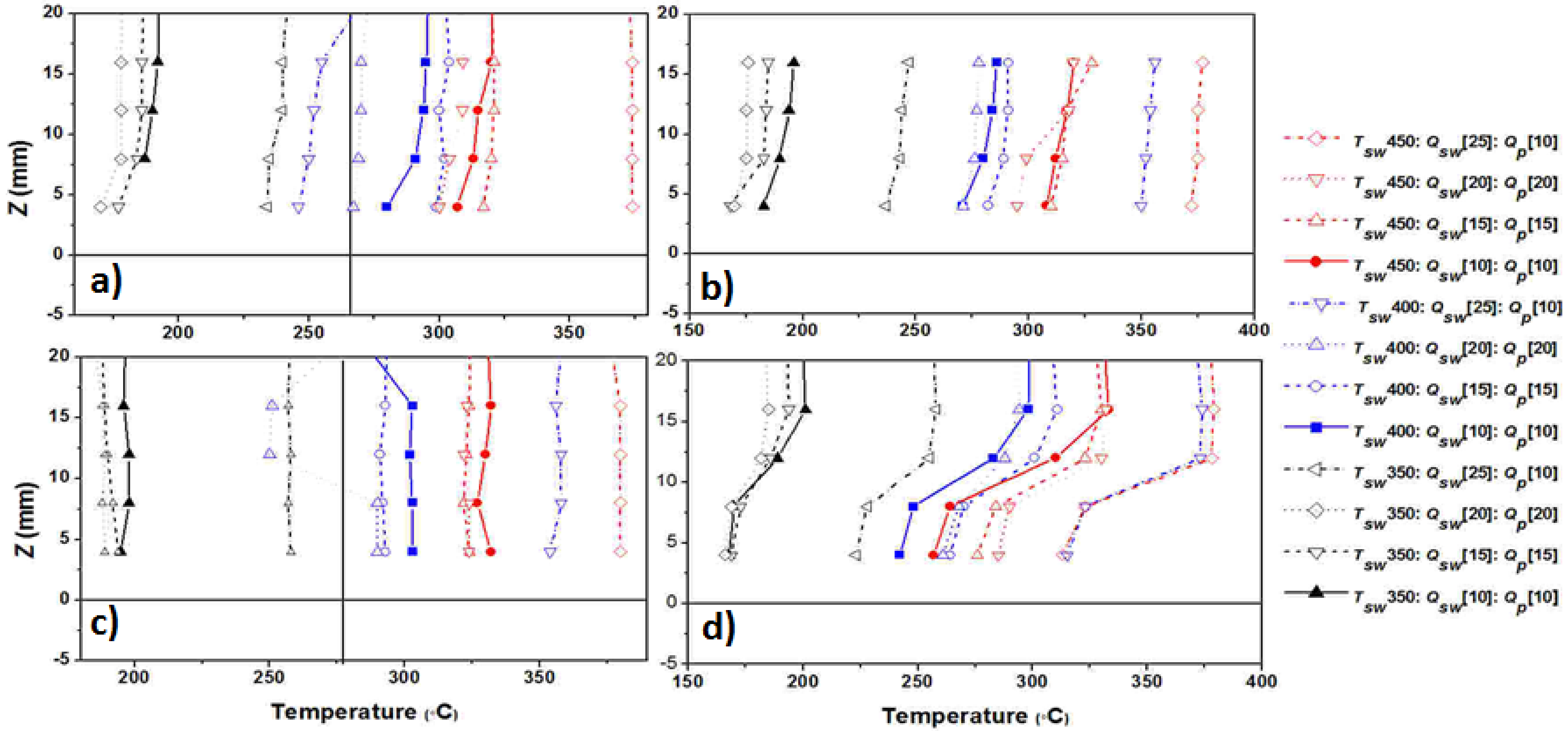

Figure 4.8: Measurements of temperature at positive z from inlet position when different confined jet reactors are used, **a)** d_o-d_i = 3.98, **b)** d_o-d_i = 3.57, **c)** d_o-d_i = 6.63, **d)** 6.22 . Common key for each of the geometries evaluated identifying reactor condition (see table 4.1 for reaction point components).

As identified by others, growth of ZnO nanoparticles is normally resolved as crystallite anisotropy when in the hydrothermal solution a particle growth phase occurs. (Demianets and Kostomarov 2001; Sue *et al.,* 2004) To further evaluate the particle morphology, the aspect ratio distributions of each of the samples were measured (*ca.* 150 particles), yielding values close to 1 as summarised in table 4.6. This observation suggests further the similarity in the growth of these nanoparticles. In the case of hydroxyapatite (figure 4.10), a similar observation in terms of both crystallite size and aspect ratio were made (summarised in table 4.6). However, hydroxyapatite samples produced using the 6.63 mixer showed a notably smaller crystallite size and narrower polydispersity. This suggested a moderate difference in the crystallisation of this sample. The variation in PSD of both HA and ZnO samples is presented graphically in figure 4.11a and 4.11b which identifies each sample as a function of d_o/d_i. These results suggest that measurable differences in temperature profile occur between reaction points, the differences are not sufficiently large to influence the size or size distribution of nanoparticles (figure 4.11). In light of these observations, the process appears heavily dominated by particle nucleation, even in cases where continuous running is not favoured.

From the mechanisms of particle formation described in Chapter 3, the similarity in particle size obtained in each of the CJM geometries for both materials systems are consistent with those produced under equivalent processing conditions in a counter current reactor. This observation suggests that regardless of the mixing processes used for their production, nanoparticles of similar physiochemical characteristcs can be produced if the mixing reactions are sufficiently rapid. From the data presented there are likely several explanations for the similarity in particle size as a function CJM geometry and the distribution of temperature within the reaction point ; **1)** The reactions are governed by the terminal reaction temperature and this results in the complete precipitation of ions in the hydrothermal solution itself, **2)** the nanoparticle crystallisation reactions are kinetically driven and occur at high rate, **3)** nucleate formation is dominant in the process and **4)** particle growth is constrained by exhaustion of free ions in solution. From the observation presented in both Chapters 3 and 4 this defines a limit to the versatility of the CHFS process for the synthesis of nanoparticles which are not subject to elongated particle growth phases.

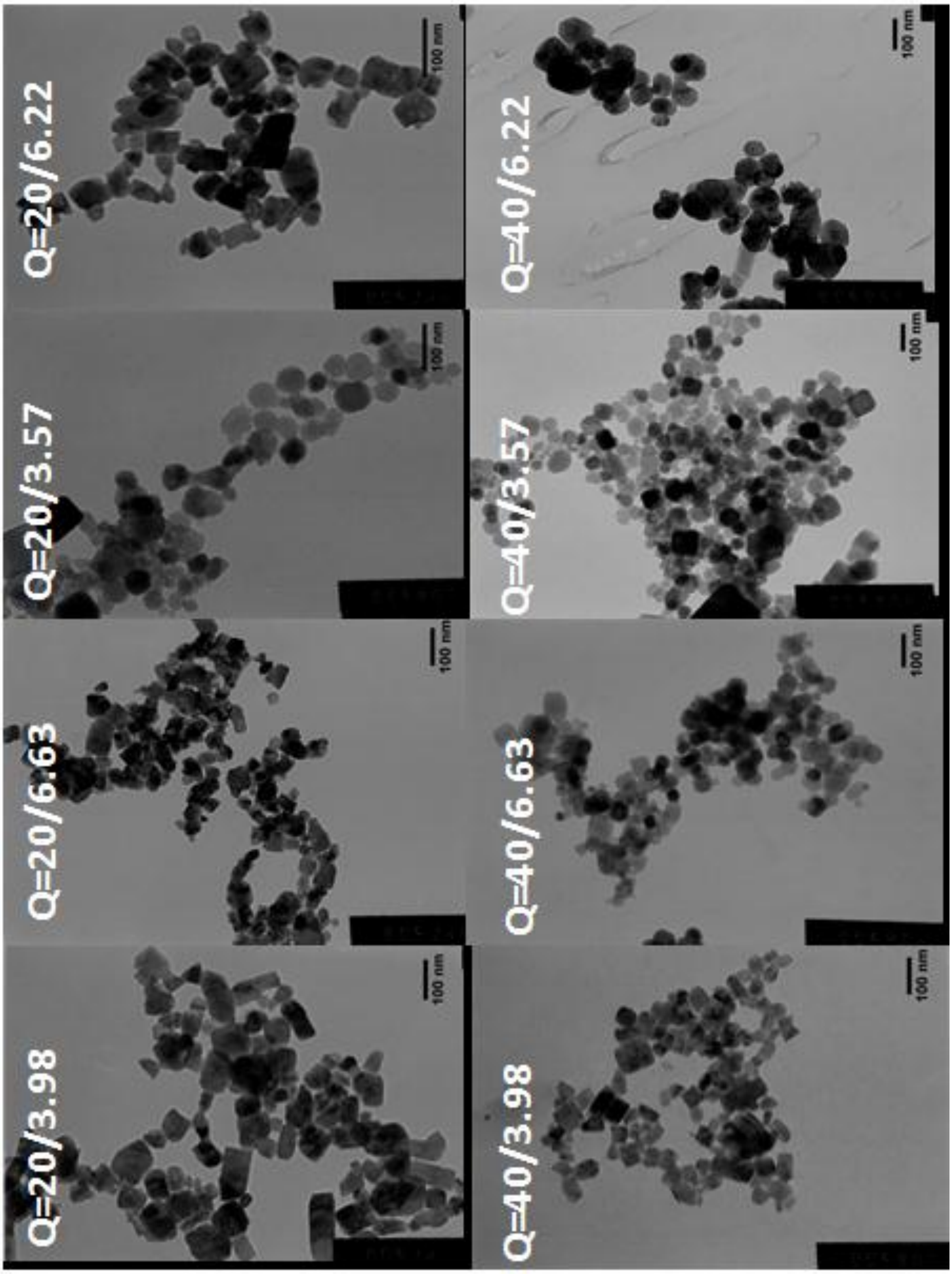

Figure 4.9: TEM images of ZnO nanoparticles produced using CJM of different physical dimensions in the figure Q identifies the flow regime (*i.e.* $Q_{sw} + Q_p = 20 = Q20$) and the reaction point geometry is identified by the value of $d_o - d_i$ summarised in table 4.1.

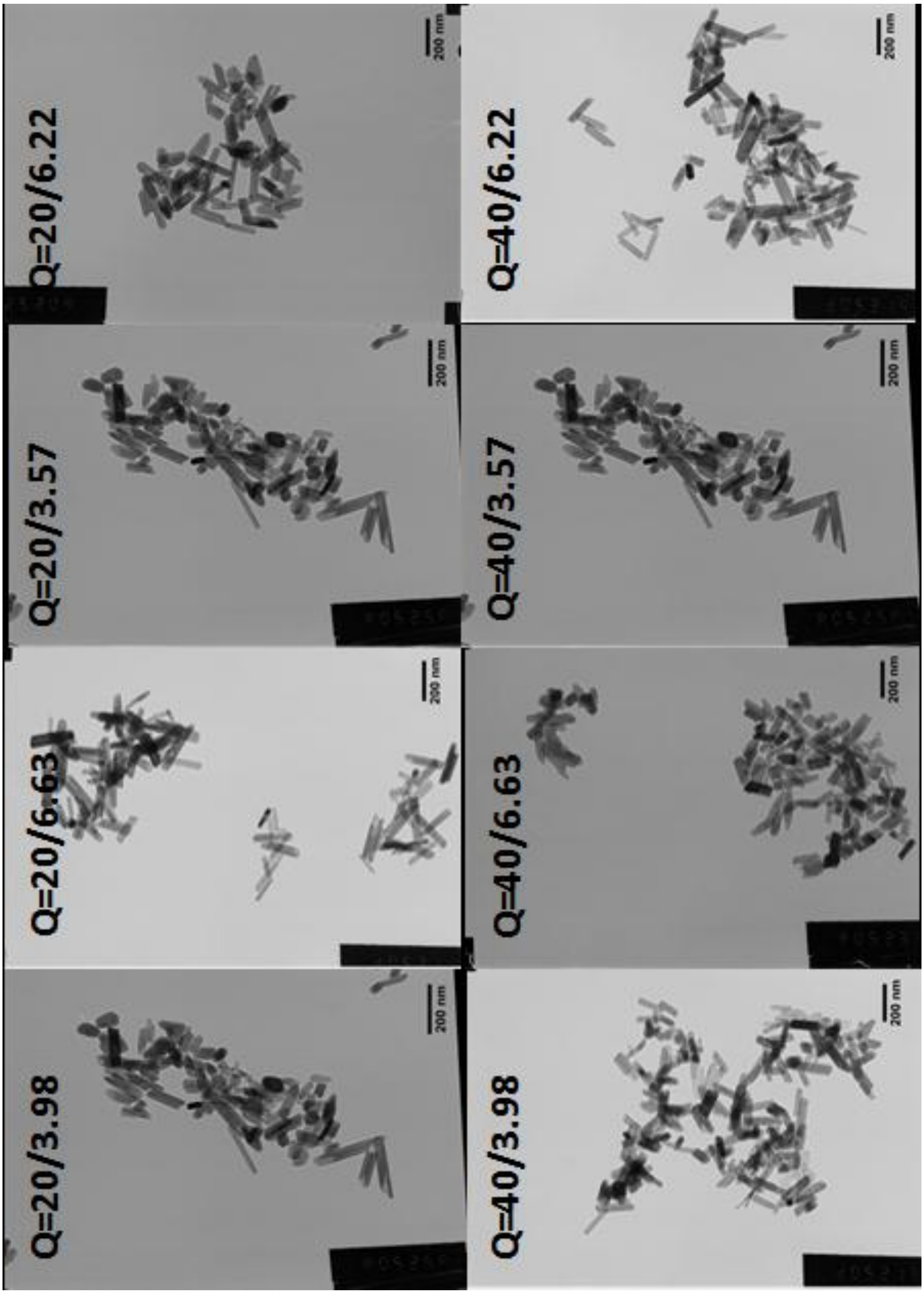

Figure 4.10: TEM images of hydroxyapatite nanoparticles produced using CJM of different physical dimensions, in the figure Q identifies the flow regime (*i.e.* $Q_{sw} + Q_p = 20 = Q20$) and the reaction point geometry is identified by the value of $d_o - d_i$ summarised in table 4.1.

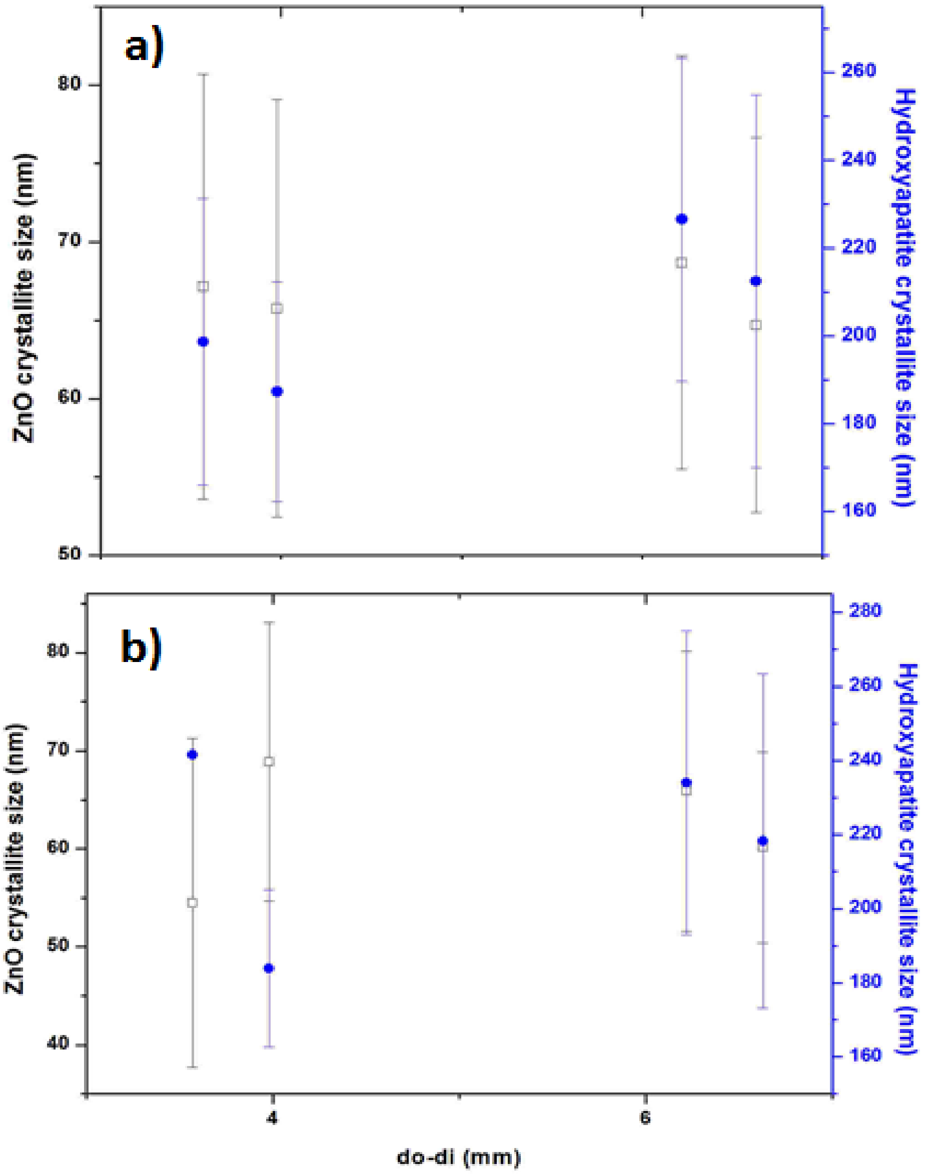

Figure 4.11: Overlay of particle size distributions produced under high and low flow regimes divided by reaction point geometry **a)** ZnO samples **b)** Hydroxyapatite samples. Samples produced using the flow regime Q_{sw} + Q_{p}= 20 are identified with circles and samples produced using the flow regime Q_{sw} + Q_{p} = 40 are identified by squares. Error bars denote each samples standard deviation in nm.

4.4 Conclusions:

In conclusion, a novel confined jet reaction suitable for the continuous hydrothermal synthesis of nanoparticles was developed and tested. The reaction point was optimised and a number of configurations were constructed and tested for their capacity to produce nanoparticles. It was shown that the particle size and size distribution were largely unaffected by slight differences in the mixing processes for both the formation of a metal oxide (ZnO), through a rapid two step dehydration reaction and a hydrothermal crystallisation reaction (hydroxyapatite). This observation is unsurprising in light of the data presented in Chapter 3. A detailed analysis of the reaction point deemed most appropriated for the synthesis of nanoparticles was also presented and showed that particles of similar crystallite size were produced owing to the similarity in temperature profile. Demonstrating, particle nucleation and growth was largely unaffected by slight differences in mixing behaviour over a spread of precursor concentrations. This suggested, supersaturation of the solution was achieved in all syntheses leading to similar particle formation steps. It was also shown by an *in-situ* temperature measurement strategy that knowledge of the heat and mass transfer processes occurring in the reactor allowed construction of a mixer which showed little material deposition. This showed the importance of controlling the mixing by confining the inlet of preheated water preventing recirculation and deposition of material within the reactor. It was also shown that rapid mixing between the preheated water feed and the precursor feed was achieved in CJM due to the dominance of momentum in dictating jet behaviour. Rapid entrainment of the precursor solutions into the rear of the jet was suggested as the mechanism of rapid mixing in this system a condition that was satisfied over a broad range of process conditions. The CJM showed a good mixing profile in all process conditions which was shown to be more versatile in terms of mixing different ratios of feeds than the counter current reactor initially presented in Chapter 3.

4.5 Future work:

The largest single contribution this work would come from CFD modelling of the mixing processes. Although, from the materials synthesis data it is unlikely this analysis would contribute significantly to altering particle nucleation and growth processes. However, it would serve to further define the processes responsible for mixing and would be of academic interest. Experimentally, the processes responsible for mixing would be better defined through measuring the centre line jet temperature and using this data to reinterpret the events occurring within the reaction point with a far greater resolution than afforded by the presented measurements. Further investigation into mechanism to control the size of particles produced by this method would be of interest. This would most likely be achieved by altering the chemical conditions within the mixing zone. Investigation of auxillary reagents which would alter the solubility of ions in the hydrothermal solution would be of interest as from the data presented in this Chapter complete precipitation of the ions in solution leads to limited particle growth.

CHAPTER 5

Synthesis and Characterisation of Magnetic Iron Oxides Produced Using CHFS

:

5.0 Aim:

This chapter outlines an investigation into the synthesis of iron oxide nanoparticles using a continuous hydrothermal method as described in Chapter 2. The synthesis of iron oxides from iron nitrate hexahydrate was initially investigated by varying the reaction point temperature over a range of temperatures. This was then compared to iron oxides synthesised using CHFS from iron (III) citrate precursor. The aim was to understand the influence of oxidizing and reducing species formed within the reactor to assess the effect of synthesis conditions on the structure, surface chemistry, morphology and magnetic properties of the iron oxide.

5.1: Introduction:

Iron oxides are widely used and well-recognised compounds, which exists in 16 identified forms. (Laurent *et al.,* 2008) Much research has focused on the synthesis and characterisation of hematite (α-Fe_2O_3), magnetite (Fe_3O_4), and maghemite (γ-Fe_2O_3), because they are the principal forms of the oxide used industrially as pigments and magnetic materials. (Teja and Koh 2009) Magnetite and maghemite particles ranging from nanometre to micrometre diameters are under study for a large number of medical applications, such as magnetic cell separation drug delivery, MRI contrast agents and magnetic hyperthermia. (Gunasekera *et al.,* 2009; Kallumadil *et al.,* 2009; Loebinger *et al.,* 2009; Pankhurst *et al.,* 2009; Pankhurst *et al.,* 2003; Thomas *et al.,* 2009) Their unique properties in terms of chemical stability, biocompatibility, low cost and magnetic properties (high saturation magnetisation), make these materials ideal for such specific applications. (Pankhurst *et al.,* 2003) Similarly, the unique magnetic properties of nanosized magnetite are also of interest in a variety of high value applications *e.g.* magnetic markings and magnetic inks. (Lam *et al.,* 2008)

Nanoparticles of maghemite and magnetite can be synthesised by many chemical routes including, co-precipitation reactions, (Babes *et al.,* 1999) mirco-emulsion routes, (Santra *et al.,* 2001) synthesis in micro-reactors, (Shchukin and Sukhorukov 2004) sol-gel, (Lu *et al.,*

2002) poly-ol processes, (Joseyphus *et al.*, 2007) thermal decomposition reactions and hydrothermal reactions. (Hyeon *et al.*, 2001; Lam *et al.*, 2008) However, the most common and simplest synthesis of magnetic iron oxides is *via* the co-precipitation of di/trivalent iron salts in a basic aqueous medium. (Babes *et al.*, 1999) Typically, commercially available iron oxide nanoparticles for MRI applications are exclusively prepared by this method and are produced in batch sizes in the range of *ca.* 10-50 g. (Kim *et al.*, 2001) The co-precipitation approach remains an economical route to synthesise large amounts of nanostructured iron oxide particles it also entails several disadvantages in terms of poor degree of size control, crystalinity and colloidal stability with the product requiring heavy refinement. (Kim *et al.*, 2001) Among the various methods for producing nanoparticles, wet chemical routes have the advantages of being simple and provide good control over particle properties which are desired in the synthesis of magnetic nanoparticles. (Mikhaylova *et al.*, 2004) Similarly, wet chemical methods allow for the introduction of a suitable capping agent during, or after the synthesis to prevent the aggregation of the nanoparticles and make the synthesis of stable colloidal dispersion possible, thereby expanding the application of many materials. (Thanh and Green 2010)

Hydrothermal methods, both continuous and batch wise have been applied to the synthesis of magnetic nanomaterials. Magnetite and maghemite have both been synthesised from solutions of $Fe(SO_4)_3$, $Fe(Ac)_2$ and iron citrate, respectively using continuous hydrothermal systems at temperatures in the range 200 to 500 °C producing materials with crystallite sizes of *ca.* 50-100 nm. (Adschiri *et al.*, 1992; Cote *et al.*, 2003; Hao and Teja 2003; Sasaki *et al.*, 2010). Although particles of this size range would find limited application in biomedical applications such as MRI or magnetic hyperthermia, the formation of these magnetic phases is of interest especially when lined to the time-scale on which they are produced. (Rosensweig 2002) The synthesis of nanoparticluate ferrites MFe_2O_4 (M = Co, Ni, Zn) has also been reported by Cabanas and Poliakoff. (Cabanas and Poliakoff 2001) Solutions of metal acetates (*e.g.* $Fe(Ac)_2$) were used to assess the formation of ferrite in near critical water. (Cabanas and Poliakoff 2001) Investigations into the mechanisms of magnetic ferrite formation in near-critical water, suggested the hydrolysis and simultaneous oxidation ($Fe^{2+} \rightarrow Fe^{3+}$) of mixtures of Fe(II) acetate leads to the formation of a spinel phase. However, disproportionation of Fe^{2+} also results in the formation of elemental Fe under some reaction conditions. (Cabanas & Poliakoff 2001) This suggests further analysis of the formation of magnetic iron oxides in such systems is required as it is often desirable to use a phase pure material. Similarly, as many of the physical properties of the magnetic particles produced using CHFS have not been evaluated, it is of interest to define these. The strong dependence of magnetic particle properties on structural characteristics such as mean size, polydispersity, particle shape, crystalinity, the presence of defects and cation vacancies is of interest in the terminal application of many of these materials. (Levy *et al.*, 2011) Hence, greater understanding of the formation and physiochemical properties of magnetic iron oxide synthesised using CHFS would be beneficial. (Cabanas & Poliakoff 2001)

In this chapter, the synthesis and characterisation of magnetic iron oxides produced by CHFS are explored. The evaluation of the materials is presented through complete characterisation of nanoparticles produced under different reaction conditions. An investigation into the mechanism of magnetic iron oxide phase formation is also presented.

5.2: Materials and methods:

5.2.1: Reagents

Iron(III) citrate ([$Fe(C_6H_5O_7)$] technical grade, >98 %), Citric acid ([$C_6H_8O_7$] 99 %) and $(NH_4)OH$ solution (28 vol%) were supplied by Sigma–Aldrich Chemical Company (Dorset, UK). Iron(III) citrate powder was dissolved in water by adding a stoichiometric amount of NH_4OH solution forming a soluble iron citrate complex (Ammonium ferric citrate [$NH_3Fe(C_6H_5O_7)$). Iron(III) nitrate hexahydrate ($Fe(NO_3)_3 \cdot 6H_2O$ [98%]) and hydrogen peroxide (H_2O_2 [28 % v/v]) were obtained from VWR international. All experiments were conducted using deionized water (>10 MΏ).

5.2.2: Synthesis of Magnetite using CHFS:

Samples of iron oxide were produced using the experimental details presented in table 5.1 and summarises 16 reactions. CHFS reactor 1, the same as that shown in Chapter 3 was used for the synthesis of all iron oxide samples within this chapter. The reaction point used in this work was a CJM type geometry as described in Chapter 4 (constructed from ¼” components and a 1/16” inlet in the optimal position defined in Chapter 4). The three pump configuration was used for all reactions with the precursor solution being pumped equally (*i.e.* Q_p / 2) by P2 and P3 to a desired flow rate. In this chapter a variety of reagents were used to evaluate mechanisms to control the phase of iron oxide produced using CHFS. After collection from the exit of the BPR, the slurry obtained from the process was allowed to flocculate, the supernatant was removed and the particles were decanted into centrifuge tubes, the particles were further concentrated by centrifuged at 4500 rpm for 3 min. Then the clear supernatant was removed and replaced. The samples were redispersed and re-centrifuged at 4500 rpm for 3 min prior to freeze drying for 24 hours at 1 $x10_{-4}$ mbar. The structure and morphology of the products of continuous hydrothermal synthesis were investigated using XRD, TEM, HRTEM, XPS, TGA and squid magnetometry the experimental details of which are presented in Chapter 2.

Table 5.1: Summary of the reaction conditions used for the synthesis of iron oxides using CHFS reactor 1, alongside characterisation data obtained for each sample. Residence time (RT) was calculated assuming T_{mix1} (theoretical mixture temperature) was obtained at the terminus of the preheated water inlet (see figure 4.1). The flowrate of supercritical water (Q_{sw}) was met by a flow of precursors Q_p being pumped equally by P2 and P3 (*i.e.* Q_p/2). All metal salt concentrations were 0.066 M. Auxiliary reagents are identified alongside the concentration used by £ =H_2O_2 and \$ =Citric acid.

ID	**Precursor**	**Auxillary**	**[Q_{sw}:Q_P](mL min^{-1})**	**HT (°C)**	**T_{mix} (°C)**	**RT (s)**	**XRD**	**Size XRD (nm)**	**TEM (nm)**	**SD**
M1	$Fe(NO_3)_3$	-	20:20	350	199	4.19	α-Fe_2O_3	14.0	13.26	2.91
M2	$Fe(NO_3)_3$	-	20:20	400	305	3.48	α-Fe_2O_3	13.3	10.18	3.06
M3	$Fe(NO_3)_3$	-	20:20	450	335	3.16	α-Fe_2O_3	15.0	12.16	3.32
M4	$Fe(NO_3)_3$	(0.022M)$^{\$}$	20:20	450	335	3.16	α-Fe_2O_3	12.1	-	-
M5	$Fe(NO_3)_3$	(0.044 M)$^{\$}$	20:20	450	335	3.16	α-Fe_2O_3	14.5	-	-
M6	$Fe(NO_3)_3$	(O.066M)$^{\$}$	20:20	450	335	3.16	Fe_3O_4	14.8	-	-
M7	Fe (cit)	-	20:20	350	199	4.19	-	-	-	-
M8	Fe (cit)	-	20:20	400	305	3.48	Fe_3O_4	4.6	11.96	3.17
M9	Fe (cit)	-	20:20	450	335	3.16	Fe_3O_4	8.1	12.02	3.08
M10	Fe (cit)	-	25:10	450	382	1.69	Fe_3O_4	11.4	12.10	2.99
M11	Fe (cit)	(0.022M)$^{£}$	25:10	450	382	1.69	Fe_3O_4	13.7	-	-
M12	Fe (cit)	(0.044M)$^{£}$	25:10	450	382	1.69	Fe_3O_4	12.2	-	-
M13	Fe (cit)	(0.066M)$^{£}$	25:10	450	382	1.69	α-Fe_2O_3	14.3	-	-
M14	Fe (cit)	0.022M$^{\$}$	25:10	450	382	1.69	Fe_3O_4	13.2	-	-
M15	Fe (cit)	0.044 M$^{\$}$	25:10	450	382	1.69	Fe_3O_4	13.9	-	-
M16	Fe (cit)	O.066M$^{\$}$	25:10	450	382	1.69	-	-	-	-

5.3 Results and Discussion:

5.3.1 Synthesis of Magnetite Nanoparticles using CHFS:

In this section, the effect of different combinations of metal ion and auxiliary precursors was evaluated as a function of reaction point temperature to assess the phase behavior of iron oxides produced using CHFS. It is clear from table 5.1 that precursor choice and reaction point temperature greatly influenced the phase of iron oxide produced in each reaction.

As shown in figure 5.1.a the hydrothermal reaction of iron(III) nitrate solutions resulted exclusively in the formation of hematite (α-Fe_2O_3) as the reaction product when compared to the ICDD pattern for hematite (ICDD:43465). Hematite was obtained at reaction point temperatures of 199, 305 and 335 °C which suggested that hematite was the thermodynamically favoured phase under these synthesis conditions. The mechanism of hematite formation is likely to be the direct hydrolysis of Fe^{3+} to $Fe(OH)_3$ followed rapidly by dehydration to form α-Fe_2O_3. (Adschiri, Kanazawa, & Arai 1992) Application of the Scherrer equation to the (104) reflection of hematite yielded crystallite size estimates of *ca.* 14, 13.3 and 15 nm, for the samples produced at 199, 305 and 335 °C. Similarly, direct observation of the products using TEM revealed that the morphology and particle size distributions were similar in each reaction (figure 5.2). Mean crystallite sizes (s.d) of 13.26 nm (2.91) (sample M1), 10.18 nm (3.06) (sample M2) and 12.16nm (3.67) (sample M3) were determined from the measurement of 300 particles and are consistent with the crystallite sizes estimated from the diffraction data (Table 4.1). The similarity in both crystallite size and reaction yield suggested that complete precipitation and crystallisation of the product had occurred within the reactor (table 4.1). The similarity of particle size distributions suggested that the extent of solution saturation (thus the extent of particle nucleation and growth) is similar over the given temperature range and the reaction point temperatures are consistent with those used in batch hydrothermal process for the production of crystalline hematite. (Sorescu *et al.*, 2004) These observations are also consistent with the work of Sue *et al.* whom suggested the low solubility of Fe ions in near-critical water leads to similar solution saturation, and thus similarity in particle nucleation (dominant) and growth process when synthesis is performed above a critical temperature. (Sue *et al.*, 2006) These observations are also consistent with the study of

ZnO nanoparticle formation presented in chapter 3 where comparatively large changes in the temperature profile within a reactor yielded materials with similar particle characteristics.

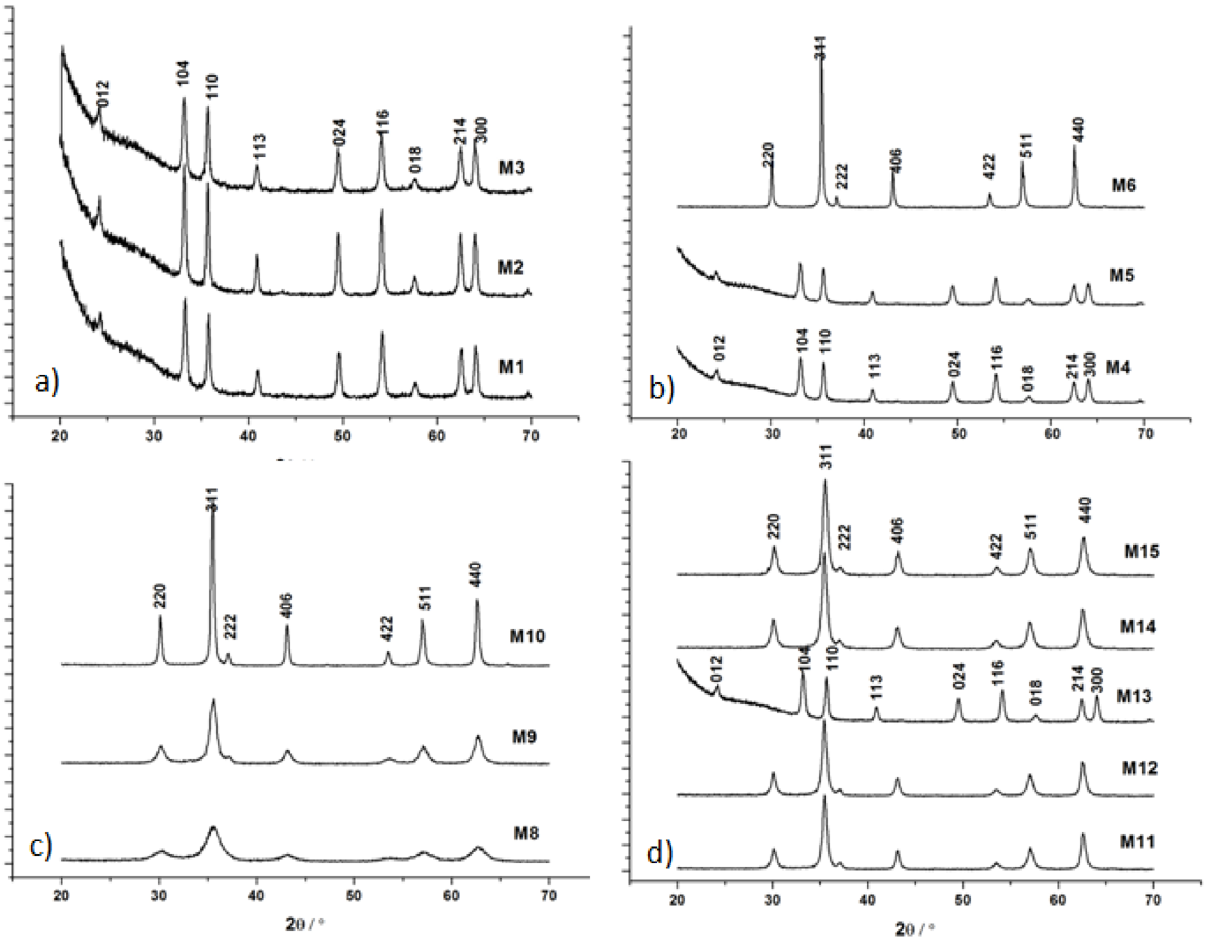

Figure 5.1: XRD patterns of iron oxide synthesised according to the conditions presented in Table 5.1 (Miller indicies of both hematite and magnetite are identified in each figure).

If iron citrate is used as the precursor, a spinel like phase was observed exclusively as the reaction product (reactions M7-10), that were similar to ICDD patterns 082234 and 79196 for magnetite and maghemite, respectively (figure 4.3.1c). Although a definitive phase identification was difficult due to the structural similarity of magnetite and maghemite, the products were all identified as a magnetic spinel phase. (Muerbe *et al.*, 2008; Muller *et al.*, 2006) Reaction point temperatures of 305, 335 and 380 °C lead to formation of the spinel phase (reactions M8-10). In contrast, reaction point temperatures of < 199 °C produced a brown-orange solutions indicative of iron ammonium citrate with no recoverable solid, suggesting the reaction point temperature was insufficient to decompose the complex and hydrolyse the iron. It is interesting to note that at a reaction point temperature of 199 °C a temperature sufficient to produce crystalline hematite (through direct hydrolysis and dehydration) no product was recovered when iron (III) citrate was used as a precursor suggesting differences in the hydrolysis and dehydration reactions when different precursors are used. This observation is consistent with the fact that citrates are known to have higher decomposition temperatures in hydrothermal solutions than nitrates. (Pannaparayil *et al.*, 1988) As shown in figure 5.1c, a sequential increase in the reaction point temperature resulted in sharper powder x-ray diffraction peaks indicating an increase in sample crystalinity. Figure 5.2 iv-vi shows TEM images representative of the nanoparticles produced in reactions M8-M10. The particle size distributions obtained from the measurement of *ca.* 300 particles showed significant similarity with crystallites of *ca.* 12 nm obtained in each synthesis as summarised in table 5.1. The decrease FWHM as a function of reaction point temperature appears to be dominated by an increase in sample crystalinity rather than crystallite size (table 5.1). HRTEM images of products of reactions M9 and M10 are presented in figure 5.3. In both samples lattice fringes corresponding to the 311 plane with measured d-spacings of *ca.* 2.54 Å are clearly visualized throughout the body of each particle suggesting the formation of a crystalline material at both reaction point temperatures. SEAD (figure 5.3 insets) are consistent with observeations made using XRD, where it can be seen that the breadth of the Scherrer rings decreased with increasing temperature suggesting an increase in sample crystallinity (order) at higher temperatures. The smaller crystallite size reported herein when compared to the work of Adischiri *et.al.* is attributed to the rapid mixing characteristic for the Confined Jet Mixer as discussed earlier in Chapter 4. (Sasaki *et al.*, 2010) Where, rapid mixing at the reaction point confers a fast transition from soluble precursors to insoluble oxides (leading to particle synthesis) this is dominated by particle nucleation with particle crystalinity being governed by temperature. (Adschiri, Kanazawa, & Arai 1992; Lester *et al.*, 2006)

The observation of different phases of iron oxides as reaction products is likely to be due to *in situ* reduction and oxidation reactions altered by the counter ion in the chosen metal salt. The decomposition of nitrates in supercritical water been shown to form some oxidizing species including hydroxyl radicals, O_2 and NO_x, which as in previous publications were shown to be suitable to oxidise divalent transition metals. (Boldrin *et al.*, 2007) Similarly, a study of the thermal decomposition of citric acid in hydrothermal conditions showed that the decomposition series formed certain reducing species which would be miscible with both near and supercritical water allowing the reduction of Fe^{3+} to a mixture of Fe^{2+} and Fe^{3+} dependent upon the extent of speciation in the decomposition products. (Shock 1995; Shock and Helgeson 1990)

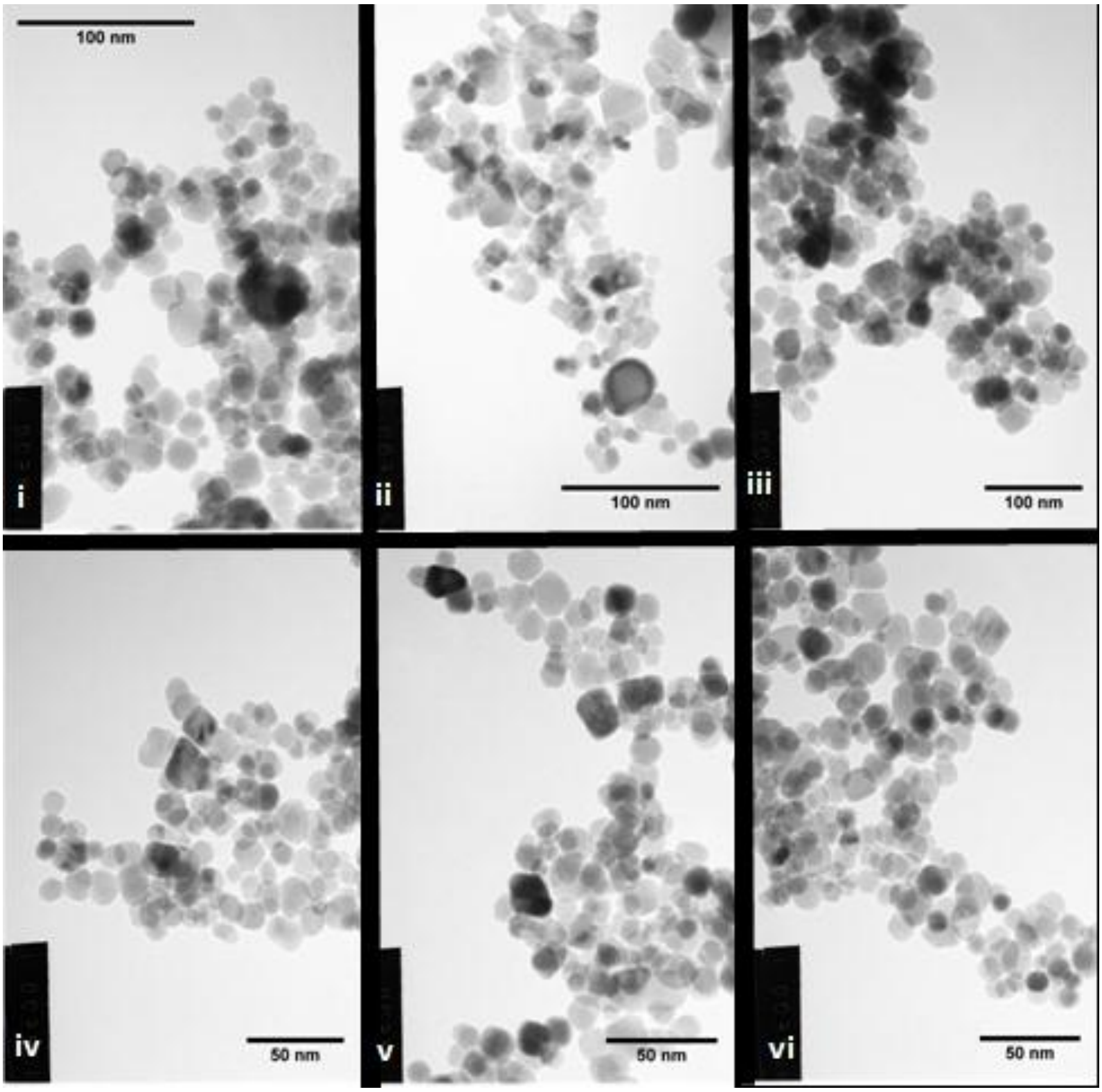

Figure 5.2: a) TEM images of Hematite (α-Fe_2O_3) synthesized as a function of reaction point temperature using **i)** M1 **ii)** M2 **iii)** M3 (scale bars 100nm) and TEM images of magnetite (Fe_3O_4) synthesised as a function of reaction point temperature **iv)** M8 **v)** M9 **vi)** M10 CHFS (images were captured using a JEOL 100CX).

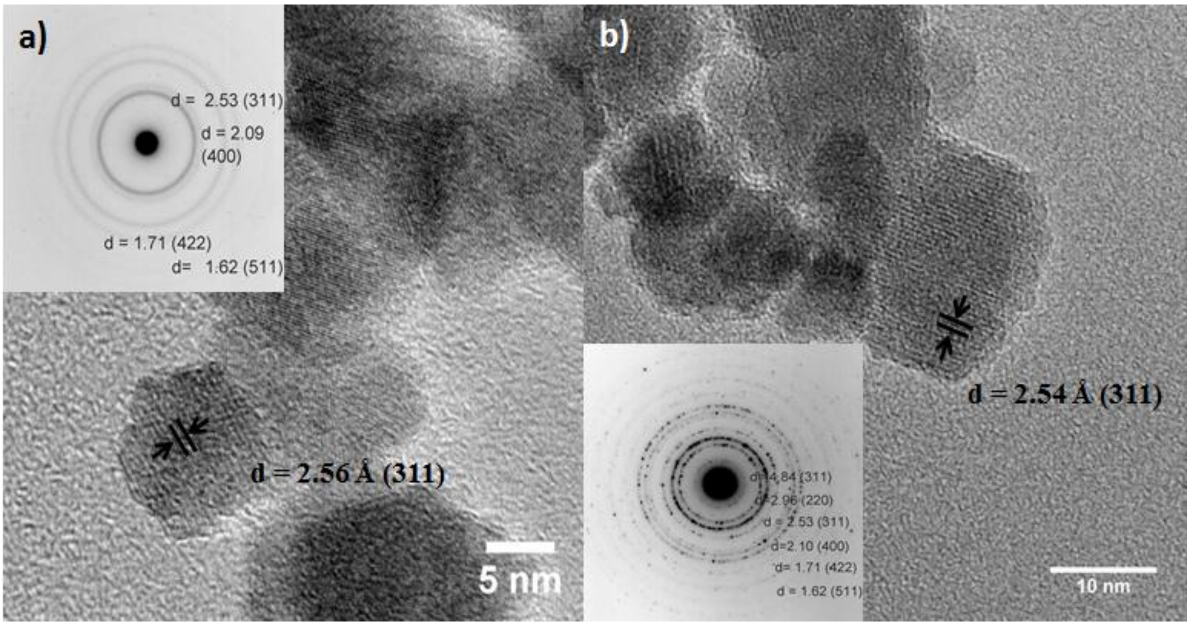

Figure 5.3: a) HRTEM image of iron oxide synthesised at 380°C using CHFS. Inset shows lattice fringes observed corresponding to (311) plane with a measured spacing of 2.56 Å (magnetite = 2.53 Å. Inset lower right shows an enhanced view of the lattice fringes corresponding to the 311 plane, **b)** indexed SEAD pattern obtained for the sample (images were captured using a JEOL 4000X).

To further understand the phase behaviour of iron oxides in CHFS systems mixtures of iron(III) nitrate solutions with different ratios of citric acid (Reactions M4 - 6), solutions of iron(III) citrate with different ratios of H_2O_2 (acting as an oxidant, reactions M14 - 16) and solutions of iron(III) citrate with different ratios of citric acid (reactions M11 - 13), were used to assess the relative effect of reducing or oxidising species concentration on the phase of phase behaviour of iron oxides in CHFS. As shown in figure 5.1, at a constant reaction point temperature (*ca.* 380 °C) either hematite or magnetite were obtained as the exclusive phases in each of the reaction sets. The crystallite sizes estimated for reactions M4 - 6, M14 - 16 and M11 - 13 from the (104) and (311) reflections of hematite and magnetite taken from the powder diffraction data are summarised in table 5.1. The data suggest similarly sized nanoparticles have been produced in each reaction (consistent with the results presented for samples M8 - M10 and M1 - M3). This is likely to be due to the low solubility of iron ions in near and supercritical water, limiting the potential for particle growth in the hydrothermal solution as discussed previously in Chapter 3 and 4.

Iron(III) nitrate: [CA] ratios of 0.5 and 0.33 produced hematite as the reaction product (runs M4 - 5). In contrast, a ratio of 1 (run M6) produced magnetite as the reaction product as shown in figure 5.1, suggesting that the concentration of reducing species formed *in situ* in the former reactions was insufficient to partially reduce a sufficient portion of Fe^{3+} to Fe^{2+} leading to the formation of hematite. However, a $[Fe(NO_3)_3]$: [CA] ratio of 1 produced magnetite as the reaction product consistent with the data presented for syntheses M7 - 10 suggesting sufficient reduction to allow the formation of the spinel phase. *In situ* reduction reactions governing the formation of magnetic phases of iron have been reported previously using hydrothermal methods. (Adschiri, Kanazawa, & Arai 1992) As presented for samples M4-6 the addition of citric acid aids the partial reduction of Fe^{3+} within the process which is an observation similar to the report of Takami *et al*. which showed that the addition of organic acids [n-decanoic acid ($C_9H_{19}COOH$) and n-decylamine ($C_{10}H_{21}NH_2$)] prevented complete oxidation of Fe^{2+} and the formation of a spinel phase. (Sasaki *et al.,* 2010)

Reactions (M11-13) investigated the effect of increasing the concentration of reducing species within the reactor. In sample M13, dissolution of the reaction product was observed at the exit of the slurry from the CHFS process. In contrast, samples M11 and 12 produced magnetite as the sole reaction product similar to ICDD 082234 (figure 5.1 d). As discussed earlier, redox reactions of Fe^{2+} and Fe^{3+} species are thermodynamically possible in water *via* hydrolysis and dehydration reactions to form the corresponding oxide. (Cabanas & Poliakoff 2001) It is interesting to note than no-disproportionation or the formation of other phases of iron oxide was observed even at relatively high citric acid concentrations (syntheses M14-16). Cabanas and Poliakoff reported the disproportionation of iron occurred when Fe^{2+} sources such as iron acetate were used as precursors for the formation of various ferrite phases although these were observed at significantly lower temperatures than those reported here *ca.* 210 °C as determined by enthalpy balance. (Cabanas & Poliakoff 2001) Scheme 5.1 shows the proposed mechanism of magnetic iron oxide formation in CHFS where the presence of decomposing counter ions (forming either oxidants or reducing agents) at the process temperatures are indicated. Reactions M1-3 appeared to follow steps ***i*** and ***iv*** following a typical hydrolysis and dehydration reaction forming hematite as the sole reaction product. Reactions M7-10 appeared to follow steps ***ii*** and ***iii*** where partial decomposition of citrate leads to the formation of reducing species *in-situ* and hydrolysis of Fe^{2+} (step ***iv***) with both $Fe(OH)_2$ and $Fe(OH)_3$ species dehydrating (steps ***viii*** and ***ix***) and crystallising into a spinel structure (steps ***x*** and ***xi***). It should be noted that magnetite can form a cation deficient structure which can accommodate complete Fe^{2+} atomic vacancy under conservation of the spinel structure, as no reliable method of quantifying bulk stoichiometry was available this mechanism is proposed in light of this possibility. (Dieckmann 1982; Dieckmann and Schmalzried 1977). Reactions M14-16 appeared to follow the reaction steps described for iron citrate alone, where increasing the relative concentration of citrate species did not show evidence of disproportionation in the reaction product (step ***vii***) as suggested by Cabanas *et. al.* to be expected if the relative proportion of Fe^{2+} was greatly increased within the synthesis. Addition of oxidants investigated in reactions M11-13 suggested the increased concentration of oxidising species influenced the reaction product as the formation of hematite was observed the sole reaction product (following reaction steps ***i*** and ***vi***, respectively) through the likely oxidation of any Fe^{2+} formed within the process (step ***v***). Low to moderate concentrations of oxidising species showed a spinel phase as the reaction product suggesting insufficient oxidation of Fe^{2+} species formed through the decomposition of citrate allowing the reaction to proceed following the same steps as the reactions presented for iron citrate alone (reactions M7 - 10).

The formation of spinel oxides in CHFS suggests a successive reaction mechanism is responsible for the formation of spinel oxides under the reaction conditions presented. The phase of iron oxide produced is dictated by the iron ion oxidation states at the point of particle nucleation as mixtures of different phases were not observed as reaction products even in reaction series which transitioned from one phase to another. The phase behaviour suggests that oxidation state of Fe^{n+} species in solution determine the structure of the reaction product through influencing the crystallite phase nucleating from solution, similar to the phase behaviour of spinel compounds produced in other rapid gas phase methods. (Kruis *et al.,* 1998) In CHFS the formation of magnetite appears metastable and dependent on the presence of organic species (choice of counter ion) within the reaction. Successive reactions are typically observed in rapid synthesis methodologies similar to metastable phases of compounds with respect to temperature. Ostwald's step-rule describes successive reactions and appears a valid explanation for the data generated. In this case, at the reaction point temperatures used *ca.* 380 °C hematite is the thermodynamically favoured phase as its structure shows the lowest free energy and is obtained exclusively if a Fe^{3+} precursor is used. Under these conditions, magnetite is the least stable state. However, in the presence of both Fe^{2+} and Fe^{3+} species magnetite lies closest to the original state of free energy and as such is a metastable product only forming in the presence of a suitable concentration of Fe^{2+} species in the hydrothermal solution. (Feenstra and Debruyn 1981; Vansanten 1984) This chapter now moves forward to describe the effects of processing conditions on the magnetic properties and magnetic structure of iron oxides produced using CHFS.

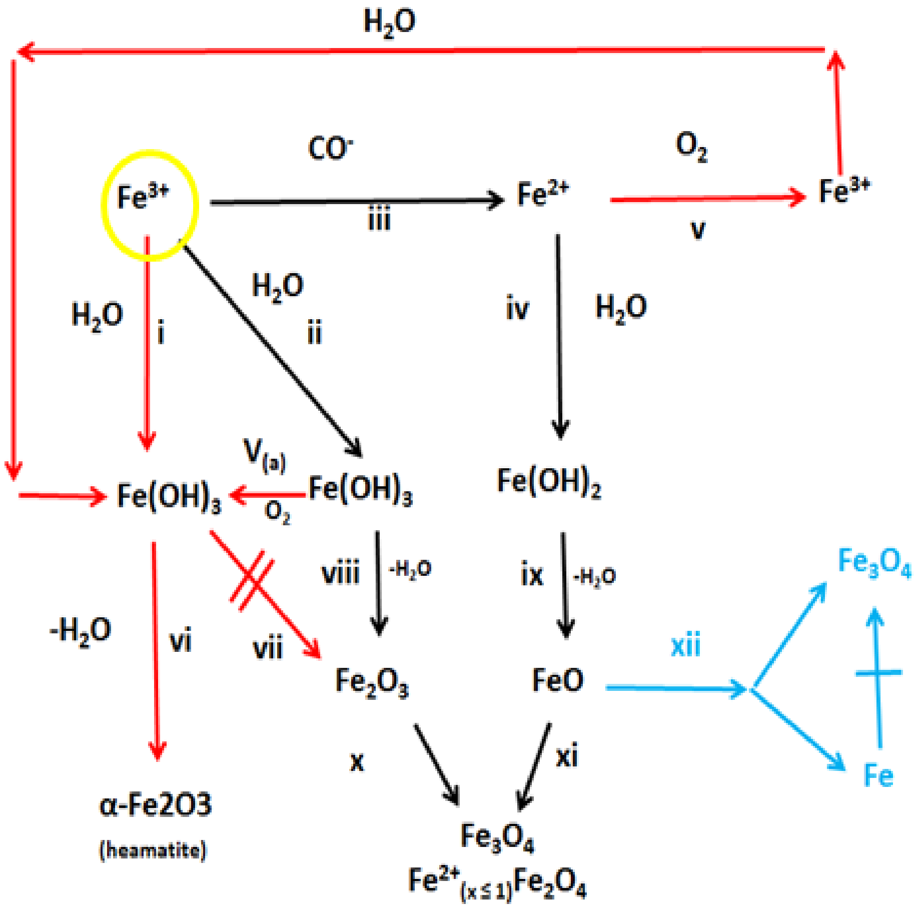

Scheme 5.1: Schematic representation of the proposed mechanism of iron oxide formation in CHFS starting from an Fe^{3+} precursor source. The steps highlighted in red correspond to syntheses in which Hematite was obtained as the exclusive reaction product. The steps highlighted in black relate to syntheses in which a magnetic iron oxide phase was obtained as the reaction product. The yellow circle identifies the starting point (*i.e.* the Fe precursor ion)

5.3.2 Magnetic Properties of Iron Oxides Produced Using CHFS

Figure 5.4 a shows M(H) curves measured for the particles produced in reactions M8-10, 15, 11-12 showing super-paramagnetic like behaviour with low coercivity at room temperature (data summarised in table 5.2). Magnetic measurements taken of samples M8-10 showed an increase of saturation magnetisation with increase of reaction point temperature ranging from 48.6 to 60.1 emu g^{-1} for samples M8- M10. The increase in saturation magnetisation is not surprising as the crystalinity of the respective samples was shown to increase with increasing reaction temperature (figure 5.1a). The highest value of saturation magnetisation was lower than the value expected for bulk magnetite (92 emu $^{-1}$g) or maghemite (77emu g^{-1}) which is commonly observed in nanosized magnetic materials. (Chatterjee *et al.*, 2003) Similar observations were made in the magnetic properties of the products produced with an excess of citric acid (likely to alter the ratio of Fe^{3+} reduced to Fe^{2+} within the product) and the addition of H_2O_2 to serve as an oxidant in runs M15, M11 and M12, respectively (figure 5.4). Increasing the relative amount of CA in the synthesis (run M6) was shown to have little effect on the magnetisation of the material yielding a saturation magnetisation of 63.1 emu g^{-1}. The addition of H_2O_2 was also shown to have little effect on the saturation magnetisation until the concentration approached *ca.* 0.044 M, whereafter a large reduction in the saturation magnetisation was observed *ca.* 31.8 emu g^{-1} (samples M11 and 12).

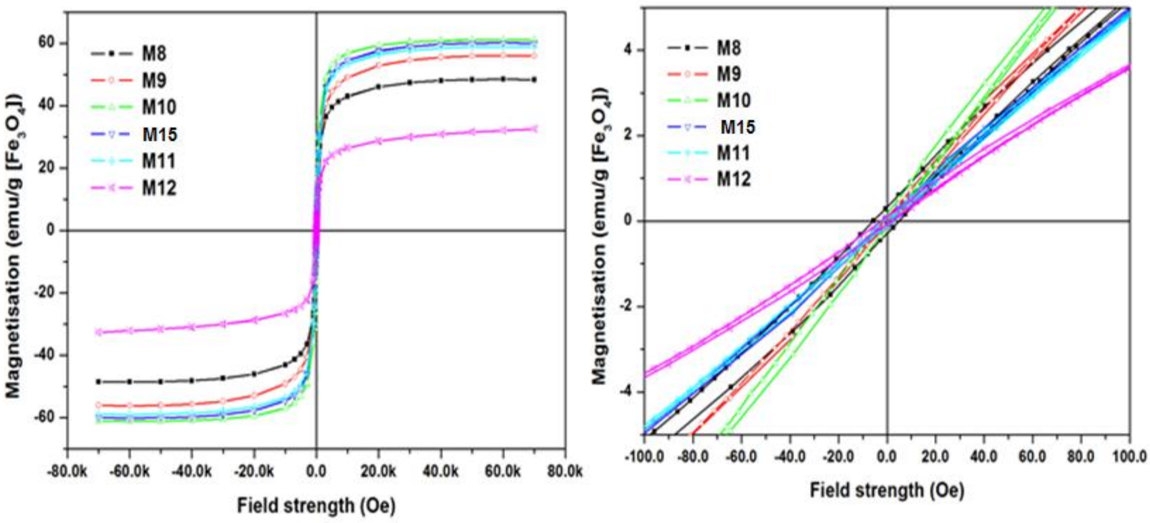

Figure 5.4: a) MH curves of citric acid coated magnetite produced using the pilot scale CHFS process **b)** expanded plot showing the near 0 Oe

The observed reduction in the value of saturation magnetisation in nanosized iron oxides can be attributed to may physiochemical and structural characteristics. In small nanoparticles *ca.* 10-15 nm reductions in saturation magnetisation are usually attributed to the surface contribution of unpaired 3d electrons of near surface atoms, although it can also be attributed to reduction in local symmetry surrounding Fe ions in the inverse spinel structure through the presence of both oxygen and Fe ion vacancies within the lattice. (Chatterjee, Haik, & Chen 2003; Sugiyama *et al.*, 1997) Equally the contributions of spin canting, surface disorder, and adsorbed species would lead to a similar measured effect on saturation magnetisation through aberration of surface spins which is particularly evident in nanomaterials which are < 15 nm in diameter. (Leslie-Pelecky and Rieke 1996) In this cases definitive phase identification from the x-ray diffraction data was complicated by the similarity in structure of both magnetite and maghemite. As, Magnetite (Fe_3O_4) and maghemite (γ-Fe_2O_3) can both crystallise in the spinel structure with ferrous and ferric ions in the octahedral sites of the spinel lattice, adopting the space group Fd3m. (Sugiyama *et al.*, 1997) Maghemite (γ-Fe_2O_3) in this context is defined as a defect spinel represented by the formula $Fe^{2+}{}_{1/3}Fe^{3+}{}_{5/3}O_4$, and cation vacancies within this structure may be randomly distributed under conservation of the spinel structure. (Zboril *et al.*, 2003) The measurements suggest loss of symmetry around Fe due to low crystalinity in the structure coupled to the presence of atom vacancies are responsible for the reduced saturation magnetisation. This is unsurprising in light of the phase behaviour observed in the reactions presented in this chapter.

Calculation of the effective ferromagnetic diameters (σ_{fm}) of the samples by fitting the magnetisation data with a Langenvin function (detailed in chapter 2) are summarised in table 5.2. In the case of sample M8-10, μ_{fm} as a percentage of the crystal volume determined by TEM was shown to increase as a function of reaction point temperature (from *ca.* 5 - 18%). This observation can be attributed to the presence of a magnetically frustrated phase within each sample and accounting for a large proportion of the nanoparticle volume as the contribution of paramagnetic-like susceptibility (χ) [accounting for the non-saturating behaviour] increased with decreasing saturation magnetisation, suggesting the discussion of a non-ferromagnetic phase (linked to loss of symmetry around Fe due to low crystalinity) as the most valid interpretation of the data. (Levy *et al.*, 2011) Sample M12 showed the largest contribution of paramagnetic like susceptibility and is consistent with the discussion presented for the formation of a defective spinel structure produced under these synthesis conditions (as the next sample in the series M13 produced hematite). The nature of the synthesis method suggests that this observation would stem primarily from the presence of partially coordinated iron atoms within the sample consistent with the discussion presented earlier within this chapter. For comparison, the ferromagnetic diameter of sample M15 was similar to that calculated for sample M10, which also showed a similar paramagnetic susceptibility on the approach to saturation suggesting that the contribution of near surface atoms in these samples is quite large and attributable to their small size. (Chen *et al.*, 2009)

Table 5.2: Summary of the magnetic properties of magnetic iron oxides produced using CHFS. Where, H_c is the coercivity of the sample at H = 0, μ is the mean ferromagnetic diameter (nm), σ is the ferromagnetic diameter polydispersity (nm) and χ is a dimensionless value representing the paramagnetic like region on approach to saturation as observed in figure 5.4. These values were derived from fitting performed by an algorithm written by Dr Paul Southern. (Chen et al. 2009)

Sample	**TEM (nm)**	**Ms (emu g^{-1})**	**H_c (Oe)**	**μ (nm)**	**σ (nm)**	**χ x10^{-5}**
M8	12.5	48.6	1.05	7.53	0.31	3.45
M9	16.7	56.5	0.90	7.70	0.26	3.26
M10	11.1	60.1	2.23	6.03	0.34	2.09
M15	13.5	63.1	1.89	7.03	0.35	2.37
M11	13.5	60.0	2.31	7.23	0.28	2.46
M12	15.9	31.8	1.89	3.94	0.29	3.67

Key: Ms = saturation magnetisation , H_c = sample coercivity at 0 Oe, μ = ferromagnetic diameter, σ = ferromagnetic diameter polydispersity and χ = paramagnetic contribution to saturation magnetisation.

The temperature dependence of M_s was measured at 5 and 300 K for sample M10 as shown in Figure 5.5a and FC/ZFC measurements are presented in figure 5.5b to further assess the magnetic properties of the material. The increase in M_s below 5 k can be attributed to the presence of magnetic phases which undergo a magnetic transition to a frozen state below T_b (blocking temperature). The fact that we still observe a nonsaturated magnetization (paramagnetic like region on approach to saturation) at 5 K indicates that a component of this sample is intrinsically non-ferromagnetic. Similarly the increase in coercive field at 5 K measured as 62 Oe whereas at 300 K a value of 2.23 Oe reported is consistent with the sample behaving as a ferromagnet below T_b. ZFC/FC measurements performed on the sample are shown in figure 5.5.b. The positive magnetisation values observed in the ZFC and FC is the fingerprint of exchange bias, a phenomenon that takes place at interfaces between different magnetic phases. (Iglesias *et al.,* 2008; Levy *et al.,* 2011; Nogues *et al.,* 2005; Nogues and Schuller 1999) It is important to note that exchange bias requires the presence of magnetic interfaces with intimate contact (*i.e.* within a single lattice) and typically does not occur through dipolar interactions between particles typically observed as broadening in the cusp of the ferromagnetic to superparamagnetic transition. (Iglesias, Labarta, & Batlle 2008) The presented measurements suggest that the crystallites produced in reaction M10 are magnetically complex structures consisting of a ferromagnetic phase with a portion of the sample behaving non-ferromagnetically the latter not saturating at even low temperature. These results suggest the paramagnetic component noted in the magnetic fitting procedure arises through the distribution of magnetic behaviour throughout the particle (*e.g* ferromagnetic-antiferromagnetic but also ferromagnetic-ferrimagnetic, ferrimagnetic-antiferromagnetic, etc.). Similarly, the absence of a distinct transition (diffuse) associated with T_v (Verway transition temperature typically observed at 120-150 K) and T_b is consistent to a wide distribution of energy barriers from different magnetic structure within the sample transitioning to a blocked state at different temperatures. (Nogues *et al.,* 2005) The likely explanation of which is that the co-ordination of surface atoms plays a large role in the magnetic behaviour of this material. Where, there are numerous reports of disorder not necessarily related to structural differences but to fine magnetic structure within a material, such as spin disorder, anti-phase boundaries, spin canting or spin glass transitions. (Koksharov *et al.,* 2000)

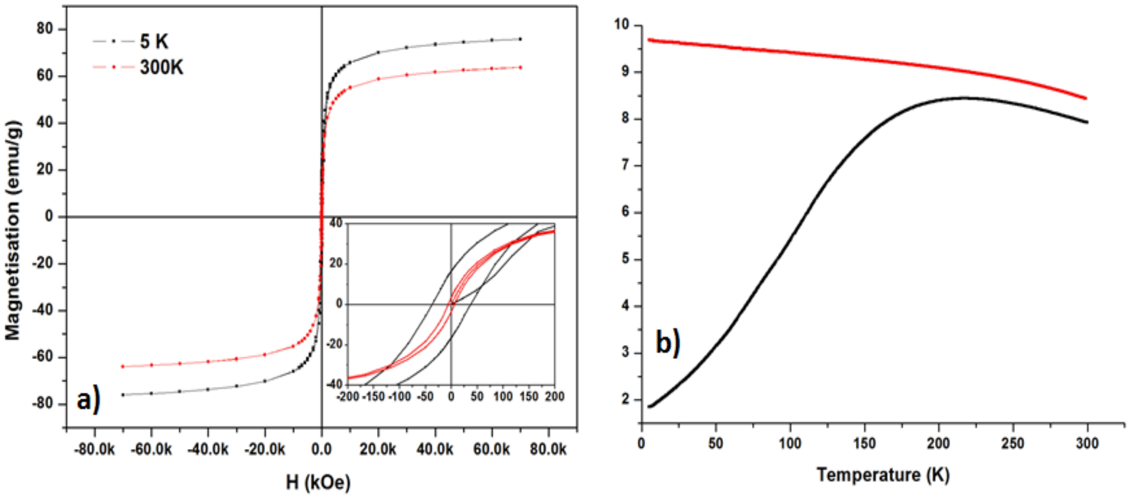

Figure 5.5: Comparison of magnetisation magnetization curves measured at 5 K and 300 K, inset shows a the near 0 Oe region magnified to show the difference in coercivity **b)** FC (red) and ZFC (black) curves under an applied field of 100 Oe.

To explain further some of the observations made using magnetic property measurements and to confirm the discussion presented for magnetite formation in CHFS, the surface oxidation state of Fe in selected samples was evaluated using XPS. Measurements were performed at a take-off angle of 45° which typically generates photoelectrons from the sample to a depth of *ca.* 3.5 nm. In light of the comparatively small particle size *ca.* 12 nm under this assumption, these measurements would represent a substantial portion of the particle volume (*ca.* 80 %). Figure 5.6 shows the Fe2p and Fe3p regions of the XPS spectra. A summary of the composition (Fe : O) stoichiometry and relative Fe^{2+}: Fe^{3+} ratios measured are presented in table 5.3. It should be noted that the Fe:O stoichiometry within the sample is likely to be influence by the presence of residual organic species (*e.g.* citrates) from synthesis and is likely not a true reflection of the materials stoichiometry. Deconvolution of the Fe3p peak with the binding energies of Fe^{2+} (53.7 eV) and Fe^{3+} (54.6 eV) reported by Grosvenor *et al.* suggested that in all cases a component of the samples surface was in a Fe^{2+} oxidation state with the bulk being Fe^{3+}. (Fujii *et al.*, 1999; Grosvenor *et al.*, 2004; McCafferty and Wightman 1998; Yamashita and Hayes 2008) The ratio of Fe^{2+} / Fe^{3+} was shown to vary with synthesis conditions in a manner consistent with the discussion presented earlier within the text. The XPS spectra of samples M8 - 10 gave Fe^{2+}: Fe^{3+} ratio slightly lower than expected for stoichiometric magnetite the ratio of Fe^{2+} was shown to increase with reaction temperature, as the thermal decomposition of citrate was likely to increase with temperature (yielding a greater proportion of Fe^{2+}). Evaluation of the Fe2p photoelectron region showed the satellite peak often observed as a broad feature in the Fe2p$_{3/2}$ photoelectron region was absent, this is indicative of a non-stoichiometric spinel phase again consistent with the discussion presented earlier. (Kuznetsov *et al.*, 2012) Deconvolution of the O1s peak into three principle components was achieved with peaks centered at 532.2, 531.2 and 531.6 eV which could be attributed to the presence of free water, lattice oxygen and the presence of surface OH groups respectively (data not shown).(Yamashita & Hayes 2008) A contribution of the peak shape is expected to have originated from surface C-O, C-OH, etc. which are difficult to evaluate as moderate shifts in the binding energy are to be expected complicating the fitting procedure. Broadly, the XPS results served to confirm that a nonstoichiometric spinel phase was produced in all reactions which formed this phase. The data also supports that based on averages (table 5.3), the discussion of magnetically complexity and thus the observed magnetic behavior stems from both fine magnetic structure distributions within the sample as the bulk stoichiometry was approximately correct for each sample.

Table 5.3: XPS peak positions of magnetic iron oxides produced using CHFS. The table also shows the ratios of Fe^{2+}and Fe^{3+} for the samples de-convoluted GL ratio = 30 (Gaussian : Lorentzian = 70:30) from the Fe3p peak using the peak positions determined by Yamashita *et al.* for Fe^{2+} and Fe^{3+} of 54.6 eV and 53.7 eV respectively. (Yamashita & Hayes 2008)

Sample identifier	**Peak position (eV)**				**Fe:O**	**Fe (at%) (Fe3p)**	
	Fe 3p	**Fe 2p**					
		Fe 2p$_{3/2}$	**Satellite**	**Fe 2p$_{1/2}$**		**Fe^{2+}**	**Fe^{3+}**
M8	53.21	708.2	716.2	721.6	0.60	20	80
M9	53.30	708.5	716.2	721.5	0.72	21	79
M10	53.23	708.3	716.3	721.6	0.71	29	71
M15	53.29	708.4	716.2	721.5	0.73	22	78
M11	53.18	708.3	715.9	721.6	0.70	24	76
M12	53.22	708.3	-	721.6	0.65	8	92

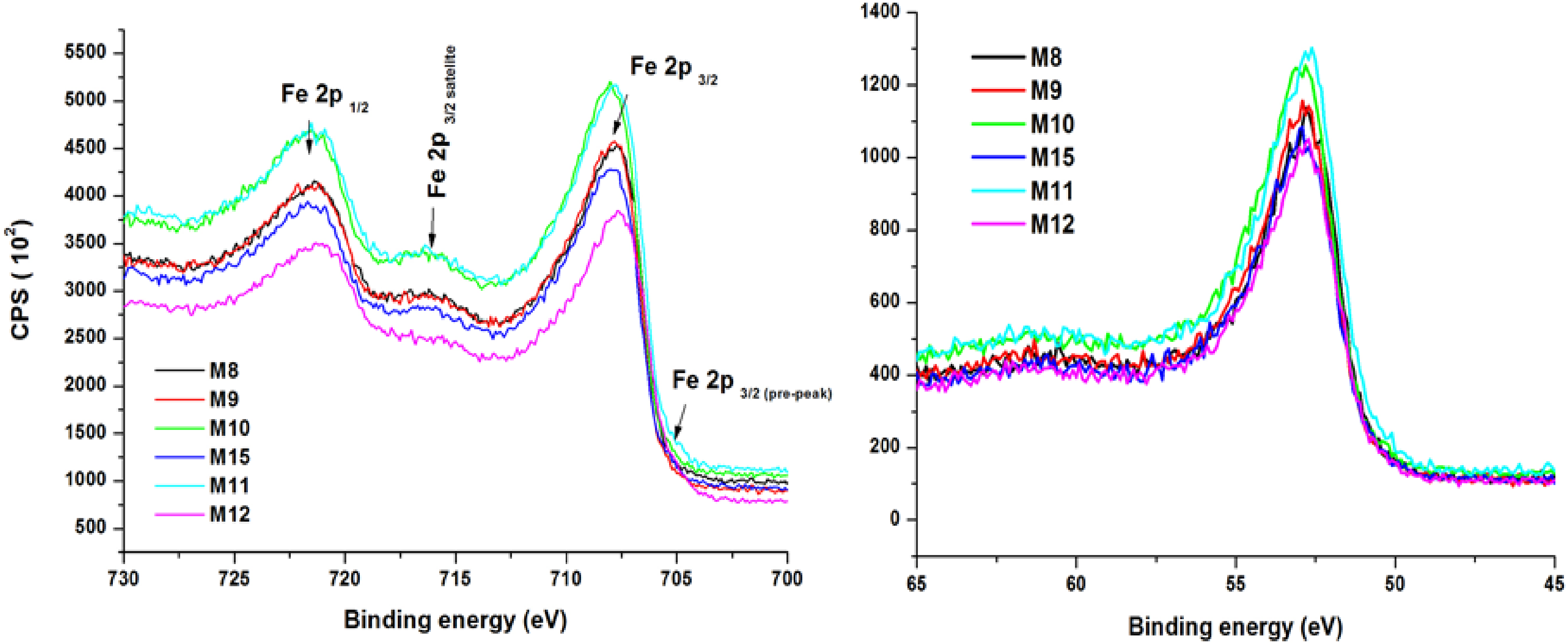

Figure 5.6: XPS spectra of magnetic iron oxides produced using CHFS showing high resolution data of the Fe2p (left) and Fe3P (right) regions

5.4 Conclusions:

CHFS was shown to be a rapid method for the synthesis of a variety of iron oxides as crystalline nanomaterials from aqueous iron precursors in a single step. The precursor choice was found to control the phase of iron obtained from the process. Iron sources which were in a Fe^{3+} oxidation state led to the formation of hematite exclusively as the reaction product (in the absence of any organic species). Fe^{3+} precursors in the presence of organic species resulted in the synthesis of a magnetic spinel phases. Phase mixtures were not observed in any of the reactions suggesting *in-situ* reactions governed the formation of different iron oxide phases at the point of particle nucleation. The yield of iron oxide (*ca.* 80%) was largely independent of temperature with similarly sized particles produced as a function of reaction point temperature if the reaction temperature was sufficient to hydrolyse the precursor. The particle size obtained from the CHFS process used herein was shown to produce significantly smaller particles than those obtained previously using CHFS which was attributed to the rapid mixing between the component streams in the confined jet mixer reactor leading to rapid precipitation of the iron ions through various hydrolysis and dehydration reactions. The magnetic phases produced using CHFS showed superparamagnetic behavior at 300 K with moderately high saturation magnetization when compared to many syntheses reported in the literature. The magnetic properties of the materials synthesised in this chapter were attributed to complexity in the fine magnetic structure of the product which was further corroborated by XPS. This observation may form an intrinsic limit to the seminal application of these materials (discussed further in chapter 6). The addition of oxidizing (H_2O_2) and reducing (citric acid) agents were used to confirm the mechanism of magnetite formation and showed an effect on the magnetic properties of the materials produced that was consistent with the phase behavior of iron oxide. Thus, demonstrating that sufficient control over the hydrothermal reaction is practicable through a judicious choice of counter-ion and chemical conditions within the reactor.

5.5 Further Work

Further investigations are needed into the effect of processing condition on the bulk stoichiometry of the reaction products through techniques more sensitive to local structure (*i.e.* XANES or Mossbauer spectroscopy). Similarly, further investigations into the control of particle size are required as the apparent low solubility of Fe results in nanoparticles of similar crystallite sizes for all the phases of iron oxides produced within this chapter could limit the application materials produced using this methodology. Further investigation is also required to assess if the unique phase behavior of the spinel oxides produced in this chapter could be reproduced on other spinel oxides (which could be of interest in self-limiting magnetic hyperthermia, discussed in greater detail within chapter 6). In addition to the iron sources reported in this chapter, other water soluble sources of Fe (or sources that can be made water soluble) would be interesting to investigate to gain a deeper understanding of iron oxide formation in CHFS. The use of other organic additives could be beneficial as the decomposition products of organic species are shown to vary in both near and supercritical water. Investigations of this type could lead to greater control of material phase and possible nanoparticle size. Similarly, it would also be beneficial to evaluate dispersion strategies for the nanoparticles produced using CHFS and possibly construct a system to produce higher order phases of iron such as FeO (at 500 - 700 °C) and ε-Fe_2O_3 (*ca.* 400 – 800 °C) which are gaining further commercial interest as components of magnetic data storage and in some biomedical applications.

Chapter 6

Investigations into the Direct Synthesis of Surface Functionalised Nanoparticles using CHFS

6.0 Aim:

The aim of this chapter is to describe how the versatility of a flow process can be exploited for production of target materials. This chapter describes the modification of a conventional CHFS reactor to allow for the direct synthesis of surface functionalised nanoparticles of magnetite. An operational envelope for the synthesis of stable aqueous dispersions of magnetite nanoparticles is defined using carboxylic acids as capping agents and is combined with an investigation into the effect of different processing conditions on the efficacy of the synthesised nanoparticles for application in magnetic hyperthermia (an emerging application of these materials).

6.1 Introduction:

Magnetic nanoparticles of many compositions have the capability to release heat under the stimulation of an alternating magnetic field. Such heat generation is attracting interest in fields such as thermobalation of cancerous cells, localised heat generation to set polymer composites and a variety of other applications in which controlled and localised heat generation is required. (Ito *et al.*, 2005) Unlike the wide spread application and evaluation of surface functionalised magnetic nanoparticles in, biological separation, diagnostics [as contrast agents for magnetic resonance imaging (MRI)], the use of magnetic nanoparticles for thermal applications is just in its infancy. (Gupta and Gupta 2005; Mornet *et al.*, 2004; Neuberger *et al.*, 2005; Pankhurst *et al.*, 2003) Many different materials have been evaluated for application in magnetic hyperthermia including Magnetite, Maghemite, ferrite nanoparticles (MFe_2O_4, where M = Mn, Fe, Co), perovskite type magnetic phases (principally for self-limiting magnetic hyperthermia), and metal nanoparticles (Fe, Co, etc). (Jordan *et al.*,1999) Moreover, there is a strong dependence of magnetic particle properties on structural characteristics such as mean size, polydispersity, particle shape, crystalinity, the presence of defects and cation vacancies. (Hergt *et al.*, 1998; Rosensweig 2002) Which, can be influenced by the synthetic protocol used to produce the materials, the choice of capping agent and the dispersion protocol used to formulate many of the materials into stable particle dispersions. (Gazeau *et al.*, 2008; Levy *et al.*,2008; Levy *et* *al.,* 2011) Much academic effort has been directed towards understanding the effects of various structural and magnetic features for hyperthermia applications. Among these, the size of the particles and their size distribution, (Fortin *et al.,* 2007; Gonzales-Weimuller *et al.,* 2009; Ma *et al.,*2004; Rovers *et al.,*2009) crystallinity, (Gloeckl *et al.,* 2006; Rovers *et al.,* 2010; Shubayev *et al.,* 2009) chemical composition, (Dennis *et al.,* 2008; Jordan *et al.,*1999) and inter-particle interactions (Gloeckl *et al.,* 2006) are intrinsically associated to the magnetic material chosen as the hyperthermia mediator. Alongside intrinsic structural effects, other aspects such as the physiological conditions or the magnetic field amplitude and frequency used, interparticle interaction in dispersion and the agglomeration of nanoparticles in dispersion also appear to also be influential factors affecting hyperthermia performance. (Chen *et al.,* 2010; Zhang *et al.,* 2010) Hence, the understanding of the ideal characteristics of magnetic nanoparticles for enhanced heat generation is still a subject of great interest and intensive research. Magnetite nanoparticles are of acute interest in hyperthermia applications as theory predicts heat generation of upto 1 kW g^{-1} for iron oxide could be obtained. (Rosensweig 2002) However, values approaching this are rarely measured experimentally. (Hergt *et al.,* 1998) As such there is significant ambiguity in the dominant physical characteristics and the properties of nanoparticle mediators influence hyperthermia performance due to the sheer number of experimental conditions which need to be considered. In Chapter 5 it was shown that CHFS can be used to produce magnetic nanoparticles showing reasonable magnetic properties although some structural magnetic features were observed which could be classed as detrimental to hyperthermia performance, many of the measurements taken correlate well with those reported for materials showing good performance in hyperthermia applications. This chapter builds upon the work presented in Chapter 5 by modifying the CHFS process to allow for the direct synthesis of surface functionalised magnetite nanoparticles and couples this process development to the application of these materials as mediators for magnetic hyperthermia.

Surface functionalised nanomaterials can be produced using a number of synthesis procedures including; co-precipitation reactions, (Jiang *et al.,* 2004) microemulsion routes, (Bagwe *et al.,* 2006) polyol processes,(Hyeon 2003; Park *et al.,* 2004) thermal decomposition reactions, (Hyeon 2003) and hydrothermal reaction (Arita *et al.,* 2010; Taguchi *et al.,* 2011) as reviewed in greater detail within Chapter 1. Many of the aforementioned processes allow for the addition of capping agents either during particle formation reactions or allow the addition of a capping agent shortly after the formation of nanoparticles and correspondingly many materials obtained from these reactions have been studied as mediators for magnetic hyperthermia. (Jordan *et al.*, 1999) Of the many processing methods used for the synthesis of surface functionalised nanoparticle, the single step processing methods are favoured as they allow for the direct synthesis of high quality dispersions as the particles are either grown in the presence of the capping agent or the capping agent is added shortly after particle formation limiting agglomeration of the particles prior to functionalisation and is desired for the application of such materials as hyperthermia mediators. (Levy *et al.*, 2011) However, many of the single step process suffer experimental limitations such as long reaction times, high production cost (associated with reagents), low production rate and are almost exclusively batch type processes, which in some cases yields a bulk product requiring heavy refinement before application. (Taguchi *et al.*, 2011) Although well reported, two-step synthesis methodologies are not favoured as the state of particle agglomeration prior to surface functionalisation is difficult to control. (Majewski and Thierry 2007) The two step reactions often use nanoparticles produced using conventional techniques and a subsequent dispersion and formulation protocol is used to functionalise the surface of the particles. A major drawback of the two-step method is that particle agglomeration is difficult to control and often yields poor dispersion reproducibility. Various efforts including ultrasonication, (Bruce and Sen 2005; Suslick and Price 1999), changing pH, (Racuciui *et al.*, 2005; Racuciu *et al.*, 2006) using dispersants/surfactants, (Racuciu, Creanga, & Calugaru 2005) and chemical surface modification (Mulvaney *et al.*, 2000; Rajh *et al.*, 2002) have been extensively investigated to improve the dispersion properties. However, in many embodiments the poor reproducibility of two step methods for the synthesis of nanoparticles are far superseded by the single step methods.

The stability of a nanoparticle dispersion can be controlled by several mechanism and the particles may be either, charge stabilized (electrostatic), or sterically stabilised (physical separation) as reviewed in greater detail within Chapter 1 and materials showing both modalities have been assessed as mediators for magnetic hyperthermia. (Pankhurst *et al.*, 2003) Typically, the surface functionalisation and stabilisation strategy employed is application dependent and is entirely dependent upon the chemical moiety grafted to the particle surface. Many of the aforementioned methods have been adapted to allow the direct synthesis of nanoparticles stablilised by these mechanisms. (Gupta & Gupta 2005)

Furthermore, the surface layer of these nanoparticles can be modified for increased aqueous stability, biocompatibility, stability and bio-recognition and a number of chemical modifications are presented in the academic literature utilising many of the free reactive groups associated with common capping agents. (Gupta & Gupta 2005; Thanh and Green 2010) Hence there is interest in processing methodologies which can either; directly produce functionalised materials, or produce materials which can be readily functionalised post synthesis (*i.e.* producing materials with a suitable anchoring molecule for further functionalisation). (Thanh & Green 2010)

Compared to many of the aforementioned methods, hydrothermal routes for the synthesis of surface functionalised nanoparticles are comparatively poorly described. (Taguchi *et al.*, 2011) Principally, this stems from the oxidation of capping agents under hydrothermal conditions making effective surface functionalisation difficult due to decomposition of the organic compound, as near critical water is often used in biomass remediation due to is oxidative potential (Supercritical water oxidation [SWO]). (Taguchi *et al.*, 2012b) However, several studies have detailed the synthesis of surface functionalised inorganic nanoparticles, such as TiO_2, ZnO,CeO_2 and $CoAl_2O_4$, where carboxylic acids (C4 - C14 acids, oleyl amine and phosphonated acids) are used conferring stability in non-aqueous media. (Arita *et al.*, 2010; Mousavand *et al.*, 2010; Taguchi *et al.*, 2012a; Taguchi *et al.*, 2012b) Adischiri *et al.* studied the synthesis of di-carboxylic acid (C4 - C8) modified CeO_2 nanocrystals and showed variation alkyl chain length altered the morphologies of the CeO_2 nanocrystals produced using a batch supercritical water process. (Taguchi *et al.*, 2011) However, the comparatively short residence times in CHFS suggest that effective functionalisation of nanoparticles shortly after particle formation steps may be possible due to the comparatively simple modification of the process to allow for the introduction of supplementary reagents.

In this chapter the development and optimisation of surface functionalised nanoparticle synthesis using a continuous hydrothermal methodology is presented. The optimisation of the process is presented through complete characterisation of nanoparticles produced under different processing conditions. The structure and morphology of the products of Continuous hydrothermal synthesis were investigated using XRD, TEM, HRTEM, DLS, electrophoretic mobility measurements, TGA and magnetometry. These investigations are coupled to an evaluation of citric acid coated magnetite produced using this method as mediators for magnetic hyperthermia.

6.2 General synthesis procedures:

6.2.1 Materials:

Iron (III) citrate ([Fe ($C_6H_5O_7$] technical grade, >98%), Citric acid ([$C_6H_8O_7$] 99%) and (NH_4)OH solution (28 vol %) were supplied by Sigma–Aldrich Chemical Company (Dorset, UK). Iron (III) citrate powder was dissolved in water by adding a stoichiomentric amount of NH_4OH solution forming a soluble iron (III) citrate complex (Ammonium ferric citrate [NH_3 Fe($C_6H_5O_7$). All experiments were conducted using deionized water (>10 Mega Ohms).

6.2.2 Synthesis:

The system used for this work is defined as CHFS system 2 and is described in greater detail within Chapter 2. The reaction point geometry used in this work is presented schematically in figure 6.1, where key dimensions and definition of the variables used within the text are highlighted. Where, the particle formation residence time (RT1) is defined as L1 in figure 6.1 (at temperature T_{mix1}, 24.1 MPa), and the post citric acid residence time (RT_2) is defined from the volume of the reaction point from the terminus of the citric acid solution inlet to the cooler (at temperature T_{mix2}, 24.1MPa) and is sometimes expressed as a the nominal volume of the system between these points. This reaction point geometry (constructed as described in Section 2.2.1) was preliminarily optimised before the completion of this work. Reactions were carried out using variable system configuration as summarised in table 6.1. As detailed in Chapter 2 the flow of P1 was used exclusively to provide a feed of supercritical water to the reactor (Q_{sw}), the combined output of P2 + 3 (Q_p) was used to supply metal salt supply precursors and the output of P4 + P5 (Q_q) was used to supply a quenching flow (containing citric acid) shortly after the formation of nanoparticles. For information the structure and molecular geometry of citric acid (CA) is presented in figure 6.2. All reactions were carried out using a heater set temperature of 450 °C and a system pressure of 24.1 MPa. Similarly, all reactions used NH_3 Fe($C_6H_5O_7$) at a concentration of 0.066 M as the sole metal precursor. In a typical synthesis *ca.* 800 mL of nanoparticle laden slurry was collected from the process and recovered using NaCl flocculation and centrifugation followed by dialysis as per the method stated in Chapter 2. Samples were retained as both freeze dried powders and cleaned dispersions for further analysis. Samples produced in this section are identified by a unique sample number and typically successive samples or sample series are referred to throughout the text. The details of several control reactions are presented in Appendix 1 all samples reported in this section were produced using the synthesis methodology presented here. Data presented in this appendix is referred to throughout the body of the text to support various discussions.

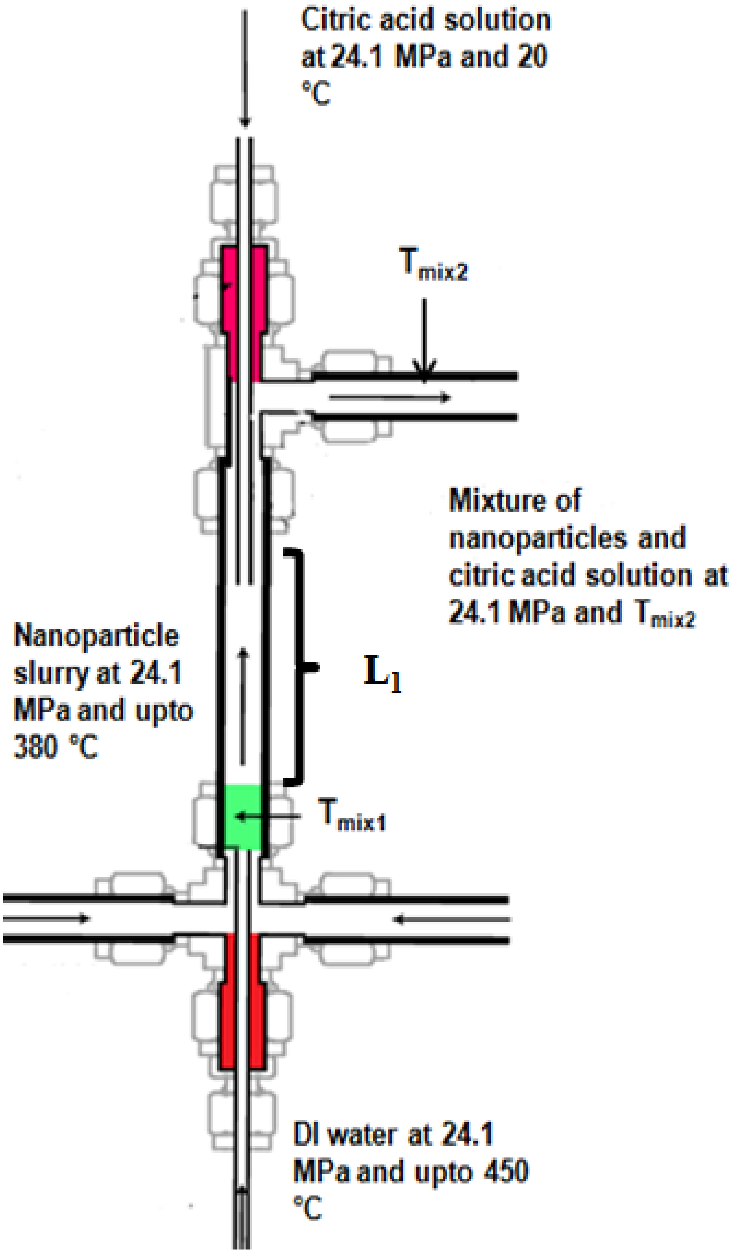

Figure 6.1: A schematic of the reaction point used for the synthesis of citric acid coated magnetite nanoparticles indicating key variables.

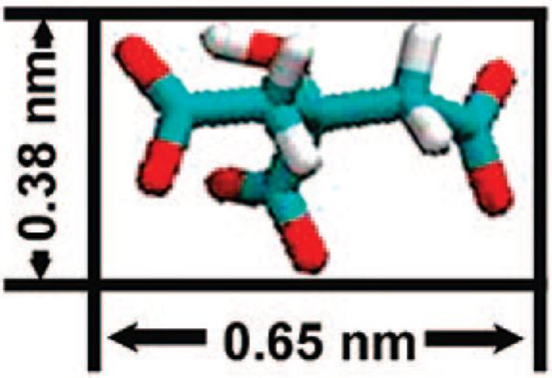

Figure 6.2: The structure and dimensions of citric acid as a molecule. (Mudunkotuwa & Grassian 2010)

In-situ temperature measurements were also performed to provide an indication of the quality of mixing between the nascent stream of particles, the output of Q_{sw} and Q_p combined at a temperature of (*ca.* 380 °C) and the flow of capping agent solution (Q_q). These measurements were performed using an analogous methodology to that presented in Chapter 3. The relative placement of thermocouples used in this analysis is defined later within the text. All reaction temperatures quoted in this work were determined by overall heat balance. Consistent with Chapter 3 the physical properties of water at 24.1 MPa were determined from the IAPWS Formulation 1995 for the Thermodynamic Properties of Ordinary Water Substance for General and Scientific Use and the associated FLUIDCAL software.(Wagner and Pruss 2002) This software was also used to calculate the density and viscosity of water for any given temperature and these values were used in the calculation of residence time.

6.2.3: Evaluation of Materials for Magnetic Hyperthermia:

This section is composed of data relating to the evaluation of citric acid coated magnetite nanoparticles produced using the two step reaction point geometry presented in Section 6.2.2. This section details the effect of processing conditions on the relative efficacy of magnetite nanoparticles as mediators in magnetic hyperthermia. The synthesis and characterisation details of materials evaluated for magnetic hyperthermia are presented in Appendix 1. Samples were prepared for calorimetric measurement using the following procedure; a batch of each sample *ca.* 800 mL of nanoparticle laden slurry (*ca.* 1g of powder) was consolidated by NaCl flocculation as described in Chapter 2. Following flocculation the sample was centrifuged to minimise the volume of the sample for dialysis the sample was re-suspended to a fixed volume of 5 mL and placed in dialysis tubing

(SLS) with a molecular weight cut-off of 12 kDa forming a magnetically actuable fluid. Dialysis was performed against DI water for between 24 - 36 hours and included two complete buffer exchanges to remove excess reagents and free citric acid. Following dialysis the samples were freeze dried for 24 h prior to being redispersed to a concentration of 50 mg mL^{-1} ($Fe_3 O_4$, basis) and the efficacy of the materials for magnetic hyperthermia was measured using calorimetric measurements as stated in Chapter 2 (Section 2.14).

6.3 Results and Discussion:

6.3.1 Effect of Capping Agent Addition:

The samples produced in this section are summarised in Table 6.1. Initially combinations of flow rates ($Q_{sw} + Q_p$), quench rates (Q_q), relative iron to citric acid ratios (Fe : CA) and post capping agent addition residence times were evaluated to assess the effect of each variable on the product obtained from the reaction. The addition of the capping agent (citric acid) after the formation of nanoparticles was used to ensure survival of the capping agent and to segregate the particle growth steps (occurring at *ca.* 380 °C) from the functionalisation steps (occurring at a lower temperature). Dissolution of the reaction product was consistently observed when CA : Fe ratios > 10, either within the CHFS system or shortly after product collection, and was attributed to the acidity of the particle slurry. Under these conditions the slurry exiting the process was at *ca.* pH 1 - 2, upon product dissolution the likely soluble complex formed was $Fe_2 C_6H_3O_7$ (a bright yellow solution). In reactions where products were recovered all samples formed stable dispersions after consolidation as exemplified by sample CAO7 (Table 6.1), shown in figure 6.3.

Figure 6.3: Photograph of the ferrofluid formed after recovery of sample CAO7 dispersed in DI water to a concentration of 50 mg mL $^{-1}$ (Fe_3O_4 basis).

Table 6.1: Summary of the reaction condition and characterisation data for citric acid coated magnetite produced using CHFS system 2. The Iron citrate concentration was fixed at 0.066 M, the heater temperature was set to 450 °C resulting in a reaction point temperature of *ca.* 380 °C (T_{mix1}) at the flow rates used Q_{sw} =10 and Q_p=5. Residence times were calculated from the reaction zone length and the velocity of the fluid at it's theoretical mixture temperature (*i.e.* T_{mix1} or T_{mix2}).

ID	**Reactor length (mm)**	**Q_q**	**$T_{mix\ 2}$ (°C)**	**CA (wt %)**	**CA:Fe**	**RT2**	**C_s (nm)**	**TGA data**		**Hydrodynamic diameter (nm)**			**TEM data**		**$CA/nm^{2\ £}$**
								Weight loss (%)	**(CA/nm^2)***	**D_h**	**PDI**	**$D_{h(number)}$**	**Mean**	**(SD)**	
CAO1	21	10	281	1.0	1.5	2.56	12.8	4.42	1.17	79	0.132	43.2	-	-	-
CAO2	21	20	210	1.0	3.1	2.06	11.8	4.22	1.03	78	0.19	46.4	-	-	-
CAO3	21	30	168	1.0	4.7	1.68	11.3	2.79	0.65	80	0.155	54.3	-	-	-
CAO4	120	10	281	0.5	0.7	5.21	13.4	7.1	1.96	100	0.215	23.5	-	-	-
CAO5	120	20	210	0.5	1.5	4.18	12.8	7.37	1.95	106	0.178	22.1	13.7	3.3	2.08
CAO6	120	30	168	0.5	2.3	3.42	13.5	7.72	2.15	72	0.149	17.6	16.6	3.3	2.64
CAO7	120	10	281	1	1.5	5.21	11.8	10.35	3.31	74	0.152	17.9	11.7	3.1	2.50
CAO8	120	20	210	1	3.1	4.18	12.9	8.64	1.71	72	0.193	20.6	11.0	2.6	1.96
CAO9	120	30	168	1	4.7	3.42	11.7	8.11	2.32	74	0.163	25.3	13.4	4.1	2.24
CAO10	120	10	281	2	3.1	5.21	12.4	8.98	1.57	73	0.165	13.9	13.5	3.5	2.50
CAO11	120	20	210	2	6.3	4.18	10.9	5.05	1.14	75	0.21	18.5	15.8	4.2	1.64
CAO12	120	30	168	2	9.4	3.42	11.6	5.95	1.42	77	0.169	22.3	11.2	2.6	1.37
CAO13	220	10	281	2	3.1	7.88	11.7	9.87	2.38	76	0.154	29.8	-	-	-
CAO14	220	20	210	2	6.3	6.33	11.8	9.0	2.19	73	0.185	34.5	-	-	-
CAO15	220	10	281	1	1.5	7.88	12.8	7.2	1.90	77	0.17	26.7	11.1	2.6	1.64
CAO16	220	20	210	1	3.1	6.33	11.5	8.23	1.94	86	0.189	25.0	14.4	3.7	2.44
CAO17	220	30	168	1	4.7	5.17	11.0	7.91	1.79	80	0.133	45.6	-	-	-
CAO18	320	10	281	3	4.7	10.6	12.3	2.09	0.53	170	0.241	67.8	-	-	-
CAO19	320	10	281	2	3.1	10.6	12.4	2.00	0.51	187	0.281	54.3	-	-	-
CAO20	320	15	241	2	4.7	9.46	9.6	1.82	0.36	192	0.332	56.9	-	-	-
CAO21	320	10	281	1	1.5	10.6	9.9	2.82	0.57	218	0.328	43.2	11.4	2.6	0.66
CAO22	320	15	241	1	2.3	9.46	9.6	2.19	0.43	200	0.28	89.3	11.7	3.0	0.53
CAO23	320	20	210	1	3.1	8.47	11.6	1.92	0.46	290	0.468	76.4	-	-	-
CAO24	320	25	187	1	3.9	7.63	11.3	-	-	273	0.402	103.4	-	-	-

*grafting density of CA determined using equation 6.1 and the crystallite size determined from the Scherrer equation (C_s), $^\$$ denotes the same calculation using the TEM based particle size, Q_q is the flowrate of citric acid solution (mL min^{-1}), T_{mix2} is the theoretical mixture temperature post citric acid addition, D_h = hydrodynamic diameter (nm) measured using DLS and $D_{h(number)}$ is the number weighted distribution (explained in Chapter 2), TGA = weight loss in the 200 - 500 °C region (attributed to the thermal decomposition of citric acid).The reactor length is defined as the length of the reactor post addition of citric acid.

XRD patterns of the products of the reactions presented in table 6.1 are shown in figure 6.4. All diffraction patterns were in good agreement with those of both magnetite (ICDS 082234) and Maghemite (ICDS 79196), respectively (figure 6.4 a). As discussed in greater detail within Chapter 5, magnetite is the only mixed-valence iron oxide and it has an inverse spinel structure which is often difficult to differentiate from other magnetic spinel iron oxide phases (figure 6.4 b), hence the phase of these materials will be referred to as magnetite. The addition of the capping agent through Q_q was shown to have no effect on the absolute phase determined by XRD consistent with the discussion presented in Chapter 5. Application of the Scherrer equation to the (311) reflection gave estimates of crystallite size between 10 and 13 nm and the data for each sample is summarised in table 6.1, with the crystallite size being largely invariant of synthesis condition (figure 6.4 b). The similarity between crystallite sizes determined from application of the Scherer equation to the diffraction data is consistent with the data obtained in an evaluation of partial reaction quenching presented in Appendix 1. Where, the effect of partial reaction quenching was shown to have little effect on particle size or particle morphology or magnetic properties even when $RT_1 = 0.21$ s, suggesting that the particle formation steps were independent of both Q_p and CA:Fe ratio (until the onset of dissolution CA:Fe >10) and that particle formation occurs on vanishingly small timescales.

Figure 6.5 shows TEM images of the products of each of the reactions summarised in table 6.1. The average particle sizes and size distribution were found from the measurement of *ca.* 300 particles and are detailed in table 6.1. From TEM the primary crystallite size ranged from *ca.*11-15 nm, with particle size being largely invariant of Q_q or CA:Fe consistent with the observations made using XRD. Direct observation using TEM confirmed the independence of crystallite size on both Q_q and CA:Fe ratio. The TEM data is also consistent with the observations noted in Chapter 5 and the experiments presented in Appendix 1 where partial quenching of the reaction was shown to have little influence on the crystallite size produced in the reaction, suggesting the particle formation and surface functionalisation steps are effectively segregated in this system and that particle formation is complete on vanishingly small timescales. It is also evident from figure 6.5 that the state of agglomeration in the sample varied with both Q_q and CA:Fe suggesting optimal dispersion in a narrow operational space which is discussed further in the text below. HRTEM confirmed that a highly crystalline single phase material was produced in the median synthesis condition (Sample CAO7) as shown in figure 6.6a and the phase of the material under observation was confirmed using SAED and the indexed diffraction pattern is shown in figure 6.6b. In figure 6.6a lattice fringes corresponding to the (311) plane with a measured d-spacing of 2.54 Å are visualised extending towards the edge of each crystallite confirming that a highly crystalline and single phase product was obtained in the reaction. The results obtained from the HRTEM and SAED data are in good agreement with the lattice parameters reported for the inverse cubic spinel structure of Fe_3O_4 and consistent with the diffraction data obtained for the sample.

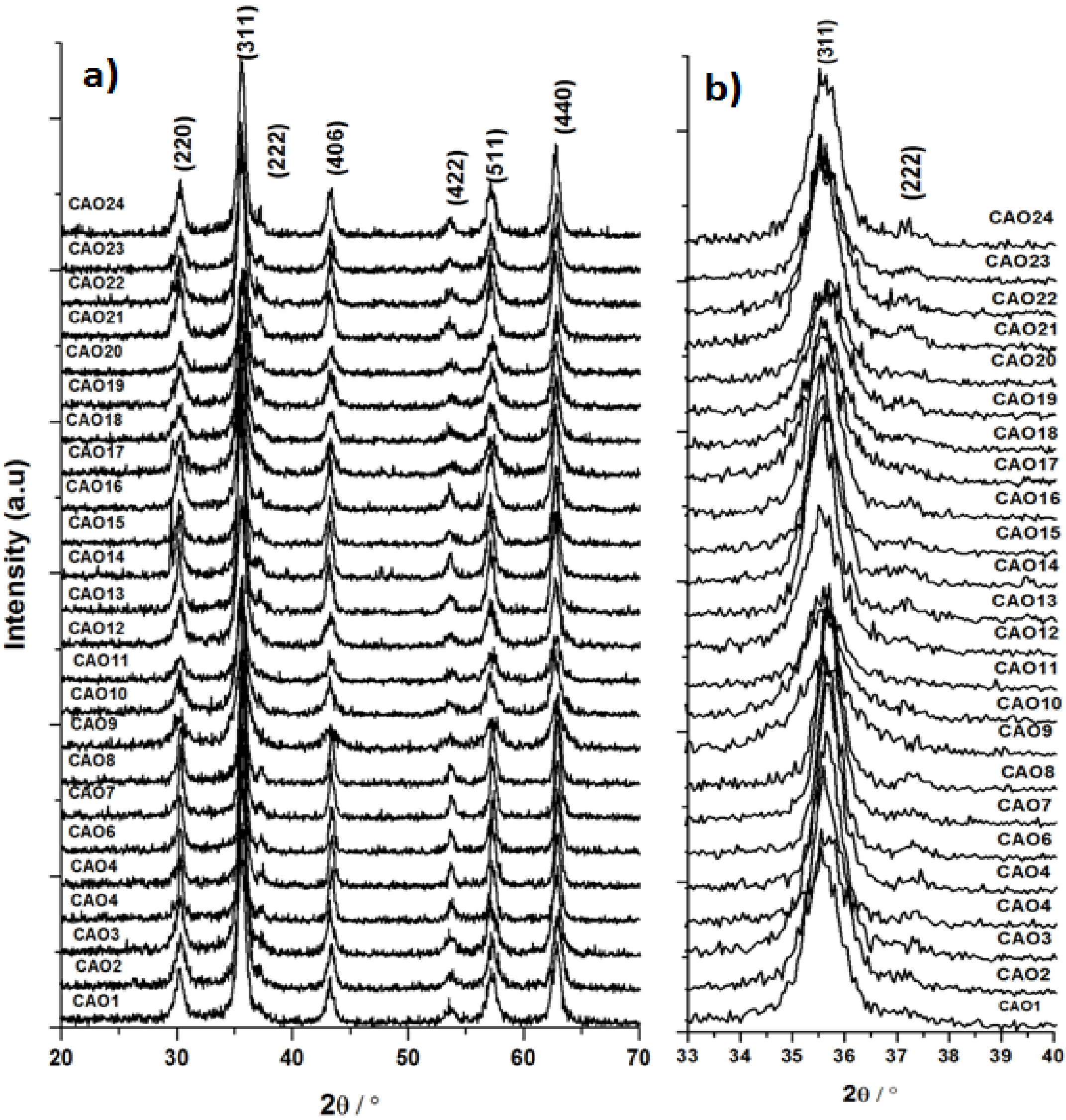

Figure 6.4: XRD patterns obtained for magnetite nanoparticles synthesised in **a)** experimental runs CAO1-24 b) shows an expanded view of the 33 - 40 ° 2θ region from which the crystallite size was determined by application of the Scherer equation.

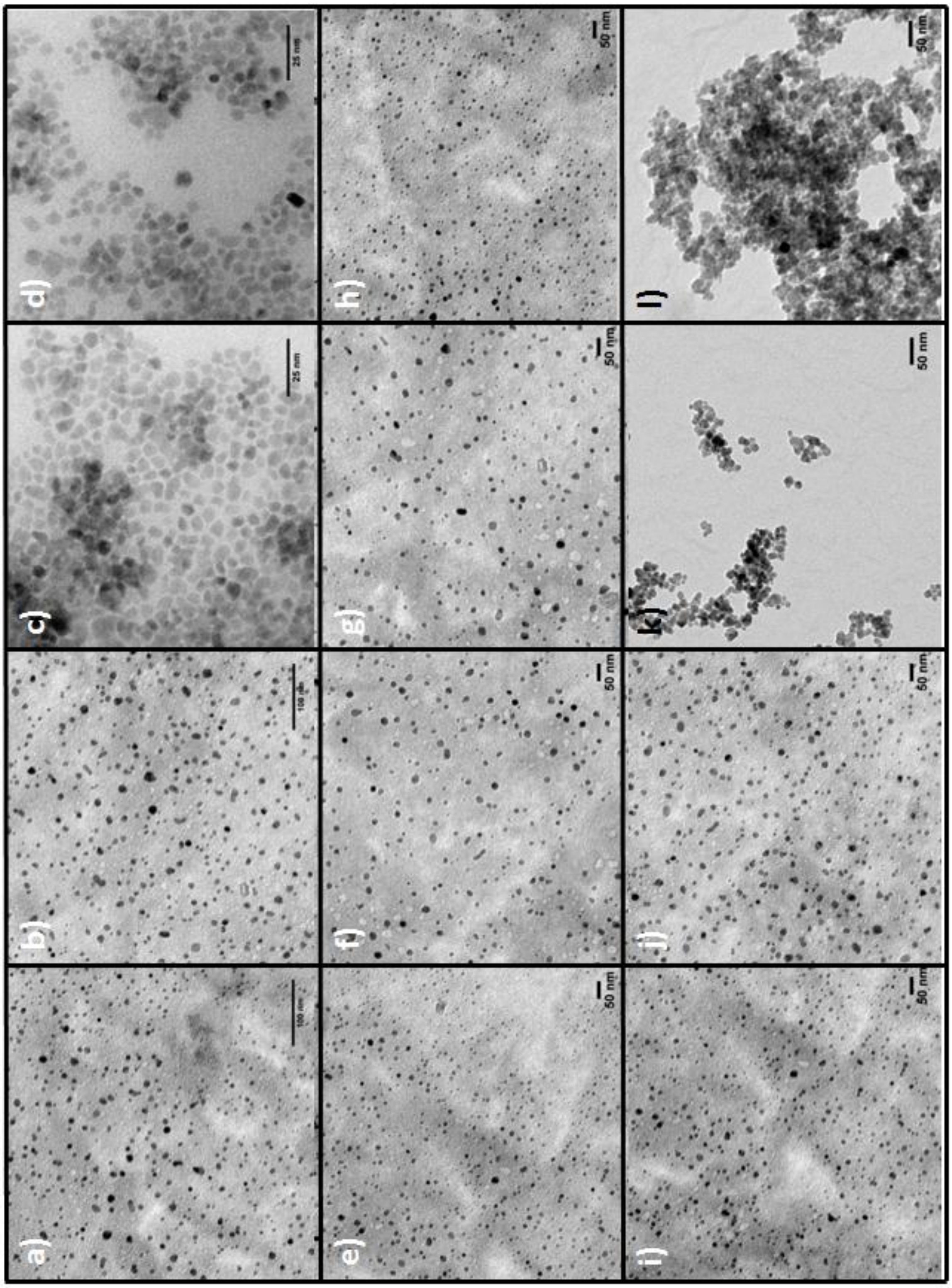

Figure 6.5: TEM images of the products of reactions; **a)** CAO5, **b)** CAO6, **c)** CAO7, **d)** CAO8, **e)** CAO9, **f)** CAO10, **g)** CAO11, **h)** CAO12, **i)** CAO15, **j)** CAO16, **k)** CAO21 and **l)** CAO22.

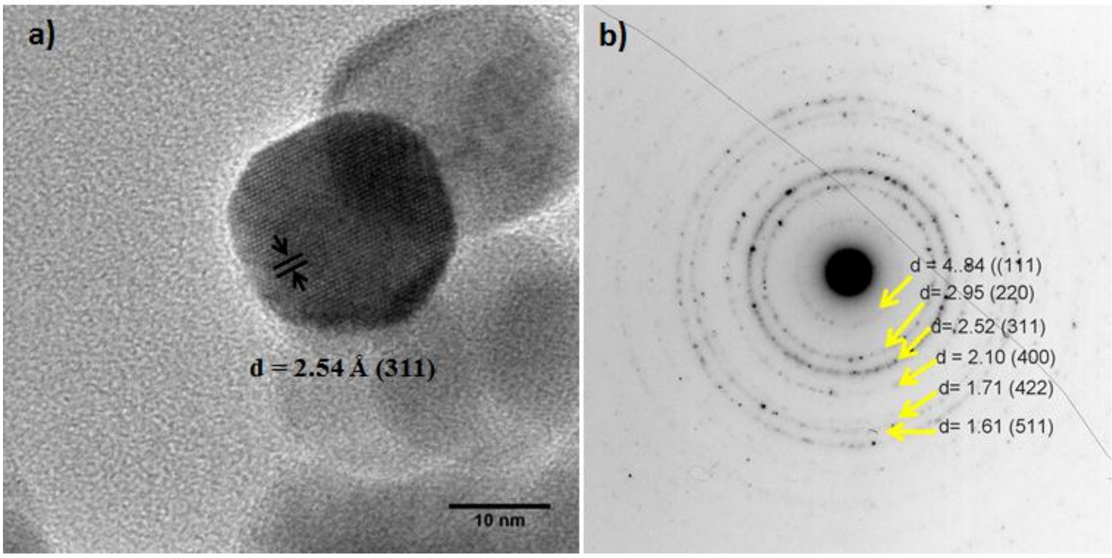

Figure 6.6: a) HRTEM image of sample CAO7 showing visualisation of lattice fringes corresponding to 311 plane with a measured spacing of 2.54 Å (magnetite = 2.53 Å), **b)** indexed SEAD pattern obtained for the sample.

ATR-FTIR was used to confirm the presence of citric acid on the surface of the nanoparticles produced in runs CAO1-24 (figure 6.7). The spectra obtained from bulk citric acid showed modes originating from (ν) C=O present at 1735 cm^{-1}, (ν_s) COO$^-$ (~ 1390 cm^{-1}) and (ν) OC-OH (~1200 cm^{-1}) and (νs) OC-OH (~1429 cm^{-1}). The (ν_{as}) COO$^-$ (~1569 cm^{-1}) mode was absent in the spectrum of bulk citric acid (data not shown). Spectra obtained for the coated magnetite particles showed modes origination from (ν) C=O present at 1735 cm^{-1}, (ν_s) COO$^-$ (~1390 cm^{-1}), (ν) OC-OH (~1204 cm^{-1}), (νs) OC-OH (~1429 cm^{-1}) and (ν_{as}) COO$^-$ (~1569 cm^{-1}) confirming the presence of citric acid on the surface of the products. The observation of the (ν_{as}) COO$^-$ stretching mode centred at 1569 cm^{-1} suggests a proportion of the acid groups present in the sample are coordinated to the particle surface. (Goodarzi *et al.*, 2004) In previous studies of carboxylic acid coated nanoparticles the wavenumber separation between the (ν_s) COO$^-$ (*ca.* 1390 cm^{-1}) and the (ν_{as}) COO$^-$ (*ca.* 1569 cm^{-1}) modes have been used to determine the binding state of the carboxylate group and the metal oxide surface using the wavenumber separation (Δ) between the asymmetric (υ_{as}) and symmetric (υ_s) IR modes. (Kirwan *et al.*, 2003; Taguchi *et al.*, 2011; Zhang *et al.*, 2006) Unidentate complexes exhibit Δ values (ranging from 200 to 320 cm^{-1}) that are much greater than those of bidentate complexes (ranging from 140 to 190 cm^{-1}) as depicted in figure 6.8. (Zhang, He, & Gu 2006) The values of Δ determined for the citric acid coated magnetite samples varied between 190 and 220 cm^{-1} as clearly shown in figure 6.7 through variation in the V_{as} COO^- mode position suggesting mixtures of monodentate and bridging coordination with the particle surface consistent with the coordination typically reported for many citric acid coated nanomaterials. (Illes and Tombacz 2006) A shift in the value of Δ was observed with increasing grafting density from bridging coordination to monodentate binding which could be attributed to a greater number of CA molecules co-ordinated to the particle surface (quantified later). From the data presented no realistic information could be derived to assess if significant decomposition of citrate species occurred under the processing conditions used, hereafter the species present at the surface of the nanoparticles will be referred to as citric acid.

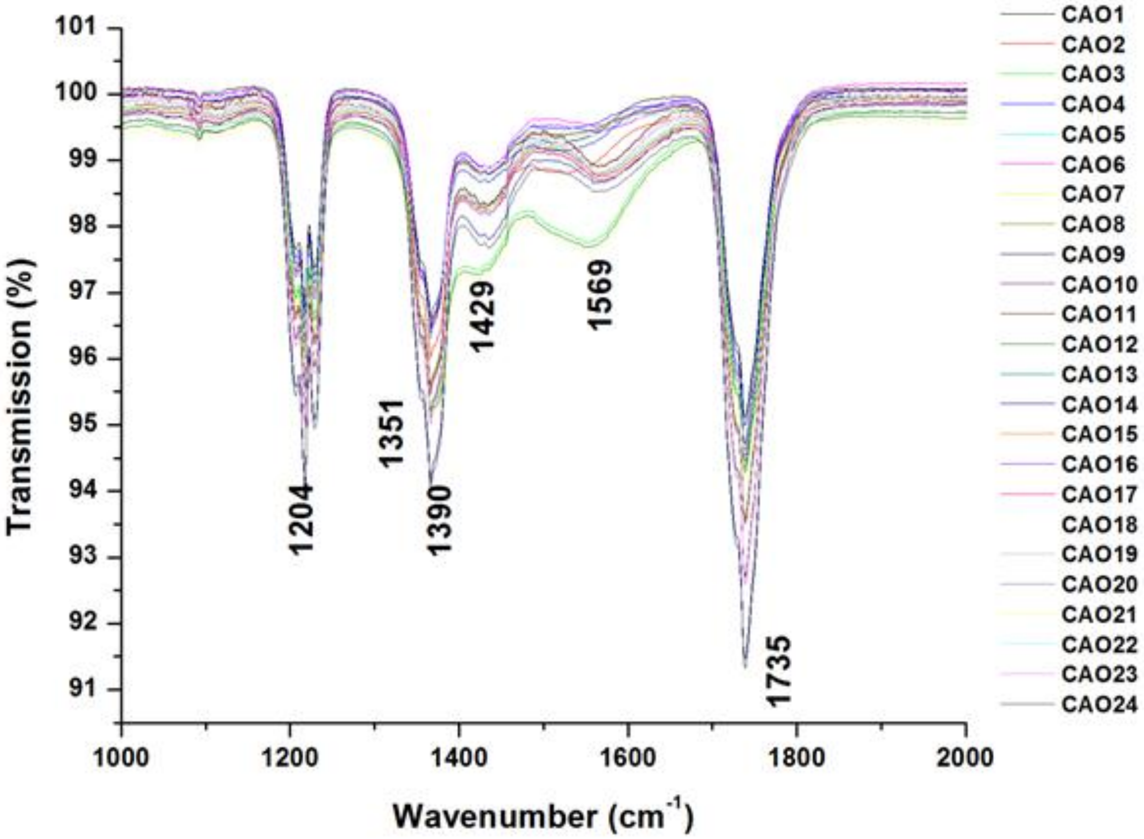

Figure 6.7: Stacked FTIR spectra of the products from each reaction CAO1-24 showing an expanded region of the complete spectra (range 1000 - 2000 cm^{-1}) identifying the IR active mode positions.

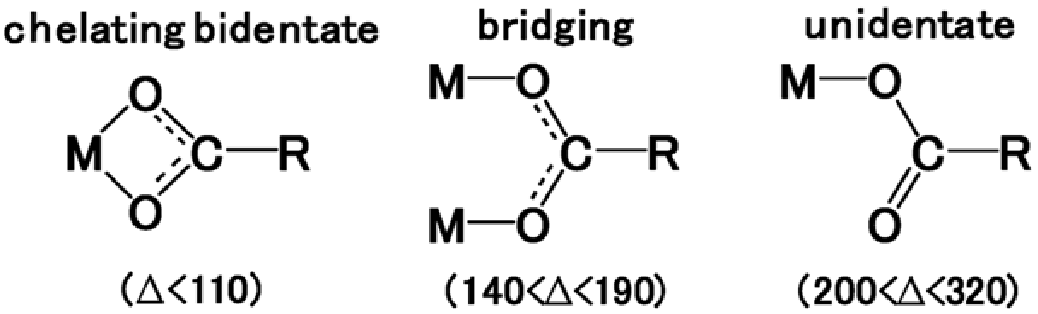

Figure 6.8: Schematic representation of possible coordination geometries of carboxylate groups coordinating surface metal ions. Where, M is the metal ion. Δ (cm^{-1}): is the wave number separation between the ν_{as} and ν_s stretching vibration of COO^- indicative of the coordination environment of the carboxyl group. (Zhang, He, & Gu 2006)

Thermogravimetric analysis was used to quantify the proportion of the sample mass attributable to organic species. Figure 6.9a shows the TGA data obtained for samples CaO4-11 showing variation in the regions of weight loss. The TG curve can be divided into two dominant stages of weight loss, the region below 90 °C, over which the mass loss ranged from *ca.5 - 10 %* (expressed as a percentage of sample mass) can be attributed to the removal of weakly associated water and physisorbed water. The second region of weight loss in the 180 - 400 °C region can be attributed to the decomposition of organic species. The decomposition temperature observed is consistent with the decomposition temperature of bulk citric acid (*ca.* 220°C) and has been confirmed using TGA-MS (data not shown). (Carlsson *et al.,* 1994) DSC data obtained for each of the samples is presented in figure 6.9b and shows two characteristic endotherms, the first was attributed to the evaporation of physisorbed water consistent with the first weight loss observed in TGA, and the second endotherm observed can be attributed to the decomposition of organic species (principally citrates) consistent with the second region of weightloss observed in figure 6.9a. A third small endotherm was also observed at *ca.* 600 °C which corresponds well with the phase transition temperature of Fe_3O_4 / $\gamma Fe_2O_3 \rightarrow \alpha\text{-}Fe_2O_3$. (Carlsson *et al.,* 1994) The measured weighloss for each sample is summarised in table 6.1, it is evident from the data that processing condition influenced the density of citric acid on the surface of the nanoparticles.

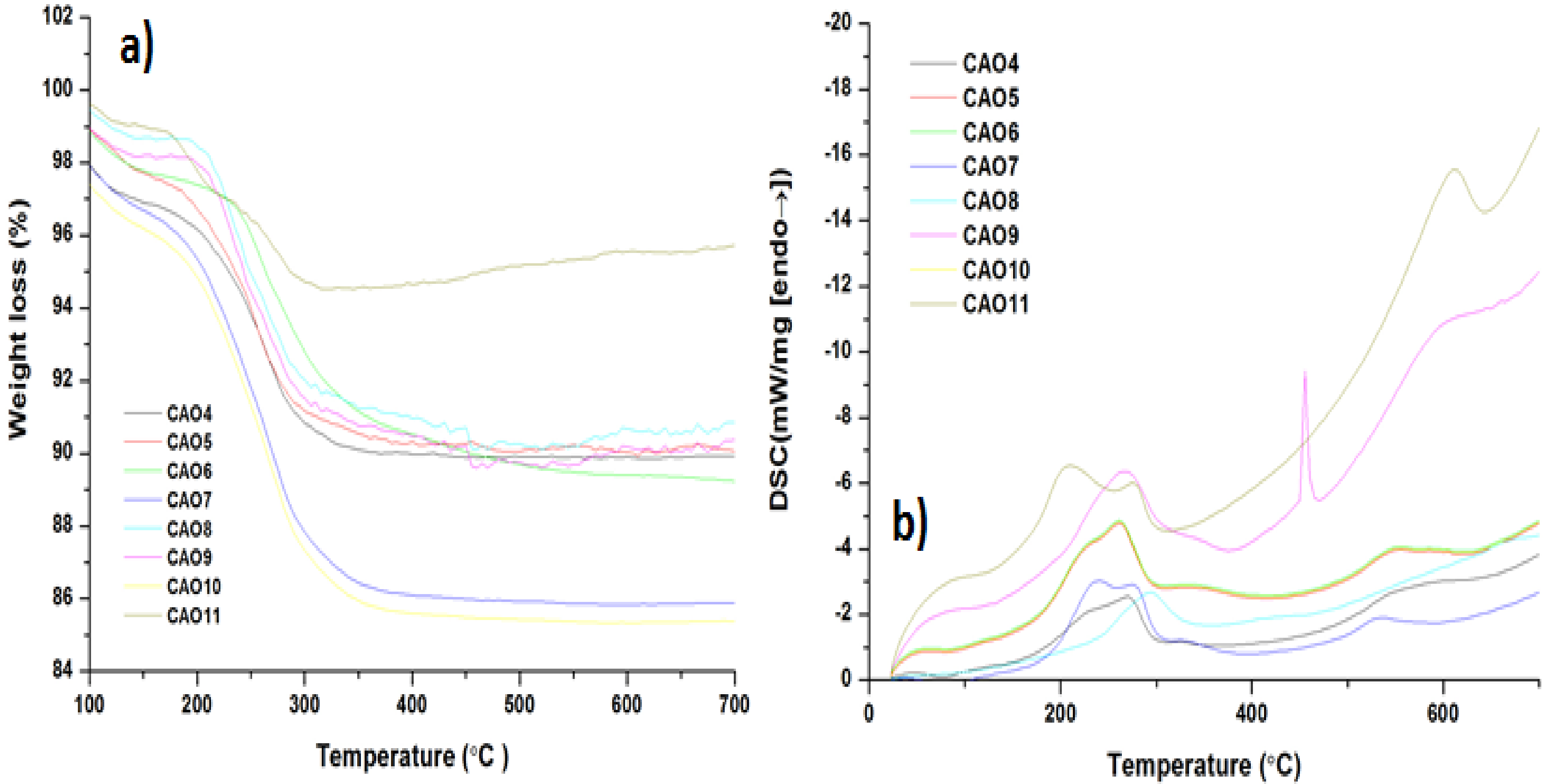

Figure 6.9: **a)** TGA data obtained for sample CAO4-11 and **b)** DSC traces of samples CAO4-11

The grafting densities of CA on the surface of magnetite nanoparticles was calculated from the composition and surface area data derived from either the equivalent surface area calculated from the crystallite size determined by XRD and in selected samples the mean crystallite size determined from TEM using equation 6.1. Under this evaluation it is assumed that CA co-ordination to the particle surface is irreversible as widely reported for citric acid coordination to nanoparticle surfaces at 300 K and any binding events occur within the reaction point. (Mudunkotuwa and Grassian 2010; Pettibone *et al.,* 2008)

$$\sigma = \left(\frac{m_{ca}}{m_{fe3o4}}\right)\frac{N_a}{M_n A_{sp}} \quad \textbf{(Equation 6.1)}$$

In Equation 6.1, σ is the grafting density expressed as the number of molecules per square nm (CA / nm^2), $m_{ca/}m_{Fe3O4}$ is the mass ratio of capping agent to magnetite (determined by TGA), and N_A is Avogadro’s number, M_n is the density of magnetite (assumed to be 5.15 g cm^{-3}) and A_{sp} is the particles equivalent sphere surface area calculated from either the average diameter determined by TEM or the crystallite size determined by XRD (as stated in table 6.1). The number of carboxylate groups available for adsorption per square nanometer (binding area *ca.* 21 Å^2) of the nanoparticle surfaces was not used in the calculation of the grafting density due to the number of possible binding configurations citric acid could adopt at the surface of the nanoparticles (monodentate or bidentate binding configurations). (Pettibone *et al.,* 2008) As an example the grafting density calculated using the monodentate carboxylic acid binding area resulted in theoretical surface coverage values of *ca.* 40 - 60 % although from calculation derived from equation 6.1 an apparent surface saturation of *ca.* 2.6 CA/nm^2 was determined (sample CAO7). The observed surface saturation of *ca.* 2 - 2.6 CA/nm^2 is consistent with the typical saturation density reported in the literature for both inorganic metal oxides and calcium phosphates. (Fauconnier *et al.,* 1996; Jiang *et al.,* 2008) Figure 6.10a shows the variation in CA grafting density as a function of both CA:Fe ratio used in synthesis plotted against the reactor volume post CA addition. Where, it can been seen that the reactor volume post addition of the CA feed was the most influential factor in determining the CA grafting density and was largely invariant of all other processing conditions. To confirm the accuracy of the grafting densities shown in figure 6.10 a the same calculation was made using the crystallite size directly observed using TEM was used to accurately quantify the grafting density for selected samples and yielded almost identical values of CA grafting density (figure 6.10b).

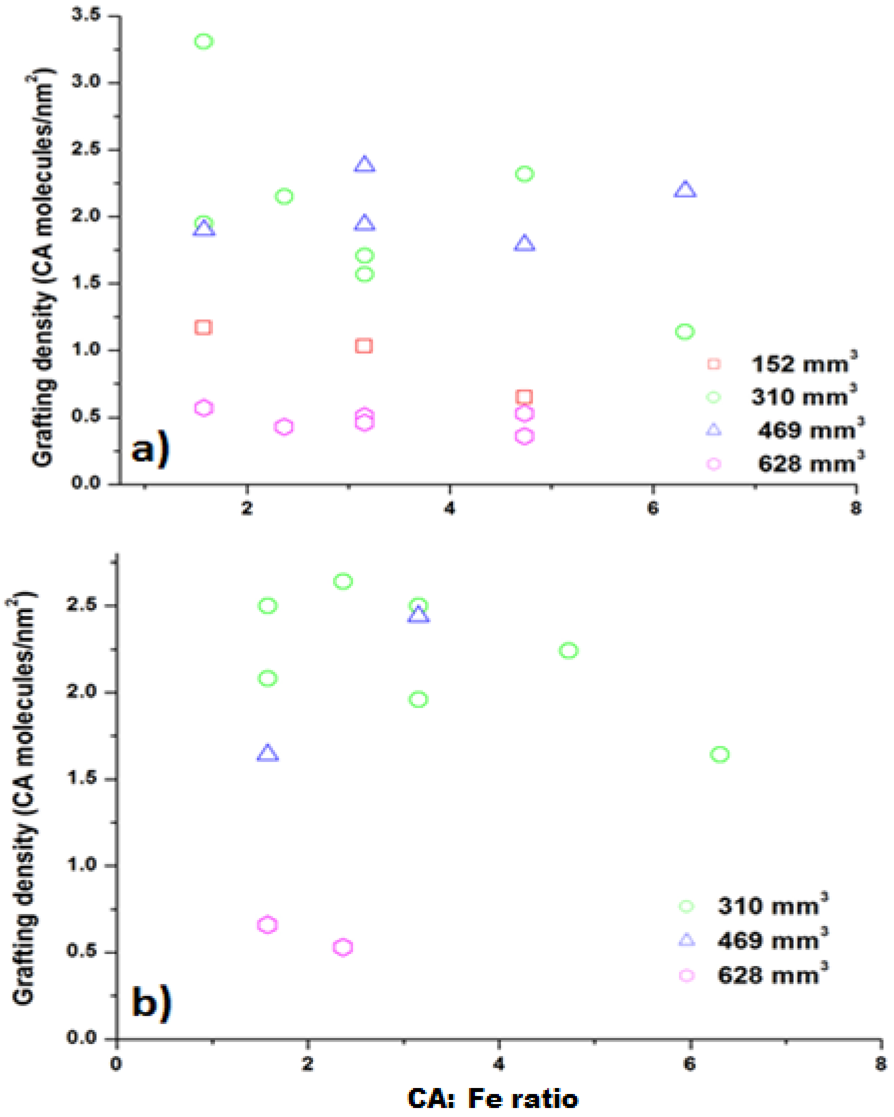

Figure 6.10: a) Citric acid grafting density derived from the crystallite size estimated from the diffraction data as a function of synthesis condition plotted as a function of reaction point volume post addition of Q_q, **b)** variation in grafting density calculated from equation 6.1 using TEM based crystallite size plotted against relative CA:Fe ratio used in the synthesis of each product as a function of reaction point volume post addition of Q_q.

Estimation of the residence time (RT_2) for each synthesis condition is presented in table 6.1 assuming the feeds are completely mixed at the terminus of the Q_q inlet and the mixture (Q_{sw} + Q_p + Q_q) is at the temperature defined by enthalpy balance (T_{mix2}). Residence times of *ca.* 1.68 - 2.56 s resulted in a calculated citric acid grafting density of *ca.* 50% of that calculated as the saturation density (runs CAO1 - 3). Suggesting a limitation of citric acid binding likely related to the diffusion of citric acid to the nascent particle surface (an artefact of mixing the two feeds). Increase of RT2 to *ca.* 4.42 - 5.21 s resulted in increased grafting density with an apparent surface saturation of 2 - 2.6 CA/nm^2. Further suggesting the lower grafting density calculated in runs (CAO1-3) is linked to diffusion of citric acid to the particle surface. Increasing the residence time post citric acid addition to *ca.* 6.33 -7.8 s (runs CAO12 - 17) resulted in a lower citric acid grafting density than those presented for residence times of *ca.* 4.42 - 5.21 s which is likely to result from the decomposition of citric acid to lower molecular weight acids through decarboxylation reactions forming itaconic acid (130.1 g mol^{-1}) and citraconic and (130.1 g mol^{-1}) known hydrothermal decarboxylation products of CA. (Carlsson *et al.,* 1994) Similarly, when residence times of *ca.* 7.63-10.6 s yield similarly low grafting densities. Substitution of the mass of itaconic and citraconic acid into equation 6.1 yields grafting densities similar to those obtained for citric acid in runs CAO4-11 of *ca.* 1.8 - 2.4 CA/nm^2 (runs CAO12 - 24). Suggesting decarboxylation of citrate is responsible for the reduced grafting density determined from equation 6.1. FTIR specta obtained for each sample series confirmed the presence of COO- groups however, no definitive identification of the species present at the surface of the nanoparticles could realistically obtained due to the similarity in IR spectra between the decarboxylation products (figure 6.5).

Figure 6.11 shows the variation in hydrodynamic diameter (z-average) as a function of both CA:Fe ratio and the reactor volume post citric acid addition. As shown in figure 6.11 the most significant contribution to the reduction in hydrodynamic diameter was the volume of the reactor post addition of citric acid. Typically, the measured hydrodynamic diameter and relative polydispersity was reflected by the samples grafting density as compared in table 6.1. For samples CAO1-17 hydrodynamic diameters in the region of 60-100 nm were measured suggesting similarity in the dispersions of nanoparticles. Samples CAO4-11 showed the narrowest hydrodynamic diameter distributions consistent with the high grafting density determined for each of the samples (table 6.1). However, it is interesting to note that the hydrodynamic diameter of the samples produced with the longest residence time were the least disperse suggesting agglomeration of the samples has occurred which could be linked to the lower grafting density discussed earlier or an alteration in the mechanism of particle stabilisation due to longer hydrothermal treatment (discussed further later). It is worthwhile to note that the intensity of the distribution in this measurement is biased towards larger particles in the sample as scattering by particles is proportional to r^6 (r = particle radius) *i.e.* particles of *ca.* 10 nm scatter 10^5 fewer photons than particles of *ca.* 100 nm typically leading to under-representation of small particles in the calculated distribution which has been explained further in Chapter 2. Quoting the hydrodynamic diameter corrected to particle number yielded average sizes in each dispersion slightly larger than those obtained from diffraction and TEM as summarised in table 6.1. Nonetheless it is reasoned that the smaller nanoparticles represented the majority of the sample by mass on the basis of the high citric acid grafting densities calculated for each of the samples and direct observation of particles using TEM (Figure 6.5).

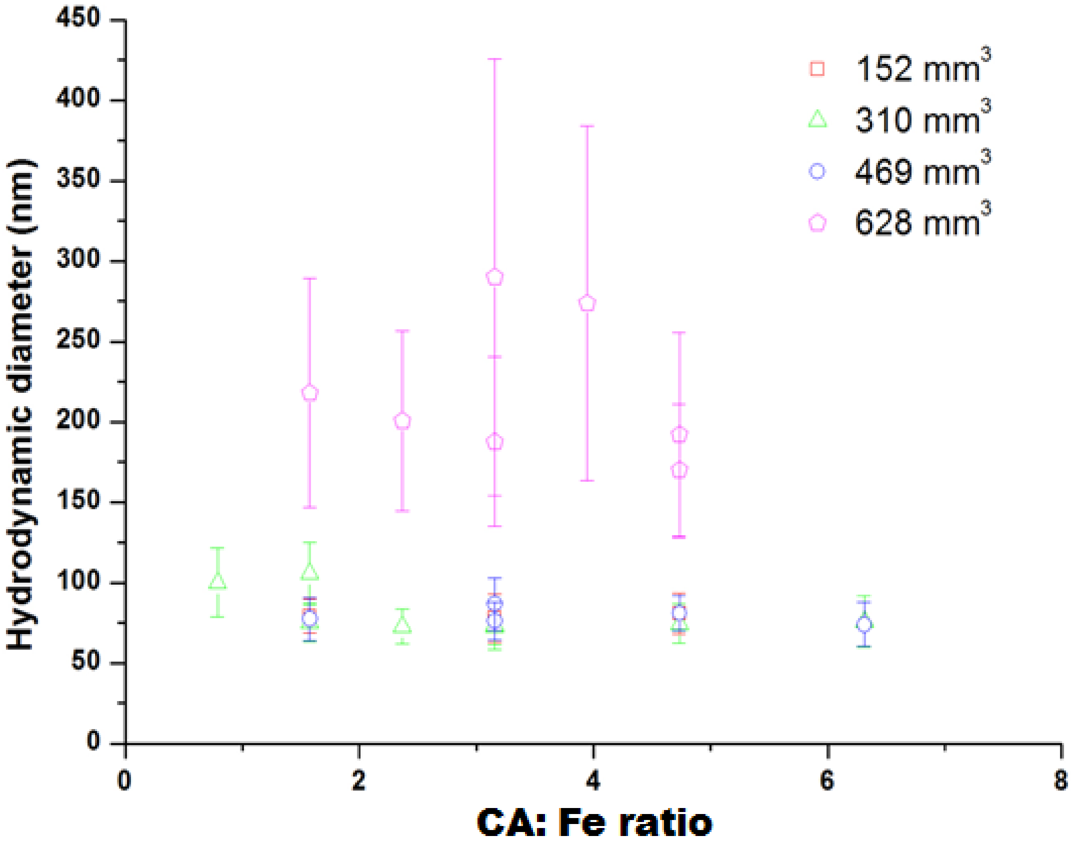

Figure 6.11: Grouped DLS data showing the difference in hydrodynamic diameter of samples CAO1-24, the z-average hydrodynamic diameter is plotted as a function of the relative CA:Fe ratio used in synthesis and the reaction point volume post citric acid addition (error bars represent the sample polydispersity in nm).

The electrophoretic properties of iron oxide nanoparticles produced using CHFS in reactions CAO1-24 were investigated by zeta-potential measurements as a function of pH (figure 6.12). From the measurements presented in figure 6.12 a reduction in the magnitude of the surface charge is observed at pH 6 suggesting suppression of the dissociation of the weakest acid group of citric acid and suspension stability is conferred through an electrostatic mechanism. The reported pKa values of CA as a tricarboxylic acid are pKa_1 = 3.13, pKa_2 = 4.76 and pKa_3 = 6.40. The zeta-potential of samples which showed CA grafting densities of >1 CA / nm^2 showed titrations characteristic of the protonation and deprotonation of free acid groups on the surfaces of the particles (samples CAO1 - 3 and CAO12 - 24). The magnitude of the Zeta-potential followed the trend of grafting density, as samples CAO4-11 showed the largest negative surface charge. These results suggest the weakest acid remains free and binding to the surface of the particle occurs through the strongest acid groups consistent with many other reports in the literature. (Mudunkotuwa & Grassian 2010) The liability of the different acid groups of citric acid to decarboxylation as reported by Shock *et al.* suggest that the acid group with a pKa of 4.76 is the most labile and de-carboxylates preferentially, possibly providing an explanation for the similarity in surface charge even in samples which showed a reduction in grafting density attributed to thermal decomposition. (Shock 1993; Shock and Helgeson 1988) The similarity in the magnitude of the zeta-potential measured for samples CAO 15, 16, 21 and 22 is consistent with the decarboxylation proposed by Carlsson *et al*. where the free carboxlic acid group present in the sample is the same as that observed for samples showing a high-citric acid grafting density with an apparent pKa of *ca.* 6.40. (Carlsson *et al.*, 1994) The surface charge observed for samples showing low CA grafting densities (Samples CAO2-5) can be attributed to the amphoteric behaviour of magnetite, which can develop surface charge in the protonation ($Fe\text{-}OH + H^+ \rightarrow Fe\text{-}OH_2^+$) and deprotonation ($Fe\text{-}OH \rightarrow Fe\text{-}O^- + H^+$) reactions of Fe-OH sites. The IEP (iso-electric point) of magnetite is often quoted at pH 7-8 for both bulk and nanosized variants as evaluated by others. (Illes & Tombacz 2006) In this work, only slight amphoteric behaviour (observed as a smooth transition in the zeta-potential) was observed principally due to the presence of citrates in all samples (table 6.1). With all samples showing CA grafting densities >1 CA / nm^2 yielding dispersions which are electrostatically stabilised and characterised as stable as values of > 30 mV are indicative of stable dispersions. (Illes & Tombacz 2006)

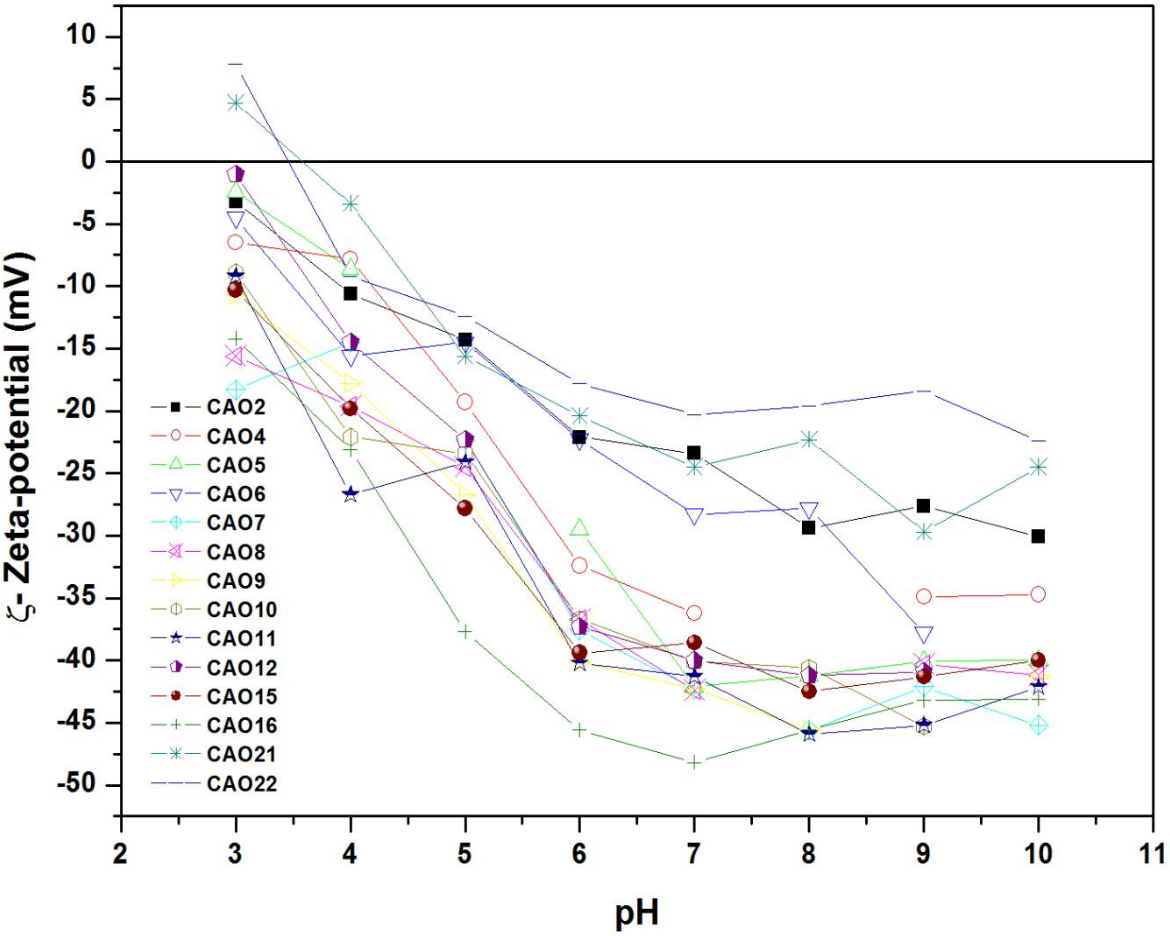

Figure 6.12: Zeta-potential titrations of CAO samples (measurement standard deviations were typically *ca.* ±3 mV and have been omitted for clarity).

6.3.2 The Effect of High Flow Regimes on Surface Functionalisation:

To further assess the effects of processing condition on surface functionalisation in the modified CHFS process materials produced under a high flow regime ($Q_{sw} + Q_p = 35$ mL min^{-1}) similar to that used initially for the synthesis of magnetite nanoparticles in Chapter 5 were compared to those obtained in samples CAO1 - 22 ($Q_{sw} + Q_p = 15$). Under a higher flow regime a different optimisation condition was observed. Detailed characterisation data for the samples described in this section is presented in Appendix 1 and tabulated in table A1.2. Samples presented in this section are identified by the series HCAO1-12.

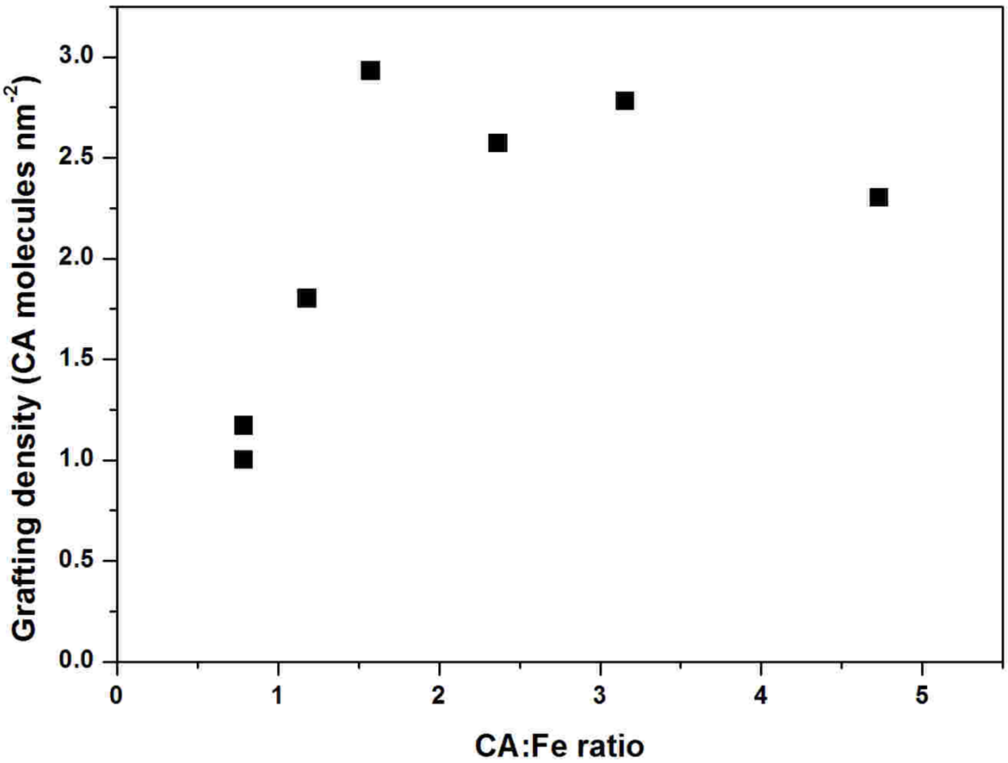

Figure 6.13: Variation in the calculated citric acid grafting density obtained for samples HCAO1-12 plotted as a function of CA:Fe ratio used in synthesis.

XRD patterns of the materials produced in runs HCAO1-10 suggest that all products are well crystallised and have a cubic inverse spinel structure (space group Fd3m) known for bulk magnetite and maghemite (ICDS 082234 and ICDS 79196), respectively (Appendix 1). TEM images of selected samples produced in the series HCAO1-12 are shown in Appendix 1 figure A1.2 showing similar degrees of dispersion as shown in figure 6.5. The crystallite size measured for samples HCAO1-12 (*ca.* 5.6 - 10.4 nm) was smaller than those observed for materials produced in runs CAO1-24 (*ca.* 11 - 15 nm). The reduced crystallite size produced in these reactions is tentatively attributed to latent process variation. However, correspondingly greater weight loss attributed to the thermal decomposition of organic species was measured in TGA, which ultimately yielded saturation grafting densities of *ca.* 2.6 - 2.9 CA / nm^2 consistent with the saturation grafting density calculated for samples CAO4 - 12. Figure 6.13 shows the variation in citric acid grafting density calculated using equation 6.1 plotted as a function of CA:Fe ratio used in each synthesis. It can be seen from Figure 6.13 that saturation of the particle surface occurred at a CA:Fe ratio of *ca.* 1.8 and the grafting density appeared proportional to CA:Fe ratio below this value indicative of a diffusion limit to functionalisation in this process. The calculated residence time post synthesis addition was lower (*ca.* 1.87 - 2.20 s) than the optimum residence time observed in the low flow regime (*ca.* 4.42 - 5.21 s). Achieving similar CA grafting densities at shorter residence times, suggests differences in the degree of mixing between Q_{sw} + Q_p (containing the nascent nanoparticles) and Qq (citric acid feed) which in a lower flow rate limited the rate of citrate diffusion to the nascent particle surface. FTIR confirmed the presence of citric acid in this sample series and yielded wavenumber separation between the (ν_s) COO^- (*ca.* 1390) and the (ν_{as}) COO^- (*ca.* 1569) values of 190 and 220 cm^{-1} suggesting a mixture of both mono-dentate and bridging coordination with the particle surface as inferred for samples CAO1 - 24. Hydrodynamic diameters measured using DLS are presented in Appendix 1, and showed similar dispersion properties to those presented in figure 6.11 and were shown to be consistent with the grafting density determined for each of the samples. Zeta-potential measurements characterised the samples showing CA grafting densities > 1 CA / nm^2 as stable dispersions with magnitudes > - 30 mV similar to those presented for samples CAO4-12. Titration of this sample series confirmed an electrostatic mechanism of particle stabilisation, a reduction in the magnitude of the samples zeta-potential around pH 6 further suggests a similar co-ordination of citric acid to the particle surface.

6.3.3 Proposed Mechanism of Surface Functionalisation:

As the density of citric acid was shown to vary with flow regime chosen for synthesis. In samples CAO1-24 (Q_{sw} + Q_p =15) estimated residence times post CA addition of *ca.* 5 s were required to achieve saturation of the particle surface. However, at a higher flow regime (Q_{sw} + Q_p =35) residence times of *ca.* 2 s were shown to give products with equivalent CA grafting densities when the CA:Fe ratio used in synthesis > 4 suggesting the degree of functionalisation was governed by diffusion of CA to the nascent particle surface and was likely linked to mixing between the component streams. In the stated flow regime the mixture issuing from the reaction point (defined by T_{mix1}) is a highly turbulent flow with a Reynolds number between 6.12 x 10^4 (Q_{sw} + Q_p = 15) and 11.23 x 10^4 (Q_{sw} + Q_p = 35) with corresponding Fr^2 of 100 and 160 being a momentum driven flow. Mixing of the feed containing nascent nanoparticles and the feed containing citric acid is likely to be complex due to; **1)** the density difference between the feeds (*ca.* 280 kg m^{-3} ($T_{mix\ 1}$) and 1002 kg m^{-3} (Q_q) **2)** the differences in flow velocity attributed to the difference in density and the mass flow rate. However, an estimation of the flow type occurring in the system under the different flow conditions suggested the mixture after the addition of citric acid (Q_q) was a turbulent flow in the high flow regime (Re = 3.4 - 4.5 x 10^4 (Qq = 10 - 40 mL min^{-1}) if the mixture is assumed to be at T_{mix2}, whereas in the low flow regime Re = 1.9 - 2.6 x 10^4 (Qq= 10 - 40 mL min^{-1}) suggesting a transient flow. This analysis would offer a straight forward interpretation if surface functionalisation was linked to mixing at high temperature and thus diffusion of CA to the particle surface as in a turbulent flow diffusion of CA to the particle surface would be enhanced yielding more rapid saturation of the particle surface.

To confirm if differences in flow regimes were responsible for the variation in grafting density *in-situ* temperature measurements were used to establish the extent of mixing between the component streams as a function of $Q_{sw} + Q_p$ and Qq. The relative placement of thermocouples is represented graphically in Figure 5.14. The temperature profiles measured are presented in figures 5.14b and 5.14c for flow regimes of $Q_{sw}+Q_p$ = 35 and $Q_{sw} + Q_p$ = 15 with a variable Q_q as 30 s time averaged temperature measurements. It should be noted that significant noise was recorded in the measurements suggesting the mixing process is not in a steady state. Figure 5.16 clearly shows that the introduction of a feed post nanoparticle formation results in complex mixing of the two feeds as the theoretical mixture temperature as an average was not met in any flow condition. However, one interesting feature of the data is the degree to which the cold water feed penetrates into the stream of nascent particles and appears related to Q_q leading to a reduction in T_{mix1}. These results suggest a significant density difference between the incoming stream and the nascent stream provides an explanation as the significantly denser Q_q falls through the less dense stream of nanoparticles. To confirm that the discrepancy in temperature did not arise as the result of heat loss a slow response thermocouple (of greater thermal mass) just before the cooling apparatus gave measurements of temperature within 5 -10 °C of those expected from enthalpy balance further suggesting the system is not steady state and that some phase separation in the mixture is possible and averages over a longer time period (data not shown). These measurements suggest the analysis of different flow types based on T_{mix2} determined from enthalpy balance may not be locally correct throughout the geometry. Although, characterisation data supports a diffusion limit to grafting density further process evaluation using this methodology was inconclusive.

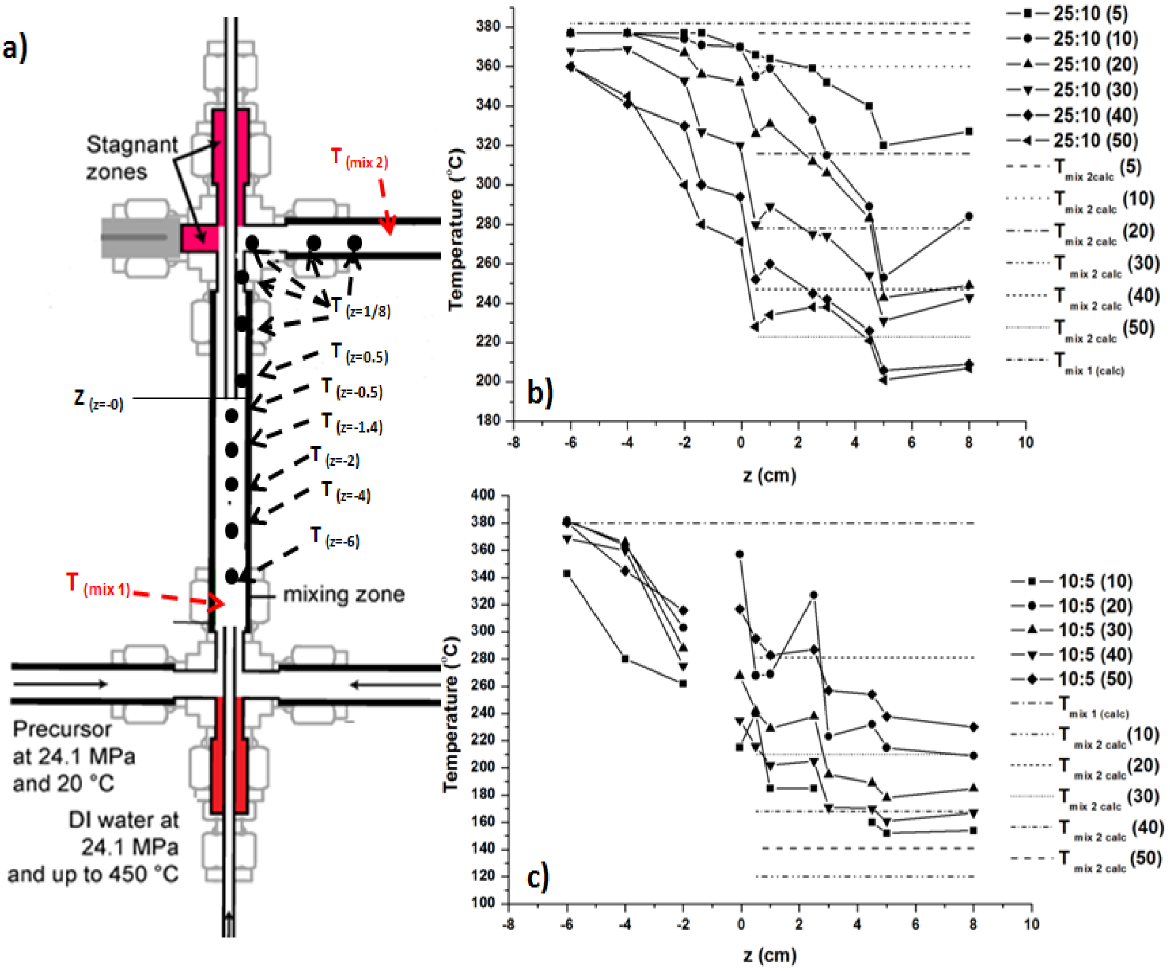

Figure 6.14: *In-situ* temperature measurement representing the mixing of Q_{sw} + Q_p and Q_q **a)** Schematic showing the relative placement of thermocouples, **b)** Temperature measurements for the reaction point operated at $Q_{sw}+Q_p = 35$ and **c)** Temperature measurements for the reaction point operated at $Q_{sw}+Q_p = 15$. Dashed lines represent the temperature determined by overall enthalpy balance.

A number of authors have investigated the adsorption of carboxylic acids to the surface of metal oxide nanoparticles in ambient aqueous dispersion, including Hematite (α-Fe_2O_3), (Hwang and Lenhart 2008; Kirwan, Fawell, & van Bronswijk 2003) magnetite (Fe_3O_4), (Kundu *et al.*, 2006) titania (TiO_2).(Mudunkotuwa & Grassian 2010) Typically, citric acid coating protocols presented in the literature suggest adsorption of the citrate tri-ion occurs when the surface of the substrate is positively charged (*i.e.* at low pH for an amphoteric metal oxide). (Illes & Tombacz 2006; Mudunkotuwa & Grassian 2010) It should be noted that Mudunkotuwa and Grassian and Pettibone *et al.* found differences in the affinity constants of citric acid to the surface of TiO_2 nanoparticles which were heavily dependent upon the pH of the suspension and in the case of the CHFS process presented here it is not beyond reasonable doubt that differences in citric acid affinity to the particle surface varied across the reaction conditions presented and observation of this was beyond the resolution of sample characterisation. (Mudunkotuwa & Grassian 2010; Pettibone *et al.,* 2008) It is assumed that under the hydrothermal conditions used for the production of carboxylic acid functionalised magnetite, speciation of citrate would lead to the formation of the Citrate ($^{3-}$) ion as indicated by the work of Shock *et.al*. and coordination occurs through the strongest acid groups as inferred from the pH dependent charge state of the samples surface. (Shock *et al.,* 1989) Although the results presented here suggest a diffusion limitation to the efficacy of capping, the pH of the dispersion could play a significant role although from experimental limitation, this could not be assessed further.

6.3.4 Magnetic Properties of Citric acid Coated Nanomaterials:

As the co-ordination of functional groups to the surface of magnetic nanomaterials is well known to alter the magnetic fine structure of a material it is important to characterise the effects of capping agent grafting. (Itoh and Sugimoto 2003; Sahoo *et al.,* 2005) Materials which showed slight variance in citric acid grafting density were evaluated to identify the effects of citric acid grafting on the magnetic properties of the material. As presented in Appendix 1 the magnetic and physiochemical properties of magnetite were shown to be largely invariant of Q_q and residence time at T_{mix1}. MH measurements performed on samples CAO4 – 11 (showing citric acid grafting densities ranging from 1.37 - 2.50) are presented in figure 6.15a. All samples showed superparamagnetic behaviour at 300 K and low coercivity values of between 0.5 - 1.6 Oe (figure 6.15a inset) consistent with what would be expected in light of the structural characterisation of these materials (table 6.1). The MH data showed a slight reduction in the saturation magnetisation as a function of increasing CA grafting density. Correspondingly, calculation of the effective ferromagnetic diameter (as detailed in Chapter 2) also showed a slight trend of decreasing ferromagnetic diameter on increasing CA grafting density (figure 6.15b). Similarly, the paramagnetic contribution in the calculation of ferromagnetic diameter was shown to increase (in all cases) from 1.05 - 1.97 x10^{-5} (a.u) when the grafting density increased from 1.37 - 2.50 CA/ nm^2 suggesting a proportional increase in a non-ferromagnetic phase. Carboxylic acids bound to the surface of magnetic nanoparticles are known to induce spin canting inducing disorder in Fe 3d spins due to chelation type bonding and this often results in a reduction in the net magnetic moment of the particle. (Daou *et al.,* 2008) The observed reduction presented here *ca.* 5 - 10 emu g^{-1} when compared to the highest saturation magnetisation produced for magnetite under partial reaction quenching (Appendix 1) are similar to the reduction published previously *ca.* 5 - 7 emu g^{-1}. (Itoh & Sugimoto 2003) However, this observed trend was well within the bounds of magnetic polydispersity observed in samples produced using CHFS (discussed later).

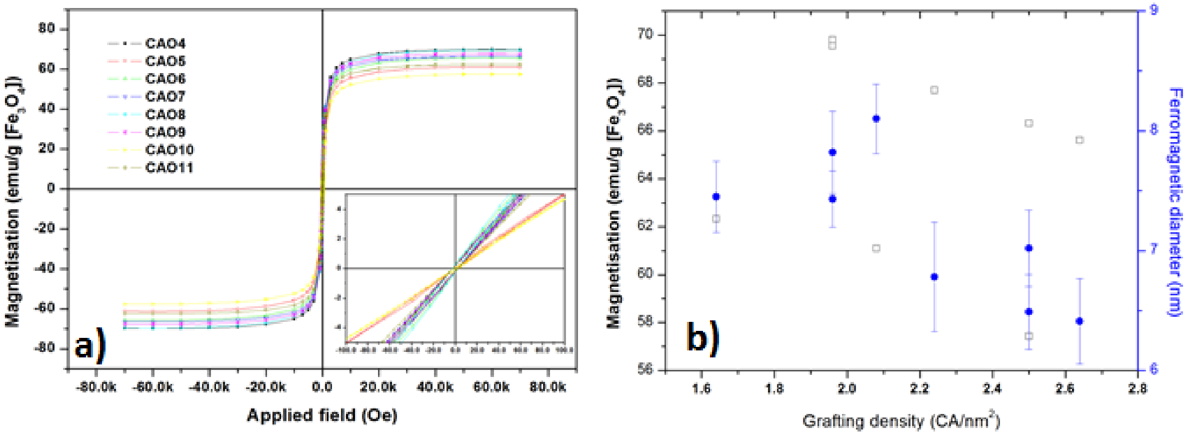

Figure 6.15: a) MH curves of citric acid coated magnetite produced using CHFS showing different citric acid grafting densities; inset shows an expanded plot of the near 0 Oe region. **b)** Variation in saturation magnetisation (squares) and ferromagnetic diameter (circles) as a function of calculated citric acid grafting density.

To further assess the contribution of citric acid on the magnetic properties of the material. The temperature dependence of Ms was measured at 5 and 300 K for sample CAO7 as shown in Figure 6.16. The increase in M_s below 5 k can be attributed to the presence of abhorrent spins which undergo a magnetic transition to a frozen state increasing the measured value of M_s. (Koksharov *et al.*, 2000) Similarly, the increase in coercive field at 5 K measured as 25 Oe whereas at 300 K a value of 0.4 Oe reported is consistent with the sample behaving as a ferromagnetic at lower temperatures. (Nogues *et al.*, 2005) ZFC / FC measurements performed on the sample are shown in figure 6.16.b and show an increase in sample magnetisation in the FC condition with decreasing temperature indicative of magnetic moments transitioning to a frozen state over a distribution of temperatures, which is consistent with the observations noted in chapter 5 on the low temperature magnetic behaviour of magnetite produced using CHFS. In the ZFC condition the lack of distinct magnetic transitions is consistent with a wide distribution of energy barriers within the sample and is typically referred to as a distribution of magnetic frustration which can originate from many sources (spin disorder, anti-phase boundaries, spin canting or spin glass transitions) which is further emphasised by the single crystal structure of the particles identified using HRTEM and shown in figure 6.6. (Nogues *et al.*, 2005) As initially highlighted in Chapter 5, the positive magnetisation values observed in the ZFC and FC is the fingerprint of exchange bias, a phenomenon that takes place at interfaces between different magnetic phases and again suggests a distribution of magnetic phases (in intimate contact) within the particles (*e.g.* ferromagnetic-antiferromagnetic but also ferromagnetic- ferri-magnetic, ferri-magnetic-antiferromagnetic, etc). (Iglesias *et al.*, 2008; Levy *et al.*, 2011) The presented measurements suggest that the crystallites in this sample (CAO7) are magnetically complex structures and show magnetic properties very similar to those initially discussed in Chapter 5. As carboxylic acids bound to the surface of magnetic nanoparticles are known to induce spin disorder on association with Fe 3d electrons of the surface iron atoms. (Leslie-Pelecky and Rieke 1996) This surface disorder would be observed as a slight broadening of the blocking temperature or transition from superparamagnetic to ferromagnetic state (normally observed at *ca.* 10 - 40 K in magnetite) and a slight increase in M_s below this temperature. The magnetic complexity of the sample effectively masks the observation of these effects making any inference about the finite effects of grafting tenuous. (Koksharov *et al.*, 2000)

Further analysis of the magnetic properties of samples produced at higher flow rates, which showed slightly smaller crystallite sizes as determined by TEM (samples HCAO5, 6 and 7) are presented in Appendix 1. As anticipated these samples showed coercivity values of between 0.1 - 1.2 Oe showing superparamagnetic behaviour at 300 K. However, in this sample series lower values of M_s were measured than those observed for samples CAO4 - 11 with values of 45.3, 53.1 and 47.6 emu g^{-1}, respectively. The measured values correlated well with the CA grafting density determined for each of the samples 1.0, 2.93 and 2.57 CA / nm^2 consistent with the observation made in samples CAO4-11. The reduced saturation magnetisation of this sample series can be attributed principally to the reduction in crystallite size as determined by TEM and XRD (Appendix 1). Several studies suggest that the lower magnetic saturation values for smaller Fe_3O_4 nanoparticles are caused either by increasing spin-disorder effects at the particle surface or by the existence of canted spins if the particle is sufficiently small (*ca.* > 10 nm). In either case this would yield a lower magnetisation. (Chatterjee *et al.*, 2003; Sugiyama *et al.*, 1997) ZFC - FC measurements performed on sample HCAO6 showed coercive field at 5 K of 35 Oe whereas at 300 K, a value of 0.8 Oe was recorded yielding similar observations to those discussed for sample CAO7 and discussed further in Chapter 5.

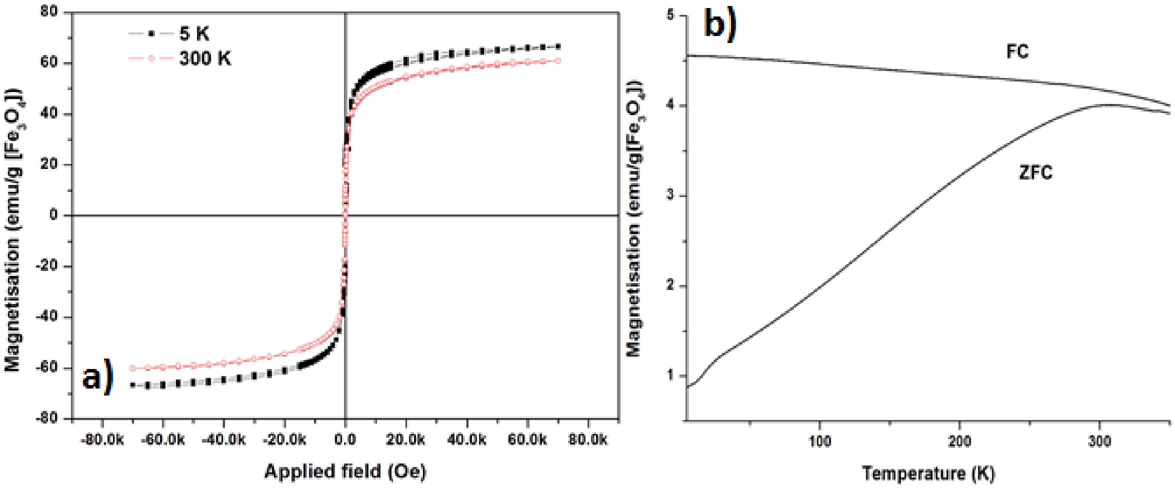

Figure 6.16: a) Comparison of magnetisation magnetization curves measured at 10 K and 300 K, **b)** FC and ZFC curves under an applied field of 100 Oe.

6.3.5 Evaluation of Materials for Magnetic Hyperthermia:

As stated earlier within this chapter, localised heat generation under the stimulation of an alternating magnetic field using nanoparticles as mediators is of interest in a variety of biomedical and other applications. (Gupta and Gupta 2005) To evaluate the efficiency of the citrate coated iron oxide nanoparticles produced using CHFS as mediators for therapeutic hyperthermia, their SLP (specific loss power) was measured. This was expressed in Watts per iron oxide unit mass (g), in a magnetic field of 6.664 kA m^{-1} oscillating at a frequency of 1.05 MHz. As only a single magnetic field strength and frequency were investigated the SLP was converted to ILP (intrinsic loss power) expressed in nH kg m^{-2} as detailed within Chapter 2 to allow a broader comparison to published materials. (Kallumadil *et al.*, 2009) The evolution of heat from a magnetic particle under the influence of an AC magnetic is heavily dependent upon the size and magnetic characteristics of the materials under actuation by the AC field (crystallite polydispersity, particle shape, crystalinity, the presence of defects and cation vacancies) as detailed earlier. (Gazeau *et al.*, 2008; Gonzales-Weimuller *et al.*, 2009) Where, the evolution of heat from ferro or ferrimagnetic (multi domain) particles arises through hysteretic loss. However, in superparamagnetic nanoparticles loss occurs through either Brownian (physical rotation of the particle and heat is generated through friction) or Neel relaxation (where heat loss occurs through the re-orientation of magnetic moments to their equilibrium state). (Zhang *et al.*, 2010) In the case of the nanoparticles presented in this section heat loss is likely to be almost exclusively generated by the latter mechanism. In this section the synthesis and evaluation of 100 samples produced at varying processes conditions as mediators for magnetic hyperthermia is presented. The synthesis details and characterisation data of which are presented in Appendix 1. All samples assessed in this section formed stable magnetically actuable fluids at particle concentration of 50 mg mL^{-1}. All samples were prepared for measurement using the procedure highlighted in section 6.2.4, the reproducibility of the calorimetric measurements used for the calculation of ILP showed high internal reliability (data not shown).

Despite our best attempts, large variations in the performance of magnetic iron oxides produced using CHFS were observed. However, a preliminary characterisation of the materials from XRD yielded a slight correlation with crystallite size determined from the application of the Scherer equation to the diffraction data (figure 6.17a). Similarly, figure 6.17b shows a moderate correlation with increasing residence time (RT1) which superficially would indicate that sample crystalinity yields an increase in energy yield. Although as shown in figures 6.17a and b, there appeared to be significant variance in both trends. To clarify the correlations simple regression analysis was used to assess if any one synthesis variable could be used as a predictor for the performance of the material. The products of Pearson correlation coefficients between ILP, crystallite size (volume weighted mean) and residence time (RT1) [inferring an increase in material crystalinity] are summarised in table 6.2 as these are likely the most influential characteristics of hyperthermia performance (regressions were performed using SPSS). From this analysis, moderate and positive correlations between crystallite size, residence time and ILP were recorded with all factors showing statistical significance. It is well known in the academic literature that there is an optimal size for maximum heat generation in magnetite nanoparticles which is centred at *ca.* 12 nm for a perfect dispersion of nanoparticles. (Hergt *et al.*, 1998; Rosensweig 2002a) Similarly, it is well know that even moderate crystallite polydispersity can significantly reduce the efficacy of the material for magnetic hyperthermia alongside a plethora of other factors as indicated in the introduction.(Hergt *et al.*, 1998) Although variance was observed in ILP, it is interesting to consider the difference in magnitude of the value of ILP when compared to that of materials (of similar size *ca.* 12 nm) reported in the literature. (Kallumadil *et al.*, 2009) The highest reported SAR values have been reported by Fortin *et al.* and Hergt *et al*. as 1650 W/g (H = 24.8 kA m^{-1}, f = 700 kHz) and 600 W/g (H = 11.2 kA m^{-1} , f = 410 kHz) respectively. Calculation of the ILP from the reported data resulted in ILP values of 3.8 and 11.7 nHm^2 kg^{-1}, respectively which are significantly greater than the values of any sample prepared using CHFS. The reports by Herght *et al.* and Fortin *et al.* described mediators which characteristics very similar to those reported for the samples produced by CHFS with an average crystallite size of 15.3 nm (σ_{fm} =15 nm). (Fortin *et al.*, 2007; Hergt *et al.*, 2004)

Table 6.2: Products of Pearson's correlation between ILP, crystallite size and residence time (RT1).

	ILP	Cs	RT
ILP	1.000	.646** .000	.511** .000
Cs		1.000	0.519** .000
RT1			1.000

** Correlation is significant at the $p < 0.01$ level (2-tailed). Cs is the volume weighted mean crystallite size determined from XRD and RT1 is the residence time (s) prior to the addition of citric acid.

To further investigate which material properties showed the largest influence on hyperthermia performance, a selection of materials was taken from the data shown in figure 6.17a. The samples chosen for further analysis are detailed in table 6.3 alongside relevant materials characterisation data. These samples were identified for comparison due to their similarity in dispersion (as assessed by DLS) and initially by the similarity in crystallite size as estimated by XRD data, and a near uniform spread of ILP values between 0.12 and 1.02 nH kg m^{-2}. To highlight the difference in heat generation figure 6.18 shows the raw calorimetric data recorded for the sample series presented in table 6.3.

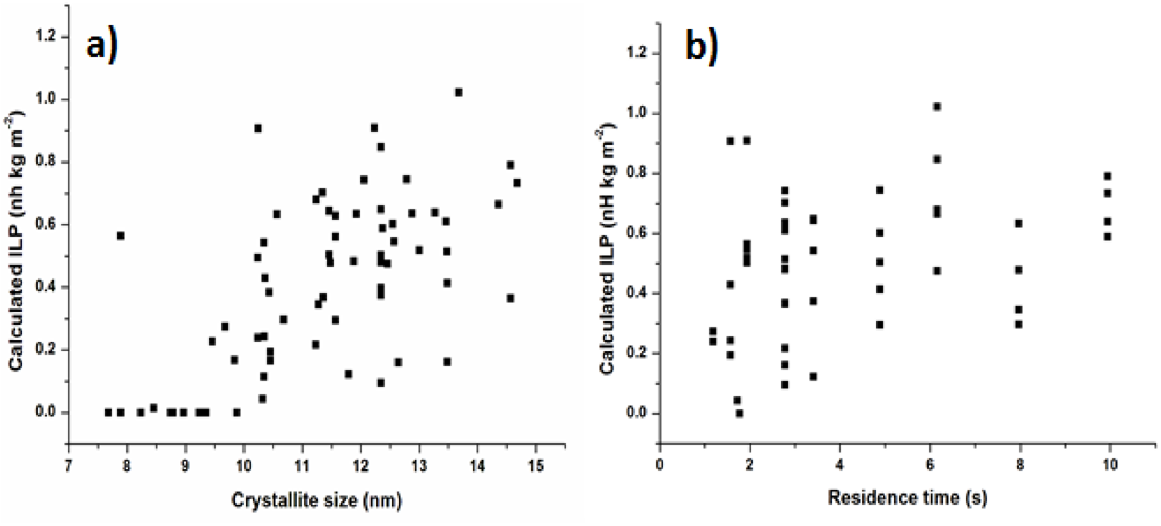

Figure 6.17: a) Correlations between the ILP of different ferrofluid samples and the volume weighted mean crystallite size determined from XRD, **b)** Correlations between ILP and residence time (RT1) used in the synthesis of all materials. **n.b.** the ILP values quoted for these samples have been calculated assuming no contribution to the sample mass from the capping agent, in all cases this would yield an underestimate of ILP of upto 15 %. Tablulated synthesis and characterisation data can be found in Appendix 1.

As summarised in table 6.3, the structural characterisation of the materials yielded results very similar to those initially reported for citric acid coated magnetite produced using CHFS. Consistent with the results of Section 6.3.2 and Chapter 5 there was no evidence of contaminating phases observed in any of the samples as inferred from the XRD data. The synthesis of highly crystalline materials was also inferred by the similarity in crystallite size determined from both application of the Scherrer equation (311 reflection) and the direct measurement of *ca.* 300 crystallites per sample by TEM, as summarised in table 6.3. Further characterisation of this sample series using DLS and TGA showed that materials with similar dispersion properties and citric acid grafting densities (determined using Equation 6.1) approaching the saturation value determined earlier within this Chapter. The polydispersity indices (PDI) for the hydrodynamic diameters of the samples chosen for further evaluation ranged from 0.12–0.25,which indicate low to moderate polydispersity within the samples which are also not significantly greater than the hydrodynamic polydispersity reported for commercially available ferrofluids measured using the same technique. (Kallumadil *et al.*, 2009)

Table 6.3: Synthesis and characterisation details of samples chosen to assess the effect of material characteristics on hyperthermia performance.

Sample	Q_{sw}:Q_p	Q_q	RT1 (S)	ILP (nH kg m^{-2})	XRD (nm)	TEM data (nm)		Magnetic properties				Dh nm (PDI)	TGA (%)	CA/nm^2
						Mean	SD	M_s	μ	σ	χ (x 10^{-5})			
MHO1	15:8	15	1.94	0.51	13.0	12.0	2.4	40.9	5.8	0.40	1.09	80.6 (0.138)	7.32	1.94
MHO2	15:8	20	1.94	0.90	12.2	12.7	2.7	42.0	5.9	0.38	1.13	79.27(0.179)	8.24	2.15
MHO3	10:5	15	2.78	0.36	11.3	11.4	2.8	43.3	4.8	0.44	1.24	77.9 (0.155)	6.58	2.55
MHO4	10:5	25	2.78	0.51	10.4	10.5	2.2	42.9	5.4	0.41	1.22	77.0 (0.169)	7.89	2.70
MHO5	15:8	15	3.41	0.12	11.7	13.6	3.4	51.5	4.6	0.47	1.63	75.99(0.210)	7.81	2.19
MHO6	15:8	20	3.41	0.54	10.3	13.7	3.2	50.7	5.9	0.38	1.48	76.56(0.193)	5.98	2.59
MHO7	10:5	15	4.89	0.50	11.4	15.6	4.6	46.6	6.1	0.33	1.65	75.8 (0.165)	8.32	2.04
MHO8	10:5	20	4.89	0.41	11.4	11.4	2.8	57.0	6.7	0.34	1.12	76.1 (0.154)	7.13	2.44
MHO9	10:5	15	6.15	0.66	10.3	10.8	2.5	43.6	5.7	0.41	1.14	74.46(0.162)	5.67	2.10
MHO10	10:5	20	6.15	1.02	11.5	12.8	3.3	40.4	6.0	0.38	1.05	73.4 (0.182)	4.59	2.14
MHO11	10:5	15	7.96	0.63	10.5	14.7	3.2	52.6	6.9	0.31	1.64	74.5 (0.194)	5.67	2.56
MHO12	10:5	20	7.96	0.29	10.6	16.1	3.8	58.9	6.4	0.30	1.43	74.5 (0.164)	5.9	2.43

Key: M_s = saturation magnetisation (emu g^{-1}), μ = effective ferromagnetic diameter (nm), σ = ferromagnetic diameter polydispersity (nm), χ = paramagnetic contribution on approach to magnetic saturation, Dh = hydrodynamic diameter (nm) measured using DLS, TGA = weight loss in the 200-500 °C region (attributed to the thermal decomposition of citric acid) and CA/nm^2 is the citric acid grafting density determined using Equation 6.1.

To further assess the variance within this sample series on both the low hyperthermia performance (when compared to materials showing similar structural characteristics) and the variance in heat generation the magnetic properties of the samples presented in table 6.3 were measured at 300 K (figure 6.19 a). Consistent with the structural charcterisation of these materials presented in table 6.3, all samples showed superparamagnetic behaviour at 300 K. All data from the magnetic measurements is summarised in table 6.3. From the characterisation of magnetic properties a slight trend emerged between the ferromagnetic diameter, $M_{s,}$ μ and χ as a function of ILP (using the magnetic fitting procedure detailed in Chapter 2). This variation is presented graphically in figure 6.19 a. Where, a slight increase in ILP was observed with increasing ferromagnetic diameter and decreasing paramagnetic contribution (figure 6.19b). As the heating power of these nanoparticles was far below the expected value due to a clear discrepancy between the physical crystal size (table 6.3) and the effective magnetic volume it can be interpreted that these particles behave in a manner indicative of smaller particles (*i.e.* particles of a much smaller physical size displaying ideal magnetic properties). (Levy *et al.*, 2011) As initially identified in Chapter 5 and observed again in this Chapter, magnetic disorder was particularly evident for magnetic nanoparticles produced using CHFS, and has been attributed to magnetic complexity in the sample (Section 6.3.3). As a consequence, the effective magnetic volumes of the particles were significantly reduced as well as their magnetic polydispersity dispersions enlarged (represented by σ in table 6.3) forming a likely explanation for the lower than expected hyperthermia performance. (Levy *et al.*, 2008; Levy *et al.*, 2011)

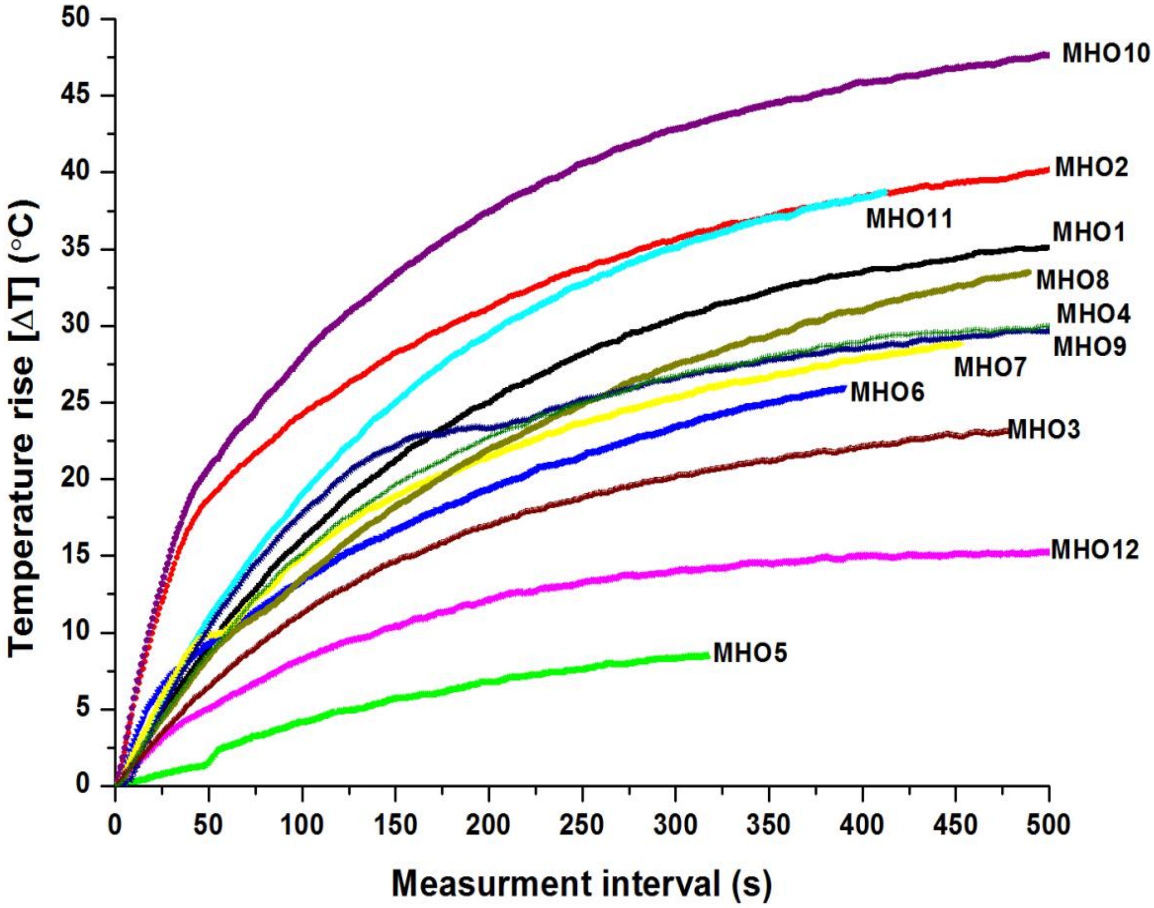

Figure 6.18: A sample of the calorimentric data recorded for ferrofluid samples presented in table 6.3 using a magnetic field strength of 6.664 kA m^{-1} and a frequency of 1.05 MHz. From which the SAR and corresponding ILP values were calculated using a corrected M_{fe} value. (samples are identified in table 6.3).

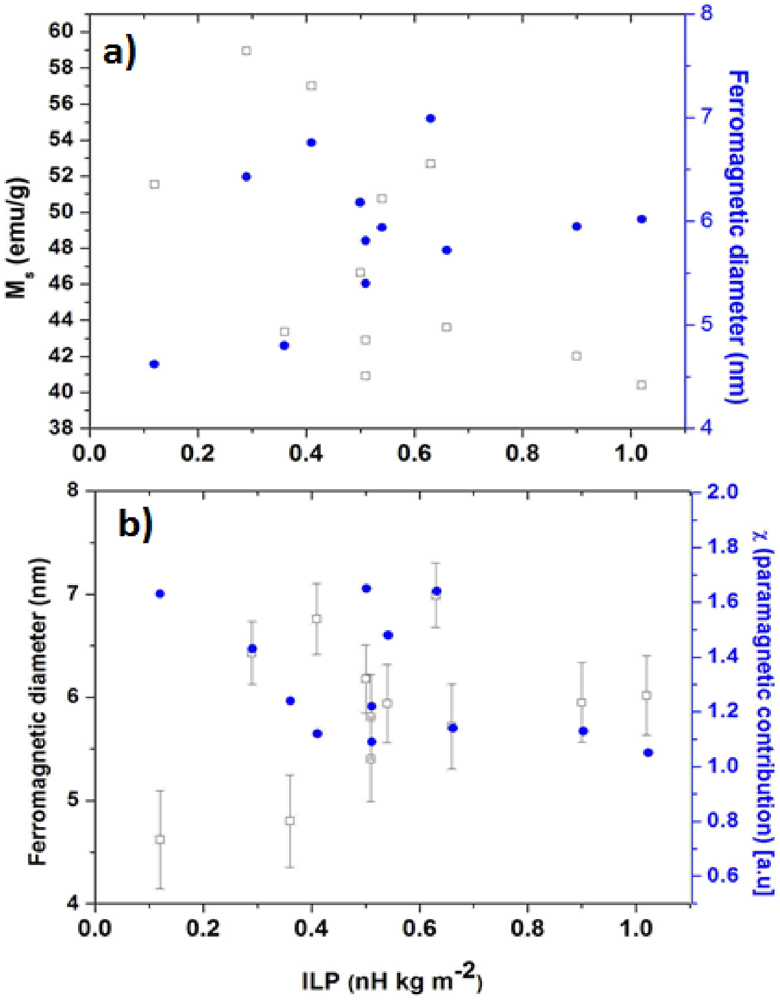

Figure 6.19: a) correlations between Ms and effective ferromagnetic diameter plotted against measured ILP and **b)** Correlations between effective ferromagnetic diameter and the contribution of paramagnetic like susceptibility in the samples plotted against ILP.

From figures 6.19a and b it is still implied that other factors relating to the sample may also contribute to the variation in hyperthermia performance as the slight trend in increasing hyperthermia performance with crystallite size is still rather ambiguous. As summarised in table 6.3 the variation in the effective magnetic particle size is comparatively small *ca.* 1.5 nm between the best mediator and the poorest. The theoretical work of Rosenweig and the experimental evaluation of Herght, suggest nanoparticles displaying magnetic polydispersity in the region of as little as 10 % could reduce the expected hyperthermia performance by upto 50 % and this has recently been shown experimentally, which could be a valid interpretation of this variance. (Levy *et al.*, 2011; Muller *et al.*, 2006; Rosensweig 2002) As such a much smaller investigation was performed to test the reproducibility of three discrete syntheses in CHFS. Figures 6.20

shows the variation of ILP from repeat syntheses conducted at various residence times RT1 = 1.94, 4.89 and 6.15 s. From these samples a selection of three samples produced at each residence time was further evaluated and a similar set of data generated to that presented for the broader study presented in Table 6.3. Run numbers 3, 6 and 9 (of figure 6.20) were evaluated for each residence time. As shown previously, these materials showed significant similarity in crystallite morphology and particle size as determined by TEM (*ca.* 300 particles measured). Interpretation of the MH curves of these samples by the magnetic fitting procedure detailed in Chapter 2 assuming *ca.* 7 % of the particle mass could be attributed to capping agent as shown in figure 6.21 b. This analysis suggested that although reasonable crystallite size reproducibility was obtained in each synthesis the magnetic frustration in the samples differed, plotted as a function of ILP (figure 6.21 b). In many regards the observations made for this sample series mirrored those described in table 6.3. This observation formed the basis of the brief discussion of capping agents and their effects on magnetite produced using CHFS (Section 6.3.4). For comparison, the crystallite size including the standard deviation determined for each of the samples (*ca.* 200 particles measured) is presented alongside the ferromagnetic diameter calculated from the MH data, suggesting further that polydispersity in the samples could be attributed to magnetic frustration rather than large differences in crystallite size figure 6.21 a.

This analysis showed that fine variation in the magnetic structure of the materials was the likely cases for the variation in hyperthermia performance, and this variation is likely to be intrinsic to CHFS due to the comparatively harsh and rapid reactions occurring at the point of particle nucleation. The variation in magnetic structure (*i.e.* magnetic disorder) inferred from this analysis could arise from many sources; spinel ferrite iron oxide nanoparticles can be found in the form of stoichiometric magnetite, cation deficient magnetite, maghnemite or a mixture with significant dependency on the size and synthesis protocol chosen. (Gonzales-Weimuller, Zeisberger, & Krishnan 2009) In the case of CHFS, rapid particle nucleation and growth suggest that the cation deficiency is the major cause of reduced ferromagnetic diameter and magnetic frustration. (Levy *et al.*, 2011) The presence of highly strained regions within the lattice of each crystallite as it accommodates defects could account for the discrepancies, in light of knowledge of the processing conditions used for synthesis. However, if it is assumed that crystallinity rather than structural disorder influenced the magnetic properties to a greater extent, one would assume a measurable increase proportional to residence time, as this was not observed even when RT1 was varied between 0.21 and 9.67 seconds, suggesting atomic vacancies reside within the lattice (and the variation in concentration of these vacancies) results in the moderated difference in magnetic frustration observed.

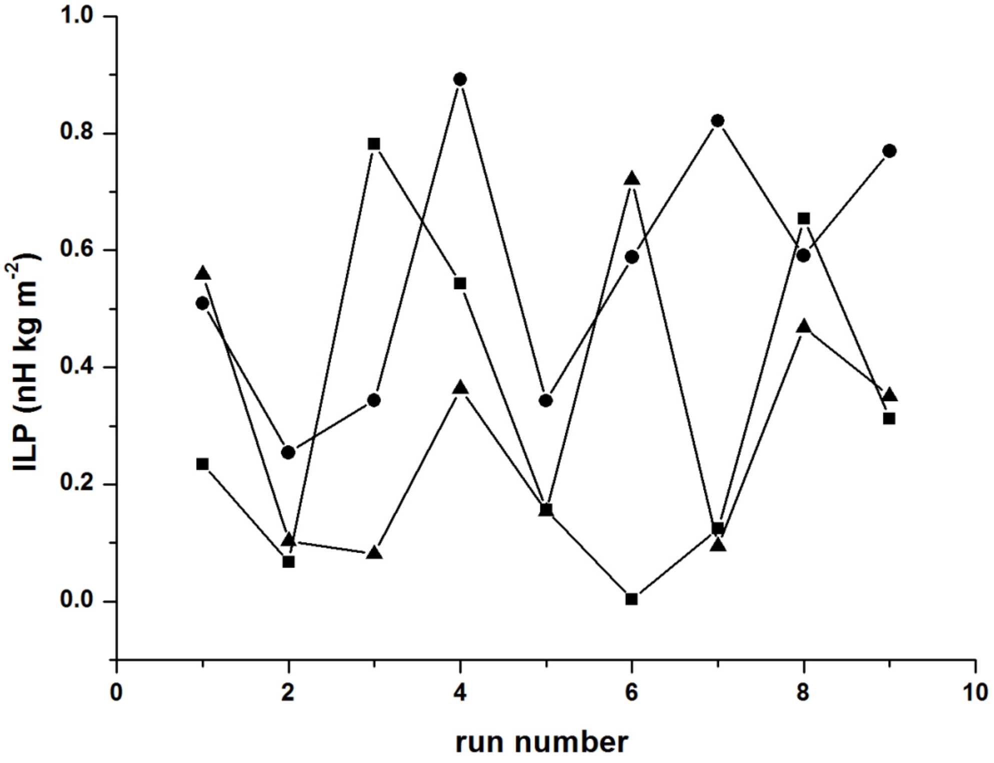

Figure 6.20: a) Plot of ILP variation from three discrete reaction conditions repeated 9 times at 3 different residence times. 1.94 s (triangles), 4.89s (circles) and 6.15 s (squares). The iron salt concentration was fixed at 0.066 M and a 1 wt% CA concentration under the following flow condition Q_{sw} = 10, Q_p = 5 and Q_q = 20 (*n.b.* these ILP values were corrected assuming a contribution of 7 wt % capping agent).

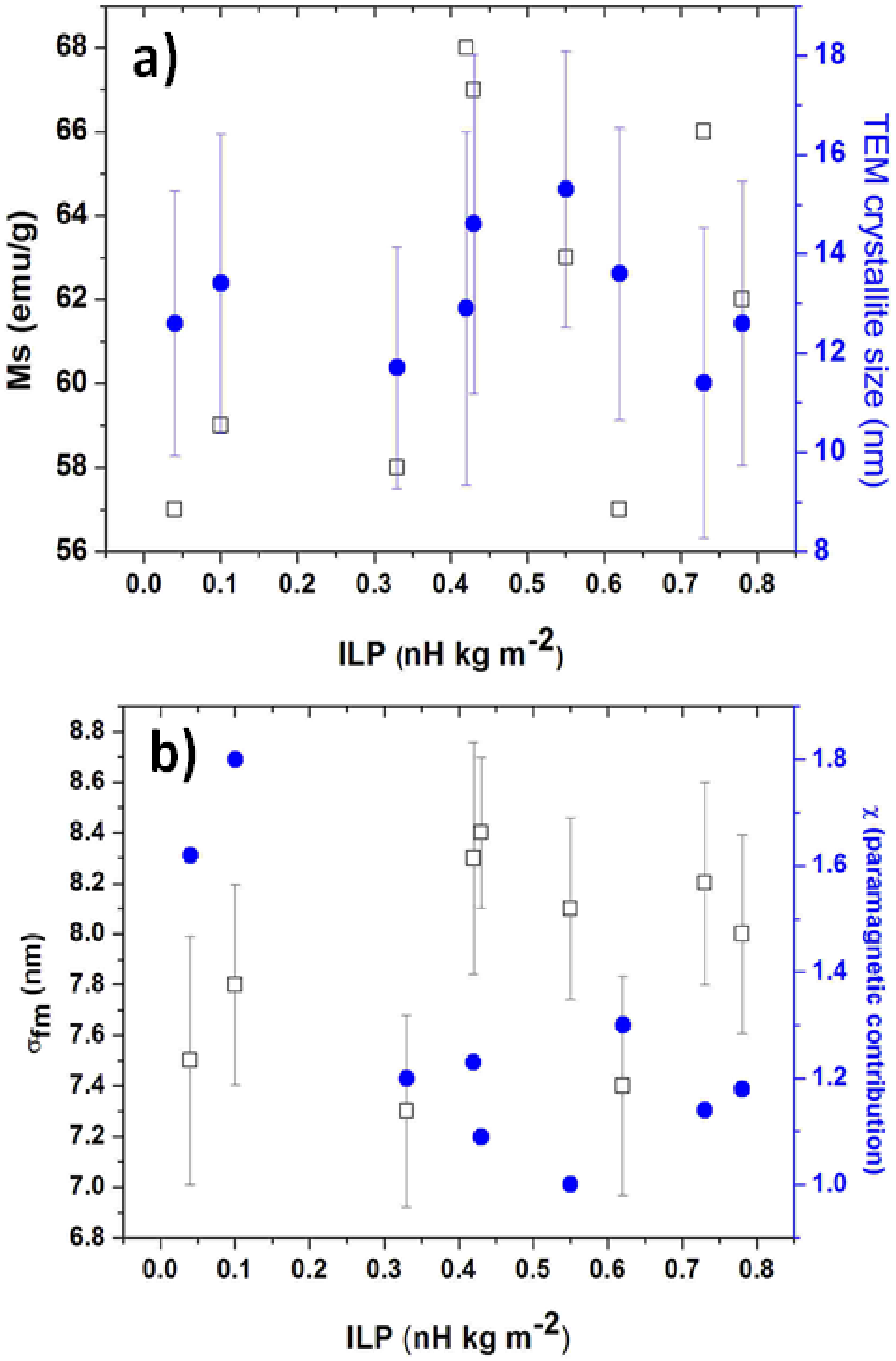

Figure 6.21: a) Plot showing the variation of Ms of the samples chosen from figure 6.20 and their crystallite size determined from TEM plotted against ILP, **b)** Results from magnetic fitting plotted against ILP for the same sample series.

6.4 Conclusions:

For the first time the successful modification of a CHFS flow reactor has been demonstrated, and allows for the introduction of a capping agent shortly after the formation of nanoparticles. The process was shown to be capable of producing nanomaterials which had a high grafting density of citric acid on the surface to confer a stabilising effect to the particles. Grafting citric acid to the surface of the nanoparticles yielded reasonable particle dispersions in light of the limitations of DLS. Zeta-potential measurements confirmed that the particles were stabilised by an electrostatic mechanism consistent with the deprotonation of the weakest reported acid group of citric acid and that consolidated nanoparticles formed stable ferrofluids. From FTIR, it was found that coordination of the acid to the particle surface occurred through a mixture of unidentate and bridging coordination with the particle surface. A complete process envelope was established by operating the reaction point at a variety of temperature and flow rate regimes, allowing the identification of regions where the process could be operated to allow for the direct synthesis of surface functionalised magnetite nanoparticles. A series of samples suggested that the mixing between the feed containing citric acid and the feed containing nascent nanoparticles was influential in determining the amount of capping agent adsorbed onto the particle surface. It was observed that in a low flow regime a much longer residence time post citric acid addition was required to achieve saturation of the particle surface. However, in a higher (“more turbulent”) flow regime grafting of citric acid occurred with higher efficiency. Characterisation of the products showed that the crystallite size of the nanomaterials was largely invariant of the processing conditions used and this observation suggested complete segregation of the particle formation and capping steps.

It was demonstrated that the crystallite size and the magnetic properties of the nanomaterials produced using partial reaction quenching to residence times of *ca.* 0.21 s were shown to have little effect on the size or magnetic properties of magnetite produced using CHFS (data shown in Appendix 1). These reactions showed the particle nucleation and growth phase in CHFS is rapid and that particle formation occurring where the precursors and preheated water meet can effectively be segregated from reactions occurring downstream of particle formation. As initially discussed in Chapter 5 the magnetic properties of the material were again shown to be affected by intrinsic process limitations and the magnetic frustration within the samples was attributed to lattice defects.

The investigation of magnetic nanoparticles produced using this methodology was disappointing because the process superficially yielded materials which satisfied many of the requirements for high energy conversion hyperthermia mediators. However, the large number of samples evaluated, allowed some discrimination amongst several structural and magnetic features and served to highlight the sensitivity of hyperthermia mediators to magnetic frustration. It is suggested that the rapid nature of the synthesis yields the magnetic frustration in these materials through the incorporation of atomic defects in the materials structure and may be inherent to the process.

6.5 Future work:

Principally, it would be of interest to assess the cytotoxicity of citric acid coated nanoparticles produced using the methodology presented herein. Similarly, it would be of interest to apply the processing methodology to materials of different compositions. The presence of a free acid group anchored to the nanoparticle surface could also be exploited for further surface functionalisation of the nanomaterials produced using this methodology which could broaden the application of these materials in the future. The use of simple post processing to further engineer the particle surface would be of interest as the methodology presented could find application as a method for the synthesis of a precursor nanomaterial which could be functionalised for application in many fields. It would be of interest to further assess and evaluate the reproducibility of magnetite synthesis specifically for application in magnetic hyperthermia. As shown in Appendix 1 and Section 6.3.4, comparatively small variation in the physiochemical characteristics of magnetite had a very large effect on the efficacy of the materials for hyperthermia (*i.e.* crystallite size and magnetic volume). It would be of interest to investigate the CHFS processing methodology presented herein as a solvothermal system in which an organic solvent is substituted for water, this would possible allow greater control over; **1)** the particle nucleation and growth steps, **2)** the choice of capping agent, and **3)** possibly the synthesis of quantum dot type materials in a flow process.

Chapter 7

The Continuous Hydrothermal Synthesis and Characterisation of ($Y_{0.96}Eu_{0.04}$) OOH Phosphor Nanoparticles for Cell Imaging Applications

7.0 Aim:

The aim of this chapter is to develop new routes for the production of visibly bright phosphor nanoparticles which can be formulated in aqueous dispersions. Phosphor nanoparticles may be produced with varying compositions, and are typically based on a host lattice doped with an activator atom (*i.e.* a lanthanide). Many efficient phosphor material compositions are obtained through high temperature processing, leading to significant increases in particle size through sintering of the precursor material. This chapter initially describes the use of CHFS to produce visibly bright ($Y_{1-x}Eu_x$) OOH nanoparticles directly. These materials are then evaluated as nanosized precursors for the synthesis of higher temperature phases through a flash heat treatment protocol to further dehydrate the product to form the corresponding metal oxide, whilst minimizing the effects of sintering. As the properties of phosphor nanoparticles are heavily influenced by surface effects, materials produced using a similar processing methodology to that presented in chapter 6 were used to assess the effects of surface functionlisation on this system. Similarly, further formulation of these nanoparticles for use in biological imaging was also evaluated.

7.1 Introduction:

Nanosized phosphor materials have a number of advantages over their bulk material counterparts, such as, ease of formulation into stable dispersions and higher packing densities for application as security inks. (Ronda *et al., 1*998) Nanosized phosphor materials often show reduced quantum efficiency when compared to their bulk material counterparts due to structural defects and apparent lower crystalinity limiting their application in many fields. (Tissue 1998) However, the luminescent characteristics and chemical stability of rare-earth-activated phosphors have attracted significant research interest as both a bulk and nanosized materials for emerging applications (*i.e.* as non-cadmium based biological imaging probes and security taggants). (Bruchez *et al.*, 1998)

A common dopant for the synthesis of nanoparticle phosphors is trivalent europium (Eu^{3+}) due to its broad UV excitation and strong red emission spectrum originating from ^5D_J (J =

0,1,2) → ^7F_J (J = 0,1,2,3) transitions. (Holsa *et al.*,1985a) Europium (Eu^{3+}) doped rare-earth oxides, oxysulfides, hydroxides, phosphates and fluorides have been investigated as possible alternatives to conventional fluorescent probes and many have been produced and evaluated as nanomaterials. (Bruchez *et al.*, 1998) The literature highlights lanthanide doped phosphor materials as having several advantages over both conventional organic molecular probes and functionalised quantum dots; including, high photochemical stability (non-blinking), narrow emission, low cytotoxicity and tunable emission. Therefore, significant research effort has been directed toward producing these materials as nanoparticles in a crystalline form. (Huignard *et al.*, 2000)

Phosphor nanoparticles have been synthesised by a number of both bottom up and top down strategies; solid state, sol-gel, gas phase/deposition methods, co-precipitation, alkali reduction and combustion/flame syntheses are all well represented in the literature. (Bruchez *et al.*, 1998; Buissette *et al.*, 2006; Hebbink *et al.*, 2002; Tissue 1998) Despite the promising prospect of lanthanide-doped nanoparticles in labelling and other applications, their widespread use is often limited by the lack of nanosized materials. (Tissue 1998) As many processing methods require high temperature and lengthy annealing to increase PL yield and quantum efficiency, many of the materials require significant post processing to formulate a nanosized material. (Buissette *et al.*, 2006) Similarly, particles from many synthetic processes are formed without any ligands on the surface and thus they have no dispersibility in solvents, which is a basic requirement for terminal application/evaluation of many phosphors as nanomaterials. (Bruchez *et al.*, 1998) Therefore, further refinement in the synthetic process is required to eliminate the need for high temperature annealing of as-prepared materials. However, some phosphor systems have been prepared as colloidal dispersions (without the requirement for high temperature annealing), several research groups have reported the synthesis of colloids based upon yttrium vanadate, lanthanum fluoride, and lanthanum phosphate nanoparticles doped with a variety of lanthanide (III) ions (e.g. Ce^{3+}, Tb^{3+}, Yt^{3+}, Eu^{3+} Er^{3+}, Nd^{3+}). (Haase *et al.*, 2000; Huignard, Gacoin, & Boilot 2000; Meyssamy *et al.*, 1999; Riwotzki and Haase 2001; Stouwdam *et al.*, 2005) However, many know phosphor compositions are not accessible using these synthesis methodologies as the reaction temperatures involved are not always sufficiently high to crystallise the desired product. (Tissue 1998)

Hydrothermal methods often require relatively lower synthesis temperatures to access complex oxides when compared to conventional methods (as reviewed in greater detail within Chapter 1). (Darr and Poliakoff 1999) As highlighted in Chapter 3 the short timescales and relatively high temperatures used in CHFS result in the rapid nucleation and growth of nanoparticles and the homogenous precipitation of component metal ions (desirable in the synthesis of phosphor materials). As such, a number of phosphor compositions have been produced as nanomaterials in batch hydrothermal reactors.(Choi et al. 2010;Hakuta et al. 2003;Li et al. 2009) More recently, Lin *et. al.* published work describing the automation of CHFS allowing the rapid synthesis and evaluation of $Y_{1-x}Eu_x(OH)_3$ [where, x = 0.05-0.30] nanoparticles as precursor solids for the production of $(Y_{1-x}Eu_x)_2O_3$ after heat treatment (200-1200°C, 6 hours). The work allowed the rapid optimisation of luminescence efficiency for the preparation method chosen. (Lin *et al.,* 2010) Other CHFS type methods have produced phosphor materials based on a YAG (Yttriun Aluminium Garnet), Europium doped YAG ($YAG:Eu^{3+}$) and Terbium doped YAG ($YAG:Tb^{3+}$). (Hakuta *et al.*, 1999; Hakuta *et al.*, 2003) In these reports, continuous tubular reactors (comprising of a pipe running through a heated zone) were used, which have been shown to produce nanomaterials with a much larger crystallite sizes than the embodiment of CHFS evaluated within this thesis.

This chapter describes the direct synthesis and characterisation of $(Y_{1-x}Eu_x)$ OOH phosphor nanoparticles using a continuous hydrothermal process. The materials have been characterised by XRD, TGA, TEM, BET, HREM, photoluminescence measurements and time resolved photoluminescence. An investigation into the moderate calcinations of $(Y_{1-x}Eu_x)$ OOH is also presented. Moreover, the method can be adapted as described in Chapter 6 to provide precursor materials which can be potentially be formulated into stable colloids for luminescent security inks and probes for biological imaging.

7.2 Materials and Methods:

7.2.1: Materials:

$Y(NO_3)_3{\cdot}6H_2O$, (99.99 %), Citric acid [$C_6H_8O_7$] (99 %), HCl (99 %), NaCl (99 %), NaOH (99 %) and H_2O_2 (30 % v/v) were supplied by Sigma-Aldrich Chemical Co. (Dorset, U.K.). $Eu(NO_3)_3{\cdot}6H_2O$ (99.99 %) was supplied by AMR Europe (Abingdon, U.K.). KOH (96 %) was supplied by VWR International (Leicestershire, U.K.). All experiments were conducted using deionized water (> 10 Mega Ohms).

7.2.2: Synthesis of $Y_{1-x}Eu_xOOH$ Nanoparticles

Table 6.1 summaries the reaction conditions used for the synthesis of phosphor samples. CHFS reactor 1, the same as that shown in Chapter 5 was used for the synthesis of all samples within this section. The three pump configuration was used for all reactions with the precursor solution being pumped equally by P2 and P3 (*i.e.* Q_p) to a desired flow rate meeting a feed of supercritical water (*i.e.* Q_{sw}) being supplied by P1. The metal salt solution containing $Eu(NO_3)_3 \cdot 6H_2O$ and $Y(NO_3)_3 \cdot 6H_2O$ were fed by pump 2 and all auxillary precursors were pumped by pump 3. The products of the presented experiments were recovered using the same method as that used for the consolidation of magnetite presented in Chapter 5.

Table 7.1: Details of Experimental Conditions and Products of Hydrothermal Flow Reactions

Run	**[Y] (M)**	**[Eu] (M)**	**H_2O_2 added (M)**	**Q_{sw}:Q_p**	**Product [XRD]**	**XRD (nm)**	**BET (m$_2$/g)**		**TEM**	
							(m^2/g)	**ED (nm)**	**Avg (nm)**	**SD**
1	0.048	0.002	0^1	25:10	$Y(OH)_3$ / YOOH	-	-	-	-	-
2	0.048	0.002	0^2	25:10	YOOH	35.7	-	-	-	-
3	0.048	0.002	0^3	25:10	YOOH	41.1	-	-	-	-
4	0.048	0.002	0^4	25:10	YOOH	31.5	-	-	-	-
5	0.048	0.002	0.2^2	25:10	YOOH	43.8	-	-	-	-
6	0.048	0.002	0.4^2	25:10	YOOH	46.5	-	-	-	-
7	0.048	0.002	0.6^2	25:10	YOOH	34.3	-	-	-	-
8	0.048	0.002	0.8^2	25:10	YOOH	33.0	-	-	-	-
9	0.049	0.001	0.8^2	20:20	$Y(OH)_3$ / YOOH	-	-	-	-	-
10	0.048	0.002	0.8^2	20:20	$Y(OH)_3$ / YOOH	-	-	-	-	-
11	0.047	0.003	0.8^2	20:20	$Y(OH)_3$ / YOOH	-	-	-	-	-
12	0.050	0.000	0.8^2	25:10	YOOH	37.6	33.0	38.6	35.6	7.8
13	0.049	0.001	0.8^2	25:10	YOOH	40.8	34.3	37.1	37.4	6.7
14	0.046	0.002	0.8^2	25:10	YOOH	40.8	31.2	40.9	35.8	9.4
15	0.044	0.003	0.8^2	25:10	YOOH	45.4	31.9	39.9	40.1	10.3
16	0.042	0.004	0.8^2	25:10	YOOH	37.4	34.8	36.6	39.6	6.9
17	0.040	0.005	0.8^2	25:10	Y(OH)3 / YOOH	-	27.8	45.8	56.7	7.4
18	0.038	0.006	0.8^2	25:10	Y(OH)3 / YOOH	-	29.3	43.5	54.7	15.6
19	0.036	0.007	0.8^2	25:10	Y(OH)3 / YOOH	-	22.7	56.2	67.9	17.2

Key: Flow rates used in all syntheses were fixed at 25 mL min^{-1} (P1), 5 mL min^{-1}(P2) and 5 mL min^{-1}(P3) generating a reaction point temperature of (382° C mixing point and residence time 1.69 s). *N.b.* in the case of runs 9-11, the flow rates were increased to Q_p = 20 and Q_{sw} = 20 generating a reaction point temperature of (335° C mixing point and residence time 3.16 s). Reaction yield is quoted as the dry mass of product obtained from a fixed volume of process slurry. Parenthesis denote concentration of KOH added to H_2O_2 feed, ^{1}= 0.5 M, ^{2} = 1.0 M, ^{3} = 2.0 M and ^{4} = 3.0 M

7.2.3 Heat Treatment of $Y_{1-x}Eu_xOOH$ Nanoparticles

A mild heat treatment method was used for the conversion of as obtained (Y_{1-x} Eu_x)OOH nanoparticles to the corresponding oxide $(Y_{1-x}Eu_x)_2O_3$. A ceramic tube furnace was used to allow easy access to any heat-treated materials for relatively short times. Samples were fed into the middle of a preheated tube furnace set to 550 °C and held at the centre for the desired time. In a typical experiment *ca.* 0.5 g of freeze dried powder ((Y_{1-x} Eu_x) OOH) was placed into a platinum crucible and fed into the tube furnace. All materials characterisation was undertaken on materials obtained directly from the furnace without further processing.

7.2.4 Direct Synthesis of Surface Functionalised $Y_{1-x}Eu_xOOH$ Nanoparticles

Yttrium oxyhydroxide nanoparticles doped with europium ((Y_{1-x} Eu_x) OOH, where x = 0.04) were synthesised using CHFS system 2 and were produced directly as citric acid coated materials. In this section an operational envelope for the synthesis of surface functionalised phosphors was established using the previously optimised reaction point geometry presented in figure 6.3 and described in Chapter 6. The optimised reaction point geometry yielding post citric acid addition residence times of between 3.4 - 5.2 s after citric acid addition was used. In a typical reaction a 0.05 M metal ion solution (Yttrium nitrate hexahydrate (0.048 M) europium nitrate hexahydrate 0.002 M) was fed into the system using pump 2 and pump 3 was used to supply a 0.1M KOH solution (combined output of pump 2 and 3 is referred to as Q_p) and pump 1 was used to supply supercritical water at 450 °C (Q_{sw}), and the combined output of pumps 4 and 5 were used to feed a 0.05-0.15 M citric acid solution into the system at a combined flow rate of between 10 and 30 mL min^{-1} (Q_q). All reactions presented are defined in table 7.2. The reaction products (nominal 1L nanoparticle laden slurry) were concentrated by NaCl flocculation as described in Chapter 2, the concentrated sol was dialysed against > 10 Mega Ohm DI water for 72 h. The cleaned particle sol was either freeze dried for analysis or retained as an aqueous sol for further evaluation or post-synthesis modification.

Table 7.2: Summary of the reaction condition and characterization data for samples produced with the addition of citric acid (CA). The metal ion concentration was fixed at 0.05M, the heater temperature was set to 450 °C. Q_{sw} = 25 mL min^{-1} and Q_p = 10 mL min^{-1}.

ID	Q_p (mL min^{-1})	T_{mix2} (°C)	CA (Wt%)	CA:M ion ratio	XRD (nm)	TEM (nm)		TGA		(CA/nm^2)	Dynamic Light scattering		
						AVG	SD	200-400 (%)	425-700 (%)		HD(nm)	PDI	Hd number (nm)
3:10	10	358	3	4.1	29.2	25.2	5.6	2.67	5.86	1.38	173.9	0.214	43.6
3:20	20	312	3	8.3	-	-	-	-	-	-	-	-	
3:30	30	273	3	12.4	-	-	-	-	-	-	-	-	
2:10	10	358	2	2.7	28.3	24.4	6.3	2.73	6.59	1.37	152.2	0.184	32.6
2:20	20	312	2	5.5	28.2	27.8	7.7	3.2	6.20	1.42	133.2	0.21	33.8
2:30	30	273	2	8.3	-	-	-	-	-	-	-	-	
1:10	10	358	1	1.3	28.5	25.5	7.08	2.10	6.41	0.92	136.7	0.148	56.7
1:20	20	312	1	2.7	27.2	24.0	6.29	1.50	6.59	0.81	260.8	0.562	52.5
1:30	30	273	1	4.1	26.0	24.8	7.31	2.7	5.28	1.36	168.5	0.33	35.6
1.5:10	10	358	1.5	2.0	31.1	24.7	8.9	1.75	6.47	1.06	136.8	0.211	48.9
1.5:20	20	312	1.5	4.1	29.2	26.2	6.4	2.57	6.38	1.39	128.2	0.149	38.6
1.5:30	30	273	1.5	6.2	30.5	28.2	6.3	2.01	6.13	1.16	126.7	0.189	63.2

Key: Flow rates used in all syntheses were fixed at 25 mL min^{-1} (P1), 5 mL min^{-1} (P2) and 5 mL min^{-1}(P3) generating a reaction point temperature of 382° C mixing point and residence time 1.69 seconds equal to that quoted in Table 7.1) [Q_{sw} = 25 and Q_p= 10]. *N.b.* samples are identified by the concentration of CA used in each synthesis (expressed as wt %) and the citric acid introduction flow rate Q_q . CA : M = the ratio of citric acid to metal ions, Dh = intensity weighted hydrodynamic diameter, HD number = the number weighted hydrodynamic diameter, PDI = the hydrodynamic diameter polysidpersity, CA/nm^2 = Citric acid grafting density calculated using equation 6.1, and T_{mix2} = the theoretical temperature of the mixture Q_{sw} + Q_p + Q_q determined by enthalpy balance (°C).

7.2.5 Post Synthesis CA Coating of Phosphor Nanoparticles

For comparison to $(Y_{1-x}Eu_x)OOH$ nanoparticles produced as surface functionalised nanomaterials (table 7.2) nanoparticles of $(Y_{1-x} Eu_x)_2O_3$ and $(Y_{1-x} Eu_x)OOH$ were functionalised with citric acid post synthesis. Nanoparticles of both $(Y_{1-x} Eu_x)$ OOH or $(Y_{1-x} Eu_x)_2O_3$ were accurately weighed and dispersed ultrasonically using a tip sonicator (Branson USP 4000) at 80 W for 5 minutes in DI water. In a typical preparation 0.5 g of nanoparticles were dispersed in DI water and the pH of the solution was adjusted to pH 4 using HCl after the addition of *ca.* 2.0 g of citric acid. The solution was stirred using a magnetic stirrer and heated to a temperature at 60 °C, the reaction was allowed to proceed overnight. After completion the solution was dialysed against DI water to remove unbound citric acid and neutralise the solution. After dialysis the samples were retained as both dispersions and as freeze dried powders for further characterisation.

7.2.6 Pegylation of CA-coated (Y_{1-x} Eu_x) OOH Nanoparticles

CA-coated nanoparticles (50 mg) of sample 1.5:20 prepared as described in table 7.2 were ultrasonically dispersed (Branson USP ultrasonic probe, UK) from a 50 mg mL^{-1} (concentrate) in 10 mL of DI water (> 10 MΏ) and filtered through a 220 nm syringe filter (Millipore, UK). The ratio of particles (dry mass) to NH_2-PEG was used in excess for all NH_2-PEG variants (2 kDa and 5 kDa, respectively) used to ensure complete reaction of all free carboxylic acid groups on the particle surface. In a typical material preparation; 0.1 g of NH_2-PEG (2 or 5 kDa) was added to solution 1, followed by 0.05 g of EDC ((1-Ethyl-3-(3-dimethylaminopropyl) carbodiimide hydrochloride*)* and 0.08 g of NHS (*N*-Hydroxysuccinimide). The pH of the solution was adjusted to pH 9 with the addition of NaOH and HCl, respectively. The mixture was stirred vigorously for 24 h at ambient temperature and subsequently dialyzed against an aqueous solution for 2 days. Excess NH_2-PEG was removed after the reaction was complete by dialysis against DI water using a cellulose membrane (dialysis tubing) with pores having a cutoff size of 100 kDa for > 100 hours. The material was either retained as a cleaned variant of solution or freeze dried for further analysis.

7.2.7 Preparation of Sample for Cell Imaging Experiments

Stable colloidal dispersions of nanoparticles in DI water at known particle concentrations were made up in a 2 x PBS solution to the desired particle concentration (166 μg mL^{-1}) and passed through a 0.22 μm syringe (Millipore, UK). Phosphor nanoparticles (filtered) were incubated with mounted COS7 cells for 4 hours (we predicted that constitutive uptake of the particles would occur). Visualisation of the cells was undertaken using fluorescence microscopy using 470 nm excitation and emission was captured at 620 nm as described in Chapter 2. COS-7 cells characteristically display adherent growth to glass and plastic surfaces and are typically use as a model system to study changes alongside viral transfection.(Alarid 2006) Preparation and mounting of cells was conducted by Dr J Muir.

7.3 Results and Discussion

7.3.1 Direct Synthesis of $Y_{1-x}Eu_xOOH$ Nanoparticles

This section describes the continuous hydrothermal synthesis of phosphor nanoparticles using CHFS. The effects of different processing variables and reactor conditions are evaluated. Phosphor materials were synthesised using CHFS system 1 operated under the reaction conditions summarised in Table 7.1. Initially, the effect of reaction point temperatures (mixture of precursors and pre-heated water feeds) above and below the critical point of pure water (T_c = 372 °C, 24.1 MPa) was investigated on a single material composition (4 mol % europium) and the effects of auxiliary reagents such as KOH and H_2O_2 were assessed.

A reaction point temperature of *ca.* 383 °C (with 0.5 M KOH added to the auxiliary feed (run 1) produced a mixed phase product of $Y(OH)_3$ / YOOH as determined by XRD when compared to ICDS card numbers 20098 and 28442, respectively (Figure 7.1a). Whereas, the addition of KOH at concentrations >1.0 M was sufficient to produce a material in good agreement with ICDS pattern 28442 for monoclinic YOOH (run 2 and 3) as shown in figure 7.1a. This suggests that a stronger oxidizing environment is present in these experiments conducted with high KOH concentrations further facilitating the partial dehydration of $Y(OH)_3 \rightarrow$YOOH and the overall reaction is summarised by equations 7.1 and 7.2 for the formation of the hydroxide and oxyhydroxide phases, respectively. The decomposition of nitrate species in supercritical water is known form various oxidizing species including hydroxyl radicals, O_2 and NO_2, although alone these appeared to be insufficient to produce the YOOH phase. (Boldrin *et al.*, 2007) Similarly, the addition of H_2O_2 (previously used as an oxidant aiding dehydration) to the metal salt feed did not alter the structure of the reaction product (runs 5-8) data not shown. Materials synthesised at a reaction point temperature of *ca.* 338 °C using the same solution compositions used in experimental run 8 produced a mixed phase product of $Y(OH)_3$ / YOOH as determined by XRD (figure 7.1 b). The products of runs 9 - 11 were similar crystallographically to the material produce in run 1 at europium concentrations of 2 - 6 mol% as presented in figure 7.1a. Supercritical water is known to be more oxidizing than sub-critical water and the higher hydrothermal reaction temperatures used in this work provide a simple explanation for the formation of YOOH instead of the hydroxide produced using other hydrothermal methods. (Li, Yanagisawa, & Kumada 2009)

The results presented suggest a thermodynamic limitation to the direct synthesis of Y_2O_3 directly under the processing conditions presented.

$1\text{-x}\ Y(NO_3)_{3\,(aq)} + x\ Eu(NO_3)_{3(aq)} + 6\ KOH \rightarrow Y_{1\text{-}x}\ Eu_x(OH)_{3\,(s)} + K(NO_3) + 5H_2O$ **(Equation 7.1)**

$1\text{-x}\ Y(NO_3)_3 + x\ Eu(NO_3)_3 + KOH \rightarrow Y_{1\text{-}x}\ Eu_x(OH)_3 \rightarrow (Y_{1\text{-}x}\ Eu\ _x)OOH + H_2O$ **(Equation 7.2)**

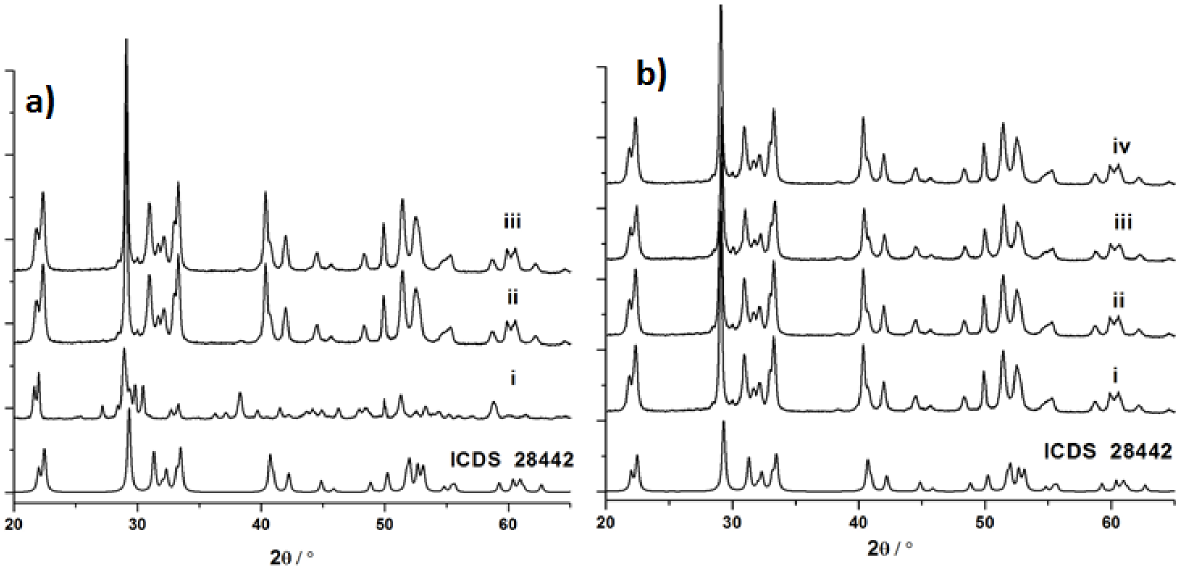

Figure 7.1: a) XRD patterns of the products from experimental runs 1-3 synthesised with different concentrations of KOH in the auxiliary feed **i)** ICDS 28442, **ii)** 0.5M, **iii)** 1.0 M and **iv)** 2.0M. **b)** XRD patterns obtained for the reaction products obtained from reactions conducted at a reaction point temperature of *ca.* 335 °C, **i)** ICDS 20098, **ii)** 2 mol% Eu, **iii)** 4 mol% Eu, and **iv)** 6 mol% Eu.

To investigate the effect of increasing dopant concentration on the phase behavior of $(Y_{1\text{-}x}\ Eu_x)$ OOH a series of compositions were produced in the range x = 0.00 - 0.14 (runs 12-19). All materials in this composition series showed visibly bright red emission under UV irradiation (λ = 254 nm) as both particle slurries and freeze dried powders (figure 7.2). A comparison of the nominal and measured Eu content of the samples produced in the series x = 0.00 - 0.14 (runs 12-19) is presented in figure 7.3b, measured using a calibrated EDX. The measured composition values were in good agreement with nominal values in the sample series for values of x = 0.02 - 0.08 (figure 7.3a). The largest divergence between nominal and measured composition was found in the 14 mol% Eu sample (run 19) with a measured 11.6 mol% Eu content. This discrepancy has been attributed to the incomplete precipitation of the Eu ion during the reaction.

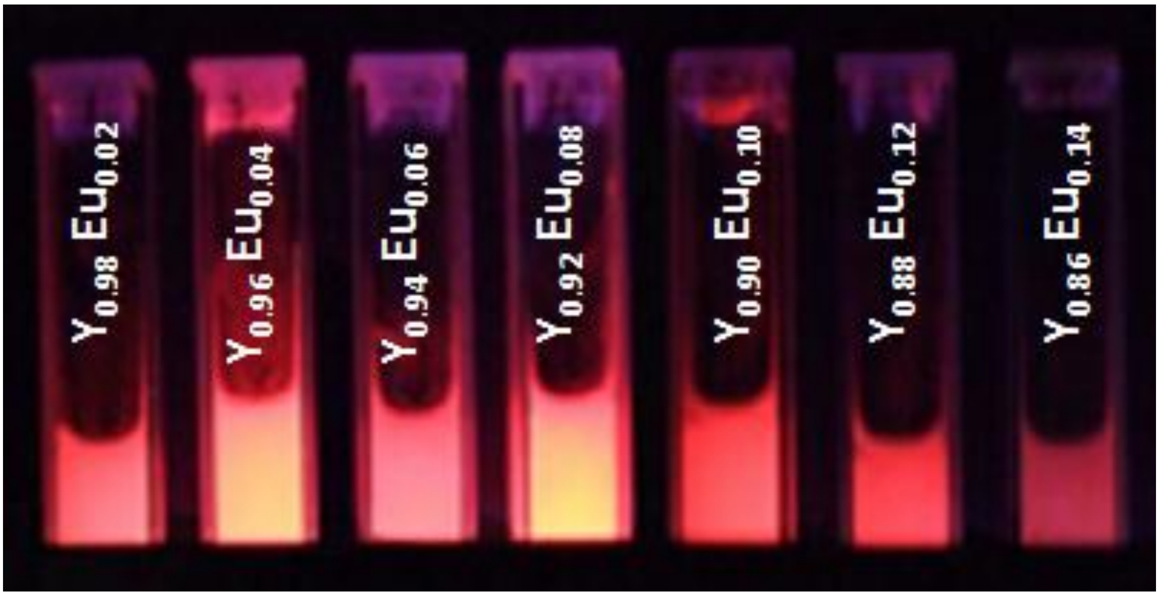

Figure 7.2: A photograph of $(Y_{1-x}Eu_x)$ OOH phosphor particle slurries as obtained from the CHFS process under UV irradiation (λ = 254 nm).

Materials produced in the series x = 0.00 - 0.08 were identified as $(Y_{1-x}\ Eu\ _x)$OOH using XRD when compared to ICDS pattern 28442 (figure 7.3a). Whereas, Eu doping > x = 0.10 produced a mixed phase product composed of $Y(OH)_3$ / YOOH when compared to (ICDS 20098 and 28442, respectively). It is postulated that higher Eu substitution favours the nucleation of $Y(OH)_3$ from the hydrothermal solution and the reaction point temperatures are insufficient to dehydrate Eu, which is known to have higher phase transition temperatures than $Y(OH)_3$. (Brittain and Posluszny 1987) A slight shift in the diffraction peak positions (to lower 2θ) was observed for the samples produced in the series x = 0.00 - 0.08 consistent with the incorporation of a larger guest ion into the YOOH host lattice. The results from Le-bail fitting of this sample series are presented in table 7.3 and showing the observed increase in unit cell volume as a function of increasing dopant concentration. Lattice parameters calculated for the undoped sample (run 12) were in good agreement with those previously reported in the literature. (Holsa *et al.,* 1985a)

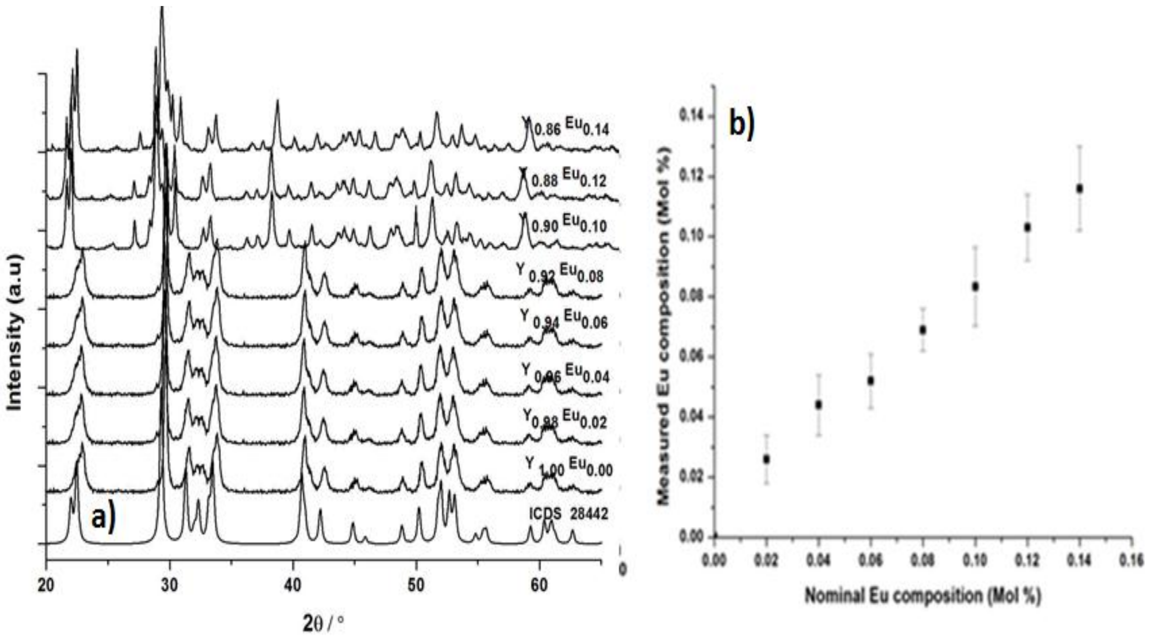

Figure 7.3: a) Stacked powder diffraction patterns obtained for (Y_{1-x} Eu_x)OOH (where, x = 0.00 - 0.14) phosphor materials synthesised using CHFS compared to ICDD pattern 28442, **b)** Comparison of the nominal and measured Eu concentration of (Y_{1-x} Eu_x)OOH nanoparticles [error bars indicate the standard deviation of the measurement].

Table 7.3: Summary of Lattice parameters determined by le-bail fitting for (Y_{1-x} Eu_x) OOH (where, x = <0.10)

Sample	Phase	Lattice parameter (Å)			R_p	R_{wp}
		a	b	c		
$Y_{1.00}$ $Eu_{0.00}$	P_{121}/M_1	4.282	3.660	6.071	0.073	0.060
$Y_{0.98}$ $Eu_{0.02}$	P_{121}/M_1	4.285	3.670	6.079	0.0802	0.084
$Y_{0.96}$ $Eu_{0.04}$	P_{121}/M_1	4.289	3.671	6.101	0.038	0.028
$Y_{0.94}$ $Eu_{0.06}$	P_{121}/M_1	4.299	3.678	6.109	0.031	0.034
$Y_{0.92}$ $Eu_{0.08}$	P_{121}/M_1	4.294	3.683	6.112	0.026	0.022

Key: R_p = Quality of fit overall (without background subtraction) and R_{wp} = Quality of fit overall (with background subtraction).

Transmission electron microscopy (Figure 7.4) was used to assess the crystallite morphology and particle size distribution of composition range ($Y_{1-x}Eu_x$)OOH (x = 0.00 - 0.14). The morphology of ($Y_{1-x}Eu_x$) OOH was shown to transition from spherical crystallites at low Eu dopant concentrations (x = 0.02 - 0.10) to particles with a rod like morphology at higher dopant substitutions (x = 0.12 - 0.14) and particle size data obtained for each composition are presented in table 7.1. The morphology of samples produced with Eu concentrations of 10 - 14 mol% europium were identified as $Y(OH)_3$ and the rodlike products are consistent with

$Y(OH)_3$ nanoparticles synthesised using other hydrothermal methods suggesting differences in crystal growth at the point of particle nucleation as suggested above. (Li, Yanagisawa, & Kumada 2009) Comparison of the crystallite sizes obtained for the diffraction data by application of the Scheerer equation, the equivalent sphere diameter (calculated from surface area measurements and the crystallite size determined from TEM are all consistent and are summarised in table 7.1 suggesting the synthesis of highly crystalline materials. Similarly, BET surface areas of the sample showed crystallite size estimates equivalent to those determined from other methods, a slight reduction in surface area was also measured which is also consistent with the evolution of a rod-like particle morphology in this sample series (table 7.1).

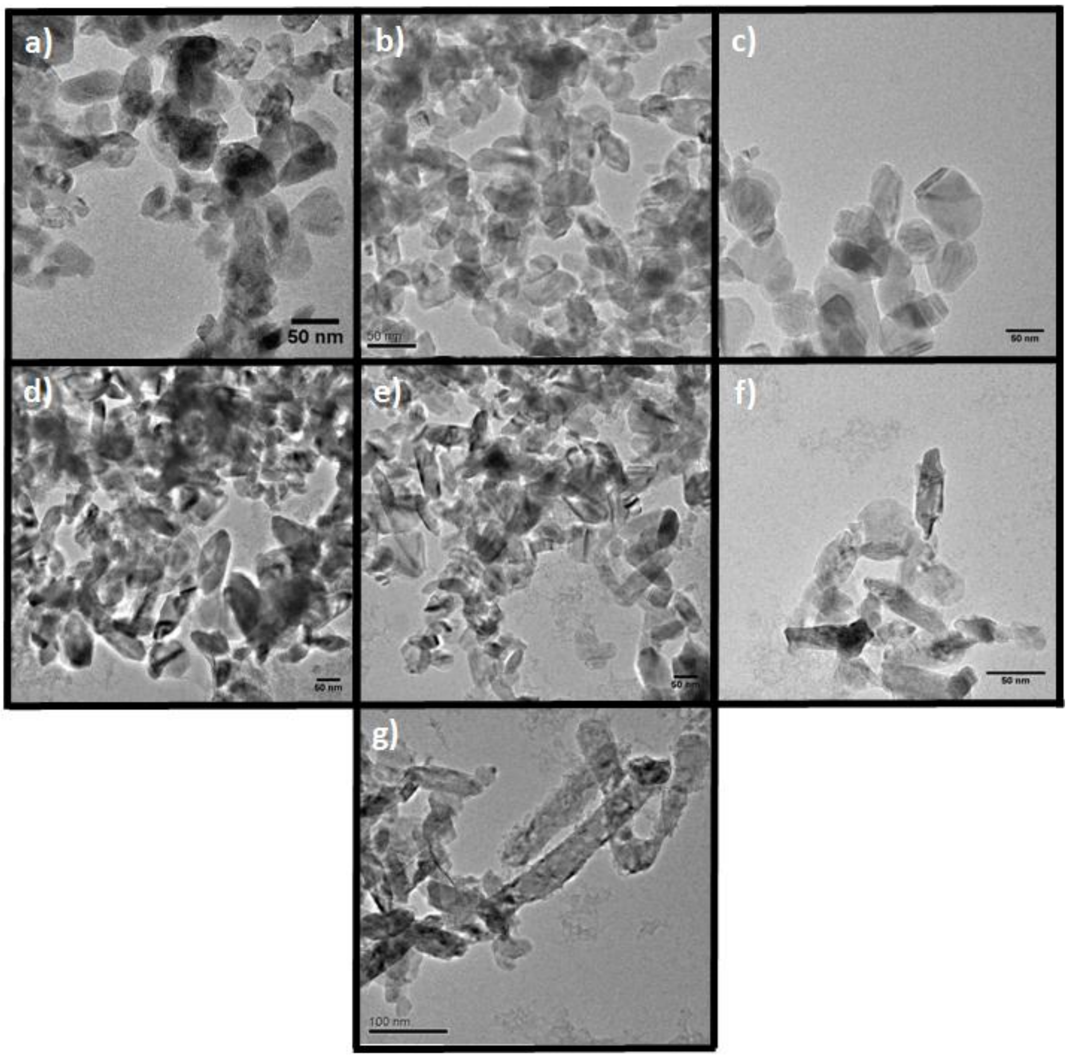

Figure 7.4: TEM images of the nanoparticles produced in the composition series ($(Y_{1-x}Eu_x)OOH$: **a)** x = 0.02 **b)** x = 0.04 **c)** x = 0.06 **d)** x = 0.08 **e)** x = 0.10 **f)** x = 0.12 **g)** x = 0.14.

HREM confirmed that highly crystalline nanomaterial were obtained in each synthesis. Figure 7.5 summarises HREM data obtained for the samples identified as $Y_{0.90}Eu_{0.14}(OH)_3$ and $(Y_{0.96}Eu_{0.04})OOH$, respectively. SEAD diffraction (Figure 7.5 insets) confirmed the phase of the material under observation. Figure 7.5 a shows lattice fringes extending towards the surface of the crystallite and visualisation of the (210) and (201) lattice planes with measured d-spacings of 3.12 and 2.13 Å, in good agreement with the theoretical values of 3.13 and 2.14 Å of $Y(OH)_3$ [ICDD 23811]. Figure 7.5b shows visualisation of the (101) plane of YOOH with a measured d-spacing of 4.01 Å (theoretical, 4.03 Å) which again was shown the constitute the bulk of each crystallite confirming the synthesis of highly crystalline nanoparticles through the sample series.

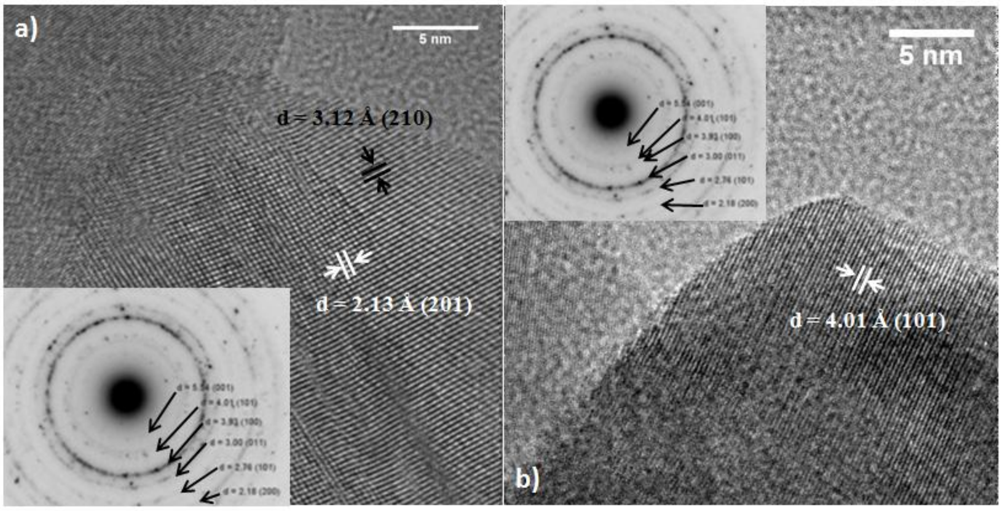

Figure 7.5: a) HREM images of $Y_{0.90}Eu_{0.14}(OH)_3$ (run 19) produced using CHFS (inset; indexed SAED pattern of confirming the phase of the material) **b)** HREM image of $(Y_{0.96}Eu_{0.04})OOH$ (run 13) showing visualisation of the [101] lattice fringe with a measured d-spacing of 4.01 Å (inset; indexed SAED pattern of confirming the phase of the material).

The optimal doping level for high photoemission in phosphors is dependent on many factors including synthesis method, size of the particles, post treatment temperature, and the existence of segregated phases. (Meltzer *et al.*, 1999; Tissue 1998) Hence, both the excitation and emission photoluminescence of the materials produced in the series x = 0.00 - 0.14 were measured as shown in figure 7.6 a and b, respectively. The excitation spectra (λ_{em} = 617 nm) of $(Y_{1-x} Eu_x)OOH$ [where x = 0.02 - 0.14] showed regions of strong absorbance in the 200-500 nm range, absorbance in the 200-300 nm range originates from transitions to charge transfer states from europium-oxygen bonds and absorbance in the region 350-500 can be attributed to transitions from $^7F_0$ to excited states as indicated in figure 7.6 b. (Holsa *et al.*, 1985a; Holsa *et al.*, 1985b) All excitation spectra showed significant similarity which could be expected as absorption in both the charge transfer region and transitions between ground state $^7F_0$ to excited states occur in both defined material phases. (Holsa *et al.*, 1985a) The emission spectra measured for samples x = 0.02 - 0.14 showed strong emission in the range 600-630 nm, corresponding to transitions of $^5D_0 \rightarrow {}^7F_{2(1\text{-}4)}$. (Holsa *et al.*, 1985b) A weak emission region (580-600 nm) was observed which can be assigned to the transitions of $^5D_0 \rightarrow {}^7F_{1(1\text{-}2)}$. The intensity of the emission spectra was similar for materials synthesised in runs x = 0.02 - 0.08, however in runs x = 0.10 - 0.14 the intensity was lower which is not surprising in light of the mixed phase product identified using XRD (Figure 7.6b). Where, in the presented data concentration quenching (*i.e.* quenching due to energy transfer between acceptor ions and traps [non-radiative emission centres]) appears to occur at > 4 mol% europium for the phase pure material synthesised in the series $(Y_{1-x}\,Eu_x)OOH$ [where, x = 0.00 - 0.08]. The onset of concentration quenching in this system occurs at a similar level of dopant substation to that reported for many Eu doped phosphor materials. (Meltzer *et al.*, 1999)

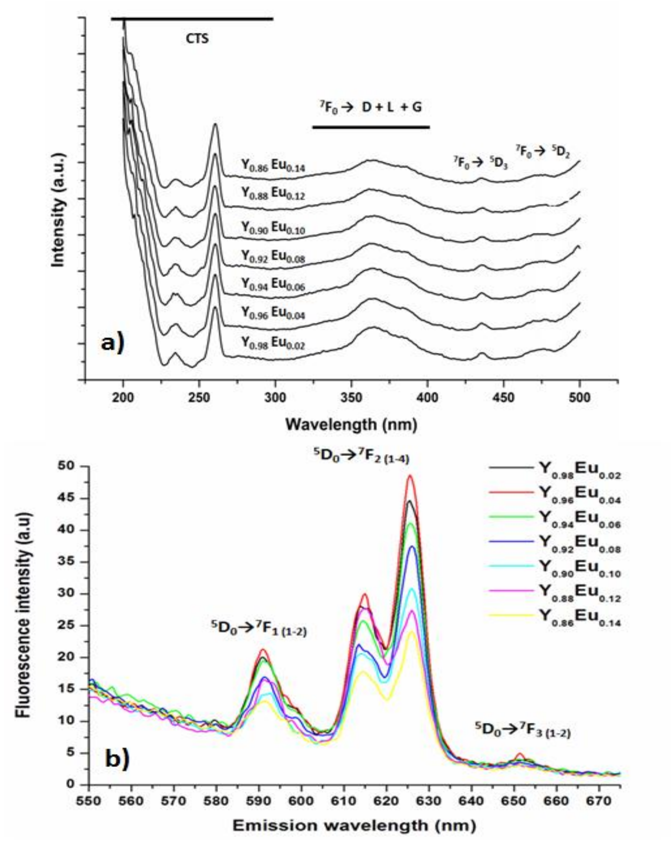

Figure 7.6: a) Excitation spectra ($\lambda_{emission}$ = 617 nm) of $(Y_{1-x}\,Eu_x)OOH$ nanoparticles (where x = 0.00 - 0.14), **b)** Photoluminescence spectra ($\lambda_{excitation}$ = 254 nm) of $(Y_{1-x}\,Eu_x)OOH$ (where x = 0.00 - 0.14) nanoparticles.

In addition to the excitation and emission spectral characteristics shown in figure 7.6, time-resolved emission has been analysed to investigate the dynamics of luminescence for each of the samples produced in the series Y_{1-x} Eu_xOOH (x = 0.02 - 0.08) [experimental runs 13-17]. This technique is sensitive to local variations in electron density (caused by differences in the site of europium within a host lattice) and can therefore detect defect structures and be used to infer the mechanisms responsible for the emission lifetimes of phosphor materials if the analysis is performed on electric dipole transitions. To identify both the electronic and magnetic-dipole transitions in this phosphor system lifetime measurements were taken at 594, 617 and 624 nm (corresponding to the transitions $^5D_0 \rightarrow {}^7F_1$, $^5D_0 \rightarrow {}^7F_2$ and $^5D_0 \rightarrow {}^7F_4$, respectively) of the sample with a nominal composition ($Y_{0.96}$ $Eu_{0.04}$) OOH which yielded lifetimes (equation 7.1) of 3.04, 0.50 and 0.42 ms, respectively. Where, the longer lifetime observed for the $^5D_0 \rightarrow {}^7F_1$ transition (3.04 ms) and those observed for $^5D_0 \rightarrow {}^7F_2$ and $^5D_0 \rightarrow {}^7F_4$ transitions are consistent with lifetime values indicative of electronic dipole transitions and magnetic dipole transitions. (Holsa *et al.,* 1985a) This analysis is consistent with the theoretical work of Holsa *et al.* which identified the $^5D_0 \rightarrow {}^7F_1$ as the magnetic dipole transition in this phosphor system. (Holsa, Leskela, & Leskela 1985b) Figure 7.7 shows the time-resolved luminescence data obtained from Y_{1-x} Eu_x OOH (x=0.02 - 0.08) measured at 617nm. The emission lifetimes of each sample were obtained from a single-exponential fit to the decay curves using the following equation;

$$I = I_0 \, e^{\frac{-t}{\tau}} \qquad \textbf{(Equation 7.1)}$$

Where, I is the signal intensity, I_0 is the maximum intensity, t is the time and τ is the decay constant. Where, in this system on the $^5D_0 \rightarrow {}^7F_2$ and $^5D_0 \rightarrow {}^7F_4$ transitions would be sensitive to local and electron structural variation. The lifetime of the $^5D_0 \rightarrow {}^7F_2$ transition of the sample series x = 0.02 - 0.08 showed an increase in nominal dopant concentration resulted in a corresponding decrease in the radiative lifetime (Figure 7.7 inset). The observed decrease in photoluminescence lifetime as a function of Eu^{3+} substitution is consistent with the increase of non radiative transition rate observed in other phosphor systems in this electronic dipole transition. (Meltzer *et al.,* 1999) Typically, the non-radiative transition rate increases with dopant substitution leading to either a reduction in local symmetry surrounding the activator ion or activator segregation with more atoms located at or near the particle surface. As a consequence, the radiative transition rate of $^5D_1 \rightarrow {}^7F_2$ decreases as a greater proportion of excited states de-excite through non-radiative pathways. These observations are consistent with the concentration based fluorescence quenching observed within this phosphor system, suggesting the concentration quenching occurs through the activation of non-radiative pathways for de-excitation attributed to slight electronic structure variation through increasing dopant substitution in the host lattice (figure 7.6b). (Stouwdam, Raudsepp, & van Veggel 2005)

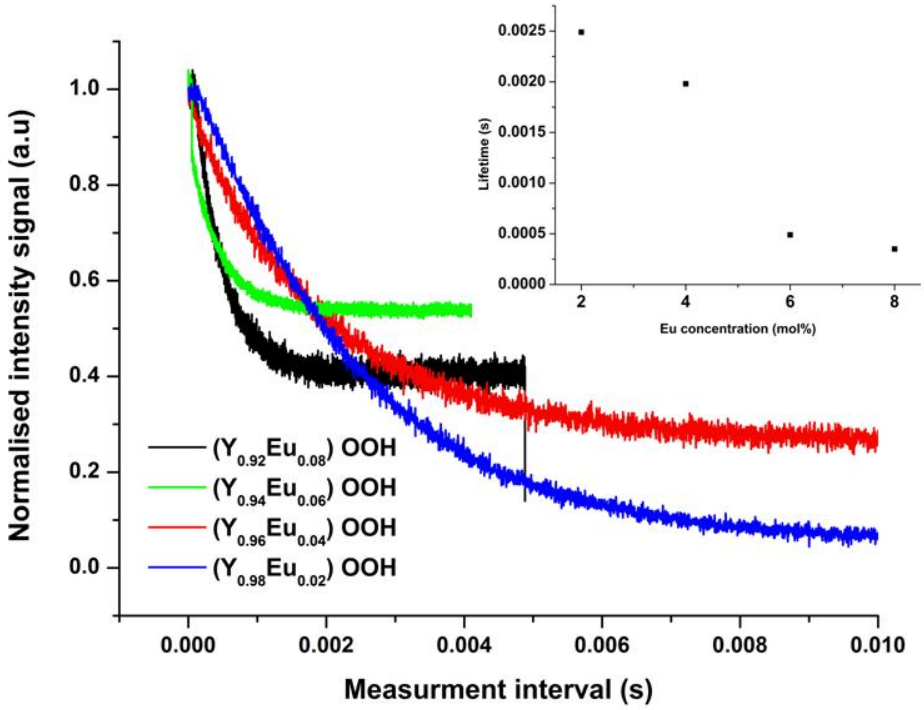

Figure 7.7: Photoluminecence lifetime measurements recorded for the $^5D_0 \rightarrow {}^7F_2$ transition in $(Y_{1-x}\ Eu_x)OOH$ [where x = 0.00 - 0.08] nanoparticles. Inset shows the variation in the lifetime determined by single exponential fitting as a function of nominal Eu concentration.

7.3.2 Calcination of $Y_{1-x}Eu_xOOH$ Nanoparticles

In addition to size related variables, the influence of post-synthetic processes that are often necessary to produce phosphor materials must be investigated as many of the properties depend upon synthesis method, size of the particles, post treatment temperature, and the existence of segregated phases. (Tissue 1998) Nanoparticle annealing is a common necessity to optimise optical properties of many phosphor systems to either increase crystallite size or reduce the contribution of non-radiative de-excitation process from adsorbed surface species. (Tissue 1998) This section describes the effect of moderate annealing on the physical characteristics and PL properties of $(Y_{0.96}Eu_{0.04})OOH$. as, annealing will induce a degree of grain growth, annealing durations need to be minimized for some applications that require disperse, small particles. (Tanner and Fu 2009)

$(Y_{0.96}Eu_{0.04})OOH$ nanoparticle produced as described in table 7.1 were annealed for durations of 20, 30, 60, 120, 180, 300, 600, 1200 and 1800 s at 550°C. Where, the phase transition from $(Y_{0.96}Eu_{0.04})OOH$ to $(Y_{0.96}Eu_{0.04})_2O_3$ is shown in figure 7.8. Phase identifications made through XRD showed that annealing times < 300 seconds are not suitable to completely dehydrate the material. All XRD data obtained for samples annealed for < 60 seconds showed the dominant material phase was monoclinic $(Y_{0.96}\ Eu_{0.04})OOH$ (ICDD 28442), after *ca.* 180 s a mixed phase product was obtained showing characteristic diffraction peaks of a cubic phase in good agreement with ICDS pattern 23811. The Scherer equation has been used to assess if any significant particle growth or coarsening of the material occurs as a function of annealing time and the data is summarised in figure 7.9. An increase in volume weighted mean crystallite size was observed which suggests slight crystallite growth as a function of annealing duration after phase change to the oxide**.** To confirm the complete dehydration of the material produced after annealing for 300 seconds TGA/DSC of the sample gave no distinct region of weight-loss or any conclusive endotherm attributed to phase transitions suggesting the complete dehydration of the precursor material has been achieved (data not shown).

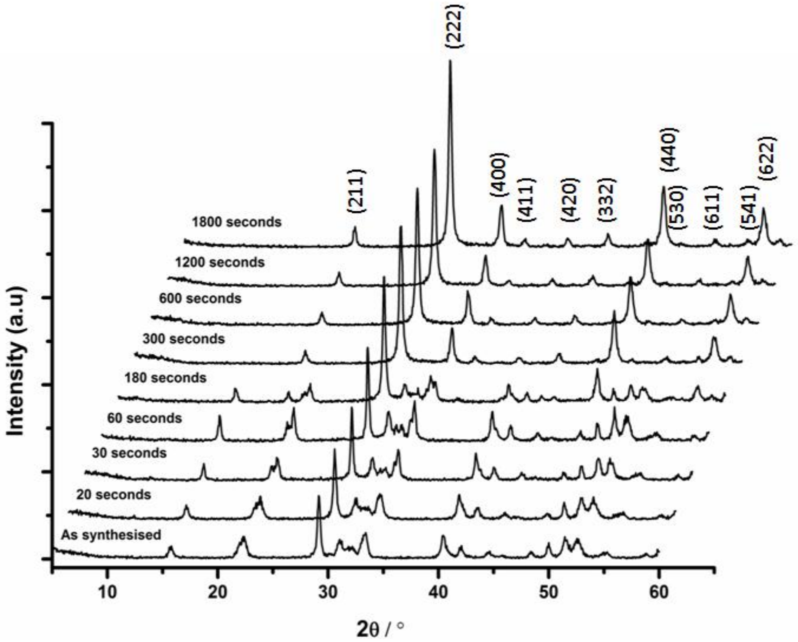

Figure 7.8: XRD patterns of $(Y_{0.96}: Eu_{0.04})$ OOH annealed at 550 °C for the indicated time (Miller indices for the cubic oxide system are indicated on the figure).

To assess the degree of sintering transmission electron micrographs taken for the annealed materials identified as $(Y_{0.96}Eu_{0.04})_2O_3$ (annealed for > 300 s) showed that the annealing procedure induced a moderate degree of grain growth (Figure A2.2 shown in Appendix 2). The particle size distributions measured for the samples are compared to the as synthesised material are presented in figure 7.9, where the crystallite size and standard deviation are presented (*ca.* 300 particle measured). A comparison of the crystallite sizes obtained from XRD and TEM show a discrepancy between the crystallite size from the diffraction data and the crystallite size obtained from TEM, this suggests that coarsening occurs through a necking mechanism rather than bulk crystal growth. (Arcidiacono *et al.,* 2004; Zhu and Averback 1996) To further assess grain growth, surface areas of the samples were measured using the BET method and showed a consistent reduction in surface area as a function of annealing time. Calculation of the equivalent sphere diameter (Cs = 6000/(ρ x S.A) where; Cs is the equivalent sphere diameter, ρ is the material density (*ca.* 4.170 g cm^{-3}) and S.A. is the measured surface area) gave size estimates consistent with those obtained from TEM, suggesting a necking mechanism of particle coarsening rather than complete densification of the nanomaterial through plastic flow. (Arcidiacono *et al.,* 2004) The minimal degree of growth observed can be attributed to misaligned particles also creating an energetic boundary to conventional coarsening at the relatively short annealing durations used. (Zhu & Averback 1996) Pore size calculation using the BJH adsorption/desorption method yielded a near consistent pore size equivalent to the diameter of the initial nanoparticles and has been excluded from this discussion.

HREM was used to further asses the phase transformation the structure of the material produced after annealing at 550 °C for 300s (figure 7.10) and the phase of the material under observation was confirmed using SAED (figure 7.10 inset). In this sample clear visualisation of the (211) and (222) planes with measured d-spacings of 4.33 and 3.08 Å were observed throughout the body of each crystallite which were in good agreement with the theoretical; 4.36 and 3.10 Å (ICDD 23811) allowing for imperfect alignment of the crystal. Direct observation confirmed that both complete phase transformation of $(Y_{0.96}Eu_{0.04})OOH$ to the corresponding cubic oxide $(Y_{0.96}Eu_{0.04})_2O_3$ and the formation of a fully crystalline nanomaterial.

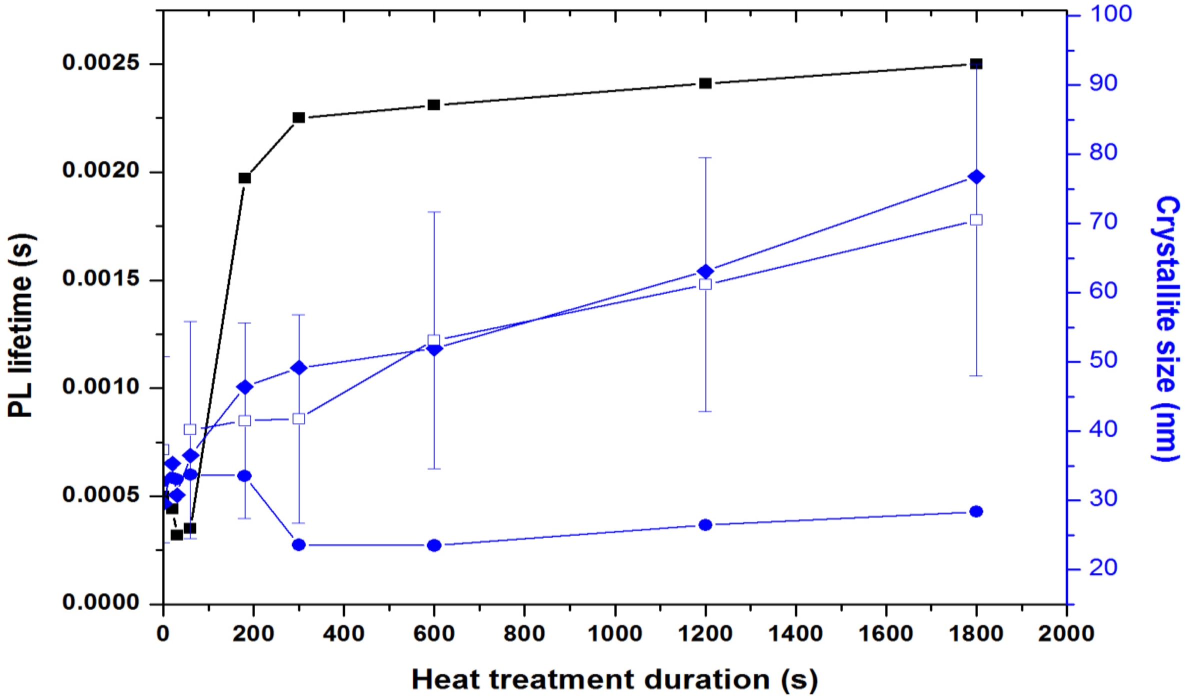

Figure 7.9: ■ Measured emission lifetime □ Crystallite size by TEM (error bars = SD) ♦ BET equivalent sphere diameter ● Crystallite size from diffraction [***n.b*** Lifetime quoted for < 180 s measured at 617 nm ($^5D_0 \rightarrow ^7F_2$) in $(Y_{0.96}Eu_{0.04})OOH$ and > 300s at 612 nm ($^5D_0 \rightarrow ^7F_2$) in $(Y_{0.96}Eu_{0.04})_2O_3$].

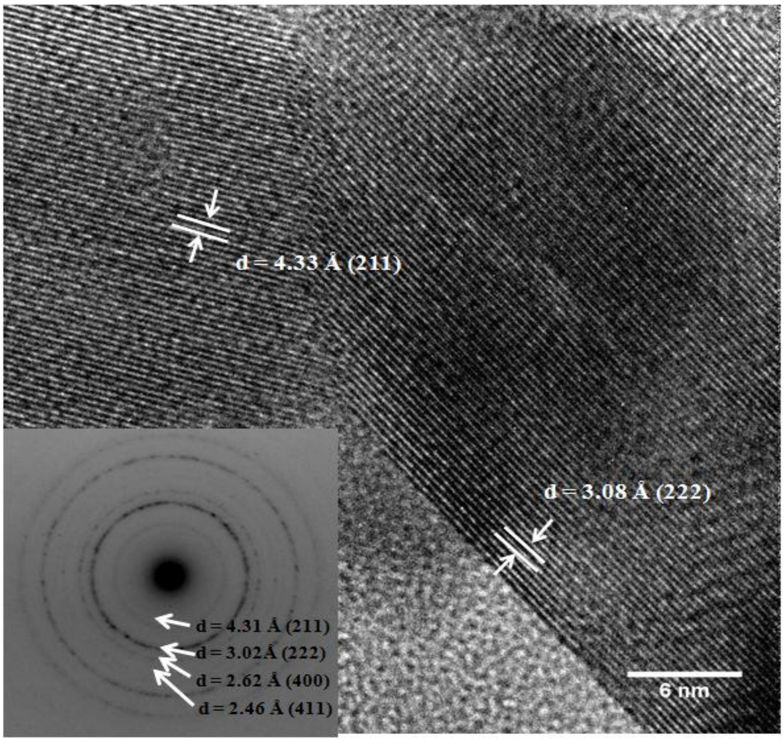

Figure 7.10: HREM images of $(Y_{0.96}Eu_{0.04})_2O_3$ produced by annealing $(Y_{0.96}Eu_{0.04})OOH$ at 550 °C for 300 (indexed lattice fringes are indicated within the image). Figure inset; indexed SAED pattern of confirming the phase of the material.

The dynamics of luminescence in the annealed samples were measured using photoluminescence emission spectra (λ_{ex} = 473 nm) as shown in figure 7.11. The spectra clearly show a reduction in luminescence intensity from the $^5D_0 \rightarrow ^7F_2$ transitions in ($Y_{0.96}Eu_{0.04}$) OOH until a partial phase transition to the cubic oxide at *ca.* 180 s. In general, the emission spectra of ($Y_{0.96}Eu_{0.04})_2O_3$ (formed at 550 °C for times > 300 s) gave rather broad peaks under 473 nm excitation consisting of red emission peaks centred at 581 (corresponding to $^5D_0 \rightarrow ^7F_0$), 587, 593, 600 (corresponding to $^5D_0 \rightarrow ^7F_{1(1-3)}$), 612 (highest intensity and asymmetric peak corresponding to $^5D_0 \rightarrow ^7F_2$ transitions of Eu^{3+} ions) and 630 nm (corresponding to $^5D_0 \rightarrow ^7F_3$ transition). (Holsa *et al.*, 1985b) The luminescence intensity of the $^5D_0 \rightarrow ^7F_2$ transitions in $(Y_{0.96}Eu_{0.04})_2 O_3$ was show to increase gradually with annealing time suggests a decrease in non-radiative (de-excitation) processes occurring within the sample. This observation is commonly indicative of a decrease in the surface-to-volume ratio consequent to the growth of the small crystals yielding a reduction in non-radiative de-excitation associated with near surface Eu^{3+} ions, consistent with much of the available literature. (Tanner & Fu 2009) Offering a straightforward explanation for the increased radiative intensity we see for nanocrystalline $(Y_{0.96}Eu_{0.04})_2 O_3$ in light of the characterisation data summarised in Figure 7.9.

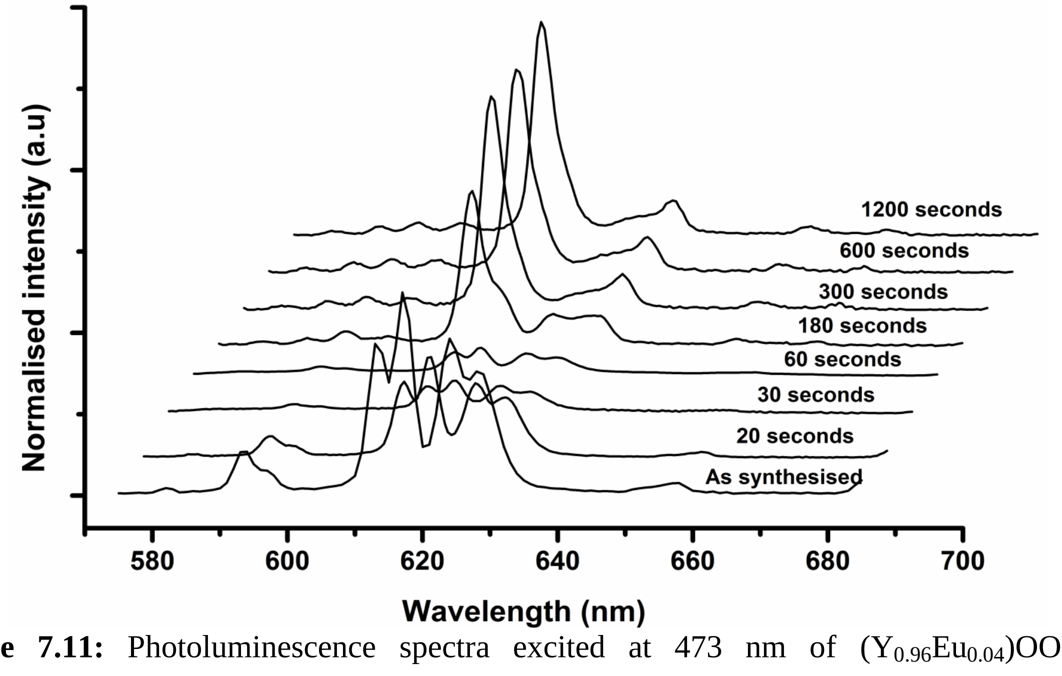

Figure 7.11: Photoluminescence spectra excited at 473 nm of $(Y_{0.96}Eu_{0.04})OOH$ or $(Y_{0.96}Eu_{0.04})_2O_3$ annealed at 550 °C for the indicated time.

The emission lifetime is a dependent parameter with can be influenced by many intrinsic structural properties of the material, and has been used to further qualitatively assess the effect of annealing time on the dynamics of luminescence in this phosphor series. The measured emission lifetime (λ_{em} = 617 nm [$^5D_0 \rightarrow {}^7F_2$]) was show to gradually decrease with calcinations time for materials identified as $Y_{0.96}$ $Eu_{0.04}$ OOH until *ca.*180 second where a phase change occurred (figure 7.9). The reduction in emission lifetime (determined from equation 7.1) for annealing durations of < 180 s suggests a distortion of the crystal field associated with Eu^{3+} within the lattice until the phase change occurred, allowing non-radiative pathways for de-excitation processes, consistent with the sequential reduction of PL intensity observed in figure 7.11.(Brown et al. 1995;Schmechel et al. 2001a;Schmechel et al. 2001b) The lifetime measured ($^5D_0 \rightarrow {}^7F_2$ at 612 nm) for samples annealed for > 300 s was shown to increase gradually with increasing annealing time (data summarised in figure 7.9) alongside a corresponding increase in PL intensity. The observed lifetimes > 2.25 ms (calculated using equation 7.1) are considerably greater than values typically reported for reported for bulk $(Y_{1-x}Eu_x)_2O_3$ samples *ca.*1.7 ms. (Schmechel *et al.*, 2001a) However, other investigators have found that the lifetime of the $^5D_0 \rightarrow {}^7F_2$ transition is actually longer by a factor of 3 (*ca.* < 5.1 ms) for nanocrystalline Eu doped Y_2O_3, rather than shorter as one might expect if surface recombination is enhanced. (Tissue 1998) Schmechel and co-workers also suggested a possible explanation for the increased lifetimes in nanocrystalline $(Y_{0.96}Eu_{0.04})_2$ O_3 is the effect of strain in the crystal lattice and the reduction in local symmetry of Eu^{3+} at the surface of the nanoparticles leading to de-excitation processes occurring through step-wise processes, through energy transfer between the host and activator atoms and attributed their observations to crystal field complexity around Eu^{3+}, a complex sum of structural and surface effects. (Schmechel *et al.*, 2001a; Schmechel *et al.*, 2001b) In this annealed series, a further increase in emission lifetime was observed with annealing duration which is indicative of a decrease in non-radiative (de-excitation) processes, and is probably mediated by inter-granular growth giving an explanation for the longer emission lifetimes through a reduction in the contribution of non-radiative surface recombination counterbalanced by slight structure differences associated with particle growth. (Brown, Mascher, & Kitai 1995) These results suggest only minimal “crystalisation” (*i.e.* onset of bulk like emission lifetime) of $(Y_{0.96}Eu_{0.04})_2$ O_3 as a function of annealing time and suggesting that the increase in PL intensity arises as a result of increasing crystallite size and a reduction in local symmetry surrounding Eu^{3+} induced through crystallite coarsening leads to an increasing lifetime. (Schmechel *et al.*, 2001a)

Investigation into the moderate annealing of $(Y_{0.96}Eu_{0.04})$ OOH identified a compromise for the annealing of phosphor nanoparticles. Moderate annealing identified that the increase in PL emission intensity was counter balanced by crystallite growth showing a summarised in figure 7.9 and complete dehydration of $(Y_{0.96}\ Eu_{0.04})$ OOH to $(Y_{0.96}Eu_{0.04})_2\ O_3$ only yielded fractional increases in PL intensity for quite large coarsening of the particles. Suggesting direct processing and the use of $(Y_{0.96}Eu_{0.04})$ OOH obtained by CHFS would yield the most useful phosphor material if the characteristic PL emission of $(Y_{0.96}Eu_{0.04})_2\ O_3$ was not required for a given application. This chapter now moves forward to assess the effect of surface functionalisation on $(Y_{0.96}Eu_{0.04})$ OOH nanoparticles.

7.3.3 Effects of Surface Functionalisation of $Y_{1-x}Eu_xOOH$ and $Y_{2-y}Eu_yO_3$ Nanoparticles

The surface of small particles, where the coordination of atoms differs from the bulk and where different chemical species may be adsorbed, is suspected to be the most important source of alteration of the luminescence efficiency in nanosized phosphor materials. (Bruchez *et al.,* 1998; Haase *et al.,* 2000) In this section a description of the effects of citric acid functionalisation on the optical properties $(Y_{0.96}Eu_{0.04})$ OOH of is presented. The materials were produced either directly from the CHFS using the processing methodology presented in Chapter 5 or through the post synthesis coating process described in Section 7.2.4. Samples are identified by the concentration of CA used in synthesis and the value of Q_q used in the synthesis as detailed in table 7.2 or alternatively by the composition of the nanomaterial used followed by CA.

The results of investigation into the direct synthesis of surface functionalised phosphors are summarised in table 7.2. Broadly, the ratio of citric acid to metal ions which resulted in the dissolution of the material (CA : M > 7) within the system was consistent with that observed for the synthesis of citric acid coated magnetite as shown in Chapter 6 (CA : Fe > 6). Figure 7.13 shows TEM images of the citric acid coated phosphors summarised in table 7.2. The morphology of the materials was similar to that obtained for $(Y_{0.96}\ Eu_{0.04})$ OOH nanoparticles produced in Section 7.3.1. Consistent with the observations presented in Chapter 6, the crystallite size determined from TEM (*ca.* 300 particles measured) was largely invariant of processing condition (Q_q, M / CA ratio, *etc*) suggesting that once again effective segregation of the particle-formation and functionalisation steps is observed (data summarised in table 7.2). XRD patterns identified the products being as a phase pure material in good agreement with IDCS pattern 28442 (figure 7.12a). Consistent with the product produced in run 10 (Table 7.1) Comparison of the crystallite size estimated from the diffraction data (011 reflection) and the crystallite size determined from TEM were consistent, suggesting the synthesis of a highly crystalline nanomaterials over the processing range.

ATR-FTIR was used to confirm the presence of citric acid on the surface of $(Y_{0.96}Eu_{0.04})$ OOH nanoparticles (figure 7.13.b). Spectra obtained for the citric acid coated phosphor showed modes origination from (ν) C = O (~ 1730 cm^{-1}), (ν_s) COO^- (~ 1400 cm^{-1}), (ν_{as}) COO^- (~ 1569 cm^{-1}) and (ν) OC - OH (~ 1200 cm^{-1}). Consistent with the discussion presented in Chapter 6. The wavenumber separation between the (ν_s) COO^- and the (ν_{as}) COO^- modes has been used to determine the binding state of the carboxylate group at the nanoparticle surface. Carboxylate binding showed wavenumber separation (Δ) values which varied between 190 and 220 cm^{-1} suggesting a mixture of unidentate and bidentate coordination with the particle surface consistent with the data provided in Chapter 6 (figure 6.4). (Adschiri *et al.,* 2007; Kaneko *et al.,* 2007) Similarly, the (ν) C = O mode present as a broad split peak in the bulk citric acid sample had shifted to higher wavenumbers (*ca.* 1740 cm^{-1}) suggesting that both free acid and coordinated acid groups are present in the sample (figure 7.13b). (Mudunkotuwa and Grassian 2010)

TGA was used to quantify the grafting density of citric acid on the nanoparticle surface for the as-synthesised phosphor materials (data summarised in table 7.2). The weight loss as a function of temperature in the 200 - 350 °C region (attributed to the thermal decomposition of citric acid) was measured and the results are summarized in table 7.2. The grafting density of citric acid was calculated using the theoretic density of the material determined from XRD (4.710 g/cm^3) and the crystallite size determined by TEM using equation 6.1. Syntheses conducted with CA : M ratios > 2.8 consistently showed the highest grafting density *ca.* > 1.3 CA/nm^2 and an apparent surface saturation at this value, which is lower than that obtained for magnetite in Chapter 6 (figure 7.14). Hereafter, samples are identified by the grafting density calculated from TGA as many of the properties of the dispersions are intrinsically linked to this value. A possible explanation for the lower grafting density is that COOH groups preferentially coordinate metal ion terminated crystal facets, and has previously been observed in anatase nanoparticles where the carboxylic acid group binds preferentially to Ti terminated facets of the 100 family. (Mudunkotuwa & Grassian 2010) Although not independently confirmed, carboxylic acid groups binding preferentially to certain crystal facets is known in batch hydrothermal reactions allowing the synthesis of different morphologies of nanoparticles by mediating particle growth to bare crystal facets. (Zhang *et al.*, 2007)

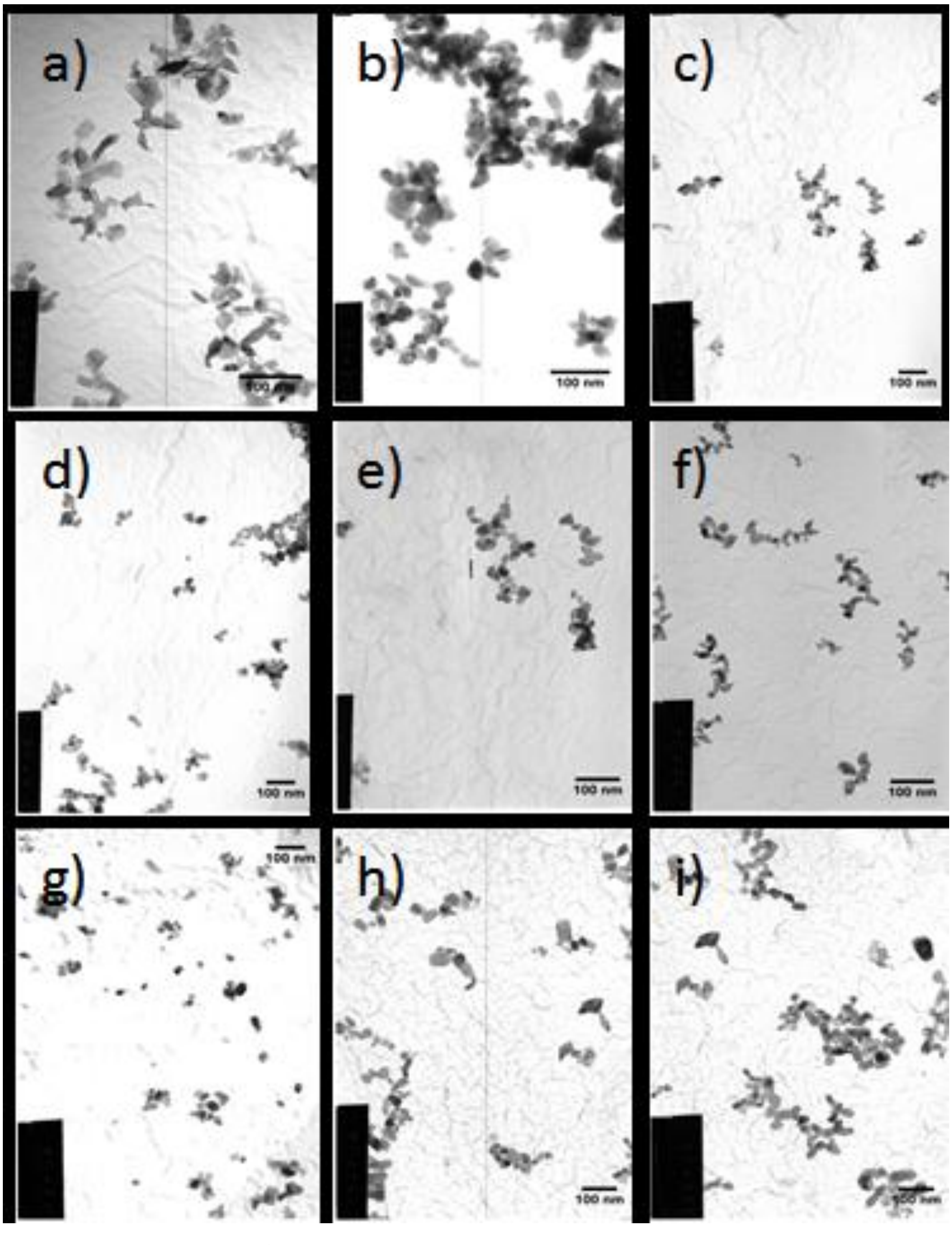

Figure 7.12: TEM images of phosphor nanoparticles produced in runs; **a)** 3:10, **b)** 2:10, **c)** 2:20, **d)** 1:10, **e)** 1:20, **f)** 1:30, **g)** 1.5:10, **h)** 1.5:20 and **i)** 1.5:30. Samples are identified by the CA concentration used in synthesis and the Q_q flow-rate.

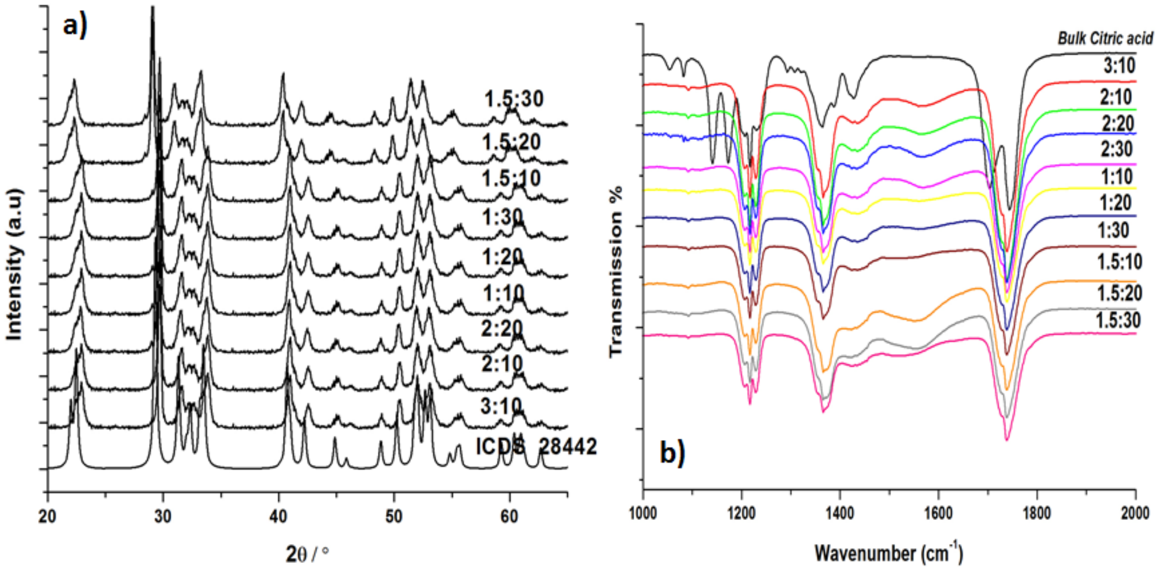

Figure 7.13: a) XRD patterns of phosphor samples produced with the addition of citric acid (samples are identified by the CA concentration used in synthesis and the Q_q flowrate), **b)** ATR-FTIR spectra of CA coated phosphor samples (showing the spectral range 1000 - 2000 cm^{-1}).

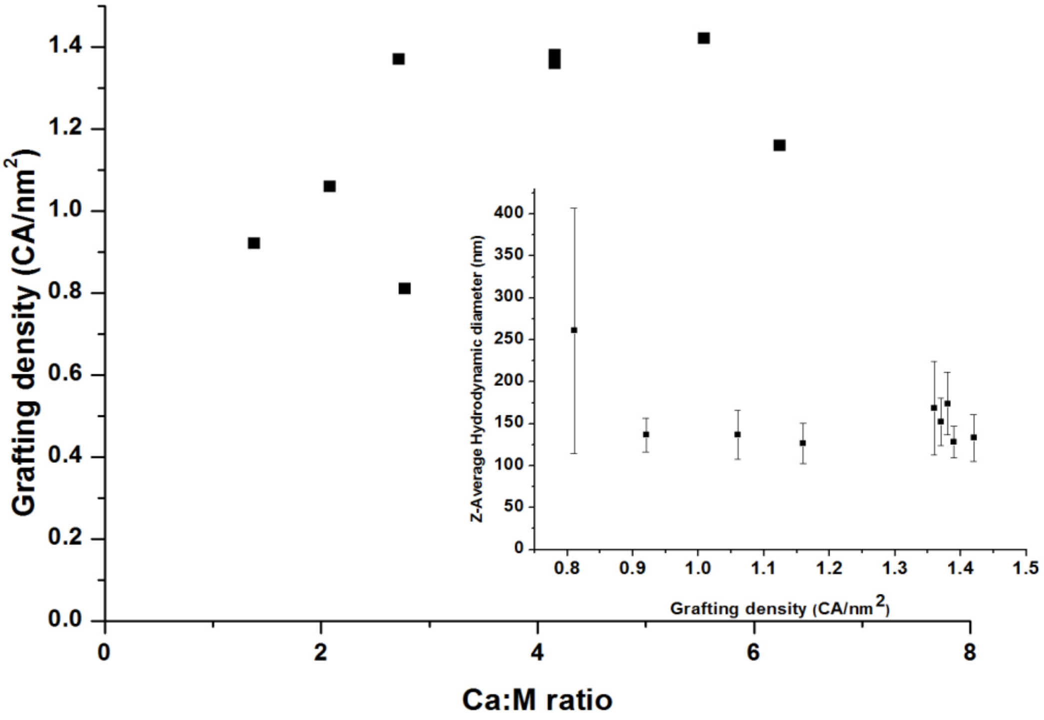

Figure 7.14: Plot of grafting density against CA:M ratio used in synthesis. Inset, shows the variation of hydrodynamic diameter against CA grafting density.

Dynamic light scattering was used to measure the hydrodynamic diameter of the particles in aqueous solution. The materials all showed relatively broad size distributions described by their polydispersity indices (table 7.2) when compared to samples produced in chapter 6. Figure 7.14 (inset) shows the variation in hydrodynamic diameter as a function of CA grafting density and citric acid grafting densities >1 CA/nm^2 gave similar hydrodynamic diameter distributions. Particle number weighting the data presented in figure 7.14 yielded particle diameters similar to that expected from direct observation using TEM (table 7.2) again reasoning that a majority of the sample was well dispersed. Figure 7.15 shows the variation in the magnitude of zeta-potential (indicative of dispersion stability) as a function of pH, plotted against the calculated CA grafting density for each sample. The magnitude of the zeta-potential was shown to correlate well with the CA grafting density. Particle dispersions showing CA grafting densities > 1 CA/nm^2 were characterised as stable as the magnitude of the Zeta-potential > - 30 mV, consistent with the electrostatic mechanism of stabilisation conferred by de-protonation of carboxylylic acids (discussed in greater detail within chapter 6). The measurements presented in figure 7.15 show a reduction in the magnitude of the surface charge at pH 6 suggesting suppression of the dissociation of the weakest acid group of citric acid (pKa_3 = 6.40). Where, the most acidic groups bind to the surface of the nanoparticle suggesting a similar coordination to that presented in chapter 6. Sample showing < 1 CA/nm^2 showed amphoteric behavior with a PZC at pH 8.5 which is consistent with the protonation ($M - OH + H^+ \rightarrow M - OH_2^+$) and deprotonation of ($M - OH \rightarrow M\text{-}O^- + H^+$) reactions of surface metal ions.

The dynamics of luminescence in CA coated ($Y_{0.96}Eu_{0.04}$) OOH and the emission characteristics were assessed. Figure 7.16 shows the PL emission spectra of CA coated ($Y_{0.96}Eu_{0.04}$) OOH from excitation at 254 nm. Consistent with previously reported spectra strong red emission (600-630 nm) attributed to transitions of $^5D_0 \rightarrow {}^7F_2$ dominated each spectra. Similarly, a weak emission range (580-600 nm) was observed and attributed to $^5D_0 \rightarrow {}^7F_1$ with the emission characteristics being similar to those presented in section 7.3.1. The PL intensity varied considerably between samples and showed no consistency with any one change in processing condition *i.e.* a decrease in the temperature at T_{mix2} (increase in Q_q) or relative CA / M ratio. However, increasing grafting density showed a sequential reduction in PL intensity where similar reductions were observed for all emission wavelengths (as presented in figure 7.16 inset). Quenching of luminescence in red emitting phosphor systems has been described previously. (Huignard, Gacoin, & Boilot 2000; Ronda, Justel, & Nikol

1998) The mechanism of quenching in these samples may arise from two effects; **1)** the partial OH quenching of the Eu red emission is significant since the energy of the $^5D_0 \rightarrow {}^7F_{2\ 1\text{-}4}$ transition corresponds well with the absorption energy of OH oscillation (3rd harmonic) increasing the ratio of surface species adsorption in the sample. (Ozawa 1979; Tissue 1998) **2)** increase in non-radiative de-excitation due to differences in Eu^{3+} ion coordination through surface complex formation with carboxylate groups. (Chen *et al.*, 2008) The latter mechanism appears more prominent in these samples as the intensity ratios of all transitions are consistent with increasing CA grafting density. However, a very slight increase in the ratio of $^5D_0 \rightarrow {}^7F_{2(1\text{-}2)}$: $^5D_0 \rightarrow {}^7F_{2\ (3\text{-}4)}$ with increasing CA grafting density suggests slight adsorption through adsorbed surface species. Overall, the difference between low and high grafting densities *ca.* 0.8 to 1.4 CA/nm^2 showed a 40 % reduction in PL yield which would be significant for any imaging application.

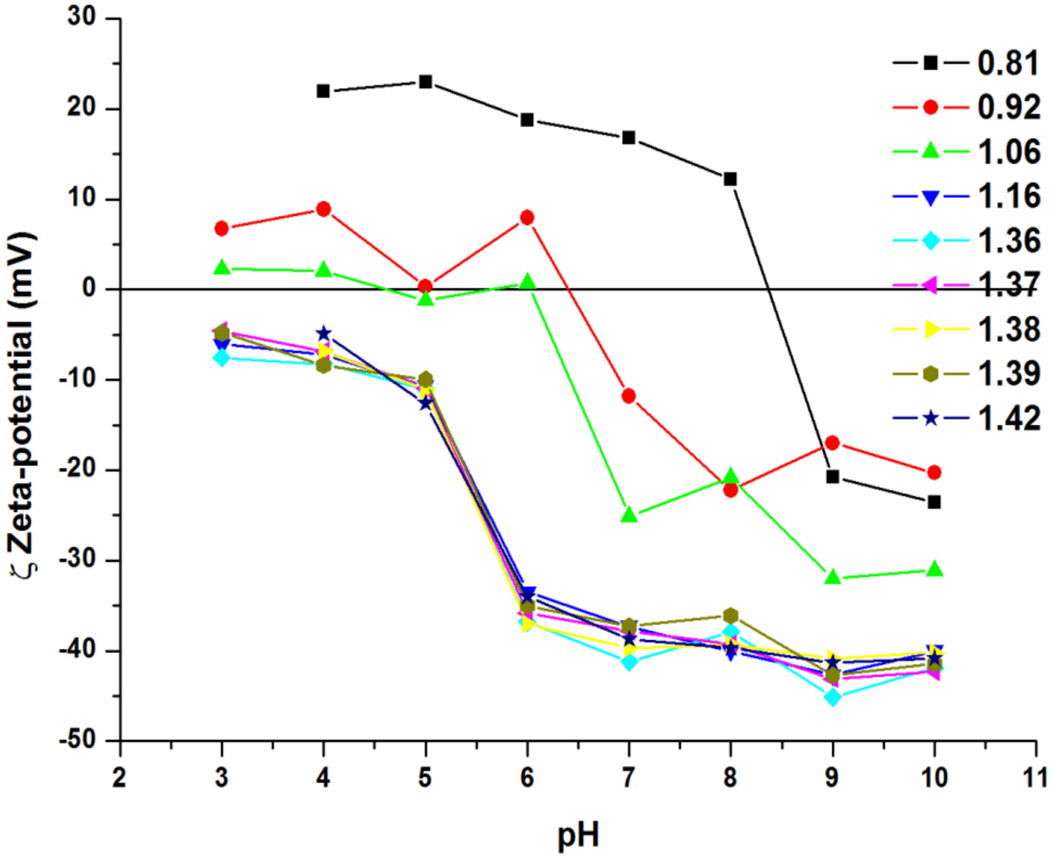

Figure 7.15: Zeta-potential titrations of citric acid coated $(Y_{0.96}Eu_{0.04})OOH$ nanoparticles plotted as a function of CA grafting density. (The standard deviation of the measurements has been omitted for clarity).

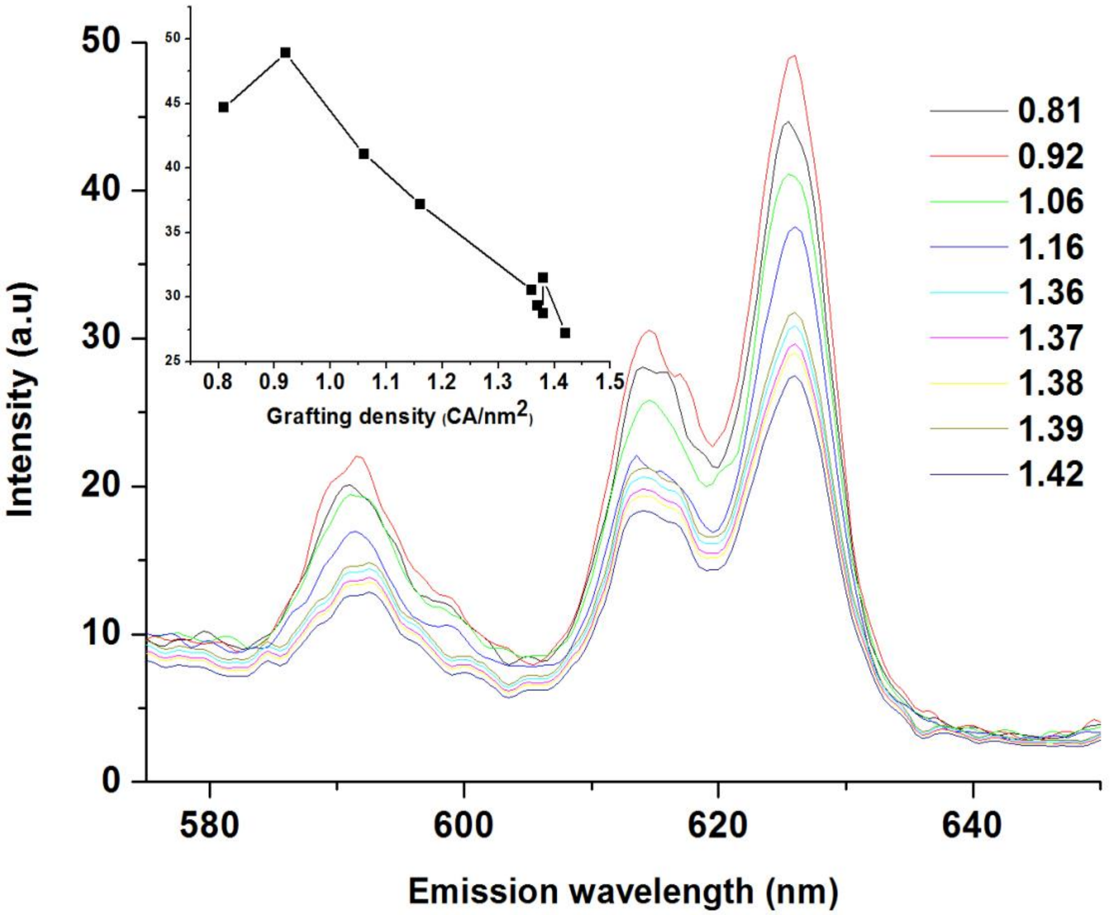

Figure 7.16: Pl emission spectra (λ_{ex} = 254 nm) of CA coated phosphors plotted as a function of CA grafting density (figure key). Inset, shows the variation of PL intensity ($^5D_0 \rightarrow {}^7F_{2\ [625\ nm]}$) against the CA grafting density.

To ensure that the reduced PL yield (*ca.* 40 %) was not intrinsic to the system. Samples for comparison were synthesised by post synthesis functionalisation with citric acid of both $(Y_{0.96}Eu_{0.04})_2 O_3$ and $(Y_{0.96}Eu_{0.04}) OOH$ nanoparticles (section 7.2.4). ATR-FTIR confirmed that similar citrate coordination to that produced directly was observed, the wavenumber separation values (ν_s COO$^-$ and the (ν_{as}) COO$^-$ modes) were 210 and 215 cm^{-1} suggesting a mixture of unidentate and bi-dentate co-ordination. (Mudunkotuwa & Grassian 2010) For comparison, the grafting density for the $(Y_{0.96}Eu_{0.04}) OOH$ and $(Y_{0.96}Eu_{0.04})_2 O_3$ samples was calculated as 1.46 and 2.4 CA/nm^2 for $(Y_{0.96}Eu_{0.04})_2 O_3$ and $(Y_{0.96}Eu_{0.04}) OOH$ samples, respectively. Consistent with the results outlined earlier. In both samples, a significant reduction in fluorescence intensity is observed (*ca.* 52 and 48 % for $(Y_{0.96}Eu_{0.04})_2 O_3$ and $(Y_{0.96}Eu_{0.04}) OOH$ samples, respectively) when the coated samples are compared to the precursor particles. Confirming, that the PL reduction was attributed principally to adsorption of citrate occurring through a mechanism of increase in non-radiative de-exciation in the coated phosphor systems.

7.3.4: Post synthesis Modification of Citric acid Coated Phosphors:

As discussed in Chapter 6 electrostatically stabilised dispersions of nanoparticles are not often suitable for application in high electrolyte media such as in physiological buffers. The addition of electrostatically stabilised colloidal dispersions to electrolyte solutions leads to the collapse of the double layer preventing particle interaction. (Graf *et al.,* 2003) This section details an investigation into the steric stabilization through EDC amidation of citric acid coated ($Y_{0.96}Eu_{0.04}$) OOH using two amine mono-end functionalised polyethylene glycol (NH_2-PEG) derivatives with molecular weights of 2 and 5 kDa. The experimental details of the coupling reaction are presented in Section 7.2.4. (Lattuada and Hatton 2007) A schematic of the coupling mechanism is presented in Appendix 2.

FTIR was used to confirm the presence of PEG variants coupled to citric acid coated ($Y_{0.96}Eu_{0.04}$) OOH nanoparticles. The spectra of both free NH_2-PEG (2 kDa and 5 kDa) and coated particles are presented in figure 7.17. The spectra are dominated by the expected –(C)O-C vibration at 1104 cm^{-1}, characteristic of the PEG chains, this IR active mode is present in both bound and unbound NH_2- PEG. The spectra obtained for both bulk PEG variants showed a very weak mode centred at 1584 cm^{-1}, characteristic of $–NH_2$. However, upon amidation the mode has shifted to 1540 cm^{-1}, characteristic of formation of an amide bond. The low intensity of the mode centred at 1540 cm^{-1} is expected as *ca.* 200 amide bonds would be present per particle assuming a grafting density of 1.4 molecules (CA)/nm^2 and a crystallite size of *ca.* 25 nm. Other characteristic modes observed for the PEG coated samples, such as the modes centred at 2943, 2880, 2821, 2804, 2704, 1466, 1359, 1342, 1279, 1241, 1060, 961, 949, and 842 cm^{-1}, indicate that the PEG grafted onto the particle surface is ordered (after drying), where the aforementioned modes are typically attributed to harmonics of -COC- stretches and suggestive of a dense coverage of PEG on the ($Y_{0.96}Eu_{0.04}$) OOH nanoparticle cores. (Zhang *et al.,* 2006)

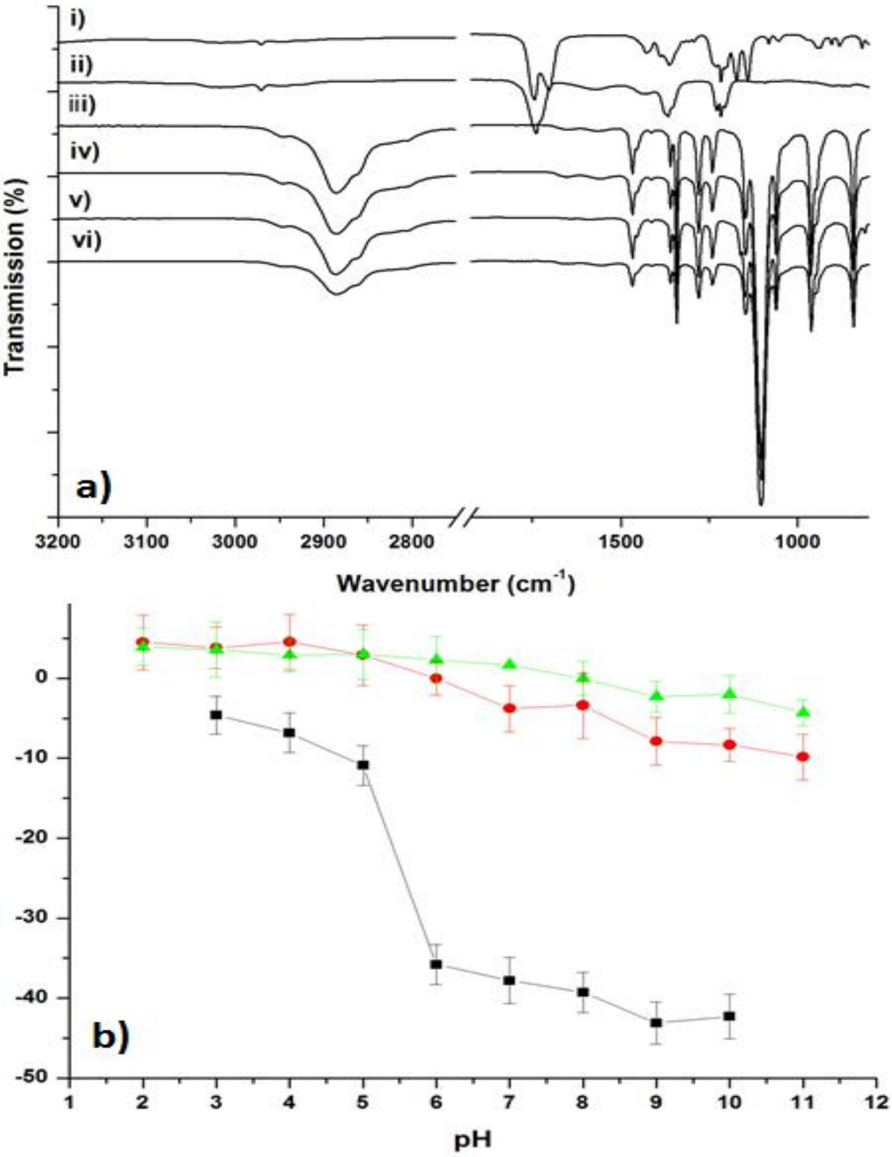

Figure 7.17: a) FTIR spectra of citric acid coated $(Y_{0.96}Eu_{0.04})OOH$ nanoparticles and NH_2-PEG variants produced through EDC coupling of the as synthesised citric acid coated particles; **i)** Bulk citric acid, **ii)** Citric acid coated $(Y_{0.96}Eu_{0.04})$ OOH nanoparticles, **iii)** Bulk 2 kDa NH_2-PEG, **iv)** 2 kDa NH_2-PEG modified $(Y_{0.96}Eu_{0.04})$ OOH, **v)** Bulk 5 kDa NH_2-PEG and **vi)** 5 kDa NH_2 - PEG modified $(Y_{0.96}Eu_{0.04})$ OOH. **B)** Comparison of Zeta-potential titrations performed on CA-coated $(Y_{0.96}Eu_{0.04})OOH$ (squares), 2 kDa PEG coated $(Y_{0.96}Eu_{0.04})$ OOH (circles) and 5 kDa PEG coated $(Y_{0.96}Eu_{0.04})$ OOH. Error bars represent the standard deviation of the measurements.

Figure 7.17b, shows the zeta-potential titration of both PEG variants compared to the titration of citric acid coated $(Y_{0.96}Eu_{0.04})$ OOH. It is apparent from Figure 7.17.b that no significant surface charge is observed for PEG coated variants. This result is expected as PEG does not have any readily ionisable groups under the presented measurement conditions. Hence, the moderate surface charge observed is attributed to amphoteric behaviour of OH groups within the PEG chains. (Yoncheva *et al.,* 2007) To further confirm the colloidal stability of the samples functionalised with 2 and 5 kDa PEG a colloidal stability study was performed by measuring the evolution of hydrodynamic diameter as a function of increasing electrolyte concentration as shown in figure 7.18. Typically, if the thickness of the polymer is large enough, the Van der Waals attraction between the particles is negligible in comparison to the Brownian thermal energy leading to a sterically stabilised dispersion even when the double layer is entirely suppressed by the electrolyte concentration. (Napper 1977; Raghavan *et al.*, 2000) The slope of the $R_{(\mathrm{H})}$ versus time curve for $t \rightarrow 0$ at each salt concentration (estimated with low-order polynomial fitting) has been used to estimate the stability ratio for each electrolyte concentration. The stability ratio (W) is commonly used as a measure to infer the type of coagulation within the colloidal system. At a fixed particle concentration the colloidal stability, W is calculated from equation 7.2.

$$\mathrm{W} = \frac{\left(\left(\frac{\delta \mathrm{r}}{\delta \mathrm{t}}\right)_{\mathrm{t}\rightarrow 0}^{(\mathrm{f})}\right)}{\left(\frac{\delta \mathrm{r}}{\delta \mathrm{t}_{\mathrm{t}\rightarrow 0}}\right)} \quad \textbf{(Equation 7.2)}$$

Where, r is the measured hydrodynamic diameter and t is the measurement interval, the term $\delta r/\delta t_{\ (t\rightarrow 0)}^{\ (f)}$ is defined the fast coagulation state (the slope of the curve when it becomes independent of electrolyte concentration) and $\delta r/\delta t_{\ (t\rightarrow 0)}$ is the slope of the measurement. (van der Zande *et al.,* 2000) When $W > 1$ only a fraction of the particle collisions leads to aggregates because of the presence of an energy barrier generated by the sum of the attractive and repulsive forces acting between the particles (principally electrostatic). When W = l every collision produces an aggregate (lack of the energy barrier) and the diffusion limited aggregation rate (fast) occurs. As shown in figure 7.18 the sample grafted with 5 kDa PEG was very stable ($W \approx \infty$) over the measured electrolyte range suggesting that a significant steric component was present. Whereas, the electrostatically stabilised particles showed significant agglomeration and settling behaviour at even moderate electrolyte concentrations $W = 1$ occurring at *ca.* 100 mM NaCl (figure 7.18 a). The sample grafted with 2 kDa PEG showed colloidal stability greater than that observed for citric acid coated particles alone with $W = 1$ occurring at *ca.* 200 mM NaCl. These results suggest the thickness of the PEG layer is insufficient to confer a steric mechanism of particle stabilisation as the polymer layer is too thin to confer a sufficient energy barrier to particle agglomeration and Van der Waals interactions between particles are of similar (if not greater in) magnitude to the Brownian thermal energy of the system. Showing relatively thick polymer layers are required to stabilise a material in this size range.

The effect of further functionalisation using PEG was investigated on the emission characteristics of the phosphor system. The emission spectra from excitation at 254 nm showed strong red emission in the 600 - 630 nm regions corresponding to transitions of $^5D_0 \rightarrow {}^7F_2$ and a weaker emission region (580 - 600 nm) attributed to $^5D_0 \rightarrow {}^7F_1$ transitions with the emission characteristics being similar to those presented in Section 6.3.1. The PL intensity of the $^5D_0 \rightarrow {}^7F_{2\ \mathrm{and}}$ $^5D_0 \rightarrow {}^7F_1$ transitions was completely invariant of grafting with both PEG moiety as 2 kDa and 5 kDa variants. This result was expected as PEG shows little absorption in the visible region and similarly in the Hard UV region > 300 nm and correspondingly good light transmission was observed in the red region.

7.3.5 Evaluation of $Y_{1-x}Eu_xOOH$ nanoparticles as probes in biological imaging

In biological imaging applications where UV radiation can damage organic structures, blue excitation has been employed with Eu^{3+} complexes and other lanthanide doped nanophosphors as a suitable excitation wavelength to allow live cell imaging. (Sun *et al.*, 2011) To demonstrate the use of both citric acid coated $(Y_{1-x}Eu_x)$ OOH and $(Y_{1-x}Eu_x)_2$ O_3 nanoparticles as potential probes for bioimaging, optical phantoms containing various concentrations of coated nanoparticles (0.01, 0.05, 0.1, 0.5, 1.0 mg mL^{-1}) were analyzed in an photoluminescence spectrometer using an excitation wavelength of λ_{ex} = 473 nm and measuring emission at wavelengths summarised in figure 7.19. The results of optical phatoms containing $(Y_{0.96}Eu_{0.04})OOH$ - CA (Method 6.2.3), $(Y_{0.96}Eu_{0.04})_2$ O_3 - CA (Method 6.2.3) , CA - $(Y_{0.96}Eu_{0.04})OOH$, 2kDa NH_2 - PEG $(Y_{0.96}Eu_{0.04})OOH$ and 5kDa NH_2 - PEG $(Y_{0.96}Eu_{0.04})OOH$ particles are shown comparatively in figure 7.19 as a function of particle concentration. Where, using 473 nm excitation ($^7F_0 \rightarrow {}^5D_0$) resulted in almost complete quenching in samples functionalised with PEG when compared to the materials which were coated with citric acid alone. The reduction in intensity of PEG coated samples was attributed to the adsorption of PEG in the 300 - 500 nm region, preventing down conversion by the phosphor core (data not shown). (Choi, Moon, & Jung 2010) Whereas, when hard UV excitation was used no apparent reduction in PL intensity was observed. Suggesting that samples showing only a minimal coating would be suitable for application in assays using blue excitation.

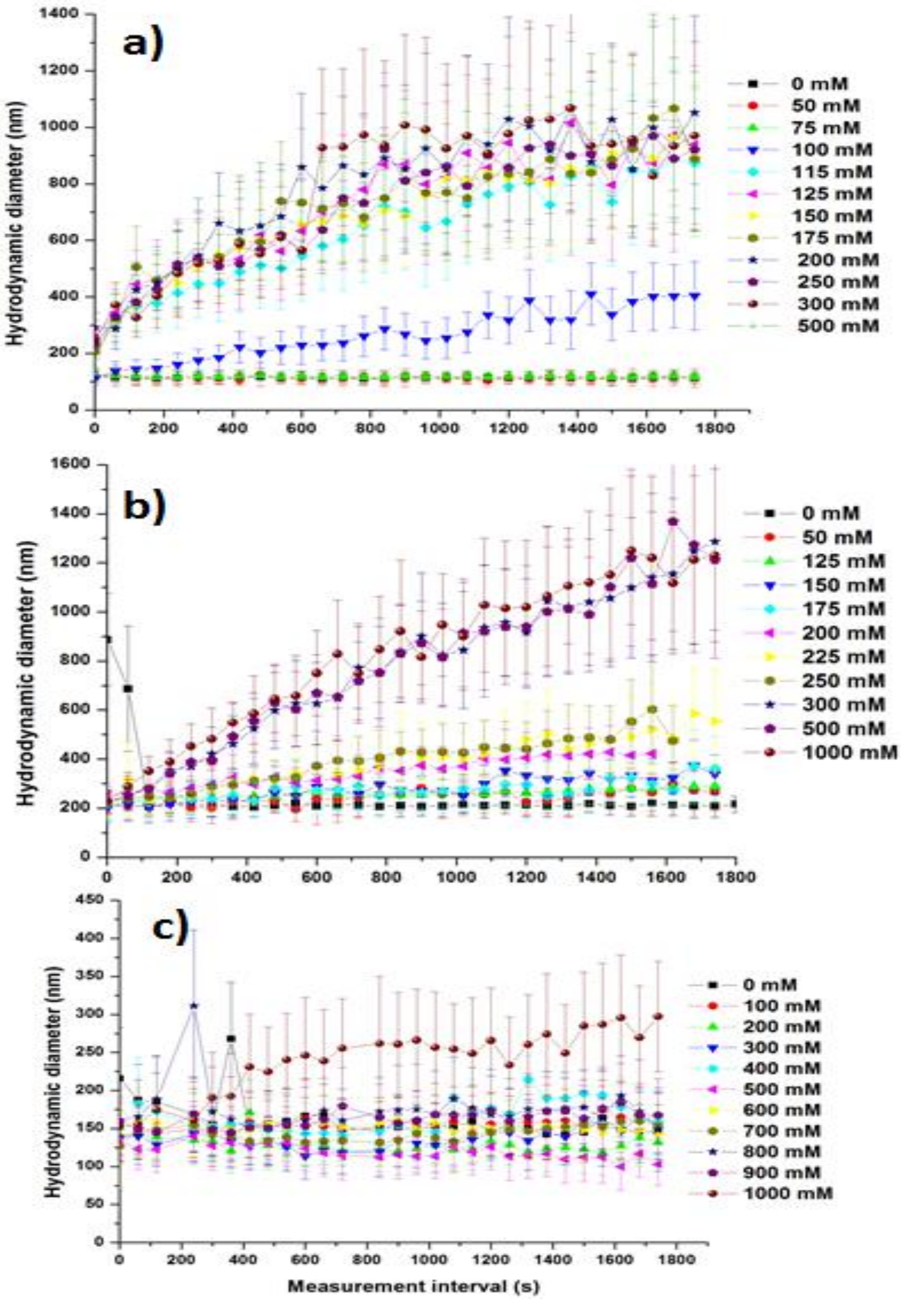

Figure 7.18: The effect of different electrolyte concentrations on the evolution of hydrodynamic diameter measured using DLS; **A)** Citric acid coated nanoparticles obtained directly from the CHFS process, **B)** NH_2-PEG [2 kDa] $(Y_{0.96}Eu_{0.04})OOH$ and **C)** NH_2-PEG [5 kDa] $(Y_{0.96}Eu_{0.04})OOH$. The relative sample polydispersity of the sample measured in nm is presented for each data-point. Lines are drawn in each of the data series to serve as a guide to the eye only.

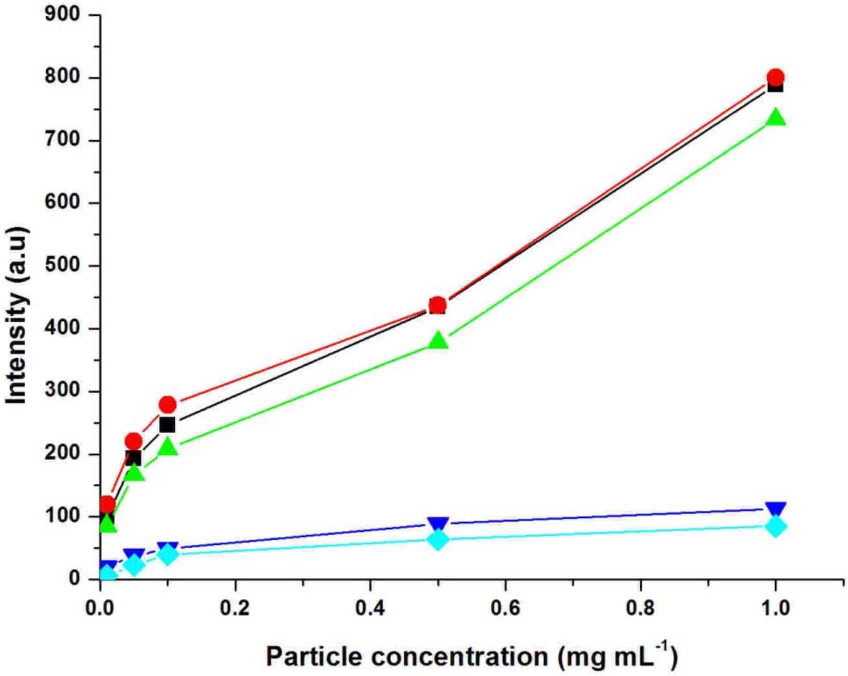

Figure 7.19: Comparison of Optical phantoms of coated phosphor materials using 473 nm excitation; $(Y_{0.96}Eu_{0.04})OOH$-CA ($^5D_0 \rightarrow {}^7F_2$) [squares], $(Y_{0.96}Eu_{0.04})_2O_3$-CA ($^5D_0 \rightarrow {}^7F_2$) [circles], CA-$(Y_{0.96}Eu_{0.04})OOH$ ($^5D_0 \rightarrow {}^7F_2$) [triangles], 2kDa NH_2-PEG $(Y_{0.96}Eu_{0.04})OOH$ [inverted triangles] and 2kDa NH_2-PEG $(Y_{0.96}Eu_{0.04})$ OOH [diamonds].

To demonstrate the potential application of citric acid coated $(Y_{0.96}Eu_{0.04})$ OOH and $(Y_{0.96}Eu_{0.04})_2$ O_3 NPs as fluorescent probes they were visualised under conditions analogous to a typical *in-vitro* fluorescence imaging experiment. Particles were sparsely dispersed on coverglass and visualised using 470 nm excitation / 620 nm emission and resolvable fluorescence from both dispersions of particles was observed (Figure 7.20). The diameter of fluorescence signals was typically in the order of 1 - 2 pixels (*ca.* 1 pixel = 270 nm) suggest that most of the luminescence observed is from single citric acid coated NPs when the approximated wave spread function of the microscope is considered (λ / 2 = 320 nm). The data were analysed from fluorescence images over a 60 × 60 µm area, and high photochemical stability was observed with no blinking. (Sun *et al.*, 2011) The size data determined from optical methods was consistent with the data presented from light scattering techniques (figure 7.19). Fluorescence from particles was not visualised using 470 nm excitation / 540 nm emission consistent with the PL data recorded for the samples. Suggesting resolvable fluorescence from the particles could be visualised in a typical fluorescence cell imaging experiment.

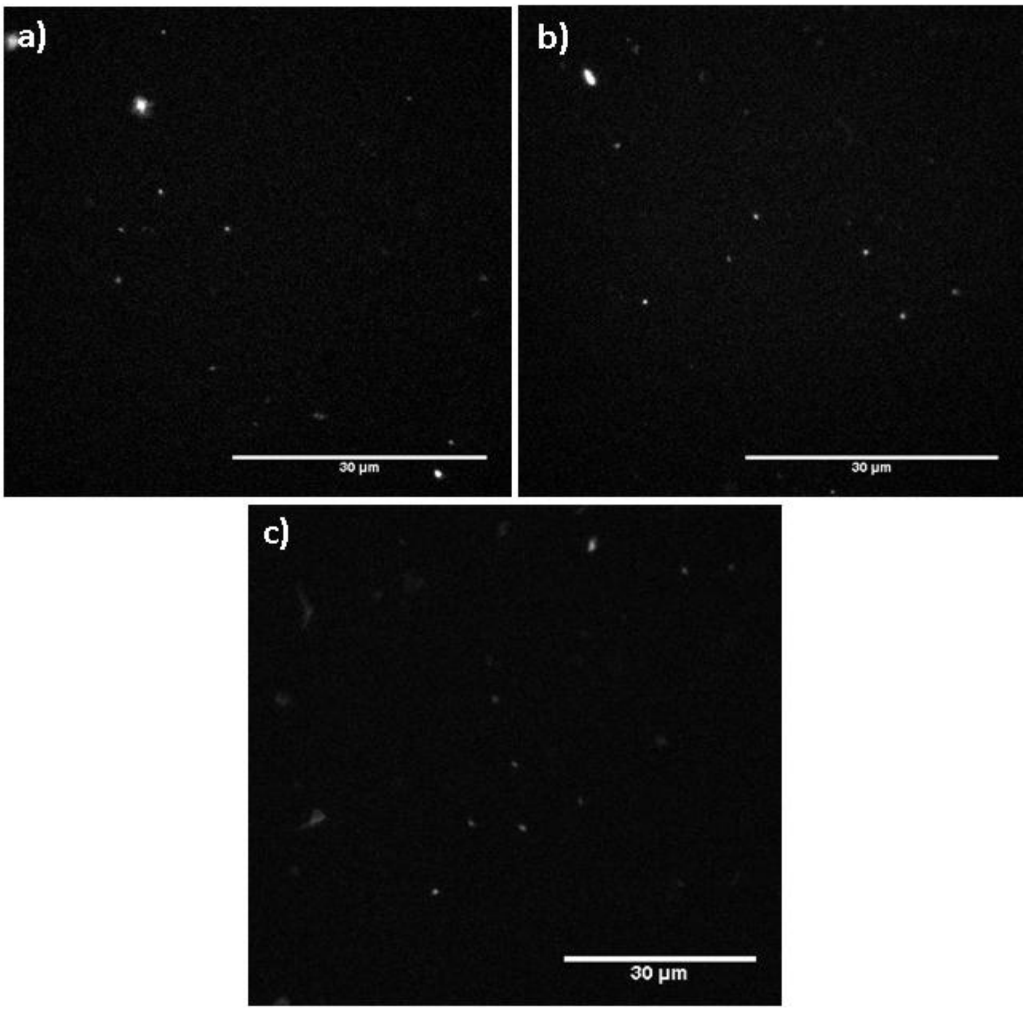

Figure 7.20: The diameter of fluorescence signals from nanoparticles dispersed on cover-glass visualised using 470 nm excitation / 620 nm emission **a)** citric acid coated $(Y_{0.96}Eu_{0.04})OOH$ nanoparticles, **b)** citric acid coated $(Y_{0.96}Eu_{0.04})_2O_3$ nanoparticles and **c)** citric acid coated $(Y_{0.96}Eu_{0.04})OOH$ nanoparticles produced directly using CHFS.

To further assess the visualisation of phosphors the dispersed phosphor systems an assay was designed to evaluate if fluorescence from phosphor nanoparticles could be resolved from cellular autofluorescence (Figure 7.21). In the assay phosphor NPs (filtered through a 0.22 µm syringe filter) were dispersed in PBS to a concentration of 166 µg mL^{-1} and COS7 cells were incubated in the solution for 4 hours. We predicted that constitutive uptake of the particles would occur consistent with previous publications. (Bruchez *et al.*, 1998; Sun, Carpenter, Pratx, & Xing 2011) Bright field image of a COS7 cell following incubation with nanoparticles of coated $(Y_{0.96}Eu_{0.04})$ OOH and $(Y_{0.96}Eu_{0.04})_2$ O_3, are shown to identify the cell body visulaised in each of the fluorescence signal measurement conditions. In the bright field images (figure 7.21 a, d, g) evidence of particle agglomeration is observed through the visualisation of sub-micron particle agglomerates surrounding the cell membrane. Agglomerate formation was expected as the electrostatically stabilised dispersion suffers compression of the double layer at physiological salt concentrations resulting in agglomeration (figure 7.19). A degree of cellular autofluorescence was observed using 470 nm excitation/ 540 nm which is likely to arise from flavoproteins and serves to identify the cellular organelles likely to fluoresce as shown in Figure 7.21 b, e, h. (Sun *et al.,* 2011) However, no fluorescence from the phosphor nanoparticles was observed at this measurement wavelength, consistent with our fluorescence measurements. Figures 7.21 c, f, I show effective visualisation of the phosphor particles coating the cell membrane. As the phosphors were not targeted to cell membrane proteins, a near uniform coverage of the particles was observed. Experiments performed in the absence of the phosphor nanoparticles using 470 nm excitation / 620 nm emission showed some overlap between the fluorescence observed at 540 nm emission and was attributed to the broad fluorescence profile of flavoproteins, explaining the overlap between fluorescence signals in images 7.21 c, f, I and 7.21 b, e, h. Where all particle types showed resolvable fluorescence and visualisation was consistent with that inferred from the optical phantom experiment.

7.4 Conclusions

The CHFS process was shown to be capable of directly producing a visibly bright phosphor nanoparticle without the requirement for post synthesis annealing when reaction point temperatures above the critical point of pure water. Alongside temperature, base was shown to influence the phase behaviour of the phosphor host with efficient phosphor materials only being produced at high base concentrations (> 0.1 M KOH). Similarly, the phase behaviour of the host system was shown to differ upon the level of Eu^{3+} substitution within the synthesis, suggesting the nucleation of different nanoparticles within the reaction point (which is currently not fully understood). Phosphor nanoparticles produced directly from the process were shown to be highly crystalline single phase materials and as such show high PL intensity, a large benefit of many other bottom up processes used for their production in terms of retaining a small particle size.

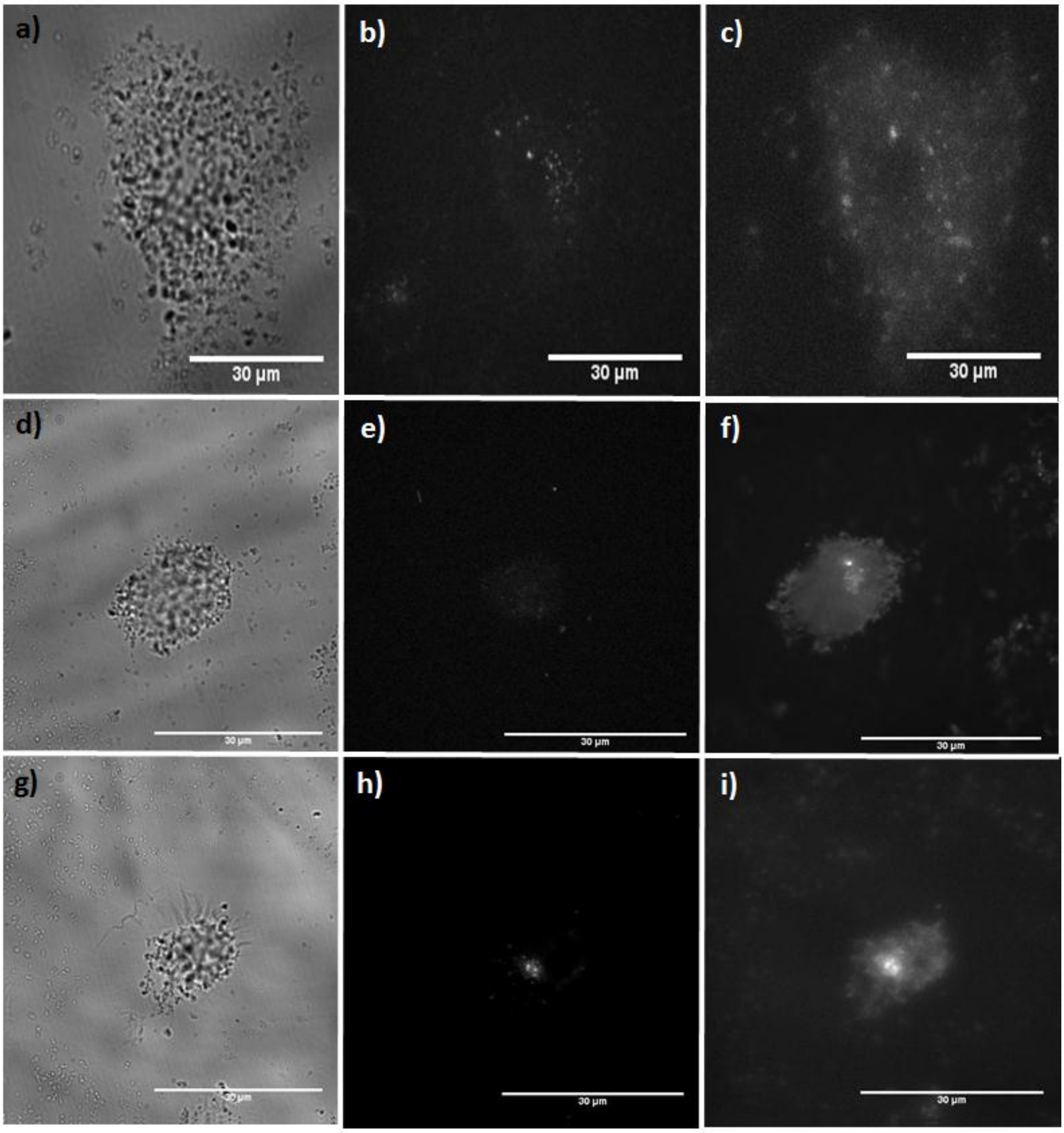

Figure 7.21: Visulalisation of COS7 cells using citric acid coated $(Y_{0.96}Eu_{0.04})OOH$ [a, b, c] $(Y_{0.96}Eu_{0.04})_2O_3$ nanoparticles[d, e, f] and citric acid coated $(Y_{0.96}Eu_{0.04})OOH$ produced directly from CHFS [g, h, i]. Images [a, d and g] show bright-field image of incubated cells. Images [b, e and h] show the location of cellular auto-fluorescence measured at 470 nm excitation / 540 nm emission and Images [c, f, I] show down converted luminescence following 470 nm excitation / 620 nm emission showing cellular uptake.

The rapid and efficient conversion of one of the $(Y_{0.96}Eu_{0.04})OOH$ nanoparticles to the corresponding oxide phosphor $(Y_{0.96}Eu_{0.04})_2O_3$ was conducted using a flash heat treatment strategy, showing complete dehydration of the ($Y_{0.96}Eu_{0.04}$) OOH nano-precursor can be achieved with limited agglomeration and particle growth on timescales significantly shorter than those typically reported in the literature. Showing that the use of nanoparticles as precursors is a suitable strategy for the synthesis of higher order oxide structures as nanomaterials if a suitable annealing strategy is employed. Time resolved PL measurements of the annealed samples suggested the grain growth of the annealed materials was responsible for the altered PL characteristics of the materials upon heat treatment. Analysis of the evolution of crystallite size showed that even moderate annealing durations (much shorter than those typically used for the production of Y_2O_3 nanoparticles) rapidly grew to sizes > 100nm. This work provided an indication of how quickly coarsening occurs in annealed nanomaterials.

Modification of the CHFS process as initially presented in Chapter 6 allowed the systematic evaluation of producing surface functionalsed phosphor nanoparticles directly using CHFS. Where, the core particle formation steps were effectively segregated from the functionalisation steps allowing the influence of surface functionalisation to be accurately determined. Several observations were presented which differed from those initially presented in Chapter 6. Where, a different saturation grafting density of citric acid was observed which could be tentatively attributed to the preferential coordination of CA to metal terminated crystal facets. Similarly a degree of fluorescence quenching was observed that was linked to the grafting density of citric acid on the phosphor nanoparticle suggesting that functionalisation for a near consistent particle size increases the proportion of non-radiative de-excitation processes in the phosphor system. Comparisons to materials produced using a more common surface functionalisation method yielded a similar reduction in PL yield confirming the observation for materials produced directly using the modified CHFS process.

The nanoparticles produced in this work which were either produced directly from the process or suitably formulated as dispersions were found to suitable as probes in biological imaging and could be readily resolved from cellular autofluorescence . Limitations were identified in the choice of post synthesis functionalisation strategies due to the absorption characteristics of the coating materials which limit the detection of these materials in common fluorescence assays. Although disappointing these results showed that efficient post-synthesis functionalisation of nanoparticles was possible suggesting the use of nano-materials such as these could be diversified in more targeted applications.

In closing, the results presented herein highlight a desirable methodology for the synthesis method of phosphors as this strategy eliminates the need for high-temperature and prolonged heat treatment of as-prepared materials.

6.5 Future work

Further optimisation of the process specifically for the production of citric acid coated $(Y_{0.96}Eu_{0.04})OOH$ nanoparticles would be beneficial as the quality of the dispersion (relative polydispersity) would hinder application of the material in many analytical fields (without refinement). Although, the apparent saturation grafting density could be a physical factor limiting the quality of the dispersion in this host system. Alternatively, the use of further material refinement steps to improve the dispersion of the particles would be useful, as this is a well know refinement step (Field-flow fractionation and the like) and is commonly used in the production of many nanomaterials. The effect of different processing conditions on the relative quantum efficiency of the material would be useful to investigate quantitively as it would allow further optimisation of the material allowing greater visualisation in any future cell work, although a qualitative analysis presented here was shown to be satisfactory to identify materials as probes in cellular imaging. As stated in Chapter 6 it would be useful to assess the cytotoxicity of both coated and non-coated nanoparticles. Similarly, identification of this phosphor system as a promising biological imaging probe suggests that the further evaluation of an amidation or other coupling strategy to allow for the specific targeting of nanoparticles to certain cellular compartments/receptors would also be of interest. Terminally, one of the most interesting applications would include the use of antibody fragments or localising peptides, allowing the visualisation of receptors or cellular compartments respectively (analogous to the current application of quantum dots, without the detrimental effects of photobleaching) .

The development and evaluation of alternative rare-earth ion doped nanoparticles phosphors would also be an interesting avenue of investigation to assess if the CHFS process would allow for the synthesis of known higher efficiency phosphor materials. In fact several europium doped systems ($Eu_xY_{1-x}VO_4$ and $Eu_xLn_{1-x}PO_4$) have also been produced by the author and will be reported in due course. The literature highlights several examples of rare-earth ion doped oxide phosphors which would be suitable for imaging applications especially those based on a $LaPO_4$ host lattices. The bottom up CHFS process would convey certain synthetic advantages over the methods commonly used to produce such materials as highlighted previously. Upconverting phosphor systems are becoming of acute interest in the biomedical application of phosphor nanoparticles, as IR transmission through tissue is high a substantial research effort is now focusing on the synthesis of upconverting phosphor compositions. It may be of interest to assess the application of CHFS to the synthesis of these materials.

Chapter 8

Scale up of Nanoparticle Synthesis using CHFS

8.0 Aim:

The primary objective of this Chapter is to evaluate the practical aspects of CHFS process scale up. This Chapter details investigations into the construction and operation of a pilot scale CHFS process with a nominal flow output of 800 mL min^{-1} of nanoparticle laden slurry. The overall objective of this Chapter can be summarised into the following areas; **1)** investigation into the volumetric scale up of the confined jet mixer as evaluated in Chapter 4, **2)** the effects of volumetric scale up on nanoparticle characteristics and the effects of mass based scale up on particle properties, **3)** Investigation into the scale up of surface functionalised nanoparticle synthesis at pilot scale, **4)** Application of the pilot scale CHFS process to combinatorial materials synthesis. The presented work is intended to demonstrate that the CHFS process is readily scaled to a volumetric enlargement of 20X that of the laboratory scale process.

8.1 Introduction:

"Scale up" is generally defined as the process of increasing the batch size or the production rate of a process dependent upon its operation. Scale up of a process can also be viewed as a procedure for applying the same process to different output volumes through either larger reaction / reactor volumes or multiplicity in synthesis commonly referred to as "scale out". (Roco 2001; Trambouze 1981) The latter suffers complications if the process is difficult to reproduce or suffers batch variation. (Jongen *et al.,* 2003) There is a subtle difference between these two definitions, as batch size enlargement does not always translate into a size increase of the processing volume *i.e.* increasing the yield of a product or by increasing the concentration of reagents to increase yield per unit process volume (mass based scale up). (Kreuter 1990; Pennemann *et al.,* 2004)

Inorganic nanoparticles have reached annual production volumes of several metric megatons. (Djerdj *et al.,* 2008; Journet *et al.,* 1997; Yoshimura 1998) Most of the worldwide production on an industrial scale can be assigned to carbon black, silica and titania. (Liu *et al.,* 2009; Madler *et al.,* 2002; Roco 2001; Stark and Pratsinis 2002) The large production volume of the highlighted nanomaterials is counterbalanced by the high production capacity of a very limited range of elemental compositions; the reasons for this are elaborated further in Chapter 1. There is significant interest in expanding the capacity of nanomaterial synthesis methods to produce materials of more diverse composition, whilst retaining the physiochemical characteristics of nanomaterials often initially identified from synthesis on a smaller scale. (Tretyakov and Goodilin 2009) One of the major reasons for the lack of variety in material composition and a wider range of nanoparticles is often limited by a complication with the scale up of a previously identified process for their manufacture. (Kreuter 1990) Not all processes are amenable to scale up, for example the chemical synthesis of proteins, peptides and nucleic acids requires a reduction in batch size to increase product quality *i.e.* “scale-down”. (Sweere *et al.,* 1987)

The complexity in scaling a nanoparticle production process is often reduced to complications associated with ensuring a uniform particle nucleation environment, as a result control over particle size and polydispersity. (Marchisio *et al.,* 2006) The difficulty in scaling up production lies in achieving a stable and uniform reaction environment, whether this takes the form of nanoparticles synthesis in large chemical baths (liquid phase) or combustion of precursors in a flame (stability of flame front) most endeavours of scale up strive to ensure uniform quality of the resulting nanoparticles across production scales. (Dirksen and Ring 1991; Tsuzuki 2009) Although there are many general complications with increase in production rate; particle agglomeration during particle growth, elongated particle growth phases, loss of control over particle nucleation, compositional differences in materials (*e.g.* material phase and homogeneity). (Chen *et al.,* 2000; Cushing *et al.,* 2004; Dirksen & Ring 1991) Many of these complications arise from a reduction in the intimate control normally attainable over a small scale chemical reaction. (Dirksen & Ring 1991) This lack of reaction control is often attributed to, concentration gradients, thermal gradients and inhomogeneity in mixing reagents in large volumes (*i.e.* heat and mass transfer differences in the large scale analogue). (Tsuzuki 2009) Similarly, increasing the production rate yielding high particle concentration which can cause particle agglomeration, elongated particle growth phases and an increase in particle polydispersity. (Dirksen & Ring 1991) As a result, the production of nanoparticles on a commercial scale often produces materials which are different to those produced by analogous small scale processes, and in many cases require lengthy reoptimisation for each material composition to be produced. (Liu *et al.,* 2009)

As CHFS is a continuous flow process, in which reactants undergo a rapid change to a condition of high supersaturation which leads to the formation of nanoparticles. As highlighted in Chapter 1 and further discussion presented in this thesis, CHFS can be adapted to many synthetic challenges often forming products which are not readily accessible through more conventional methodologies (*e.g.* kinetic or metastable products). (Boldrin *et al.*, 2007; Chaudhry *et al.*, 2006; Gruar *et al.*,2010; Parker *et al.*, 2011; Weng *et al.*, 2009; Zhang *et al.*, 2009) The high supersaturation (*i.e.* dominance of particle nucleation) afforded by continuous hydrothermal methods generally leads to a large number of nucleation events and results in smaller particles than equivalent reactions performed on much longer time scales (*i.e.* batch reactions) with particles of similar physicochemical properties being obtained over broad ranges of synthesis variables (Chapters 3, 4 ,5 and 6). Reactions which produce nanoparticles in CHFS are rapid often with residence times in the order of a few seconds. (Adschiri *et al.*, 2011; Marre *et al.*, 2012) Many material phases and compositions are accessible directly, as highly crystalline and phase pure nanomaterials. (Chaudhry *et al.*, 2006; Gruar *et al.*, 2010; Zhang *et al.*, 2009) It has been demonstrated that hydrothermal flow reactions can be conducted using large scale reactors similar to those used by Sue *et al.*, which are reviewed in greater detail within Chapter 1. (Adschiri *et al.*, 2011) These reactors rely on a different engineering mechanism for achieving metal salt hydrolysis and dehydration, and are based upon feeding precursors through a heated pipe (analogus to the already commercially operated SCWO plants) resulting in nanoparticles which do not nucleate as uniformly resulting in broader size distributions. (Adschiri *et al.*, 2011)

In the embodiment of CHFS presented throughout this thesis it has been shown that the rapid rates of particle crystallisation lead to the formation of similarly sized nanomaterials if the mixing processes are sufficiently similar and appear to not be affected by small fluctuations in thermal gradients or mixing events occurring on *(sic)* small timescales. As the scale up of a chemical process is typically complex, and often suffers from unforeseen complications such as loss of size control or phase separation, etc. The purpose of this Chapter is to evaluate the potential of CHFS as a large scale nanoparticle manufacturing technique. In this chapter variants of the above scale up practices are evaluated with regard to the CHFS process as defined previously within this thesis. Within this work many materials have been evaluated on the basis of volumetic scale up, with distinct reaction types from Chapters 4 and 5 and 6 being evaluated. In selected cases, scale up strategies based on both a volumetic and mass basis have been used to further explore scale up methodologies using a pilot scale CHFS process.

8.2 General Synthesis and Procedures:

All experiments presented in this Chapter were conducted using the pilot scale CHFS process as defined in Chapter 2. The process was designed and constructed in collaboration with Dr Christopher Tighe. The details of the process equipment are presented in Chapter 2 alongside descriptions of major process modifications and the reactor configurations used for materials synthesis. Sections are presented to address the objectives of this chapter as highlighted in the aims. This chapter uses a variety of material compositions to highlight different aspects of scale up reactions.

8.2.1 Materials:

Iron (III) citrate ([Fe ($C_6H_5O_7$] technical grade, > 98 %), Citric acid ([$C_6H_8O_7$] 99 %) and $(NH_4)OH$ solution (28 vol %) were supplied by Sigma–Aldrich Chemical Company (Dorset, UK). Iron(III) citrate powder was dissolved in water by adding a stoichiomentric amount of NH_4OH solution forming a soluble Iron citrate complex (Ammonium ferric citrate [NH_3 $Fe(C_6H_5O_7)$ and was used exclusively as the metal precursor solution for iron based samples (Sections 8.3.4)). Zinc nitrate ($Zn(NO_3)_2{\cdot}6H_2O$, > 98 %), Cerium ammonium nitrate ($(NH_4)_2Ce(NO_3)_6\ {\cdot}6H_2O$ > 98.5 %) and potassium hydroxide (KOH, > 85 %) were obtained from Sigma-Aldrich (Dorset, UK). These precursors were used for the synthesis of ZnO samples and Ce-Zn samples as presented in sections 8.3.2 and 8.3.3. All experiments were conducted using deionised water (>15 MΩ).

8.2.2 *In-situ* Temperature Measurements:

In-situ temperature measurements have been uses to assess the degree of mixing between the precursor (Q_p) and supercritical water feed (Q_{sw}) in the pilot scale CHFS process. The system configuration was analogous to the three pump system typically used for the synthesis of nanoparticles (described in Chapter 2 section 2.3). An analogous temperature measurement strategy to that presented in Chapter 3 was used to evaluate a suitably scaled mixer geometry (detailed in table 8.1, compared to the laboratory scale mixer chosen as the basis of scale up) and explained further in section 8.3.1. In the pilot scale process, eight simultaneous measurements of temperature were taken at different locations within the reaction point as a function of total system flow rate ($Q_p + Q_{sw}$) and at different heater set temperatures (350 – 450 °C). All measurement positions were normalised to z/d_i where d_i is the internal pipe diameter and z is the relative position of the thermocouple from the terminus of the preheated water inlet (shown pictorially in figure 8.1). The physical dimensions of reaction point (mixer) used in the pilot scale CHFS process are presented in table 8.1. Measurement at reaction temperatures and pressures was allowed through the use of a spectate fitting which is detailed in Chapter 2. In the pilot scale process the length of the cooling apparatus meant that thermocouples were fed into the reactor upstream of the reactor and were insulated from the high temperatures at the reaction point by *ca.* 1 M of 3/8” 316 SS tubing. Again, measurements of temperature could not be taken during materials synthesis due to fouling of the thermocouples. All calculations derived from temperature measurements were evaluated using the IAPWS formulations as detailed in Chapter 2.

8.2.3 Investigation into the mass based scale up of CHFS:

Table 8.3 provides a summary of the solution compositions and synthesis conditions used for the production of ZnO nanoparticles using the pilot scale CHFS process. Chapter 4 section 4.3.2 provides a summary of the materials produced on the laboratory scale process chosen as the basis for scale up reactions and are identified here as they were in Chapter 4. ZnO nanoparticles were produced on the pilot scale CHFS process using a four pump configuration as shown in Chapter 2 (figure 2.7). All ZnO samples reported in this Chapter are identified by the concentration of zinc nitrate and the total system flow rate ($Q_p + Q_{sw}$) *i.e.* a sample produced using 0.1 M zinc nitrate (KOH was always used as a mineraliser in a 1:1 ratio with zinc nitrate) and a total system flow rate of 800 ($Q_{sw} = 400$, $Q_{pkoh} = 200$, $Q_{pzn} = 200$) is identified as 0.1M800. In this section, two sets of reactions are presented, the first set assessed the effect of volumetric scale up (0.05M400 - 0.05M800 and 0.1M400 - 0.1M800) as defined in table 8.3, the second set (0.1M700 - 0.9M700) assessed the effect of mass based scale up. Samples 0.05M400 - 0.05M800 and 0.1M400 - 0.1M800 were produced by using Pump 1 (P-1) to supply supercritical water (scH_2O) to the reaction point and pumps 2 and 3 were used to supply the reaction precursors (KOH and $Zn(NO_3)_2{\cdot}6H_2O$) always in a 1:1 ratio, Pump 4 was isolated. In the case of experimental runs 0.1M700-0.9M700, P4 was used to allow for inline dilution of the combined $Zn(NO_3)_2{\cdot}6H_2O$ and KOH feed in a static mixer and a complete process description is provided in Chapter 2. Consistent with the materials recovery procedures used in Chapters 3, 4 and 5. Samples of *ca.* 5L nanoparticle laden slurries were recovered and freeze dried for characterisation.

8.2.4 Investigation into the Synthesis of Binary Oxide Systems Using the Pilot Scale CHFS Process:

A summary of the experimental conditions used for the synthesis of the Ce-Zn oxide binary system is provided in table 8.4. For the synthesis of these materials the pilot scale process was operated using a four pump configuration as described in Chapter 2. In this configuration, Pump 1 (P-1) supplied supercritical water (scH_2O) to the reaction point whilst the rest of the pumps (P-2, P-3 and P-4) were dedicated to pumping precursors. The output of pumps P3 and P4 was used to control the ratio of Ce and Zn salts (completely dissolved in tanks) combining with the output of P2 (DI water) before entering the reaction point as shown in figure 2.6 (Chapter 2). A static mixer was used to ensure homogenisation of the precursor solution after they were mixed in a tee-piece (1/4” Swagelok) prior to entering the reaction point (CJM as described in table 8.1). In all experiments the heater was operating at an outlet water temperature of 450 °C at a pressure of 240 bar. The flow rates of both metal salt solutions (0.1 M) were controlled as indicated in Table 8.4. The temperature at the mixing point was estimated as 337 ºC, determined from overall enthalpy balance. (Wagner and Pruss 2002) Samples were assigned names on the basis of the nominal Zn contents used in each synthesis, *e.g.* sample 30 Zn – Ce was assumed to have 30 : 70 ratio of Zn : Ce. In this section, ten samples were made using the pilot scale CHFS process. In a typical synthesis, a sample of two litres (nanoparticle-laden aqueous slurry) was repeatedly centrifuged and washed with deionised water until pH neutral using the method described in Chapter 2. All materials were freeze dried for characterization and were treated in an analogous manner to those produced in Chapter 4. The work of kellici *et al.* to which the materials produced on the pilot scale process are compared were synthesised using a laboratory scale CHFS process (identical to the system used in Chapter 3).(Kellici *et al.,* 2010) However, all other experimental variables were scaled and the reaction point temperature used in this work (337°C) was similar to that used by kellici *et al.* evaluated experimentally from the temperature measurement method presented in Chapter 3. (Kellici *et al.,* 2010)

8.2.5 Volumetric Scale up of Magnetite Nanoparticle Synthesis

In this section a series of nine reactions were performed using the reaction point geometry described in table 8.1. Synthesis of magnetite nanoparticles on the pilot scale process used a three pump configuration (figure 2.5). Precursor concentration was controlled by inline dilution to the target concentration from a 0.2 M feed stock of ammonium ferric citrate and the output of Q_{sw} and Q_p were changed to assess volumetric scale up of magnetic nanoparticle synthesis. Pump 1 (P-1) was used to supply supercritical water (scH_2O) to the reactor whilst pump 2 (P-2) was dedicated to pumping the solubalised iron precursor and the feed issuing from P3 was used to dilute the feed issuing from P2, allowing inline control of precursor concentration. In these reactions the precursor concentration was varied (0.05, 0.1 and 0.2 M) to assess the concentration dependence of magnetite formation in the pilot scale process. A sample at each concentration was produced at $Q_{sw} = 400$ / $Q_p = 360$, $Q_{sw} = 300$ / $Q_p = 270$ and $Q_{sw} = 200$ / $Q_p = 180$ mL min^{-1}. Typically, sample volumes of 5 L (nanoparticle laden slurry) were collected and allowed to sediment under gravity. The concentrated slurry was further reduced through repeated centrifugation and decantation steps until the supernatant was neutral (pH 7 from the as obtained slurry pH10). All materials were freeze dried for characterisation and were treated in an analogous manner to those produced in Chapter 5. In all experiments the heater was operating at an outlet water temperature of 450 °C. The temperature at the mixing point was estimated to be in the range of 350 - 360 ºC as calculated from overall enthalpy balance. These reactions were performed to assess whether the slightly lower reaction point temperature significantly influenced the properties of the nanoparticles prior to the detailed investigation described in section 8.2.6. and only a summary of the results is presented for this purpose.

8.2.6 Investigations into the Volumetric Scale up of Surface Functionalised Nanoparticle Synthesis using CHFS

A summary of the experimental conditions used for the synthesis of the surface functionalised magnetite are provided in table 8.6. The Pilot scale CHFS process was operated using a three pump configuration. As shown in figure 2.6 (Chapter 2), Pump 1 (P-1) was used to supply supercritical water (scH_2O) to the reactor whilst pump 2 (P-2) was used to feed the solubalised iron precursor into the reaction point at a concentration of 0.066 M. The feed issuing from P3 was rerouted through the system and fed into the reaction point after the formation of nanoparticles in a geometry analogous to that developed in Chapter 6 and described in greater detail within Chapter 2. In all experiments the heater (H-1) was operating at an outlet water temperature of 450 °C. The temperature at the mixing point where the precursor and preheated water mix was estimated at between 350 - 360 ºC and the reaction temperature after the addition of the citric acid flow (T_{mix2}) are summarised in table 8.6, determined by overall enthalpy balance. Materials were recovered from the process as dilute nanoparticle laden slurry, sedimentation was induced by adding an appropriate amount of NaCl to allow for a 1.0 M salt solution leading to flocculation of the stable particle dispersions, *ca.* 10 L of nanoparticle laden slurry (autogenous), decantation of the slurry supernatant, centrifugation and cleaning were undertaken as described previously in Chapter 2 and in Chapter 6. All materials were freeze dried for characterization and were treated in an analogous manner to those produced in Chapter 6.

8.3 Results and Discussion:

8.3.1: Investigations into the Volumetric Scale up of the CJM reactor

8.3.1.1 Scale up Methodology

The purpose of this section is to describe the methodology used for the scale up of the confined jet mixer developed within this thesis, to process a 20x greater volumetric flow rate *ca.* 800 *vs.* 40 mL min^{-1}. According to the theory of dimensionless models, two processes may be considered similar if they take place in similar geometric space and if all the dimensionless numbers necessary to describe the process have a similar numerical value, this has formed the basis of the scale up methodology employed here. (Lerou and Ng 1996) The dimensions of the mixer used on the pilot scale process were determined empirically by calculation and a justification for the choice of these dimensions is provided later in the text. This section also describes the experimental evaluation of the scaled process for similarity to the laboratory scale process and serves to identify the limitations of the scale up.

8.3.1.2 Scale up Methodology (Calculations):

Figure 8.1 summarises the processes of heat and mass transfer expected within the confined jet reactor as discussed in greater detailed within Chapter 4. Initially, the scale up methodology was simplified to an analysis of the Re (equation 8.1) and $(Fr)^2$ (equation 8.2) of Q_{sw} at the exit of the inlet ($z = 0$) assuming no contribution of heat transfer (ΔQ in figure 8.1) *i.e.* the properties of Q_{sw} were assumed to be those at T_{sw} (inlet water temperature). As shown in Chapter 4, the magnitude of ΔQ was extremely difficult to estimate experimentally due to large temperature changes occurring in a relatively small geometric space (although in Chapter 4 it was estimated to provide an indication to the reader of the mixing events occurring near the terminus of the supercritical water inlet). Data presented in Chapter 4, showed that rapid mixing between Q_{sw} and Q_p was observed in all flow regimes where both high Re and $(Fr)^2$ were determined. This rapid mixing was attributed to the behaviour of turbulent buoyant jets which are known to readily entrain co-flow. As such, in the laboratory scale process rapid mixing was observed in all mixer sizes and was attributed to the similarity in the magnitude of the Re and $(\mathrm{Fr})^2$ of the process in the temperature and flow regimes evaluated (Chapter 4). (Pitts 1991a; Pitts 1991b) These observations initially suggested this mixer would scale well if the magnitude of forces represented by these numbers were similar and the mixing occurred rapidly. (Ricou and Spalding 1961)

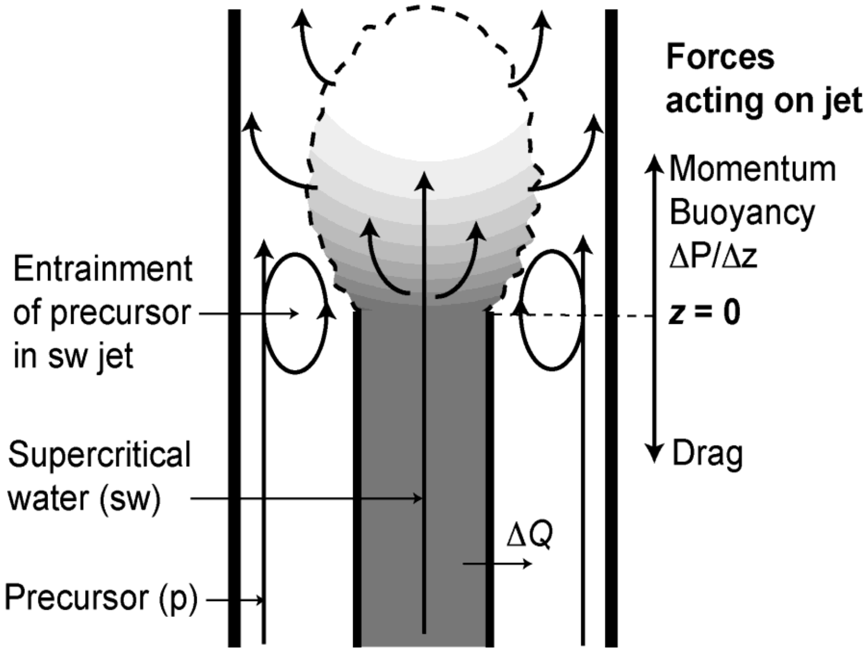

Figure 8.1: Representation of the processes of heat and mass transfer occurring within the confined jet reactor.

As initially discussed in Chapter 4, the relative magnitude of the momentum of the flow of $Q_{sw\ z=0}$ compared to the viscous drag force can be represented by the Reynolds number, $\mathrm{Re}_{\mathrm{sw\ z=0}}$, of the flow :

$$\mathrm{Re}_{\mathrm{sw\ z=o}} = \frac{\rho_{\mathrm{sw\ z=o}} u_{\mathrm{sw\ z=o}} di}{\mu_{\mathrm{sw\ z=o}}} = \frac{4G_{\mathrm{sw\ z=o}}}{\pi di \mu_{\mathrm{sw\ z=o}}}$$ **(Equation 8.1)**

Where, $\rho_{sw\ \mathrm{z=o}}$, $u_{sw\ \mathrm{z=o}}$ and $\mu_{sw\ \mathrm{z=o}}$ are the density, velocity and dynamic viscosity of Q_{sw}, respectively, $\mathrm{G}_{\mathrm{sw\ z=o}}$ is the mass flow rate of supercritical water and d_i is the internal diameter of the inlet. Similarly, the relative magnitude of the momentum of the jet acting upwards compared to the buoyancy forces can be represented by the square of the Froude number, $(\mathrm{Fr}_{\mathrm{sw\ z=0}})^2$ (equal to the reciprocal of the Richardson number, Ri):

$$(\mathrm{Fr}_{\mathrm{sw\,z=o}})^2 = \mathrm{Ri}^{-1} = \frac{\rho_{\mathrm{sw\,z=o}} u_{\mathrm{sw\,z=o}}^{\;\;2}}{g d_i(\rho_p - \rho_{hw})} = \frac{16 G_{\mathrm{sw\,z=o}}^{\;\;2}}{\pi^2 d_i^{\,5} \rho_{sw}(\rho_p - \rho_{sw}) g}, \qquad \textbf{(Equation 8.2)}$$

Where, ρ_m is the density of $Q_{sw,\ z=0}$. As summarised in table 8.2 the laboratory scale reactions forming the basis of scale up the yielded $Re_{sw,\ z=0}$ with a magnitude ranging from 7.5 - 15.1 x 10^4 increasing as expected for G_{sw} and T_{sw}, defining the flow in the mixer as turbulent at the point of issue. Similarly, the magnitude of $(Fr_{sw\ z=0})^2$ for the laboratory scale mixer chosen as the basis of scale up reactions increased as expected with $T_{hw,in}$ and $Q_p : Q_{sw}$. Suggesting that over the range of T_{sw} and $Q_p : Q_{sw}$ the rapid movement of flow towards the outlet of the mixer is driven by momentum $(Fr_{sw,\ z=0})^2 >> 1$ and thus the rapid entrainment of Q_p into Q_{sw}. The work of Augustine *et al.* accompanied by data presented in Chapter 4 showed that significant entrainment of the co-flowing fluid under conditions similar to those presented in this work was expected at < 2.4 inner pipe diameters when the $(Fr)^2 = 25 - 400$, and appeared the most dominant characteristic for good mixing *i.e.* rapid entrainment of Q_p into Q_{sw}. (Augustine and Tester 2009; Zhdanov and Chorny 2011) It was chosen to scale the mixer on the basis of a similar $(Fr_{sw,\ z=0})^2$ to ensure the magnitude of momentum to buoyancy forces were similar to those used in the laboratory scale process. (Augustine & Tester 2009) Table 8.1, provides a summary of the dimensions, maximum flow rates and reactor sizes for the laboratory scale and the pilot scale which yielded the most “equivalent” magnitudes of Re and $(Fr_{sw,\ z=0})^2$ in the scaled reactor. As detailed in table 8.2 the magnitudes of both the Re and $(Fr_{sw,\ z=0})^2$ could not be matched exactly and this was limited by the availability of suitably sized high pressure components for the pilot scale mixer.

Table 8.1: Comparison of maximum flowrates and optimum confined jet reactor size for laboratory and pilot scale processes.

	Lab Scale	**Pilot Scale**
Q_{sw} / mL min^{-1}	20	400
Q_p / mL min^{-1}	20	400
d_i / mm	0.99	3.97
d_o / mm	4.57	13.51
$(d_o - d_i) / d_o$	0.78	0.71
L / mm	20	40

Table 8.2: Summary of the laboratory scale mixer conditions chosen as the basis of scale up

Q_{sw} (mL min-1)	**Q_p** (mL min^{-1})	**T_{sw}** (°C)	**T_{mix}** (°C)	**Re_{sw}** 10^4	**$(Fr)_{sw}^2$**
Laboratory scale mixer (d_i = 0.99 and d_o = 4.67 mm)					
10	10	400	305	7.6	40
15	15	400	305	11.4	89
20	20	400	305	15.3	159
10	10	450	335	7.5	55
15	15	450	335	11.3	123
20	20	450	335	15.6	219
Pilot scale mixer (d_i = 3.97 and d_o = 13.51 mm)					
200	200	400	305	38.8	17
300	300	400	305	58.8	37
400	400	400	305	67.6	66
200	200	450	335	38.2	23
300	300	450	335	57.3	51
400	400	450	335	76.8	91

As summarised in tables 8.2 the magnitude of the $Re_{sw,\ z=0}$ number for both the laboratory (7.5 - 15.1 x 10^4) and pilot scale (37.5 - 74.4 x 10^4) differ in magnitude between the process scales owing largely to the difference in G_{sw} between each condition (Equation 8.1). As such, it was decided that this variance could be accepted if the magnitude of $(Fr_{(sw,\ z=0)})^2$ could be maintained between the process scales and the flow remained turbulent at issue (figure 8.1). As, if the pilot scale mixer was sized appropriately to conserve similarity in the Reynolds number (equation 8.1) the d_i of the confining tube containing the mixture would have to be significantly larger *ca.* 8x that of the size summarised in table 8.2 to yield numbers of similar magnitude to the laboratory scale process. However, scale up on this basis would also yield a reduction in the $(Fr_{(sw,\ z=0)})^2$ of Q_{sw} which would approach unity and alter the behaviour of the flow issuing from the inlet. (Ricou & Spalding 1961) Therefore, to ensure equivalency between the process scales and to maintain Q_{sw} as a turbulent momentum driven jet as it emerged from the inner pipe (ignoring the contribution of ΔQ), rather than becoming a more diffuse buoyancy-driven plume on increasing d_i, it was decided to scale up the confined jet reactor based on maintaining $(Fr_{(sw,\ z=0)})^2$ close to that used on the laboratory scale process.

8.3.1.3 Temperature Profiles within the Scaled CJM:

This section experimentally evaluates the mixer size chosen for use on the pilot scale CHFS process. Measured temperature profiles between the pilot scale and laboratory scale process are presented in Figures 8.2a (T_{sw} = 400 °C) and b (T_{sw} = 450 °C) as summarised in Table 8.2. The dashed lines in Figures 8.2 a) and b) show the maximum theoretical temperature calculated for the outlet of the mixer (*i.e.* the inlet to the cooler) assuming mixing is complete and any heat losses from the outer pipe to the surroundings are negligible as determined by overall enthalpy balance (as described in Chapter 4).

It can be seen in Figures 8.2a and 8.2b, that on both the lab scale and the pilot plant, the measured temperature reached T_{mix} (theoretical mixture temperature) within five inner pipe diameters ($z/d_i \sim 5$) downstream of the outlet of the supercritical water. This represents a mixing time of ~ 40 ms at the highest flowrates ($Q_{sw} + Q_p = 40$ and $Q_{sw} + Q_p = 800$ mL min^{-1}) of each process scale assuming T_{mix} occurs at the terminus of the inlet ($Rt(s) = \pi d_o z/ V_{mix}$). It is also evident that the temperature of Q_{sw} decreases as heat is transferred to Q_p. The normalised temperature in the region $z/d_i < 0$ shows a slight discrepancy in the temperature rise in Q_p when the reaction point is scaled. This could be attributed to the larger diameter of $d_o - d_i$ in the pilot scale mixer, the free floating nature of the thermocouple or a thermal gradient across the annulus. (Ma *et al.,* 2011) The magnitude of the heat transfer coefficient (U_o) occurring in the annulus bound by $d_o - d_i$ was calculated to be between 2130 - 3280 W m^{-2} K^{-1} on the laboratory scale mixer and 6238 - 7436 W m^{-2} K^{-1} on the pilot scale analogue, increasing as would be expected with both increasing Q_{sw} and T_{sw}. Where, the heat transfer on the pilot scale is much larger owing to the higher G_{sw} and G_p. Estimation in this manner yielded heat transfer coefficients (U_o) which were comparable to those determined in previous work, albeit for another mixer which suggest that U_o in the region 908 – 3208 W m^{-2} K^{-1} could be expected under these measurement conditions. (Ma *et al.,* 2011; Tighe *et al.,* 2012) Although, the probable formation of a boundary layer around the inlet or a large temperature gradient across the annulus bound by $d_o - d_i$ would mean that the value of U_o could be much higher than experimentally determined (discussed in greater detail within Chapter 4). (Augustine & Tester 2009) To further assess the temperature profile at $z / d_i > 5$ the magnitude of the distance required to closely approach within 20 °C of T_{mix} through the conduction of heat between the inlet of supercritical water (diameter d_i) and the annulus in which the precursors flow (width $d_o - d_i$) between the mixers was compared. In stratified flows of steam and water, U_o has been reported to vary between 3 and 30 kW m^{-2} K^{-1} giving a length to approach within 20 °C of T_{mix} in this case of z/d_i = 400 to 40 on the pilot scale and z/d_i = 210 - 30 on the laboratory scale, *i.e.* much greater than the measured z/d_i = 5 as determined by equation 8.3. (Jaster and Kosky 1976)

$$A_o = \frac{\Delta Q_m}{U_o \Delta T_{lm}} \quad \textbf{(Equation 8.3)}$$

Where, A_o is the heat transfer area required for a known mixer size (table 8.1) of inner pipe, ΔQ_m is the heat transferred, U_o is the inferred heat transfer coefficient and ΔT_{lm} is the log mean temperature difference (taken from enthalpy balance). (Chorny and Zhdanov 2012) Consequently, the measured temperature profiles must be the result of mixing events occurring near the terminus of d_i. The observation of complete mixing between the two streams at and beyond z/d_i = 5 is consistent between both scales. The similarity of the normalized temperature profiled in the case of both ΔQ and z/d_i suggests that the temperature difference at the terminus of the inlet in both $Q_{sw,\ z=0}$ and $Q_{p,\ z=0}$ are similar across the reaction scales and that similar mixing events are occurring in both the process scales. As similar temperature profiles exclusively yielded nanoparticles with exceptionally similar crystallite size and size distribution, the finer details of mixing are not discussed further, as it is likely they make little difference to the formation of nanoparticles as implied by the results presented in Chapter 4, due to the rapid rates of reaction in the CHFS system.

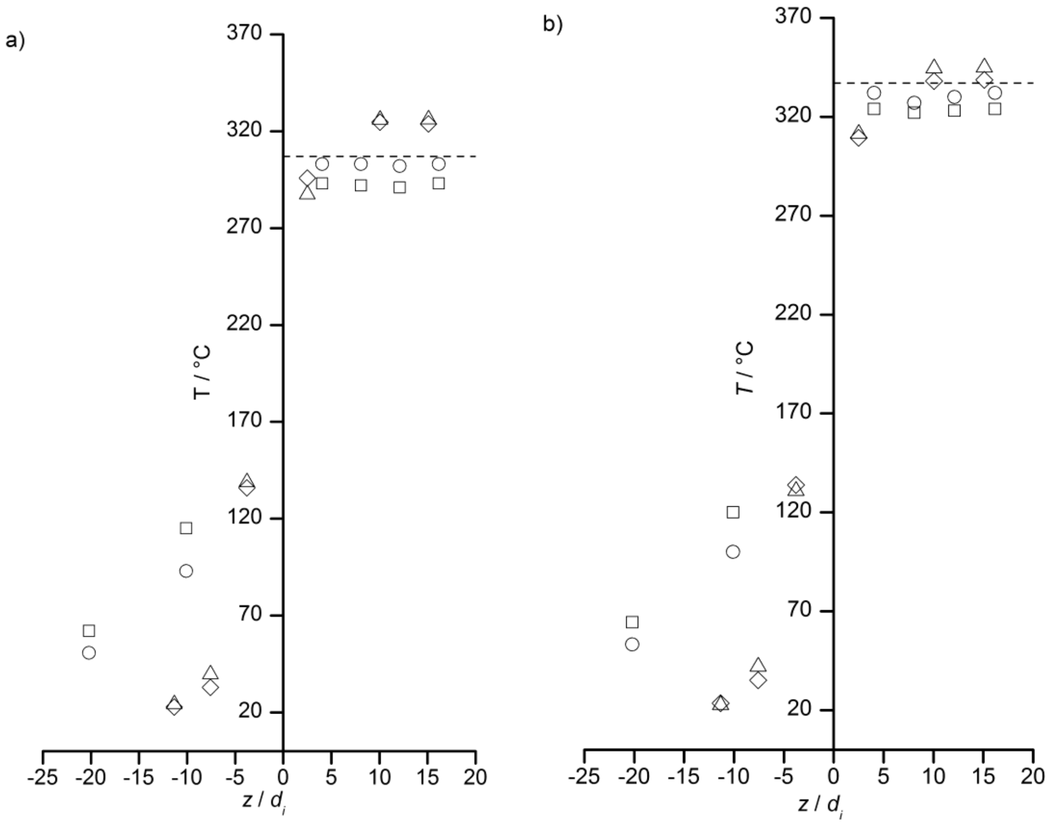

Figure 8.2. Temperature profiles in lab scale (Δ Q_{sw} = Q_p = 15 mL min^{-1}, ○ 20 mL min^{-1}) and pilot plant reactors (△Q_{sw} = Q_p = 300 mL min^{-1}, ◊ 400 mL min^{-1}) for a supercritical water temperature, T_{sw} of **a)** 400 °C and **b)** 450 °C. Dashed lines in a) represents T_{mix} [Q_{sw} = Q_p, T_{sw} = *400 °C]* and in b) [Q_{sw} = Q_p, T_{sw} = 450 °C]. Measurements performed at Q_{sw} = 200 and Q_p=200 have been omitted for clarity in the figure.

8.3.1.4: Limitations of Scale up

In the pilot scale CJM temperature and pressure fluctuations were observed (*ca.* ± 120 °C and ± 50 bar) when the ratio of Q_{sw} : Q_p > 1.3 under these conditions, it was deemed unsafe to use the process. In the laboratory scale CJM, no evidence of pressure or temperature fluctuations were observed even when Q_{sw}:Q_p > 1.5 (Chapter 4). This observation was thought to arise due to a large momentum of the flow $(Fr_{sw, z=0})^2$ having insufficient co-flow to entrain *e.g.* when Q_{sw} = 400 and Q_p = 300 the $Re_{sw, z=0}$ and $(Fr_{sw, z=0})^2$ of 7.6 x10^4 and 91 were determined (assuming no contribution of ΔQ). However, Q_p is reduced so the jet is probably unable to entrain sufficient flow generating a zone of recirculation. (Chorny & Zhdanov 2012) In this context severe recirculation is thought to be a plausible explanation for the fluctuations as recirculation in pressurised flows of steam and water are known to cause pressure fluctuations. (Viollet 1987) The work of Thring and

Newby suggested that severe recirculation would be observed if C_{tn} (defined in Chapter 4) approached 0. (Thring and Newby 1980) As initially presented in Chapter 4 even if the temperature of $Q_{p, z=0}$ reached 320 °C and $Q_{sw, z=0}$ was reduced to 392 °C (80 % of balance) a value of C_{tn} of only 0.06 is determined, this would suggest that recirculation is highly likely, as the issuing jet could not entrain sufficient co-flow. (Pitts 1991a; Pitts 1991b) Ultimately, the observation of system instability meant that many of the reactions previously performed on the laboratory scale CHFS process could not be readily reproduced on the pilot scale process to allow for direct comparison. Although, it was shown by *in-situ* temperature measurements that conservative scale up (*i.e.* values falling within the range of those used on the laboratory scale process) the process could be operated in a similar regime to that initially observed on the laboratory scale process (figure 8.2). Thus, the scale up of mixer scale up was further limited to $(Fr_{sw, z=0})^2$ within the range of those previously found suitable for the production of nanoparticles in flow regimes where $Q_{sw} : Q_p < 1.3$.

8.3.1.5 Summary:

The scale up methodology chosen to increase the physical dimensions of the CJM to process larger volumes was shown to be effective. The scale up of the reaction point on a near constant $(Fr)^2$ of the jet issuing at Z = 0 was shown to be effective strategy to allow similar normalised temperature profiles within the scaled mixers. Mixing between the supercritical water feed and the precursor flow was shown to be complete within z / di ~ 5 over a large range of scale up ratios and consistent with the mixing distance observed in the laboratory scale system (data presented in Chapter 4). *In-situ* temperature measurements also identified a limitation to scale up using this methodology, in that flow regimes where $Q_{sw}:Q_p > 1.3$ yielded temperature and pressure instabilities within the process which limited the flow regimes which could be safely used on the pilot scale. This chapter now moves forward to describe the effect of both volumetric and mass based scale up on the synthesis of nanoparticles.

8.3.2: Investigation into the Volumetric and Mass Based Scale up of CHFS of ZnO Nanoparticles

The aim of this section is to assess the volumetric (serving to confirm speculation made in previous sections of this Chapter) and mass based scale up of nanoparticles synthesis using the pilot scale CHFS process to define the limitations of each strategy for the synthesis of nanoparticles. ZnO has been used as a model system to characterise the influence of both scale up strategies. Data is presented which relates to both methods of scale up and detailed characterisation of ZnO nanoparticles produced using both methodologies are presented. Table 8.3, summarises the reaction conditions used in the synthesis of materials presented herein. Reactions presented in this section are compared to materials produced under equivalent reaction conditions preformed on the laboratory scale presented in Chapter 4 section 4.3.2. Samples are identified by the precursor concentration and the total flowrate used in synthesis.

8.3.2.1 Volumetric Scale up of ZnO Nanoparticle Synthesis

Initially, the effect of volumetric scale up was investigated at analogous synthesis conditions to those used to produce ZnO on the laboratory scale process using the reaction conditions summarised in tables 4.3 (Chapter 4) and 8.3. Figure 8.3 shows a comparison of the diffraction patterns of ZnO nanoparticles produced using the laboratory scale process (Samples 0.05M20 – 0.05M40 and 0.1M20 – 0.1M40 and 0.2M20 - 0.2M40, summarised in table 4.3) and the products produced from volumetric scale up of 10, 15 and 20x (1x is defined as $Q_p + Q_{sw} = 40$) at two precursor concentrations (Samples, 0.05M400 – 0.05M800 and 0.1M400 – 0.1M800). Diffraction patterns obtained from both series showed significant similarity and can be indexed to the hexagonal wurtzite structure of ZnO in good agreement with ICDD 26170. No evidence of contaminating phases was present in the data, consistent with the observations initially made in Chapter 3 and ZnO was obtained as the exclusive reaction product. As a comparison the crystallite sizes estimated from the [101] reflection are presented in tables 4.3 and table 8.3 for sample series 0.05M20 – 0.05M40 and 0.1M20 – 0.1M40 and 0.05M400 – 0.05M800 and 0.1M400 – 0.1M800 , respectively. Where, crystallite size appears to be consistent between sample series, and size estimates in the region of 30 - 40 nm were obtained from application of the Scheerer equation). Raman spectra of samples series 0.05M20 – 0.05M40, 0.1M20 – 0.1M40 and 0.05M400 – 0.05M800, 0.1M400 – 0.1M800 were recorded to confirm the structural observations made using XRD. The spectra of both series showed significant similarity and modes were observed centred at 435 and 404 cm^{-1} attributed to the $E_{2(high)}$ and $E_{1(TO)}$ phonons, and a mode centred at 327 cm^{-1} was attributable to the (E_{2H} - E_{2L}) second order phonon reaffirming the Wurtzite structure (data not shown). (Damen *et al.*, 1966)

A comparison of the UV-Vis absorption spectra for ZnO nanoparticles produced on the laboratory scale process (0.05M20 - 0.2M40) and the samples scaled up on a volumetric basis (0.05M400 - 0.1M800) are summarised in tables 4.3 and 8.3 as band gap values calculated using the K-M method detailed in Chapter 2. All the samples showed good absorption over the entire range of UV and little or no visible absorbance, consistent with all data presented in Chapters 3 and 4. The calculated band gap values showed significant similarity and in all cases were slightly red shifted when compared to the band gap of bulk ZnO (3.37 eV), which can be attributed to the comparatively small particle size. (Li et al. 1999) The similarity in band gap suggested significant compositional and structural similarity as inferred from other methods. (Liu and Zeng 2003)

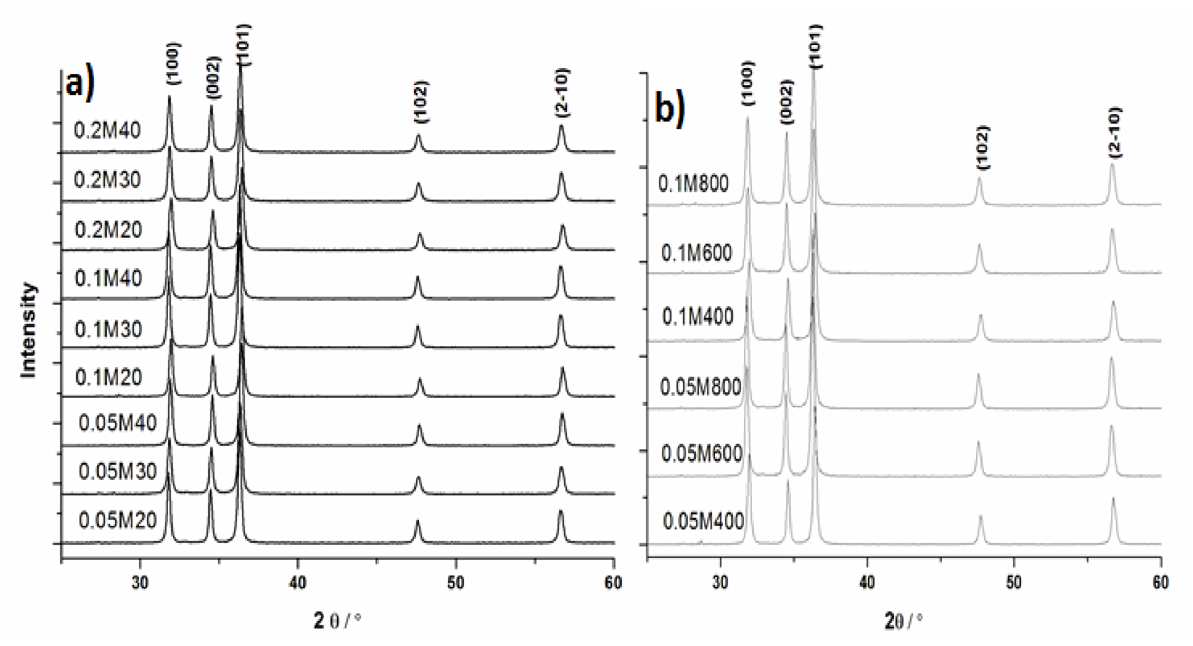

Figure 8.3: a) XRD patterns of ZnO nanoparticles synthesis using the laboratory scale CHFS process (Experimental runs 0.05M20 – 0.2M40) **b)** XRD patterns of ZnO nanoparticles produced at different volumetric scale up ratios (experimental runs 0.05M400 – 0.1M800).

Table 8.3: Summary of the reaction conditions used for the synthesis of ZnO using the CHFS pilot plant.

ID	**[Zn] (M)**	**Flowrates / mL min^{-1}**				**Phase (XRD)**	***Cs(nm)***	**BET**		**TEM (nm)**			**E_g (eV)**	**Yield (%)**
		Q_{sw}	**Q_{Zn}**	**Q_K**	**Q_d**			***(m^2 g^{-1})***	***ESD (nm)***	***Avg***	***S.D***	***AR***		
0.05M800	0.05	400	200	200	-	ZnO	33.61	16.30	65.6	59.5	18.0	1.13	3.26	92
0.05M600	0.05	300	150	150	-	ZnO	33.47	15.00	71.3	58.5	16.3	1.15	3.26	88
0.05M400	0.05	200	100	100	-	ZnO	34.17	15.79	67.7	59.6	16.7	1.11	3.26	91
0.10M800	0.1	400	200	200	-	ZnO	30.45	18.69	57.2	51.8	13.8	1.19	3.27	96
0.10M600	0.1	300	150	150	-	ZnO	30.85	17.55	60.9	55.9	15.7	1.20	3.27	92
0.10M400	0.1	200	100	100	-	ZnO	29.61	20.84	51.3	48.7	12.3	1.27	3.26	90
0.20M700	0.2	350	35.0	35.0	280	ZnO	-	17.16	62.33	81.8	37.8	1.32	3.25	93
0.30M700	0.3	350	52.5	52.5	245	ZnO	-	14.13	75.70	91.1	45.1	1.87	3.26	87
0.40M700	0.4	350	70.0	70.0	210	ZnO	-	12.47	85.76	94.5	45.1	1.90	3.26	94
0.50M700	0.5	350	87.5	87.5	175	ZnO	-	13.03	82.10	103.2	40.1	1.82	3.24	89
0.60M700	0.6	350	105.0	105.0	140	ZnO	-	12.58	85.03	112.5	48.2	1.90	3.26	93
0.70M700	0.7	350	122.5	122.5	105	ZnO	-	12.00	89.14	114.0	55.6	2.10	3.26	89
0.80M700	0.8	350	140.0	140.0	70	ZnO	-	11.68	91.62	112.3	44.2	2.10	3.26	93
0.90M700	0.9	350	157.5	157.5	35	ZnO	-	11.58	92.41	121.9	47.4	2.04	3.26	90

Key: Q_{sw} = the flowrate of supercritical water (450 °C), Q_{zn} = the flowrate of zinc nitrate precursor, Q_{KOH} = the flowrate of KOH solution ([KOH] = [Zn]), Q_d = the flowrate of the dilution feed, Cs = the crystallite size determined from application of the Scheerer equation to the (101) reflection of ZnO, ESD = the equivalent sphere diameter determined from the BET surface area, AR = the aspect ratio determined from TEM (*ca.* 150 particles measured) and Eg = the direct bandgap of the material determined from UV-Vis (using the KM method).

TEM was used to assess the crystallite morphology and allow the comparison of crystallite size distributions of the materials produced in runs 0.05M20 - 0.2M40 (shown in Figure 4.5 and runs 0.05M400 - 0.1M800 are shown in figure 8.4). Measurement of *ca.* 300 particles of each sample produced in the laboratory scale process (samples 0.05M20 - 0.2M40), showed that the PSD were largely invariant over the experimental range presented as summarised in table 4.3, an observation attributed to similarity in particle nucleation and growth within the reactor. The size of the ZnO nanoparticles produced on the pilot scale process in reactions 0.05M400 - 0.1M800 are summarised in table 8.4 and confirmed that particles with similar morphology and size distribution similar to those observed for the laboratory scale runs were produced in the range, *ca.* 55 - 63 and 60 - 68 nm, respectively. The similarity in PSD between the sample series is shown graphically in figure 8.5, showing an overlay of the particle size distributions from the laboratory scale process and the equivalent materials produced on the pilot scale process, the samples are identified by precursor concentration and total flow rate (Q_{sw} + Q_p). To confirm the similarity in particle size, BET surface area measurements of the two sample series are summarised in table 4.3 and 8.3 giving crystallite size estimations similar to those obtained by TEM using the equivalent sphere approximation. Where, mean values of surface area were 16.5 and 16.7 m^2 g^{-1} for sample series 0.05M20 - 0.2M40 and 0.05M400 - 0.1M800, respectively.

It was anticipated that in the scaled reactions a degree of anisotropic growth of ZnO would be evident if a particle growth phase had occurred. (Kolb *et al.,* 1967) To confirm that no anisotropic particle growth occurred the aspect ratio distributions were measured (*ca.* 150 particles) which yielded values close to 1 (range 1.0 - 1.2) in the case of all samples. Anisotropic growth of ZnO is often observed if there are two stages of particle formation *i.e.* particle nucleation followed by a growth phase and are commonly observed in many hydrothermal methods. (Liu & Zeng 2003) Which, suggests that the materials produced on the laboratory scale and the pilot scale occur in a particle formation regime where nucleation >> particle growth when scaled on a volumetric basis alone. These observations are consistent with the inference made about the similarity in mixing between the laboratory and pilot scale CHFS processes as discussed in greater detail within Section 8.3.1.

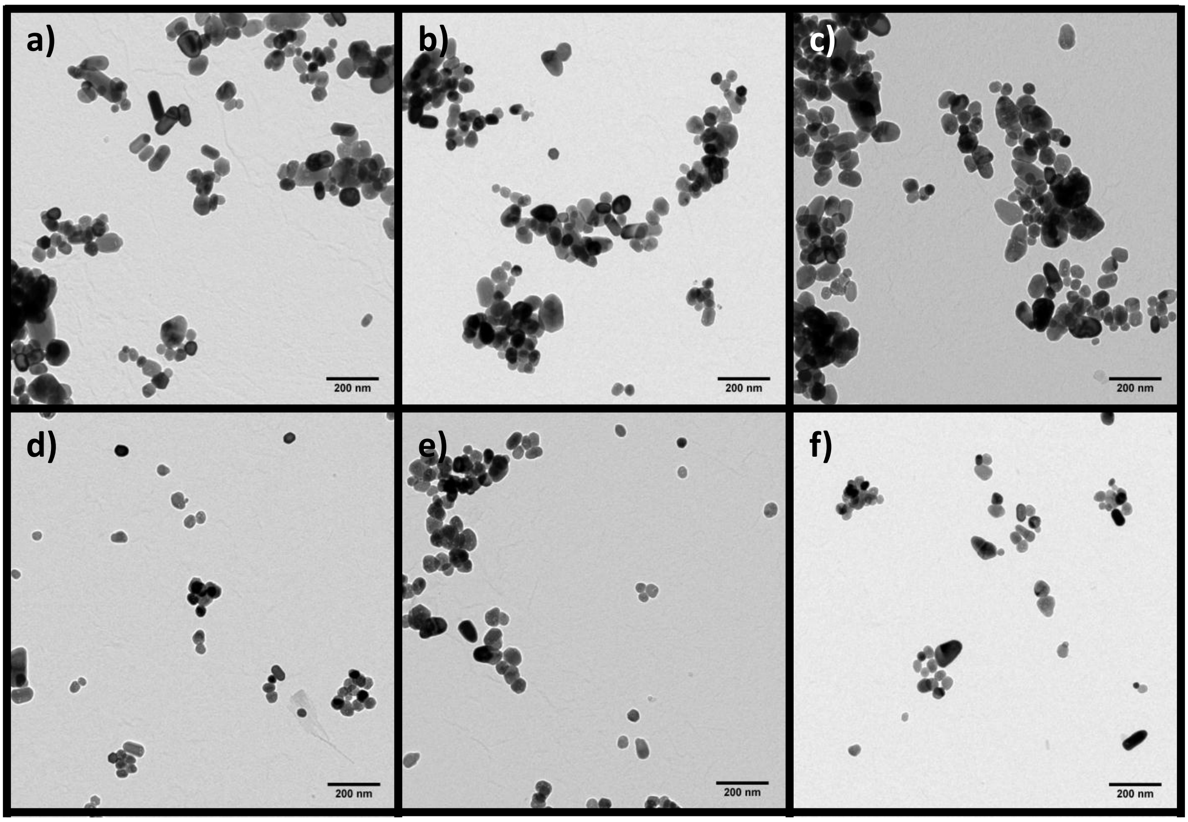

Figure 8.4: TEM images representative of ZnO nanoparticles produced on the pilot scale CHFS process through a volumetric scale up strategy; **a)** 0.05M400, **b)** 0.05M600, **c)** 0.05M800, **d)** 0.1M400, **e)** 0.1M600 and **f)** 0.1M800 [scale bar = 200nm]. Images were taken using a JEOL 1200 operated at 120 KeV.

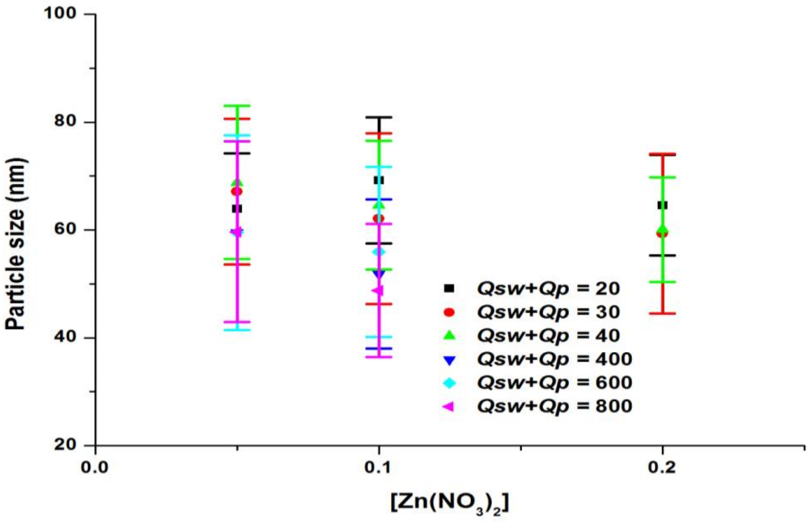

Figure 8.5: Overlay showing the similarity of ZnO nanoparticles produced on the laboratory scale to those obtained for equivalent materials produced on the pilot scale CHFS process.

It is well known that ZnO preferentially grows along the crystallographic c-axis (*i.e.* the [0001] direction). HREM images of the samples were captured and used to assess the crystal structure in the products. Figure 8.6 shows a compilation of HREM images of ZnO samples produced in experimental runs 0.1M40 and 0.1M800. Figures 8.6a and 8.6d show low magnification image representative of the particle obtained in each synthesis and figures 8.6 b and 8.6e show HREM images of the faceted particles observed in the centre of figures 8.6a and 8.6d allowing visualisation of lattice fringes with a measured d-spacing of 2.54 Å [0002] and 2.83 Å $[10\bar{1}0]$ (sample 0.1M40) and 2.83 Å $[10\bar{1}0]$ for sample 0.1M800, respectively. Indexed electron diffraction patterns of the particles are shown in Figures 8.6c and 8.6f. In each case the electron diffraction patterns diffraction suggest no preferential particle growth in the samples and confirming visualisation along the crystallographic c-axis. ZnO is known to have preferential growth directions due to the terminating atom on a given crystal facet, addition to the (0001) facet verses the $(10\bar{1}1)$ facet occurs at twice the rate. (Demianets *et al.*, 2002) The absence of growth along the crystals fast direction (inferred from aspect ratio) suggests particles are obtained as a result of synthesis in a nucleation dominated regime and minimal pure particle growth occurs, consistent on volumetric scale up and consistent with the discussion presented in Chapters 3 and 4. As was anticipated from the temperature measurements presented in section 8.3.1 the mixing process *(sic)* governing the formation of nanoparticles would appear to be well scaled and were not found to be sufficiently different to induce a difference in crystal growth. (Li, Shi, Zhong, & Yin 1999)

8.3.2.2 Mass based Scale up of ZnO Nanoparticle Synthesis

In the previous section it was shown that scale up of CHFS on a volumetric basis yielded nanoparticles with similar physiochemical characteristics to those produced in a laboratory scale process. However, if the scale up was performed on a mass basis, differences in the particle nucleation and growth processes were observed on increasing precursor concentration, identified by reactions 0.2M700 - 0.9M700 (summarised in table 8.3). These observations were made at much higher precursor concentrations than could be used safely on the laboratory scale due to rapid pressure regulator failure. This section discusses the characterisation data obtained for nanomaterials synthesis performed on increasing scale by mass using CHFS.

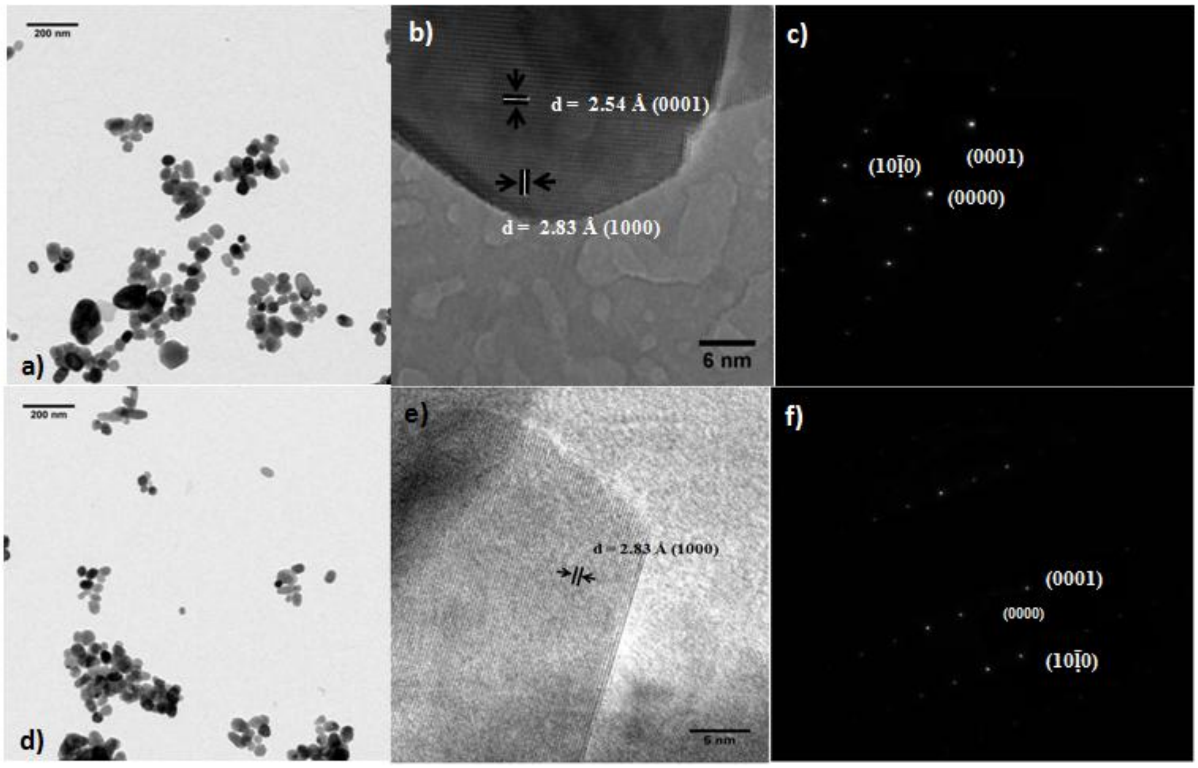

Figure 8.6: Compilation of HREM images of the ZnO sample produced in runs 0.1M40 and 0.1M800 **a)** and **d)** Low magnification image representative of the particles 0.1M40 and 0.1M800, **b)** and **e)** HREM images of ZnO nanoparticles produced in runs 0.1M40 and 0.1M800, respectively. **c)** and **f)** Electron diffraction pattern of the single crystallite presented in image [b and e] the spot patterns could be indexed to the (0001) and $(10\bar{1}0)$ planes confirming the growth direction presented in images **b** and **e.** .

Figure 8.7 shows the XRD patterns of samples scaled up through precursor concentration (samples 0.2M700 - 0.9M700). All XRD patterns can be indexed as the hexagonal wurtzite structure of ZnO and are in good agreement with the ICDD file of ZnO. The structure of the products was also confirmed with raman spectroscopy, yielding spectra similar to those reported for samples 0.1M20 – 0.1M40, noted in section 8.3.2.1 (data not shown). It can be seen that compared to the XRD patterns collected for samples 0.05M20 - 0.2M40 and 0.05M400 - 0.1M800, a slight variation in the intensity between the (100) and (002) reflection is observed (in samples 0.05M400 - 0.1M800 this was invariant), increasing as a function precursor concentration suggesting a degree of preferential growth within the samples. These observations suggest that the growth rate of the (002) plane was increased and the crystallites produced showed anisotropy in the [0001] direction consistent with the common growth directions of ZnO nanoparticles produced by many hydrothermal methods. (Demianets and Kostomarov 2001) Calculation of the diffraction peak FWHM of the (100) and (002) reflections showed anisotropy consistent with that observed in the corresponding relative peak intensities as shown in figure 8.8 providing further evidence for preferential growth within the sample, the latter narrowing as a function of precursor concentration. UV-Vis absorption spectra for ZnO nanoparticles which showed morphology dependence on precursor concentration (Runs 0.2M700-0.9M700) are shown in figure A3.4. The samples showed similar UV-Vis absorption profiles to those measured for samples 0.05M20 - 0.2M40 and 0.05M400 - 0.1M800. The calculated band gap values derived using the K-M method (described in Chapter 2) are shown in table 8.3 and ranged from 3.25 - 3.30 eV, consistent with values determined for all other samples produced using CHFS, being slightly red-shifted from the reported bulk value (3.37 eV). (Li, Shi, Zhong, & Yin 1999) There was no apparent shift in the band gap even as the average crystallite size and morphology increased. The absence of a shift in the band gap is likely due to the particles being much larger than the excitation Bohr radius required to observe quantum size effects in ZnO, yet still much smaller that materials considered as bulk samples. This yielded a slight red shift in our materials. (Liu & Zeng 2003)

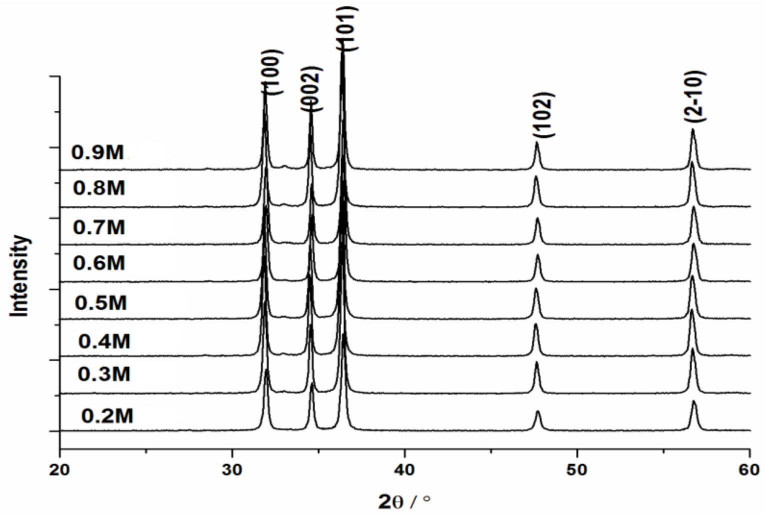

Figure 8.7: XRD patterns of ZnO nanoparticles produced on the pilot scale CHFS process as a function of Zn precursor concentration ($Q_p + Q_{sw} = 700$).

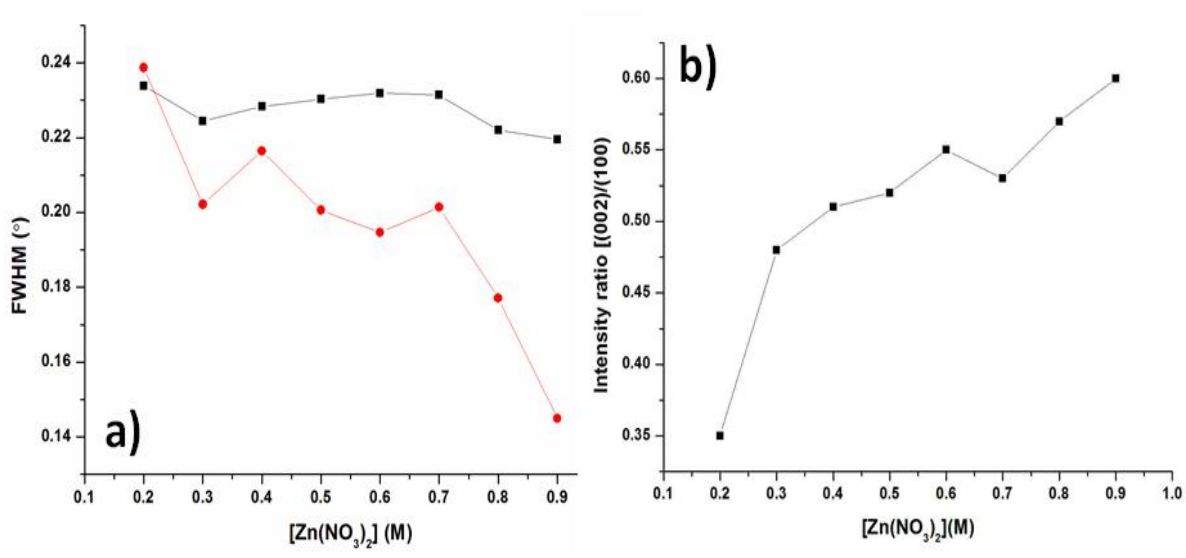

Figure 8.8: a) Variation of the full with half maximum value determined from the (100) [red circles] and (002) [black squares] reflections of ZnO, **b)** variation of the intensity ratio of the (100) and (002) reflections of ZnO nanoparticles plotted as a function of increasing precursor concentration.

To confirm the anisotrophic growth of ZnO suggested by XRD, selected samples were evaluated with HRTEM and TEM. Electron micrographs of the samples produced within the series 0.2M700 – 0.9M700 are shown in figure 8.9. A slight morphology change was observed as a function of increasing precursor concentration consistent with that inferred from the diffraction data (figure 8.9). Figure 8.10a, summarises the size data obtained from TEM, BET and XRD as a function of Zn precursor concentration with all measured values showing consistency. As suggested by XRD, the morphology of the nanoparticles was shown to evolve from hexagonal like particles to more rodlike particle morphology as a function of precursor concentration, with a corresponding increase in the particle aspect ratio (*ca.* 150 particles measured) occurring with sequential increase in precursor concentration (figure 8.10b). SAED patterns obtained from each of the images confirmed the phase of the material observed a selection of indexed electron diffraction patterns are presented in figure A3.1. Suggesting, that in the synthesis of this sample series a particle growth phase was responsible for the evolution of particle morphology.

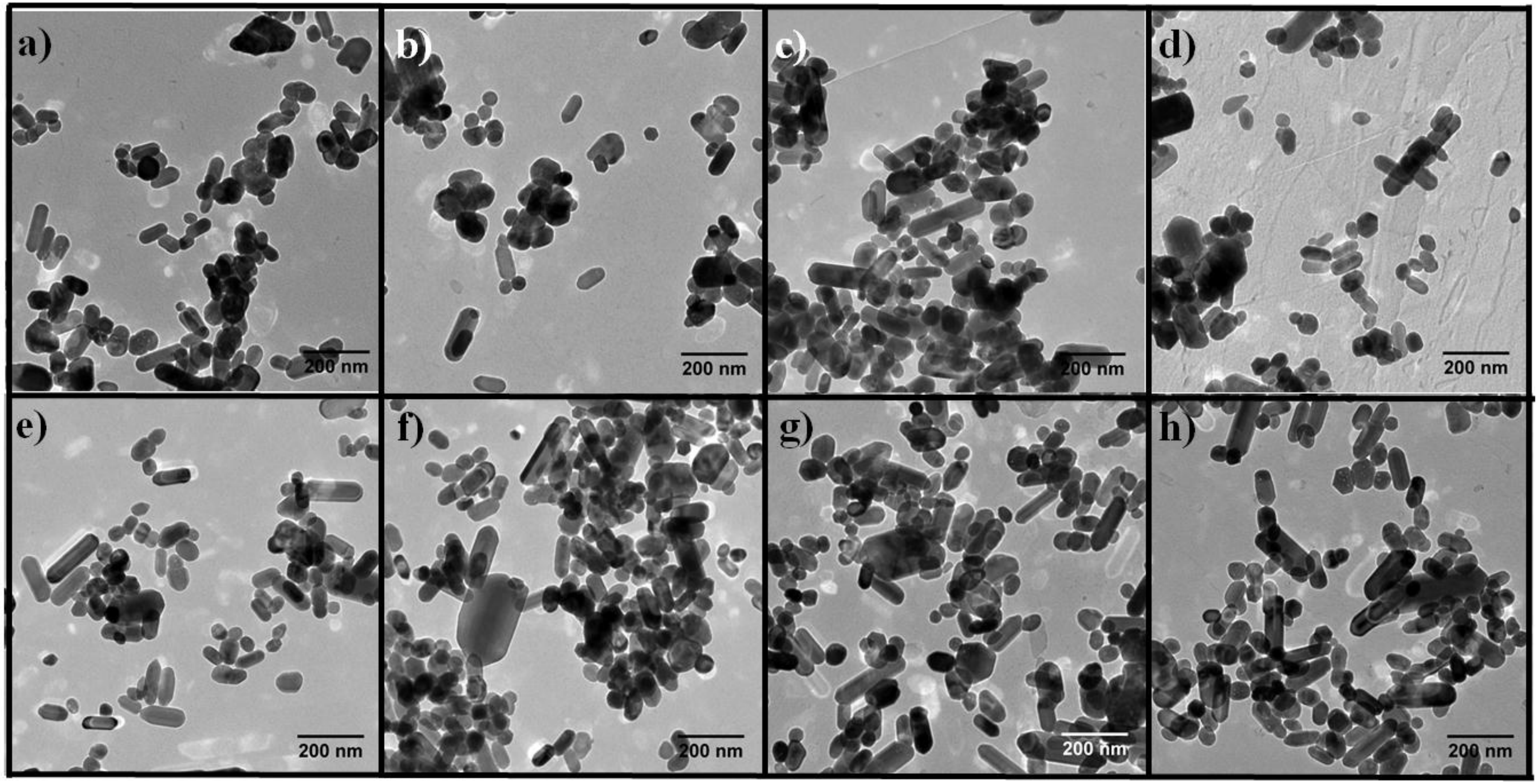

Figure 8.9: TEM images of ZnO nanoparticles produced through concentration based scale up of the CHFS process; **a)** 0.2M700, **b)** 0.3M700, **c)** 0.4M700, **d)** 0.5M700, **e)** 0.6M700, **f)** 0.7M700, **g)** 0.8M700, **h)** 0.9M700 (scale bar = 100 nm).

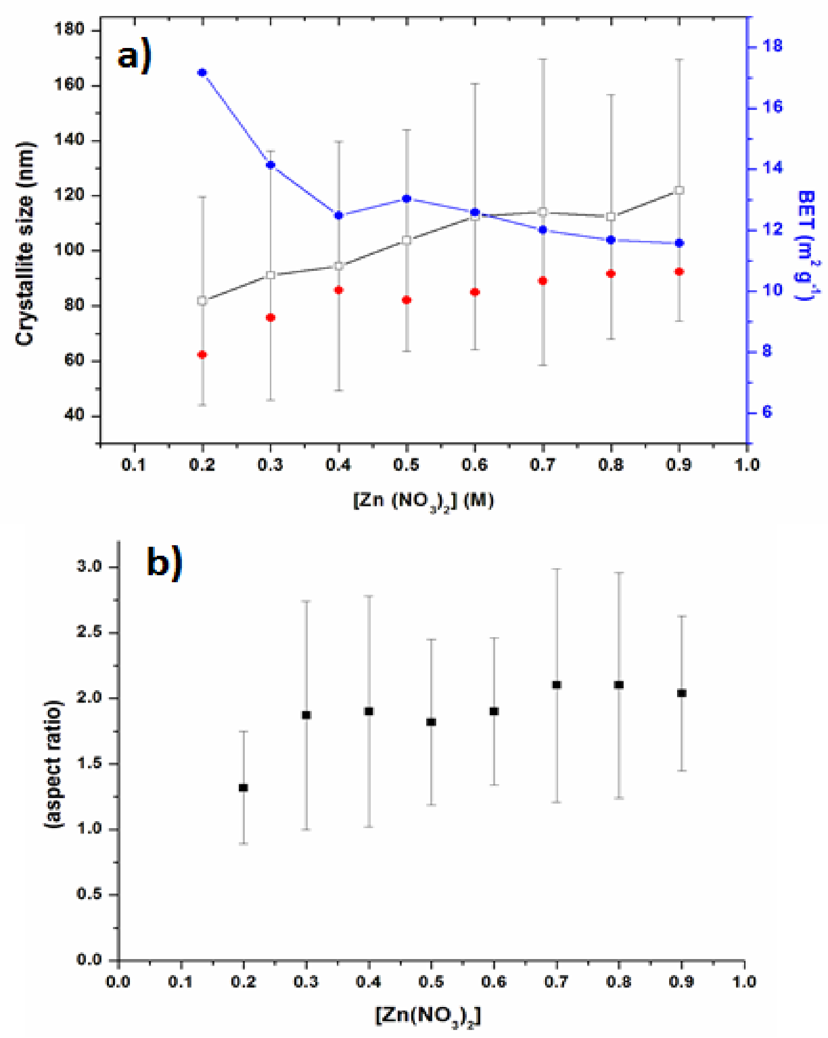

Figure 8.10: a) Comparison of the PSD obtained from TEM of the products of reactions 0.2M700 – 0.9M700 plotted as a function of precursor concentration (squares, error bars denote SD [nm]), BET equivalent sphere diameter [for indication only] (red circles), BET surface area (blue circles), TEM determined crystallite length (error bar = S.D), **b)** Evolution of particle aspect ratio as a function of Zn concentration *ca.* 150 particles measured.

HRTEM was used to confirm the growth direction of the materials produced in experimental runs 0.4M700 and 0.8M700. Compilations of the data obtained for each sample are presented in figure A3.5 and 8.11, respectively. Figure 8.11a shows a low magnification image representative of the nanoparticles obtained from reaction 0.8M700. HREM images of this particle population showed highly faceted particles consistent with those observed for the products of reactions 0.1M40 and 0.1M800. Lattice fringes were identified for particles within the population that showed different morphology, hexagonal and rodlike, as shown in figures 8.11b and 8.11c, respectively. Visualisation of the $(10\bar{1}0)$ lattice fringes with a measured d-spacing of 2.80 Å is shown for a rodlike particle, and lattice fringes corresponding to the (0002) plane were observed for a hexagonal like particle with a measured d-spacing of 2.60 Å. These observations suggest that growth occurs along the crystallographic c-axis in particles which show elongated morphology. The growth direction was also confirmed using SAED as shown in figure 8.11 d and the diffraction spots could be indexed to the (0001) and $(10\bar{1}0)$ reflections confirming the growth direction as [0001], equivalent to the crystal systems c-axis. In the case of samples 0.4M700 equivalent HRTEM data to that presented for sample 0.8M700 is presented in the Appendix to this Chapter, in which crystallite anisotropy was once again attributed to the crystal systems c-axis (Figure A3.3).

The growth mechanism of ZnO under hydrothermal conditions has already been explained by Laudise *et al.*, and Demianets and Kostomarov, amongst others. (Demianets *et al.*, 2002; Demianets & Kostomarov 2001; Kolb *et al.*, 1967) From experimental data generated in Chapter 3, the mechanism of particle nucleation and growth, including reaction mechanisms appear to be consistent between both reported batch hydrothermal processes and continuous hydrothermal synthesis of nanoparticles. (Sondergaard *et al.*, 2011) In hydrothermal systems, it is known that the preferential growth of ZnO along the crystals c-axis occurs after particle nucleation if discrete particle nucleation and growth phases are present under the reaction conditions employed. (Liu & Zeng 2003) Zinc oxide rods, bars and whiskers have been previously synthesised in other continuous hydrothermal systems. Where, differences in the nucleation of particles were cited as the cause for the observed morphology. (Li *et al.*, 2011; Ohara *et al.*, 2008; Sue *et al.*, 2004) Ohara *et al.* reported the synthesis of ZnO micron scale rods using low concentrations of Zn precursors (0.05 - 0.02 M) where the aspect ratio of the bars was found to increase with decreasing concentration suggesting the extent of nucleation (driven by supersaturation) differed between synthesis, in part attributed to a large thermal gradient within the reactor. (Ohara *et al.*, 2008) Similarly, methods which have defined nucleation and growth steps typically produce ZnO materials showing crystallite anisotropy. (Yoshimura 1998) These observations differ from those presented herein (samples 0.2M700 to 0.9M900), where a morphology change was observed for an incremental increase in precursor concentration suggesting a different mechanism for particle growth in which the kinetics of particle growth play an equal, or larger role as nucleation (as nucleation is assumed to be near instantaneous).

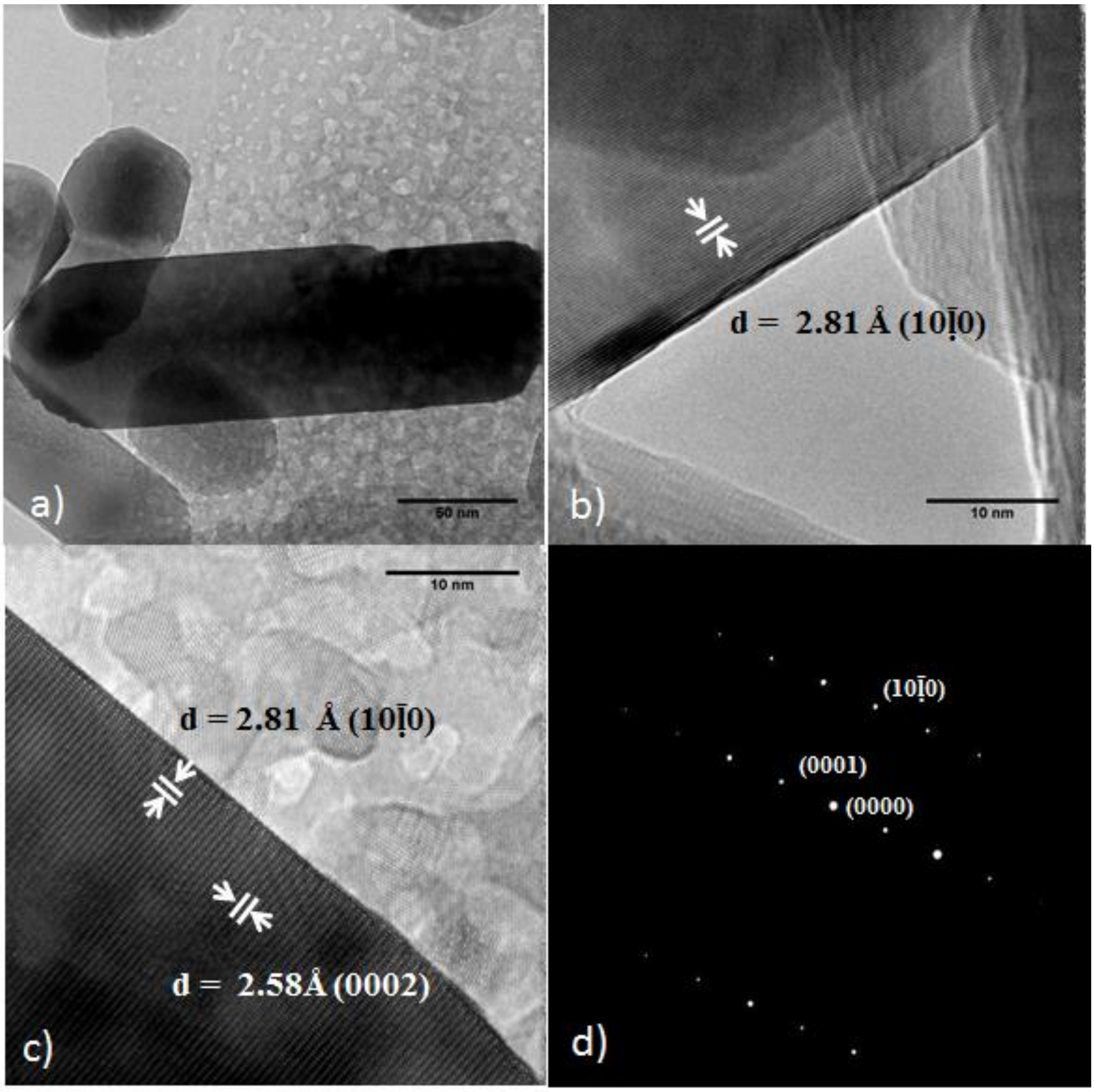

Figure 8.11: Compilation of HREM images of the ZnO sample produced in run 0.8M700; **a)** Low magnification image of a typical rod like particle, **b)** HREM image of a hexagonal particle, **c)** HREM image of the facets of the rod like particle visualised along a zone axis showing intersecting lattice planes, **d)** Indexed electron diffraction pattern of the single crystallite presented in image [a].

In hydrothermal solution, the driving force reported for both ZnO nucleation arises from the high concentration of Zn species (ZnOOH, Zn(OH)$_4^{2-}$, ZnO$_2^{2-}$) which builds the extent of supersaturation necessary induce ZnO nuclei formation. (Demianets *et al.,* 2002) Identified in Chapter 3, this appears to occur through the dehydration of soluble zinc species as a function of temperature with the Zn salt forming a soluble intermediate prior to crystallisation as ZnO as described by equations 8.4 -8.6. (Demianets & Kostomarov 2001) The overall reaction describing the formation of ZnO in continuous hydrothermal synthesis is described by equation 8.6 where the dehydration step occurs at high temperature (See Chapter 3 for further details).

$Zn(OH)_2 + 2OH^- \rightarrow Zn(OH)_4^{2-}$. **(Equation 8.4)**

$Zn(OH)_4^{2-} \rightarrow 2H^+ + ZnO_2^{2-}$(Zinc peroxide). **(Equation 8.5)**

$Zn(NO_3)_2 \bullet 6H_2O + 4OH^- \rightarrow Zn(OH)_2^{4-} + O^{2-} \rightarrow Zn(OH)_2 + 2OH- \rightarrow ZnO_2^{2-}$

$+ 2H+ \rightarrow ZnO$ (crystal) $+ 2e^-$ **(Equation 8.6)**

The preferential growth of ZnO along the [0001] direction is well described and is commonly observed in many aqueous methodologies used for the synthesis of ZnO nanoparticles, especially if nucleation and growth phases are difficult to control. (Darr and Poliakoff 1999) As ZnO is a polar crystal, and the "polar growth unit" $ZnO_2^{\ 2-}$ (formed by dehydration in CHFS) adds to both the positive [0001] and negative $[000\bar{1}]$ monohedron facets of the crystal, which likely involve the reactions represented by equations 8.7 and 8.8. (Li *et al.*, 1999)

Zn^{2+} (surface) $+ ZnO_2^{2-} \rightarrow 2ZnO$ (crystal) ; [0001] **(Equation 8.7)**

O^{2-} (surface) $+ ZnO_2^{2-} + 2H_2O \rightarrow 4OH^- + ZnO$ (crystal); $[000\bar{1}]$ **(Equation 8.8)**

Simply, the extent of preferential growth observed in ZnO nanoparticles can be reduced to the ratio of formed ZnO units ($Zn(OH)_4^{2-}$, ZnO_2^{2-}) to the ratio of particle nucleates formed (*i.e.* the ratio of Zn species in solution to Zn in a crystal). In the case of the pilot scale CHFS process, the observed morphology change has been attributed to the rapid formation of insoluble zinc species in the solution ($Zn(OH)_4^{2-}$, ZnO_2^{2-}) and their rapid concentration increase within the reactor due to the rapid change in temperature associated with mixing, yielding complete formation of insoluble Zn species as observed by the high reaction yields (table 8.3). In the case of CHFS, it is proposed that as a function of precursor concentration the populous of initial nucleates is similar in each case, where after a critical particle size is reached there is sufficient polarity in the crystal to drive the addition of Zn to certain facets indicative of a rate of crystal growth. (Li *et al.*, 1999) Li *et al.* performed experiments to determine the rate of growth along each facet and showed that the rate of addition to the (0001) face is double that observed to addition to the $(10\bar{1}0)$ face. Where, as observed in CHFS the a and b directions of the crystals was almost unchanged for relatively large changes in the c direction reflected in the HREM data presented for samples 0.4M700 and 0.8M700. (Demianets *et al.*, 2002) The unique reaction conditions of CHFS where, supersaturation and thus nucleate formation is largely dominated by particle concentration, control the formation of nucleates and the initial population of particles and occur on very short time scales (estimated as < 100 ms). The aspect ratio distributions observed suggests similar formation and growth processes to those observed under all conditions. However, at high concentration sufficient Zn species remain in solution to allow preferential growth once a critical particle size is reached suggesting the rate of crystal growth under these conditions drives the morphology change increasing as expected with Zn concentration. These reactions have served to demonstrate the limitations of mass based scale up in CHFS in one material system.

8.3.2.3 Section Summary and Conclusions:

In summary, ZnO was a useful system to evaluate the effect of precursor concentration on nanoparticle size and morphology. The mechanism of particle formation highlighted in Chapter 3 was shown to be correct and the synthesis of ZnO nanoparticle synthesis was successfully scaled on a volumetric basis, giving nanoparticles of ZnO with very similar physiochemical characteristics to those obtained using equivalent synthesis conditions on a laboratory scale reactor. An investigation into the mass based scale up of ZnO nanoparticle synthesis showed that particle morphology changes above a 0.2 M $Zn(NO_3)_2$ precursor concentration with the particles showing evidence of a growth phase, this resulted in preferential growth along the particles crystallographic c-axis, a commonly reported fast crystal growth direction. This work has highlighted the requirement for further investigation into the mass based scale up strategy to explore the influence of particle growth. This section has served to highlight that CHFS is readily scaled on a volumetric basis. However, on a mass based scale up strategy nanoparticle growth can be observed above a critical precursor concentration which could be a limit to the overall output of this process, if particle growth phases are not desirable. Although informative this section does not evaluated some of the more complicated material compositions which are commonly produced using CHFS. As such this chapter now moves forward to assess the synthesis of binary oxides using the pilot scale CHFS process.

8.3.3 Synthesis and Characterisation of Doped Nanomaterials Produced using the Pilot Scale CHFS Process:

The aim of this section is to compare the properties of doped nanoceramics produced on the pilot scale CHFS process to those previously produced on a laboratory scale. It is well known that the chemical and physical properties of the nanoceramics can be tuned towards desired applications by doping the host metal oxide structure with various elements. (Chai and Wang 2007; Jang *et al.,* 2009; Li *et al.,* 2002; Morinaga *et al.,* 1997) For example, doping can introduce significant changes in the structure of the host material, creating various lattice defects such as cation / oxygen vacancies and lattice strain dependent upon the ionic radii mismatch / valence of the dopant and host, resulting in different functional properties from those of the host material. (Morinaga *et al.,* 1997; Yoshimura 1998) Hence, there is an interest in scaling up unique properties identified in materials produced on a small scale to usable quantities of material. (Kreuter 1990) This section aims to demonstrate that slight modification of the pilot scale process allows combinatorial work similar to that used on the laboratory scale to be; **1)** readily recreated on the pilot scale process, **2)** is capable of producing similar materials to those produced under analogous conditions using the laboratory scale process. The details of the reactions presented in this section are summarised in table 8.4. Samples were assigned names on the basis of their nominal Zn contents used in each synthesis as per elemental composition, *e.g.* sample 30:70 was assumed to have 30 : 70 ratio of Zn : Ce. In this section, 10 samples were made using the pilot scale CHFS process modified to allow for combinatorial materials synthesis of large volumes of nanomaterials for preliminary materials characterisation / evaluation.

Table 8.4: Flow rates of metal salt precursors used in the synthesis of all the mixed oxide samples. Zn/Ce content (at %, metals basis) in the samples is indicated. Conditions were chosen based on the work of Kellici *et al.* and based on a volumetric scale up of *ca.* 17.5 x (Qsw was fixed at 350 mL min^{-1}) the flow rates initially reported. (Kellici *et al.,* 2010)

Sample Zn:Ce	**Q_{zn}**	**Q_{ce}**	**Q_{KOH}**	**Measured atomic ratios**		**BET (m^2/g)**	**Eg (eV)**	**CIE colour coordinates**			**TEM**	
	(ml min^{-1})			**Zn *(at%)***	**Ce *(at%)***			***a****	***b****	***L****	***Mean***	***SD***
0:100	18*	157	175	0.55	99.45	211	3.21	0.1	31.2	87.2	4.81	1.21
10:90	18	157	175	5.08	94.92	248	3.22	0.5	28.6	88	3.18	1.12
20:80	35	140	175	18.2	81.80	209	3.28	-1.8	25.5	94.3	3.32	2.32
30:70	53	123	175	29.73	70.27	206	3.38	-2	25.1	96.3	3.65	0.98
40:60	70	105	175	37.46	62.54	189	3.28	-2.7	21.5	97.3	-	-
50:50	88	88	175	54.8	45.20	160	3.33	-2.1	19.5	96	-	-
60:40	105	70	175	62.86	37.14	128	3.3	-2.3	18.5	97.5	-	-
70:30	123	53	175	67.52	32.48	114	3.31	-2.9	16.1	99.6	-	-
80:20	140	35	175	78.9	21.10	87	3.31	-2.4	15.8	101.7	-	-
90:10	158	18	175	88.95	11.05	69	3.3	-2.5	11.5	100.9	-	-
100:0	158	18*	175	97.69	2.31	30	3.29	-1.8	3.4	103.1	53.2	10.5

Key: * Indicates a flow of DI water was used instead of the Zn precursor solution through use of a ball valve to switch between tank 2 and Pump 1. $^{\&}$ Likely deviation of approximation from spherical particle morphology due to phase separated product. Q_{zn} = the flow rate of zinc nitrate solution, Q_{ce} = the flow rate of ammonium cerium nitrate solution, Q_{KOH} = the flow rate of KOH solution and E_g = the direct band gap determined from UV-Vis using the KM method.

Reaction yields of > 90 % (metals basis) were obtained in each reaction suggesting near complete precipitation of the component metal ions in the hydrothermal solution. Results obtained from the laboratory scale process were quoted as > 70 % (metals basis) in good agreement with the presented results. (Kellici *et al.,* 2010) An evaluation of nominal and measured Zn content in the samples was performed after the determination of Zn : Ce ratios from EDX analysis and the data is summarised in table 8.4. Where, the previously published results gave a linear fit (r^2 = 0.999) of measured composition against nominal composition, the pilot scale materials showed a similar quality of fit (r^2 = 0.996). The largest divergence was found in 10 : 90 Zn : Ce sample, which can be explained by the error associated with displacement volume from the process pumps *ca.* 5% at the flow rates quoted (table 8.4). The most accurate value was found for the 30 : 70 sample (29.75 at% Zn) and a Zn content average difference of 0.75 at% was estimated over the complete binary series. A broad analysis of the particles produced in the range fron 100:0 to 0:100 (Zn:Ce) was completed using BET and the surface area of the composites produced is shown in figure 8.12 compared to the results of Kellici *et al.*. The BET surface area generally decreased with increasing Zn substitution in both series showing suggesting similarly sized composites were produced in each of the scaled reactions.

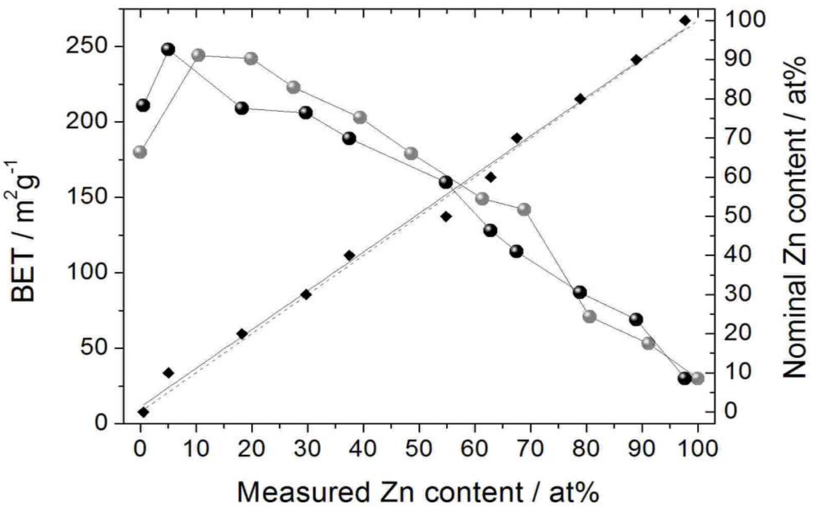

Figure 8.12: BET surface areas of pure CeO_2, pure ZnO and Zn / Ce oxide samples upon increasing Zn metal content in at%. A linear fit between nominal (solid line) and measured Zn content (dashed line).

Figure 8.13 shows the XRD patterns obtained for the materials synthesis in the 100 : 0 to 0 : 100 (Zn : Ce) series using the pilot scale process. Diffraction patterns of the materials produced with 100 % Ce and Zn compositions showed good agreement with fluorite phase CeO_2 (ICDS pattern 78-694) and hexagonal ZnO (ICDS pattern 79-2205). With crystallite sizes of 4 nm for CeO_2 and 32 nm for ZnO calculated from the diffraction data by applying the Scherer equation to the most intense [111] and [101] reflections for CeO_2 and ZnO, respectively. Diffraction patterns obtained for the binary oxide system showed a single phase fluorite (CeO_2) structure upto *ca.* 30 at% Zn, thereafter evidence of phase separation was observed (figure 8.13b). The samples produced using the pilot scale CHFS process showed similar phase behaviour to the materials produced by Kellici *et al.* (figure 8.13a) In both data sets Zn appeared to be soluble in the fluorite lattice upto 30 at% nominal Zn.

Whereas, phase separation was observed in all samples with > 30 % Zn and < 90 % Zn. As the ionic radius of Ce^{4+} (1.03 Å) is much larger than that of Zn^{2+} (0.74 Å) it is unsurprising that Ce shows poor solubility in the ZnO structure. Phase separation was observed as a broad feature in the diffraction patterns centred at 2θ = 27 ° as identified in figure 8.13b. The diffraction data presented for this sample series has showed an apparent solubility of *ca.* 20 - 30 % Zn in the fluorite lattice. However, the low resolution afforded by diffraction from nanocrystalline solids could possibly mask the presence of segregated phases. For this purpose several other complimentary structural characterisation techniques have been employed later in the text to corroborate the observations made using XRD.

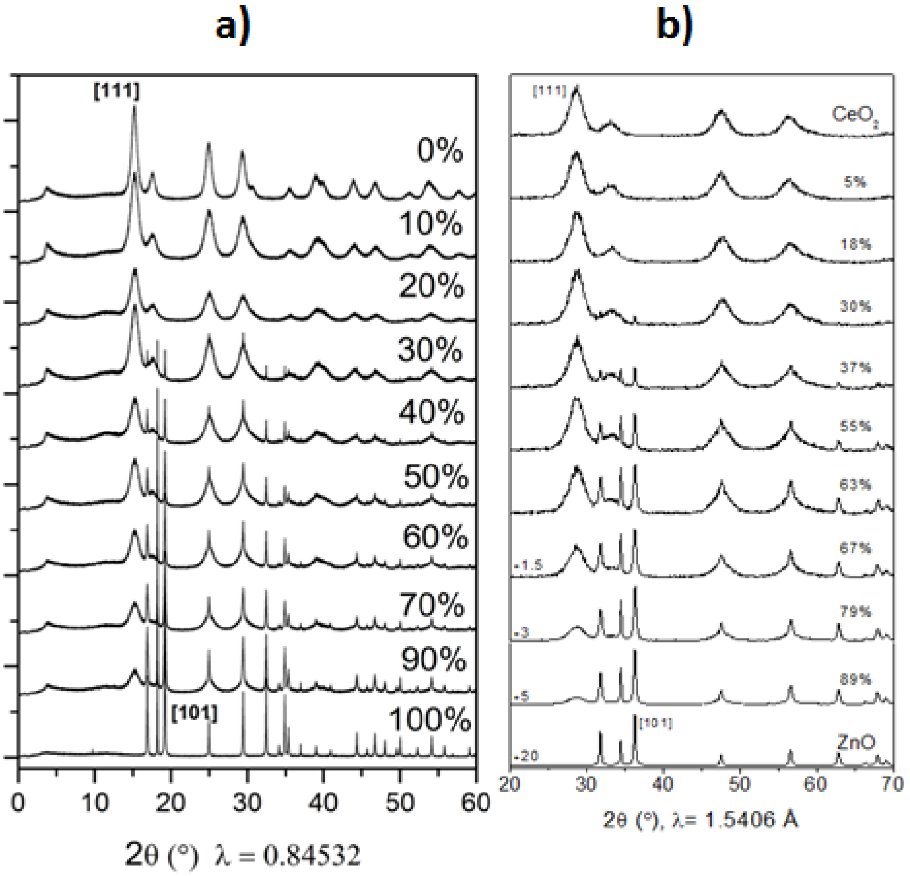

Figure 8.13: Comparison of the diffraction data obtained by Kellici *et al.* and the data obtained for the samples produced on the pilot scale CHFS process; **a)** Diffraction patterns taken from the original report [*n.b.* note wavelength difference], **b)** X-ray diffraction patterns of pure CeO_2, pure ZnO and Zn : Ce oxide mixtures. Zn content in the mixed oxides is given in at%. The relative intensity of 70 - 90 at% Zn oxides and ZnO patterns is adjusted as indicated. Key reflections (111)and (101) for CeO_2 and ZnO, are indicated. (Diffraction data was collected by Dr Raul Quasada-Caberra)

The Raman spectra of all binary oxide samples are shown in figure 8.14 and allowed further comparison between the structural characteristics of both sample series. The spectra of all samples doped with cerium were dominated by the most intense ceria mode a characteristic Ce-O vibration (F_{2g}) centered at 465 cm^{-1}. (Spanier et al. 2001) Defects related to oxygen vacancies, strain and phonon confinement are reported to induce redshift and broadening of this mode.(Spanier, Robinson, Zheng, Chan, & Herman 2001;Weber et al. 1993) Raman spectra for samples containing from 100 - 10 at% cerium (as oxide) showed a slight red-shift of the (F_{2g}) mode position which was nearly linear with increasing Zn substitution upto 40 at% Zn, beyond this limit the mode position remained nearly constant consistent with the incorporation of Zn into the fluorite structure observed in Figure 8.14. The broad modes observed below 400 cm^{-1} and the spectral features in the 500-600 cm^{-1} region have previously been assigned to oxygen vacancies and dopant defects and were present in all samples containing cerium and are commonly observed in doped fluorite phase materials. (Spanier *et al.*, 2001) As the Raman spectrum of ZnO is significantly less intense than the spectrum of CeO_2 the presence of ZnO was only observed in samples containing above 70 at% Zn (as oxide). The spectrum of pure ZnO confirmed its wurtzite structure. (Damen, Porto, & Tell 1966) Modes centered at 435 and 404 cm^{-1} are attributed to the $E_{2(high)}$ and $E_{1(TO)}$ phonons of ZnO with the hexagonal space group P63/mc (Wurtzite structure) and the mode centered at 327 cm^{-1} is attributable to the (E_{2H}-E_{2L}) second order phonon. All observations were consistent with those initially reported, and reaffirmed the characterisation made by XRD. (Kellici *et al.*, 2010)

To further assess the similarity in structure and composition of the materials produced in the scaled process. The single-crystalline structural details of samples 0 : 100, 10 : 90, 20 : 80 and 30 : 70 (Zn:Ce) were further characterised by HREM as shown in figures 8.15. The particle size distributions (S.D) determined for the series (*ca.* 500 particles measured) were 4.81 (1.21), 3.18 (1.12), 3.32 (2.32) and 3.65 (0.98) nm for samples 0 : 100, 10 : 90, 20 : 80 and 30 : 700 (Zn : Ce), respectively. In all samples, the dominant crystal facets for each material composition were the (100) and (111) planes which are typical of the octahedral crystal habit of CeO_2 nanoparticles produced by many other methods, and consistent with the observations of Kellici *et al.* (Kuo and Shen 2000) Typically, materials were visualised down the [110] zone axis with measured angles of intersection of 56.1 ± 2.34° between the 111 and 100 planes (theoretical 54.7 °). Similarly, the angle of intersection between 220 and 200 was observed as 48.6 ± 1.35 (theoretical 45.0 °). In all cases lattice spacings were consistent with those reported for fluorite phase CeO_2. (Mogensen *et al.*, 1994) Surveys of the images did not show lattice spacings characteristic of the larger expected d-spacings of the (100) and (002) planes of ZnO, further suggesting solubility of Zn in fluorite structure. SAED confirmed the presence of a single fluorite phase (CeO_2) upto a zinc concentration of 30 at % where a reflection from the hexagonal ZnO crystal system could be observed in the data (figure 8.16). Table 8.5 provides a summary of the measured lattice spacings and indexed reflections from the materials produced in this series consistent with the observation made using XRD although the interpretation of the SAED data is subject to the presence of an undetected secondary phase (figure 8.13).

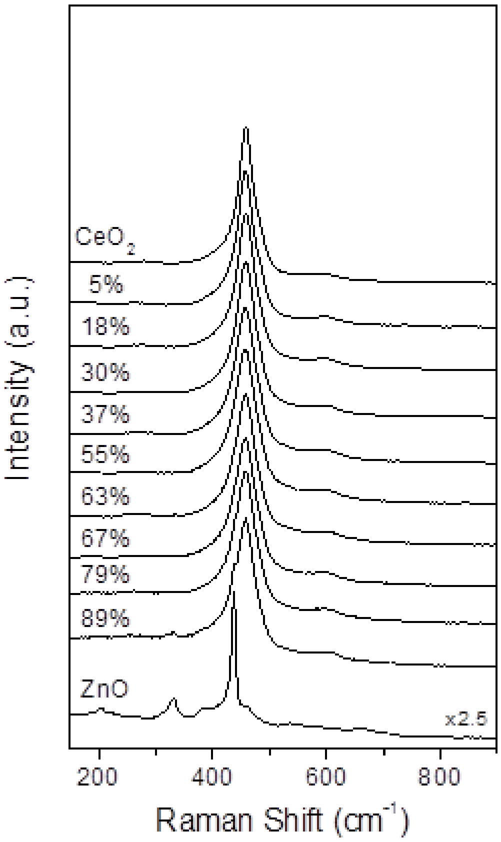

Figure 8.14: Normalised Raman spectra of Zn/Ce oxides containing an increasing amount of Zn from top to bottom. Zn content (at %) and intensity ratio for the ZnO spectrum are indicated.

The optical properties of the nanoparticles prepared using the pilot scale process were assessed using UV-Vis and compared to the optical properties of the nanoceramics reported previously. The band gaps of pure CeO_2, pure ZnO and mixed Ce/Zn oxides were calculated using the Kubelka-Munk function, $F(R) = (1-R)^2/2R$, where R is the value of reflectance (converted from the absorbance data), plotted as a Tauc plot for direct bandgaps, $F(R)*E^2$ *vs E*, where *E (eV)* is photon energy as described in Chapter 2. The calculated band gap for pure CeO_2 nanoparticles was 2.29 eV, which was within the range of 2.00 – 2.63 eV reported in the literature. (Masui *et al.*, 1997; Phoka *et al.*, 2009) Figure 8.17 shows a comparison of the band gap reported previously and the band gap values determined in this work (plotted against measured composition). A gradual blue shift in the direct optical band gap was observed with increasing Zn content, with calculated values of 3.28, 3.35, 3.45 and 3.40 for the samples produced with nominal 10, 20, 30 and 40 at% Zn, respectively. Materials produced with high Zn content > 50 at% showed a reduction in the optical band gap between samples 50 % Zn and 70 % Zn to 3.3 eV with the calculated band gap trending towards 3.35 eV with further increase in Zn content (Bulk ZnO bandgap = 3.35 eV). This is thought to be due to an increase in the UV absorption of the samples owing to the transition to a majority ZnO phase. As shown in figure 8.17 the optical properties of the pilot scale materials showed significant similarity to those previously obtained allowing for slight differences in the measured compositions.

To further explore the similarity in the optical properties of the materials, colorimetric data for all the Zn-Ce oxide sample series produced on the pilot scale CHFS process was compared to those initially reported. Within the binary series, no dramatic change in colour coordinates was observed in the red-green axis (*a**), a linear colour shift was recorded along the yellow-blue axis (*b**) as the Zn content increased, resulting in a virtually white ZnO sample (figure 8.18). The colour change from yellow to white upon increasing Zn content was also inferred from lightness measurements (*L**), as they range from 85 % for pure CeO_2 to almost 100 % for pure ZnO (yellow to white). The results of Kellici *et al.* showed similar trends although the degree of difference in the *a** (the green-red axis) b* (the blue-yellow axis) was greater in the laboratory scale materials which can be attributed to a slight difference in the nominal Ce and Zn contents of the samples (Figure 8.14). The lightness coordinate (*L**) increased almost linearly with increasing zinc concentration for samples 20 at % Zn up to ZnO with L* values of 83% to 100% for the sample series. The colour coordinates for both series change in a similar fashion where, *a** values and b* values decrease codependently on Zn substitution, consistent with the change of colour from dark yellow/brown for CeO_2 (suggesting a majority Ce^{4+} oxidation) to very near white for ZnO. The pure CeO_2 and 10 at % Zn sample did not appear to follow the trends of the other samples, which suggested that the presence (or absence) of separate ZnO nanoparticles dominated the trends in *L*a*b** properties which can be considered broadly consistent with the phase behaviour of the binary system. Nevertheless, the pilot scale materials showed exceptionally similar optical properties to those reported allowing for reasonable experimental error.

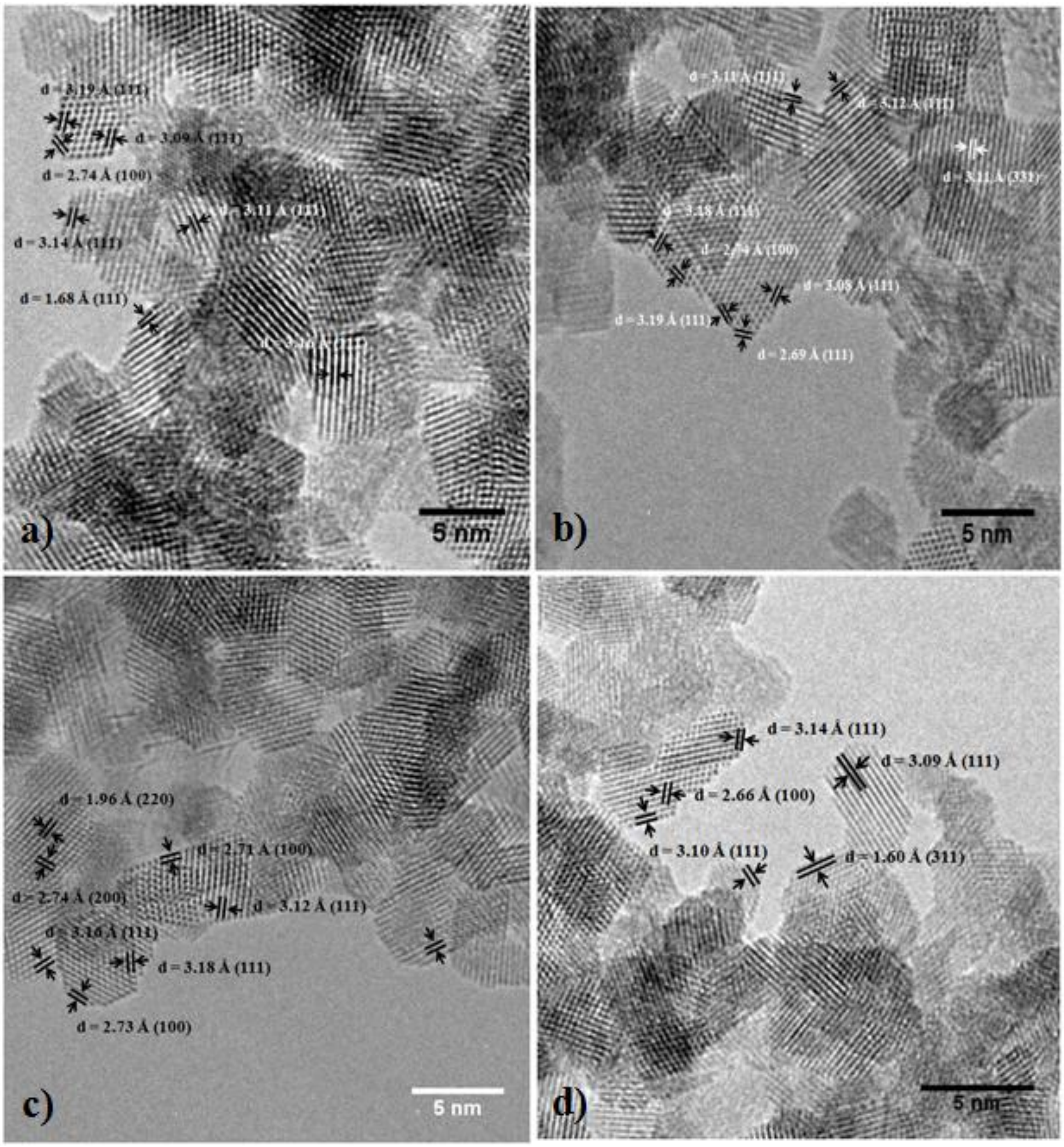

Figure 8.15: HREM images of Ce-Zn oxide nanoparticles produced using a pilot scale CHFS process; **a)** 0 : 100, **b)** 10 : 90, **c)** 20 : 80, **d)** 30 : 70 (Zn:Ce). Inter atomic spacing and corresponding miller indices are noted on each figure (JEOL 4000x was used to capture images at a magnification 350,000 x, scale bar = 5 nm).

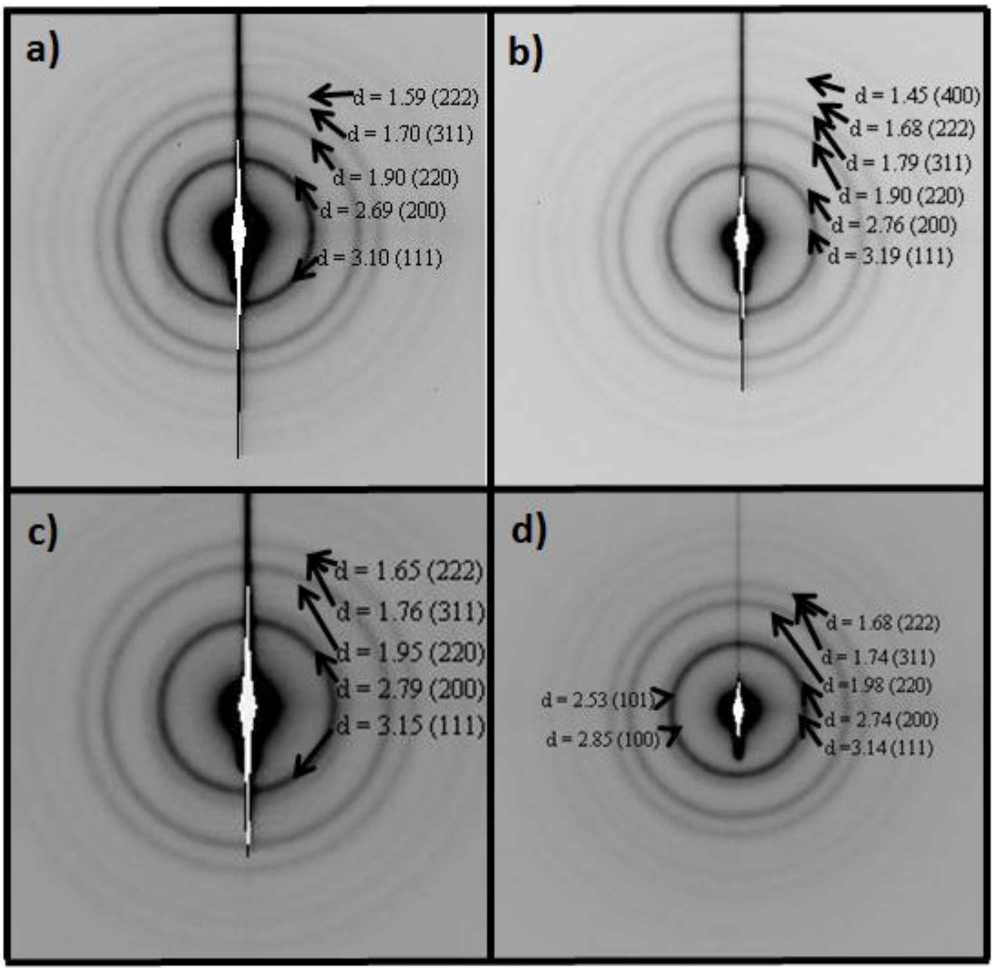

Figure 8.16: Indexed SAED patterns for Zn-Ce oxide nanoparticles produced using a pilot scale CHFS process: **a)** 0:100, **b)** 10:90, **c)** 20:80, **d)** 30:70 (Zn:Ce).

Table 8.5: Summary of lattice parameters measured from SAED data

	Theoretical d-spacings from CeO_2 Fm -3m (ICDS 621705)										**ZnO observed reflections**	
Miller indicie	**(111)**	**(200)**	**(220)**	**(311)**	**(222)**	**(400)**	**(331)**	**(420)**	**(422)**	**(511)**	**(100)**	**(101)**
Theoretical	3.12	2.70	1.91	1.63	1.56	1.35	1.24	1.20	1.10	1.04	2.81	2.47
Samples	**Measured d-spacings (Å)**										**d-spacings (Å)**	
0:100	3.10	2.69	1.90	1.70	1.59	1.39	1.18	*	*	*	-	-
10:90	3.19	2.76	1.90	1.79	1.68	1.45	1.24	*	*	*	-	-
20:80	3.20	2.79	1.95	1.76	1.65	1.53	1.28	*	*	*	-	-
30:70	3.14	2.74	1.98	1.74	1.68	1.48	1.31	*	*	*	2.85	2.53

*Observed reflection although diffuse consequently the diameter was not measured. *N.b.* The profile of each diffraction ring was treated as a Guassian function and the centre point was used to calculate the d-spacing.

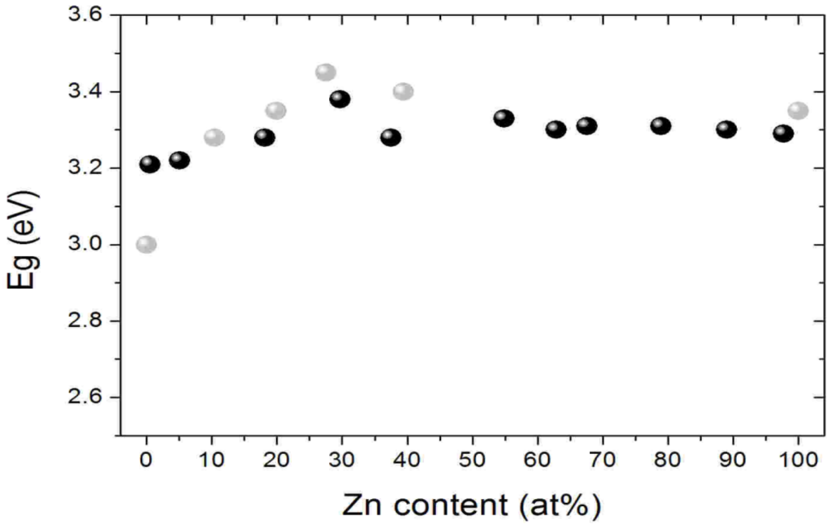

Figure 8.17: Variation in Band gap upon increasing Zn content (at %) in the Zn/Ce oxide binary system. A comparison between the present work (Black symbols) and previous work (grey symbols).

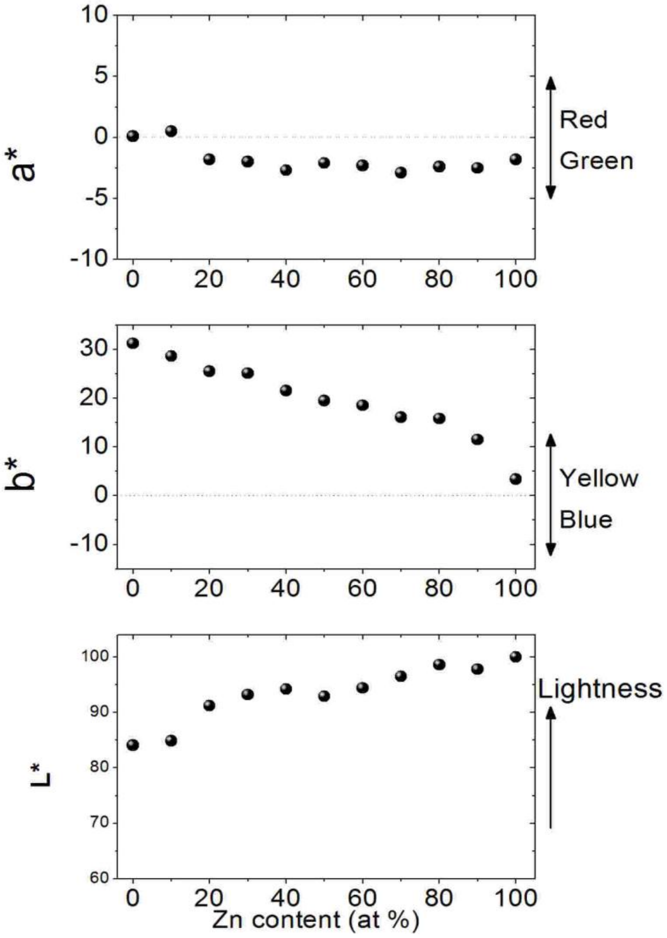

Figure 8.18: CIE colorimetric parameters for Zn-Ce oxides *vs* measured Zn content (at%) produced using the pilot scale CHFS process.

8.3.3.1 Summary of Section:

In summary, an experiment previously performed using a high throughput continuous hydrothermal methodology which allowed a combination of particle properties to be identified (*e.g.* unusual phase stability, tuneable optical band gap, high crystallinity and small particle size) that was difficult to achieve using more conventional synthesis routes was successfully recreated using the pilot scale CHFS process at a volumetric scale up of 17.5 x. The pilot scale process was operated in a configuration which allowed a complete range of Zn : Ce oxide nanomaterials to be sequentially synthesised analogous to previously reported high throughput experiments. All the nanomaterials produced using the pilot scale process were shown to have similar physical characteristics to those published previously as determined by XRD, Raman spectroscopy, UV–Vis, BET surface area and elemental analysis (allowing for reasonable experimental error). Synthesis on the pilot scale process yielded materials which showed similar phase behaviour, morphology and optical properties to those produced on the laboratory scale process. Ultimately, this section has demonstrated that combinations of particle properties which are difficult to produce using more conventional synthetic methodologies (*e.g.* band gap, crystallinity, size, etc.) could be replicated on a large scale in CHFS at a 17.5x volumetric scale up of the laboratory process which allowed the synthesis of nanoparticles in sufficient quantity for through evaluation in any potential application.

8.3.4 Scale up of Magnetite Nanoparticle Synthesis using CHFS

Initially, this section describes an investigation into the volumetric scale up of magnetite nanoparticle synthesis. The physical characteristics of the products are identified and the data is summarised briefly. This section then moves forward to assess the volumetric scale up of surface functionalised nanoparticle synthesis using the process methodology presented in Chapter 6. Rather than assessing if this processing methodology can be sequentially enlarged on a volumetric basis, data is presented which has assessed if the process can be enlarged. Where, previously magnetite was used as a simple nanoparticles system to study the influence of different processing conditions on the state of dispersion, grafting density and magnetic properties. An equivalent investigation to that initially presented in Chapter 6 has been reproduced on the pilot scale process. This section serves to demonstrate that reactions optimised on the laboratory scale can be adequately reproduced on a larger scale.

8.3.4.1: Synthesis of Magnetite Nanoparticles:

In this section the effects of both volumetric scale up and precursor concentration were assessed co-dependently on the formation of magnetite nanoparticles in the pilot scale CHFS process. The reactions reported in this section are summarised in table A3.2 (Appendix 3).

Although the reaction point temperature used in the production of magnetite nanoparticles on the pilot scale CHFS process *ca.* 348 °C was lower when compared to the temperature typically used on the laboratory scale CHFS process *ca.* 383 °C. Similar materials were produced over all processing conditions. In all reactions summarised in Appendix 3, a single phase product was obtained in each reaction, consistent with the data presented in Chapters 5 and 6, where it was shown that large differences in the chemical environment within the reactor were required before the phase of the reaction product was altered. Characterisation data obtained for the sample series, showed that the crystallite size determined by standard structural methods (TEM, XRD and BET) was similar to that observed when the laboratory scale process (data summarised in Appendix 3, Section A3.2). In the pilot scale process, nanoparticles of magnetite with a crystallite size of *ca.* 13 nm were produced which are very similar to those initially produced in Chapter 5. Which, as shown in Appendix 3.2, appeared to be invariant of both the volumetric flow rate of the system and the precursor concentration over the range tested. The similarity between particle sizes as a function of volumetric scale and precursor concentration are likely to arise from similar particle formation processes over the experimental range with particle formation occurring at high supersaturation leading to minimal growth as initially discussed for the scale up of ZnO synthesis (Section 8.3.2.1).

The variance in magnetic properties previously identified using the laboratory scale process, initially attributed to inhomogeneous magnetic domains, was also observed when synthesis was recreated using the pilot scale process. The measured magnetic properties of properties of each sample are summarised in table A3.2 (Appendix 3). M_s of each of the samples was shown to vary considerably (48 to 69 emu g^{-1}), but no definitive trend in saturation magnetisation could be established with any one volumetric scale up or precursor concentration used (figure A3.6). All samples behaved superparamagnetically at 300 K with low coercivity (0.04 - 2.3 Oe). The observed reduction in the value of M_s in nanosized iron oxides can be attributed to may physiochemical and structural characteristics as discussed in greater detail within Chapter 5. As such, calculation of the effective ferromagnetic diameters (μ_{fm}) of the samples by fitting the magnetisation data with a Langenvin function (detailed in Chapter 2) are summarised in table A3.2. The calculated ferromagnetic diameter ranged from 4.9 to 7.0 nm, and varied consistently with M_s. In all samples which showed lower values of saturation magnetisation the paramagnetic contribution (accounting for the non-saturating behaviour), was notably much larger than samples showing higher saturation magnetisation. This observation can be attributed to the presence of a magnetically frustrated phase within each sample and accounting for a large proportion of the nanoparticle volume as discussed in greater detail within Chapter 5. These observations are consistent with those presented in Chapter 6 where some magnetic polydispersity was observed in each of the samples. From fitting of the magnetisation curves it has been inferred that the magnetic structure of the particles is difficult to reproduce using this synthesis methodology and on scale up this observation was also made for materials, as materials appeared to scaled up well in structure and physical properties. Similarly, low temperature MH cures and ZFC/FC measurements showed significant similarity to the characteristics of magnetic iron oxides previously noted in Chapters 5 and 6 (Appendix A3.2, figure A3.7). The measurements suggest that the crystallites produced in the scaled reactions are magnetically complex structures which show evidence of magnetic frustration, as consistently observed throughout this thesis. Again, these measurements suggest that disorder not necessarily related to structural differences but magnetic domain disorder within the crystallites. The magnetic polydispersity observed means only limited conclusions can be drawn from this evaluation in light of the data presented in Chapters 5 and 6 as the variance of magnetic properties appeared completely random in the reactions performed on the pilot scale process. However, it has been shown that particles with properties within the range identified on the laboratory scale process could be produced in terms of both material structure, particle size and magnetic properties reaffirming the observations made in Sections 8.3.2 and 8.3.3. This section now moves forward to assess the surface functionalisation of magnetite nanoparticles using the pilot scale CHFS process.

8.3.4.2 Investigation of the Volumetric Scale up of Surface Functionalised Nanoparticle Synthesis using CHFS

This section details an investigation into the direct synthesis of citric acid coated nanoparticles using the pilot scale CHFS process. The reactions detailed in this section are presented in table 8.6.

A reaction point temperature of *ca.* 350 °C (just below the supercritical point of pure water at 24.1 MPa) was found to be suitable for the synthesis of single phase magnetite using the pilot scale CHFS process (Section 8.3.4.1). The synthesis of citric acid coated nanoparticles using the pilot scale process scaled on a volumetric basis alone was evaluated to define an operational space in which stable dispersions of particles could be produced. All reported materials formed ferrofluids after consolidation as demonstrated in figure 8.19 consistent with the observations initially presented in Chapter 6. A discrepancy was observed between the syntheses presented in Chapter 6 and the results presented for sample PPCAN1 - 15 identified herein. In the pilot scale process CA :Fe ratios > 2 resulted in dissolution of the product whereas in the laboratory scale process much higher ratios (CA : Fe ratios > 10) resulted in the dissolution of product. The likely explanation is that the pH of the mixture exiting the system is different to that in the laboratory scale process and an explanation for this is most likely complex and multifactoral. Otherwise, similar product characteristics were observed in the scaled reaction which will be discussed further in the text below.

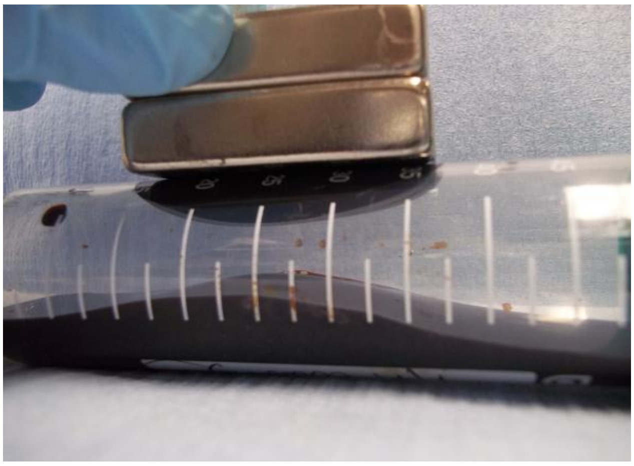

Figure 8.19: Photograph of the ferrofluid produced by the recovery of sample PPCAM14 under the influence of a rare earth magnet.

Table 8.6: Summary of the reaction conditions used for the synthesis of citric acid coated magnetite on the pilot scale CHFS process.

ID	**Pump flow rates (mL min^{-1})**			**T_{mix2} (°C)**	**CA:Fe**	**RT $_{mix1}$ (s)**	**RT $_{mix2}$ (s)**	**Cs (nm)**	**Surface area**		**TGA data**		**Hydrodynamic diameter (nm)**			**TEM data**	
	Q_{sw}	**Q_p**	**Q_q**						**(m^2/g)**	**S_{BET} (nm)**	**Weight loss (%)**	**GD (CA nm^{-2})**	**HD**	**PDI**	**H_{Dn}**	**Mean**	**SD**
PPCAM1	200	160	137	283	0.66	2.30	1.82	15.67	66.3	17.6	1.44	-	113	0.231	47.5	-	-
PPCAM2	200	160	183	263	0.90	2.30	1.83	13.42	55.4	21	4.39	-	118	0.204	45.6	-	-
PPCAM3	200	160	229	245	1.12	2.30	1.85	12.67	67.4	17.3	2.47	0.63	142	0.134	50.4	12.5	2.9
PPCAM4	200	160	274	230	1.35	2.30	1.9	11.37	74.5	15.6	2.95	0.70	120	0.154	38.5	11.6	3.4
PPCAM5	300	260	206	277	0.625	1.55	1.69	10.78	83.4	14	3.28	-	96	0.168	34.9	-	-
PPCAM6	300	260	274	257	0.831	1.55	1.63	13.67	72.1	16.2	2.41	0.67	91	0.120	39.7	13.5	3.3
PPCAM7	300	260	343	240	1.04	1.55	1.62	10.94	68.2	17.1	2.92	0.35	60	0.101	29.3	16.6	3.3
PPCAM8	300	260	411	225	1.24	1.55	1.61	12.56	79.3	14.7	2.57	0.52	70	0.245	28.3	11.7	3.1
PPCAM9	350	310	240	275	0.61	1.33	1.59	13.98	67.2	17.3	5.45	2.23	69	0.341	35.6	11.0	2.6
PPCAM10	350	310	261	270	0.66	1.33	1.58	14.25	60.3	19.3	6.75	1.89	54	0.101	20.3	13.4	4.1
PPCAM11	350	310	343	251	0.86	1.33	1.56	10.65	73.1	15.9	7.60	2.11	49	0.082	19.5	13.5	3.5
PPCAM12	400	360	300	268	0.657	1.17	1.51	13.96	69.2	16.8	8.11	2.64	42	0.132	16.7	15.8	4.2
PPCAM13	400	360	400	248	0.871	1,17	1.48	10.79	67.2	17.3	7.48	1.78	40	0.135	22.8	11.6	3.3
PPCAM14	400	360	500	231	1.09	1.17	1.46	14.36	73.4	15.9	9,80	2.57	60	0.167	19.4	12.8	4.5
PPCAM15	400	360	600	216	1.53	1.17	1.45	15.67	59.2	14.98	8.64	2.02	43.2	0.131	20.3	11.4	1.2

Key: GD = grafting density of CA determined using equation 6.1 and the crystallite size determined from TEM, Q_{sw} = the flow rate of supercritical water (450 °C), Q_p = the flow rate of ammonium iron citrate (0.066 M), Q_q = the flow rate of citric acid solution (mL min^{-1}), T_{mix2} = the theoretical mixture temperature post citric acid addition, CA : Fe = the molar ratio of iron to citric acid used in the synthesis, RT_{mix1} = the reaction residence time prior to citric acid addition, RT_{mix2} is the reactor residence time post citric acid addition, Cs = the crystallite size determined from the application of the Scheerer equation to the (311) reflection of magnetite, S_{bet} = the equivalent sphere diameter calculated from the surface area, D_h = hydrodynamic diameter (nm) measured using DLS and $D_{h(n)}$ is the number weighted distribution (explained in Chapter 2), TGA = weight loss in the 200 - 500 °C region (attributed to the thermal decomposition of citric acid).

XRD patterns of the products of reactions PPCAN1-15 are shown in figure 8.20. XRD showed that the products are well crystallised and have a cubic inverse spinel structure (space group Fd3m) known for bulk magnetite and maghemite (ICDS 082234) and maghemite (ICDS 79196), respectively. Volume weighted crystallite size estimates taken from the most intense reflection (311) yielded sizes in the range 8 to 11 nm (table 8.6), which appeared largely invariant of the processing conditions, consistent with the data presented in Chapter 6 and also the crystallite sizes determined for samples produced in Section 8.3.4.1.

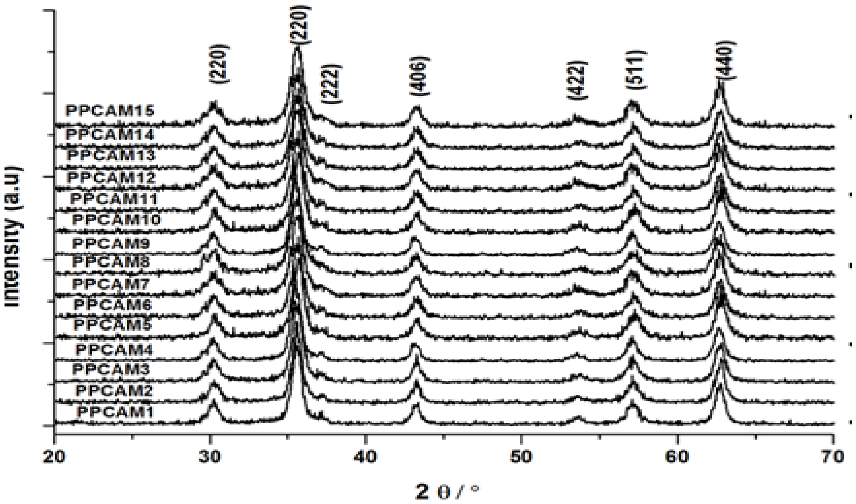

Figure 8.20: XRD patterns of citric acid coated magnetite produced on the pilot scale CHFS process as detailed in table 8.6.

TEM images representative of the particles produced in each synthesis are presented in figure 8.21. The average particle sizes and distribution were calculated from the measurement of *ca.* 300 particles are summarised in table 8.6, and confirmed that crystallite size was largely independent of processing condition (consistent with data presented in Chapter 6, as crystallite size was shown to be invariant of reaction quenching and CA : Fe, to the point of dissolution). The crystallite sizes obtained were in good agreement with the crystallite size determined from the diffraction data. However, BET surface area measurements of samples PPCAM1-15 gave surface areas lower than anticipated ranging from 55 to 79 m^2 g^{-1}, as summarised in table 8.6. Estimation of the crystallite size using the equivalent sphere approximation (equation 2.6) assuming a material density of 5.15 g/cm^3 gave values which were *ca.*1 - 5 nm larger than observed from both diffraction data and particle size directly observed using TEM. If it is assumed that the citric acid molecules formed an impenetrable layer as the particle surface and the geometry of the molecule is taken into account *ca.* 1.2 nm would be added to the effective particle diameter determined using this approximation, which suggests if this interpretation is valid all size estimates give equivalent values.

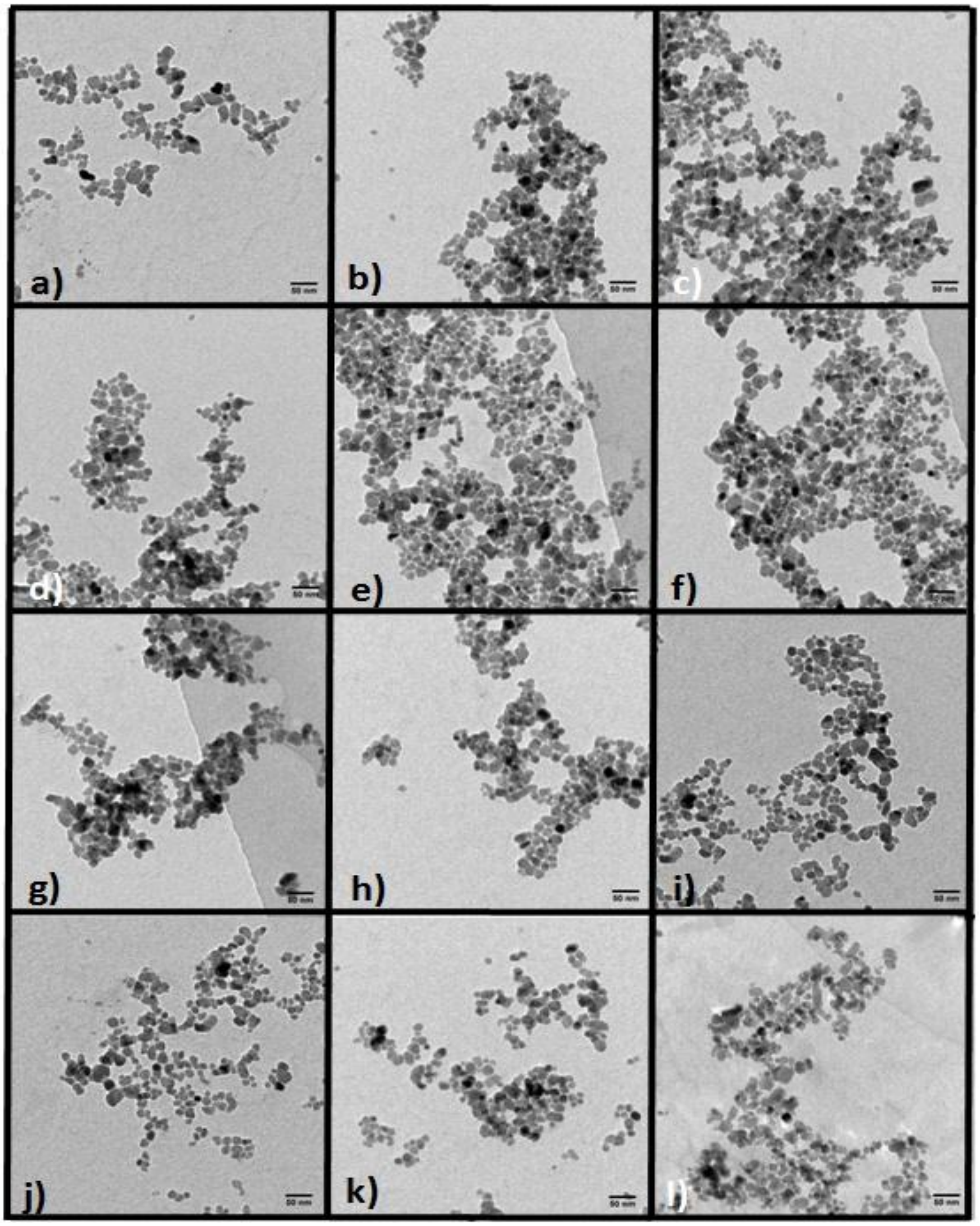

Figure 8.21: TEM images of citric acid coated magnetite nanoparticles produced using the pilot scale CHFS; **a)** PPCAM3, **b)** PPCAM4, **c)** PPCAM6, **d)** PPCAM7, **e)** PPCAM8, **f)** PPCAM9, **g)** PPCAM10, **h)** PPCAM11, **i)** PPCAM12, **j)** PPCAM13, **k)** PPCAM14, **l)** PPCAM15 (scale bar = 50 nm).

To confirm functionalisation of the products of run PPCAN1-15, ATR-FTIR spectra were collected as shown in figure 8.22. Spectra obtained for the coated magnetite particles showed modes origination from (ν) C=O present at *ca.* 1735 cm^{-1}, (ν_s) COO$^-$ (~ 1390 cm^{-1}), (ν) OC-OH (~ 1204 cm^{-1}), (νs) OC-OH (~ 1429 cm^{-1}) and (ν_{as}) COO$^-$ (~1569 cm^{-1}) confirming the presence of citric acid. The apparent wavenumber separation between (ν_s) COO$^-$ (*ca.* 1390) and the (ν_{as}) COO$^-$ (*ca.* 1569), varied between 190 and 220 cm^{-1} suggesting a mixture of monodentate and bidentate coordination to the surface of magnetite. The weak and broad nature of the observed modes makes a definitive binding state difficult to confirm using the presented data. However, a tentative approximation from the data suggests a mixture of monodentate and bidentate coordination, consistent with the data presented in Chapter 6 and 7.

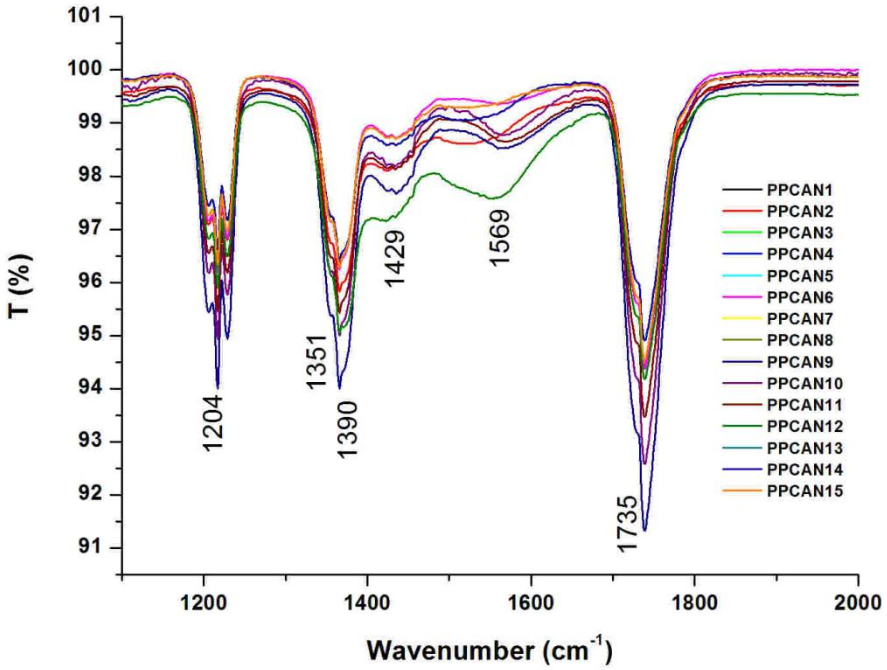

Figure 8.22: Stacked FTIR spectra of the products from each reaction PPCAM1-15 showing an expanded region of the complete spectra (range 1000 to 2000 cm^{-1}) identifying the IR active mode positions.

The grafting density of citric acid bound to the surface of magnetite produced using the pilot scale process was calculated from the composition and surface area (from the mean crystallite size determined using TEM) using equation 6.1 as presented in Chapter 6. TGA data collected for the products of reactions PPCAN1-15 is shown in figure 8.23a and the weight loss data summarised in table 8.6. The variation in grafting density as a function of scale up ratio ([Q_{sw} = 400, Q_p = 360 = 20x], [Q_{sw} = 350, Q $_p$= 310 = 17.5x], [Q_{sw}= 300 Q_p = 260, = 15x] and [Q_{sw} = 200, Q_p =160 = 10x]) is presented in figure 8.23b showing an apparent surface saturation of *ca.* 2.6 CA nm^{-2}, consistent with the saturation density calculated for magnetite produced on the laboratory scale process (Chapter 6) and saturation values reported in the literature. (Mudunkotuwa and Grassian 2010; Racuciu *et al.*, 2006) The observations of increasing grafting density as a function of increasing flow rate are assumed to be due to differences in the mixing environment between successive volumetric scales as initially suggested in Chapter 6. The degree of mixing between the citric acid feed (Q_q) and the nascent nanoparticle stream (Q_{sw} + Q_p) was not experimentally validated using the pilot scale process due to the size of the process equipment. However, to provide an indication of whether this is a reasonable evaluation of these observations, the flow type occurring within the system was estimated for each condition presented by calculating the Re of the flow. In the stated flow regimes the mixture issuing from the reaction point (defined by T_{mix1}) is a highly turbulent flow with a Reynolds numbers ranging from 6.46 x 10 ^{4} ($Q_{sw\ =\ 200}$ + $Q_{p\ =\ 160}$) to 12.65 x 10 ^{4} ($Q_{sw\ =\ 400}$ + $Q_{p\ =\ 360}$) with corresponding Fr^2 of 65 and 110 being a momentum driven flow. Mixing of the feed containing nascent nanoparticles and the feed containing citric acid is likely to be complex due to the reasons outlined in Chapter 6 and was unlikely to be a steady state system as shown by *in-situ* temperature measurements. However, an estimation of the flow type occurring pilot scale system under the different flow conditions suggested the mixture after the addition of citric acid was a turbulent flow in the highest scale up ($Q_{sw\ =\ 400}$ + $Q_{p\ =\ 360}$) flow regime yielding Re = 12.5 to 12.9 x 10^4 (*Qq* = 300 - 600 ml min^{-1}) if the mixture is assumed to be at T_{mix2}, and Re 11.6 to 11.9 x 10^4 when $Q_{sw\ =\ 350}$+$Q_{p\ =\ 310}$ and $Q_{q=\ 240\ -\ 343}$ mL min^{-1}. However, in the lower flow regimes ($Q_{sw\ =\ 200}$ + $Q_{p\ =\ 160}$ and $Q_{sw\ =\ 300}$ + $Q_{p\ =\ 260}$) Reynolds numbers ranging from Re = 4.38 to 7.89 x 10^4 ($Q_{q=\ 137-411}$ ml min^{-1}) were calculated, significantly lower in magnitude that those obtained in the high flow regime suggesting a transient flow type in the lower flow regimes and a turbulent flow in the high flow regimes. Which, is consistent with the observations presented in the laboratory scale process where higher grafting densities of citric acid were obtained in a turbulent flow regime. Again, suggesting surface functionalisation was linked to mixing at high temperature and thus diffusion of CA to the particle surface as in a turbulent flow diffusion of CA to the particle surface would likely be enhanced. This interpretation is presented in light of the data presented in Chapter 6.

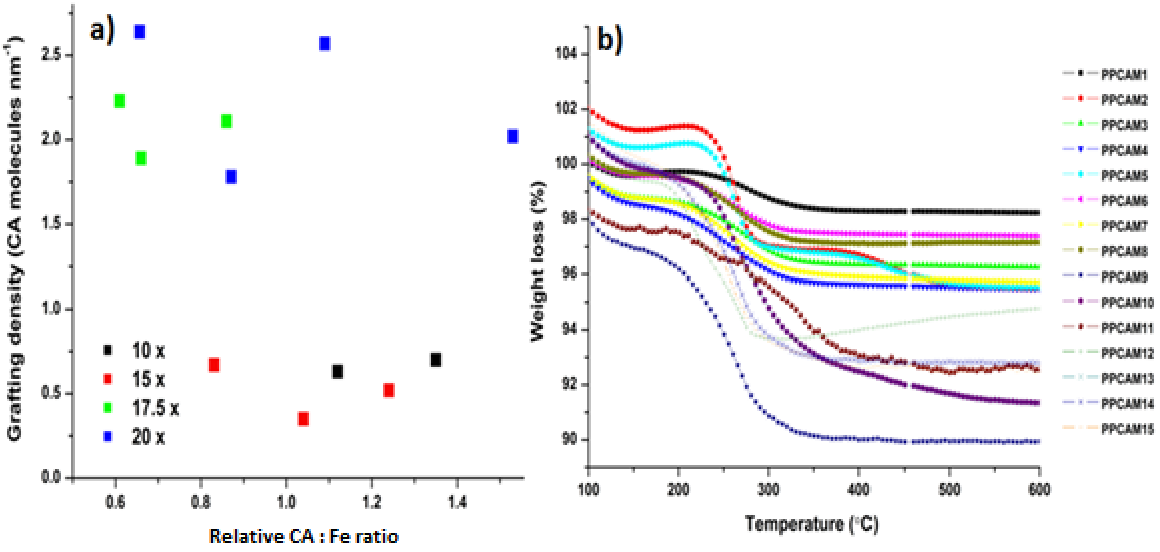

Figure 8.23: a) Variation in calculated grafting density calculated from equation 6.1 plotted against relative CA : Fe ratio used in the synthesis of each product. **b)** TGA data of the pilot scale reaction products.

To assess the dispersion of the products from the pilot scale process the hydrodynamic diameter of the samples was measured using DLS, a plot showing the Z-average hydrodynamic diameter (polydispersity plotted in nm) as a function of scale up ratio and CA : Fe ratio is shown in figure 8.24 (tabulated summary is provided in table 8.6). As shown in figure 8.24, the polydispersity indices (PDI) of the samples ranged from 0.09–0.25 which indicates low to moderate polydispersity. In general the measured hydrodynamic diameters decreased as anticipated with increasing grafting density and dispersions of similar quality to those produced in Chapter 6 were reproduced. Measurements of hydrodynamic diameter gave size values larger than those anticipated by TEM suggesting a degree of agglomeration in the samples. However, when the limitations of DLS are considered in terms of the r^6 relationship between particle size and scattered light, conversion to number weighted values (table 8.6) yielded hydrodynamic diameters slightly larger than those expected from TEM suggesting a majority of the sample was in dispersion as single crystallites in agreement with the results presented in Chapter 6.

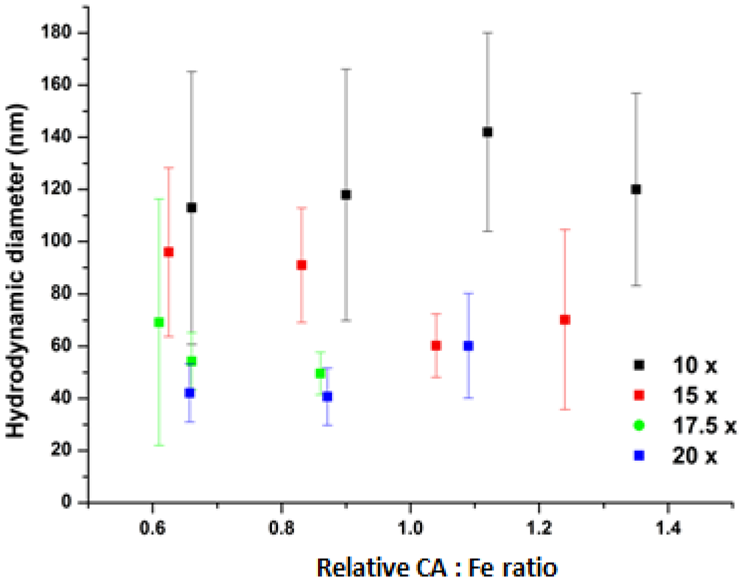

Figure 8.24: Grouped DLS data showing the difference in hydrodynamic diameter from samples PPCAM1-15, the z-average hydrodynamic diameter is plotted as a function of the relative CA : Fe ratio used in synthesis and the volumetric scale up factor (error bars represent the sample polydispersity in nm).

Figure 8.25 shows the variation in the magnitude of the zeta-potential as a function of dispersion pH for samples produced on the pilot scale CHFS process. The zeta-potential of samples which showed CA grafting densities of > 1 CA nm^{-2} (PPCAM9 to 15) gave characteristic features of the protonation and deprotonation of free acid groups on the surfaces of the particles, yielding values of similar magnitude to those presented in Chapter 6. A characteristic change in surface charge around pH 6 corresponding well with the pKa of the weakest acid group of citric acid (pKa 6.13) suggests similar coordination of the acid to the particle surface as observed for the materials presented in Chapter 6, serving to confirm the electrostatic stabilisation of the dispersion. Positive values of zeta-potential were recorded for all samples below pH 5 consistent complete protonation of the surface species and the onset of sample dissolution occurring at pH 3. In the case of samples PPCAM 1-9 amphoteric behaviour was observed as a smooth transition in the magnitude of the zeta-potential as a function of pH likely to arise through protonation (low pH) and deprotonation (high pH) of FeOH surface groups as explained in greater detail within Chapter 6. When the grafting density of CA varied in the region of 0.5 - 0.9 CA/nm^2 comparatively large variations in the magnitude of the zeta-potential were measured, suggesting a combination of surface charge associated with free amphoteric sites on the particle surface and the deprotonation of a free acid group both played a role in the stabilisation of the sol at high pH (PPCAM4 to 6).

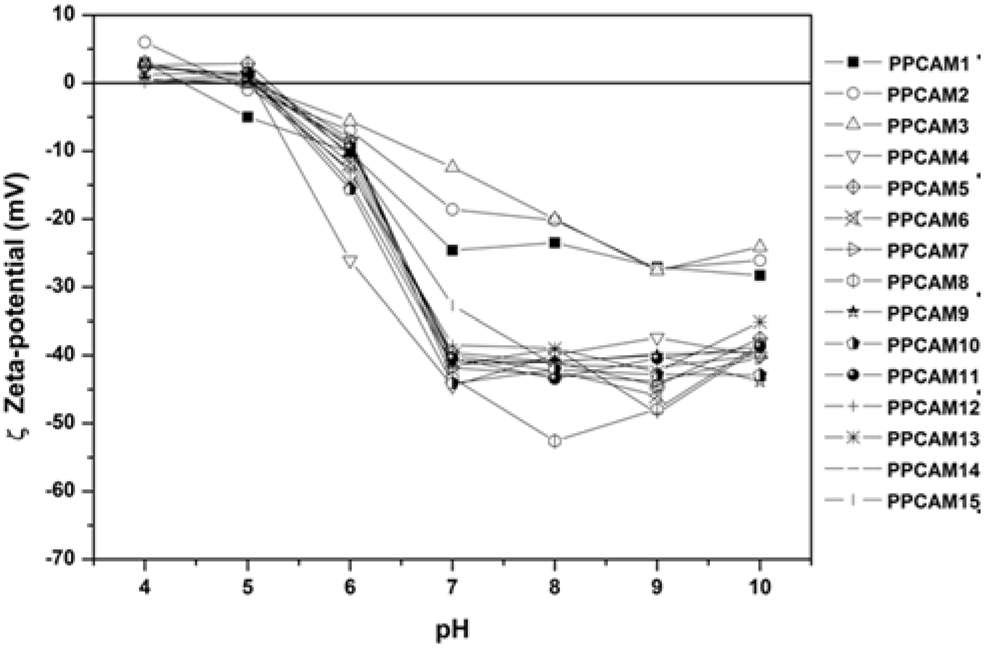

Figure 8.25: Zeta-potential as a function of titration against pH for citric acid coated magnetite nanoparticles produced on the pilot scale CHFS process.

As the magnetic properties of disperse nanoparticles are of interest in many applications the room temperature the magnetic properties of the CA coated magnetite produced on the pilot scale process were measured. As shown in figure 8.26, the nanoparticles showed superparamagnetic like behaviour with low coercivity as summarised in table 8.7, as coercive forces of < 10 Oe at 300 K are cited as indicative of the magnetite in a superparamagnetic state. (Dennis *et al.*, 2008; Itoh and Sugimoto 2003; Levy *et al.*, 2011) The saturation magnetization of the coated nanoparticles was found to be lower than the expected value for bulk magnetite consistent with all other samples produced in this thesis and in this sample series showed a degree of polydispersity, which has previously been attributed to some form of magnetic structural disorder (Chapter 6). The effective ferromagnetic size (calculated as detailed in Chapter 2) was found to be significantly smaller than that expected for the crystallite sizes determined from both XRD and TEM as summarised in table 8.7. This observation can be attributed to the presence of a magnetically frustrated phase within each sample and accounting for a proportion of the nanoparticle volume as the contribution of paramagnetic-like susceptibility (χ) accounting for the non-saturating behaviour, increased with decreasing saturation magnetisation, suggesting the synthesis of magnetically complex structure as initially observed in Chapters 5 and 6. (Mikhaylova *et al.*, 2004)

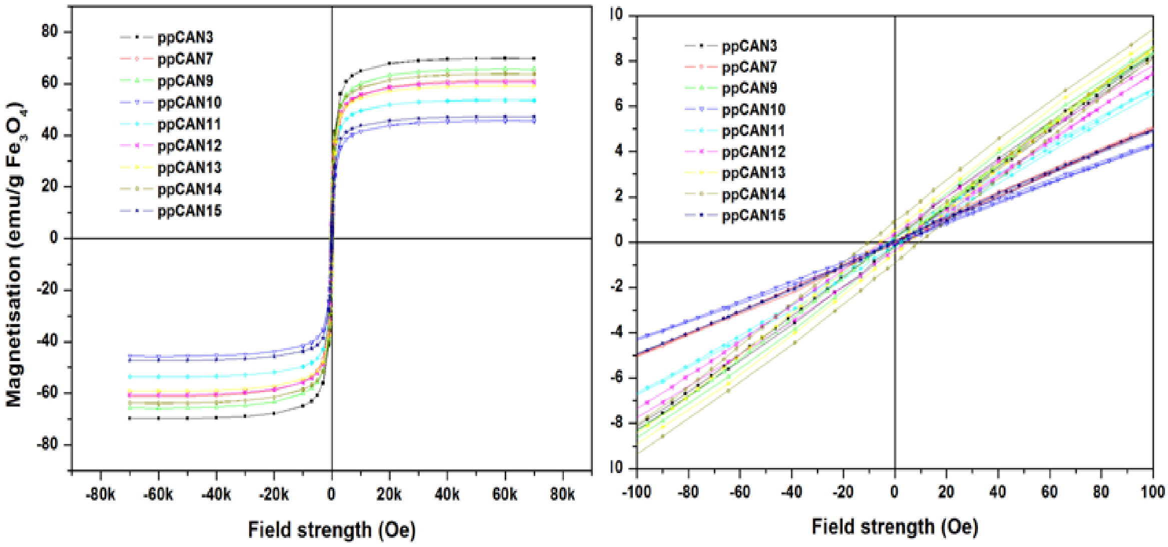

Figure 8.26: a) MH curves of citric acid coated magnetite produced using the pilot scale CHFS process, **b)** expanded plot showing the near 0 Oe region.

Table 8.7: Summary of the magnetisation data and results from magnetic fitting for samples synthesised with the addition of citric acid in the pilot scale CHFS process

Sample	**TEM (nm)**	**Ms (emu g^{-1})**	**Hc (Oe)**	**μ (nm)**	**σ(nm)**	**χ (10^{-5})**
PPCAM3	12.5	74.81	1.05	7.35	0.34	0.23
PPCAM7	16.69	62.24	0.9	6.82	0.31	0.26
PPCAM9	11.08	64.69	2.23	6.76	0.37	0.29
PPCAM10	13.49	46.65	1.89	6.68	0.33	0.37
PPCAM11	13.55	56.10	2.31	6.2	0.35	0.29
PPCAM12	15.87	60.99	1.89	6.18	0.31	0.34
PPCAM13	11.6	57.00	1.69	5.65	0.34	0.32
PPCAM14	12,8	63.37	2.10	5.62	0.31	0.28
PPCAM15	11.4	45.95	0.13	5.61	0.28	0.38

Key: Values of μ (mean) and σ (standard deviation) represents the log-normal ferromagnetic diameter calculated from fitting the Langevin equation to the (M-H) curves assuming a bulk magnetisation value of 92 emu g^{-1}, M_s is the saturation magnetisation, Hc is the room temperature coercivity of the sample and χ is a number representing the paramagnetic like region on the approach to saturation.

To confirm that highly crystalline materials were produced in the scaled process HRTEM was used to assess the single crystalline structural details of sample PPCAM14 as shown in figure 8.27(a). Lattice fringes were clearly visualised throughout each crystallite showing that a crystalline single phase (structural) material had been produced in the scaled reaction consistent with observations presented in Chapters 5 and 6. Figure 8.21 (b) shows an indexed SAED diffraction pattern of the sample confirming the phase of the material under observation.

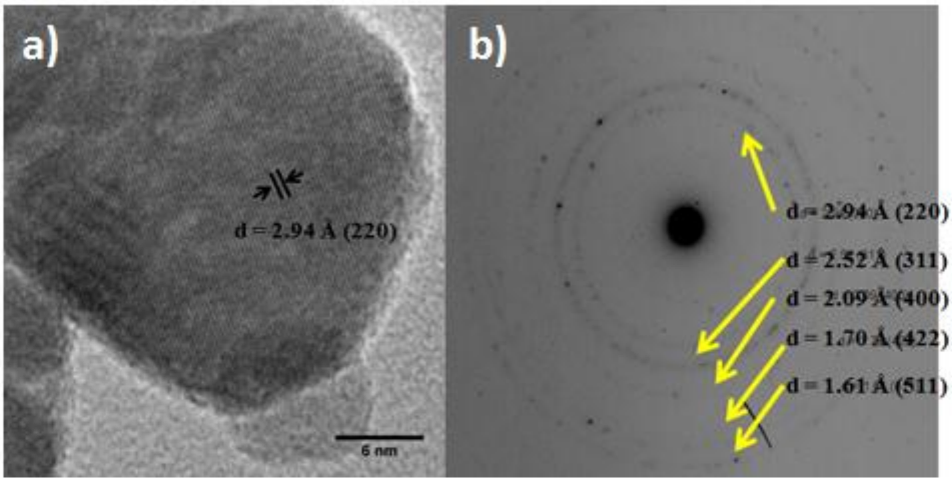

Figure 8.27: a) HRTEM image of sample PPCAM14 showing visualisation of the (220) lattice fringe **b)** Indexed SAED pattern of the sample.

To further evaluate the magnetic properties of the scaled materials, low temperature magnetisation and FC/ZFC measurements were performed on sample PPCAN14 which was shown by HRTEM to be single crystalline phase (figure 8.27). The temperature dependence of M_s was measured at 5 and 300 K for sample PPCAN14 as shown in figure 8.28 a. The increase in coercive field at 5 K to 62 Oe compared to the room temperature value of 2.10 Oe is consistent with the sample behaving as a ferromagnet below T_b. Similarly, the increase in M_s at 5 K suggests a proportion of the sample magnetic moment transitions to a blocked state, consistent with previous discussion of magnetic frustration within the samples. To further assess the low temperature magnetic behaviour, ZFC/FC measurements were taken and are presented in figure 8.28 b. The shift in low temperature magnetisation to positive values is the fingerprint of exchange bias, a phenomenon that takes place at interfaces between different magnetic phases and is commonly observed in magnetically complex structures showing magnetic interfaces in intimate contact as would be expected in a material showing lattice and surface defects. (Itoh and Sugimoto 2003;

Levy *et al.*, 2011) As the magnetisation in the FC measurement increases with decreasing temperature and the absence of distinct magnetic transitions associated with T_v and T_b is consistent with a wide distribution of energy barriers from different magnetic structure within the sample transitioning to a blocked stat at different temperatures. These features also appeared in samples produced in the laboratory scale process and shows that production of these materials in CHFS results in the synthesis of magnetically complex structures as nanomaterials.

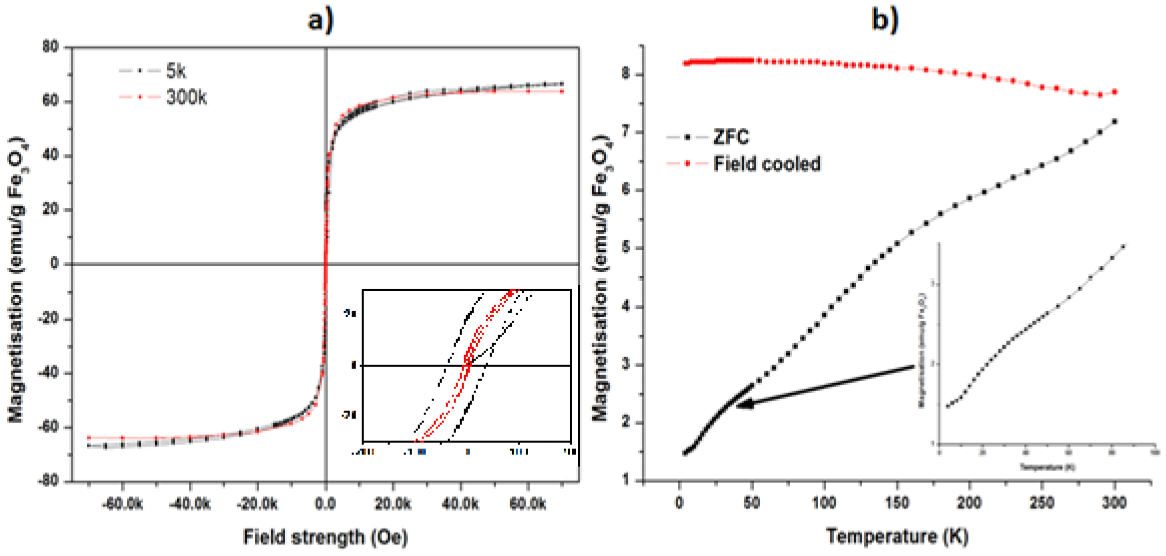

Figure 8.28: a) FC and ZFC curves under an applied field of 100 Oe, the figure inset shows an expanded plot of the near 0 Oe region **b)** Comparison of magnetisation magnetisation curves measured at 10 K and 300K, inset shows the low temperature region of the ZFC curve showing the magnetic transition features.

8.3.4.3 Section Summary and Conclusions:

In summary, the synthesis of citric acid coated magnetite previously produced using a novel processing methodology was successfully reproduced using the pilot scale CHFS process. Characterisation data obtained for the materials showed that reaction products similar to those initially obtained using the laboratory scale process could be obtained, albeit for a slightly different optimisation condition. Where, it appears that improved mixing and thus higher CA grafting densities were observed in more turbulent flows irrespective of residence time after the introduction of citric acid. Zeta-potential measurements confirmed the mechanism of particle stabilisation and showed that coordination similar to that initially reported in Chapter 6 was responsible for stabilisation of the particle dispersions. The magnetic properties of the nanopaticles produced on the pilot scale CHFS process were also shown to be similar to those measured for laboratory scale equivalents and were subject to a similar degree of magnetic frustration as that initially observed in Chapters 5 and 6. This work has highlighted that the nucleation dominance (resulting in similar nanoparticles) and the versatility of a flow system can be exploited at large scale to produce large quantities of functional nanoparticles when the processes involved in producing the desired materials are suitably well characterised. This section has demonstrated that more complex reactions can also be recreated on the pilot scale CHFS process and yield materials with similar characteristics to those initially identified on the laboratory scale.

8.4: Chapter Conclusions

In summary, this chapter has detailed several investigations into the aspects of scaling up nanoparticle synthesis using CHFS. In section 8.3.1 it was shown that the CJM evaluated in Chapter 4 could be successfully scaled for processing *ca.* 20 x the volume used for the synthesis of nanoparticles in the laboratory scale. The successful scale up strategy, showed that scale up conserving a constant $(Fr)^2$ of the supercritical water exiting the inlet of the mixer yielded the best compromise to scale the mixing events occurring within the reactor. The corresponding experimental evaluation of scaling the mixer with this strategy gave normalised temperature profiles which were similar to those initially obtained on the laboratory scale process, when the physical mixing length was normalised to d_i of the inlet used in both processes. In the pilot scale process the maximum operating conditions were shown to vary from those practicable in the laboratory scale as they resulted in temperature and pressure fluctuation in the scaled process. The temperature and pressure fluctuations were thought to arise from severe recirculation occurring in the scaled process which served to identify the operational limits.

ZnO was used as a model system to characterise the effects of both volumetric scale up and mass based scale up of the formation of nanoparticles using CHFS. Characterisation of the nanoparticles showed that the formation of nanoparticles in the scaled process was exceptionally similar to the laboratory scale process yielding materials of similar physical size and polydispersity. Suggesting that in the embodiment of the scaled process evaluated the reactions were sufficiently similar (as inferred by our temperature measurements) not to yield a measurable difference in the size or phase of the nanoparticles produced.

However, the output the process was limited by what appeared to be a particle growth phase as the process was sequentially scaled on precursor concentration. The onset of particle growth was shown to occur at the maximum precursor concentration usable in the laboratory scale process. The corresponding growth of particles was proportional to the precursor concentration. This observation suggests that the dominance of particle nucleation and minimal particle growth observed on volumetric scale up is superseded by a growth phase in mass based scale up, yielding materials with different physical properties identifying a limit to the reproduction of materials using different scale up strategies in the pilot scale process.

Further investigation of the scale up of nanoparticle synthesis lead to the evaluation of a Ce:Zn binary oxide system which originally yielded interesting phase behaviour and optical properties, in materials produced using a laboratory scale reactor. Ce–Zn oxide nanoparticles produced at a x 17.5 volumetric scale up of the existing laboratory process were produced at analogus synthesis conditions in terms of reactor temperature and reagent concentrations so that a comparison of the physical properties of the products could be made. Important nanoparticle properties related to BET surface area, phase behaviour and crystallite size were shown to be virtually indistinguishable from those produced by the laboratory scale apparatus. In particular, the solubility of Zn in the nanoparticle fluorite lattice was observed with a limit of 20 – 30 at% (Zn in CeO_2) for the as-prepared nanomaterial and as little as 10 – 20 at% Ce into ZnO consistent with the initial work. Doping Zn into CeO_2 altered the shape and position of the UV–visible absorption edge, an observation consistent with the previous publication. This similarity was despite the substantive volumetric scale up of the pilot process and other slight differences in apparatus. This suggests that the processes underlying the nucleation and growth of nanoparticles occur at similar rates, yielding materials showing notably similar physical characteristics (allowing for slight experimental error). Highlighting, that the CHFS process is highly scalable when the output of the process is increased on a volumetric basis alone even when slightly more complex syntheses than homometallic oxides are evaluated.

Section 8.3.4 demonstrated that the pilot scale process could also be used for the production of more complex nanomaterials, and it was shown to be possible to recreate the production of surface functionalised nanoparticles of magnetite, initially described in Chapter 6. Characterisation data obtained for the materials showed that reaction products similar to those initially obtained using the laboratory scale process could be obtained, albeit for a slightly different optimisation condition. Showing that further complexity in the reactions beyond simple particle formation in the CHFS process can be effectively reproduced. Consistent with the observations initially noted in the laboratory scale process where improved mixing (in highly turbulent flows) yielded higher CA grafting densities and a high quality particle dispersion in solution. The magnetic properties of the nanopaticles produced on the pilot scale CHFS process were also shown to be similar to those measured for laboratory scale equivalents and were subject to a similar degree of magnetic frustration initially observed in Chapters 5 and 6. This work has highlighted that the nucleation dominance (resulting in similar nanoparticles) and the versatility of a flow system can be exploited at large scale to produce large quantities of functional nanoparticles, when the processes involved in producing the desired materials are suitably well characterised.

In closing, the scale up of nanoparticle synthesis using CHFS was shown to be reproducible on a volumetric basis and many reaction types *i.e.* the synthesis of homometallic oxides, binary oxides and surface functionalised nanoparticles could be readily recreated on the large scale CHFS process. Limitations to the scale up of the process were only identified at extremes of process conditions *i.e.* precursor concentration where evidence of particle growth occurred yielding materials with different physical properties to those of the laboratory scale. This is a major proof of concept for the large scale production of different types of nanoparticles and a comparatively simple method for their production. As the CHFS process has been demonstrated to produced nanomaterials of many compositions it can be regarded as a platform technology which could find broader application in nanomaterials synthesis.

8.5: Future Work

The investigations presented in this Chapter have highlighted that the CHFS process is a scalable methodology for the synthesis of nanomaterials. The high ouput capacity (*ca.* 2 kg/h at the highest flow rates and concentrations presented here) of this process could be evaluated in a number of contexts to produce materials which could be commercially exploited or to provide sufficient material for latter stage R&D into the application of nanomaterials.

This process may also find application in producing nanosized metal precursor co-precipitates for solid state reactions. (Weng *et al.*, 2009) These nanosized solid state reaction precursors have been shown to be an effective route for the production of many complex oxides. The scale up of these types of reactions would be beneficial as many complex oxides find application and electrical and ion conductors in SOFC amongst other applications and often are required in substantial quantities for investigation. Similarly, as many nanoparticles find application as gas sensors and photocatalysis it may be of interest to apply the large scale processing method presented here to the synthesis of materials as activities in both applications are intimately linked to surface area.

Overall, this chapter has demonstrated that the CHFS process is scalable on a volumetric basis alone and only suffers complications at extremes of processing conditions. For this reason the process validated in this chapter may find application as a platform technology for the synthesis of a diverse range of nanoparticle compositions and functionalities. Currently, investigations into the application of the CHFS pilot plant for the synthesis of Li ion battery cathodes and anodes are underway ($Li_4Ti_5O_{12}$, $LiCo_{1-x-y}Ni_xMn_yO_2$, $LiFePO_4$ and doped $LiFePO_4$). Similarly, the process is being applied to the synthesis of phosphor compositions based upon a La PO_4 host lattice and are also being evaluated as citric acid coated nanoparticles.

Chapter 9

Conclusions

At the end of the literature review, it was concluded that CHFS may be a useful technique for the production of nanomaterials for a wide range of applications. It was suggested by the literature, that the formation of nanoparticles within CHFS systems was heavily dependent on the mixing between precursor and preheated water feeds leading to the formation of nanoparticles and that the formation of nanomaterials maybe difficult to control. However, the literature also identified many key benefits of the process; namely that it was an aqueous process and that all nanomaterials formation and collection steps could be undertaken in the aqueous phase, many materials of interest could be produced without the requirement for expensive or environmentally damaging chemicals or heat treatments, and that many combinations of system and processing parameters could be used to produce functional materials. As such, this thesis has evaluated many of these aspects and applied the concept of continuous hydrothermal synthesis to the production of nanoparticles at both a laboratory and pilot scale.

The work presented in this thesis has shown that a wide range of materials can be produced using CHFS, and the reaction conditions controlled by either external factors (such as the choice of precursor reagents, reaction temperature) or through the addition of auxiliary reagents to the process were very influential in determining the products of reaction. This thesis has used nanomaterials ranging from simple metal oxides, binary metal oxides, doped materials and surface functionalised nanoparticles to describe different aspects of the CHFS process which terminally allowed a successful scale up procedure to be identified.

In-situ temperature measurements (a novel evaluation strategy) were useful in defining the key differences in the temperature profile within reaction points, and reaction points used for processing different flow rates, allowing a much finer analysis of the events occurring around the point of mixing precursors with supercritical water. This region is commonly defined as the point of particle nucleation, and much time and effort has been spent on ensuring rapid changes in the temperature of hydrothermal solutions at this point *i.e.* driving the formation of nanoparticles. *In-situ* temperature measurements showed that the CHFS process and the mixing process in the reactor are dynamic and are highly system dependent, in a number of reactor configurations. These measurements showed that even simple variation in the flow rate yielded significant differences in the temperature at the point of particle formation and the distribution of temperature within the reaction point (due to differences in the magnitude of heat transfer), an observation either ignored or simply overlooked in the academic literature. This analysis provided the only conclusive evidence of the dominance of precipitation process occurring in the reactor and has eluded that the short time scale of the reactions dominates all other process in the formation of nanoparticles. This strategy was also useful to define the reactor criteria allowing the successful scale up of the process. Overall, reactor and process scale measurements served to identify that the microscale mixing processes occurring between the preheated water and precursor feeds are probably not important for the formation of nanoparticles, and as such the kinetics of particle formation probably play a greater role in particle formation, yielding surprisingly similar nanoparticles due to complete precipitation of the metal ions in solution. These measurements also allowed unfavourable heat and mass transfer processes occurring in reactors to be identified, allowing sufficient resolution for the effective development of a novel reaction point geometry suitable for the synthesis of nanoparticles in both a laboratory scale and pilot scale CHFS process.

The successful scale up strategy of the CJM developed in this work, showed that scale up conserving a near constant $(Fr)^2$ of the supercritical water exiting the inlet of the mixer was the most suitable strategy. This strategy, allowed the best compromise to scale the mixing events occurring within the reactor. The corresponding experimental evaluation of scaling the mixer gave normalised temperature profiles which were similar to those initially obtained on the laboratory scale process, when the physical mixing length was normalised to the internal diameter of the preheated water inlet used in both processes. In the pilot scale process the maximum operating conditions were shown to vary from those practicable in the laboratory scale, as they resulted in temperature and pressure fluctuation in the scaled process and served to define the limits of scale up (an important observation if the process is to be scaled further). Limitations to the scale up of the process were only identified at extremes of process conditions (*i.e.* precursor concentration) where evidence of particle growth occurred, yielding materials with different physical properties to those of the laboratory scale. However, on a volumetric basis even complex particle systems, Ce–Zn oxide nanoparticles produced at a 17.5x volumetric scale up of the existing laboratory process, showed that important nanoparticle properties related to BET surface area, phase behaviour and crystallite size were shown to be virtually indistinguishable from those produced by the laboratory scale.

This thesis also demonstrated the successful modification of a CHFS flow reactor, to allow for the introduction of a capping agent shortly after the formation of nanoparticles. These investigations showed how the versatility of a flow process can be exploited for the synthesis of target nanoparticles. The process was shown to be capable of producing nanomaterials which had a high grafting density of citric acid conferring a stabilising effect to the particle dispersion. A complete process envelope was established by operating the reaction point at a variety of temperature and flow rate regimes, allowing the identification of regions where the process could be operated for the direct synthesis of surface functionalised magnetite nanoparticles, this data was then successfully interpreted to allow for the synthesis to be conducted at a much larger scale which yielded materials with similar physiochemical characteristics to those initially identified on the laboratory scale (albeit for a slightly different optimisation condition). This processing methodology was then successfully applied to the synthesis of phosphor nanoparticles as dispersions and the products were shown to be suitable probes for biological imaging. Further investigation of the particle dispersions also showed that citric acid was a suitable chemical moiety to allow further functionalisation of the particle surface. Coupled together, these investigations showed that citric acid coated nanoparticles produced using CHFS could be used as precursor nanoparticles for further functionalisation for a given application giving a wider application area than citric acid functionalised nanoparticles alone, as the process was also shown to be scalable.

The nanoparticles from the CHFS process were also found to be suitable precursor nanomaterials for conversion to higher order phases. In Chapter 7, a flash heat-treatment strategy allowed the complete dehydration of the $(Y_{0.96}Eu_{0.04})OOH$ nanoprecursor could be achieved with limited agglomeration and particle growth. It was also shown that the reaction occurred on time scales significantly shorter than those used in the literature. Showing that the use of nanoparticles as precursors, is a suitable strategy for the synthesis of higher order oxide structures, and under suitable conditions the effects of sintering can be minimised yielding materials which can subsequently be dispersed as nanomaterials.

In closing, the process of Continuous Hydrothermal Flow Synthesis in the embodiments presented in this thesis have shown considerable potential as a technique for the synthesis of nanomaterials on both a laboratory or research scale and as a large scale process capable of producing *ca.* 2 kg of nanomaterials per hour. The scale up of nanoparticle synthesis using CHFS was shown to be reproducible on a volumetric basis and many reaction types *i.e.* the synthesis of homometallic oxides, binary oxides and surface functionalised nanoparticles could be readily recreated on the large scale CHFS process. Limitations to the scale up of the process were only identified at extremes of process conditions (*i.e.* precursor concentration) where evidence of particle growth occurred yielding materials with different physical properties to those of the laboratory scale. This is a major proof of concept for the large scale production of different types of nanoparticles and of a comparatively simple method for their production. As the CHFS process has been demonstrated to produce nanomaterials of many compositions it can be regarded as a platform technology which could find broader application in nanomaterials synthesis. Further work should be conducted to assess the full range of materials which can be produced using this technique. In addition, further benefits may be gained by improving control over particle properties through modifications to the process embodiments presented in the future work sections of each chapter.

Chapter 10

Future work

At the end of the literature review, it was concluded that CHFS may be a useful technique for the production of nanomaterials for a wide range of applications. It was suggested by the literature, that the formation of nanoparticles within the CHFS process was heavily dependent on the mixing between precursor and preheated water feeds leading to the formation of nanoparticles, and that the formation of nanomaterials maybe difficult to control. However, the literature also identified many key benefits of the process; namely that it was an aqueous process and that all nanomaterials formation and collection steps could be undertaken in the aqueous phase, many materials of interest could be produced, and that many combinations of system and processing parameters could be used to produce functional materials. As such, this thesis has evaluated many of these aspects and applied the concept of continuous hydrothermal synthesis to the production of nanoparticles at both a laboratory and pilot scale. Many material systems and caveats to the process were identified which in future work would warrant investigation. The purpose of this chapter is to summarise some of these future investigations and how they would benefit the subject of the thesis described thus far.

In the early Chapters of this thesis, investigations of the mixing and particle formation processes within continuous hydrothermal reactors were presented. The difficulties associated with working at system pressures limited the resolution of the experimental data and as such many of the transient mixing processes responsible for particle formation were only speculated upon. In the final chapter the experimental evaluation of a pilot scale CHFS process was presented utilising the knowledge gained from these measurements. Although successful the methodology used to scale the process was experimentally simple it required a significant amount of trial and error (a large time and capital investment) to define an optimum scale up reactor. If the process was to be scaled further it maybe useful to investigate alternate scale up strategies based upon modelling and combining this with experimental data presented in this thesis or further experimental data which could be gathered using both working reactor scales (an alternate data collection strategy would be measuring the centreline temperature within the CJM). In particular, it would probably be beneficial to combine computational fluid dynamics and simple precipitation models (taken from first principles) to derive scale-up criteria for the production of nanoparticles in the CHFS process if the processing volume is to be further increased. The use of CFD would also allow the visualisation of complex flow patterns, fluid velocity contours to be mapped and the addition of tracers would the state of complete mixing to be modelled on the experimental results obtained. In this embodiment further evidence for the causes of adverse mixing behaviour in the CJM could be identified and possibly remedied as at larger scales it could cause processing issues. Further investigation into mechanism to control the size of particles produced by this method would be of interest across any production scale. This would most likely be achieved by altering the chemical conditions and coupling these investigations to CFD modelling and particle precipitation models within the mixing zone to better define scale up criteria. Investigation of auxillary reagents which would alter the solubility of ions in the hydrothermal solution would be of interest as from the data presented in this thesis complete precipitation of the ions in solution leads to limited particle growth and minimal control of particle size.

The work presented in this thesis has shown that a wide range of materials can be produced using CHFS, and the reaction conditions controlled by either external factors (such as the choice of precursor reagents, reaction temperature) or through the addition of auxiliary reagents to the process were also shown to be very influential in determining the products of reaction. Further investigations into the control of particle size are required as the apparent low solubility metal ions results in nanoparticles of similar crystallite sizes for all the materials produced within this thesis and detailed explanations of various methodologies are presented in the various synthesis Chapters. This could probably be achieved by using different metal ion precursors which may allow the thermal decomposition temperatures of the soluble metal sources to control the rates of particle growth. This may also be achieved through the use of other organic additives to control the precipitation of the metal ions in hydrothermal solution.

An area of materials chemistry not explored in this thesis was the use of nanoparticles produced by the CHFS as nanosized metal precursor co-precipitates for solid state reactions. (Weng *et al.*, 2009) These nanosized solid state reaction precursors have been shown to be an effective route for the production of many complex oxides and could be applicable to the production of SOFC components as the lower sintering temperatures of nanomaterials are desirable for the densification of cell components whilst retaining microstructure. The scale up of these types of reactions would be beneficial as many complex oxides are often required in substantial quantities for device level investigation. Similarly, as many nanoparticles find application as gas sensors and photocatalysis it may be of interest to apply the large scale processing method presented here to the synthesis of materials as activities in both applications are intimately linked to surface area as devices. In a similar vein investigation of the pilot scale CHFS process as a platform technology for the synthesis of a diverse range of nanoparticle compositions would be beneficial (this is addressed in more detail within each of the experimental Chapters).

A large area of the future work highlighted by the work presented in Chapters 6, 7 and 8 based on the introduction of a capping agent shortly after the formation of nanoparticles would be useful to investigate further using different chemical moieties to functionalise the particle surface. As The modified CHFS process was shown to be capable of producing nanomaterials which had a high grafting density of citric acid conferring a stabilising effect to the particle dispersion a further investigation of capping agents which would confer colloidal stability in apolar solvents could be beneficial. Similarly, investigations into the large scale synthesis of nanoparticles functionalised with different chemical moieties would also be of interest from a commercialisation point of view (conjugation to antibody fragments or proteins for example). As quantum dots are becoming increasingly commercially viable and required in large quantities. It would be of interest to investigate the CHFS processing methodology presented herein as a solvothermal system in which an organic solvent is substituted for water, this would possible allow greater control over; **1)** the particle nucleation and growth steps, **2)** the choice of capping agent, and **3)** possibly the synthesis of quantum dot type materials in a flow process.

Taking an applications based perspective upon the surface functionalised nanoparticles produced by the CHFS process it would be of interest to assess the cytotoxicity of citric acid coated nanoparticles produced using the methodology presented herein. Similarly, it would be of interest to assess the broader toxicity of the materials produced to fully assess the environmental impact of the process. As investigations of this type could identify candidate materials for biological imaging applications or as identifying markers on security documents as discussed further in the future work section of Chapter 7. Alongside these general statements for future work much more detailed descriptions can be found at the end of each of the experimental chapters.

References

Adschiri, T. (2007). Supercritical hydrothermal synthesis of organic-inorganic hybrid nanoparticles. *Chemistry Letters,* 36, (10) 1188-1193.

Adschiri, T. & Byrappa, K. (2009). *Supercritical Hydrothermal Synthesis of Organic-Inorganic Hybrid Nanoparticles*. Wiley, New York, 103-109.

Adschiri, T., Hakuta, Y., & Arai, K. (2000). Hydrothermal synthesis of metal oxide fine particles at supercritical conditions. *Industrial & Engineering Chemistry Research 39*, 4901-4907.

Adschiri, T., Hakuta, Y., Sue, K., & Arai, K. (2001). Hydrothermal synthesis of metal oxide nanoparticles at supercritical conditions. *Journal of Nanoparticle Research 3*, 227-235.

Adschiri, T., Kanazawa, K., & Arai, K. (1992a). Rapid and Continuous Hydrothermal Crystallization of Metal-Oxide Particles in Supercritical Water. *Journal of the American Ceramic Society 75*, 1019-1022.

Adschiri, T., Kanazawa, K., & Arai, K. (1992b). Rapid and Continuous Hydrothermal Synthesis of Boehmite Particles in Subcritical and Supercritical Water. *Journal of the American Ceramic Society 75*, 2615-2618.

Adschiri, T., Lee, Y. W., Goto, M., & Takami, S. (2011). Green materials synthesis with supercritical water. *Green Chemistry 13*, 1380-1390.

Aimable, A., Muhr, H., Gentric, C., Bernard, F., Le Cras, F., & Aymes, D. (2009). Continuous hydrothermal synthesis of inorganic nanopowders in supercritical water: Towards a better control of the process. *Powder Technology 190,* 99-106.

Aizawa, T., Masuda, Y., Minami, K., Kanakubo, M., Nanjo, H., & Smith, R. L. (2007). Direct observation of channel-tee mixing of high-temperature and high-pressure water. *Journal of Supercritical Fluids 43*, 222-227.

Alarid, E.T. 2006. Lives and times of nuclear receptors. *Molecular Endocrinology*, 20, (9) 1972-1981.

Alivisatos, A. P. (1996). Semiconductor clusters, nanocrystals, and quantum dots. *Science 271*, 933-937.

Arcidiacono, S., Bieri, N.R., Poulikakos, D., & Grigoropoulos, C.P. 2004. On the coalescence of gold nanoparticles. *International Journal of Multiphase Flow*, 30, (7-8) 979-994.

Arita, T., Moriya, K. i., Yoshimura, T., Minami, K., Naka, T., & Adschiri, T. (2010a). Dispersion of Phosphonic Acids Surface-Modified Titania Nanocrystals in Various Organic Solvents. *Industrial & Engineering Chemistry Research 49,* 9815-9821.

Arita, T., Yoo, J., & Adschiri, T. (2010b). Synthesis and characterization of a fatty acid self-assembled monolayer on CeO_2 nanoparticles: to explore solution-state property of a SAM. *Journal of Nanoparticle Research 12*, 2567-2578.

Arita, T., Moriya, K.i., Minami, K., Naka, T., & Adschiri, T. (2010). Supercritical Hydrothermal Synthesis of Carboxylic Acid-surface-functionalised TiO_2 Nanocrystals: pH Sensitive Dispersion and Hybridization with Organic Compounds. *Chemistry Letters*, 39, (9) 961-963.

Augustine, C. & Tester, J.W. (2009). Hydrothermal flames: From phenomenological experimental demonstrations to quantitative understanding. *Journal of Supercritical Fluids*, 47, (3) 415-430.

Babes, L., Denizot, B., Tanguy, G., Le Jeune, J.J., & Jallet, P. (1999). Synthesis of iron oxide nanoparticles used as MRI contrast agents: A parametric study. *Journal of Colloid and Interface Science*, 212, (2) 474-482.

Bagwe, R.P., Hilliard, L.R., & Tan, W.H. (2006). Surface modification of silica nanoparticles to reduce aggregation and nonspecific binding. *Langmuir*, 22, (9) 4357-4362.

Balbuena, P. B., Johnston, K. P., & Rossky, P. J. (1996). Molecular dynamics simulation of electrolyte solutions in ambient and supercritical water .1. Ion solvation. *Journal of Physical Chemistry 100*, 2706-2715.

Bandow, S., Kimura, K., Konno, K., & Kitahara, A. (1987). Magnetic-Properties of Magnetite Ultrafine Particles Prepared by W/O Microemulsion Method. *Japanese Journal of Applied Physics Part 1-Regular Papers Short Notes & Review Papers 26*, 713-717.

Basset, D., Matteazzi, P., & Miani, F. (1993). Designing A High-Energy Ball-Mill for Synthesis of Nanophase Materials in Large Quantities. *Materials Science and Engineering A-Structural Materials Properties Microstructure and Processing 168*, 149-152.

Biswas, P. & Wu, C. Y. (2005). 2005 Critical Review: Nanoparticles and the environment. *Journal of the Air & Waste Management Association 55*, 708-746.

Blood, P. J., Denyer, J. P., Azzopardi, B. J., Poliakoff, M., & Lester, E. (2004). A versatile flow visualisation technique for quantifying mixing in a binary system: application to continuous supercritical water hydrothermal synthesis (SWHS). *Chemical Engineering Science 59*, 2853-2861.

Boldrin, P., Hebb, A.K., Chaudhry, A.A., Otley, L., Thiebaut, B., Bishop, P., & Darr, J.A. (2007). Direct synthesis of nanosized $NiCo_2O_4$ spinel and related compounds via continuous hydrothermal synthesis methods. *Industrial & Engineering Chemistry Research*, 46, (14) 4830-4838.

Brittain, H.G. & Posluszny, J.V. (1987). FTIR and High-Resolution Photoluminescence Studies of the Thermal-Decomposition of Crystalline Europium Hydroxide. *Thermochimica Acta*, 118, 25-34.

Brown, J., Mascher, P., & Kitai, A.H. (1995). Positron Lifetime Spectroscopy and Cathodoluminescence of Polycrystalline Terbium-Doped Yttria. *Journal of the Electrochemical Society*, 142, (3) 958-960.

Bruce, I.J. & Sen, T. (2005). Surface modification of magnetic nanoparticles with alkoxysilanes and their application in magnetic bioseparations. *Langmuir*, 21, (15) 7029-7035.

Bruchez, M., Moronne, M., Gin, P., Weiss, S., & Alivisatos, A.P. (1998). Semiconductor nanocrystals as fluorescent biological labels. *Science*, 281, (5385) 2013-2016.

Brust, M., Walker, M., Bethell, D., Schiffrin, D. J., & Whyman, R. (1994). Synthesis of Thiol-Derivatized Gold Nanoparticles in A 2-Phase Liquid-Liquid System. *Journal of the Chemical Society-Chemical Communications* 801-802.

Buissette, V., Giaume, D., Gacoin, T., & Boilot, J.P. (2006). Aqueous routes to lanthanide-doped oxide nanophosphors. *Journal of Materials Chemistry*, 16, (6) 529-539.

Burda, C., Chen, X. B., Narayanan, R., & El-Sayed, M. A. (2005). Chemistry and properties of nanocrystals of different shapes. *Chemical Reviews 105*, 1025-1102.

Byrappa, K. & Adschiri, T. (2007). Hydrothermal technology for nanotechnology. *Progress in Crystal Growth and Characterization of Materials 53*, 117-166.

Byrappa, K., Ohara, S., & Adschiri, T. (2008). Nanoparticles synthesis using supercritical fluid technology - towards biomedical applications. *Advanced Drug Delivery Reviews 60*, 299-327.

Cabanas, A., Darr, J. A., Lester, E., & Poliakoff, M. (2000). A continuous and clean one-step synthesis of nano-particulate $Ce_{1-x}Zr_xO_2$ solid solutions in near-critical water. *Chemical Communications* 901-902.

Cabanas, A. & Poliakoff, M. (2001). The continuous hydrothermal synthesis of nano-particulate ferrites in near critical and supercritical water. *Journal of Materials Chemistry 11*, 1408-1416.

Calleja, J.M. & Cardona, M. (1977). Resonant Raman-Scattering in ZnO. *Physical Review B*, 16, (8) 3753-3761.

Carlsson, M., Habenicht, C., Kam, L.C., Antal, M.J., Bian, N.Y., Cunningham, R.J., & Jones, M. (1994). Study of the Sequential Conversion of Citric to Itaconic to Methacrylic-Acid in Near-Critical and Supercritical Water. *Industrial & Engineering Chemistry Research*, 33, (8) 1989-1996

Casaletto, M.P., Kaciulis, S., Mattogno, G., Mezzi, A., Ambrosio, L., & Branda, F. (2002). XPS characterization of biocompatible hydroxyapatite-polymer coatings. *Surface and Interface Analysis*, 34, (1) 45-49.

Casas, L. I., Roig, A., Molins, E., Greneche, J. M., Asenjo, J., & Tejada, J. (2002). Iron oxide nanoparticles hosted in silica aerogels. *Applied Physics A-Materials Science & Processing 74*, 591-597.

Chai, X. & Wang, D. (2007). UV-shielding and catalytic characteristics of nanoseale zinc-cerium oxides. *Journal of Wuhan University of Technology-Materials Science Edition*, 22, (4) 622-625.

Chatterjee, J., Haik, Y., & Chen, C.J. (2003). Size dependent magnetic properties of iron oxide nanoparticles. *Journal of Magnetism and Magnetic Materials*, 257, (1) 113-118

Chaudhry, A.A., Haque, S., Kellici, S., Boldrin, P., Rehman, I., Fazal, A.K., & Darr, J.A. (2006). Instant nano-hydroxyapatite: a continuous and rapid hydrothermal synthesis. *Chemical Communications* (21) 2286-2288.

Chen, D., Sanchez, A., Taboada, E., Roig, A., Sun, N., & Gu, H. (2009). Size determination of superparamagnetic nanoparticles from magnetization curve. *Journal of Applied Physics 105.*

Chen, J.F., Wang, Y.H., Guo, F., Wang, X.M., & Zheng, C. (2000). Synthesis of nanoparticles with novel technology: High-gravity reactive precipitation. *Industrial & Engineering Chemistry Research*, 39, (4) 948-954.

Chen, S., Chiang, C.l., & Hsieh, S. (2010). Simulating physiological conditions to evaluate nanoparticles for magnetic fluid hyperthermia (MFH) therapy applications. *Journal of Magnetism and Magnetic Materials*, 322, (2) 247-252.

Chen, Z., Chen, H., Hu, H., Yu, M., Li, F., Zhang, Q., Zhou, Z., Yi, T., & Huang, C. (2008). Versatile synthesis strategy for carboxylic acid-functionalised upconverting nanophosphors as biological labels. *Journal of the American Chemical Society*, 130, (10) 3023-3029.

Choi, S., Moon, Y.M., & Jung, H.K. (2010). Luminescent properties of PEG-added nanocrystalline $YVO_4:Eu^{3+}$ phosphor prepared by a hydrothermal method. *Journal of Luninescence*, 221, (60) 345-352.

Chorny, A. & Zhdanov, V. (2012). Turbulent mixing and fast chemical reaction in the confined jet flow at large Schmidt number. *Chemical Engineering Science,* 68, (1) 541-554

Corrias, A., Casula, M. F., Ennas, G., Marras, S., Navarra, G., & Mountjoy, G. (2003). X-ray absorption spectroscopy study of FeCo-SiO2 nanocomposites prepared by the sol-gel method. *Journal of Physical Chemistry B 107*, 3030-3039.

Cote, L. J., Teja, A. S., Wilkinson, A. P., & Zhang, Z. J. (2003). Continuous hydrothermal synthesis of CoFe2O4 nanoparticles. *Fluid Phase Equilibria 210*, 307-317.

Coulson,J. M., Backhurst, J. R., Harker, J. H (1999). *Chemical Engineering Vol. 1,* Butterworth-Heinemann, Oxford, ed. 6th.

Cushing, B. L., Kolesnichenko, V. L., & O'Connor, C. J. (2004). Recent advances in the liquid-phase syntheses of inorganic nanoparticles. *Chemical Reviews 104*, 3893-3946.

Damen, T.C., Porto, S.P.S., & Tell, B. (1966). Raman Effect in Zinc Oxide. *Physical Review*, 142, (2) 570.

Daou, T., Greneche, J., Pourroy, G., Buathong, S., Derory, A., Ulhaq-Bouillet, C., Donnio, B., Guillon, D., & Begin-Colin, S. (2008). Coupling agent effect on magnetic properties of functionalised magnetite-based nanoparticles. *Chemistry of Materials*, 20, (18) 5869-5875.

Darab, J. G. & Matson, D. W. (1998). Continuous hydrothermal processing of nano-crystalline particulates for chemical-mechanical planarization. *Journal of Electronic Materials 27*, 1068-1072.

Darr, J. A. & Poliakoff, M. (1999). New directions in inorganic and metal-organic coordination chemistry in supercritical fluids. *Chemical Reviews 99*, 495-541.

Demianets, L.N. & Kostomarov, D.V. (2001). Mechanism of zinc oxide single crystal growth under hydrothermal conditions. *Annales de Chimie-Science des Materiaux*, 26, (1) 193-198.

Demianets, L.N., Kostomarov, D.V., Kuz'mina, I.P., & Pushko, S.V. (2002). Mechanism of growth of ZnO single crystals from hydrothermal alkali solutions. *Crystallography Reports*, 47, S86-S98.

Dennis, C., Jackson, A., Borchers, J., Ivkov, R., Foreman, A., Hoopes, P., Strawbridge, R., Pierce, Z., Goerntiz, E., Lau, J., & Gruettner, C. (2008). The influence of magnetic and physiological behaviour on the effectiveness of iron oxide nanoparticles for hyperthermia. *Journal of Physics D-Applied Physics*, 41, (13).

Dieckmann, R. (1982). Defects and Cation Diffusion in Magnetite (Iv) - Nonstoichiometry and Point-Defect Structure of Magnetite Fe-3-Delta-O-4. *Berichte der Bunsen-Gesellschaft-Physical Chemistry Chemical Physics*, 86, (2) 112-118.

Dieckmann, R. & Schmalzried, H. (1977). Defects and Cation Diffusion in Magnetite .1. *Berichte der Bunsen-Gesellschaft-Physical Chemistry Chemical Physics*, 81, (3) 344-347.

Dirksen, J. A. & Ring, T. A. (1991). Fundamentals of Crystallization - Kinetic Effects on Particle-Size Distributions and Morphology. *Chemical Engineering Science 46*, 2389-2427.

Djerdj, I., Arcon, D., Jaglicic, Z., & Niederberger, M. (2008). Nonaqueous synthesis of metal oxide nanoparticles: Short review and doped titanium dioxide as case study for the preparation of transition metal-doped oxide nanoparticles. *Journal of Solid State Chemistry*, 181, (7) 1571-1581.

Dzyaloshinskii, I. E., Lifshitz, E. M., & Pitaevskii, L. P. (1961). The General Theory of Vanderwaals Forces. *Advances in Physics 10*, 165-209.

Eroglu, S., Zhang, S. C., & Messing, G. L. (1996). Synthesis of nanocrystalline Ni-Fe alloy powders by spray pyrolysis. *Journal of Materials Research 11*, 2131-2134.

Fauconnier, N., Bee, A., Roger, J., & Pons, J.N. (1996). Adsorption of gluconic and citric acids on maghemite particles in aqueous medium. *Trends in Colloid and Interface Science X*, 100, 212-216.

Feenstra, T.P. & Debruyn, P.L. (1981). The Ostwald Rule of Stages in Precipitation from Highly Supersaturated Solutions - A Model and Its Application to the Formation of the

Nonstoichiometric Amorphous Calcium-Phosphate Precursor Phase. *Journal of Colloid and Interface Science*, 84, (1) 66-72.

Feynman, R. P. & Vernon, F. L. (1963). The Theory of A General Quantum System Interacting with A Linear Dissipative System. *Annals of Physics 24*, 118-173.

Fletcher, P. D. I., Howe, A. M., & Robinson, B. H. (1987). The Kinetics of Solubilisate Exchange Between Water Droplets of A Water-In-Oil Microemulsion. *Journal of the Chemical Society-Faraday Transactions I 83*, 985-1006.

Fortin, J.P., Wilhelm, C., Servais, J., Menager, C., Bacri, J.C., & Gazeau, F. (2007). Size-sorted anionic iron oxide nanomagnets as colloidal mediators for magnetic hyperthermia. *Journal of the American Chemical Society*, 129, (9) 2628-2635.

Fujii, T., de Groot, F.M.F., Sawatzky, G.A., Voogt, F.C., Hibma, T., & Okada, K. (1999). In situ XPS analysis of various iron oxide films grown by NO2-assisted molecular-beam epitaxy. *Physical Review B*, 59, (4) 3195-3202.

Fukushima, Y. & Wakayama, H. (1999). Nanoscale casting using supercritical fluid. *Journal of Physical Chemistry B 103*, 3062-3064.

Gazeau, F., Levy, M., & Wilhelm, C. (2008). Optimizing magnetic nanoparticle design for nanothermotherapy. *Nanomedicine*, 3, (6) 831-844.

Geohegan, D. B., Puretzky, A. A., Duscher, G., & Pennycook, S. J. (1998). Time-resolved imaging of gas phase nanoparticle synthesis by laser ablation. *Applied Physics Letters 72*, 2987-2989.

Gloeckl, G., Hergt, R., Zeisberger, M., Dutz, S., Nagel, S., & Weitschies, W. (2006). The effect of field parameters, nanoparticle properties and immobilization on the specific heating power in magnetic particle hyperthermia. *Journal of Physics-Condensed Matter*, 18, (38) S2935-S2949.

Gonzales-Weimuller, M., Zeisberger, M., & Krishnan, K.M. (2009). Size-dependant heating rates of iron oxide nanoparticles for magnetic fluid hyperthermia. *Journal of Magnetism and Magnetic Materials*, 321, (13) 1947-1950.

Goodarzi, A., Sahoo, Y., Swihart, M.T., & Prasad, P.N. (2004). Aqueous ferrolluid of citric acid coated magnetite particles. *Journal of Magnetism and Magnetic Materials*, 284, (13) 1923-1945.

Graf, C., Vossen, D.L.J., Imhof, A., & van Blaaderen, A. (2003). A general method to coat colloidal particles with silica. *Langmuir*, 19, (17) 6693-6700.

Grosvenor, A.P., Kobe, B.A., Biesinger, M.C., & McIntyre, N.S. (2004). Investigation of multiplet splitting of Fe 2p XPS spectra and bonding in iron compounds. *Surface and Interface Analysis*, 36, (12) 1564-1574.

Gruar, R., Tighe, C.J., Reilly, L.M., Sankar, G., & Darr, J.A. (2010). Tunable and rapid crystallisation of phase pure Bi_2MoO_6 (koechlinite) and $Bi_2Mo_3O_{12}$ via continuous hydrothermal synthesis. *Solid State Sciences*, 12, (9) 1683-1686.

Gu, Y. F., Li, G., Meng, G. Y., & Peng, D. K. (2000). Sintering and electrical properties of coprecipitation prepared Ce0.8Y0.2O1.9 ceramics. *Materials Research Bulletin 35*, 297-304.

Gunasekera, U., Pankhurst, Q.A., & Douek, M. (2009). Imaging applications of nanotechnology in cancer. *Targeted Oncology*, 4, (3) 169-181.

Gupta, A.K. & Gupta, M. (2005). Synthesis and surface engineering of iron oxide nanoparticles for biomedical applications. *Biomaterials*, 26, (18) 3995-4021.

Gupta, S. M. & Tripathi, M. (2011). A review of TiO2 nanoparticles. *Chinese Science Bulletin 56*, 1639-1657.

Hakuta, Y., Adschiri, T., Hirakoso, H., & Arai, K. (1999a). Chemical equilibria and particle morphology of boehmite (AlOOH) in sub and supercritical water. *Fluid Phase Equilibria 158*, 733-742.

Hakuta, Y., Seino, K., Ura, H., Adschiri, T., Takizawa, H., & Arai, K. (1999b). Production of phosphor (YAG : Tb) fine particles by hydrothermal synthesis in supercritical water. *Journal of Materials Chemistry 9*, 2671-2674.

Hakuta, Y., Haganuma, T., Sue, K., Adschiri, T., & Arai, K. (2003). Continuous production of phosphor YAG : Tb nanoparticles by hydrothermal synthesis in supercritical water. *Materials Research Bulletin*, 38, (7) 1257-1265.

Haase, M., Riwotzki, K., Meyssamy, H., & Kornowski, A. (2000). Synthesis and properties of colloidal lanthanide-doped nanocrystals. *Journal of Alloys and Compounds*, 303, 191-197.

Hale, P.S., Maddox, L.M., Shapter, J.G., Voelcker, N.H., Ford, M.J., & Waclawik, E.R. (2005). Growth kinetics and modeling of ZnO nanoparticles. *Journal of Chemical Education*, 82, (5) 775-778.

Hao, Y. L. & Teja, A. S. (2003). Continuous hydrothermal crystallization of alpha-Fe_2O_3 *Journal of Alloys and Compounds*, 309, 170-175.

Hebbink, G.A., Stouwdam, J.W., Reinhoudt, D.N., & van Veggel, F.C.J.M. (2002). Lanthanide(III)-doped nanoparticles that emit in the near-infrared. *Advanced Materials*, 14, (16) 1147-1150.

Hergt, R., Andra, W., d'Ambly, C.G., Hilger, I., Kaiser, W.A., Richter, U., & Schmidt, H.G. (1998). Physical limits of hyperthermia using magnetite fine particles. *Ieee Transactions on Magnetics*, 34, (5) 3745-3754.

Hergt, R., Hiergeist, R., Hilger, I., Kaiser, W.A., Lapatnikov, Y., Margel, S., & Richter, U. (2004). Maghemite nanoparticles with very high AC-losses for application in RF-magnetic hyperthermia. *Journal of Magnetism and Magnetic Materials*, 270, (3) 345-357.

Hirai, H., Aizawa, H., & Shiozaki, H. (1992). Preparation of Nonaqueous Dispersion of Colloidal Silver by Phase-Transfer. *Chemistry Letters* 1527-1530.

Ho, G. S., Huang, C., & Carter, E. A. (2007). Describing metal surfaces and nanostructures with orbital-free density functional theory. *Current Opinion in Solid State & Materials Science 11*, 57-61.

Hoffmann, M. M. & Conradi, M. S. (1997). Are there hydrogen bonds in supercritical water? *Journal of the American Chemical Society 119*, 3811-3817.

Hoffmann, M. R., Hua, I., & Hochemer, R. (1996). Application of ultrasonic irradiation for the degradation of chemical contaminants in water. *Ultrasonics Sonochemistry 3*, S163-S172.

Holsa, J., Chateau, C., Leskela, T., & Leskela, M. (1985a). Optical Study of Phase-Transformations in Rare-Earth Oxyhydroxides. *Acta Chemica Scandinavica Series A-Physical and Inorganic Chemistry*, 39, (6) 415-421.

Holsa, J., Leskela, T., & Leskela, M. (1985b). Luminescence Properties of Europium$^{(3+)}$-Doped Rare-Earth Oxyhydroxides. *Inorganic Chemistry*, 24, (10) 1539-1542.

Holthoff, H., Egelhaaf, S. U., Borkovec, M., Schurtenberger, P., & Sticher, H. (1996). Coagulation rate measurements of colloidal particles by simultaneous static and dynamic light scattering. *Langmuir 12*, 5541-5549.

Huignard, A., Gacoin, T., & Boilot, J.P. (2000). Synthesis and luminescence properties of colloidal YVO_4 : Eu phosphors. *Chemistry of Materials*, 12, (4) 1090-1094.

Hyeon, T., Lee, S. S., Park, J., Chung, Y., & Bin Na, H. (2001). Synthesis of highly crystalline and monodisperse maghemite nanocrystallites without a size-selection process. *Journal of the American Chemical Society 123*, 12798-12801.

Hyeon, T. (2003). Chemical synthesis of magnetic nanoparticles. *Chemical Communications* (8) 927-934.

Hwang, Y.S. & Lenhart, J.J. (2008). Adsorption of C4-Dicarboxylic Acids at the Hematite/Water Interface. *Langmuir*, 24, (24) 13934-13943.

Iglesias, O., Labarta, A., & Batlle, X. (2008). Exchange bias phenomenology and models of core/shell nanoparticles. *Journal of Nanoscience and Nanotechnology*, 8, (6) 2761-2780.

Ikushima, Y., Hatakeda, K., Saito, N., & Arai, M. (1998a). An in situ Raman spectroscopy study of subcritical and supercritical water: The peculiarity of hydrogen bonding near the critical point. *Journal of Chemical Physics 108*, 5855-5860.

Ikushima, Y., Saito, N., & Arai, M. (1998b). Raman spectral studies of aqueous zinc nitrate solution at high temperatures and at a high pressure of 30 MPa. *Journal of Physical Chemistry B 102*, 3029-3035.

Illes, E. & Tombacz, E. (2006). The effect of humic acid adsorption on pH-dependent surface charging and aggregation of magnetite nanoparticles. *Journal of Colloid and Interface Science*, 295, (1) 115-123.

Ito, A., Shinkai, M., Honda, H., & Kobayashi, T. (2005). Medical application of functionalised magnetic nanoparticles. *Journal of Bioscience and Bioengineering*, 100, (1) 1-11.

Itoh, H. & Sugimoto, T. (2003). Systematic control of size, shape, structure, and magnetic properties of uniform magnetite and maghemite particles. *Journal of Colloid and Interface Science*, 265, (2) 283-295.

Jang, M., Ryu, M., Yoon, M., Lee, S., Kim, H., Onodera, A., & Kojima, S. (2009). A study on the Raman spectra of Al-doped and Ga-doped ZnO ceramics. *Current Applied Physics*, 9, (3) 651-657.

Jang, Y. I., Wang, H. F., & Chiang, Y. M. (1998). Room-temperature synthesis of monodisperse mixed spinel $(Co_xMn_{1-x})_3O_4$ powder by a coprecipitation method. *Journal of Materials Chemistry 8*, 2761-2764.

Jarvie, H. P., Neal, C., Leach, D. V., Ryland, G. P., House, W. A., & Robson, A. J. (1997). Major ion concentrations and the inorganic carbon chemistry of the Humber rivers. *Science of the Total Environment 194*, 285-302.

Jaster, H. & Kosky, P.G. (1976). Condensation Heat-Transfer in A Mixed Flow Regime. *International Journal of Heat and Mass Transfer*, 19, (1) 95-99.

Jiang, W.Q., Yang, H.C., Yang, S.Y., Horng, H.E., Hung, J.C., Chen, Y.C., & Hong, C.Y. (2004). Preparation and properties of superparamagnetic nanoparticles with narrow size distribution and biocompatible. *Journal of Magnetism and Magnetic Materials*, 283, (2-3) 210-214.

Jiang, W., Pan, H., Cai, Y., Tao, J., Liu, P., Xu, X., & Tang, R. (2008). Atomic Force Microscopy Reveals Hydroxyapatite-Citrate Interfacial Structure at the Atomic Level. *Langmuir*, 24, (21) 12446-12451.

Jongen, N., Donnet, M., Bowen, P., Lemaitre, J., Hofmann, H., Schenk, R., Hofmann, C., Aoun-Habbache, M., Guillemet-Fritsch, S., Sarrias, J., Rousset, A., Viviani, M., Buscaglia, M. T., Buscaglia, V., Nanni, P., Testino, A., & Herguijuela, J. R. (2003). Development of a continuous segmented flow tubular reactor and the "scale-out" concept - In search of perfect powders. *Chemical Engineering & Technology 26*, 303-305.

Joseyphus, R., Kodama, D., Matsumoto, T., Sato, Y., Jeyadevan, B., & Tohji, K. (2007). Role of polyol in the synthesis of magnetic nanoparticles. *Journal of Magnetism and Magnetic Materials*, 253, (5) 210-214.

Jordan, A., Scholz, R., Wust, P., Fahling, H., & Felix, R. (1999). Magnetic fluid hyperthermia (MFH): Cancer treatment with AC magnetic field induced excitation of biocompatible superparamagnetic nanoparticles. *Journal of Magnetism and Magnetic Materials*, 201, 413-419.

Journet, C., Maser, W. K., Bernier, P., Loiseau, A., delaChapelle, M. L., Lefrant, S., Deniard, P., Lee, R., & Fischer, J. E. (1997). Large-scale production of single-walled carbon nanotubes by the electric-arc technique. *Nature 388*, 756-758.

Kafizas, A. & Parkin, I. P. (2010). The combinatorial atmospheric pressure chemical vapour deposition (cAPCVD) of a gradating N-doped mixed phase titania thin film. *Journal of Materials Chemistry 20*, 2157-2169.

Kallumadil, M., Tada, M., Nakagawa, T., Abe, M., Southern, P., & Pankhurst, Q. A. (2009). Suitability of commercial colloids for magnetic hyperthermia. *Journal of Magnetism and Magnetic Materials 321*, 1509-1513.

Kamat, P. V. (2002). Photophysical, photochemical and photocatalytic aspects of metal nanoparticles. *Journal of Physical Chemistry B 106*, 7729-7744.

Kaneko, K., Inoke, K., Freitag, B., Hungria, A.B., Midgley, P.A., Hansen, T.W., Zhang, J., Ohara, S., & Adschiri, T. (2007). Structural and morphological characterization of cerium oxide nanocrystals prepared by hydrothermal synthesis. *Nano Letters*, 7, (2) 421-425.

Kashchiev, D. (1982). On the Relation Between Nucleation Work, Nucleus Size, and Nucleation Rate. *Journal of Chemical Physics 76*, 5098-5102.

Kashchiev, D. & van Rosmalen, G. M. (2003). Review: Nucleation in solutions revisited. *Crystal Research and Technology 38*, 555-574.

Kawasaki, S. i., Sue, K., Ookawara, R., Wakashima, Y., & Suzuki, A. (2010a). Development of Novel Micro Swirl Mixer for Producing Fine Metal Oxide Nanoparticles by Continuous Supercritical Hydrothermal Method. *Journal of Oleo Science 59*, 557-562.

Kawasaki, S. i., Sue, K., Ookawara, R., Wakashima, Y., Suzuki, A., Hakuta, Y., & Arai, K. (2010b). Engineering study of continuous supercritical hydrothermal method using a T-shaped mixer: Experimental synthesis of NiO nanoparticles and CFD simulation. *Journal of Supercritical Fluids 54*, 96-102.

Kay, M.I., Young, R.A., & Posner, A.S. (1964). Crystal Structure of Hydroxyapatite. *Nature*, 204, (496) 1050.

Kellici, S., Gong, K., Lin, T., Brown, S., Clark, R.J., Vickers, M., Cockcroft, J.K., Middelkoop, V., Barnes, P., Perkins, J.M., Tighe, C.J., & Darr, J.A. (2010). High-throughput continuous hydrothermal flow synthesis of Zn-Ce oxides: unprecedented solubility of Zn in the nanoparticle fluorite lattice. *Philosophical Transactions of the Royal Society A-Mathematical Physical and Engineering Sciences*, 368, (1927) 4331-4349.

Kim, D.K., Zhang, Y., Voit, W., Rao, K.V., & Muhammed, M. (2001). Synthesis and characterization of surfactant-coated superparamagnetic monodispersed iron oxide nanoparticles. *Journal of Magnetism and Magnetic Materials*, 225, (1-2) 30-36.

Kirwan, L.J., Fawell, P.D., & van Bronswijk, W. (2003). In situ FTIR-ATR examination of poly(acrylic acid) adsorbed onto hematite at low pH. *Langmuir*, 19, (14) 5802-5807.

Klaine, S. J., Alvarez, P. J., Batley, G. E., Fernandes, T. F., Handy, R. D., Lyon, D. Y., Mahendra, S., McLaughlin, M. J., & Lead, J. R. (2008). Nanomaterials in the environment: Behavior, fate, bioavailability, and effects. *Environmental Toxicology and Chemistry 27*, 1825-1851.

Kolb, E.D., Coriell, A.S., Laudise, R.A., & Hutson, A.R. (1967). Hydrothermal Growth of Low Carrier Concentration Zno at High Water and Hydrogen Pressures. *Materials Research Bulletin*, 2, (12) 1099.

Kodama, R. H. (1999). Magnetic nanoparticles. *Journal of Magnetism and Magnetic Materials 200,* 359-372.

Koksharov, Y.A., Gubin, S.P., Kosobudsky, I.D., Beltran, M., Khodorkovsky, Y., & Tishin, A.M. (2000). Low temperature electron paramagnetic resonance anomalies in Fe-based nanoparticles. *Journal of Applied Physics*, 88, (3) 1587-1592.

Konya, Z., Vesselenyi, I., Niesz, K., Kukovecz, A., Demortier, A., Fonseca, A., Delhalle, J., Mekhalif, Z., Nagy, J. B., Koos, A. A., Osvath, Z., Kocsonya, A., Biro, L. P., & Kiricsi, I. (2002). Large scale production of short functionalized carbon nanotubes. *Chemical Physics Letters 360*, 429-435.

Koutsopoulos, S. (2002). Synthesis and characterization of hydroxyapatite crystals: A review study on the analytical methods. *Journal of Biomedical Materials Research*, 62, (4) 600-612.

Kreuter, J. (1990). *Large-Scale Production Problems and Manufacturing of Nanoparticles*.

Kuznetsov, M., V, Linnikov, O., & Rodina, I., V (2012). X-ray photoelectron spectra of magnetite nanopowders after chromium(VI) sorption from aqueous solutions. *Inorganic Materials,* 48, (2) 169-175.

Kruis, F. E., Fissan, H., & Peled, A. (1998). Synthesis of nanoparticles in the gas phase for electronic, optical and magnetic applications - A review. *Journal of Aerosol Science 29,* 511-535.

Kuo, L.Y. & Shen, P. (2000). Shape dependent coalescence and preferred orientation of CeO2 nanocrystallites. *Materials Science and Engineering A-Structural Materials Properties Microstructure and Processing*, 277, (1-2) 258-265.

Kuo, P. C. & Tsai, T. S. (1989). New Approaches to the Synthesis of Acicular Alpha-Feooh and Cobalt-Modified Iron-Oxide Particles. *Journal of Applied Physics 65,* 4349-4356.

Kundu, T.K., Rao, K.H., & Parker, S.C. (2006). Atomistic simulation studies of magnetite surface structures and adsorption behavior in the presence of molecular and dissociated water and formic acid. *Journal of Colloid and Interface Science*, 295, (2) 364-373.

Lam, C., Zhang, Y. F., Tang, Y. H., Lee, C. S., Bello, I., & Lee, S. T. (2000). Large-scale synthesis of ultrafine Si nanoparticles by ball milling. *Journal of Crystal Growth 220,* 466-470.

Lam, C. W., James, J. T., McCluskey, R., Arepalli, S., & Hunter, R. L. (2006). A review of carbon nanotube toxicity and assessment of potential occupational and environmental health risks. *Critical Reviews in Toxicology 36*, 189-217.

Lam, U.T., Mammucari, R., Suzuki, K., & Foster, N.R. (2008). Processing of iron oxide nanoparticles by supercritical fluids. *Industrial & Engineering Chemistry Research*, 47, (3) 599-614.

Lattuada, M. & Hatton, T. (2007). Functionalization of monodisperse magnetic nanoparticles. *Langmuir*, 23, (4) 2158-2168.

Laurent, S., Forge, D., Port, M., Roch, A., Robic, C., Elst, L.V., & Muller, R.N. (2008). Magnetic iron oxide nanoparticles: Synthesis, stabilization, vectorization, physicochemical characterizations, and biological applications. *Chemical Reviews*, 108, (6) 2064-2110.

Lerou, J.J. & Ng, K.M. (1996). Chemical reaction engineering: A multiscale approach to a multiobjective task. *Chemical Engineering Science*, 51, (10) 1595-1614.

Lessing, P. A. (1989). Mixed-Cation Oxide Powders Via Polymeric Precursors. *American Ceramic Society Bulletin 68*, 1002-1007.

Leslie-Pelecky, D.L. & Rieke, R.D. (1996). Magnetic Properties of Nanostructured Materials. *Chemistry of Materials*, 8, (8) 1770-1783.

Lester, E., Blood, P., Denyer, J., Azzopardi, B., Li, J., & Poliakoff, M. (2010). Impact of reactor geometry on continuous hydrothermal synthesis mixing. *Materials Research Innovations 14*, 19-26.

Lester, E., Blood, P., Denyer, J., Giddings, D., Azzopardi, B., & Poliakoff, M. (2006). Reaction engineering: The supercritical water hydrothermal synthesis of nano-particles. *Journal of Supercritical Fluids 37*, 209-214.

Levy, M., Quarta, A., Espinosa, A., Figuerola, A., Wilhelm, C., Garcia-Hernandez, M., Genovese, A., Falqui, A., Alloyeau, D., Buonsanti, R., Davide Cozzoli, P., Angel Garcia, M., Gazeau, F., & Pellegrino, T. (2011). Correlating Magneto-Structural Properties to Hyperthermia Performance of Highly Monodisperse Iron Oxide Nanoparticles Prepared by a Seeded-Growth Route. *Chemistry of Materials*, 23, (18) 4170-4180.

Levy, M., Wilhelm, C., Siaugue, J.M., Horner, O., Bacri, J.C., & Gazeau, F. (2008). Magnetically induced hyperthermia: size-dependent heating power of gamma-Fe_2O_3 nanoparticles. *Journal of physics.Condensed matter : an Institute of Physics journal*, 20, (20) 204133.

Ljuboja, M. & Rodi, W. (1980). Calculation of Turbulent Wall Jets with An Algebraic Reynolds Stress Model. *Journal of Fluids Engineering-Transactions of the Asme*, 102, (3) 350-356.

Liu, B. & Zeng, H.C. (2003). Hydrothermal synthesis of ZnO nanorods in the diameter regime of 50 nm. *Journal of the American Chemical Society*, 125, (15) 4430-4431.

Liu, D.M., Troczynski, T., & Tseng, W.J. (2001). Water-based sol-gel synthesis of hydroxyapatite: process development. *Biomaterials*, 22, (13) 1721-1730.

Li, J. J., Wang, Y. A., Guo, W. Z., Keay, J. C., Mishima, T. D., Johnson, M. B., & Peng, X. G. (2003). Large-scale synthesis of nearly monodisperse CdSe/CdS core/shell nanocrystals using air-stable reagents via successive ion layer adsorption and reaction. *Journal of the American Chemical Society 125*, 12567-12575.

Li, W.J., Shi, E.W., Zhong, W.Z., & Yin, Z.W. (1999). Growth mechanism and growth habit of oxide crystals. *Journal of Crystal Growth*, 203, (1-2) 186-196.

Lifshitz, E. M. (1956). The Theory of Molecular Attractive Forces Between Solids. *Soviet Physics Jetp-Ussr 2*, 73-83.

Lifshitz, I. M. & Slyozov, V. V. (1961). The Kinetics of Precipitation from Supersaturated Solid Solutions. *Journal of Physics and Chemistry of Solids 19*, 35-50.

Li, R.X., Yabe, S., Yamashita, M., Momose, S., Yoshida, S., Yin, S., & Sato, T. (2002). Synthesis and UV-shielding properties of ZnO- and CaO-doped CeO(2) via soft solution chemical process. *Solid State Ionics*, 151, (1-4) 235-241.

Li, S., Gross, G., Guenther, P., & Koehler, J. (2011). Hydrothermal micro continuous-flow synthesis of spherical, cylinder-, star- and flower-like ZnO microparticles. *Chemical Engineering Journal*, 167, (2-3) 681-687.

Li, W.J., Shi, E.W., Zhong, W.Z., & Yin, Z.W. (1999). Growth mechanism and growth habit of oxide crystals. *Journal of Crystal Growth*, 203, (1-2) 186-196.

Liu, X., Zhang, P., Li, X., Chen, H., Dang, Y., Larson, C., Roco, M.C., & Wang, X. (2009). Trends for nanotechnology development in China, Russia, and India. *Journal of Nanoparticle Research*, 11, (8) 1845-1866.

Lin, M. Y., Lindsay, H. M., Weitz, D. A., Ball, R. C., Klein, R., & Meakin, P. (1990). Universal Reaction-Limited Colloid Aggregation. *Physical Review A 41*, 2005-2020.

Lin, T., Kellici, S., Gong, K., Thompson, K., Evans, J. R., Wang, X., & Darr, J. A. (2010). Rapid Automated Materials Synthesis Instrument: Exploring the Composition and Heat-Treatment of Nanoprecursors Toward Low Temperature Red Phosphors. *Journal of Combinatorial Chemistry 12*, 383-392.

Liu, B. & Zeng, H.C. 2003. Hydrothermal synthesis of ZnO nanorods in the diameter regime of 50 nm. *Journal of the American Chemical Society*, 125, (15) 4430-4431

Lin, W., Huang, Y. w., Zhou, X. D., & Ma, Y. (2006). In vitro toxicity of silica nanoparticles in human lung cancer cells. *Toxicology and Applied Pharmacology 217*, 252-259.

Liu, X., Zhang, P., Li, X., Chen, H., Dang, Y., Larson, C., Roco, M. C., & Wang, X. (2009). Trends for nanotechnology development in China, Russia, and India. *Journal of Nanoparticle Research 11*, 1845-1866.

Loebinger, M.R., Kyrtatos, P.G., Turmaine, M., Price, A.N., Pankhurst, Q., Lythgoe, M.F., & Janes, S.M. (2009). Magnetic Resonance Imaging of Mesenchymal Stem Cells Homing to Pulmonary Metastases Using Biocompatible Magnetic Nanoparticles. *Cancer Research*, 69, (23) 8862-8867.

Lu, A. H., Salabas, E., & Schueth, F. (2007). Magnetic nanoparticles: Synthesis, protection, functionalization, and application. *Angewandte Chemie-International Edition 46*, 1222-1244.

Lu, H.B., Campbell, C.T., Graham, D.J., & Ratner, B.D. (2000). Surface characterization of hydroxyapatite and related calcium phosphates by XPS and TOF-SIMS. *Analytical Chemistry*, 72, (13) 2886-2894.

Lu, Y., Yin, Y.D., Mayers, B.T., & Xia, Y.N. (2002). Modifying the surface properties of superparamagnetic iron oxide nanoparticles through a sol-gel approach. *Nano Letters*, 2, (3) 183-186.

Ma, C. Y., Tighe, C. J., Gruar, R. I., Mahmud, T., Darr, J. A., & Wang, X. Z. (2011). Numerical modelling of hydrothermal fluid flow and heat transfer in a tubular heat exchanger under near critical conditions. *Journal of Supercritical Fluids 57*, 236-246.

Ma, M., Wu, Y., Zhou, H., Sun, Y.K., Zhang, Y., & Gu, N. (2004). Size dependence of specific power absorption of Fe3O4 particles in AC magnetic field. *Journal of Magnetism and Magnetic Materials*, 268, (1-2) 33-39.

Mae, K., Suzuki, A., Maki, T., Hakuta, Y., Sato, H., & Arai, K. (2007). A new micromixer with needle adjustment for instant mixing and heating under high pressure and high temperature. *Journal of Chemical Engineering of Japan 40*, 1101-1107.

Madler, L., Kammler, H.K., Mueller, R., & Pratsinis, S.E. (2002). Controlled synthesis of nanostructured particles by flame spray pyrolysis. *Journal of Aerosol Science*, 33, (2) 369-389.

Majewski, P. & Thierry, B. (2007). Functionalised magnetite nanoparticles - Synthesis, properties, and bio-applications. *Critical Reviews in Solid State and Materials Sciences*, 32, (3-4) 203-215.

Malow, T. R. & Koch, C. C. (1998). Mechanical properties, ductility, and grain size of nanocrystalline iron produced by mechanical attrition. *Metallurgical and Materials Transactions A-Physical Metallurgy and Materials Science 29*, 2285-2295.

Marchisio, D. L., Rivautella, L., & Barresi, A. A. (2006). Design and scale-up of chemical reactors for nanoparticle precipitation. *Aiche Journal 52*, 1877-1887.

Marre, S., Roig, Y., & Aymonier, C. (2012). Supercritical microfluidics: Opportunities in flow-through chemistry and materials science. *Journal of Supercritical Fluids*, 66, 251-264.

Masala, O. & Seshadri, R. (2004). Synthesis routes for large volumes of nanoparticles. *Annual Review of Materials Research 34*, 41-81.

Masuda, Y., Aizawa, T., & Suzuki, A. (2009). Flow Visualization and Numerical Simulation of T-Junction Mixing of High-Temperature High-Pressure Water. *Journal of Chemical Engineering of Japan 42*, 64-70.

Masui, T., Fujiwara, K., Machida, K., Adachi, G., Sakata, T., & Mori, H. (1997). Characterization of Cerium(IV) oxide ultrafine particles prepared using reversed micelles. *Chemistry of Materials*, 9, (10) 2197-2204.

Matson, D. W., Linehan, J. C., & Bean, R. M. (1992). Ultrafine Iron-Oxide Powders Generated Using A Flow-Through Hydrothermal Process. *Materials Letters 14*, 222-226.

McCafferty, E. & Wightman, J.P. (1998). Determination of the concentration of surface hydroxyl groups on metal oxide films by a quantitative XPS method. *Surface and Interface Analysis*, 26, (8) 549-564.

McMahon, J. M. & Emory, S. R. (2007). Phase transfer of large gold nanoparticles to organic solvents with increased stability. *Langmuir 23*, 1414-1418.

McNeil-Watson, F. & Kaszuba, M. (2010). A Novel Method for Measuring Zeta Potential of High-Concentration, Low-Volume Protein Samples. *American Laboratory 42*, 15-16.

Meltzer, R.S., Feofilov, S.P., Tissue, B., & Yuan, H.B. (1999). Dependence of fluorescence lifetimes of Y_2O_3: $Eu^{(3+)}$ nanoparticles on the surrounding medium. *Physical Review B*, 60, (20) 14012-14015.

Meng, X. D., Wang, D. Z., Liu, J. H., & Zhang, S. Y. (2004). Preparation and characterization of sodium titanate nanowires from brookite nanocrystallites. *Materials Research Bulletin 39*, 2163-2170.

Messing, G. L., Zhang, S. C., & Jayanthi, G. V. (1993). Ceramic Powder Synthesis by Spray-Pyrolysis. *Journal of the American Ceramic Society 76*, 2707-2726.

Meyssamy, H., Riwotzki, K., Kornowski, A., Naused, S., & Haase, M. (1999). Wet-chemical synthesis of doped colloidal nanomaterials: Particles and fibers of $LaPO_4$: Eu, $LaPO_4$: Ce, and $LaPO_4$: Ce,Tb. *Advanced Materials*, 11, (10) 840-+

Middelkoop, V., Boldrin, P., Peel, M., Buslaps, T., Barnes, P., Darr, J. A., & Jacques, S. D. (2009). Imaging the inside of a Continuous Nanoceramic Synthesizer under Supercritical Water Conditions Using High-Energy Synchrotron X-Radiation. *Chemistry of Materials 21*, 2430-2435.

Mikhaylova, M., Kim, D.K., Bobrysheva, N., Osmolowsky, M., Semenov, V., Tsakalakos, T., & Muhammed, M. (2004). Superparamagnetism of magnetite nanoparticles: Dependence on surface modification. *Langmuir*, 20, (6) 2472-2447.

Mills, A., Elliott, N., Parkin, I. P., O'Neill, S. A., & Clark, R. J. H. (2002). Novel TiO_2 CVD films for semiconductor photocatalysis. *Journal of Photochemistry and Photobiology A-Chemistry 151*, 171-179.

Mizuno, M., Sasaki, Y., Inoue, M., Chinnasamy, C. N., Jeyadevan, B., Hasegawa, D., Ogawa, T., Takahashi, M., Tohji, K., Sato, K., & Hisano, S. (2005). Structural and magnetic properties of monolayer film of CoPt nanoparticles synthesized by polyol process. *Journal of Applied Physics 97*.

Mogensen, M., Lindegaard, T., Hansen, U.R., & Mogensen, G. (1994). Physical-Properties of Mixed Conductor Solid Oxide Fuel-Cell Anodes of Doped CeO_2. *Journal of the Electrochemical Society*, 141, (8) 2122-2128.

Mornet, S., Vasseur, S., Grasset, F., & Duguet, E. (2004). Magnetic nanoparticle design for medical diagnosis and therapy. *Journal of Materials Chemistry*, 14, (14) 2161-2175.

Morinaga, Y., Sakuragi, K., Fujimura, N., & Ito, T. (1997). Effect of Ce doping on the growth of ZnO thin films. *Journal of Crystal Growth*, 174, (1-4) 691-695.

Mousavand, T., Ohara, S., Naka, T., Umetsu, M., Takami, S., & Adschiri, T. (2010). Organic-ligand-assisted hydrothermal synthesis of ultrafine and hydrophobic ZnO nanoparticles. *Journal of Materials Research*, 25, (2) 219-223.

Mudunkotuwa, I.A. & Grassian, V.H. (2010). Citric Acid Adsorption on TiO_2 Nanoparticles in Aqueous Suspensions at Acidic and Circumneutral pH: Surface Coverage, Surface Speciation, and Its Impact on Nanoparticle-Nanoparticle Interactions. *Journal of the American Chemical Society*, 132, (42) 14986-14994.

Muerbe, J., Rechtenbach, A., & Toepfer, J. (2008). Synthesis and physical characterization of magnetite nanoparticles for biomedical applications. *Materials Chemistry and Physics*, 110, (2-3) 426-433.

Muller, R., Steinmetz, H., Zeisberger, M., Schmidt, C., Dutz, S., Hergt, R., & Gawalek, W. (2006). Precipitated iron oxide particles by cyclic growth. *Zeitschrift fur Physikalische Chemie-International Journal of Research in Physical Chemistry & Chemical Physics*, 220, (1) 51-57.

Mulvaney, P., Liz-Marzan, L.M., Giersig, M., & Ung, T. (2000). Silica encapsulation of quantum dots and metal clusters. *Journal of Materials Chemistry*, 10, (6) 1259-1270.

Napper, D.H. (1977). Steric Stabilization. *Journal of Colloid and Interface Science*, 58, (2) 390-407.

Navarro, E., Baun, A., Behra, R., Hartmann, N. B., Filser, J., Miao, A. J., Quigg, A., Santschi, P. H., & Sigg, L. (2008). Environmental behavior and ecotoxicity of engineered nanoparticles to algae, plants, and fungi. *Ecotoxicology 17*, 372-386.

Nel, A., Xia, T., Madler, L., & Li, N. (2006). Toxic potential of materials at the nanolevel. *Science 311*, 622-627.

Nogues, J. & Schuller, I.K. (1999). Exchange bias. *Journal of Magnetism and Magnetic Materials*, 192, (2) 203-232.

Nogues, J., Sort, J., Langlais, V., Skumryev, V., Surinach, S., Munoz, J.S., & Baro, M.D. (2005). Exchange bias in nanostructures. *Physics Reports-Review Section of Physics Letters*, 422, (3) 65-117.

Neuberger, T., Schopf, B., Hofmann, H., Hofmann, M., & von Rechenberg, B. (2005). Superparamagnetic nanoparticles for biomedical applications: Possibilities and limitations of a new drug delivery system. *Journal of Magnetism and Magnetic Materials*, 293, (1) 483-496.

Oberdorster, G., Oberdorster, E., & Oberdorster, J. (2005a). Nanotoxicology: An emerging discipline evolving from studies of ultrafine particles. *Environmental Health Perspectives 113*, 823-839.

Oberdorster, G., Maynard, A., Donaldson, K., Castranova, V., Fitzpatrick, J., Ausman, K., Carter, J., Karn, B., Kreyling, W., Lai, D., Olin, S., Monteiro-Riviere, N., Warheit, D., & Yang, H. (2005b). Principles for characterizing the potential human health effects from exposure to nanomaterials: elements of a screening strategy. *Particle and fibre toxicology 2*, 8.

Oberdorster, G., Stone, V., & Donaldson, K. (2007). Toxicology of nanoparticles: A historical perspective. *Nanotoxicology 1*, 2-25.

Ohara, S., Mousavand, T., Umetsu, M., Takami, S., Adschiri, T., Kuroki, Y., & Takata, M. (2004). Hydrothermal synthesis of fine zinc oxide particles under supercritical conditions. *Solid State Ionics 172*, 261-264.

Ong, J.L., Lucas, L.C., Raikar, G.N., Weimer, J.J., & Gregory, J.C. (1994). Surface Characterization of Ion-Beam Sputter-Deposited Ca-P Coatings After In-Vitro Immersion. *Colloids and Surfaces A-Physicochemical and Engineering Aspects*, 87, (2) 151-162.

Ozawa, L. (1979). Determination of Self-Concentration Quenching Mechanisms of Rare-Earth Luminescence from Intensity Measurements on Powdered Phosphor Screens. *Journal of the Electrochemical Society*, 126, (1) 106-109.

Palgrave, R. G. & Parkin, I. P. (2006). Aerosol assisted chemical vapor deposition using nanoparticle precursors: A route to nanocomposite thin films. *Journal of the American Chemical Society 128*, 1587-1597.

Pankhurst, Q., Thanh, N., Jones, S., & Dobson, J. (2009). Progress in applications of magnetic nanoparticles in biomedicine. *Journal of Physics D-Applied Physics 42*.

Pankhurst, Q., Thanh, N., Jones, S., & Dobson, J. (2009). Progress in applications of magnetic nanoparticles in biomedicine. *Journal of Physics D-Applied Physics*, 42, (22), 135-145.

Pankhurst, Q.A., Connolly, J., Jones, S.K., & Dobson, J. (2003). Applications of magnetic nanoparticles in biomedicine. *Journal of Physics D-Applied Physics*, 36, (13) R167-R181.

Pannaparayil, T., Marande, R., Komarneni, S., & Sankar, S.G. (1988). A Novel Low-Temperature Preparation of Several Ferrimagnetic Spinels and Their Magnetic and Mossbauer Characterization. *Journal of Applied Physics*, 64, (10) 5641-5643.

Parak, W. J., Gerion, D., Pellegrino, T., Zanchet, D., Micheel, C., Williams, S. C., Boudreau, R., Le Gros, M. A., Larabell, C. A., & Alivisatos, A. P. (2003). Biological applications of colloidal nanocrystals. *Nanotechnology 14*, R15-R27.

Park, J., An, K. J., Hwang, Y. S., Park, J. G., Noh, H. J., Kim, J. Y., Park, J. H., Hwang, N. M., & Hyeon, T. (2004). Ultra-large-scale syntheses of monodisperse nanocrystals. *Nature Materials 3*, 891-895.

Parker, J. E., Thompson, S. P., Cobb, T. M., Yuan, F., Potter, J., Lennie, A. R., Alexander, S., Tighe, C. J., Darr, J. A., Cockcroft, J. C., & Tang, C. C. (2011). High-throughput powder diffraction on beamline I11 at Diamond. *Journal of Applied Crystallography 44*, 102-110.

Penel, G., Leroy, G., Rey, C., & Bres, E. (1998). MicroRaman spectral study of the PO_4 and CO_3 vibrational modes in synthetic and biological apatites. *Calcified Tissue International,* 63, (6) 475-481.

Pennemann, H., Hessel, V., & Lowe, H. (2004). Chemical microprocess technology - from laboratory-scale to production. *Chemical Engineering Science 59*, 4789-4794.

Pettibone, J.M., Cwiertny, D.M., Scherer, M., & Grassian, V.H. (2008). Adsorption of organic acids on TiO_2 nanoparticles: Effects of pH, nanoparticle size, and nanoparticle aggregation. *Langmuir,* 24, (13) 6659-6667.

Phoka, S., Laokul, P., Swatsitang, E., Promarak, V., Seraphin, S., & Maensiri, S. (2009). Synthesis, structural and optical properties of CeO_2 nanoparticles synthesized by a simple polyvinyl pyrrolidone (PVP) solution route. *Materials Chemistry and Physics*, 115, (1) 423-428.

Pitts, W.M. (1991a). Effects of Global Density Ratio on the Centerline Mixing Behavior of Axisymmetrical Turbulent Jets. *Experiments in Fluids*, 11, (2-3) 125-134.

Pitts, W.M. (1991b). Reynolds-Number Effects on the Mixing Behavior of Axisymmetrical Turbulent Jets. *Experiments in Fluids*, 11, (2-3) 135-141.

Poland, C. A., Duffin, R., Kinloch, I., Maynard, A., Wallace, W. A., Seaton, A., Stone, V., Brown, S., MacNee, W., & Donaldson, K. (2008). Carbon nanotubes introduced into the abdominal cavity of mice show asbestos-like pathogenicity in a pilot study. *Nature Nanotechnology 3*, 423-428.

Porter, D. A. & Easterling, K. E. (1992), "Solidification," in *Phase Transformations in Metals and Alloys*, 2 edn, Stanley Thornes, Cheltenham. 185-260.

Pratsinis, S. E. & Vemury, S. (1996). Particle formation in gases: A review. *Powder Technology 88*, 267-273.

Racuciu, M., Creanga, D., & Airinei, A. (2006). Citric-acid-coated magnetite nanoparticles for biological applications. *European Physical Journal e*, 21, (2) 117-121.

Racuciu, M., Creanga, D.E., & Calugaru, G. (2005). Synthesis and rheological properties of an aqueous ferrofluid. *Journal of Optoelectronics and Advanced Materials*, 7, (6) 2859-2864.

Raghavan, S.R., Hou, J., Baker, G.L., & Khan, S.A. (2000). Colloidal interactions between particles with tethered nonpolar chains dispersed in polar media: Direct correlation between dynamic rheology and interaction parameters. *Langmuir*, 16, (3) 1066-1077.

Rajh, T., Chen, L.X., Lukas, K., Liu, T., Thurnauer, M.C., & Tiede, D.M. (2002). Surface restructuring of nanoparticles: An efficient route for ligand-metal oxide crosstalk. *Journal of Physical Chemistry B*, 106, (41) 10543-10552.

Reverchon, E. & Adami, R. (2006). Nanomaterials and supercritical fluids. *Journal of Supercritical Fluids 37*, 1-22.

Ricou, F.P. & Spalding, D.B. (1961). Measurements of Entrainment by Axisymmetrical Turbulent Jets. *Journal of Fluid Mechanics*, 11, (1) 21-32.

Riwotzki, K. & Haase, M. (2001). Colloidal YVO_4 : Eu and $YP_{0.95}V_{0.05}O_4$: Eu nanoparticles: Luminescence and energy transfer processes. *Journal of Physical Chemistry B*, 105, (51) 12709-12713.

Robinson, I., Alexander, C., Tung, L. D., Fernig, D. G., & Thanh, N. T. (2009). Fabrication of water-soluble magnetic nanoparticles by ligand-exchange with thermo-responsive polymers. *Journal of Magnetism and Magnetic Materials 321*, 1421-1423.

Roco, M.C. (2001). International strategy for nanotechnology research and development. *Journal of Nanoparticle Research*, 3, (5-6) 353-360.

Rodi, W. & Srivatsa, S.K. (1980). A Locally Elliptic Calculation Procedure for 3-Dimensional Flows and Its Application to A Jet in A Cross-Flow. *Computer Methods in Applied Mechanics and Engineering*, 23, (1) 67-83.

Ronda, C.R., Justel, T., & Nikol, H. (1998). Rare earth phosphors: fundamentals and applications. *Journal of Alloys and Compounds*, 275, 669-676.

Rosensweig, R. E. (2002). Heating magnetic fluid with alternating magnetic field. *Journal of Magnetism and Magnetic Materials 252*, 370-374.

Rosner, D. E. (2005). Flame synthesis of valuable nanoparticles: Recent progress/current needs in areas of rate laws, population dynamics, and characterization. *Industrial & Engineering Chemistry Research 44*, 6045-6055.

Rovers, S.A., Dietz, C.H., van der Poel, L.A., Hoogenboom, R., Kemmere, M.F., & Keurentjes, J.T. (2010). Influence of Distribution on the Heating of Superparamagnetic Iron Oxide Nanoparticles in Poly(methyl methacrylate) in an Alternating Magnetic Field. *Journal of Physical Chemistry C*, 114, (18) 8144-8149.

Rovers, S.A., van der Poel, L.A., Dietz, C.H., Noijen, J.J., Hoogenboom, R., Kemmere, M.F., Kopinga, K., & Keurentjes, J.T. (2009). Characterization and Magnetic Heating of Commercial Superparamagnetic Iron Oxide Nanoparticles. *Journal of Physical Chemistry C*, 113, (33) 14638-14643

Sahoo, Y., Goodarzi, A., Swihart, M.T., Ohulchanskyy, T.Y., Kaur, N., Furlani, E.P., & Prasad, P.N. (2005). Aqueous ferrofluid of magnetite nanoparticles: Fluorescence labeling and magnetophoretic control. *Journal of Physical Chemistry B*, 109, (9) 3879-3885.

Sahraneshin, A., Takami, S., Hojo, D., Minami, K., Arita, T., & Adschiri, T. (2012). Synthesis of shape-controlled and organic-hybridized hafnium oxide nanoparticles under sub- and supercritical hydrothermal conditions. *Journal of Supercritical Fluids 62*, 190-196.

Santra, S., Tapec, R., Theodoropoulou, N., Dobson, J., Hebard, A., & Tan, W. H. (2001). Synthesis and characterization of silica-coated iron oxide nanoparticles in microemulsion: The effect of nonionic surfactants. *Langmuir 17*, 2900-2906.

Sasaki, T., Ohara, S., Naka, T., Vejpravova, J., Sechovsky, V., Umetsu, M., Takami, S., Jeyadevan, B., & Adschiri, T. (2010). Continuous synthesis of fine MgFe2O4 nanoparticles by supercritical hydrothermal reaction. *Journal of Supercritical Fluids*, 53, (1-3) 92-94.

Sayes, C. M. & Warheit, D. B. (2009). Characterization of nanomaterials for toxicity assessment. *Wiley Interdisciplinary Reviews-Nanomedicine and Nanobiotechnology 1*, 660-670.

Schmechel, R., Kennedy, M., von Seggern, H., Winkler, H., Kolbe, M., Fischer, R.A., Li, X.M., Benker, A., Winterer, M., & Hahn, H. (2001a). Luminescence properties of nanocrystalline Y_2O_3 : Eu^{3+} in different host materials. *Journal of Applied Physics*, 89, (3) 1679-1686.

Schmechel, R., Winkler, H., Li, X.M., Kennedy, M., Kolbe, M., Benker, A., Winterer, M., Fischer, R.A., Hahn, H., & von Seggern, H. (2001b). Photoluminescence properties of nanocrystalline Y_2O_3 : Eu^{3+} in different environments. *Scripta Materialia*, 44, (8-9) 1213-1217.

Shchukin, D.G. & Sukhorukov, G.B. (2004). Nanoparticle synthesis in engineered organic nanoscale reactors. *Advanced Materials*, 16, (8) 671-682.

Shock, E.L. & Helgeson, H.C. (1988). Calculation of the Thermodynamic and Transport-Properties of Aqueous Species at High-Pressures and Temperatures - Correlation Algorithms for Ionic Species and Equation of State Predictions to 5-Kb and 1000-Degrees-C. *Geochimica et Cosmochimica Acta*, 52, (8) 2009-2036.

Shock, E.L., Helgeson, H.C., & Sverjensky, D.A. (1989). Calculation of the Thermodynamic and Transport-Properties of Aqueous Species at High-Pressures and Temperatures - Standard Partial Molal Properties of Inorganic Neutral Species. *Geochimica et Cosmochimica Acta*, 53, (9) 2157-2183.

Shock, E.L. & Helgeson, H.C. (1990). Calculation of the Thermodynamic and Transport-Properties of Aqueous Species at High-Pressures and Temperatures - Standard Partial Molal Properties of Organic-Species. *Geochimica et Cosmochimica Acta*, 54, (4) 915-945.

Shock, E.L. (1993). Hydrothermal Dehydration of Aqueous-Organic Compounds. *Geochimica et Cosmochimica Acta*, 57, (14) 3341-3349.

Shock, E.L. (1995). Organic-Acids in Hydrothermal Solutions - Standard Molal Thermodynamic Properties of Carboxylic-Acids and Estimates of Dissociation-Constants at High-Temperatures and Pressures. *American Journal of Science*, 295, (5) 496-580.

Shubayev, V.I., Pisanic, T.R., & Jin, S. (2009). Magnetic nanoparticles for theragnostics. *Advanced Drug Delivery Reviews*, 61, (6) 467-477.

Si, R., Zhang, Y. W., Li, S. J., Lin, B. X., & Yan, C. H. (2004). Urea-based hydrothermally derived homogeneous nanostructured $Ce_{1-x}Zr_xO_2$ (x=0-0.8) solid solutions:

A strong correlation between oxygen storage capacity and lattice strain. *Journal of Physical Chemistry B 108*, 12481-12488.

Simonet, V., Calzavara, Y., Hazemann, J. L., Argoud, R., Geaymond, O., & Raoux, D. (2002a). Structure of aqueous ZnBr2 solution probed by x-ray absorption spectroscopy in normal and hydrothermal conditions. *Journal of Chemical Physics 116*, 2997-3006.

Simonet, V., Calzavara, Y., Hazemann, J. L., Argoud, R., Geaymond, O., & Raoux, D. (2002b). X-ray absorption spectroscopy studies of ionic association in aqueous solutions of zinc bromide from normal to critical conditions. *Journal of Chemical Physics 117*, 2771-2781.

Sondergaard, M., Bojesen, E.D., Christensen, M., & Iversen, B.B. (2011). Size and Morphology Dependence of ZnO Nanoparticles Synthesized by a Fast Continuous Flow Hydrothermal Method. *Crystal Growth & Design*, 11, (9) 4027-4033.

Sorescu, M., Diamandescu, L., Tarabasanu-Mihaila, D., Teodorescu, V.S., & Howard, B.H. 2004. Hydrothermal synthesis and structural characterization of alpha-Fe_2O_3-SnO_2 nanoparticles. *Journal of Physics and Chemistry of Solids*, 65, (5) 1021-1029.

Sorescu, M., Diamandescu, L., & Tarabasanu-Mihaila, D. (2005). Recoilless fraction of tin-doped hematite nanoparticles obtained by hydrothermal synthesis. *Materials Letters 59*, 22-25.

Souza, M. M. V. M., Aranda, D. A. G., & Schmal, M. (2001). Reforming of methane with carbon dioxide over Pt/ZrO2/Al2O3 catalysts. *Journal of Catalysis 204*, 498-511.

Spanier, J.E., Robinson, R.D., Zheng, F., Chan, S.W., & Herman, I.P. (2001). Size-dependent properties of CeO2-y nanoparticles as studied by Raman scattering. *Physical Review B*, 64, (24).

Sreenivasan, K.R., Raghu, S., & Kyle, D. (1989a). Absolute Instability in Variable Density Round Jets. *Experiments in Fluids*, 7, (5) 309-317.

Sreenivasan, K.R., Ramshankar, R., & Meneveau, C. (1989). Mixing, Entrainment and Fractal Dimensions of Surfaces in Turbulent Flows. *Proceedings of the Royal Society of London Series A-Mathematical Physical and Engineering Sciences*, 421, (1860) 79.

Stark, W.J. & Pratsinis, S.E. (2002). Aerosol flame reactors for manufacture of nanoparticles. *Powder Technology*, 126, (2) 103-108.

Stouwdam, J.W., Raudsepp, M., & van Veggel, F.C.J.M. (2005). Colloidal nanoparticles of $Ln^{(3+)-}$doped $LaVO_4$: Energy transfer to visible- and near-infrared-emitting lanthanide ions. *Langmuir*, 21, (15) 7003-7008.

Strykowski, P.J. & Niccum, D.L. (1991). The Stability of Countercurrent Mixing Layers in Circular Jets. *Journal of Fluid Mechanics*, 227, 309-343.

Suchanek, W.L., Shuk, P., Byrappa, K., Riman, R.E., TenHuisen, K.S., & Janas, V.F. (2002). Mechanochemical-hydrothermal synthesis of carbonated apatite powders at room temperature. *Biomaterials*, 23, (3) 699-710.

Sugiyama, J., Atsumi, T., Koiwai, A., Sasaki, T., Hioki, T., Noda, S., & Kamegashira, N. (1997). The effect of oxygen deficiency on the structural phase transition and electronic and magnetic properties of the spinel LiMn2O4-delta. *Journal of Physics-Condensed Matter*, 9, (8) 1729-1741.

Sue, K., Kimura, K., & Arai, K. (2004a). Hydrothermal synthesis of ZnO nanocrystals using microreactor. *Materials Letters 58*, 3229-3231.

Sue, K., Kimura, K., Murata, K., & Arai, K. (2004b). Effect of cations and anions on properties of zinc oxide particles synthesized in supercritical water. *Journal of Supercritical Fluids 30*, 325-331.

Sue, K. W., Kimura, K., Yamamoto, M., & Arai, K. (2004c). Rapid hydrothermal synthesis of ZnO nanorods without organics. *Materials Letters 58*, 3350-3352.

Sue, K., Sato, T., Kawasaki, S. i., Takebayashi, Y., Yoda, S., Furuya, T., & Hiaki, T. (2010). Continuous Hydrothermal Synthesis of Fe2O3 Nanoparticles Using a Central Collision-Type Micromixer for Rapid and Homogeneous Nucleation at 673 K and 30 MPa. *Industrial & Engineering Chemistry Research 49*, 8841-8846.

Sue, K., Suzuki, M., Arai, K., Ohashi, T., Ura, H., Matsui, K., Hakuta, Y., Hayashi, H., Watanabe, M., & Hiaki, T. (2006). Size-controlled synthesis of metal oxide nanoparticles with a flow-through supercritical water method. *Green Chemistry 8*, 634-638.

Sun, S. H., Murray, C. B., Weller, D., Folks, L., & Moser, A. (2000). Monodisperse FePt nanoparticles and ferromagnetic FePt nanocrystal superlattices. *Science 287*, 1989-1992.

Sugiyama, J., Atsumi, T., Koiwai, A., Sasaki, T., Hioki, T., Noda, S., & Kamegashira, N. (1997). The effect of oxygen deficiency on the structural phase transition and electronic and magnetic properties of the spinel LiMn2O4-delta. *Journal of Physics-Condensed Matter*, 9, (8) 1729-1741.

Sun, C., Carpenter, C., Pratx, G., & Xing, L. (2011). Facile Synthesis of Amine-Functionalised Eu$^{(3+)}$-Doped La(OH)$_3$ Nanophosphors for Bioimaging. *Nanoscale Research Letters*, 6, 134-139.

Sun, S. H. & Zeng, H. (2002). Size-controlled synthesis of magnetite nanoparticles. *Journal of the American Chemical Society 124*, 8204-8205.

Sun, S. H., Zeng, H., Robinson, D. B., Raoux, S., Rice, P. M., Wang, S. X., & Li, G. X. (2004). Monodisperse MFe$_2$O$_4$ (M = Fe, Co, Mn) nanoparticles. *Journal of the American Chemical Society 126*, 273-279.

Sun, Y. G. & Xia, Y. N. (2002). Large-scale synthesis of uniform silver nanowires through a soft, self-seeding, polyol process. *Advanced Materials 14*, 833-837.

Suslick, K.S. & Price, G.J. (1999). Applications of ultrasound to materials chemistry. *Annual Review of Materials Science*, 29, 295-326.

Sweere, A.P.J., Luyben, K.C.A.M., & Kossen, N.W.F. (1987). Regime Analysis and Scale-Down - Tools to Investigate the Performance of Bioreactors. *Enzyme and Microbial Technology*, 9, (7) 386-398.

T

Taguchi, M., Takami, S., Adschiri, T., Nakane, T., Sato, K., & Naka, T. (2011a). Supercritical hydrothermal synthesis of hydrophilic polymer-modified water-dispersible CeO_2 nanoparticles. *Crystengcomm 13*, 2841-2848.

Taguchi, M., Takami, S., Adschiri, T., Nakane, T., Sato, K., & Naka, T. (2011b). Supercritical hydrothermal synthesis of hydrophilic polymer-modified water-dispersible CeO_2 nanoparticles. *Crystengcomm 13*, 2841-2848.

Taguchi, M., Takami, S., Adschiri, T., Nakane, T., Sato, K., & Naka, T. (2012). Simple and rapid synthesis of ZrO_2 nanoparticles from $Zr(OEt)_4$ and $Zr(OH)_4$ using a hydrothermal method. *Crystengcomm 14*, 2117-2123.

Takami, S., Sugioka, K. i., Tsukada, T., Adschiri, T., Sugimoto, K., Takenaka, N., & Saito, Y. (2012). Neutron radiography on tubular flow reactor for hydrothermal synthesis: In situ monitoring of mixing behavior of supercritical water and room-temperature water. *Journal of Supercritical Fluids 63*, 46-51.

Tanner, P.A. & Fu, L. (2009). Morphology of Y_2O_3: Eu^{3+} prepared by hydrothermal synthesis. *Chemical Physics Letters*, 470, (1-3) 75-79.

Teja, A.S. & Koh, P.Y. (2009). Synthesis, properties, and applications of magnetic iron oxide nanoparticles. *Progress in Crystal Growth and Characterization of Materials*, 55, (1-2) 22-45.

Teow, Y., Asharani, P., V, Hande, M., & Valiyaveettil, S. (2011). Health impact and safety of engineered nanomaterials. *Chemical Communications 47*, 7025-7038.

Thanh, N. T. & Green, L. A. (2010). Functionalisation of nanoparticles for biomedical applications. *Nano Today 5*, 213-230.

Thomas, L.A., Dekker, L., Kallumadil, M., Southern, P., Wilson, M., Nair, S.P., Pankhurst, Q.A., & Parkin, I.P. (2009). Carboxylic acid-stabilised iron oxide nanoparticles for use in magnetic hyperthermia. *Journal of Materials Chemistry*, 19, (36) 6529-6535.

Thring, W. M. and Newby, M. P. (1980) Length of Enclosed Turbulent Jets. Fourth symposium on Combustion (international), Williams & Wilkins (1980), 789-796.

Tighe, C.J., Gruar, R.I., Ma, C.Y., Mahmud, T., Wang, X.Z., & Darr, J.A. (2012). Investigation of counter-current mixing in a continuous hydrothermal flow reactor. *Journal of Supercritical Fluids*, 62, 165-172.

Tissue, B.M. (1998). Synthesis and luminescence of lanthanide ions in nanoscale insulating hosts. *Chemistry of Materials*, 10, (10) 2837-2845.

Toft, L. L., Aarup, D. F., Bremholm, M., Hald, P., & Iversen, B. B. (2009). Comparison of T-piece and concentric mixing systems for continuous flow synthesis of anatase nanoparticles in supercritical isopropanol/water. *Journal of Solid State Chemistry 182*, 491-495.

Togashi, T., Naka, T., Asahina, S., Sato, K., Takami, S., & Adschiri, T. (2011). Surfactant-assisted one-pot synthesis of superparamagnetic magnetite nanoparticle clusters with tunable cluster size and magnetic field sensitivity. *Dalton Transactions 40,* 1073-1078.

Trambouze, P. (1981). Methodology of Scaling Up Chemical Reactors. *Chemie Ingenieur Technik*, 53, (5) 344-351.

Tretyakov, Y.D. & Goodilin, E. (2009). Key trends in basic and application-oriented research on nanomaterials. *Russian Chemical Reviews*, 78, (9) 801-820.

Tsuda, H. & Arends, J. (1994). Orientational Micro-Raman Spectroscopy on Hydroxyapatite Single-Crystals and Human Enamel Crystallites. *Journal of Dental Research*, 73, (11) 1703-1710.

Tsuzuki, T. (2009). Commercial scale production of inorganic nanoparticles. *International Journal of Nanotechnology 6,* 567-578.

van der Zande, B.M.I., Dhont, J.K.G., Bohmer, M.R., & Philipse, A.P. (2000). Colloidal dispersions of gold rods characterized by dynamic light scattering and electrophoresis. *Langmuir*, 16, (2) 459-464.

Vansanten, R.A. (1984). The Ostwald Step Rule. *Journal of Physical Chemistry,* 88, (24) 5768-5769.

Vemury, S., Kusters, K. A., & Pratsinis, S. E. (1994). Time-Lag for Attainment of the Self-Preserving Particle-Size Distribution by Coagulation. *Journal of Colloid and Interface Science 165*, 53-59.

Viollet, P.L. (1987). The Modeling of Turbulent Recirculating-Flows for the Purpose of Reactor Thermal-Hydraulic Analysis. *Nuclear Engineering and Design*, 99, 365-377.

Vissokov, G. P., Stefanov, B. I., Gerasimov, N. T., Oliver, D. H., Enikov, R. Z., Vrantchev, A. I., Balabanova, E. G., & Pirgov, P. S. (1988). Plasmachemical Technology for High-Dispersion Products. *Journal of Materials Science 23*, 2415-2418.

Viswanathan, R. & Gupta, R. B. (2003). Formation of zinc oxide nanoparticles in supercritical water. *Journal of Supercritical Fluids 27*, 187-193.

Wagner, C. (1961). Theorie der Alterung Von Niederschlagen Durch Umlosen (Ostwald-Reifung). *Zeitschrift fur Elektrochemie 65*, 581-591.

Wagner, W. & Pruss, A. (2002). The IAPWS formulation 1995 for the thermodynamic properties of ordinary water substance for general and scientific use. *Journal of Physical and Chemical Reference Data 31*, 387-535.

Wakashima, Y., Suzuki, A., Kawasaki, S. i., Matsui, K., & Hakuta, Y. (2007). Development of a new swirling micro mixer for continuous hydrothermal synthesis of nano-size particles. *Journal of Chemical Engineering of Japan 40*, 622-629.

Wang, C. X. & Yang, G. W. (2005). Thermodynamics of metastable phase nucleation at the nanoscale. *Materials Science & Engineering R-Reports 49*, 157-202.

Wang, J. Q., Zheng, S. H., Yue, Y. L., Tao, Z. D., & Sun, X. D. (2003). Fabricating transparent yttria ceramics at low temperature. *Journal of Inorganic Materials 18*, 1222-1228.

Wang, T., Smith, R. L., Inomata, H., & Arai, K. (2002). Reactive phase behavior of aluminum nitrate in high temperature and supercritical water. *Hydrometallurgy 65*, 159-175.

Wang, X. & Li, Y. D. (2003). Rare-earth-compound nanowires, nanotubes, and fullerene-like nanoparticles: Synthesis, characterization, and properties. *Chemistry-A European Journal 9*, 5627-5635.

Warheit, D., Sayes, C., & Reed, K. (2009). Nanoscale and Fine Zinc Oxide Particles: Can in Vitro Assays Accurately Forecast Lung Hazards following Inhalation Exposures? *Environmental Science & Technology 43*, 7939-7945.

Weber, W.H., Hass, K.C., & Mcbride, J.R. (1993). Raman-Study of CeO_2 Second Order Scattering, Lattice-Dynamics, and Particle-Size Effects. *Physical Review B*, 48, (1) 178-185.

Weingartner, H. & Franck, E. U. (2005). Supercritical water as a solvent. *Angewandte Chemie-International Edition 44*, 2672-2692.

Weng, X., Boldrin, P., Abrahams, I., Skinner, S. J., & Darr, J. A. (2007). Direct syntheses of mixed ion and electronic conductors $La_4Ni_3O_{10}$ and $La_3Ni_2O_7$ from nanosized coprecipitates. *Chemistry of Materials 19*, 4382-4384.

Weng, X., Boldrin, P., Abrahams, I., Skinner, S. J., Kellici, S., & Darr, J. A. (2008). Direct syntheses of $La_{(n+1)}Ni_{(n)}O_{(3n+1)}$ phases (n = 1, 2, 3 and infinity) from nanosized co-crystallites. *Journal of Solid State Chemistry 181*, 1123-1132.

Weng, X., Cockcroft, J. K., Hyett, G., Vickers, M., Boldrin, P., Tang, C. C., Thompson, S. P., Parker, J. E., Knowles, J. C., Rehman, I., Parkin, I., Evans, J. R., & Darr, J. A. (2009). High-Throughput Continuous Hydrothermal Synthesis of an Entire Nanoceramic Phase Diagram. *Journal of Combinatorial Chemistry 11*, 829-834.

Wooding, A., Kilner, M., & Lambrick, D. B. (1991). Studies of the Double Surfactant Layer Stabilization of Water-Based Magnetic Fluids. *Journal of Colloid and Interface Science 144*, 236-242.

Xia, T., Kovochich, M., Brant, J., Hotze, M., Sempf, J., Oberley, T., Sioutas, C., Yeh, J. I., Wiesner, M. R., & Nel, A. E. (2006). Comparison of the abilities of ambient and manufactured nanoparticles to induce cellular toxicity according to an oxidative stress paradigm. *Nano Letters 6*, 1794-1807.

Xia, Y. N., Yang, P. D., Sun, Y. G., Wu, Y. Y., Mayers, B., Gates, B., Yin, Y. D., Kim, F., & Yan, Y. Q. (2003). One-dimensional nanostructures: Synthesis, characterization, and applications. *Advanced Materials 15*, 353-389.

Yamaguchi, T. (1998). Structure of subcritical and supercritical hydrogen-bonded liquids and solutions. *Journal of Molecular Liquids 78*, 43-50.

Yamashita, T. & Hayes, P. (2008). Analysis of XPS spectra of Fe^{2+} and Fe^{3+} ions in oxide materials. *Applied Surface Science*, 254, (8) 2441-2449.

Yoncheva, K., Guembe, L., Campanero, M., & Irache, J. (2007). Evaluation of bioadhesive potential and intestinal transport of pegylated poly(anhydride) nanoparticles. *International Journal of Pharmaceutics*, 334, (1-2) 156-165.

Yoshimura, M. (1998). Importance of soft solution processing for advanced inorganic materials. *Journal of Materials Research*, 13, (4) 796-802.

Yoshimura, M., Suchanek, W. L., & Byrappa, K. (2000). Soft solution processing: A strategy for one-step processing of advanced inorganic materials. *Mrs Bulletin 25*, 17-25.

Yoshimura, M., Suda, H., Okamoto, K., & Ioku, K. (1994). Hydrothermal Synthesis of Biocompatible Whiskers. *Journal of Materials Science*, 29, (13) 3399-3402.

Zarur, A. J. & Ying, J. Y. (2000). Reverse microemulsion synthesis of nanostructured complex oxides for catalytic combustion. *Nature 403*, 65-67.

Zboril, R., Mashlan, M., Machala, L., & Bezdicka, P. (2003). Iron(III) oxides formed during thermal conversion of rhombohedral iron(III) sulfate. *Material Research in Atomic Scale by Mossbauer Spectroscopy*, 94, 21-30.

Zeng, H.T. & Lacefield, W.R. (2000). XPS, EDX and FTIR analysis of pulsed laser deposited calcium phosphate bioceramic coatings: the effects of various process parameters. *Biomaterials*, 21, (1) 23-30.

Zhang, C., Luo, N., & Hirt, D.E. (2006). Surface grafting polyethylene glycol (PEG) onto poly(ethylene-co-acrylic acid) films. *Langmuir*, 22, (16) 6851-6857.

Zhang, D. L. (2004). Processing of advanced materials using high-energy mechanical milling. *Progress in Materials Science 49*, 537-560.

Zhang, J., Ohara, S., Umetsu, M., Naka, T., Hatakeyama, Y., & Adschiri, T. (2007). Colloidal ceria nanocrystals: A tailor-made crystal morphology in supercritical water. *Advanced Materials*, 19, (2) 203.

Zhang, L., He, R., & Gu, H.C. (2006). Oleic acid coating on the monodisperse magnetite nanoparticles. *Applied Surface Science*, 253, (5) 2611-2617.

Zhang, T., Ge, J., Hu, Y., & Yin, Y. (2007). A general approach for transferring hydrophobic nanocrystals into water. *Nano Letters 7*, 3203-3207.

Zhang, X., Chen, S., Wang, H.M., Hsieh, S.L., Wu, C.H., Chou, H.H., & Hsieh, S. (2010). Role of Neel and Brownian Relaxation Mechanisms for Water-Based Fe3O4 Nanoparticle Ferrofluids in Hyperthermia. *Biomedical Engineering-Applications Basis Communications*, 22, (5) 393-399.

Zhang, Z., Goodall, J. B., Brown, S., Karlsson, L., Clark, R. J., Hutchison, J. L., Rehman, I., & Darr, J. A. (2010). Continuous hydrothermal synthesis of extensive 2D sodium titanate (Na2Ti3O7) nano-sheets. *Dalton Transactions 39*, 711-714.

Zhdanov, V. & Chorny, A. (2011). Development of macro- and micromixing in confined flows of reactive fluids. *International Journal of Heat and Mass Transfer*, 54, (15-16) 3245-3255.

Zhu, H.L. & Averback, R.S. (1996). Sintering processes of two nanoparticles: A study by molecular-dynamics. *Philosophical Magazine Letters*, 73, (1) 27-33.

Appendix 1

This appendix contains supplementary data referred to in Chapter 6. This data is used to supplement some of the discussions presented. Data in this Appendix is divided by the section to which it is referred to in Chapter 6.

A1.1 Effect of Partial Reaction Quenching:

Introduction of a feed shortly after the formation of nanoparticles could reduce the crystallinity or reduce the degree of particle growth providing further insight into the dominant factors affecting the properties of magnetic iron oxides produced using CHFS. Table A.1, provides a summary of the reaction conditions and reactor configurations used to assess the effects of partial reaction quenching alongside characterisation data obtained for the materials produced in each synthesis.

Table 5.1: Summary of the reaction conditions used to assess the effect of partial reaction quenching

ID	**R1 (mm)**	**Q_{sw}: Q_p**	**Q_q**	**T_{mix1}**	**$T_{mix 2}$**	**RT1**	**RT2**	**XRD (nm)**	**TEM Crystallite size (nm)**		**Reaction yield (%)**
									Avg	SD	
MPQ1	21	25:10	10	382	358	0.16	1.66	11.6	9.11	1.89	79.2
MPQ2	21	25:10	30	382	272	0.16	1.53	9.4	8.90	2.03	77.1
MPQ3	21	25:10	50	382	216	0.16	1.28	12.6	8.08	2.30	69.4
MPQ4	75	25:10	10	382	358	0.58	2.27	8.4	9.49	1.78	84.3
MPQ5	75	25:10	30	382	272	0.58	2.09	10.7	7.58	1.67	74.2
MPQ6	75	25:10	50	382	216	0.58	1.75	9.5	8.29	2.10	69.8
MPQ7	125	25:10	10	382	358	0.96	2.84	10.3	8.65	2.16	79.7
MPQ8	125	25:10	30	382	272	0.96	2.62	11.3	8.36	2.07	80.2
MPQ9	125	25:10	50	382	216	0.96	2.19	11.1	9.18	1.65	78.6

Key: R1 = the reactor length between the quench inlet and the preheated water inlet as mm of ¼” tubing, Q_{sw} = the flow rate of preheated water (450 °C), Q_p = the flow rate of precursor (Ammonium iron (III) citrate), Q_q = the quenching flow rate, T_{mix1} = the reaction point temperature (°C), T_{mix2} = the theoretical temperature of the mixture Q_{sw} +Q_p +Q_q determined by enthalpy balance (°C), RT1 = the residence time at T_{mix1} and RT2 = the residence time at T_{mix2}. (All flow rates are quoted as mL min^{-1})

The crystallite phases of the products of reactions MPQ1-9 were evaluated by XRD to assess the effect of partial reaction quenching (data not shown). The rapid reduction of the reaction point temperature even at short reaction residence time (*ca.* 0.16 s) and lowering the reaction point temperature of the mixture to *ca.* 216 °C after the formation of nanoparticles showed no difference in crystallite phase as determined by XRD. Diffraction data obtained for samples MPQ1-9 were all identified as spinel oxides in good agreement ICDS card no. 082234 and 79196 for magnetite and maghemite, respectively. Application of the sheerer equation to the diffraction data [(311) reflection] gave results consistent with those presented previously as summarised in table A1, suggesting that the particle formation steps are very rapid and are dominated predominantly by particle nucleation and little or no particle growth occurs after *ca.* 0.16s residence time.

TEM was used to assess the crystallite size and relative sample polydispersity and crystallite sizes determined from the measurement of *ca.* 300 crystallites are summarised in table A1 (images not shown). Typically, mean crystallite sized determined by the two methods were comparable (TEM and XRD), providing further evidence for a single crystalline phase for the materials. Figure A1.1 shows the TEM determined crystallite size and polydispersity (SD) plotted as a function of quench rate and grouped by residence time. As can be seen There was little apparent variation in crystallite size even at reaction residence times of 0.16- 0.96 s and temperatures of the quenched mixture between 358 and 216°C. It is suggested that complete reaction and crystallization of magnetite occurs within the CHFS system in less than 0.16 s.

The magnetic properties of samples MPQ 2, 5 and 8 were measured to assess the effect of partial reaction quenching as shown in figure A1.2. Slight variation in the values of saturation magnetization were observed for samples MPQ2, 5 and 8 as 53.2, 62.5 and 66.3 emu g^{-1}, respectively. The observed variation in magnetisation is consistent with increasing residence time residence time although data presented later in Chapter 6 showed this variance was within the bounds of latent process variation (figure 6.20). However, the spread of magnetisation values were significantly lower than those observed in the extremes of magnetite synthesised in chapter 5. Calculation of the effective ferromagnetic diameter from the magnetisation curves gave values consistent with those presented for samples identified as magnetite in chapter 5. Similarly, with the discussion presented in chapter 5 the ferromagnetic diameters calculated from the magnetisation data were smaller than the crystallite size obtained from both TEM and XRD with diameters (polydispersity) of 6.23 (0.348), 7.01 (0.298) and 7.12 (0.341) nm for samples MPQ2, 5 and 8, respectively. The contribution of paramamagentic like susceptibility in the samples was shown to be nearly constant, increasing slightly as expected with decreasing saturation magnetisation. This observation suggests a degree of magnetic frustration is evident in the samples as discussed further in Chapter 5. Although, under the scope of further observation it can be concluded that particle reaction quenching had little effect on the magnetic properties of the reaction products.

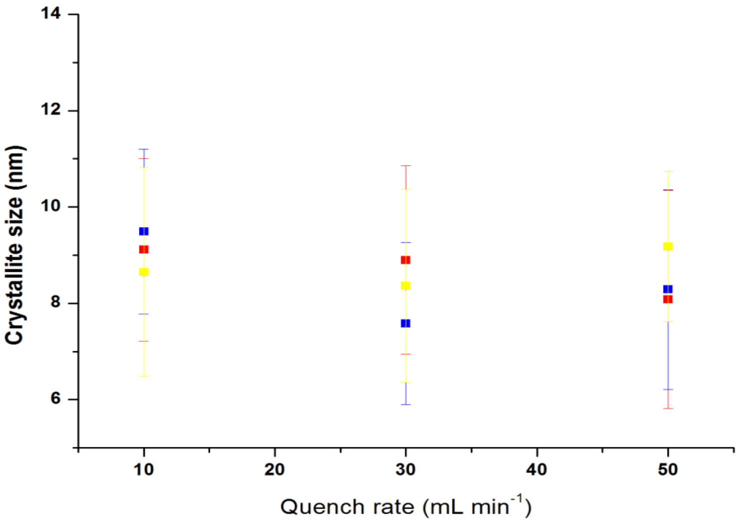

Figure A1.1: Correlations between crystallite size and standard deviation (error bars) plotted against partial reaction quenching at different residence times (blue = 0.16 s, red = 0.58 , yellow = 0.96).

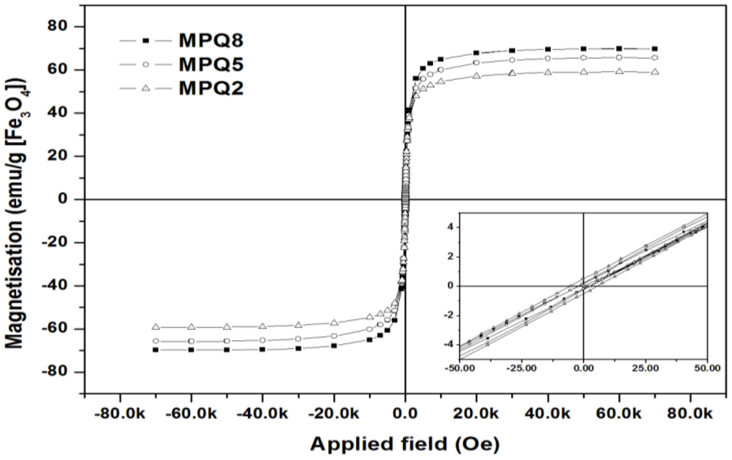

Figure A1.2: Magnetisation curves of samples MPQ2, 5 and 8 (inset shows an expanded plot showing the near 0 Oe region).

A1.2 Surface functionalization of magnetite nanoparticles using citric acid in a high flow regime

Under the high flow regime temperature measurements revealed different flow patterns within the two-step reaction point under different flow regimes. The effect of this difference in flow regime was investigated to assess differences in relation to the capacity to produce surface functionalised nanoparticles. The materials reported in this Appendix section are summarised in table A1.2. To further assess the effects of processing condition on surface functionalisation in the modified CHFS process materials produced under a high flow regime (Q_{sw}+Q_p = 35 mL min^{-1}) similar to that used initially for the synthesis of magnetite nanoparticles in Chapter 5 were compared to those obtained in samples CAO1 - 22 (Q_{sw}+Q_p = 15). Under a higher flow regime a different optimisation condition was observed. This section details the characterisation data of the samples identified in table A1.2. Samples presented in this section are identified by the series HCAO1-12.

Table A1.2: Summary of the reaction condition and characterisation data for citric acid coated magnetite produced using CHFS system 2 at the flow rates of Q_{sw} =25 and Q_p=10.

	R1	**Qq**	**T_{mix2}**	**[CA] (wt%)**	**Fe:CA**	**RT2**	**XRD (nm)**	**TGA data**		**Hydrodnamic diameter (nm)**		**TEM data**		**TEM (molecules/nm^{-2})**
								Wieght loss (%)	**molecules nm^{-2}**	**Dh (PDI)**	**PDI**	**Mean**	**SD**	
HCAO1	75	10	358	0.5	0.3	2.21	8.9	7.02	1.29	172	0.262	-	-	-
HCAO2	75	20	312	0.5	0.7	2.20	9.2	10.15	1.96	102	0.295	5.64	1.28	1.17
HCAO3	75	30	272	0.5	1.1	2.04	8.7	8.64	1.55	95	0.32	10.16	3.00	1.80
HCAO4	75	40	241	0.5	1.5	1.87	9.3	5.19	0.99	211	0.293	-	-	-
HCAO5	75	10	358	1.0	0.7	2.21	7.4	5.52	0.84	91	0.178	8.84	3.28	1.00
HCAO6	75	20	312	1	1.5	2.2	8.6	15.96	2.84	73	0.232	8.94	3.09	2.93
HCAO7	75	30	272	1	2.3	2.04	7.4	22.36	2.67	75	0.143	5.60	1.20	2.57
HCAO8	75	40	241	1	3.1	1.87	11.6	-	-	74	0.199	-	-	-
HCAO9	75	10	358	2	1.5	2.21	9.5	15.05	2.65	136	0.222	-	-	-
HCAO10	75	20	313	2	3.1	2.2	9.2	15.76	2.12	79	0.183	8.60	3.09	2.78
HCAO11	75	30	272	2	4.7	2.04	8.2	5.59	0.44	72	0.149	6.70	2.53	2.3
HCAO12	75	40	241	2	6.3	1.87	6.5	-	-	138	0.241	-	-	-

Key: R1 = the reactor length between the quench inlet and the preheated water inlet as mm of ¼” tubing, Q_{sw} = the flow rate of preheated water (450 °C), Q_p = the flow rate of precursor (Ammonium iron (III) citrate), Q_q = the quenching flow rate, T_{mix1} = the reaction point temperature (°C), T_{mix2} = the theoretical temperature of the mixture Q_{sw} +Q_p +Q_q determined by enthalpy balance (°C), RT1 = the residence time at T_{mix1} and RT2 = the residence time at T_{mix2}. (All flow rates are quoted as mL min^{-1})

XRD patterns (figure A1.3) of the materials produced in runs HCAO1-10 suggest that all products are well crystallised and have a cubic inverse spinel structure (space group Fd3m) known for bulk magnetite and maghemite (ICDS 082234 and ICDS 79196), respectively (Appendix 1). TEM images of selected samples produced in the series HCAO1-12 are shown in figure A1.4 showing similar degrees of dispersion as shown in figure 6.5 (Chapter 6). The crystallite size measured for samples HCAO1-12 (*ca.* 5.6 - 10.4 nm) was smaller than those observed for materials produced in runs CAO1-24 (*ca.* 11 - 15 nm) and are summarised in table A1.2. The reduced crystallite size produced in these reactions is tentatively attributed to latent process variation rather than an effect of the capping process. However, correspondingly greater weight loss attributed to the thermal decomposition of organic species was measured in TGA (as shown in figure A1.5a) and showed all expected endotherms in the DSC trace (as shown in figure A1.5b), which ultimately yielded saturation grafting densities of *ca.* 2.6-2.9 CA / nm^2 consistent with the saturation grafting density calculated for samples CAO4-12. Achieving similar CA grafting densities at shorter residence times as discussed further in Chapter 6, suggests differences in the degree of mixing between Q_{sw} + Q_p (containing the nascent nanoparticles) and Qq (citric acid feed) which in a lower flow rate limited the rate of citrate diffusion to the nascent particle surface. The Hydrodynamic diameters (measured using DLS)for samples HCAO1-12 are presented in figure A1.6a, and showed similar dispersion properties to those presented in figure 6.11 (Chapter 6) and were shown to be consistent with the grafting density determined for each of the samples. Zeta-potential measurements characterised the samples showing CA grafting densities >1 CA / nm^2 as stable dispersions with magnitudes > - 30 mV similar to those presented for samples CAO4-12. The magnitude of the zeta-potential was shown to transition as expected with CA grafting density (figure A1.6b). Titration of this sample series confirmed an electrostatic mechanism of particle stabilisation, a reduction in the magnitude of the samples zeta-potential around pH 6 further suggests a similar coordination of citric acid to the particle surface as discussed further in Chapter 6.

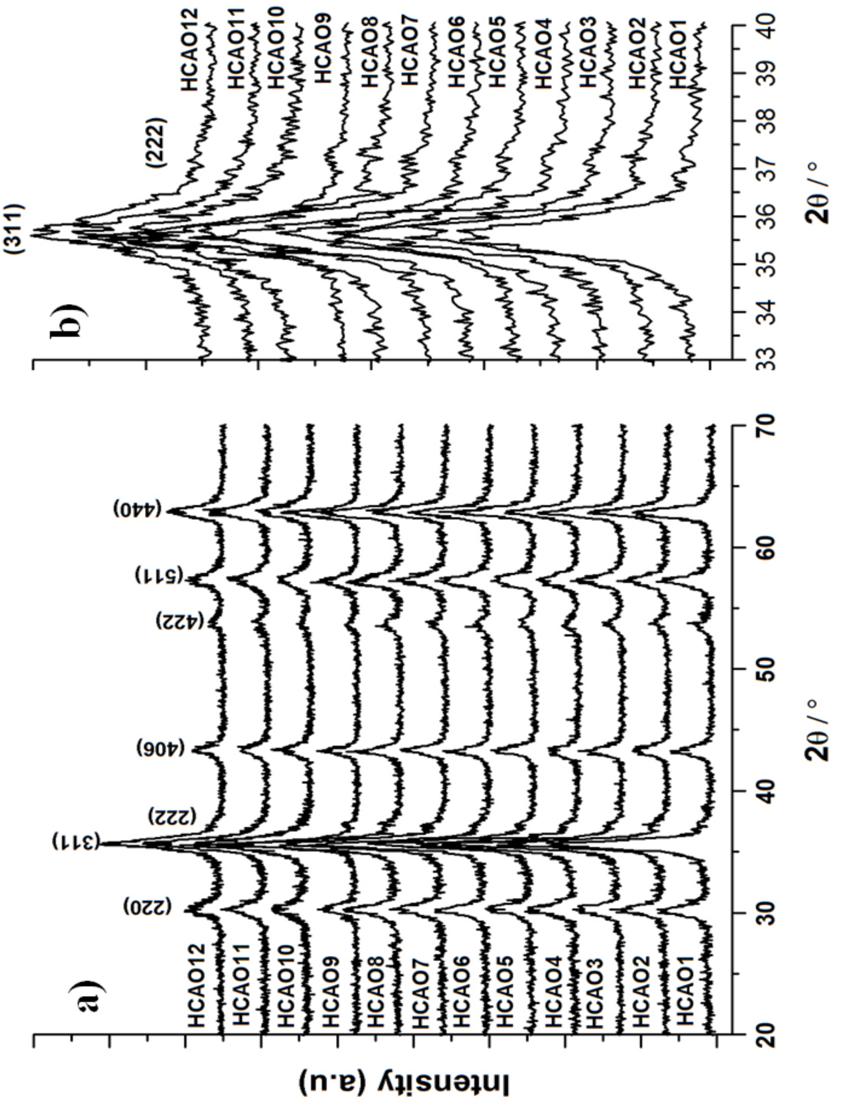

Figure A1.3: XRD patterns obtained for magnetite nanopaticles synthesised in **a)** experimental runs HCAO1-12 (inset shows a close view of the 311 reflection in magnetite) The miller indicies of each reflection are presented in each figure (inset shows an expanded view of the 311 reflection in magnetite for each sample). The data shows the similarlty in crystallite size between samples.

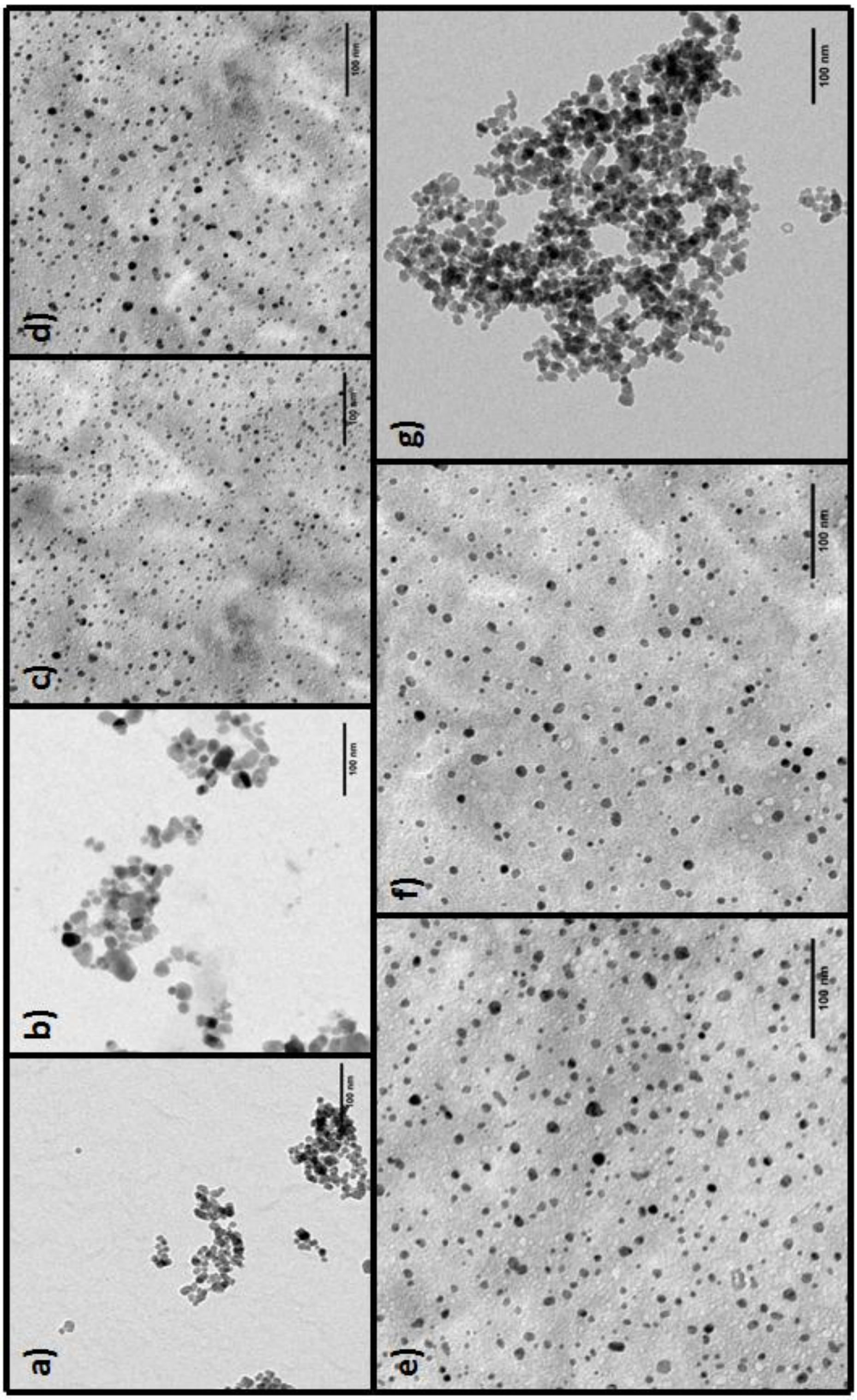

Figure A1.4: TEM images of the particles synthesised in the high flow regime as summarised in table A1.2; **a)** HCAO2 **b)** HCAO3 **c)** HCAO5 **d)** HCAO6 **e)** HCAO7 **f)** HCAO10 **g)** HCAO11.

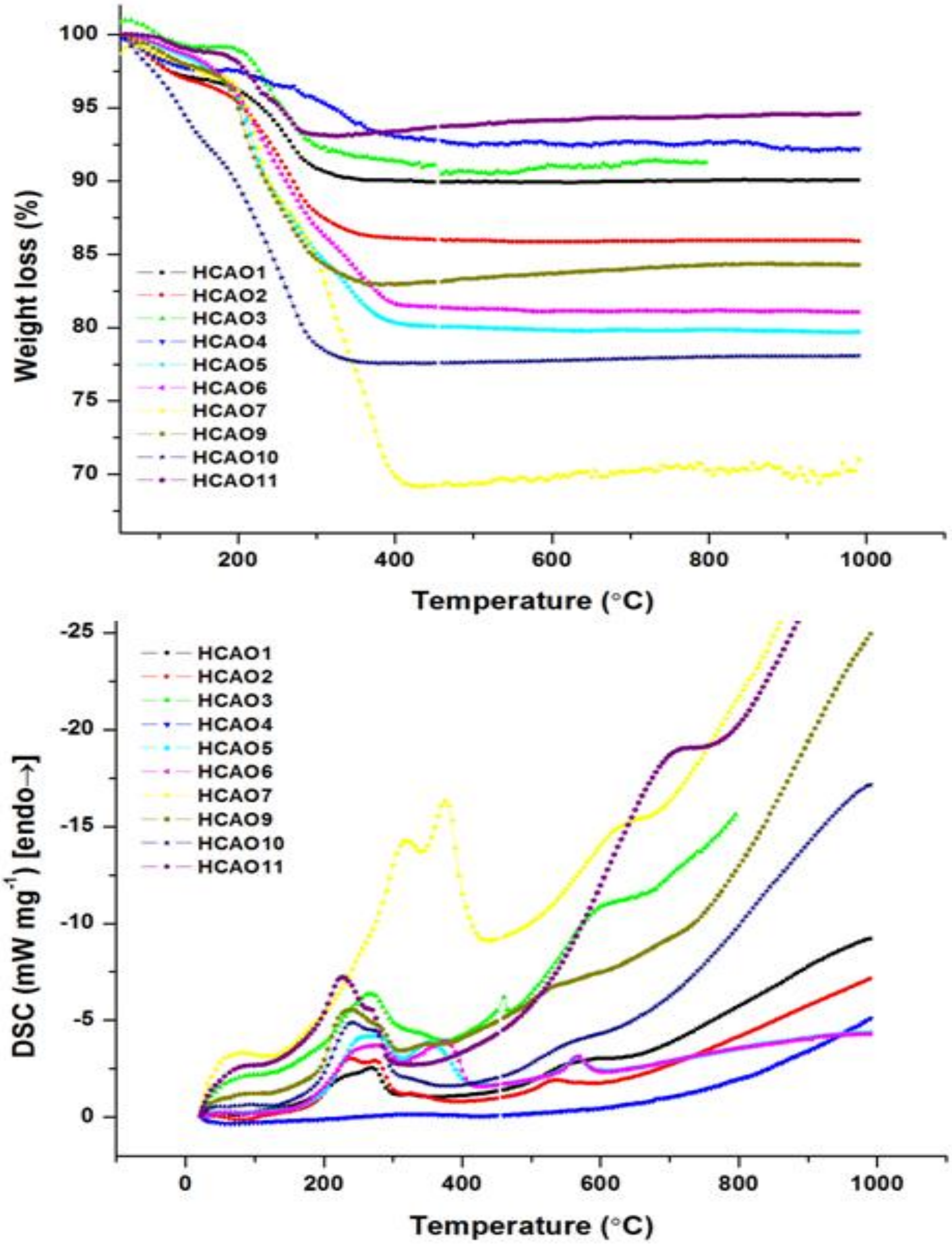

Figure A1.5: **a)** TGA data obtained for sample HCAO1 - 12 **b)** DSC traces of samples HCAO 1-12

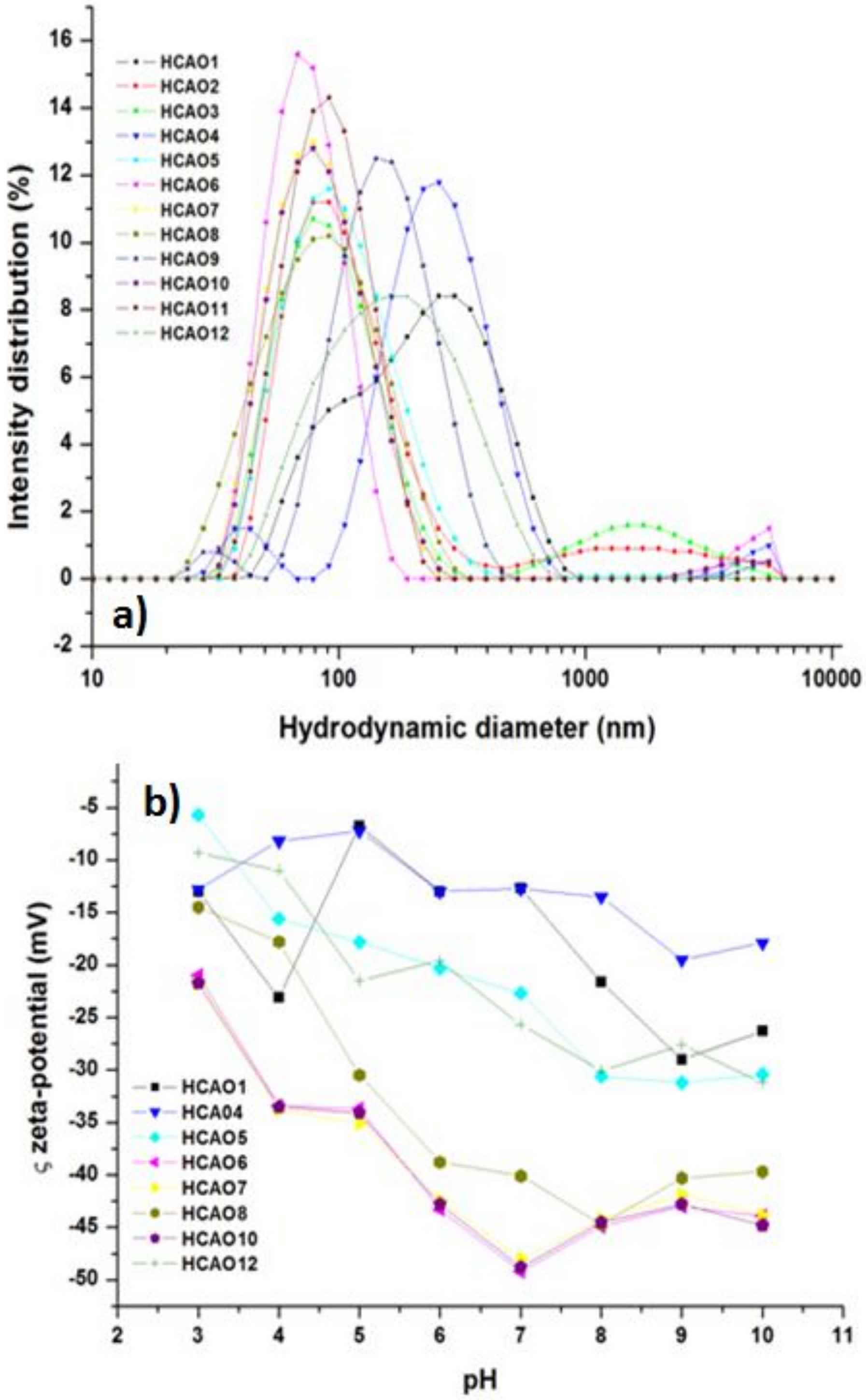

Figure A1.6: a) Grouped DLS data showing the difference in hydrodynamic diameter of samples HCAO1 - 12, plotted as hydrodynamic diameter distributions and **b)** Zeta-potential titrations of HCAO samples (measurement standard deviations were typically *ca.* ±3 mV and have been omitted for clarity)

A1.3 Synthesis and Characterisation data for Magnetic Hyperthermia

Table A1.3 provides a summary of the synthesis details and characterisation data used in the discussion resented in Chapter 6 section 6.3.4. Showing the sapread of reaction conditions used to evaluate the potential of citric acid coated magnetite produced using CHFS as mediators for magnetic hyperthermia. All calorimetric measurements were performed on samples which formed ferrofluids at particle concentrations of 50 mg mL^{-1} and prepared as described in Chapter 2 Section 2.13.

Table A1.3: Synthesis and characterisation details of ferrofluids evaluated for magnetic hyperthermia; Q_{sw} = the flow rate (mL min^{-1}) of supercritical water, Qp = the flow rate of precursor (Ammonium iron (III) citrate, 0.066 M), Qq = the flow rate of citric acid solution, T_{mix1} = the reaction point temperature (°C), T_{mix2} = the mixture temperature of $Q_{sw} + Q_p + Q_q$ (°C), Fe:CA = the ratio of iron to citric acid used in the synthesis, R_{T1} = the residence time of particle formation prior to the introduction of Q_q (s), SAR= the specific absorption rate of a ferrofluid sample, ILP = Intrinsic loss power and Cs = the crystallite size determined by application of the Scherer equation to the (311) reflection of magnetite.

Q_{sw}:Q_p	Q_q	T_{mix1}	T_{mix2}	CA (wt %)	Fe:CA	R_{T1}(s)	SAR (W g^{-1})	ILP (nH kg^{-1} m^{-2})	C_S (nm)
25:10	30	382	278	0.25	0.59	0.94	0.00	0.00	8.24
25:10	30	382	278	0.5	1.18	0.94	0.00	0.00	9.23
25:10	30	382	278	0.75	1.78	0.94	0.00	0.00	9.35
25:10	30	382	278	1	2.36	0.94	0.00	0.00	8.79
25:10	20	382	316	1	1.57	0.94	0.00	0.00	9.88
25:10	30	382	278	1	2.36	0.94	0.00	0.00	8.75
25:10	40	382	247	1	3.15	0.94	0.00	0.00	7.68
25:10	20	382	316	0.5	0.78	0.94	23.67	0.50	10.24
25:10	20	382	316	0.75	1.18	0.94	20.45	0.38	10.43
25:10	20	382	316	1	1.57	0.94	14.67	0.23	9.46

25:10	10	382	360	0.5	0.19	0.94	7.79	0.17	10.46
25:10	10	382	360	0.75	0.39	0.94	5.38	0.12	10.35
25:10	10	382	360	1	0.59	0.94	7.84	0.17	9.85
25:10	10	382	360	2	1.57	0.94	18.50	0.40	12.35
25:10	15	382	338	0.5	0.59	0.94	0.64	0.01	8.46
25:10	20	382	316	1	1.57	0.19	0.00	0.00	9.76
25:10	20	382	316	2	3.15	0.19	0.00	0.00	8.43
25:10	30	382	278	0	0	0.19	0.00	0.00	9.42
25:10	30	382	278	0.5	1.18	0.19	0.00	0.00	9.35
25:10	30	382	278	1	2.36	0.19	0.00	0.00	9.83
25:10	30	382	278	2	3.15	0.19	0.00	0.00	10.27
20:08	20	382	296	1	1.97	1.18	11.17	0.24	10.24
20:08	24	382	278	1	2.36	1.18	12.73	0.27	9.68
20:12	18.3	377	286	1	1.2	1.57	11.32	0.24	10.35
20:12	13.7	377	308	1	0.9	1.57	42.26	0.91	10.25
20:12	18.2	377	284	1	1.19	1.57	20.04	0.43	10.37
20:12	22.86	377	266	1	1.5	1.57	9.06	0.19	10.45
20:15	18.2	365	254	1	0.95	1.72	2.04	0.04	10.32
20:20	20	338	247	1	0.78	1.77	0.00	0.00	8.97
15:08	10	379	316	1	0.98	1.94	26.31	0.56	7.89
15:08	15	379	284	1	1.47	1.94	24.22	0.52	13.00
15:08	20	379	257	1	1.97	1.94	42.40	0.91	12.24
15:08	25	379	239	1	2.46	1.94	26.14	0.56	11.57
15:08	30	379	219	1	2.95	1.94	25.46	0.55	12.57
15:08	40	379	203	1	3.94	1.94	23.42	0.50	12.35
10:5	10	380	287	1	1.57	2.78	29.62	0.64	12.87

10:5	15	380	247	1	2.36	2.78	34.66	0.74	12.06
10:5	20	380	218	1	3.15	2.78	22.57	0.48	11.88
10:5	25	380	195	1	3.94	2.78	29.60	0.63	11.93
10:5	30	380	176	1	4.73	2.78	32.77	0.70	11.35
10:5	35	380	161	1	5.52	2.78	29.24	0.63	11.57
15:8	10	379	316	1	0.98	3.41	17.45	0.37	12.35
15:8	15	379	284	1	1.47	3.41	5.72	0.12	11.79
15:8	20	379	257	1	1.97	3.41	25.32	0.54	10.35
15:8	25	379	234	1	2.46	3.41	30.24	0.65	12.35
15:8	30	379	216	1	2.95	3.41	30.06	0.64	11.46
10:5	10	380	287	1	1.57	4.89	13.78	0.30	11.57
10:5	15	380	247	1	2.36	4.89	23.49	0.50	11.46
10:5	20	380	218	1	3.15	4.89	19.28	0.41	13.48
10:5	25	380	195	1	3.94	4.89	34.70	0.74	12.79
10:5	30	380	176	1	4.73	4.89	28.07	0.60	12.55
10:5	10	360	262	1	0.98	6.15	39.50	0.85	12.35
10:5	15	360	229	1	1.47	6.15	31.03	0.67	14.36
10:5	20	360	203	1	1.97	6.15	47.70	1.02	13.68
10:5	25	360	183	1	2.46	6.15	22.18	0.48	12.46
10:5	30	360	167	1	2.95	6.15	31.70	0.68	11.24
10:5	20	380	218	5	20.73	2.78	0.00	0.00	10.27
10:5	30	380	176	5	31.1	2.78	0.00	0.00	10.23
10:5	20	380	218	3	12.44	2.78	0.00	0.00	9.23
10:5	30	380	176	3	18.66	2.78	0.00	0.00	7.93
10:5	15	380	247	3	9.33	2.78	0.00	0.00	10.24
10:5	20	380	218	2	8.29	2.78	0.00	0.00	10.23

10:5	30	380	176	2	12.44	2.78	0.00	0.00	11.03
10:5	15	380	247	2	9.33	2.78	7.48	0.16	12.64
10:5	10	380	287	2	4.14	2.78	7.53	0.16	13.48
10:5	10	380	287	3	6.22	2.78	10.08	0.22	11.24
10:5	15	380	247	1	1.57	2.78	4.41	0.09	12.35
10:5	15	380	247	1	1.57	2.78	17.02	0.36	14.57
10:5	15	380	247	1	1.57	2.78	17.14	0.37	11.36
10:5	25	380	195	1	3.94	2.78	23.95	0.51	13.47
10:5	25	380	195	1	3.94	2.78	28.47	0.61	13.46
10:5	25	380	195	1	3.94	2.78	22.38	0.48	12.35
10:5	15	380	241	1	1.57	7.96	32.77	0.63	10.57
10:5	20	380	211	1	1.57	7.96	29.24	0.30	10.68
10:5	25	380	187	1	1.57	7.96	17.45	0.48	11.48
10:5	30	380	169	1	1.57	7.96	5.72	0.35	11.28
10:8	15	360	222	1	1.57	9.94	25.32	0.64	13.27
10:8	20	360	196	1	1.57	9.94	30.24	0.73	14.68
10:8	25	360	179	1	1.57	9.94	30.06	0.59	12.38
10:8	30	360	159	1	1.57	9.94	13.78	0.79	14.57
10:5	10	380	222	2	1.57	7.96	23.49	0.70	11.73
10:5	10	380	196	1	1.57	7.96	19.28	0.63	11.85
10:5	20	380	179	1	1.57	7.96	34.70	0.37	12.99
10:5	30	380	159	1	1.57	7.96	28.07	0.12	11.77
10:5	10	380	222	2	1.57	9.63	39.50	0.54	11.78
10:5	20	380	222	2	1.57	9.63	31.03	0.65	11.85
10:5	10	380	196	1	1.57	9.63	47.70	0.64	12.88
10:5	20	380	179	1	2.45	9.63	22.18	0.30	11.51

10:5	30	380	159	1	3.45	9.63	20.32	0.50	11.04
10:5	10	380	287	2	8.88	2.78	17.09	0.37	12.99
10:5	20	380	218	1	8.88	2.78	14.82	0.32	11.77
10:5	15	380	247	1	6.66	2.78	17.80	0.38	11.78
10:5	10	380	287	1	4.44	2.78	18.23	0.39	11.85
10:5	10	380	287	1.5	6.66	2.78	22.85	0.49	12.88

Appendix 2

The purpose of this Appendix is to provide data supporting the discussion presented in Chapter 7. Figures are identified by legends which are referred to within the text of Chapter 7.

Figure A2.1 shows XRD patterns of YOOH phosphor nanoparticles produced with different concentration of hydrogen peroxide in the auxiliary feed showing an relative increase in the concentration of oxidising species in the reaction had no influence on material phase.

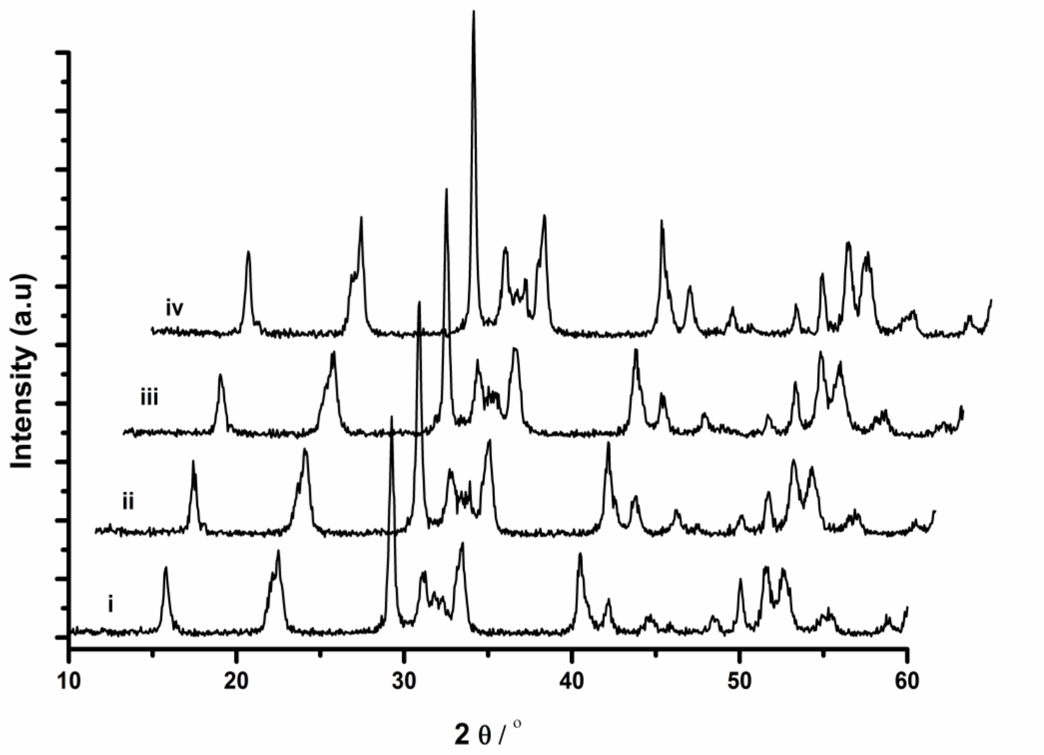

Figure A2.1: XRD patterns obtained for YOOH phosphors synthesised with the addition of hydrogen peroxide to the metal salt solution and 1.0 M KOH in the auxiliary feed, **i)** 0.2 M, **ii)** 0.4 M, **iii)** 0.6 M, **iv)** 0.8 M hydrogen peroxide added to the auxiliary feed.

Figure A2.2 shows TEM images of $(Y_{0.96}Eu_{0.04})OOH$ nanoparticle annealed for durations of 60, 180, 300, 600, 1200 and 1800 s at 550°C. These materials were converted from $(Y_{0.96}Eu_{0.04})OOH$ to $(Y_{0.96}Eu_{0.04})_2O_3$. Phase identifications made through XRD showed that annealing times < 300 seconds are not suitable to completely dehydrate the material. Figure A2.3 shows the evolution of crystallite size determined from *ca.* 300 particles observed in figure A2.2 as a box plot to clearly show coarsening events occurring in the samples.

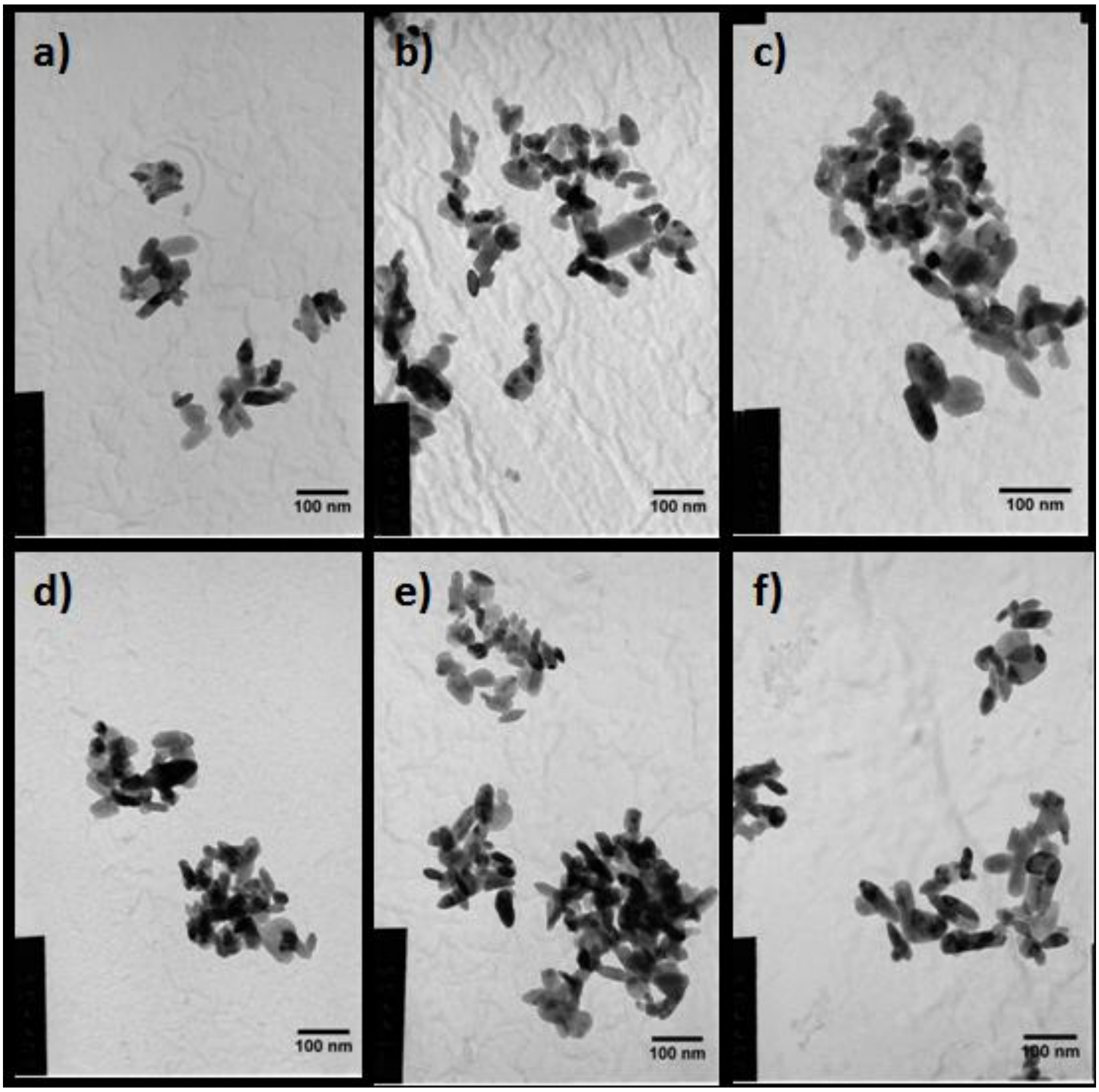

Figure A2.2: TEM images of $(Y_{0.96}Eu_{0.04})OOH$ phosphor nanoparticles heat treated at 500 °C for **a)** 60 s **b)** 180 s **c)** 300 s **d)** 600 s **e)** 1200 s **f)** 1800 s (Images were captured using JEOL 100CX)

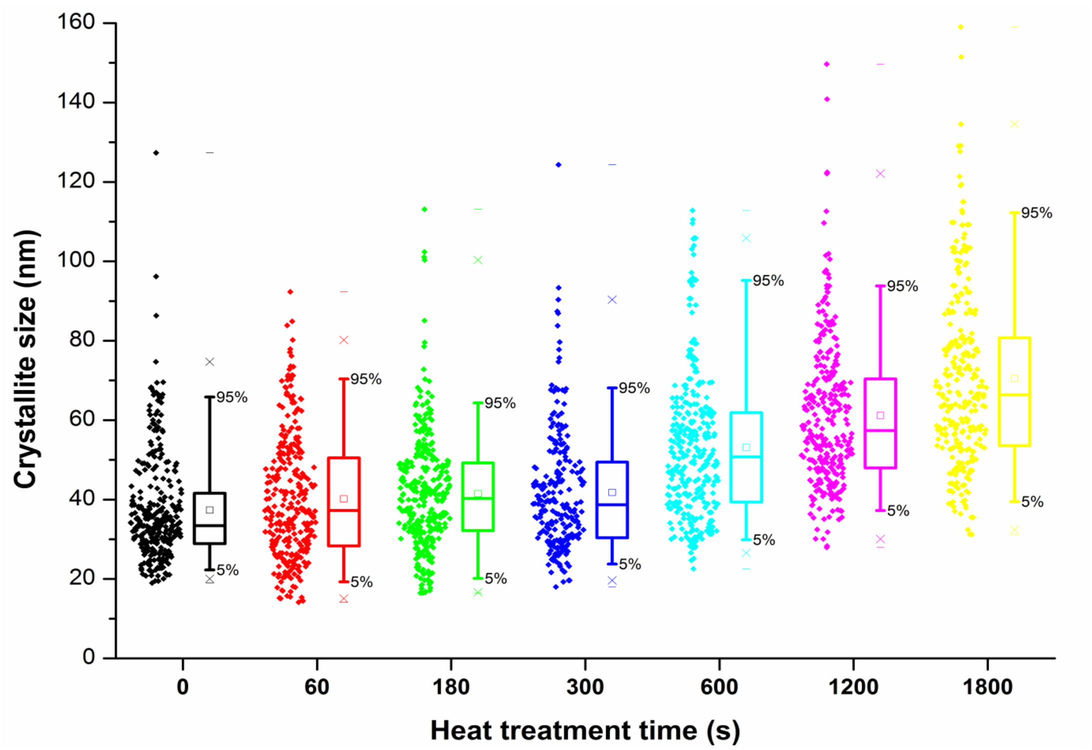

Figure A2.3: Box plot representing the particle size distributions measured from Figure A2.2 as a function of heat treatment time.

Figure A6.4 shows a schematic of the carbodiimide coupling reaction used to graft mono end NH_2-PEG molecules of 2 and 5 kDa to the surface of citric acid coated $(Y_{0.96}Eu_{0.04})$ OOH nanoparticles.

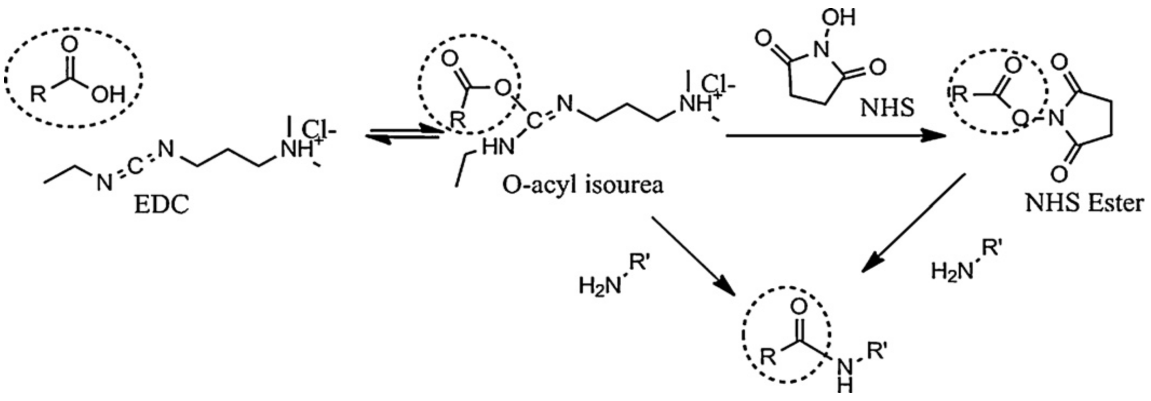

FigureA6.4 : Schematic representation of the carbodiimide coupling reaction used to functionalise the surface of citric acid coated $(Y_{0.96}Eu_{0.04})$ OOH nanoparticles.

To demonstrate the potential application of citric acid coated $(Y_{0.96}Eu_{0.04})OOH$ and $(Y_{0.96}Eu_{0.04})_2O_3$ NPs as fluorescent probes they were visualised under conditions analogous to a typical in-vitro fluorescence imaging experiment. Particles were sparsely dispersed on cover-glass and visualised using 470 nm excitation / 620 nm emission and resolvable fluorescence from both dispersions of particles was observed as shown in figure 7.20). The diameter of fluorescence signals was typically in the order of 1-2 pixels (*ca.* 1 pixel = 270 nm) and histograms representing the diameter of *ca.* 50 down converted fluorescence signals are shown in figure A2.5. These observations suggest that most of the luminescence observed is from single citric acid coated-coated NPs when the approximated wave spread function of the microscope is considered ($\lambda/2$ =320 nm).

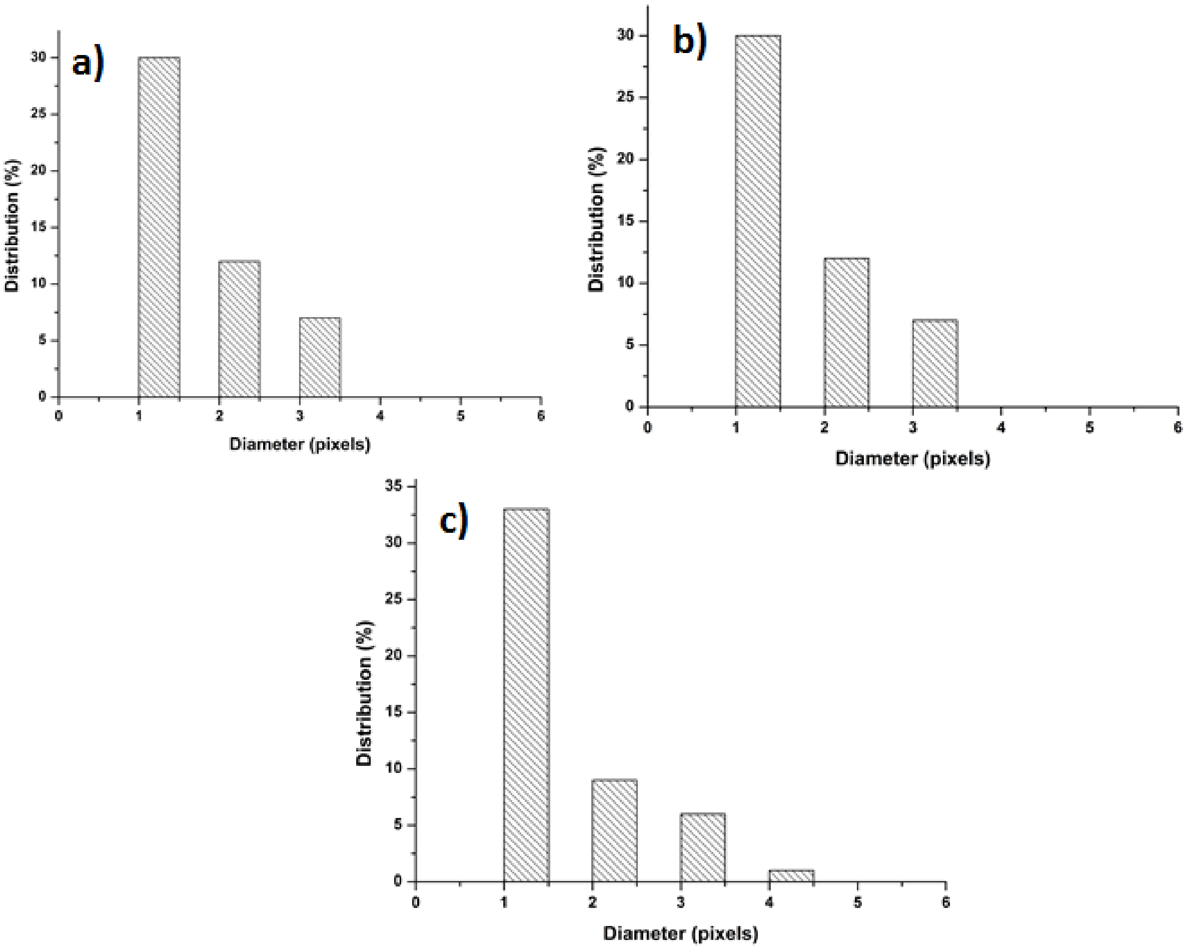

Figure A2.5: Histograms based distribution of down converted fluorescence from 50 down-converted luminescent spots **a)** $(Y_{0.96}Eu_{0.04})OOH$-CA **b)** CA-$(Y_{0.96}Eu_{0.04})OOH$ and **c)** $(Y_{0.96}Eu_{0.04})_2O_3$-CA.

Appendix 3

Scale up of nanoparticle synthesis using CHFS

This appendix contains supplementary data and discussion relevant to the topics addressed in chapter 8. The data is presented in the order in which it is referred to within the text of chapter 8.

A3.1: Synthesis and Characterisation of ZnO Nanoparticles (Chapter 8, Section 8.3.2)

Figure A3.1 shows a selection of TEM images and associated indexed SAED patterns of ZnO synthesised using the pilot scale CHFS processes confirming the phase of the material under observation. Figure A3.2 shows the UV-VIS absorption spectra and KM functions calculated for the samples produced in Section 8.3.3 which assessed the mass based scale up of ZnO nanoparticle synthesis.

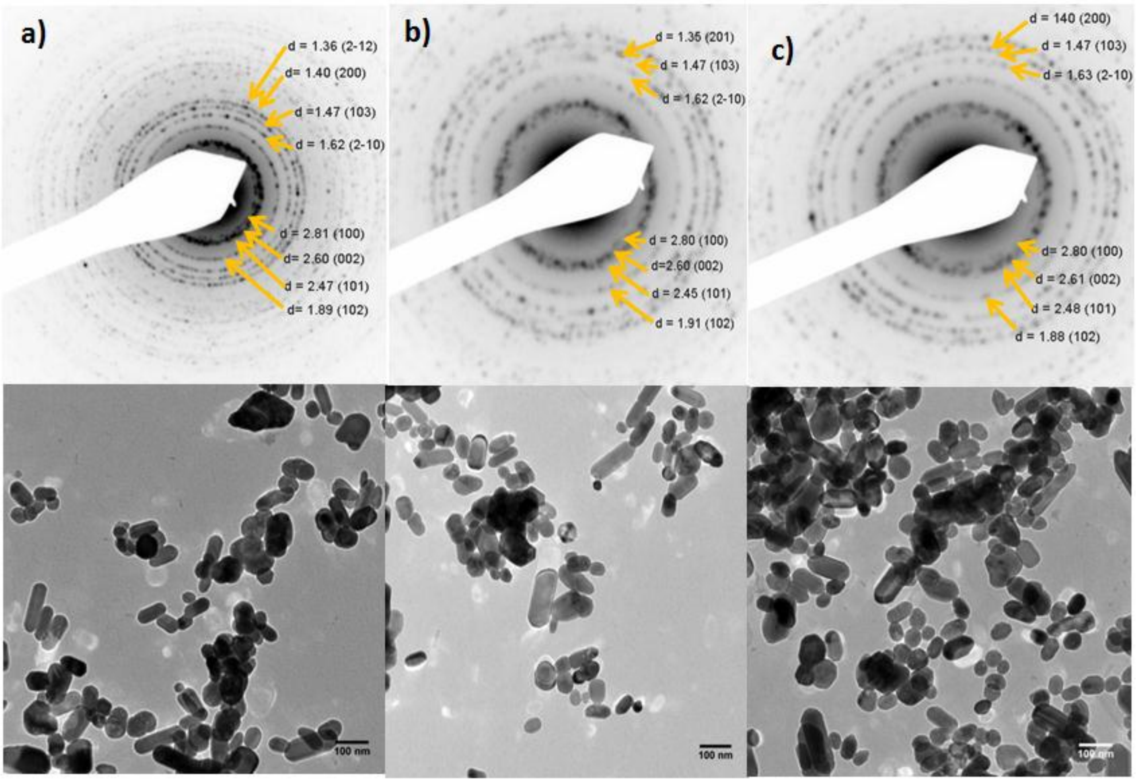

Figure A3.1: Indexed SAED patterns of ZnO synthesised using the pilot scale CHFS process using a) 0.2M $Zn(NO_3)_2$ [0.1M700] b) 0.6M $Zn(NO_3)_2$ [0.2M700] c) 0.9 M $Zn(NO_3)_2$ [0.9M700] alongside images representative of the particles produced in each synthesis confirming the morphology change of ZnO as a function of precursor concentration.

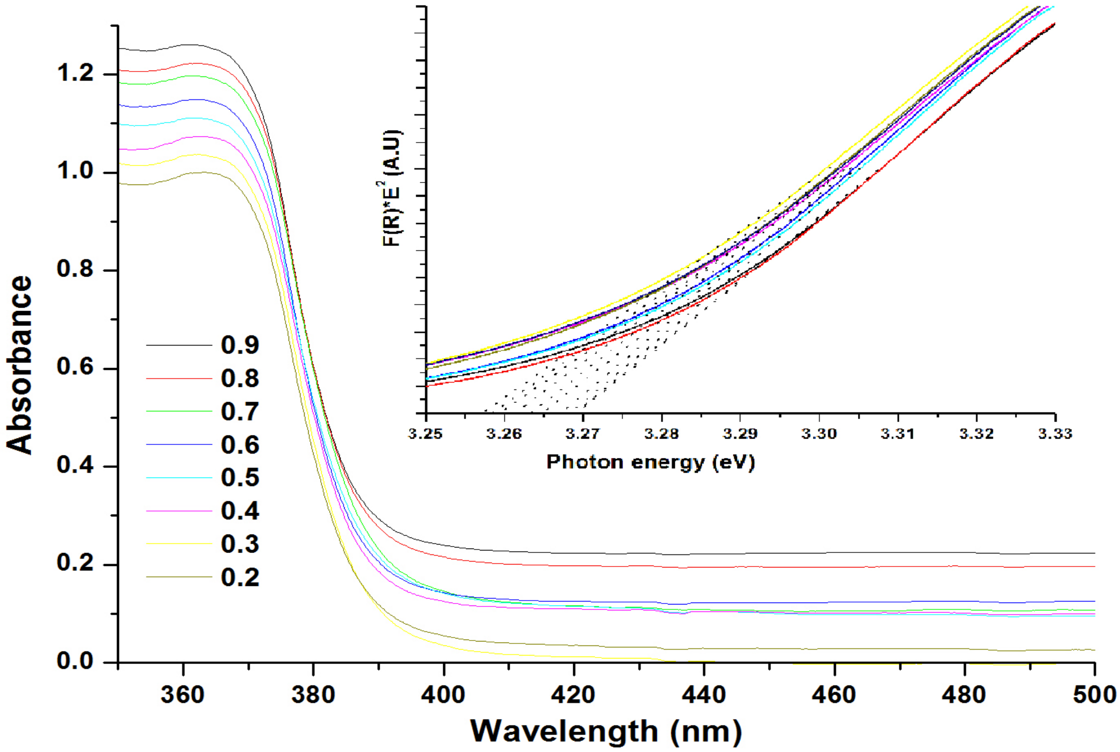

Figure A3.2: Normalised UV-VIS spectra of ZnO nanoparticles produced as a function of precursor concentration. Figure inset, shows the KM function of the data (Both figure and inset have a common key)

Figure A3.3 shows a further analysis of the growth of ZnO nanoparticles produced in Section 8.3.3. This data severs to confirm that the growth direction of the nanoparticles was consistent in the sample series.

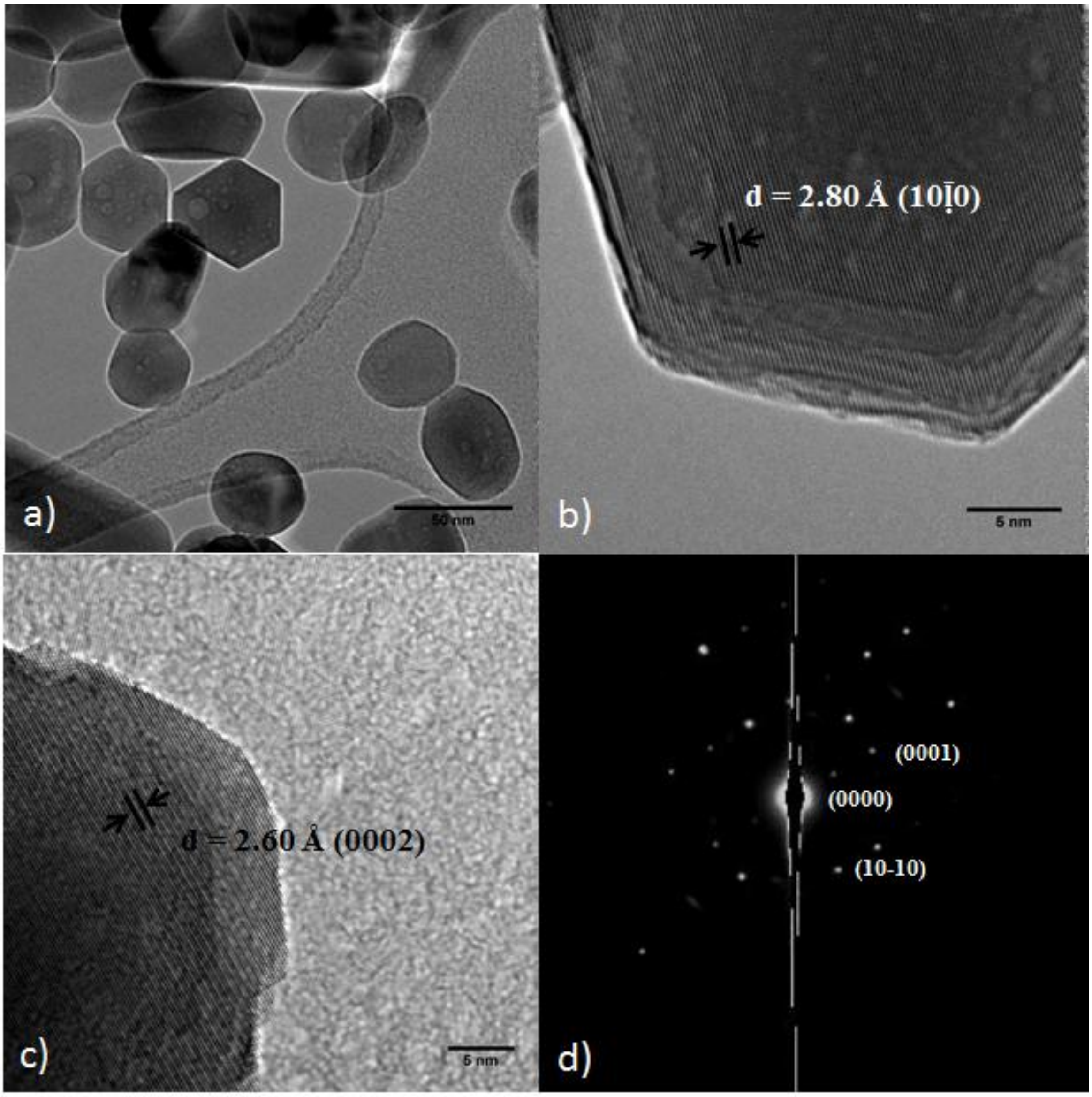

Figure A3.3: Compilation of HREM images of the ZnO sample produced in PPZnO10 **a)** Low magnification image representative of the particle population **b)** HREM image of the hexagonal ZnO nanoparticle **c)** HREM image of the tip of the rod like particle **d)** Indexed electron diffraction pattern of the single crystallite presented in image [c] the spot pattern could be indexed to the (0002) and $(10\bar{1}0)$ planes.

A3.2: Characterisation data for Magnetite Nanoparticles:

This Appendix section serves to present data for the scale up of magnetite nanoparticle synthesis using the pilot scale CHFS process. The data forms a data set used for the comparison of magnetite nanoparticles produced at different volumetric scale up and mass based scale up ratios as presented in Chapter 8. Table A3.2 provides a summary of the synthesis conditions used (alongside sample identifiers) and a summary of the characterization data obtained for each sample. Figure A3.4 shows the XRD patterns of samples PPM1-9 which indicate that the products are well crystallised and have a cubic inverse spinel structure (space group Fd-3m) known for bulk magnetite and maghemite (ICDS 082234 and 79196, respectively). Application of the Scheerer equation to the (311) reflection gave crystallite size estimates which ranged from 9.4 – 17.4 nm (as summarised in table A3.2) consistent with size estimates for samples obtained previously (Chapter 5).

Table A3.2: Summary of the synthesis conditions and characterisation data obtained for magnetite nanoparticles produced at different volumetric scale up ratios.

	Flow rates (mL min^{-1})		Precursor (M)	T_{mix1} (°C)	RT (s)	C_s (nm)	BET surface area		TEM data		Yield (%)
	Q_{sw}	Q_p					S.A (m^2 g^{-1})	ESD (nm)	Mean	SD	
PPM1	400	360	0.066	348	1.17	10.1	85.0	13.69	12.9	4.30	87
PPM2	400	360	0.1	348	1.17	9.5	95.7	12.17	13.1	3.88	82
PPM3	400	360	0.2	348	1.17	9.6	89.4	13.02	15.1	4.93	85
PPM4	300	270	0.066	348	1.55	11.6	73.3	15.88	16.5	4.59	87
PPM5	300	270	0.1	348	1.55	9.1	90.1	12.92	14.5	4.36	83
PPM6	300	270	0.2	348	1.55	9.9	97.3	11.96	14.6	5.78	80
PPM7	200	180	0.066	348	2.30	9.3	70.1	16.60	14.1	5.34	77
PPM8	200	180	0.1	348	2.30	8.8	85.2	13.66	13.1	3.90	79
PPM9	200	180	0.2	348	2.30	9.1	85.0	13.70	13.3	6.55	86

Key: T_{mix1} = The reaction point temperature (°C) determined from enthalpy balance, RT = the reaction residence time (residence time is defined by the reactor volume and the velocity of the reactor contents at T_{mix1}), Q_{sw} = the flow rate of preheated water (450 °C, 24.1 MPa), Q_p = the precursor flow rate (ammonium iron (III) citrate), C_s = is the crystallite size determined from the application of the Scheerer equation to the (311) reflection in the XRD data and ESD = the equivalent sphere diameter calculated using the BET surface area data using equation 2.6.

As discussed initially in Chapter 5 magnetite (Fe_3O_4) and maghemite (γ-Fe_2O_3) can both crystallizes in the spinel structure with ferrous and ferric ions in the octahedral sites of the spinel lattice, adopting the space group Fd3m. It is likely the reaction products from the scaled CHFS process have similar coordination environments for iron contained within the spinel structure to those initially produced in Chapter 5. The observations initially presented in Chapter 5 for the formation of magnetite using continuous hydrothermal systems showed large differences in the concentration of oxidising or reducing species were required to alter the phase of the product. The reactions governing the formation of magnetite *i.e.* the thermal decomposition of the citrate anion seems to have scaled although have not been explicitly evaluated as a spinel phase iron oxide was obtained as the only reaction product. The slight variation in reaction residence time as summarised in table A3.2 was shown to have little influence on the crystalinity or crystallite size produced in reactions PPM1-9 consistent with the data and discussion presented in Chapter 5.

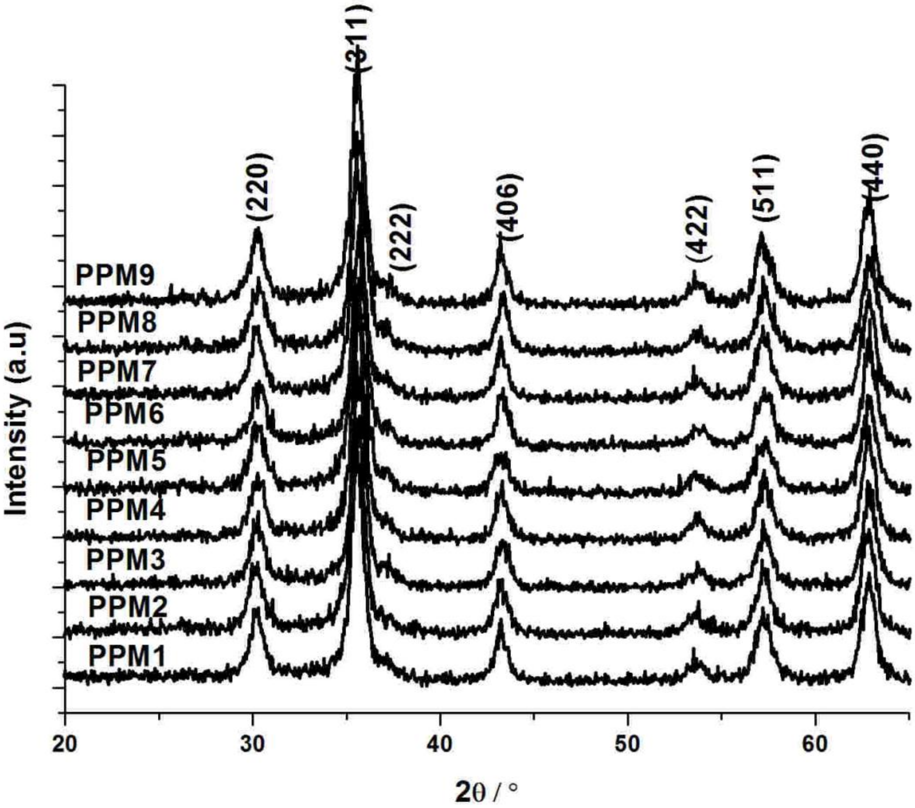

Figure A3.4: Comparison of diffraction patterns of magnetite nanoparticles produced using the pilot scale CHFS process (samples PPM1-9).

TEM was used to further assess the physical characteristics of samples PPM1-9. The TEM images (figure A3.5) show that the particle morphology was largely invariant of processing conditions or volumetric scale-up ratio chosen for each synthesis, consistent with the observations presented earlier within this thesis. The average particle sizes and distribution were calculated from the measurement of *ca.* 300 particles as summarised in table A3.2. Particle size was shown to be largely invariant of processing condition or precursor concentration.

As the sample size (quantity of material) produced on the pilot scale process was invariably large, BET surface area data was also generated for each of the samples to ensure observation made using both XRD and TEM were consistent. The measured surface area and equivalent sphere diameter assuming a material density of 5.15 g cm^{-3} are summarised in table A3.2 and yielded size estimates consistent with all other methods. This observation has been attributed to the comparatively low solubility of Fe in near critical water (Chapter 5). This sample series is also consistent with the synthesis occurring in a reaction condition in which particle nucleation dominates particle growth phases.

The magnetic properties of the magnetite samples produced on the pilot scale CHFS process to assess whether scale up had any influence on the magnetic structure of the material. Figure A3.6a shows M(H) curves measured at 300 K for the particles produced in reactions PPM1-9. All samples showed superparamagnetic like behaviour with low coecivity in the near 0 Oe region as shown in figure A3.6b. The magnetic properties of each sample taken from these measurements are summarised in table A3.3. Figure A3.6a shows that M_s of each of the samples varied considerably but no definitive trend could be established with any one experimental variable. The magnetic properties of nanosized iron oxides are known to vary and these observations can be attributed to many physiochemical and structural characteristics as discussed in greater detail within Chapter 5. As such, calculation of the effective ferromagnetic diameters (μ_{fm}) of the samples produced using the pilot scale CHFS process by fitting the magnetisation data with a Langenvin function (detailed in Chapter 2) are summarised in table A3.3. Where, the estimation of size from magnetic fitting showed significantly smaller magnetic particle diameter's to those determined by other structural techniques. This observation can be attributed to the presence of a magnetically frustrated phase within each sample and accounting for a large proportion of the nanoparticle volume as the contribution of paramagnetic-like susceptibility (χ) [accounting for the non-saturating behaviour] increased with decreasing M_s, suggesting a degree of magnetic polydispersity is observed in these samples. These observations are consistent with those presented in Chapter 5 and Chapter 6. From this analysis of the magnetisation curves it has been inferred that the magnetic structure of the particles is difficult to reproduce using this synthesis methodology (as initially discussed in Chapter 6) and on scale up this observation was also made for materials that scaled up well in structure and physical properties.

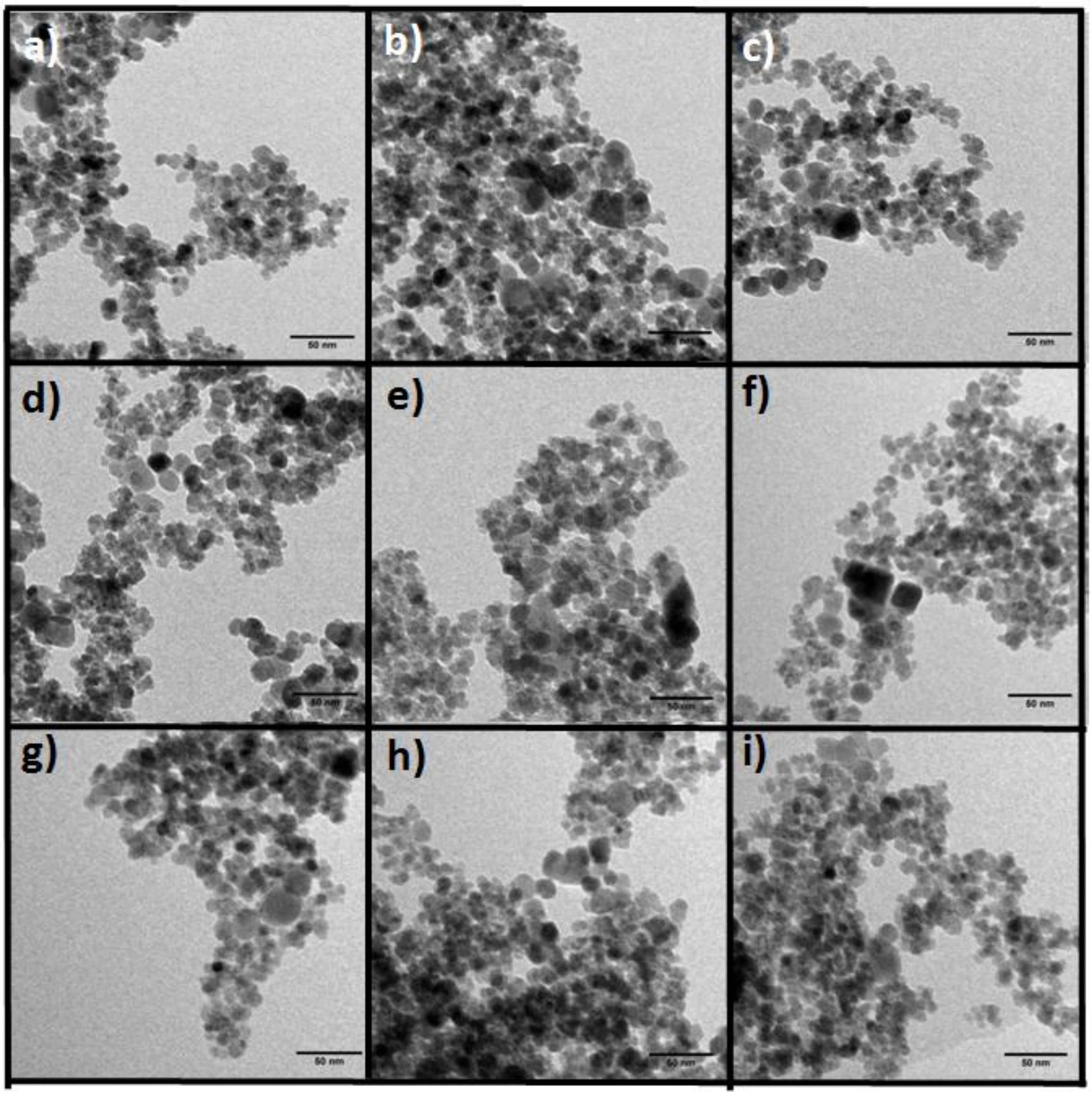

Figure A3.5: TEM images of magnetite nanoparticles synthesised on the pilot scale CHFS process; **a)** PPM1, **b)** PPM2, **c)** PPM3, **d)** PPM4, **e)** PPM5, **f)** PPM6, **g)** PPM7, **h)** PPM8, **i)** PPM9 (scale-bar = 50 nm).

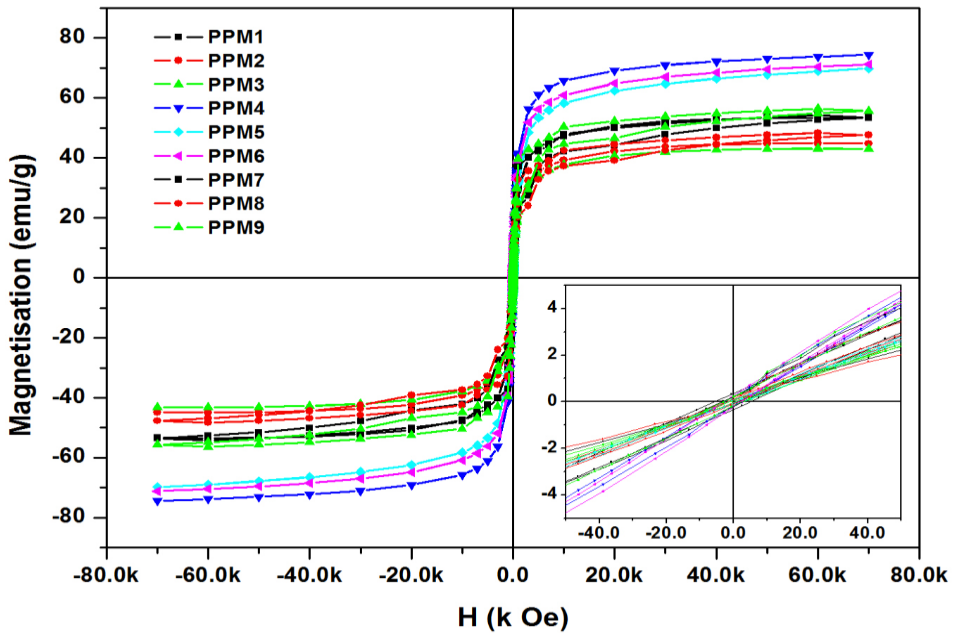

Figure A3.6: a) MH curves of citric acid coated magnetite produced using the pilot scale CHFS process **b)** expanded plot showing the near 0 Oe region.

Table A3.3: Summary of the magnetic properties of magnetic iron oxides produced using CHFS.

Sample	Crystallite size TEM (nm)	Ms (emu g^{-1} [Fe_3O_4])	Hc (Oe)	μ (nm)	σ (nm)	χ $x10^{-4}$
PPM1	12.9	57.7	2.3	5.89	0.45	0.40
PPM2	13.1	48.5	1.89	5.91	0.34	0.38
PPM3	15.1	48.0	1.56	4.92	0.29	0.47
PPM4	16.5	68.7	2.1	5.99	0.32	0.38
PPM5	14.5	69.7	1.1	6.18	0.34	0.33
PPM6	14.6	72.4	2.3	6.98	0.32	0.34
PPM7	14.1	48.4	1.56	5.98	0.36	0.41
PPM8	13.1	45.8	1.80	6.56	0.42	0.38
PPM9	13.3	59.6	1.47	4.93	0.72	0.44

Key: M_s = saturation magnetisation (emu g^{-1}), μ = effective ferromagnetic diameter (nm), σ = ferromagnetic diameter polydispersity (nm), χ = paramagnetic contribution on approach to magnetic saturation,

To further evaluate the magnetic properties, the temperature dependence of M_s was measured at 5 and 300k for sample PPM5 as shown in figure A3.7a. The increase in M_s below 5 k can be attributed to the presence of a spin-glass like surface layer that undergoes a magnetic transition to a frozen state below T_b as initially discussed in Chapter 5. The fact that nonsaturated magnetization is still observed at 5 K indicates that a component of this sample is intrinsically nonferromagnetic, an observation made initially in Chapter 5. Similarly the increase in coercive field at 5 K measured as 53 Oe whereas at 300K a value of 1.1 Oe reported is consistent with the sample behaving as a ferromagnet below T_b (figure A3.7a inset). ZFC/FC measurements further suggested a magnetically complex sample as the magnetisation in the FC measurement increases with decreasing temperature, suggesting that the broad cusp in the ZFC measurement this is not a blocking temperature but a freezing transition temperature where moments from different magnetic environments are blocking an observation consistent with those made initially in Chapter 5. Where, in this case the broad transition in the ZFC curve is indicative of a wide distribution of energy barriers (despite the narrow physical size distribution) leading to a spread distribution of magnetic frustrations and suggests the presence of multiple magnetic phases in the sample. These measurements suggest that disorder not necessarily related to structural differences but magnetic domain disorder is also evident in the materials produced on the pilot scale process as was found to be the case in most magnetic nanoparticles produced using this methodology.

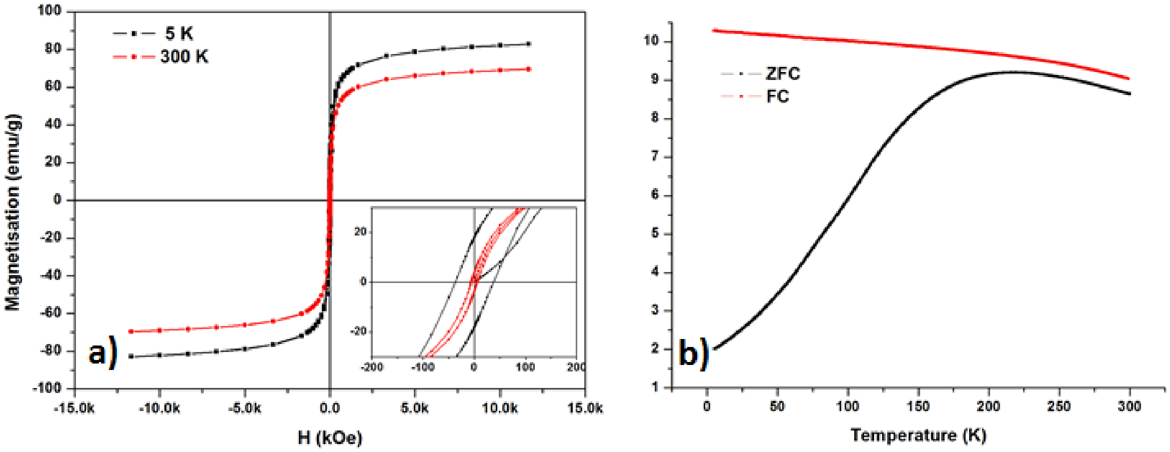

Figure A3.7: Comparison of magnetisation magnetization curves measured at 5 K and 300K, inset shows a the near 0 Oe region magnified to show the difference in coercivity **b)** FC (red)and ZFC (black) curves under an applied field of 100 Oe.